

---

**Sensitizing mechanisms, reaction mechanisms and reactive intermediate states in photocatalytic reactions on time scales from femto- to microseconds**

Matthias Wenninger

---

Dissertation  
an der Fakultät für Physik  
der Ludwig-Maximilians-Universität  
München

vorgelegt von  
Matthias Klaus Wenninger  
aus München

München 2014

Erstgutachter: Prof. Dr. Eberhard Riedle

Zweitgutachter: Privatdozent Dr. Bert Nickel

Tag der mündlichen Prüfung: 6. November 2014

## Kurzfassung

Die Erforschung nachhaltiger und ressourcenschonender Energiequellen bildet ein stetig wachsendes, interdisziplinäres Forschungsfeld. Neben der Photovoltaik, die inzwischen eine etablierte Energiequelle darstellt, ist die chemische Photokatalyse noch ein kleines, aber stets wachsendes Teilgebiet. In der Photokatalyse dient das einfallende Licht dazu, chemische Verbindungen umzuformen. Nicht nur die Anwendung der Photokatalyse für die Energiegewinnung, sondern auch der Einsatz in der chemischen Synthese stößt dabei auf wachsendes Interesse. Um photokatalytische Systeme zu optimieren ist ein fundamentales Verständnis der Prozesse erforderlich. Die transiente Absorptionsspektroskopie hat sich dabei als geeignetes Werkzeug erwiesen. Der Betrieb eines Aufbaus zur Messung transienter Spektren auf verschiedenen Zeitskalen und die gezielte Datenauswertung erfordert fundiertes physikalisches und mathematisches Verständnis, wohingegen die Interpretation der Ergebnisse nicht ohne chemisches Wissen erfolgen kann. Im Rahmen dieser Arbeit hat sich die Kooperation zwischen der organischen Chemie und der Physik als erfolgreiche Zusammenarbeit erwiesen. Gegenstand der vorliegenden Arbeit sind die Sensibilisierungsmechanismen, die Reaktionsmechanismen und die reaktiven Intermediate in photokatalytischen Reaktionen auf Zeitskalen von Femto- bis Mikrosekunden.

Es wird gezeigt, dass die Auswertung von Datensätzen mit Standardmethoden, wie der Anpassung einer Summe von Exponentialfunktionen an die zeitliche Entwicklung des Signals oft nicht ausreichend ist, um die Messdaten hinreichend zu interpretieren. Erst eine der Problemstellung exakt angepasste Datenanalyse führt zum Verständnis der zugrundeliegenden Prozesse.

Zunächst werden lichtinduzierte intramolekulare Ladungstransferprozesse behandelt. Die theoretische Basis für die Beschreibung solcher Prozesse bildet die Marcus-Theorie, die kurz eingeführt wird. Anhand eines molekularen Donor-Bridge-Acceptor-Systems wird gezeigt, dass der exponentielle Dämpfungskoeffizient  $\beta$  oft ungeeignet ist um der Reaktion einen kohärenten Tunnelprozess oder einen inkohärenten Transfermechanismus zuzuweisen.

DNS-Haarnadelstrukturen, welche kovalent mit einem Flavin-Chromophor verbunden sind, dienen als Modellsystem für die Untersuchung intramolekularer Ladungstransferprozesse. Nach Anregung induziert Flavin eine Elektronenfehlstelle in dem benachbarten DNS-Strang, die den Strang entlangwandern kann. Es wird gezeigt, dass durch die geeignete Wahl der Basensequenz eine Quantenausbeute von  $\Phi_{CS} = 14\%$  für langlebige ladungstrennte Zustände erreicht wird.

In einem weiteren Abschnitt wird untersucht, ob die Bausteine der DNS als chirale Umgebung für die enantioselektive Photokatalyse geeignet sind. Mit Hilfe einer auf der Marcus-Theorie basierenden Interpretation der Messergebnisse wird die konformationsabhängige Ladungstransferdynamik in Benzophenon-DNS-Dinukleotiden beschrieben. Es wird gezeigt, dass die Dinukleotide nicht uneingeschränkt für die enantioselektive Photokatalyse geeignet sind.

Schließlich wird eine echte bimolekulare photokatalytische Reaktion untersucht. Dabei wird mit Hilfe von Flavin ein Alkohol in ein Aldehyd umgesetzt. Mit einer angepassten Datenauswertung werden diffusive Prozesse auf der ps-Zeitskala genau quantifiziert. Die gewonnenen Informationen dienen dazu, die Reaktionsbedingungen zu optimieren um über einen Triplett-Reaktionsmechanismus höhere Quantenausbeuten zu erzielen.

Nachdem photoinduzierte Ladungstransferprozesse ausgiebig diskutiert wurden, liegt der Fokus im zweiten Teil auf der [2+2] Photocycloaddition: Als Grundlage für die Interpretation späterer Messungen wird zunächst die [2+2] Photocycloaddition an substituierten Chinolonen untersucht. Die einzelnen Reaktionsschritte der Ringbildung werden auf der Zeitskala von ps bis ns quantifiziert und charakterisiert, wobei der Triplettzustand den zentralen Zustand bildet. Anschließend wird die [2+2] Photocycloaddition an substituierten Chinolonen durch einen chiralen, auf dem organischen Chromophor Xanthon basierenden Photokatalysator initiiert. Es wird gezeigt, dass innerhalb des Katalysator-Substrat-Komplexes, in dem beide Moleküle einen Abstand von wenigen Ångström haben, neue elektronische Eigenschaften auftreten. Die Anregung eines neuen Zustands initiiert nicht nur die [2+2] Photocycloaddition sondern stellt auch einen neuen Sensibilisierungsmechanismus dar, der bisher in photokatalytischen Reaktion organischer Moleküle nicht beobachtet wurde. Der Triplettzustand des Chinolons tritt hierbei nicht mehr auf. Ob sich dieser Sensibilisierungsmechanismus auch auf andere Systeme übertragen lässt, muss durch weitere Arbeiten auf diesem Gebiet geklärt werden.





## Summary

The development of renewable energy sources depicts a constantly growing interdisciplinary research field. Beyond photovoltaics chemical photocatalysis plays a small role, but is gaining more and more importance. In photocatalysis, light serves as an energy source for the chemical conversion of certain molecules. However, not only the application of photocatalysis as energy source but also the utilization of photocatalysis in chemical synthesis has attracted a deep scientific interest. For the optimization of photocatalytic systems a fundamental understanding of the underlying processes is more than essential. Thereby, transient absorption spectroscopy has proved to be a very useful tool. On the one hand, the operation of a setup for transient absorption spectroscopy and on the other hand the systematic data evaluation requires physical and mathematical skills whereas the results cannot be interpreted without deep chemical knowledge. Within the framework of the present thesis the cooperation between the fields of organic chemistry and physics has turned out as a very productive cooperation. Sensitizing mechanisms, reaction mechanisms and reactive intermediate states in photocatalytic reactions on time scales from femto- to microseconds are the object of the present work.

The present thesis will prove that the analysis of measurement data on the basis of established standard methods, such as the fitting of a sum of exponential functions to the temporal evolution of the measured signal, often is not sufficient for a complete interpretation of the data. Only a data analysis precisely adapted to the problem can lead to a fundamental understanding of the underlying processes.

In the first part of the present thesis, the focus lies on light-induced intramolecular charge transfer processes. Marcus Theory, which depicts the theoretical background, will be briefly introduced. On the basis of a molecular donor-bridge-acceptor system it will be shown that the damping coefficient  $\beta$  is not sufficient to differ unambiguously between coherent tunneling and incoherent hopping mechanism.

Flavin-capped DNA hairpins serve as a model for the investigation of intramolecular charge transfer processes. After photo-excitation, flavin induces a hole which migrates through the DNA strand. It will be shown that an adapted base sequence allows for quantum yields of  $\Phi_{CS} = 14\%$  for long-lived charge separated states.

In the next section it will be discussed if the building blocks of the DNA are adapted to serve as chiral backbone for enantioselective photocatalysis. The conformation-dependent charge-transfer dynamics in benzophenone-DNA dinucleotides will be put on solid ground with the help of Marcus Theory. It will be shown that these dinucleotides are generally not suited to serve as an inert backbone for every kind of photochemical reaction.

In the following section a true bimolecular photocatalytic reaction will be discussed. Flavin serves as photocatalyst for the conversion of an alcohol to the corresponding aldehyde. A precisely adapted data analysis allows an exact quantification of the diffusion controlled reaction dynamics on the ps time scale. The understanding of the process allows optimizing the reaction conditions. The targeted utilization of triplet chemistry within this reaction can help to increase the quantum yield for product formation.

As photo-induced charge transfer processes have been intensively discussed, the focus in the second part of the thesis lies on the [2+2] photocycloaddition. As basis for the interpretation of subsequent measurements, the [2+2] photocycloaddition of substituted quinolones will be investigated. The formation of the cyclobutane ring in which the quinolone triplet state plays the central role will be characterized and quantified on the time scale from ps to ns. Afterwards the [2+2] photocycloaddition of substituted quinolones will be initiated by a chiral xanthone-based photocatalyst. It will be shown that within this catalyst-substrate complex in which both constituents have a distance of only few Ångströms, new electronic properties appear. The photo-excitation of a new electronic state not only initiates the [2+2] photocycloaddition of the quinolone but also depicts a new sensitizing mechanism, which has to the author's best knowledge not been observed in photocatalysis of organic molecules. The quinolone triplet state does not appear in this mechanism. The question, if this mechanism can be transferred to other photocatalytic systems has to be answered within the framework of further studies.



## Publications

This thesis is based on the following publications reprinted in the Appendices A1-A7:

- 1 Time resolved spectroscopy in photocatalysis**  
Eberhard Riedle, Matthias Wenninger  
*Chemical Photocatalysis*, pp. 319-378, Burkhard König (Editor), De Gruyter, **2013**
- 2 Exponential Distance Dependence of Photoinitiated Stepwise Electron Transfer in Donor-Bridge-Acceptor Molecules: Implications for Wire-like Behaviour**  
Annie Butler Ricks, Kristen E. Brown, Matthias Wenninger, Steven D. Karlen, Yuri A. Berlin, Dick T. Co, Michael R. Wasielewski  
*Journal of the American Chemical Society* **2012**, *134*, 4581-4588.
- 3 Flavin-induced DNA photooxidation and charge movement probed by ultrafast transient absorption spectroscopy**  
Matthias Wenninger\*, Danila Fazio\*, Uwe Megerle, Christian Trindler, Stefan Schiesser, Eberhard Riedle, Thomas Carell  
*ChemBioChem* **2011**, *12*, 703-706.  
\* these authors contributed equally to the work
- 4 Conformational control of benzophenone-sensitized charge transfer in dinucleotides**  
Thomas Merz\*, Matthias Wenninger\*, Michael Weinberger, Eberhard Riedle, Hans-Achim Wagenknecht, Martin Schütz  
*Physical Chemistry Chemical Physics* **2013**, *15*, 18607-18619.  
\* these authors contributed equally to the work
- 5 Unraveling the flavin-catalyzed photooxidation of benzylic alcohol with transient absorption spectroscopy from sub-pico- to microseconds**  
Uwe Megerle, Matthias Wenninger, Roger-Jan. Kutta, Robert Lechner, Burkhard König, Bernhard Dick, Eberhard Riedle  
*Physical Chemistry Chemical Physics* **2011**, *13*, 8869-8880.
- 6 Intramolecular [2+2] Photocycloaddition of 3- and 4-(But-3-enyl)oxyquinolones: Influence of the Alkene Substitution Pattern, Photophysical Studies and Enantioselective Catalysis by a Chiral Sensitizer**  
Mark M. Maturi\*, Matthias Wenninger\*, Rafael Alonso\*, Andreas Bauer, Alexander Pöthig, Eberhard Riedle, Thorsten Bach  
*Chemistry – A European Journal* **2013**, *19*, 7461-7472.  
\* these authors contributed equally to the work

A further contribution to a scientific publication performed in the framework of the present thesis which is not directly related to the thesis' title and therefore not discussed in the present summary is reprinted in Appendix A.7:

**7 Electronic transient spectroscopy from the deep UV to the NIR: unambiguous disentanglement of complex processes**

Eberhard Riedle, Maximilian Bradler, Matthias Wenninger, Christian F. Sailer, Igor Pugliesi

*Faraday Discussions* **2013**, *135*, 139-158.

*The author of this dissertation received written permission by the journals to include printed copies of the original versions for all publications in this thesis.*

## Table of Contents

<b>1. Introduction .....</b>	<b>1</b>
<b>2. Transient Absorption Spectroscopy on Time Scales from Femto- to Microseconds .....</b>	<b>9</b>
2.1 Experimental Approaches for Time-Resolved Transient Absorption Spectroscopy on Multiple Time Scales .....	9
2.2 Dynamics of Photo-Induced Bimolecular Reactions in Transient Absorption Spectroscopy.....	11
<b>3. Photo-Induced Electron Transfer Processes and Their Application in Photocatalysis .....</b>	<b>13</b>
3.1 Theory of Photo-Induced Electron Transfer.....	13
3.2 Photo-Induced Electron Transfer in Donor-Bridge-Acceptor Molecules .....	19
3.3 Photo-Induced Electron Transfer in DNA .....	25
3.4 DNA as Chiral Environment for Enantioselective Photocatalysis? .....	33
3.5 Diffusion Controlled Intermolecular Charge Transfer Processes in Flavin Photocatalysis.....	45
<b>4. Beyond Photoredox Catalysis: [2+2] Cycloaddition Reactions.....</b>	<b>55</b>
4.1 The Intramolecular Photo-Induced [2+2] Cycloaddition in Quinolones.....	55
4.2 Delocalized Excited States for Light-Induced Enantioselective Organocatalysis.....	63
4.2.1 Chirality in Nature and the Enantioselective Sensitization of the [2+2] Photocycloaddition by a Chiral Xanthone-Based Photocatalyst.....	63
4.2.2 Experimental Section .....	69
4.2.3 For a Basic Understanding: Diffusion Controlled Sensitization of the [2+2] Photocycloaddition with Pure Xanthone as Sensitizer.....	85
4.2.4 Accessing the Mechanistic Details of Enantioselective Photocatalysis with Transient Absorption Spectroscopy on Multiple Time Scales and Quantum Chemistry .....	95
4.2.5 Exciplex and Excimer States in DNA and Radical Cation Mediated [2+2] Photocycloaddition Reactions.....	135
<b>5. Conclusion and Outlook.....</b>	<b>139</b>
<b>References .....</b>	<b>143</b>
<b>Appendices A1-A7 .....</b>	<b>157</b>



## 1. Introduction

“When you study natural science and the miracles of creation, if you don't turn into a mystic you are not a natural scientist.”

Albert Hofmann

The desire of mankind to utilize sunlight as an energy source to satisfy the global energy demand has become one of the most essential questions in face of the enduring growth of the world population. Whereas nowadays the direct conversion of sunlight into electricity has emerged as an important part of the global energy supply and the increasing application of photovoltaics has led to an enormous growth of many related sectors of the worldwide industry, the conversion of sunlight into solar fuels still leads a niche existence in our global energy supply. Photochemical processes offer the direct conversion of light energy, provided for free by the sun, into solar fuels, such as hydrogen, which can be physically transported and utilized elsewhere. However, for the direct and efficient storage of the excitation energy of a solar photon in the absorbing molecule a rather complex chemical structure is required. Therefore the application of photocatalysis, in which a photocatalyst absorbs the photon and utilizes its energy for the conversion of a substrate molecule, which is low in energy, into a product molecule, which is higher in energy, seems to be a promising approach toward the goal of chemical exploitation of the sunlight. One of the most intensive investigated applications of photocatalysis for solar fuel production is the photocatalytic water splitting, in which the reduction process of water produces molecular hydrogen [1, 2]. However, not only the direct production of solar fuels with the help of photocatalytic processes has attracted an enormous scientific interest in the past decades. Photocatalysis can be also applied to drive processes in chemical synthesis, in which the formed product molecule not necessarily has to be adapted to serve as solar fuel. Nevertheless, the use of sunlight can play an important role in promoting sustainability and saving resources in the chemical industry by replacing energy consuming conventional synthesis pathways by energy efficient photocatalytic processes. Already in the beginning of the 20<sup>th</sup> century, the chemist Giacomo Luigi Ciamician, one of the pioneers of photochemistry, stated how photochemistry at a time in the future will serve as abundant, inexpensive, renewable and nonpolluting energy source for mankind [3]:

*“On the arid lands there will spring up industrial colonies without smoke and without smokestacks; forests of glass tubes will extend over the plains and glass buildings will rise everywhere; inside of these will take place the photochemical processes that hitherto have been the guarded secret of the plants, but that will have been mastered by human industry which will know how to make them bear even more abundant fruit than nature, for nature is not in a hurry and mankind is.”*

For the sustained improvement of existing photocatalytic systems and the further development of new, innovative photocatalysts a fundamental understanding of the underlying reaction mechanism is more than essential. In contrast to this, literature, which is dealing with photocatalysis, often provides only a very limited insight into the understanding of the involved reaction mechanism of the investigated reaction. Sometimes the most fundamental steps of a catalytic process are rather imprecisely discussed instead of put on solid ground with the help of the application of suitable and reliable analytical methods. Exemplarily for this lack of understanding is the following summary of quotes from recently published articles on photocatalysis:

- *"At present, the mechanistic picture of this reaction is not complete. It is evident, however, that eosin Y acts as a photoredox catalyst after its excitation with visible light (...)"* [4]
- *"Regarding the excitation, it remains to be elucidated which mechanism accounts for the excitation of the quinolone in its reactive triplet state."* [5]
- *"The mechanism of the eosin Y photocatalysis has not been investigated in detail at this stage. However, on the basis of our results (...) the following mechanism can be suggested (...)." [6]*
- *"The mechanism of the alkylation reaction presumably follows the proposed pathway for photoredox catalysis"* [7]
- *"(...) the reaction possibly proceeds through a radical mechanism."* [8]

These questions, which are covered and still remain unclear are for instance regarding the direction of the primary photo-induced electron transfer step [4] or concerning the actual sensitizing mechanism within a formed catalyst-substrate complex which is applied for enantioselective photocatalysis [5]. Often chemists tend to apply well established textbook opinions to propose a mechanism, which seems to be qualified to explain the present results. In many cases a convincing and reliable verification of the proposed mechanism by analytical methods is not provided. At this point time-resolved spectroscopic techniques come into play. These methods allow the direct observation and quantification of individual reaction steps of a photo-induced reaction and therefore are well suited for the investigation of sensitizing mechanisms, reaction mechanisms and reactive intermediate states in photocatalytic reactions on largely different time scales.

The present thesis finds answers to questions related to the mechanistic understanding of photocatalytic processes. Particularly questions on the actual sensitizing mechanism, the occurring intermediate states and the involved species are answered in detail. Also the influence of pre-association and diffusional motion of the reactants on the reaction pathway and how these processes can be thoughtfully tuned in order to achieve highly efficient reaction conditions are fundamentally discussed.



As basis for the following discussion in this thesis, the term “photocatalysis” has to be defined accurately. The International Union of Pure and Applied Chemistry (IUPAC) defines this term as indicated below [9]:

*“Change in the rate of a chemical reaction or its initiation under the action of ultraviolet, visible, or infrared radiation in the presence of a substance—the photocatalyst—that absorbs light and is involved in the chemical transformation of the reaction partners.”*

The presented classification has been defined in wide terms. In contrast to the IUPAC definition of the term “catalysis” [10] this definition does not require that the photocatalyst is not consumed within the catalyzed reaction. In contrast to this, in this thesis a narrower definition is applied and therefore it is required that the photocatalyst is not consumed within the catalyzed reaction.

In the past decades largely different approaches have been evolved for the photochemical utilization of light energy, which generally can be divided into the field of homogeneous and heterogeneous photocatalysis. The photo-electrochemical water splitting on TiO<sub>2</sub> surfaces was discovered in 1971 by Fujishima and Honda [11] and has emerged as an important milestone in the field of heterogeneous photocatalysis [12, 13, 14]. Since semiconductor photocatalysis is both limited in scope and tunability, the enhancement of purely inorganic solar cells by organic dyes, which was first discovered and applied by Grätzel and coworkers in the early 1990s [15, 16], represents a groundbreaking improvement in the field of photo-electrochemistry. From the use of dye-sensitized solar cells for electricity production to the application of dye-sensitized solar cells in photoredox-catalysis, such as water splitting, it is only a minor step: After the conversion of an incident photon into a spatially separated electron/hole pair, the charges are just required to be captured from catalysts that mediate the water splitting process [17, 18]. Recently reported quantum efficiencies of dye-sensitized solar cells for water splitting were 2.3% [19] and 3.1% [20], respectively. These values are still low in comparison to the quantum efficiency of silicon-based photovoltaic solar cells, but the rapid improvement of these techniques is still going on.

### **Homogeneous Photocatalysis**

In contrast to the heterogeneous catalysis of water splitting, the present thesis focuses on the investigation of homogeneous photocatalysis utilizing organic photocatalysts. The underlying photo-induced charge transfer processes—both on the inter- and intramolecular domain which are the basis in particular for photoredox catalysis, are fundamentally investigated and discussed within this thesis. The outstanding importance of photocatalysis in organic chemistry with the focus on homogeneous organocatalysis is well illustrated in recent review articles by Albin and coworkers [21, 22, 23].

The central experimental technique used in the framework of the present thesis is transient absorption spectroscopy. Time resolved spectroscopic methods both on the fs-ps and on the ns- $\mu$ s time scale are applied to gain deep insights into the molecular mechanisms of photocatalytic reactions.

The modern version of transient absorption spectroscopy is a direct successor of the flash photolysis technique developed by Ronald George Wreyford Norrish and George Porter around 1950 [24, 25], which earned them the Nobel Prize in chemistry in 1967. In the 1980s first femtosecond lasers based on dye technology became available and allowed seminal investigations of fundamental dynamic processes. Only with the discovery of the modelocked Ti:Sa laser, utilizing a solid-state laser material with the necessary broad gain bandwidth, laser pulses with fs duration became readily and reliably accessible [26, 27]. This discovery made the investigation of complex chemical reaction dynamics on the fs time scale possible. The initial work that was relying on the more complex colliding pulse modelocked technology (CPM) [28] was rewarded with a Nobel Prize in chemistry for Ahmed Zewail in 1999.

A summary of the application of time resolved spectroscopic techniques and related, valuable methods for efficient data analysis in contemporary research dealing with chemical photocatalysis can be found in a contribution to *Chemical Photocatalysis*, which was evolved within the framework of this thesis (see Appendix A.1):

### **Time resolved spectroscopy in photocatalysis**

Eberhard Riedle and Matthias Wenninger

*Chemical Photocatalysis*, pp. 88-120, Burkhard König (Editor), De Gruyter, **2013**

The focus of this book chapter lies on the one hand on the introduction of time-resolved spectroscopic methods on largely differing time scales and how they can be profitably applied for the investigation of photocatalytic processes. Since the aim of photocatalysis is the conversion of the starting material to the desired product, and therefore the over-all processes entails a change in reaction conditions, this work covers the question how related problems in time-resolved spectroscopy can be circumvented. Also experimental approaches for the determination of exact values of the product quantum yield  $\Phi_p$ , a quantity describing the efficiency of a photo-chemical reaction, are introduced. Furthermore it is discussed how these methods support the verification of a proposed reaction mechanism. On the other hand a detailed overview of the accurate data analysis of time-resolved absorption spectra is presented in this work. Since this book chapter describes all experimental techniques and most of the methods and models applied in this thesis, the interested reader is referred to this work.

---

## Sensitizing Mechanisms in Photocatalysis

Before going into detail of the own work, a brief overview of different sensitizing mechanisms in molecular homogeneous photocatalysis is given in the next section since the definition of the term “photocatalysis” still leaves questions open regarding the mechanistic details of the sensitization process.

The most conservative approach of photocatalysis is the photo-induced sensitization of a substrate by excitation energy transfer (EET) from a light absorbing photocatalyst, as schematically shown in Figure 1.1 a), which often occurs after inter-system crossing to the photocatalysts triplet state. This mechanism comprises the Förster resonance energy transfer (FRET) [29] mechanism in the uncommon case of singlet EET and the Dexter mechanism [30] in case of a triplet EET mechanism. The photocatalyst has not substantially changed its electronic configuration after this process and therefore regains its full catalytic capability immediately after the sensitization step. This type of sensitization is typically applied when the substrate undergoes the desired conversion via triplet photochemistry and only exhibits low triplet quantum yields or if its optical accessible transitions are too high in energy. For instance, triplet sensitization can be applied for the xanthone-sensitized conversion of substituted quinolones, which undergo a [2+2] photocycloaddition via triplet mechanism, since the lowest optical accessible transition of xanthone is lower in energy than of quinolone [5].

Photoredox catalysis involves an electron transfer between photocatalyst and substrate and therefore changes the redox state both of the substrate and the catalyst. From the point of view of time-resolved spectroscopy, this is one of the most fascinating types of sensitization, since the different redox states of a chromophore are often well distinguishable by their absorption properties. Since excited states are usually more reactive than their corresponding ground states, the catalyst in its excited state is capable to directly reduce or oxidize the substrate which then undergoes further chemical transformations [31]. After the initial photo-induced charge transfer step, the photocatalyst is required to be regenerated in order to retrieve its full photocatalytic capability and to complete the catalytic cycle. This is often achieved by re-oxidation or re-reduction with the help of a sacrificial electron donor (D) or electron acceptor (A). A scheme of the catalytic cycle of this type of sensitization is shown in Figure 1.1 b). Also more complex photoredox processes, in which more than two redox states of photocatalyst and substrate are involved, will be discussed within the present thesis. For instance, the chromophore flavin offers capabilities to directly convert an alcohol to the corresponding aldehyde, which requires two consecutive redox steps.

For the sake of completeness, a third type of sensitization is given in Figure 1.1 c). In this case, the catalytically active species is not the photocatalyst in its excited state. The first step after photo-excitation in this type of process, in which the photocatalytic active species needs to be formed, is the charge transfer between the precursor of the photocatalyst in its excited state and a sacrificial electron donor (D) or acceptor (A). Then, this newly formed species exhibits the desired catalytic capability. Since this type of sensitization is not readily accessible by time-resolved spectroscopy, it is not discussed in detail in the course of this

thesis. An example for this type of mechanism, which is referred to in Chapter 4.2, is from the group of MacMillan [32].

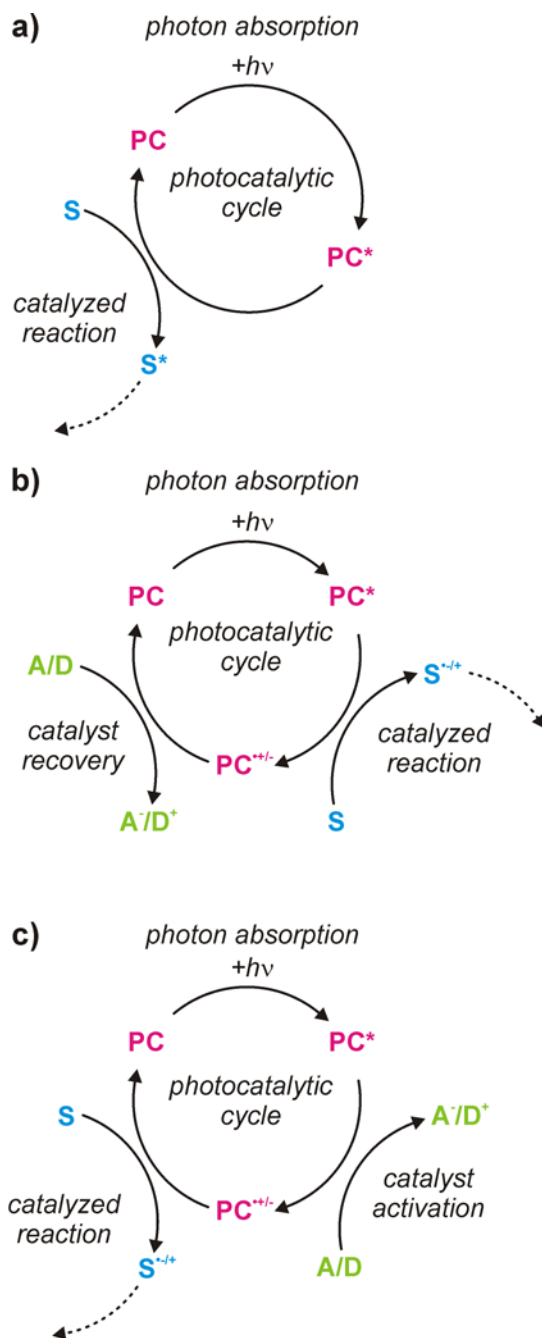


**Figure 1.1** Different sensitizing mechanisms in photocatalysis: sensitization by excitation energy transfer, primarily in the triplet state of the photocatalyst (a), direct sensitization by electron transfer in photoredox catalysis (b), and indirect sensitization, where the catalytic active species is formed by photo-induced electron transfer (c).

Although photocatalysis can involve the photo-induced transfer of an atom, i.e. hydrogen [23], or of a more complex group, the most frequently utilized sensitization mechanisms in homogeneous photocatalysis are energy-transfer and electron-transfer reactions [21, 22, 31].

Today, the research on photocatalysis understandably belongs to the field of chemistry. While intensive research on organic photoredox catalysts, which are capable of water splitting, is often conducted in the subfield of physical chemistry, the research on valuable photocatalytic systems for chemical synthesis takes place in the subfield of organic chemistry. Whereas nowadays ultrafast transient absorption spectroscopy has emerged as well established standard method in the field of physics and physical chemistry, in organic photochemistry the breakthrough of this technique has not yet come. Due to major differences in analytical approaches and prevalent philosophy between the fields of physics or physical chemistry on the one hand and organic chemistry on the other hand only very few examples can be found in the recent literature, where transient absorption spectroscopy accounts for the mechanistic understanding of a reaction applied in photochemical organic synthesis. The time-resolved spectroscopic investigation of the fundamental mechanisms of photocatalytic processes, which are utilized in chemical synthesis, reveals a relatively new and fascinating facet of the widespread research field of photocatalysis.

The present thesis tries to provide mechanistic insights of unexpected quality into the field of organic photocatalysis, which were put on solid ground by utilizing time resolved spectroscopy both in the ultrafast fs-ps and in the ns- $\mu$ s time domain and applying advanced data evaluation methods. In the following summary of this thesis, the main aspects of previously published results are briefly introduced and basically discussed with the focus on physical motivated questions and considering the background of a physically interested reader.

A short summary of the applied experimental methods for time-resolved absorption spectroscopy both on the fs-ps and on the ns- $\mu$ s time scale is given in Chapter 2.1. The related data analysis, which focuses on the kinetics of diffusion controlled bimolecular reactions and the calculation of species associated spectra is briefly commented in Chapter 2.2. A detailed description of the experimental methods and the data analysis is given in Appendix A.1.

A basic introduction into Marcus Theory, which describes the dynamics of molecular charge transfer processes, is presented in Chapter 3.1. Then, in Chapter 3.2 and Chapter 3.3 molecular charge transfer processes in selected model systems, such as organic donor-bridge-acceptor systems and artificial DNA oligonucleotides, are investigated and discussed with respect to Marcus Theory. Strategies are introduced, how to establish long-lived charge separated states with high quantum yields by modeling the base sequence of flavin capped DNA hairpin structures. Also the question, if the well investigated and versatilely discussed damping factor  $\beta$ , which parameterizes the distance dependence of charge transfer processes, is still reliable in assessing the underlying transfer mechanism in a given electron transfer reaction is considered. In Chapter 3.3 some new, yet unpublished considerations on charge transfer dynamics in flavin capped DNA hairpins are discussed. Furthermore, in Chapter 3.4 the question is answered, if and under which conditions DNA is capable to serve as chiral backbone in enantioselective photocatalysis. This study not only provides answers to this initial question. Moreover, the photo-induced electron transfer dynamics between benzophenone and the different building blocks of the DNA considering the molecular

conformation in different solvents were put on solid ground. Then we turn to intermolecular photo-induced charge transfer processes in bimolecular photocatalytic reactions. In Chapter 3.5, on the basis of flavin-mediated photocatalysis it is discussed how to inhibit competing charge recombination processes in order to achieve high product quantum yields.

In Chapter 4 we leave bimolecular photoredox catalysis behind us and turn to photo-induced [2+2] cycloaddition reactions. First, in Chapter 4.1, the non-catalyzed, stepwise [2+2] photocycloaddition of differently substituted quinolones is discussed and quantified with respect to different substitution patterns. Then, in Chapter 4.2 the reaction mechanism of a stacked photocatalyst-substrate system, in which a chirally substituted xanthone chromophore catalyzes the enantioselective [2+2] photocycloaddition of quinolone, is fundamentally investigated. It turns out, that in closely stacked molecular systems, the electronic properties of the constituents no longer can be considered as independent from each other. It is shown, how these newly, due to the close stacking, formed electronic properties can be efficiently utilized to drive enantioselective photocatalytic processes and depict a new sensitizing mechanism, which has to the author's best knowledge never been found in organic photocatalysis before.

## **2. Transient Absorption Spectroscopy on Time Scales from Femto- to Microseconds**

### **2.1 Experimental Approaches for Time-Resolved Transient Absorption Spectroscopy on Multiple Time Scales**

The transient absorption measurements with sub-ps time resolution performed in the framework of this thesis rely on the experimental setup presented in Ref. [33]. Two physical processes are the basis for this type of setup: supercontinuum generation (SCG) and optical parametric amplification. In the 1970s Alfano and coworkers for the first time reported supercontinuum generation by focusing a frequency doubled mode-locked Nd:glass laser with ps pulse duration into glass [34, 35]. Depending on the experimental requirements, different types of crystals are applied for SCG [36]. In the present setup, a spectrally broad white light, covering the spectral range from ~285-720 nm, generated by focusing pulses with fs duration from a Ti:Sa amplifier (CPA 2001, Clark-MXR) with a central wavelength of 778 nm into a CaF<sub>2</sub> crystal [37] is used for probing the sample. For the generation of a spectrally well-defined pump pulse, usually in the blue or ultraviolet spectral domain, SCG is applied, as well. Within a noncollinear optical parametric amplifier (NOPA) a selected spectral region of the generated super continuum, usually low in intensity, is amplified [38, 39, 40]. Since a stable supercontinuum generated in a sapphire crystal only extends weakly into the blue and due to the absorption properties of the applied crystals, second harmonic generation (SHG) is required for accessing pump wavelengths below ~440 nm. A scheme of the applied setup is shown in Figure 2.1.

A new technical approach was applied in this thesis for the measurement of transient absorption data covering the temporal range on the ns and  $\mu$ s time scale. Pump-probe delays significantly larger than a couple of nanoseconds, are generally not accessible by changing the optical pathway of pump and probe pulse due to physical limitations. The existing setup for time-resolved spectroscopy on the fs-ps time scale was complemented by a second pulsed laser source, which can be externally triggered and therefore is electronically synchronized with the output of the master oscillator of the Ti:Sa amplifier. The fs pulses were still applied for probe white light generation, since they provide the required high intensities for the SCG process. The accessory laser source generates pulses with ns duration which are used as pump pulse. An integrated optical parametric oscillator (OPO) provides spectral tunability. The temporal delay between ns pump and fs probe pulse is controlled by an electronic delay generator. Since the ns pulses are sufficiently short (~2.5 ns), this configuration provides the essential advantage, that the covered temporal window directly attaches to the end of the time windows of the fs-ps pump setup without any gap. A scheme of this setup is shown in Figure 2.2 and a more detailed description is given in Appendix A.1.

Specific questions, which are covering issues regarding the application of time-resolved spectroscopy both on the fs-ps and on the ns- $\mu$ s time scale for the investigations of photocatalytic processes are discussed in Appendix A.1, as well.

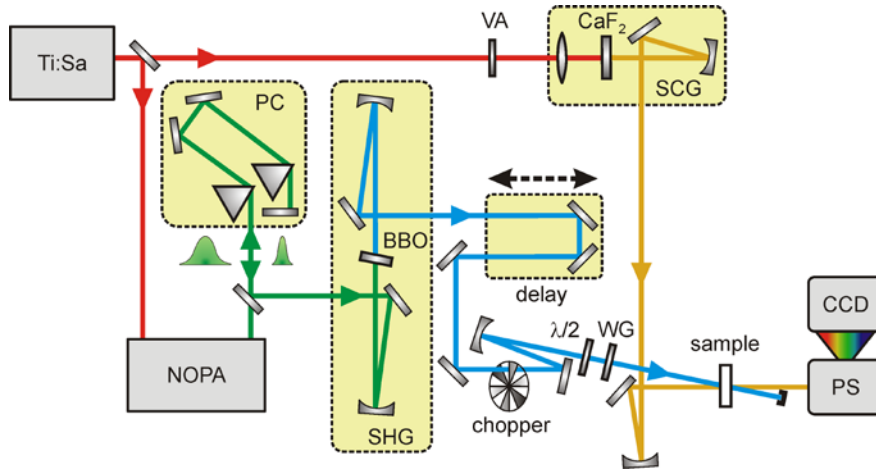


**Figure 2.1** Experimental setup for transient absorption spectroscopy with sub-ps time-resolution [33]. Spectral tunability of the pump pulse is provided by a noncollinear optical parametric amplifier (NOPA) and second harmonic generation (SHG) in a BBO crystal. The prism compressor (PC) compresses the NOPA output pulse in the time domain. The variable attenuator (VA) adjusts the energy for supercontinuum generation (SCG) in a CaF<sub>2</sub> crystal. The prism spectrometer (PS) detects the spectrally dispersed probe pulse after passing the sample at a selected pump-probe delay  $\Delta t$  with the help of a CCD array. The combined half-wave plate ( $\lambda/2$ ) and wire-grid polarizer (WG) allow adjusting the intensity of the pump pulse. Reprinted from Ref. [41].

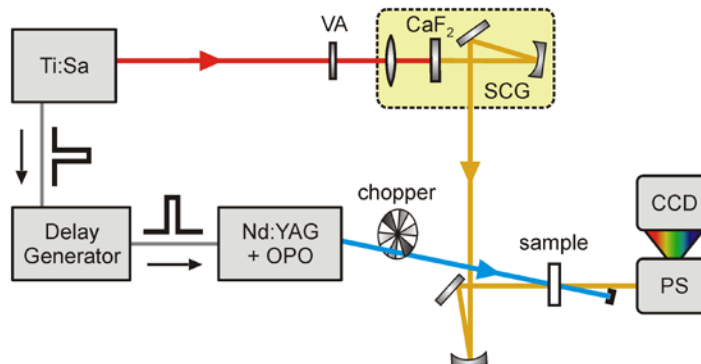


**Figure 2.2** Experimental setup for transient absorption spectroscopy on the time scale from ns to hundreds of  $\mu$ s. The fs pulse from the Ti:Sa amplifier is still used for supercontinuum generation (SCG) in the CaF<sub>2</sub> crystal. The Nd:YAG laser delivers ns pump pulses and is electronically synchronized with the Ti:Sa laser. Parametric amplification in an optical parametric oscillator (OPO) provides tunability of the pump wavelength. The prism spectrometer (PS) detects the spectrally dispersed probe pulse after passing the sample at a selected pump-probe delay  $\Delta t$  with the help of a CCD array. Reprinted from Ref. [41].



## 2.2 Dynamics of Photo-Induced Bimolecular Reactions in Transient Absorption Spectroscopy

A very widely accepted principle of data analysis in transient absorption spectroscopy is the exponential decay modeling [42]. It is based on the assumption, that the number of excited molecules which decay within an infinitesimal time period  $dt$  is proportional to the total number of molecules which are momentarily in the observed excited state. However, to describe the ultrafast population dynamics on the ps time scale of diffusion limited bimolecular reactions, which are the basis for many homogeneous photocatalytic reactions, the exponential decay modeling is inappropriate and a more sophisticated model is required. The reaction rate  $k$ , which is a constant in exponential decay modeling becomes a time dependent quantity  $k(t)$  when describing diffusion limited dynamics. The time dependency of  $k(t)$  is usually negligible for reaction dynamics on the ns time scale but causes major deviations from strictly monoexponential decay dynamics on the few ps time scale. Therefore in the framework of this thesis a model which is based on the Einstein-Smoluchowski Theory of diffusion according to Rice and coworkers [43] was employed. The resulting fit-function (Equation 2.1) describes the time dependent decay of the population of photo-excited chromophores which are quenched by a diffusion controlled reaction [43]. A detailed derivation and discussion of this function can be found in Appendix A.1.

$$N(t) = N_0 \cdot \exp \left\{ -\frac{t}{\tau} - 4\pi R D \cdot [Q_0] \cdot \left( 1 + \frac{2R}{\sqrt{4Dt}} \right) \cdot t \right\} \quad (2.1)$$

Here  $N_0$  is the number of initially excited molecules,  $D$  is the diffusion coefficient,  $[Q_0]$  the initial quencher concentration (in units of molecules per volume),  $R$  the encounter distance at which the reactants undergo the excited state quenching and  $\tau$  the intrinsic life time of the excited state. In recent literature [44, 45, 46] diffusion limited bimolecular reaction dynamics have been only qualitatively described yet. In contrast to this, the presented decay model provides a more quantitative approach toward the understanding of diffusion controlled bimolecular reactions since it reveals indications for catalyst-substrate association, the effective encounter distance and the influence of the solvent environment. In Chapter 3.5 flavin-mediated photocatalysis will be discussed in view of this model.

Deviations from a strictly monoexponential behavior can be also found when a distribution of processes with different rates depopulates an excited state [47, 48, 49]. A distribution of quenching rates is typically found, when an ensemble of chromophores is excited, in which the chromophores have a quencher in a varying but defined distance. This situation is typically found in flexibly linked donor-spacer-acceptor systems [50], DNA-oligonucleotides [51], enzymes [52] and in photo-generated radical pairs [53]. In Chapter 3.5 the electron transfer dynamics in benzophenone linked DNA nucleotides will be discussed with respect to a solvent-dependent distance distribution within the ensemble of excited chromophores.



### 3. Photo-Induced Electron Transfer Processes and Their Application in Photocatalysis

#### 3.1 Theory of Photo-Induced Electron Transfer

Photoredox catalysis relies on the general property of excited states to be more reactive than their corresponding ground states and therefore plays a major role in the field of photocatalysis [31]. Quite often one of the first steps of a catalytic photoredox reaction involves the transfer of an electron – either in the intramolecular or intermolecular [54] domain. For a fundamental understanding of the whole process, an elementary knowledge of the charge transfer dynamics is inevitable. Therefore, a brief introduction into the basics of the contemporary theory of electron transfer with respect to recent literature is given in the following section.

#### Marcus Theory – the Basis for the Explanation of Electron Transfer Dynamics

Nowadays, a substantial part of published experimental and theoretic results which are dealing with electron transfer reactions in biological, chemical or physical systems is discussed with regard to Marcus Theory [55, 56]. This theory goes back to Rudolf A. Marcus, who created in the 1950s a solid basis for the understanding of electron transfer reactions and therefore was awarded with the Nobel Prize in 1992. In his Nobel Lecture [57] Marcus accounted the introduction of new experimental techniques for the growth of the field of electron transfer in the late 1940s. One example, he referred to, was the stopped-flow apparatus which offered the time-resolved measurement of reaction kinetics on the millisecond time scale, which was fast at this time. Since that time, Marcus Theory has become a well-established theory, which is typically applied for the quantitative description of the kinetics of photo-induced charge transfer processes, regardless if they occur in the intra- or intermolecular domain. The most common form how Marcus Theory nowadays appears in literature is shown in Equation 3.1:

$$k_{\text{ET}} = \frac{2\pi}{\hbar} |H_{\text{AB}}|^2 \frac{1}{\sqrt{4\pi\lambda k_B T}} \exp\left(\frac{1}{k_B T} \cdot \frac{-(\lambda + \Delta G^0)^2}{4\lambda}\right) \quad (3.1)$$

Here  $k_B$  is the Boltzmann constant,  $\hbar$  the reduced Planck constant,  $T$  the temperature,  $H_{\text{AB}}$  describes the electronic coupling between initial state A and final state B,  $\lambda$  is the reorganization energy and  $\Delta G^0$  is the change of Gibbs energy<sup>1</sup>. The most striking phenomenon, which can be directly deduced from Marcus Theory is the inverted region, in which the electron transfer rate  $k_{\text{ET}}$  decreases with increasing exoergicity (increasing absolute value of  $\Delta G^0$ ) [55, 56, 58]. Although the predicted inverted regime seems to be

---

<sup>1</sup> Gibbs energy is the amount of work that can be extracted from a closed system at a constant temperature and pressure:  $G = U + pV - TS$

counterintuitive, experimental evidence was given by Closs and Miller investigating a series of donor-acceptor compounds in which a steroid spacer carries a 4-biphenyl group as electron donor and varying electron acceptor groups [59, 60]. In a more recent study from 2000, Lewis, Wasielewski and coworkers found charge transfer dynamics in DNA hairpins with varying caps to be in the inverted regime [61]. In agreement with Closs and Miller [59, 60] in a very recent contribution to this debate Vauthey and coworkers [62] argue that reliable effects of the inverted region are significantly more readily observable in the intramolecular and not in the intermolecular domain where diffusion sets a limit to the observable electron transfer rate. The poor understanding of the time dependence of diffusion controlled reaction kinetics, which is presented in recent literature, aggravates the problem of observing the inverted regime in bimolecular, diffusion limited reactions. According to Barbara, Meyer and Ratner, the inverted region is also considered as a key toward efficient photocatalytic processes. A photoredox catalyst in which the redox equivalents are transferred away from the initial site of excitation and are utilized elsewhere and in which recombination by back electron transfer is energetically triggered to occur in the inverted regime would provide an enormous advantage in terms of quantum efficiency [58].

Commonly, the change of Gibbs energy  $\Delta G^0$  serves as driving force for every chemical reaction and particularly for photo-induced electron transfer reactions between an electron donor (D) and an electron acceptor (A). If  $\Delta G^0$  is negative, which stands for an exergonic reaction, the reaction is thermodynamically allowed. The value of  $\Delta G^0$  of a photo-induced electron transfer reaction can be calculated according to Rehm and Weller, if the redox potentials and energies of the involved species and states are known [63]:

$$\Delta G^0 = e \left[ E^0(D^{\bullet+}/D) - E^0(A/A^{\bullet-}) \right] - \frac{e^2}{4\pi\epsilon_0\epsilon r} - \Delta E_{00} \quad (3.2)$$

Here  $E^0(D^{\bullet+}/D)$  is the one-electron standard oxidation potential of the electron donor,  $E^0(A/A^{\bullet-})$  the one-electron standard reduction potential of the electron acceptor,  $e$  the elementary charge,  $\epsilon_0$  the vacuum permittivity,  $\epsilon$  the permittivity of the solvent,  $r$  the donor-acceptor distance, and  $\Delta E_{00}$  is the energy of the photo-excited state relative to the ground state. Often the contribution of the distance dependent term describing the Coulomb interaction of the separated charges can be neglected when it is significantly smaller than the involved redox potentials.

In Equation 3.1, the reorganization energy  $\lambda$  describes the energy cost due to geometry modifications of donor, acceptor and the solvent shell following the charge transfer reaction.  $\lambda$  is defined as the energy of the reactants and the solvent at the equilibrium nuclear configuration of the products and can be divided into the inner-sphere reorganization energy  $\lambda_i$  which arises from changes in bond lengths and bond angles of donor and acceptor and the outer-sphere reorganization energy  $\lambda_o$  which describes the reorientation of the solvent molecules in response to the change in charge distribution of the reactants [64, 65]. The reorganization energy also plays an important role with regard to the inverted region: to

drive an electron transfer reaction in the inverted regime it is required that the absolute value of driving force  $|\Delta G^0|$  is larger than the reorganization energy  $\lambda$ .

#### **Typical Values of the Reorganization Energy $\lambda$**

Whereas the involved redox potentials and excited state energies can be readily determined and therefore the change of Gibbs energy  $\Delta G^0$  can be calculated directly, the reorganization energy  $\lambda$  is not easily accessible. Values for  $\lambda$  can be calculated with the help of ab initio methods or experimentally determined by fitting the Marcus parabola to a reasonable data set of electron transfer kinetics, in which the driving force  $\Delta G^0$  is systematically varied. The values of  $\lambda$ , which are presented in literature and were measured in fundamentally different systems, are only slightly distributed and remain in the 1 eV range ( $\cong 100$  kJ/mol  $\cong 8000$  cm<sup>-1</sup>). Lewis, Wasielewski and coworkers reported values of  $\lambda \cong 1$  eV for intramolecular charge transfer processes in DNA [61]. Guldi, Fukuzumi and Coworkers proposed  $\lambda$  values of an equal dimension in porphyrin-fullerene linked dyads and triads [66]. Slightly smaller values of  $\lambda$  were reported by Michel-Beyerle and coworkers in porphyrin-quinone cyclophanes in varying solvents [67]. Extremely small values for the reorganization energy of intramolecular charge transfer reactions were found by Fukuzumi and coworkers in porphyrin-fullerene ( $\lambda \cong 0.2$  eV) [68] and in flavin derivatives ( $\lambda \cong 0.26$  eV) [69].

#### **Typical Values of the Electronic Coupling $H_{AB}$**

The next term in Equation 3.1 which is to comment on, is  $H_{AB}$ , which describes the electronic coupling between initial and final state. In the weak-coupling limit, the electron transfer rate  $k_{ET}$  can be described by the Fermi golden rule, where  $k_{ET}$  is proportional to the electronic coupling amplitude  $H_{AB}$  squared. Comparable to  $\lambda$ ,  $H_{AB}$  is not directly accessible applying experimental methods. However,  $H_{AB}$  can be obtained from fitting the Marcus parabola to a reasonable data set of electron transfer kinetics. In addition to the experimental methods, there are also different strategies to calculate  $H_{AB}$  with the help of ab initio methods [70].

In contrast to the reorganization energy  $\lambda$ , typical values of  $H_{AB}$  span a wider range. Calculated values for  $H_{AB}$  in different systems range from  $H_{AB} = 10$  meV to  $H_{AB} = 500$  meV ( $\cong 1$ -50 kJ/mol  $\cong 80$ -4000 cm<sup>-1</sup>) [70]. Lewis, Wasielewski and coworkers observed values from  $H_{AB} = 3$  meV to  $H_{AB} = 30$  meV for intramolecular charge transfer processes in different DNA hairpin structures [61]. Values of about  $H_{AB} \cong 10$  meV were reported by Michel-Beyerle and coworkers for intramolecular electron transfer in porphyrin-quinone cyclophanes [67]. Electronic coupling ranging from  $H_{AB} = 80$  meV to  $H_{AB} = 400$  meV was found by Bixon, Jortner and Verhoeven in different electron donor-acceptor molecules [71].

### The Distance Dependence of the Electronic Coupling $H_{AB}$

In systems in which the electron donor-acceptor distance is well defined, a distinct value for  $H_{AB}$  can be calculated on the basis of a suitable data set. However, in systems with varying donor-acceptor distance, the electronic coupling between initial and final state changes as well. It is generally assumed, that  $H_{AB}$  falls off approximately exponentially with increasing distance and therefore electronic coupling and distance dependency can be separated [64, 72, 73, 74]. This relation is sometimes named Marcus-Levich-Jortner equation [75, 76].

$$H_{AB} = H_{AB}^0 \cdot \exp\left\{\frac{-\beta (r - r_0)}{2}\right\} \quad (3.3 \text{ a})$$

$$k_{ET} \propto |H_{AB}|^2 \rightarrow k_{ET} \propto k_0 \cdot \exp\{-\beta (r - r_0)\} \quad (3.3 \text{ b})$$

Here,  $H_{AB}^0$  is the non-distance-dependent term describing the electronic coupling between initial state A and final state B when electron donor and acceptor are at the van der Waals<sup>2</sup> contact distance  $r_0$ , which is typically between 3 and 7 Å [64]. For the sake of completeness it has to be mentioned that not only a change in donor-acceptor distance causes a change in electronic coupling. Also a varying substitution pattern of donor or acceptor with electron donating or electron withdrawing groups has effects on  $H_{AB}$  [77, 78]. In Marcus Theory the distance dependence of the electronic coupling  $H_{AB}(r)$  at a certain distance  $r$  is only given by the exponential term with the attenuation factor  $\beta$ . The damping factor  $\beta$  provides much more than only a quantitative description of the distance dependence of the electronic coupling  $H_{AB}$ . Also a mechanistic understanding of the charge transfer process can be deduced from  $\beta$ . Large values, typically  $\beta > 0.3 \text{ \AA}^{-1}$ , are assigned to a coherent single step superexchange mechanism while values of  $\beta < 0.2 \text{ \AA}^{-1}$  are generally assigned to an incoherent hopping mechanism [51, 61, 79]. Therefore determining  $\beta$  has been object of many experimental [80, 81, 82, 83] and theoretical [51, 84] studies. However, not necessarily a strictly exponential distance dependence is assigned to the hopping mechanism. For short bridges an inverse proportion of the charge transfer rate  $k_{ET}$  to the sequence length is discussed which turns to a slow exponential decay for longer sequences [85, 86, 87]. For sufficiently long bridges, theory has identified conditions under which the incoherent hopping mechanism can exhibit a strictly exponential distance dependence [51, 88, 89].

If an electron transfer reaction proceeds via incoherent hopping, the energies of the virtual states having charge on the bridge are resonant with that of the initial state and the bridge states become real. This leads to an actual localization of the transferred charge on a distinct bridge molecule [87], as shown in Figure 3.1 a). In contrast, the coherent superexchange mechanism involves mixing of virtual states having charge formally on the bridge with the initial donor state and requires the virtual states of the bridge to be energetically higher than the donor state [90]. A schematic representation of this mechanism is shown in Figure 3.1 b). Hence, the main difference between hopping and superexchange mechanism is that a

<sup>2</sup> the term “van der Waals radius” historically originates from atom physics but is often applied in literature to describe the corresponding molecular property as well [64]

substantial charge density on the bridge is present in the hopping mechanism whereas in the superexchange mechanism the charge density on the bridge is always negligible [91]. Charge transport via superexchange occurs in a single step with an exponentially decreasing rate whereas charge transport via hopping involves many charge transfer steps from the donor to the bridge as well as between the bridge sites. Ultimately, the charge is trapped at the acceptor as this step is energetically favored [92]. A coherent, single step tunneling mechanism has been found in proteins [91, 93] whereas an incoherent hopping mechanism has been observed for charge transfer processes through the  $\pi$ -way of the DNA double helix [75, 76, 81, 91, 94, 95] or donor-bridge-acceptor molecules [82, 96, 97].

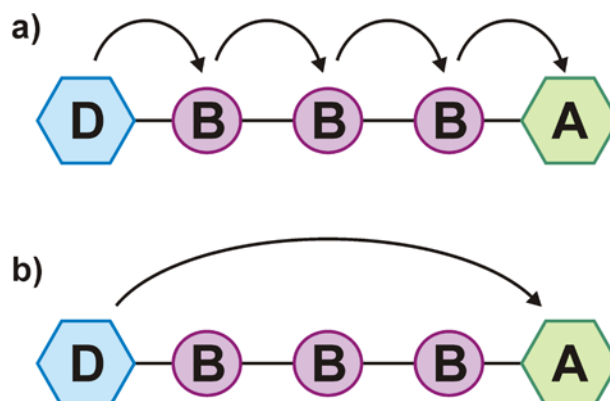


**Figure 3.1** Incoherent hopping mechanism (a) and coherent superexchange mechanism (b) of electron transfer in a donor-bridge-acceptor (DBA) system. Whereas in the hopping mechanism the electron is localized on the bridge, the electron tunnels through the bridge in the superexchange mechanism.

In recently published literature, concerns have been raised if  $\beta$  is always reliable in assessing the transfer mechanism in a given electron transfer reaction [96, 97, 98], which will be discussed in Chapter 3.2. The attenuation factor  $\beta$  was often considered to be a bridge-specific constant which also depends on the energy landscape of electron donor and acceptor and therefore the same bridge can either be poorly or strongly conducting depending on donor and acceptor [98].

So far, Marcus theory was deduced from a purely energetic point of view. However, also the spin properties of molecular orbitals are covered by a quantum mechanical treatment of the charge transfer process. Therefore the spin properties of excited states and their impact on the charge transfer dynamics and their beneficial application in photocatalysis are required to be briefly discussed as well for a basic understanding of photo-induced electron transfer processes. Particularly in the case of homogeneous photoredox-catalysis, where diffusion between photo-excited photocatalyst and substrate is the limiting step, long-lived charge separated states are desired for high quantum efficiencies. Therefore it is required to inhibit or at least to significantly slow down the charge recombination process within the photocatalyst in its charge separated state and, as well, after the first electron transfer step between catalyst and substrate. As discussed above, one approach toward this goal is to drive the nonproductive charge recombination process in the inverted regime by tweaking the energy levels of the contributing intermediate states [58]. Another well-established idea to

slow down charge recombination is to utilize charge separated triplet states, since charge recombination within a formed spin correlated radical ion pair with triplet character is a spin forbidden process [99]. This idea will be picked up again in Chapter 3.5 for flavin photocatalysis.



### 3.2 Photo-Induced Electron Transfer in Donor-Bridge-Acceptor Molecules

Molecular donor-bridge-acceptor (D-B-A) devices offer an advantageous environment to study electron transport processes, since they provide tunability of optical, energetic and conformational properties. Charge transport has been intensively studied in covalently linked donor-bridge-acceptor systems with a huge number of different bridge molecules, including proteins [65, 93, 100], DNA [61, 101], porphyrins and saturated and unsaturated hydrocarbons. In many of these systems, multiple charge-transport mechanisms and pathways exist [102]. For systems that undergo charge transfer, the electronic coupling  $H_{AB}$  between initial state A and charge separated state B not only depends on the bridge length and the relative energetics of donor, bridge and acceptor states [97, 103], but also on internal degrees of freedom such as single-bond torsions [92, 102]. Therefore, the use of donor-bridge-acceptor molecules with rigid donors and acceptors with varying bridge lengths allows for the measurement of distance dependent charge transfer dynamics in order to elucidate the superexchange and hopping regimes depending on structure within the molecular system [102].

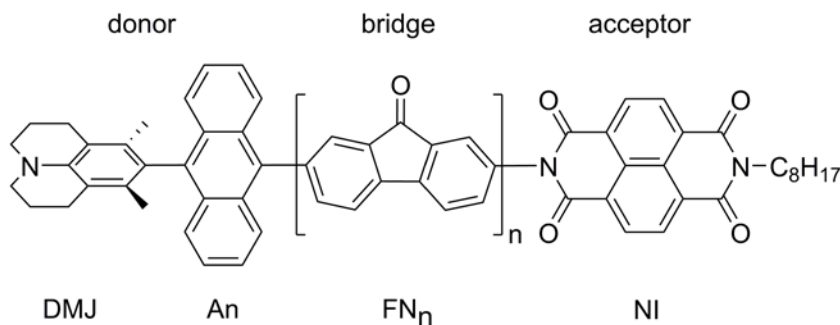
As discussed in the previous section, the damping factor  $\beta$ , which describes the distance dependence of the coupling matrix element  $H_{AB}$  (see Equations 3.3 a and 3.3 b), plays a central role in the understanding of the charge transfer dynamics and the identification of the underlying charge transport mechanism. In donor-bridge-acceptor systems, the exponential attenuation factor  $\beta$  can be written as shown in Equation 3.4 and depends on  $r_{BB}$ , the length of the individual bridge segments, on  $H_{BB}$ , the electronic coupling between adjacent bridge units and on  $\Delta E_{DB}$ , the tunneling energy gap. Therefore  $\beta$  can be written as [97, 100]:

$$\beta = \frac{2}{r_{BB}} \ln \left( \frac{\Delta E_{DB}}{H_{BB}} \right) \quad (3.4)$$

However, ambiguous definitions of the tunneling energy gap  $\Delta E_{DB}$  are found in the recent literature: on the one hand  $\Delta E_{DB}$  is defined as the vertical energy required to remove an electron from the donor and place it on the bridge [100, 102] and on the other hand  $\Delta E_{DB}$  describes the difference between the energy of the donor-acceptor system at the transition state configuration and the energy of the bridge-localized states [97, 104, 105]. Equation 3.4 clearly reveals that  $\beta$  is not a purely bridge-specific constant, since it depends on the donor energy landscape as well.

A well-established approach from the group of Michael R. Wasielewski (Northwestern University, Evanston, Illinois, USA) is the use of donor-bridge-acceptor molecules in which a 3,5-dimethyl-4-(9-anthracenyl)julolidine (**DMJ-An**) electron donor and a naphthalene-1,8:4,5-bis(dicarboximide) (**NI**) electron acceptor are covalently linked by a number of bridge molecules [92, 102, 106, 107]. Different bridge molecules, such as oligomeric 2,7-fluorenones [82, 96, 106], p-oligophenylenes [92], 1,1-diphenylethene, trans-stilbene, diphenylmethane and xanthone [107] have been applied to vary the electronic properties of the bridge and to test the effects on the charge transfer dynamics. Since the **DMJ-An** electron donor exhibits a strong charge transfer band [102], photo-excitation of the **DMJ-An**

moiety leads to an ultrafast intramolecular charge separation resulting in formation of the radical pair  $\text{DMJ}^{+\bullet}\text{-An}^{-\bullet}$  [108], which acts as high-potential electron donor. The internal charge separation process within the **DMJ-An** moiety occurs on the ultrafast time scale below 150 fs and cannot be resolved with the applied setup for transient absorption spectroscopy in this study. Then the charge travels over the oligofluorenone bridge, which consists of a series of fluorenone oligomers  $\text{FN}_n$  ( $n = 1\text{-}3$ ), to the **NI** as the final electron acceptor. Thereby a long-lived charge separated state, in which the electron is located at the  $\text{NI}^{-\bullet}$ , with a life time significantly longer than 3 ns is achieved [102]. The molecular structure of the investigated donor-bridge-acceptor molecule is depicted in Scheme 3.1.



**Scheme 3.1** Donor-bridge-acceptor molecule: electron donor (**DMJ-An**) which after photoexcitation exhibits a charge transfer state  $\text{DMJ}^{+\bullet}\text{-An}^{-\bullet}$ , bridge ( $\text{FN}_n$ ) and electron acceptor (**NI**).

The presented transient absorption measurements were conducted in the framework of the present thesis during a research stay in the group of Michael R. Wasielewski at the Northwestern University in Evanston (IL), USA. The applied experimental technologies include transient absorption spectroscopy both in the visible and infrared spectral domain and femtosecond stimulated Raman spectroscopy (FSRS). Selected transient absorption spectra in the visible spectral range of **DMJ-An-FN<sub>3</sub>-NI** in toluene after  $\lambda_{\text{EXC}} = 416$  nm excitation are shown in Figure 3.2.

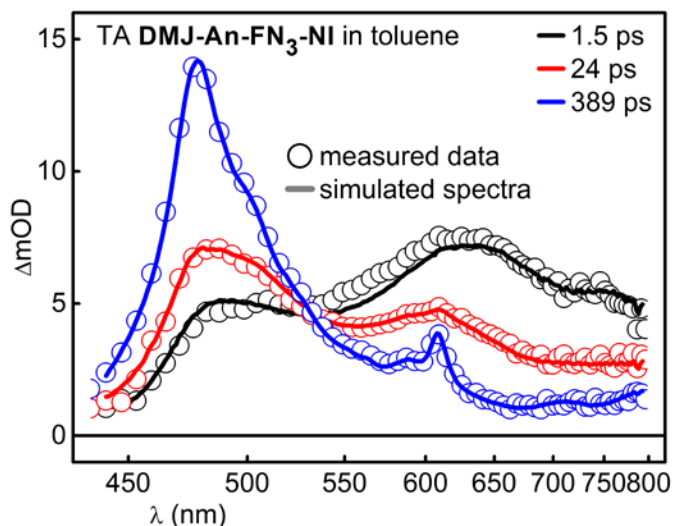


**Figure 3.2** Selected transient absorption spectra of **DMJ-An-FN<sub>3</sub>-NI** in toluene after  $\lambda_{\text{EXC}} = 416$  nm excitation. After photon absorption at the **An** moiety, the intramolecular charge separation process within the electron donor site **DMJ-An** of the D-B-A system forming the radical pair **DMJ<sup>+</sup>·-An** can be clearly identified by the broad absorption band  $\lambda > 600$  nm in the  $t = 1.5$  ps spectrum (black line) [App A.2]. The intramolecular charge separation process ( $\tau < 150$  fs) within the donor **DMJ-An** forming the radical pair **DMJ<sup>+</sup>·-An<sup>-·</sup>** could not be resolved with the applied experimental setup. The subsequent travelling of the electron over the **FN<sub>3</sub>** bridge is indicated by the slight absorption band around  $\lambda = 600$  nm in the  $t = 24$  ps spectrum (red line). Later ( $t = 389$  ps), the arrival of the electron at the acceptor site **NI** is indicated by the increase of two absorption bands at  $\lambda = 480$  nm and at  $\lambda = 610$  nm (blue line), which are associated with the radical anion state **NI<sup>-·</sup>**. The subsequent charge recombination process occurs on the ns time scale. By comparing the wavelength scale with other transient spectra presented in this thesis, it can be clearly seen, that the probed spectral range is different. This is due to different parameters and components of the setup for transient absorption spectroscopy (e.g. central wavelength of fs laser system, crystal used for supercontinuum generation), which was applied in the framework of this study.

A pump wavelength of  $\lambda = 416$  nm provides nearly selective excitation of the **DMJ-An** charge transfer band although the corresponding spectral region contains an overlap of the **FN** absorption. Since the energy of the lowest excited singlet state of **DMJ-An** is lower than of **FN**, ultrafast energy transfer [29] from **FN** to **DMJ-An** most likely occurs as the transient spectra at the earliest time points strongly resemble that of **DMJ<sup>+</sup>·-An<sup>-·</sup>**. Then the charge is injected into the **FN** bridge. Although the reduction potentials of the **FN** bridge molecules change only slightly with increasing bridge length, the rate for charge injection strongly depends on the number of bridge molecules. Since this effect is significantly weaker in a reference molecule series without an final **NI** acceptor than in the molecules with an attached **NI** acceptor, a major influence on the charge injection dynamics is caused by the **NI**

acceptor. The **NI** acceptor plausibly disturbs the electronic coupling between the **FN** units and the **DNJ-An** donor. Particularly attaching electron donating or electron withdrawing groups on donor or acceptor are known to significantly affect the coupling matrix element in charge transfer reactions [77, 78].

In the case of an incoherent hopping mechanism, the bridge states become real, if the virtual states having charge on the bridge are resonant with that of the initial state or drop below it [87]. In the present system, after charge injection into the **FN<sub>n</sub>** bridge ( $n = 2,3$ ) intra-bridge hopping cannot be spectroscopically resolved since the actual position of the electron on one of the **FN** molecules does not change the optical properties of the whole bridge. A further essential question, which has to be discussed, is regarding the character of the bridge localized states in face of a possible fluorenone-fluorenone interaction within the bridge: is it still reasonable to assign a quasi-intermolecular charge transfer mechanism between the individual **FN** bridging units or does the bridge-localized charge exhibit a fully delocalized radical anion character? The answer to this question is given by steady-state absorption spectroscopy: although an intra-bridge fluorenone-fluorenone electronic interaction can be clearly seen both in spectroelectrochemistry and in transient absorption spectroscopy, the observed spectral changes are far smaller than those expected for a fully delocalized radical anion on the bridge [109, 110, 111, 112, 113]. In Chapter 4.2 it is referred to a related question again and it will turn out that considering the individual constituents of molecular complexes as isolated molecules with independent electronic properties is not always justified, as it is in the present case.

Charge arrival on the **NI** site of the molecule can be spectroscopically clearly identified by upcoming of two strong absorption bands at  $\lambda = 480$  nm and  $\lambda = 610$  nm, which can be assigned to the radical anion **NI<sup>-•</sup>** since they were determined with the help of spectroelectrochemistry in an earlier work of the group [114].

The transient absorption measurements both in the visible and in the infrared spectral range clearly reveal, that the bridge-localized charge transfer states **DMJ<sup>+•</sup>-An-FN<sub>n</sub><sup>-•</sup>-NI** actually become real. Therefore the rate  $k_{CS1}$  is assigned to the process of charge injection into the **FN<sub>n</sub>** bridge,  $k_{CS2}$  to the process of charge arrival on the **NI** acceptor and  $k_{CR}$  describes the charge recombination process, which cannot be resolved within the ultrafast transient measurements. A scheme of all involved processes is given in Figure 3.3. In the infrared domain the **FN** localized charge transfer state is unambiguously identified by an upcoming, transient bleach of the carbonyl<sup>3</sup> stretching band of **FN** at  $1720$   $\text{cm}^{-1}$  [115]. In the visible spectral domain a more sophisticated data processing was required to extract the **FN<sup>-•</sup>** radical spectra from the transient data set. Therefore a global data analysis and a sequential rate model, as introduced in Appendix A.1, was employed for the calculation of the species associated spectra (SAS) of all involved intermediate states. A clear evidence of **FN** localized bridge states was found in the visible domain as well. The comparison of

---

<sup>3</sup> carbonyl groups are composed of a carbon atom double-bonded to an oxygen atom: C=O

spectroelectrochemistry data from partially reduced  $\text{FN}_1$  and  $\text{FN}_2$  oligomers allowed a distinct assignment of the calculated SAS to the radical states of the FN.

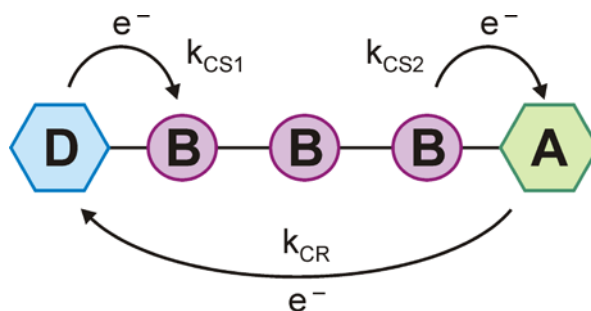


**Figure 3.3** Electron transfer cascade in D-B-A system and related rates: charge injection into the bridge ( $k_{\text{CS1}}$ ), charge arrival at on the acceptor ( $k_{\text{CS2}}$ ) and charge recombination to the ground state ( $k_{\text{CR}}$ ).

Since different compounds with a varying bridge length ( $n = 1-3$ ) were synthesized, the charge transfer rates  $k_{\text{CS1}}$  and  $k_{\text{CS2}}$  were individually determined. The comparison with the number of bridge segments reveals that the rate constant  $k_{\text{CS2}}$  for the electron arrival on the NI acceptor decreases exponentially with increasing electron donor-acceptor distance described by a damping factor of  $\beta = 0.34 \text{ \AA}^{-1}$ . This phenomenological  $\beta$  value is rather high and therefore is usually assigned to a coherent superexchange mechanism, as discussed in Chapter 3.1. In contrast, transient absorption spectroscopy both in the visible and the infrared spectral domain and an advanced data analysis clearly indicate an incoherent hopping mechanism which stands in contrast to the determined high  $\beta$  value. The stepwise charge transfer mechanism can be apparently deduced from the data since the charge transfer states become resonant with the bridge states. The results of this study and a more detailed discussion can be found in the following publication (see Appendix A.2):

**Exponential Distance Dependence of Photoinitiated Stepwise Electron Transfer in Donor-Bridge-Acceptor Molecules: Implications for Wire-like Behavior**

Annie Butler Ricks, Kristen E. Brown, Matthias Wenninger, Steven D. Karlen, Yuri A. Berlin, Dick T. Co, Michael R. Wasielewski

*Journal of the American Chemical Society* **2012**, *134*, 4581–4588

These results show, that donor-bridge-acceptor molecules designed to have stepwise, energetically downhill redox gradients do not necessarily exhibit wire-like behavior. Moreover, this study also proves that the  $\beta$  value is no longer a reliable quantity for unambiguously assessing the underlying electron transfer mechanism of a given charge transfer reaction to coherent superexchange or incoherent hopping. From an experimental point of view, this study also reveals spectroelectrochemistry as a helpful tool for the identification and assignment of transient states with radical character.



#### 3.3 Photo-Induced Electron Transfer in DNA

##### Electronically Excited States in DNA

Nature has found deoxyribonucleic acid (DNA) as the most adapted molecule to store the genetic information of nearly every living organism on earth. The requirements for a reliable genetic memory are rather high: besides the possibility of an accurate and fast replication of the genetic information, DNA has to provide long term stability under quite harsh conditions such as oxidative stress and UV irradiation [75]. Nature has established a huge number of strategies to provide effective protection against mutation [116, 117].

From the point of view of time-resolved spectroscopy, a very interesting protection mechanism is the ultrafast deactivation of photo-excited states in DNA nucleosides. Kohler and coworkers found that the excited state of common nucleosides decays within hundreds of femtoseconds by internal conversion suggesting that hydrogen bonding between solute and solvent provides efficient pathways for intermolecular vibrational energy transfer [118, 119, 120]. Recently, the formation of long-lived charge delocalization and subsequent charge recombination in DNA have been observed [121]. These deactivation pathways significantly reduce the quantum efficiency of competing deactivation processes, such as electron transfer, hydrogen abstraction or generation of reactive oxygen species, which may lead to a permanent DNA damage [122]. This has the effect, that the quantum yield  $\Phi$  for the formation of pyrimidine (6-4)pyrimidine photoproducts, cyclobutane pyrimidine dimers and other photoproducts after direct excitation of the DNA are extremely low [123]. Recent observations [124, 125] also suggest that the mechanism of DNA damage formation upon direct excitation depends on the excitation wavelength. For an understanding of these phenomena particularly the ultrafast processes on the sub-ps time scale in DNA are of major interest.

It has been shown, that predominantly the purine base guanine (G) is a major target for external oxidants [75] and therefore acts as electron loss center of the DNA since it is the nucleobase with the lowest standard oxidation potential [126, 127, 128]. As a consequence, often the first step of a photo-induced oxidation process in the presence of certain oxidants [129, 130] is the formation of a guanine radical cation ( $G^{\bullet+}$ ) [75]. However, not only the intrinsic redox properties of the guanine itself are determining its electrochemical behavior in the environment of oxidants. Moreover, the sequence context modulates the oxidation potential of the nucleobases. Ab initio calculations [131] and experimental data [132] have shown that stacked GGG sequences are more easily oxidized than stacked GG sequences, which are still more easily oxidized than a lone G [133]. Consequently, mutations will occur predominantly at G clusters. This is of outstanding interest, in particular with respect to the human genome [75, 129, 130]. After charge injection into the DNA strand, which preferentially occurs at an electron loss center, the resultant radical cation (hole) not necessarily remains located on the entrance site. The hole can migrate long distances through the DNA before being trapped [94, 133]. Accordingly, in literature it is discussed, that guanine rich domains, especially GG and GGG clusters, outside the coding regions of genes

may serve to protect the genome from permanent oxidative DNA damage [76]. Nowadays it is well established that excess charges can migrate along the stacked base pairs in the double helical DNA strand [91]. The possibility of electrical conductivity of DNA was discussed the first time in 1962 by Eley [134], not more than ten years after Watson and Crick [135] discovered the helical structure of the DNA double strand [91]. In the B form of the DNA helix, which is usually found under physiological conditions, the different nucleobases are coiled round the same axis with a pitch of only 3.4 Å. Therefore the DNA helix may be considered as a polymer with a rigid, electronically coupled aromatic column of stacked base pairs. This environment provides electron transfer capabilities due to the  $\pi$ -stacking of the aromatic groups and therefore the DNA serves as efficient “ $\pi$ -way” or molecular wire over which electron transfer reactions might be promoted efficiently [136]. An opponent contribution to the debate of electrical conductivity of DNA is from Bernard and coworkers who argue that DNA is effectively an insulator [137] relying on data, which were achieved under temperatures below 80 K. Since the measurements discussed in the framework of the present thesis were not performed under such extreme temperature conditions, the prevailing opinion that DNA is considered to be conducting is applied.

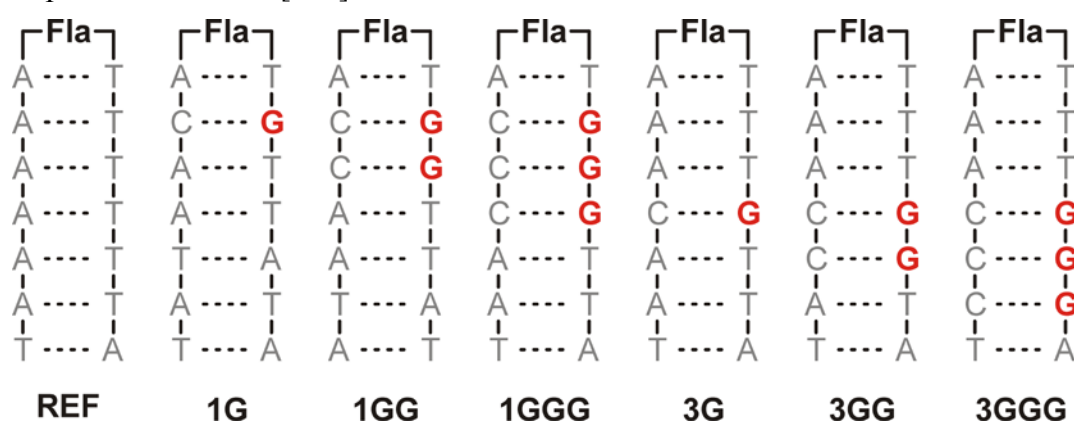
Experimental and theoretical results have emerged two different mechanisms of charge transfer through DNA: coherent superexchange, which is strongly distance dependent and incoherent multistep hopping, which exhibits only a weak distance dependency [61, 75, 81, 91, 95, 101, 138]. For long range charge transfer reactions in DNA, a hopping mechanism is proposed in which the charge tunnels between DNA bases of similar redox potential. Therefore, the overall process of long-range charge transfer in DNA consists of multiple short-range tunneling processes [75, 76, 81, 138, 139]. In case of hole transport, the guanine sites act as the stepping stones for the tunneling processes due to their low oxidation potential [76, 81, 139]. It has been shown, if two guanines are separated by an adenine (A) thymine (T) sequence, the charge tunnels through the (A:T)<sub>n</sub> sequence for  $n \leq 3$ , which is described by a strong distance dependence ( $\beta = 0.6-0.7 \text{ \AA}^{-1}$ ). In contrast, for  $n \geq 4$ , the adenines are also involved as charge carriers and the distance dependence of the charge transfer process nearly completely vanishes [81, 76]. Based on this mechanism a positive charge can be transported without any attenuation over distances of more than 50 Å, which corresponds to 15 base pairs [76, 94, 140, 141].

Another model to explain long-range charge transport processes in DNA which depends on its spontaneous structural distortion, is from Gary B. Schuster and is called phonon-assisted polaron hopping. In this model sequences of base pairs, instead of single adenines and guanines, serve as charge carriers [142]. However, the following discussion of charge transfer in DNA is based on the more common model of guanine hopping introduced in this section.



### Flavin-Capped DNA Hairpins for the Investigation of Sequence Dependent Charge Transfer Processes

The importance of intramolecular long-lived charge separated states for efficient photoredox catalysis has been already discussed. Since DNA exhibits an environment which is comparable to artificial donor-bridge-acceptor molecules, DNA is also a perfectly suited system to gain fundamental understanding of charge transfer processes in complex molecules. Moreover, particularly in DNA, the sequence dependence of charge transfer processes and the question under which conditions long-lived charge separated states are established are of major interest for biology, since long-lived charge transfer states are considered as a precursor for permanent DNA damage [143]. To investigate sequence dependent charge transfer dynamics in DNA, different DNA oligonucleotides were synthesized in the group of Thomas Carell (Ludwig Maximilian University), which are depicted in Scheme 3.2. All DNA hairpin structures have a covalently linked flavin chromophore in common [144].



**Scheme 3.2** Structures of the flavin capped DNA hairpins. **REF** serves as reference substance for the determination of the background rate of excited state quenching by ET from the AT backbone. The distance from the flavin cap to the nearest G is 6.8 Å in **1G**, **1GG** and in **1GGG** and is 13.6 Å in **3G**, **3GG** and in **3GGG**.

Flavin provides the advantage that it exhibits a strong absorption band in the visible spectral region centered around 450 nm and acts as strong oxidizing agent [145] in its excited state. Further advantages are, that the signatures of  $S_1$  state, radical anion and further protonation states are easily to distinguish in the visible spectral range [146]. Therefore flavin acts both as photo-induced oxidant and as precise optical probe for the investigation of charge transfer processes within the adjacent DNA hairpin structure. In contrast, the radical cation states of the DNA nucleobases can be hardly directly resolved with transient absorption spectroscopy in the UV and visible spectral domain due to their low cross section for photon absorption [120].

A profile plot of the transient spectrum of DNA hairpin structure **1GGG** after  $\lambda_{\text{EXC}} = 450$  nm excitation is shown in Figure 3.4. The flavin-capped DNA hairpin molecules were diluted in an aqueous solvent and the temperature was kept constant at  $T = 10$  °C during the measurements.

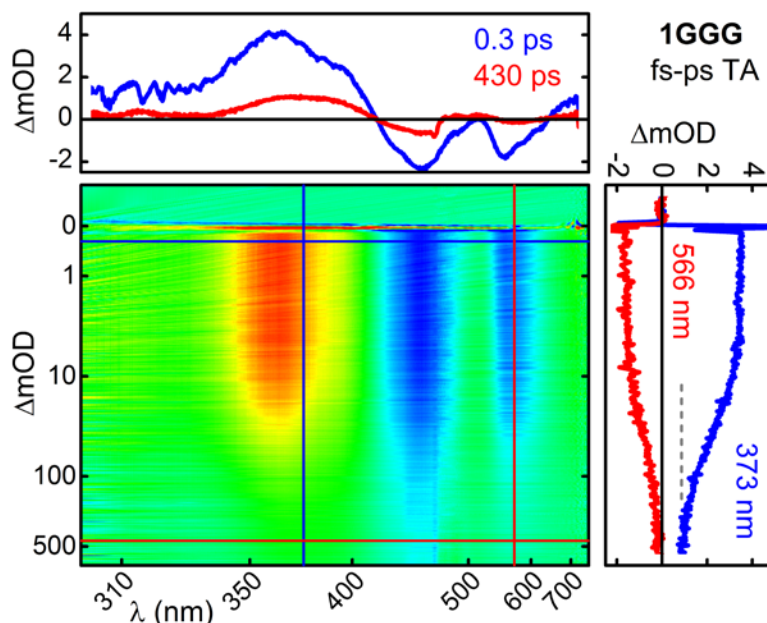


**Figure 3.4** Profile plot of the fs-ps TA measurement of flavin DNA hairpin structure **1GGG** in water after  $\lambda_{\text{EXC}} = 450$  nm excitation. The flavin  $S_1$  spectrum (blue spectral trace,  $t = 0.3$  ps, top) with the characteristic  $S_1$ -specific stimulated emission band around  $\lambda = 566$  nm (red time trace,  $\lambda = 566$  nm, right) decays within 50 ps. In contrast, the remaining spectrum (red spectral trace,  $t = 430$  ps, top), which comparably to the  $S_1$  spectrum is composed of both a ground state bleach around 450 nm and a transient absorption band around 350 nm decays on a much slower time scale. This spectrum can be associated with the flavin radical anion, which is generated by oxidation of the adjacent DNA strand. This intramolecular charge separated state is long-lived and its relative yield strongly depends on the base sequence of the DNA hairpin structure.

The detailed discussion of the experimental results with focus on the sequence dependence of the quantum yield  $\Phi_{\text{CS}}$  for long-lived charged separation is given in the following publication (see Appendix A.3):

#### **Flavin-induced DNA Photooxidation and Charge Movement Probed by Ultrafast Transient Absorption Spectroscopy**

Matthias Wenninger\*, Danila Fazio\*, Uwe Megerle, Christian Trindler, Stefan Schiesser, Eberhard Riedle, Thomas Carell

*ChemBioChem* **2011**, *12*, 703-706

\*) these authors contributed equally to this work

The experimental data reveal that within hairpin structure **3GGG**, a long-lived ( $\tau \gg 1$  ns) charge separated state is established with a quantum yield of  $\Phi_{CS} = 14\%$ . Lower values of  $\Phi_{CS} = 7\%$  in **3GG** and of  $\Phi_{CS} = 7\%$  in **3G** were found whereas in **1G**, **1GG** and **1GGG** no significant population of a long-lived charge separated state was observed. The observed charge separated state comprises the flavin radical anion **Fla<sup>-</sup>** and a radical cation state on the G site of the DNA hairpin structure.

These rather high values for long-lived charge separation in DNA have to be discussed with respect to the reported poor quantum yields for permanent DNA damage caused by direct UV irradiation of the DNA which are in the per mille region [123]. These results give evidence, that the interaction of the UV light with endogenous or exogenous chromophores has a much higher potential for mutagenesis than the direct irradiation of DNA [122]. As discussed above, nature has found strategies, which lead to the ultrafast deactivation of photo-excited states of DNA nucleobases [118, 119, 120] and therefore impedes permanent DNA damage formation after direct photo-excitation. Since in particular the aromatic amino acids absorb in the same spectral range as the DNA nucleobases do [147], photo-induced DNA oxidation mediated by external photo-induced oxidants, such as certain amino acids and light absorbing chromophores, cannot be regarded as negligible. In the case, that a hole is injected into the DNA double strand by an external oxidant, a distance of three base pairs to the next guanine charge trap is sufficient enough to significantly inhibit the desired charge recombination to prevent the formation of a long-lived charge separated state. In contrast, if the guanine charge trap is in only one base pair distance to the external oxidant, charge recombination after hole injection is much more likely. Therefore the almost only promising strategy of nature to protect DNA against photo-oxidation by external oxidants is to sterically inhibit a close proximity of potential photo-oxidants to the coding region of the DNA.

The measured data not only allow the determination of the quantum yield  $\Phi_{CS}$  for the population of a long-lived charge separated state, moreover the data provide insights into sequence dependent charge transfer dynamics in DNA. Therefore in the following section, which refers to unpublished results, the measured kinetics will be discussed with respect to Marcus Theory.

### Quantifying the Charge Transfer Dynamics in Flavin-Capped DNA Hairpins

The synthesized DNA hairpins **REF**, **1G**, **1GG**, **1GGG**, **3G**, **3GG** and **3GGG** provide a systematically varying environment for the investigation of the dependence of charge transfer processes on distance and length of the guanine site which serves as electron donor. Since the less reactive adenine (A) and thymine (T) bases are the immediate environment of the flavin cap and remain constant within the DNA hairpin series, the measured kinetics  $k_{ET}^A$  in reference hairpin **REF** are considered as the intrinsic background reaction which is apparent in all investigated DNA hairpin structures. Therefore the kinetics in the guanine containing DNA hairpins are discussed with respect to  $k_{ET}^A$ . Particularly the rate  $k_{ET}^G$  of excited state quenching by electron transfer from the guanine site is of specific interest.  $k_{ET}^G$  can be roughly estimated on the basis of the measured flavin  $S_1$  life time  $\tau_{S1}$  in each strand according to Equation 3.5:

$$\frac{1}{\tau_{S1}} = k_{ET}^A + k_{ET}^G \quad (3.5)$$

In this equation, the intrinsic rate of excited state quenching of the AT environment is  $k_{ET}^A = (63 \text{ ps})^{-1}$  obtained from hairpin **REF**. It has to be mentioned, that the determination of exact values of the  $S_1$  life time  $\tau_{S1}$  was difficult due to complex decay dynamics which required a multi-exponential decay modeling. Typically, two to three exponential terms and one constant signal lasting beyond the measurement range were required for a sufficient parameterization of the data. Therefore we used the fit curves to determine the delay time when the signal of the stimulated emission has decayed to  $1/e$  of the initial value at  $\Delta t = 0$ . The intrinsic  $S_1$  life time  $\tau_{S1} = 2 \text{ ns}$  of the free flavin compound is negligible with regard to the CT dynamics, which are found on the 100 ps time scale. The calculated values of  $k_{ET}^G$ , obtained according to Equation 3.5 are summarized in Table 3.1.

**Table 3.1** Rates of excited state quenching by electron transfer from the guanine site of the molecule to the photo-excited flavin site. The rates  $k_{ET}^G$  were calculated according to Equation 3.5 relying on the published  $S_1$  life times  $\tau_{S1}$  [App A.3].

DNA hairpin	r (Å)	$k_{ET}^G$
<b>1G</b>	6.8	$\sim (100 \text{ ps})^{-1}$
<b>1GG</b>	6.8	$\sim (50 \text{ ps})^{-1}$
<b>1GGG</b>	6.8	$\sim (50 \text{ ps})^{-1}$
<b>3G, 3GG, 3GGG</b>	13.6	$\sim (250 \text{ ps})^{-1}$

Although adjacent G bases make a single G more readily to oxidize [132], there was no significant difference in the ET dynamics between hairpins **1GG** and **1GGG**. This is due to the effect, that adding the first neighboring G base to a lone G increases the one electron ionization potential (IP) by  $\sim 0.4$  eV whereas adding a further G to an existing GG sequence lowers the IP by only  $\sim 0.2$  eV as calculations show [148, 149]. The expected differences in ET dynamics between hairpins **3G**, **3GG**, **3GGG** are also overlaid by the measurement error and due to the fact, that the simultaneous background excited state quenching mediated through the AT backbone is described by the significantly higher rate  $k_{ET}^A$ . Hence, the actually observed life time of the flavin  $S_1$  state is only slightly modulated by the additional ET reaction  $k_{ET}^G$  from the G site of the double strand.

The determined rates  $k_{ET}^G$  for two different distances between donor and acceptor allow for a rough estimate of the damping factor  $\beta$  according to Marcus Theory, which is based on an exponential distance dependence. A distance dependence of  $k_{ET}^G$  corresponding to a  $\beta$  value of roughly  $\beta = 0.2 \text{ \AA}^{-1}$  was found. Although the reliability of the determined  $\beta$  is low, on the one hand due to the fit relying only on two data points and on the other hand due to the imprecisely determined ET rates  $k_{ET}^G$ , the value corresponds very well to the results measured in a very similar system [150]: Carell and coworkers found a damping factor of  $\beta = 0.25 \pm 0.05 \text{ \AA}^{-1}$  in flavin capped DNA-hairpins.

The outstanding importance of the understanding of charge transfer dynamics in DNA has been raised by a series of experimental studies using photochemistry to initiate electron transfer. In many of them, time resolved spectroscopic techniques were applied for the detection of electron transfer dynamics, as well.

For instance, Barbara, Barton and coworkers applied ultrafast emission and absorption spectroscopy for the investigation of charge transfer dynamics in DNA. In contrast to the previously presented results, different, non-covalently bound, intercalated metal complexes served as light triggered electron donor and light-independent electron acceptor. For the damping factor  $\beta$  a value on the inverse one Ångström ( $\text{\AA}^{-1}$ ) scale was discussed [151].

A more precise value for  $\beta$  was found by Lewis, Wasielewski and coworkers, who investigated the distance dependence of charge transfer dynamics in stilbene capped DNA hairpins with the help of transient absorption spectroscopy: A damping factor of  $\beta = 0.64 \pm 0.1 \text{ \AA}^{-1}$  was found for the electron transfer from a guanine electron donor to the excited state of the stilbene cap [101].

In a more recent study, Lewis, Wasielewski and coworkers found a damping factor of  $\beta = 0.77 \text{ \AA}^{-1}$  in DNA hairpins, using different organic linker caps for the light triggered hole injection into the DNA double strand. The application of different electron donors with altered electrochemical properties in this study in combination with Marcus Theory provides a deep insight into the dependence of charge transfer dynamics on the energy landscape, which also involves the inverted region of electron transfer in DNA [61].



#### 3.4 DNA as Chiral Environment for Enantioselective Photocatalysis?

The utilization of DNA in photocatalysis research offers much greater capabilities than only to provide a well characterized environment for the investigation of intramolecular charge transfer reactions. On the one hand due to its versatile capabilities for molecular self-assembly [152], DNA is also considered as an inert backbone for the investigation of photo-induced processes of bound, photo-active chromophores in a well-defined and rigid environment [153]. On the other hand, due to the chirality of its constituents, the nucleotides<sup>4</sup>, DNA exhibits versatile capabilities to serve as a chiral template in enantioselective catalysis [154] and photocatalysis [155]. One approach toward enantioselective photocatalysis is to combine a chiral template and a photocatalyst within one molecular assembly [5, 156]. Therefore a photocatalytic chromophore is covalently linked to a chiral template, which can be a nucleotide in the case of DNA mediated photocatalysis. The light absorbing chromophore in this assembly exhibits the desired photocatalytic capability, for instance via excitation energy transfer [29, 30] or photo-induced electron transfer. The DNA backbone contributes the stereoselective information to the enantioselective catalytic process. Therefore the DNA backbone has to provide an inert environment for energy and electron transfer processes of the highly reactive photo-excited chromophore since the photocatalyst is required not to be consumed within the catalyzed reaction. Due to the well investigated charge transfer processes in DNA (Chapter 3.3) and redox chemistry of DNA [157] it was expected that the natural occurring nucleobases are not suited to serve as inert backbone for every kind of photocatalytic reaction. The question, if and under which conditions DNA can be utilized as chiral backbone for photocatalysis will be discussed in the following section. However, not only this initial question is answered. Moreover this study reveals insights into the conformational control of DNA photo-oxidation by external oxidants.

##### **Benzophenone-DNA Dinucleotides**

The organic chromophore benzophenone has been already applied in enantioselective photocatalysis [5, 156, 158] and represents an both interesting and biologically relevant system with respect to DNA damaging [122]. Hence, to answer the question if and under which conditions DNA provides capabilities as chiral backbone for enantioselective photocatalysis, benzophenone was studied as photocatalytically active model chromophore [21]. Therefore, in the group of Hans-Achim Wagenknecht (Karlsruhe Institute of Technology), benzophenone as an artificial C-nucleoside<sup>5</sup> was linked by a phosphodiester bridge to one of the natural nucleosides<sup>6</sup> of the naturally occurring nucleobases guanine (G), adenine (A),

---

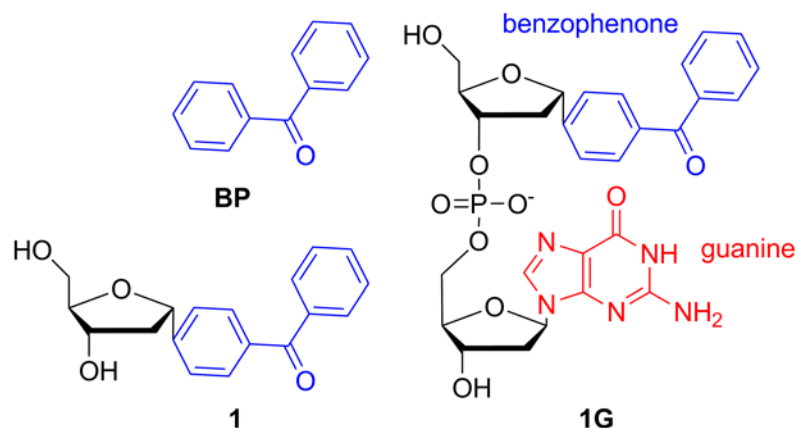
<sup>4</sup> nucleotides are composed of a nucleobase, a sugar and at least one phosphate group

<sup>5</sup> C-nucleosides are a class of nucleosides in which the pendant heterocyclic base is covalently linked to the sugar by a C-C bond instead of a C-N bond [159]

<sup>6</sup> nucleosides are composed of a nucleobase and a sugar

thymine (T) and cytosine (C). The synthesis of these dinucleotides<sup>7</sup> is described in detail elsewhere [160].

For the present investigation, an artificial nucleotide with benzophenone attached to the sugar backbone of the DNA (**1**) was synthesized as reference substance to study the intrinsic photophysical behavior of the benzophenone chromophore in the environment of the sugar backbone. The benzophenone chromophore (**BP**), the reference nucleotide **1** and the benzophenone guanine dinucleotide **1G**, which is exemplarily for all other compounds **1A**, **1T** and **1C**, are shown in Scheme 3.3.



**Scheme 3.3** Structure of the synthesized nucleotides: benzophenone **BP**, reference nucleotide **1** and dinucleotide **1G**, which is exemplarily for dinucleotides **1A**, **1T** and **1C**.

The different nucleobases of the DNA exhibit a strongly varying electrochemical behavior: the nucleobase guanine is relatively easy to oxidize in comparison to the other nucleobases [126, 127, 128]. Therefore the following discussion is first of all based on the dinucleotide **1G**. Due to the low standard oxidation potential of guanine and the fact that benzophenone acts as strong oxidant in its excited state [54], an electron transfer reaction from guanine to benzophenone in its excited state is very likely [161].

The first approach toward the discussion, if DNA is inert enough to serve as non-reactive backbone for benzophenone sensitized photoredox catalysis, was to calculate the change of Gibbs energy  $\Delta G^0$  within a possible electron transfer reaction between the benzophenone both in its excited singlet and triplet state and the corresponding nucleobase. Generally, calculating the change of Gibbs energy  $\Delta G^0$  reveals if an reaction is exergonic and therefore thermodynamically allowed or endergonic and therefore thermodynamically forbidden. Since all photophysical and electrochemical quantities of benzophenone and the nucleobases can be found in the literature, the  $\Delta G^0$  value of a photo-induced charge transfer reaction between the benzophenone in its excited state and an adjacent nucleobase can be easily calculated according to Rehm and Weller [63, 162], which is shown in Equation 3.6 (compare Equation 3.1). However, exact values of the standard redox potentials of the

<sup>7</sup> dinucleotides consist of two nucleotides joined through their phosphate groups



nucleobases in pH-neutral water environment are not easy to measure and therefore values measured in varying environments are presented in the literature [126, 127, 128]. The present work refers to the values from Seidel and Sauer [127].

$$\Delta G^0 = e \left[ E^0(G^{\bullet+}/G) - E^0(BP/BP^{\bullet-}) \right] - \Delta E_{00} - \frac{e^2}{4\pi\epsilon_0\epsilon r} \quad (3.6)$$

In this equation, the one-electron standard oxidation potential (vs. NHE<sup>8</sup>) of guanine is  $E^0(G^{\bullet+}/G) = 1.49$  V [127], the one-electron standard reduction potential (vs. NHE) of benzophenone is  $E^0(BP/BP^{\bullet-}) = -1.00$  V [163] and the energies of the excited states of benzophenone with respect to its ground state are  $\Delta E_{00}(S_1^{BP}) = 3.30$  eV [164] in its  $S_1$  state and  $\Delta E_{00}(T_1^{BP}) = 3.04$  eV [162, 165] in its  $T_1$  state. The only term in this equation still owning uncertainties is the last one describing the Coulomb interaction of the charge separated state, in which  $e$  is the elementary charge,  $\epsilon_0$  the vacuum permittivity,  $\epsilon$  the permittivity of the solvent and  $r$  the donor-acceptor distance. Therefore this term and the geometric conformation of the dinucleotide, since it particularly affects the donor-acceptor distance  $r$ , will be discussed in the following section. Without taking this distance dependent term into account, which would lead to a further decrease of  $\Delta G^0$ , the change of Gibbs energy is already  $\Delta G^0 = -0.810$  eV, which makes a charge transfer reaction thermodynamically very favored.

### Solvent Dependent Conformation of the Dinucleotide

It is well established that, depending on the solvent polarity, dinucleotides exhibit different conformations when they are diluted [166]. Since the benzophenone chromophore and the nucleobase are connected by a flexible linker, a conformational distribution, in which the distance  $r$  between electron donor and electron acceptor strongly varies, is expected. Due to the size of the dinucleotide and its low rigidity it can be safely assumed that the donor-acceptor distance  $r$  varies over a huge range of more than 10 Å. In face of typical damping coefficients for electron transfer reactions in water of  $\beta = 1.0 - 1.4$  Å<sup>-1</sup> [50, 100] this wide distance distribution largely affects the electron transfer dynamics. The actual value of  $r$  within the observed dinucleotide determines whether an electron transfer reaction is possible and strongly affects its efficiency. In order to understand the conformational motion and the distribution of conformations in varying solvents, in the group of Martin Schütz (University of Regensburg) Molecular Dynamics simulations on this dinucleotide were performed by Thomas Merz.

Before the calculated trajectories are discussed, the actual distance, which is relevant for the electron transfer reaction has to be considered. The electron transfer quenches an photo-excited state of benzophenone, which is of  $^1n\pi^*$  character [167] while the radical of the guanine nucleobase is located at the carbonyl group<sup>9</sup> of the purine base guanine [157]. Hence the distance between the benzophenone carbonyl group and the guanine carbonyl group is of

<sup>8</sup> normal hydrogen electrode

<sup>9</sup> carbonyl groups are composed of a carbon atom double-bonded to an oxygen atom: C=O

major interest, since it depicts the effective distance over which the electron is transferred in a photo-induced charge transfer reaction. Both the experiments and the calculations were performed in two different solvents: in water and in the less polar methanol. Therefore 500 steps of the trajectory of  $r = d(O_B C_G)$ , the distance between  $O_B$ , the oxygen atom of the carbonyl group of the benzophenone, and  $C_G$ , the carbon atom of the carbonyl group of the guanine, were calculated in Molecular Dynamic runs. The results of the simulation are depicted in Figure 3.5.

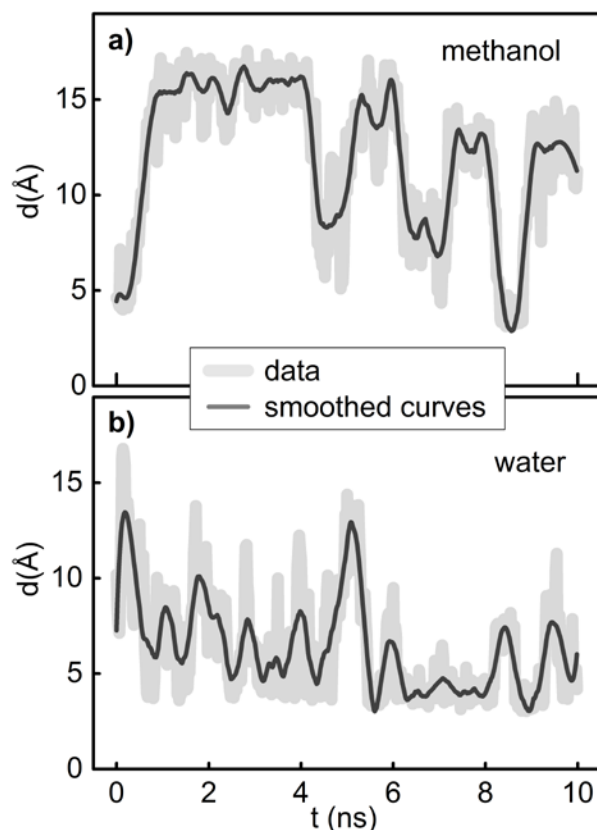


**Figure 3.5** Trajectories of Molecular Dynamics run of **1G**: distance between the oxygen atom of the carbonyl group of benzophenone ( $O_B$ ) and the carbon atom of the carbonyl group of guanine ( $C_G$ ) in methanol (a) and in water (b). Calculated values (transparent line) and smoothed values according to Savitzky-Golay algorithm (solid line).

The Molecular Dynamics simulations clearly reveal that the predominant conformation of the dinucleotide strongly depends on its solvent environment. Whereas in water a closed conformation is clearly favored, in the less polar methanol no preferred conformation of the dinucleotide is found. In methanol, the dinucleotides are switching between an open and a closed conformation. Therefore, according to the Ergodic Hypothesis an ensemble of molecules with different conformations exhibiting the same statistical behavior is found in methanol when a huge number of dinucleotides is dissolved. A closed conformation is considered at distances of  $d(O_B C_G) \leq 6 \text{ \AA}$  whereas at distances of  $d(O_B C_G) \cong 15 \text{ \AA}$  an open conformation is assumed. This is in agreement with literature, where a two-state model regarding the conformation of dinucleotides in different solvents was already discussed

[166]. Since the conformational distribution of the dinucleotides in two different solvents has been quantified, its influence on charge transfer dynamics will be discussed in the next section.

### Conformation Dependent Electron Transfer Dynamics

At close distances of both carbonyl groups, the electron transfer occurs with its full intrinsic rate  $k_{\text{ET}} = k_0$ . Then with increasing donor-acceptor distance  $r$ , the coupling matrix element  $H_{\text{AB}}$  decreases according to Marcus Theory (Equation 3.3 a and 3.3 b) exponentially. At very large distances, the electron transfer reaction is completely damped and therefore no longer detectable. For the following discussion, a contact distance of  $r_0 = 6 \text{ \AA}$  is assumed. This value is not exactly determined but is still in agreement with the literature where comparable van der Waals radii<sup>10</sup> of molecules are discussed [64, 168]. Therefore three regimes can be distinguished:

I.	Contact regime	$r \leq 6 \text{ \AA}$	$k_{\text{ET}} = k_0$
II.	Marcus regime	$6 \text{ \AA} < r \leq 11.2 \text{ \AA}$	$k_{\text{ET}} = k_0(r) \cdot \exp\{-(r - r_0)\beta\}$
III.	Non-contact regime	$r > 11.2 \text{ \AA}$	$k_{\text{ET}} = 0$

Here, the border between Marcus regime and non-contact regime was defined to be at  $r = 11.2 \text{ \AA}$  where the electron transfer rate drops below 1% of  $k_0$ . Whereas the electron transfer dynamics in regimes I and III are easily to understand, regime II requires a further discussion, since the distance dependence not only appears in the exponential term of the Marcus equation. Also the change of Gibbs energy  $\Delta G^0$  becomes distance dependent according to Equation 3.6 since the Coulomb interaction term is strongly distant dependent. Therefore,  $k_{\text{ET}}(r)$  in regime II can be written as shown in Equation 3.7, where  $k_0$  is the intrinsic electron transfer rate at contact distance,  $\beta$  the damping factor,  $\lambda$  the reorganization energy and  $\Delta G^0(r)$  the distance dependent change of Gibbs energy at donor-acceptor distance  $r$ .

$$k_{\text{ET}}(r) = k_0 \cdot \exp(-\beta(r - r_0)) \cdot \exp\left(\frac{1}{k_B T} \cdot \frac{(\lambda + \Delta G^0(r))^2}{4\lambda}\right) \quad (3.7)$$

<sup>10</sup> the term “van der Waals radius” historically originates from atom physics but is often applied in literature to describe the corresponding molecular property as well [64]

An exact value of  $k_0$  is only experimentally accessible and will be discussed in the next section. The distance dependence of  $k_{ET}(r)$  with regard to the normalized intrinsic rate  $k_0$  is depicted in Figure 3.6. Here, a damping coefficient of  $\beta = 1.2 \text{ \AA}^{-1}$  [50, 100] (see Chapter 3.1 and discussion below) for both solvents is assumed. The very slight difference of the distance dependence within regime II in methanol and in water is due to different values of the absolute permittivity  $\epsilon$  of both solvents, which causes effects in the distance dependent Coulomb term of Equation 3.6 and therefore in  $\Delta G^0(r)$ .

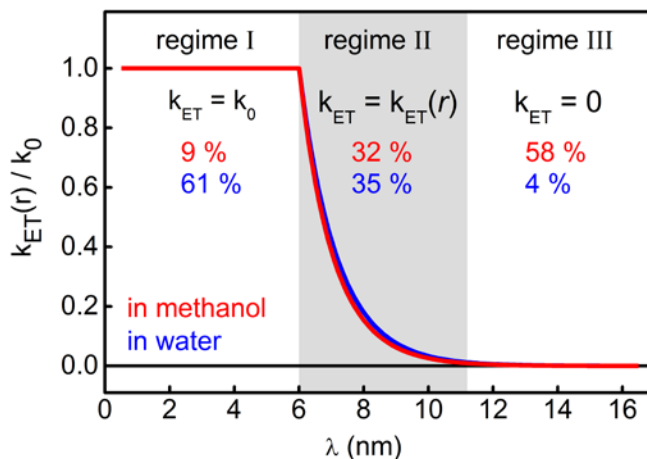


**Figure 3.6** Regimes of the distance-dependent normalized electron transfer rate  $k_{ET}(r)$  according to Equation 3.7 and probability to find a dissolved dinucleotide in one of the regimes in methanol (red) and in water (blue).

Also the probability to find a dissolved dinucleotide in one of the three regimes is given in Figure 3.6 (numbers in red and blue). It can be clearly seen that in water mainly donor-acceptor distances below  $6 \text{ \AA}$  are found and therefore the closed form of the dinucleotides is prevailing. In contrast, in methanol, the open form with donor-acceptor distances of more than  $11.2 \text{ \AA}$  is the dominating conformation.

The probability of the distance  $r$  to be found in the corresponding solvent is described by  $P(r)$  and can be directly deduced from the Molecular Dynamic runs under consideration of the Ergodic Hypothesis. Since  $P(r)$  and the distance dependence of the electron transfer dynamics  $k_{ET}(r)$  within the dinucleotide have been quantified, an average electron transfer rate  $\langle k_{ET} \rangle$  for both solvents can be estimated according to Equation 3.8.

$$\langle k_{ET} \rangle = \int_{r=0}^{\infty} dr P(r) \cdot k_{ET}(r) \quad (3.8)$$

Although a stretched exponential fit function is usually applied to describe reaction dynamics in a system exhibiting a distribution of rates [47, 49] (Chapter 2.2), an average value  $\langle k_{ET} \rangle$  of the electron transfer rate seems to be sufficient. Equation 3.8 does not reveal a numeric value of  $\langle k_{ET} \rangle$ , but a value in dependence on the intrinsic rate  $k_0$ , which is particularly of physical interest since it allows the calculation of the coupling matrix element  $H_{AB}$  for the electron transfer at contact distance ( $r \leq 6 \text{ \AA}$ ).

According to Equation 3.8 the average values of  $k_{\text{ET}}$  are  $\langle k_{\text{ET}} \rangle = 0.75 \cdot k_0$  in water and  $\langle k_{\text{ET}} \rangle = 0.17 \cdot k_0$  in methanol. This relation allows to calculate the intrinsic electron transfer rate  $k_0$  at contact distance based on the measured electron transfer rate  $\langle k_{\text{ET}} \rangle$ . To plausibly quantify the electron transfer dynamics with respect to Marcus theory, a measurement series with varying values of the change of Gibbs energy  $\Delta G^0$  is required. The four naturally occurring nucleobases span a relatively wide range of redox potential of  $\Delta E^0 = 0.62 \text{ V}$  [126, 127, 128] and provide access to electron transfer dynamics at different  $\Delta G^0$  values. The results of time resolved spectroscopic measurements of the dinucleotides **1G**, **1A**, **1T** and **1C** combined with a theoretical discussion of the excited state energy landscape based on quantum mechanical ab initio calculations are presented in the following publication (see Appendix A.4):

**Conformational control of benzophenone-sensitized charge transfer in dinucleotides**

Thomas Merz\*, Matthias Wenninger\*, Michael Weinberger, Eberhard Riedle, Hans-Achim Wagenknecht, Martin Schütz

*Physical Chemistry Chemical Physics* **2013**, 135, 1000-1010

\*) these authors contributed equally to this work

The performed time-resolved measurements clearly reveal that after excitation, both the benzophenone  $S_1$  life time and the triplet yield  $\Phi_T$  of dinucleotide **1G** in both solvents is significantly reduced in comparison to reference dinucleotide **1**. This result and the results of quantum mechanical ab initio calculations, performed by Thomas Merz give strong evidence for an intramolecular electron transfer process from the adjacent nucleobase guanine to the  $S_1$  state of benzophenone, which is competing with triplet formation. Also the remaining dinucleotides **1A**, **1T** and **1C** show a reduced  $S_1$  life time due to an intramolecular photo-induced charge transfer processes as observed in **1G**. The decrease of  $S_1$  life time within these dinucleotides is less intense than observed in **1G** due to the higher standard oxidation potential of the nucleobases cytosine, thymine and adenine.

When discussing the electron transfer in the singlet manifold one has to keep in mind that the  $S_1$  state of benzophenone undergoes a relatively fast inter-system crossing to the  $T_1$  state on the 10 ps time scale [167], which is not affected by the covalently linked sugar, and therefore electron transfer processes are only observable within this limited temporal window. However, this temporal window was long enough to substantially quantify the electron transfer dynamics of all synthesized dinucleotides.

A profile plot of the transient absorption spectrum of benzophenone dinucleotide **1C**, which is composed of cytosine instead of guanine (Scheme 3.3) after  $\lambda_{\text{EXC}} = 358 \text{ nm}$  excitation in methanol is shown in Figure 3.7. The transient spectrum is dominated by the relatively fast inter-system crossing of benzophenone on the 10 ps time scale.

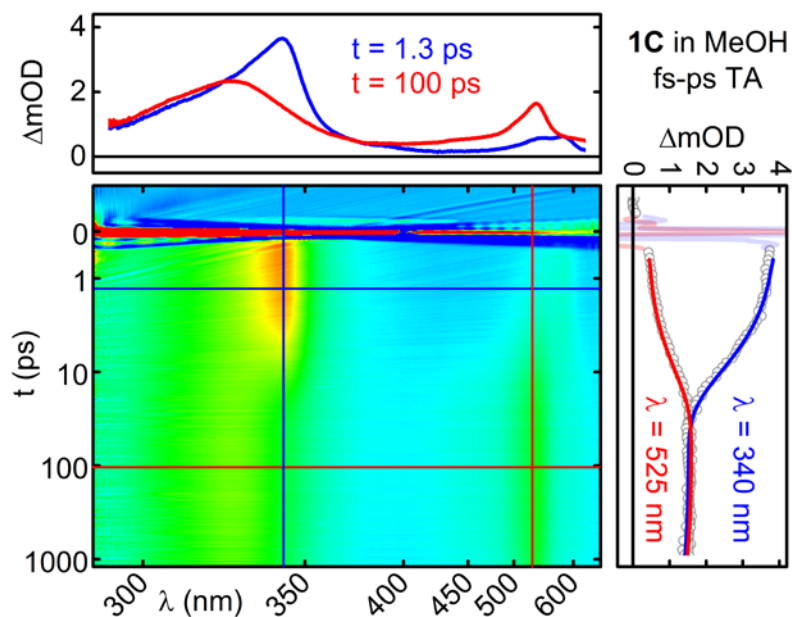


**Figure 3.7** Profile plot of the fs-ps TA measurement of benzophenone dinucleotide **1C** in methanol after  $\lambda_{\text{EXC}} = 358$  nm excitation. The benzophenone  $S_1$  state with a characteristic absorption around 340 nm (blue spectral trace,  $t = 1.3$  ps, top) undergoes inter-system crossing to the benzophenone  $T_1$  state with a characteristic absorption around 525 nm (red spectral trace,  $t = 100$  ps, top). The inter-system crossing is overlaid by an electron transfer process from cytosine quenching the benzophenone  $S_1$  state. The time constant describing the decay of the benzophenone  $S_1$  state and the population of the benzophenone  $T_1$  state (red and blue time traces, right) which also comprises information about the intramolecular charge transfer dynamics was the basis for the calculation of the electron transfer rate  $k_{\text{ET}}$ .

The electron transfer rates  $k_{\text{ET}}$  of all synthesized dinucleotides in both solvents are depicted in Figure 3.8. Based on the introduced terminology and under consideration of a strictly mono-exponential decay behavior, which is a justified simplification in face of the expected stretched exponential decay dynamics within an ensemble exhibiting a distribution of rates (vide supra), the actually observed decay rate  $k_{\text{ET}}$  corresponds to the value  $\langle k_{\text{ET}} \rangle$ , defined in Equation 3.8. Performed attempts to fit a stretched exponential function<sup>11</sup> to the transient data reveal a close to unity exponential parameter  $\beta$  which strongly supports the reliability of the applied mono-exponential decay model.

A Marcus parabola (Equation 3.7) was fitted to the data and is shown in Figure 3.8. Since the distance dependence of the change of Gibbs energy  $\Delta G^0$  considering reasonable values of  $r = d(\text{O}_\text{B}\text{C}_\text{G})$  only causes minor effects on the effective value of  $k_{\text{ET}}(r)$  at a fixed value of  $\Delta G^0$ , constant distances between electron donor and acceptor in both solvents ( $r = 12$  Å in

<sup>11</sup> stretched exponential fit function:  $f(t) = \exp\left(-\left(\frac{t}{\tau}\right)^\beta\right)$

methanol,  $r = 6 \text{ \AA}$  in water) were taken as basis for the fit of the Marcus parabola. Hence, the only remaining parameters of the fit were the reorganization energy  $\lambda$  and the coupling matrix element  $H_{AB}$ .

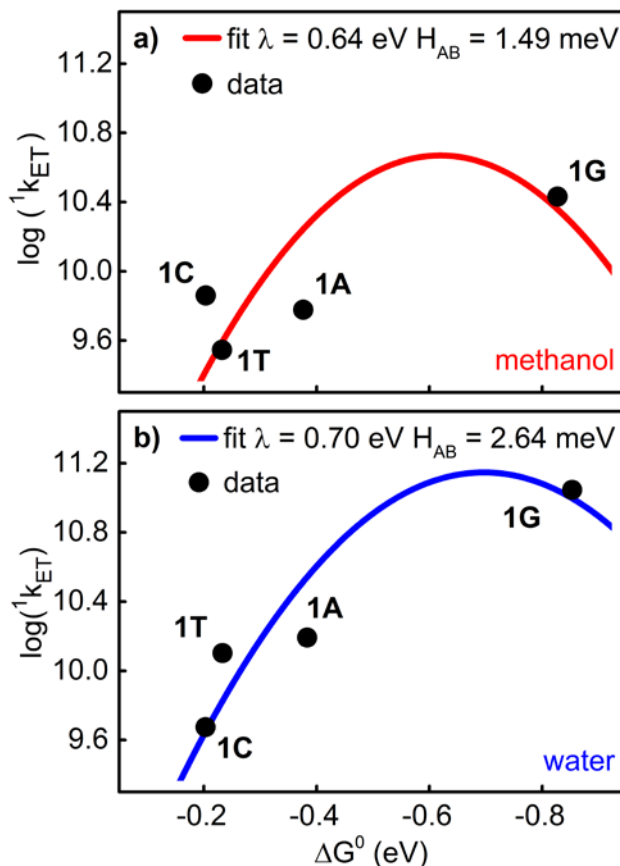


**Figure 3.8** Rates of electron transfer  $k_{ET}$  from the corresponding nucleobase to the benzophenone moiety in its  $S_1$  state in dinucleotides **1G**, **1A**, **1T** and **1C** and fit values  $\lambda$  and  $H_{AB}$  of the Marcus parabola in methanol (a) and in water (b).

The derived values for the reorganization energy  $\lambda$  in both solvents are in excellent agreement with values presented in the literature, which cover the range from  $\lambda = 0.2 \text{ eV}$  to  $\lambda = 1 \text{ eV}$  (Chapter 3.1). The coupling matrix element  $H_{AB}$ , obtained from fitting the Marcus equation to the measured data, has yet no physical meaning, since it represents the average value of the electronic coupling in an ensemble of dinucleotides exhibiting different donor-acceptor distances  $r$ . According to Equation 3.8, considering the probability  $P(r)$  of each donor-acceptor distance  $r$  to be found in the corresponding solvent, the measured values of  $\langle k_{ET} \rangle$  can be used to calculate the intrinsic electron transfer rate  $k_0$  at contact distance  $r \leq r_0$ . The intrinsic coupling matrix element  $H_{AB}$  at contact distance can be easily deduced from  $k_0$  according to Equation 3.9.

$$H_{AB} = H_{AB}^{\text{fit}} \cdot \sqrt{\frac{k_0}{\langle k_{ET} \rangle}} \quad (3.9)$$

Applying this equation, coupling matrix elements of  $H_{AB} = 3.6 \text{ meV}$  in methanol and  $H_{AB} = 3.1 \text{ meV}$  in water were found which are equal within the measurement error. This

result agrees very well with theory, since the coupling matrix element  $H_{AB}$  is the off-diagonal element of the electronic Hamiltonian  $H_{AB} = \langle \Psi_A | H | \Psi_B \rangle$  in case of through-space electronic interaction and therefore in first approximation  $H_{AB}$  is independent of the solvent environment [169]. However, there might be a minor solvent-dependent contribution caused by a varying geometric donor-acceptor orientation, which also potentially affects the electronic coupling strength between initial and final state [58]. In contrast, the reorganization energy  $\lambda$  obtained from fitting the Marcus equation to the measured data represents a value with physical meaning which does not alter when changing the analytical view from ensemble dynamics to single molecule dynamics at a defined contact distance  $r = r_0$ .

#### **DNA - a Suitable Backbone for Enantioselective Photocatalysis?**

This study clearly reveals that nucleotides are not perfectly suited to serve as inert backbone in benzophenone-mediated enantioselective photocatalysis. However, with some restrictions, the application of a cytosine- or thymine-based DNA backbone in combination with less reactive photocatalytic active chromophores might be a considerable approach toward DNA mediated enantioselective photocatalysis, since these are the nucleobases with the highest oxidation potential and therefore less reactive in the environment of an excited chromophore. Due to the limited number of different nucleobases, replacing the photocatalytic active chromophore benzophenone by a less reactive photocatalyst has to be considered to design a stable DNA-based photocatalyst. Assuming a carbostyryl compound, the parent compound of quinolones, as target for an enantioselective photocatalytic reaction, a triplet energy of the photo-sensitizer of at least  $E_T = 2.86$  eV is required to provide triplet sensitization. Benzophenone with a triplet energy of  $E_T = 2.98$  eV readily fulfils this energetic requirement [165]. The use of a photocatalyst instead of benzophenone which is slightly lower in energy of  $S_1$  and  $T_1$  state would allow to tune the change of Gibbs energy  $\Delta G^0$  of a hypothetical electron transfer reaction within the DNA-based photocatalyst to more positive values and therefore energetically prohibit a competing excited state quenching reaction.

In comparison to benzophenone ( $E_{S_1} = 3.30$  eV,) the substituted 4-amino-benzophenone provides a slightly altered energy landscape with a lower  $S_1$  energy of  $E_{S_1} = 3.03$  eV ( $\triangleq 410$  nm) and a  $T_1$  energy of  $E_T = 2.91$  eV [165], which is still sufficient for triplet sensitization of the carbostyryl target. The value of  $E_{S_1}$  indicates that 4-amino-benzophenone exhibits an optical accessible transition outside the quinolone absorption range, which is a substantial prerequisite for enantioselective photocatalysis. A calculated change of Gibbs energy of  $\Delta G^0 \approx +0.1$  eV for a hypothetical reductive excited state quenching of the  $S_1$  state within a dinucleotide consisting out of a 4-amino-benzophenone and a thymine or cytosine nucleobase seems to be a promising environment for a DNA-based photocatalyst. This model is based on the assumption, that the standard reduction potential of 4-amino-benzophenone remains comparable to pure benzophenone (vide supra). However, the drawback of replacing benzophenone by 4-amino-benzophenone is a reduced triplet quantum yield of  $\Phi_T = 0.6$  in comparison to a unity triplet quantum yield of pure



benzophenone [165]. A reduced triplet quantum yield leads to a decrease in quantum yield of triplet-sensitized reactions.

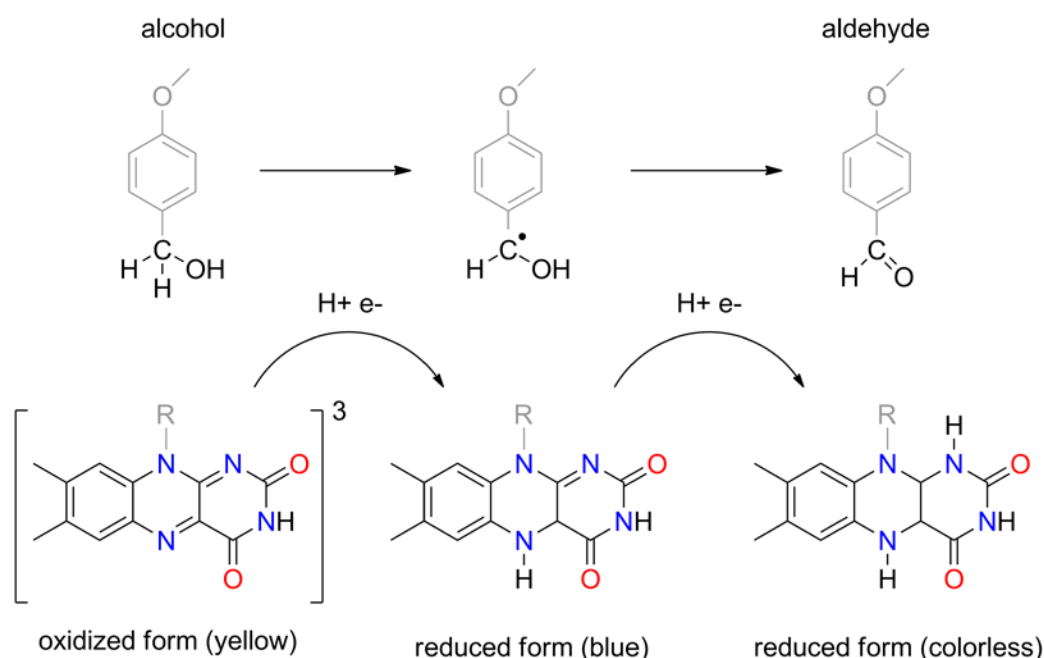
The present study did not only answer the initial question, if and under which conditions DNA provides capabilities as chiral backbone for enantioselective photocatalysis, moreover the present study revealed an insight into conformational control of charge injection into DNA. To reliably quantify charge transfer processes in DNA, the manifold of conformational states in DNA needs to be explicitly addressed. In the literature which is dealing with charge transfer processes in DNA, the manifold of different conformational states is often neglected. This assumption is, however, justified in most cases, since usually ensemble dynamics are studied and an averaged value describing the charge transfer dynamics is presented.

However, there is also literature considering the influence of the structural flexibility of the DNA on charge transfer dynamics. For instance, Ratner and coworkers present a theoretical study describing the effect of structural fluctuations on charge transfer dynamics in DNA [51]. Particularly the dependence of the coupling matrix element  $H_{AB}$  on the actual conformation of DNA hairpins is considered. Also the phonon-assisted polaron hopping model, presented by Schuster and coworkers, assumes long-range charge transfer in DNA to depend on transient structural distortions.



### 3.5 Diffusion Controlled Intermolecular Charge Transfer Processes in Flavin Photocatalysis

Since intramolecular charge transfer processes have been intensively discussed in the preceding section, now the focus is on intermolecular charge transfer processes, which are the basis for nearly every kind of homogeneous photoredox catalysis. The naturally occurring chromophore flavin is widely applied as photocatalyst for a large number of different applications both in nature [170] and in photochemistry [171, 172, 173, 174]. Flavin shows strong optical absorption up to 480 nm and is generally capable of two subsequent electron and proton transfer reactions and is versatilely applied in photoredox catalysis. Riboflavin, better known as vitamin B<sub>2</sub>, was discovered in 1879 by Alexander Wynther Blyth, who isolated a yellowish substance from cow milk, which he named lactochrome [175, 176, 177]. More than 50 years later, in 1937, the Swiss scientist Paul Karrer was awarded with the Nobel Prize for his important contributions to the chemistry of flavins and his efforts to isolate flavin and clarify its molecular structure among some other compounds. His research led to the identification of flavin as part of a complex originally thought to be vitamin B<sub>2</sub> [178]. In 1938, the Austrian chemist Richard Kuhn, who also contributed to the field of flavin chemistry, was awarded the Nobel Prize as well. Kuhn for the first time discovered, that under acidic or basic conditions, the optical absorption properties of flavin are significantly changing [179, 180]. At that time, he couldn't explain this observation but nowadays it is well established, that the absorption properties of flavin strongly depend on its redox and protonation state [146, 181].



**Scheme 3.4** The flavin-mediated photo-oxidation of methoxy benzyl alcohol to the corresponding aldehyde comprises two subsequent electron and proton transfer reactions between substrate and photocatalyst. The depicted colors refer to the singlet ground state of each oxidation state.

Due to its advantageous properties and its versatile application, flavin photochemistry has been the subject of intense research over the past 130 years [182]. In the framework of the present thesis, a model reaction was studied, in which riboflavin tetraacetate (RFTA) served as photocatalyst to oxidize methoxy benzyl alcohol (MBA) to the corresponding aldehyde (Scheme 3.4). The course of the reaction including all occurring intermediate states and partial reactions, in which basically two electrons and two protons are transferred from RFTA to MBA, was understood and quantified on the basis of the signal originating from the photocatalyst. Since the underlying study performed in the framework of this thesis has been already introduced in another thesis [183] and the underlying model, describing the dynamics of diffusion controlled processes, has been intensively discussed in Appendix A.1, the present summary provides only a very basic introduction. A more detailed presentation of early measurement data can be found in a diploma thesis [177]. The consolidated results are summarized in the following publication (see Appendix A.5):

**Unraveling the flavin-catalyzed photooxidation of benzylic alcohol with transient absorption spectroscopy from sub-pico- to microseconds**

Uwe Megerle, Matthias Wenninger, Roger-Jan Kutta, Robert Lechner, Burkhard König, Bernhard Dick, Eberhard Riedle

*Physical Chemistry Chemical Physics* **2011**, *13*, 8869-8880

The picture of the reaction, revealed from time resolved spectroscopic measurements both on the fs-ps time scale, which were performed in the group of Eberhard Riedle (Ludwig Maximilian University) and on the ns- $\mu$ s time scale, which were performed in the group of Bernhard Dick (University of Regensburg) in combination with quantum yield measurements under various conditions assigned triplet chemistry as the key element to access an efficient reaction pathway. In an equal mixture of acetonitrile (MeCN) and water (H<sub>2</sub>O) as solvent only a quantum yield of  $\sim 0.03$  for product formation was observed under optimum reaction conditions, which is low in comparison to quantum yields reported in the present thesis, for instance of  $\Phi_{CS} = 0.14$  for long-lived photo-induced charge separation in flavin capped DNA hairpins (vide supra) [App A.2] or of  $\Phi_P = 0.73$  for product formation within the intramolecular [2+2] photocycloaddition of substituted quinolones (vide infra) [App A.6]. Since the flavin-mediated photooxidation of benzyl alcohol is generally a rather complex bimolecular reaction, which comprises two consecutive electron and proton transfer steps and these reactions are strongly affected by diffusion of the reactants, an initial quantum yield of  $\Phi_P = 0.03$  seems to be a promising value.

A profile plot of the of the transient spectrum of riboflavin tetraacetate diluted in the highly viscous substrate methoxy benzyl alcohol without any solvent after  $\lambda_{EXC} = 450$  nm excitation is shown in Figure 3.9. The transient spectrum renders the reductive quenching of the flavin S<sub>1</sub> state by electron transfer from the substrate within 3.8 ps and the subsequent charge recombination process within 50 ps.

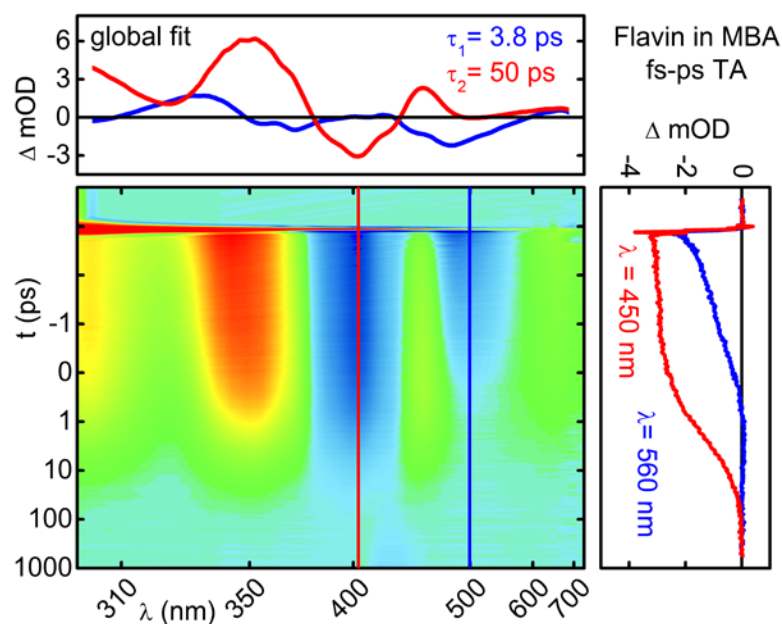


**Figure 3.9** Profile plot of the fs-ps TA measurement of riboflavin tetraacetate diluted in the highly viscous substrate methoxy benzyl alcohol without any solvent after  $\lambda_{\text{EXC}} = 450 \text{ nm}$  excitation. The fast photo-induced transfer of an electron from the substrate to the photocatalyst described by a time constant of  $\tau_1 = 3.8 \text{ ps}$  is indicated by the decay of the stimulated emission of flavin around  $560 \text{ nm}$  (blue time trace,  $\lambda = 560 \text{ nm}$ , right). The transient absorption in the near UV spectral range around  $350 \text{ nm}$  of the flavin radical anion is slightly redshifted compared to the  $S_1$  absorption in this spectral region. The corresponding DADS from the global fit (blue line,  $\tau_1 = 3.8 \text{ ps}$ , top) shows both the decay of the stimulated emission and the shift of the  $350 \text{ nm}$  absorption band. The charge separated state is relatively short-lived and decays within  $50 \text{ ps}$  by charge recombination back to the ground state. The corresponding DADS (red line,  $\tau_2 = 50 \text{ ps}$ , top) renders the decay of all transient spectral signatures.

### Triplet Chemistry – the Key to High Reaction Quantum Yields

The determining factor of the whole reaction pathway is the spin multiplicity of the photo-excited flavin chromophore at the moment when the first electron transfer between catalyst and substrate occurs. In case, that this first electron transfer happens in the  $S_1$  state of flavin, a spin correlated radical ion pair (RIP) with singlet character is formed. Since charge recombination within this intermolecular charge separated state is in principle an allowed process, it occurs with significant probability. The determined time constants were  $\tau_{\text{ET}} \cong 4 \text{ ps}$  for the electron transfer reaction, if photocatalyst and substrate are already in close proximity, and  $\tau_{\text{CR}} \cong 40 \text{ ps}$  for charge recombination. If, however, the first electron transfer occurs after inter-system crossing to the  $T_1$  state of the flavin chromophore, the formed spin correlated radical ion pair still exhibits triplet character [99]. Within such a radical ion pair, the charge recombination is significantly slowed down, since in terms of the Pauli exclusion principle two electrons with parallel spin cannot occupy the same orbital. This differentiation is fundamental for the successive course of the reaction, since a slowed charge

recombination leaves time for subsequent processes, such as proton transfer and the transfer of the second electron-proton pair, which are required partial reactions for product formation. The full scheme of the reaction is depicted in Figure 3.10. However, the time resolved spectroscopic data only give direct evidence for the first electron and for the first proton transfer based on spectroscopic data exclusively from the catalyst. Relying on time resolved spectroscopy, it cannot be unambiguously answered if the second electron and proton transfer still occurs within the same catalyst-substrate pair, which has already accomplished the first reaction step.

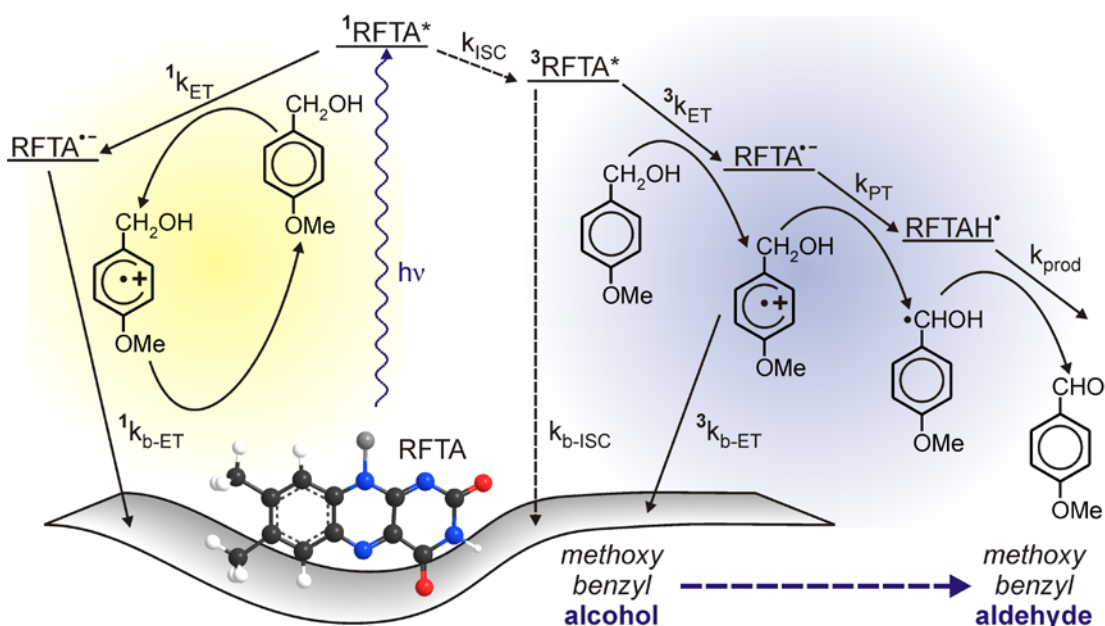


**Figure 3.10** Triplet vs. singlet chemistry: electron transfer between the  $S_1$  state of riboflavin tetraacetate (RFTA) and methoxy benzyl alcohol (MBA) in the singlet manifold leads to a nonproductive electron transfer reaction with nearly instantaneous charge recombination (left side). In contrast, an electron transfer in the triplet manifold is the starting point for a cascade of proton and electron transfer processes leading to product formation (right side). Reprinted from Ref. [183].

Since flavin exhibits a triplet yield of ~70% [182, 184, 185] it is generally a suitable catalyst for triplet chemistry with reasonable quantum yields. Hence, the essential question is how to drive the first electron transfer reaction in the triplet manifold (Figure 3.10, right side) and simultaneously inhibit the nonproductive singlet reaction pathway (Figure 3.10, left side). Toward this goal, there are generally two different approaches: one is to accelerate the inter-system crossing process of flavin and therefore increase its triplet yield. The other is to slow down the electron transfer reaction between flavin and the benzyl alcohol, in order to avoid an efficient singlet electron transfer reaction. Whereas the present study focusses on the latter one it is also possible to substitute the flavin chromophore by more heavier atoms, which would lead to a faster inter-system crossing due to the heavy atom effect [186].

Since initially there was no evidence of pre-association of catalyst and substrate, an effective approach to slow down the reaction kinetics is to adjust the substrate concentration. In the nanosecond time domain, the quenching rate  $k_Q = k_Q([S])$  linearly depends on the quencher concentration  $[S]$ . Hence the task is to find the optimum substrate concentration, which is on the one hand sufficiently high to allow for triplet chemistry in face of a limited triplet life time in aerated solvents. Here, it has to be kept in mind, that in the present reaction diluted oxygen is required as sacrificial electron acceptor to re-oxidize the photocatalyst after the catalytic cycle. On the other hand, the substrate concentration needs to be sufficiently low, to avoid the nonproductive singlet reaction pathway. In these terms a concentration of  $[S] \cong 50$  mM seems to be a good compromise which allows for a maximum quantum efficiency. To find more fundamental answers to the issue of diffusion controlled reaction kinetics, a basic understanding of diffusion controlled reactions on the picosecond time scale at rather high substrate concentrations up to the 1 M regime is required. Therefore a quantitative treatment of diffusion controlled processes on the basis of the Einstein-Smoluchowski Theory of diffusion was introduced (Chapter 2.2).

#### The Einstein-Smoluchowski Theory of Diffusion

The signal of the stimulated emission, which precisely quantifies the population dynamics of the flavin  $S_1$  state was used as a probe signal to accurately trace the electron transfer dynamics between catalyst and substrate. The underlying electron transfer reaction is clearly evident since the formed flavin radical anion is spectroscopically accessible [146]. The observed  $S_1$  quenching clearly shows non-exponential dynamics and therefore an adapted fit function (Equation 3.10) was fitted to the data. As a result, the application of this model revealed some kind of pre-association between catalyst and substrate. Therefore Equation 3.10 comprises an additional exponential term describing the dynamics in these pre-associated catalyst-substrate complexes. Whether the observed pre-association is of statistical character or based on physical interaction between RFTA and MBA cannot be answered yet.

$$n(t) = n_{\text{contact}} \cdot \exp\{-k_{\text{ET}}^0\} + n_{\text{diff}} \cdot \exp\left\{-\frac{t}{\tau_{S_1}} - 4\pi R[S]_0 \cdot \left[1 + \frac{2R}{\sqrt{4Dt}}\right] \cdot t\right\} \quad (3.10)$$

In this equation  $n_{\text{contact}}$  is the amount of excited molecules undergoing a fast, non-diffusive electron transfer reaction, described by  $k_{\text{ET}}^0$ , due to catalyst-substrate pre-association.  $n_{\text{diff}}$  is the amount of molecules undergoing diffusion controlled reaction dynamics, which are described by the second exponential term. The intrinsic life time of the excited singlet state is  $\tau_{S_1}$ . The encounter distance, at which both reactants undergo the electron transfer reaction is  $R$ , the initial concentration of substrate molecules in number of particles per unity volume is  $[S]_0$  and the diffusion constant describing the diffusional motion of both reactants is  $D$ .



For a detailed derivation of the applied fit function, based on Einstein-Smoluchowski Theory of diffusion, which typically describes diffusion limited quenching processes on the ps time scale at high quencher concentrations, the interested reader is referred to Ref. [43] and to Appendix A.1. A closer view to the determined fit parameters provides further insights into the reaction mechanism. A consistent set of fit parameters and the derived physical quantities in two different solvents are presented in Table 3.2.

**Table 3.2** Fit parameter and physical quantities derived from the fit function (Equation 3.10): diffusion constant  $D$  at a substrate concentration of  $[S] = 0$ , molecular radius, which is relevant for diffusion  $R_{\text{diff}}$ , effective viscosity of the solvent environment  $\eta$ , encounter distance  $R$ , time constant for ultrafast electron transfer within pre-associated catalyst-substrate pairs  $\tau_{\text{ET}}$  and association constant  $K_{\text{Fla-MBA}}$  for catalyst substrate association. Table reprinted from Ref. [177].

	<b>98% MeCN 2% DMSO</b>	<b>50% MeCN 50% H<sub>2</sub>O</b>
<b><math>D([S] = 0)</math></b>	$1.4 \cdot 10^{-9} \text{ m}^2 \text{ s}^{-1}$	$0.4 \cdot 10^{-9} \text{ m}^2 \text{ s}^{-1}$
<b><math>R_{\text{diff}}</math></b>	0.45 nm	0.8 nm
<b><math>\eta</math> (T = 300 K)</b>	0.34 mPas	0.68 mPas
<b>R</b>	0.38 nm	0.63 nm
<b><math>\tau_{\text{ET}}</math></b>	4.5 ps	0.95 ps
<b><math>\tau_{\text{CR}}</math></b>	39.5 ps	6.2 ps
<b><math>K_{\text{Fla-MBA}}</math></b>	$0.17 \text{ M}^{-1}$	$0.60 \text{ M}^{-1}$

The comparison of the fit parameters obtained both in nearly pure acetonitrile (98% MeCN, 2% DMSO) and in an equal mixture of acetonitrile and water (50% MeCN, 50% H<sub>2</sub>O), clearly reveals increased values of the encounter distance  $R$  and the molecular radius  $R_{\text{diff}}$ , which is relevant for diffusion, in MeCN/H<sub>2</sub>O in comparison to MeCN/DMSO. This observation strongly suggests that in presence of water, a solvent shell of water molecules surrounds the reactants and in particular the flavin chromophore. Also water seems to significantly accelerate the electron transfer dynamics within pre-associated catalyst-substrate complexes. Certainly the solvent dependent standard oxidation potential of methoxy benzyl alcohol [187, 188] is contributing to the increased electron transfer rate (vide infra). The hypothesis of a solvent shell of water is also supported by a recent publication [189], in which flavin-flavin aggregation was found to be significantly less intense in a pure water environment or in a mixture of water and acetonitrile than in pure acetonitrile. This observation corroborates the picture obtained by applying an advanced data analysis since flavin is supposed to aggregate both by  $\pi$ - $\pi$  interaction, leading to stacks of two identical chromophores which are parallel and in close proximity, and via hydrogen bonding, leading to a more loose bonding between two flavins [189, 190]. The surrounding

water shell seems to effectively inhibit this aggregation process since the water molecules are able to undergo hydrogen bonding as well and compete with hydrogen bonding mediated flavin-flavin aggregation. The altered value of the diffusion constant  $D$  in Table 3.2 is not surprising and can be easily explained with the increased molecular radii due to solvent association and with a change in solvent viscosity due to the addition of water.

### Singlet vs. Triplet Chemistry – Describing the Difference with Marcus Theory

The transient absorption measurements not only provide microscopic insights into the reaction mechanism. The transient absorption data both on the fs-ps and on the ns- $\mu$ s time scale reveal that the electron transfer dynamics are significantly slowed down in the triplet manifold in comparison to the singlet manifold. A ratio of  ${}^1k_{\text{ET}}/{}^3k_{\text{ET}} = (6.4 \text{ ns})^{-1}/(2046 \text{ ns})^{-1} \cong 320/1$  between singlet and triplet excited-state quenching, which are both diffusion limited processes was found at a substrate concentration of  $[S] = 50 \text{ mM}$ . One emerging question is, if a substantial change of the reaction mechanism or just the change of the energetics between singlet and triplet regime accounts for this observation. The lowest triplet state of the flavin chromophore ( $E_{\text{T1}} \cong 2.17 \text{ eV}$ ) [191] is lower in energy with respect to its lowest excited singlet state ( $E_{\text{S1}} \cong 2.58 \text{ eV}$ ). According to Marcus Theory [55, 56] and based on the calculated change of Gibbs energy  $\Delta G^0$  [63], the expected behavior of the reaction rate in the triplet state can be readily estimated. Therefore the redox properties of the contributing reactants are required: the potential for the one electron reduction of Flavin in its oxidized ground state is  $E^0(\text{Fla}/\text{Fla}^{\bullet-}) = -0.292 \text{ V}$  (vs. NHE) [145], the potential for the one electron oxidation of methoxy benzyl alcohol (MBA) is  $E^0(\text{MBA}^{\bullet+}/\text{MBA}) = 1.98$  (vs. NHE) in acetonitrile and  $E^0(\text{MBA}^{\bullet+}/\text{MBA}) = 1.7$  (vs. NHE) in water [187, 188]. Since the present study was performed in an equal mixture of acetonitrile and water, the use of an averaged value of  $E^0(\text{MBA}^{\bullet+}/\text{MBA}) = 1.84$  seems to be justified. According to Rehm and Weller [63] (Equation 3.2.) a change of Gibbs energy of  ${}^1\Delta G^0 = -0.45 \text{ eV}$  in the singlet manifold and  ${}^3\Delta G^0 = -0.04 \text{ eV}$  in the triplet manifold can be derived. Since the electronic coupling  $H_{\text{AB}}$  and the temperature  $T$  is supposed to remain constant in singlet and in triplet chemistry, the only term which has to be considered is the exponential term of the Marcus equation (Equation 3.1) comprising  $\Delta G^0$  and  $\lambda$ . Since reported values of the reorganization energy  $\lambda$  of common charge transfer processes only vary weakly and are in the 1 eV regime (see Chapter 3.1), a typical value of  $\lambda = 0.8 \text{ eV}$  is assumed in Equation 3.11.

$$\frac{{}^1k_{\text{ET}}}{{}^3k_{\text{ET}}} = \exp\left(-\frac{1}{k_{\text{B}}T} \cdot \frac{1}{4\lambda} \cdot \left[ \left(\lambda + {}^1\Delta G^0\right)^2 - \left(\lambda + {}^3\Delta G^0\right)^2 \right]\right) = \frac{295}{1} \quad (3.11)$$

The estimated ratio of 295/1 corresponds very well to the actually observed ratio of  ${}^1k_{\text{ET}}/{}^3k_{\text{ET}} = 320/1$  (vide supra). Hence, it is evident that only the change in energy between singlet and triplet state accounts for the significant decrease of the electron transfer rate in the triplet manifold.

The highest observed quantum yield for product formation of  $\Phi_{\text{p}} = 0.03$  in flavin-mediated photooxidation of methoxy benzyl alcohol still leaves room for improvement. Therefore in

the group of Burkhard König (University of Regensburg) the flavin chromophore was substituted by more heavier atoms such as iodine and bromine to utilize the heavy atom effect [186] for a faster and more efficient inter-system crossing. In a first measurement series on the fs-ps time scale, performed in cooperation with Roger-Jan Kutta (University of Regensburg) the effect of accelerated inter-system crossing could be observed, as well as improved reaction quantum yields were found in irradiation experiments. However, in terms of tweaking the course of the reaction toward an improved quantum efficiency, the influence of the substitution on the triplet energy of flavin has to be considered since the estimated change of Gibbs energy within the triplet reaction in the present system of  ${}^3\Delta G^0 = -0.04$  eV is only slightly below zero.

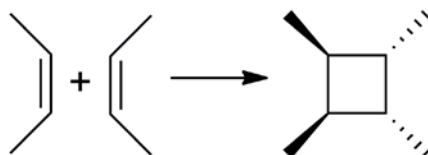
Although flavin chemistry has been subject of many scientific publications, there are still unanswered questions, particularly regarding the influence of water [192] on the total course of the reaction. It is yet not fully understood why the addition of water to the solvent causes such a dramatic increase of the reaction performance. As discussed above, one important point seems to be the solvent dependence of the one electron oxidation potential of methoxy benzyl alcohol. The question if the influence of water to the total course of the reaction is only one little piece in a complex framework or if water is the crucial element in the whole reaction cannot be answered yet.



## 4. Beyond Photoredox Catalysis: [2+2] Cycloaddition Reactions

### 4.1 The Intramolecular Photo-Induced [2+2] Cycloaddition in Quinolones

In organic synthesis, a straightforward method for the preparation of cyclobutane rings<sup>12</sup> is the [2+2] cycloaddition of olefins<sup>13</sup> [193]. The [2+2] cycloaddition reaction comprises the transformation of two independent, carbon-carbon double bonds into a four-membered ring, in which four carbon atoms are covalently linked with each other by single bonds, as shown in Scheme 4.1. Since thermal [2+2] cycloadditions are limited both in scope and usefulness [194] and due to the recent enormous development of light-driven synthesis pathways [195], photo-induced cycloaddition reactions have emerged as versatile method for the formation of cyclobutane rings. The light-induced [2+2] cycloaddition was first reported in 1908 by the Italian photochemist Giacomo Luigi Ciamician, who was already quoted in the introduction of the present thesis, when he observed the conversion of carvone (flavoring substance of, e.g., caraway, dill and spearmint) under prolonged exposure to sunlight [196, 197].



**Scheme 4.1** [2+2] Cycloaddition: a four-membered ring is formed out of two double bonds. In this scheme only one possible stereoisomer<sup>14</sup> of the product is shown.

In particular when the reaction exhibits intermolecular character, the photo-induced [2+2] cycloaddition involves the addition of a photo-activated double bond to a double bond, which is not part of the absorbing chromophore [198]. Serious considerations about the mechanism of the [2+2] photocycloaddition go back to the 1950s. Büchi and Goldman proposed two distinctly different reaction mechanisms, one involving an ionic singlet intermediate and the other involving a diradical triplet intermediate [199]. Corey and coworkers picked up this hypothesis and proposed an intermediate state of the [2+2] cycloaddition, in which only one of the new bonds is formed yet [198]. This intermediate state is discussed to exhibit a 1,4-diradical character and is supposed to appear in thermally mediated [2+2] cycloaddition reactions as well [200]. Also De Mayo and coworkers investigated the mechanism of the [2+2] photocycloaddition with focus on this intermediate state and claimed the formation of this state to be a reversible step [201]. This means that after the first bond of the cyclobutane ring is formed, there is a significant possibility for this intermediate state to decay back to the starting material by breaking up

---

<sup>12</sup> cyclobutane rings are four membered rings consisting of four carbon atoms which are covalently linked by single bonds

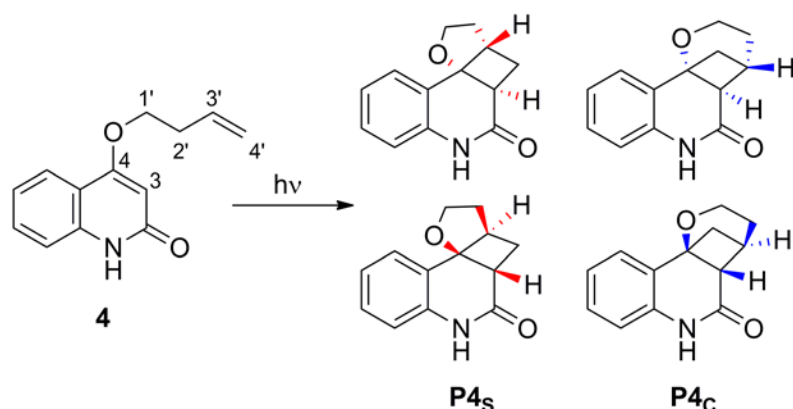
<sup>13</sup> olefins are unsaturated organic compounds containing at least one carbon-to-carbon double bond C=C

<sup>14</sup> stereoisomers exhibit the same bond structure, but the geometric positioning of atoms and functional groups in space differs; the class of stereoisomers comprises enantiomers (mirror images of each other and non-superposable) and diastereoisomers (not related as mirror images)

the recently formed bond. Although many mechanistic details of the actual mechanism of the [2+2] photocycloaddition have been intensively discussed, there is still very little literature dealing with the real time analysis of this reaction with the help of time resolved spectroscopic methods. A study of a pseudo-bimolecular photocycloaddition in the gas phase was presented by Stolow and coworkers [202]. In contrast to the previously introduced mechanism, a concerted bond formation in the excited singlet state was proposed. However, for the present thesis this mechanism is only of minor interest, since it involves the reaction of a completely different chromophore under quite artificial conditions in the gas phase.

Another important aspect, that draws major attention to the [2+2] photocycloaddition is the distinct stereochemistry of this reaction [203, 204, 205, 206, 207]. As shown in Figure 4.1 it is easily conceivable that the creation of the four-membered ring allows the formation of different stereoisomers, where the remaining bonds, which are not contributing to the newly formed cyclobutane ring, can exhibit different relative configurations: whether the uninvolved bonds points into (  $\cdots$  ) or out of (  $\nearrow$  ) the drawing plane. This leads to different stereoisomers of the product, which typically appear in equal ratios when no stereoisomer is sterically or energetically favored.

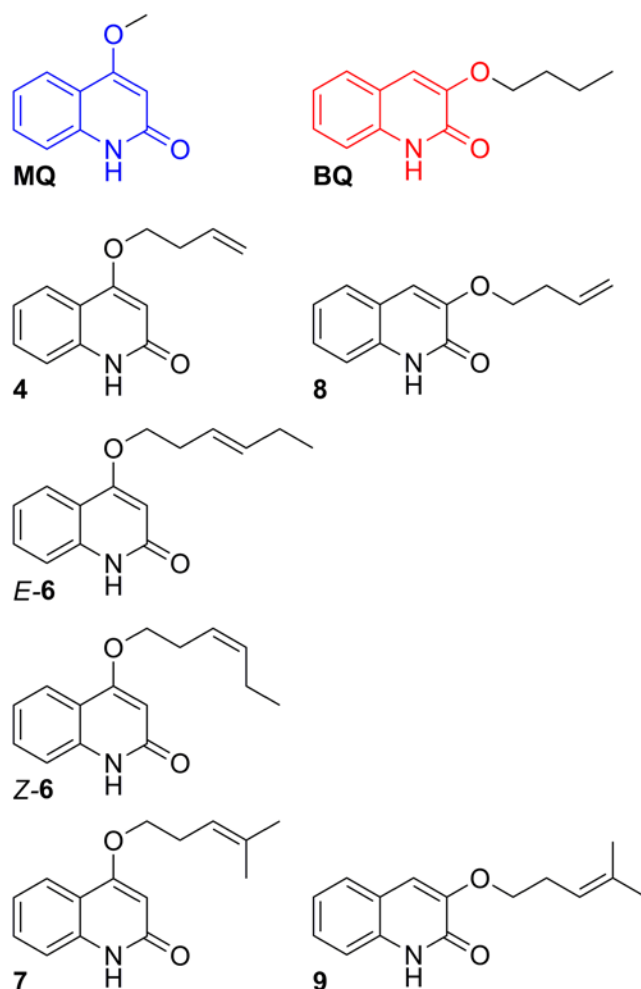
The mechanistic study performed in the framework of the present thesis is based on the intramolecular [2+2] photocycloaddition of substituted quinolones, which was first described by Kaneko and coworkers [208]. Since substituted quinolones serve as a versatile target in enantioselective photoorganocatalysis [5, 156], which will be discussed in Chapter 4.2, a fundamental knowledge and characterization of the individual steps of the photo-induced, non-catalyzed cyclobutane ring formation is essential for a mechanistic understanding of the whole catalytic reaction. Direct photo-excitation of the well studied prochiral reference compound **4** (Scheme 4.2), which comprises a 3'-butenyloxy side-chain attached to the quinolone chromophore, leads to two regioisomeric products: the predominant straight product **P4<sub>s</sub>**, and the crossed product **P4<sub>C</sub>** with a regioisomeric ratio (r.r. = **P4<sub>s</sub>**/**P4<sub>C</sub>**) of r.r. = 86/14 [156].



**Scheme 4.2** Intramolecular [2+2] photocycloaddition of 4-(3'-butenyloxy)quinolone **4** to two different enantiomers of the predominant straight product **P4<sub>s</sub>** and the crossed product **P4<sub>c</sub>**.

Since a triplet state is supposed as key intermediate state within the course of the [2+2] photocycloaddition [209], a triplet mechanism is likely in the present system as well. Since the triplet-triplet absorption band of the parent compound carbostyryl is centered around 450 nm [210, 211], transient absorption spectroscopy in the UV and visible spectral range seems to be a perfectly suited tool to provide answers to questions regarding the actual course of the [2+2] photocycloaddition.

For a systematic study of the [2+2] cycloaddition of quinolones and especially to answer the question regarding the effect of a varying side chain on the reaction dynamics and the product properties, in particular its stereochemistry, different substituted quinolones were synthesized in the group of Thorsten Bach (Technical University Munich). All compounds are depicted in Scheme 4.3. In general, effects of differently substituted side chains on two positions of the quinolone chromophore were tested in the framework of this study: the side chain was attached to carbon 4 in compounds **4**, **6** and **7** in contrast to carbon 3 in compounds **8** and **9**. 3-butoxyquinolone (**BQ**) and 4-methoxyquinolone (**MQ**) served as reference compounds to study the intrinsic photophysical properties, such as excited state absorption properties and the life time of the excited singlet and triplet state, since **BQ** and **MQ** cannot undergo a [2+2] cycloaddition due to the inexistent required second carbon-carbon double bond in the side-chain.



**Scheme 4.3** Quinolone compounds with varying substitution patterns: in compounds **4**, **6** and **7** (chromophore drawn in red) the side chain is attached to carbon 4, in compound **8** and **9** (chromophore drawn in blue) the side chain is attached to carbon 3.

One essential issue, which has to be covered for a full understanding of the mechanism, is regarding the first bond formation of the cyclobutane ring, since a stepwise mechanism is expected [196, 209]. For the sake of simplicity only the formation of the predominant straight product **P4<sub>s</sub>** will be discussed. Since all synthesized quinolones, which can undergo an intramolecular [2+2] photocycloaddition, qualitatively show the same photochemical behavior and only differ quantitatively, it is sufficient just to discuss the reaction kinetics based on quinolone **4**, which is exemplarily for all other compounds **6-9**. Generally, there are two different positions for the first cyclization reaction to occur: either the first bond is formed between carbon 4' of the side chain and carbon 3 of the chromophore forming a seven-membered ring, or the first bond is formed between carbon 3' and carbon 4 forming a five-membered ring (see Scheme 4.2). A clear answer to the question regarding the position of the first bond formation can be found in literature [212, 213], where the formation of five-membered rings is favored over formation of a seven-membered ring. This rule is sometimes called the "Rule of Five" [196, 209].



Transient absorption measurements covering time scales from ps to ns in combination with the determination of reaction quantum yields and the characterization of the photoproducts, performed in the group of Thorsten Bach, revealed a clear mechanistic picture of the [2+2] photocycloaddition. The results of this study are summarized and described in detail in the following publication (see Appendix A.6):

**Intramolecular [2+2] Photocycloaddition of 3- and 4-(But-3-enyl)oxyquinolones: Influence of the Alkene Substitution Pattern, Photophysical Studies and Enantioselective Catalysis by a Chiral Sensitizer**

Mark M. Maturi\*, Matthias Wenninger\*, Rafael Alonso\*, Andreas Bauer, Alexander Pöthig, Eberhard Riedle, Thorsten Bach

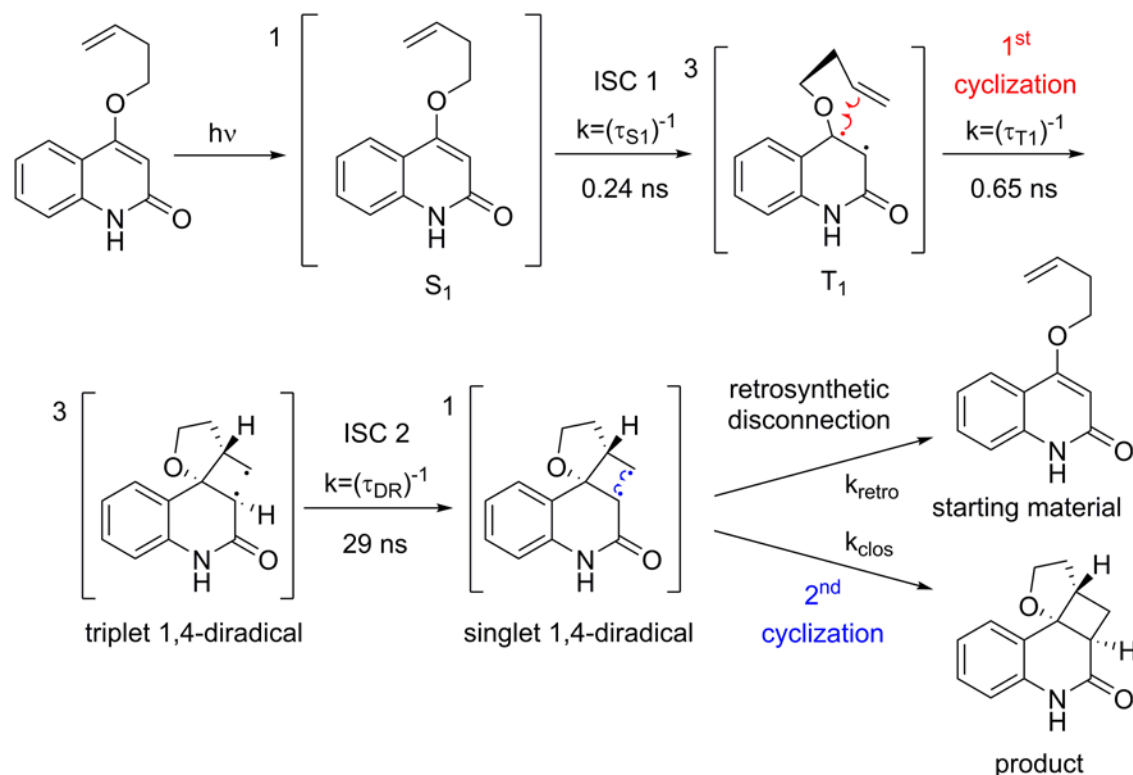
*Chemistry – A European Journal* **2013**, *13*, 7461-7472

\*) these authors contributed equally to this work

The UV/Vis absorption and fluorescence properties are found to be comparable for compounds **MQ**, **4**, **6** and **7** and for compounds **BQ**, **8** and **9**, which was expected since the substitution pattern of the side chain does not qualitatively affect the electronic properties of the light absorbing chromophore. Only the absolute intensity of the  $S_1 \leftarrow S_0$  transition increases by a factor of two going from **MQ**, **4**, **6** and **7** to **BQ**, **8** and **9**, which is still in agreement with the underlying picture. The measured absorption and fluorescence spectra were used to calculate the radiative decay rate<sup>15</sup>  $k_{\text{rad}} = (\tau_{\text{rad}})^{-1}$  according to Strickler und Berg [214]. For both chromophores the radiative decay can be described by a time constant of  $\tau_{\text{rad}} \cong 10$  ns. Since the observed excited state dynamics span a wide temporal range, time resolved spectroscopy both on the fs-ps and on the ns- $\mu$ s time scale was required for the characterization of the whole reaction pathway.

All intermediate states and processes occurring within the course of the reaction are depicted in Scheme 4.4. The reaction follows a mechanism in which the triplet 1,4-diradical plays the central role. Moreover, advanced analysis of the spectroscopic data reveal the species associated spectra (SAS) of each intermediate state and in particular of the triplet 1,4-diradical, which has not been characterized by time resolved spectroscopy yet. Since the population of the triplet state and the subsequent first bond formation both occur with nearly unity quantum yield, the determined decay time constant  $\tau_i$  of each state represents the rate of the underlying process, which populates the next state. Therefore the rate of each partial reaction can be equalized with the inverse life time of the parent state:  $k_i = (\tau_i)^{-1}$ .

<sup>15</sup> the radiative decay rate  $k_{\text{rad}}$  represents only the contribution of the fluorescence decay to the overall  $S_1$  deactivation process and should not be confused with the  $S_1$  deactivation rate  $k_{S_1}$  which can be directly derived from the  $S_1$  life time:  $k_{S_1} = (\tau_{S_1})^{-1}$



**Scheme 4.4** Stepwise mechanism of the [2+2] photocycloaddition of **4** exemplarily shown for all remaining compounds: after photo-excitation ( $h\nu$ ), **4** undergoes inter-system crossing into the triplet state (ISC 1) from where the first cyclization occurs. Since the second bond formation in the triplet state is not spin-allowed, a second inter-system crossing back to the singlet manifold (ISC 2) is required until the second cyclization results in product formation (one possible enantiomer exemplarily shown). The depicted time constants represent the reaction kinetics of quinolone **4**.

The determined life times of all occurring intermediate states are summarized in Table 4.1. The life time  $\tau_{\text{DR}}$  of the triplet 1,4-diradical is  $\tau_{\text{DR}} \cong 30$  ns for **4**, **6** and **7** and  $\tau_{\text{DR}} \cong 24$  ns for **8** and **9**. These values are in good agreement with values presented in literature, where life times of the triplet 1,4-diradical from below 25 ns up to 5  $\mu\text{s}$  were reported in Norrish-Type-II<sup>16</sup> reactions [215, 216], which are related to the present reaction. A triplet diradical life time in the order of 50 ns was estimated in photo-induced [2+2] cycloaddition reactions [209]. The dispersion of the life time of the triplet 1,4-diradical ( $\tau_{\text{DR}} = 29\text{--}34$  ns for **MQ**-based quinolones **4**, **6**, **7** and  $\tau_{\text{D}} = 23\text{--}25$  ns for **BQ**-based quinolones **8**, **9**) is not large and within the measurement error of the applied setup for ns- $\mu\text{s}$  transient absorption spectroscopy. This indicates intersystem crossing from the triplet diradical into a singlet diradical as the main, if not the only process determining the triplet diradical life time [216]. The singlet diradical is supposed to collapse on a significantly faster time scale either to the

<sup>16</sup> a Norrish-Type-II photoreaction is the intramolecular abstraction of a  $\gamma$ -hydrogen by an excited carbonyl compound to produce a 1,4-diradical as a primary photoproduct [9]

product by second bond formation ( $k_{\text{clos}}$ ) or to the starting material by retrosynthetic disconnection ( $k_{\text{retro}}$ ) of the recently formed bond [217]. Since the singlet 1,4-diradical comprises two adjacent unpaired electrons, both with radical character exhibiting anti-parallel spin, it is easily conceivable that the singlet 1,4-diradical state strongly tends to undergo a further reaction after formation. However, the singlet 1,4-diradical is spectroscopically not accessible, since its population rate is much lower as the sum of the depopulating rates  $k_{\text{retro}}$  and  $k_{\text{clos}}$ . It has to be mentioned, that the postulation of this rapidly decaying intermediate singlet diradical state is of rather theoretical nature. In order to maintain the picture of a stepwise reaction mechanism, in which every partial reaction can be individually addressed, an intermediate singlet diradical state seems to be an adequate auxiliary construction to address a physically interested reader.

**Table 4.1** Parameterization of the excited state dynamics of all synthesized quinolones:  $S_1$  life time  $\tau_{S1}$ , triplet life time  $\tau_{T1}$ , triplet 1,4-diradical life time  $\tau_{DR}$  (from transient absorption spectroscopy), quantum yield for product formation  $\Phi_P$  (from actinometric measurements), quantum yield for triplet formation  $\Phi_{T1}$ , quantum yield for triplet 1,4-diradical formation  $\Phi_{DR}$  and ratio  $k_{\text{clos}}/k_{\text{retro}}$  of the rates for second bond formation and retrosynthetic disconnection (calculated on the basis of a sequential rate model). Table reprinted from Appendix A.6.

entry	$\tau_{S1}$ (ps)	$\tau_{T1}$ (ns)	$\tau_{DR}$ (ns)	$\Phi_P$	$\Phi_{T1}$	$\Phi_{DR}$	$k_{\text{clos}}/k_{\text{retro}}$
<b>MQ</b>	229	116	—	—	0.98	—	—
<b>4</b>	237	0.651	29	0.30	0.98	0.98	31/69
<b>Z-6</b>	199	1.319	30	0.72	0.99	0.97	74/26
<b>E-6</b>	202	0.934	32	0.32	0.99	0.98	33/67
<b>7</b>	176	0.647	34	0.26	0.99	0.98	26/74
<b>BQ</b>	296	81	—	—	0.97	—	—
<b>8</b>	362	~1	23	0.73	0.96	0.95	77/23
<b>9</b>	301	0.957	25	0.54	0.97	0.96	57/43

In addition to the transient absorption measurements, the actinometric determination of the product quantum yield  $\Phi_P$  with the help of a tunable laser and UV/Vis absorption spectroscopy (for details see Experimental Section of Appendix A.6) contributed significantly to the understanding and quantification of the reaction mechanism. Technical details of the measurement of product quantum yields in photochemistry are discussed in Ref. [218] and in Appendix A.1. The determined values of  $\Phi_P$ , which are between 0.26 and 0.73, reveal that the over-all reaction is quite efficient although after photon absorption many consecutive steps are required to form a product molecule. Reported quantum yields of

#### 4. Beyond Photoredox Catalysis: [2+2] Cycloaddition Reactions

---

product formation in [2+2] photocycloaddition reactions in the literature are on a comparable scale [205, 206].

The consistent picture of the reaction mechanism and its agreement with previously published results provide a coherent basis for the investigation of the more complex photocatalytic [2+2] photocycloaddition within the catalyst-substrate complex, which will be discussed in Chapter 4.2.

## 4.2 Delocalized Excited States for Light-Induced Enantioselective Organocatalysis

### 4.2.1 Chirality in Nature and the Enantioselective Sensitization of the [2+2] Photocycloaddition by a Chiral Xanthone-Based Photocatalyst

#### Chirality in Nature and the Approach of Enantioselective Photocatalysis

Chirality is one of the most fascinating properties of matter. The quest to synthesize chiral molecules enantioselectively and the desire to understand the underlying reaction mechanism belong to the intellectually most challenging tasks of chemistry [5]. In particular with regard to the biochemical application of certain chiral compounds as pharmaceutical drug, the field of enantioselective synthesis and enantioselective catalysis is of major interest in organic chemistry. There are many catchy examples how the chirality of a molecule significantly affects its chemical interaction with the human body and other biological systems. For instance, the organic molecule carvone, which was already mentioned with respect to the [2+2] photocycloaddition (Chapter 4.1) and the research of Giacomo Luigi Ciamician, appears as flavoring substance both in caraway and in spearmint. Carvone is a chiral molecule and exhibits two enantiomers, which have significantly different effects on our gustatory system: whereas the levorotatory R-(–)-carvone<sup>17</sup> is responsible for the spearmint taste, its mirror image, the dextrorotatory S-(+)-carvone, causes the caraway taste [220]. In particular with regard to the use as pharmaceutical drug, the chirality of the active agent can lead to significantly different effects in the human body. For instance, *d*-amphetamine is three to four times more effective in central nervous system stimulation than its *l*-isomer, whereas the latter is slightly more potent in its cardiovascular action [221]. Also the versatilely applied analgesic drug ibuprofen is a well suited example for the importance of the distinct chirality of a molecule: only the (S)-(+)-ibuprofen exhibits the desired pharmaceutical effect whereas the (R)-(–)-ibuprofen is inactive [222].

Since the different enantiomers of the same molecule require huge technological effort for separation [223] from a racemic<sup>18</sup> mixture, it is strongly desired to exclusively produce one enantiomer of a chiral molecule. The enantioselective synthesis avoids on the one hand the laborious separation of both enantiomers and on the other hand increases the chemical yield of the product with the desired chirality. Not only conventional synthesis pathways but also

---

<sup>17</sup> in stereochemistry there are several terminological systems for the nomenclature of the different enantiomers of a molecule [219]:

- R and S: a chiral center is labeled S (sinister, Latin for left) or R (rectus, Latin for right) based on a system in which the substituents of the chiral center are each assigned a priority according to the CIP (Cahn-Ingold-Prelog) priority rules
- (+) and (–) or *d*- and *l*-: a molecule is labeled *d*- (dextrorotatory) or (+) for clockwise and *l*- (levorotatory) or (–) for counterclockwise rotation of polarized light
- D- and L- (not to be confused with the *d/l* system): compounds are labeled by the spatial configuration of its atoms related to the chiral compound glyceraldehyde as reference

<sup>18</sup> a racemic mixture (also named racemate) is an equimolar mixture of a pair of enantiomers

photocatalytic synthesis pathways are applied to achieve enantioselectivity. The enantioselective catalysis of a photochemical reaction requires chiral compounds, which interact with the substrate during or prior to the optical excitation process. A common approach in stereoselective photochemistry and especially in photocatalysis is to accomplish the two required partial reactions, the stereoselective step and the photo-sensitization, with two different types of catalysts. This method has the important advantage, that it allows the use of well-established standard photocatalysts which do not need to offer intrinsic enantioselectivity. A versatilely applied approach is the use of a chiral imidazolidinone-based organocatalyst providing the stereochemical information, combined with a complementary, non-chiral photoredox catalyst mediating the photosensitization. A mechanism for the enantioselective  $\alpha$ -alkylation<sup>19</sup> of an aldehyde<sup>20</sup> was proposed by MacMillan and coworkers, in which the excited state of the ruthenium centered coordination complex  $\text{Ru}(\text{bpy})_3^{2+}$  acts as photo-induced oxidizing agent for the desired reaction[224]. Also the metal-based coordination complex  $\text{Ir}(\text{ppy})_2(\text{dtb-bpy})^+$  provides capabilities in enantioselective photocatalysis. It has been shown, that the asymmetric  $\alpha$ -trifluoromethylation<sup>21</sup> of aldehydes can be performed with the help of this iridium catalyst acting as photo-induced oxidizing agent [225]. Another example from the group of MacMillan is the application of the metal centered coordination complex  $\text{fac-Ir}^{\text{III}}(\text{ppy})_3$  as photocatalyst. In this reaction, not the iridium complex in its excited state provides the photocatalytic capability. After photo-excitation, the catalyst is first oxidized by a sacrificial electron acceptor to  $\text{fac-Ir}^{\text{IV}}(\text{ppy})_3^+$ , which then acts as strong oxidizing agent for the primary reaction, the enantioselective  $\alpha$ -benzylation<sup>22</sup> and  $\alpha$ -alkylation of an aldehyde [32] (compare Figure 1.1 c). König, Zeitler and coworkers presented a very similar approach for enantioselective photocatalysis. Here, the non-chiral organic dye eosin Y and, as well, the chiral imidazolidinone organocatalyst [224] are used for the photocatalytic intermolecular C-C bond formation [4]. Although the full mechanistic picture of this reaction is not complete yet, the catalyst in its excited state is assumed to act as photoredox catalyst, either as oxidation or reduction agent.

Another approach for enantioselective photochemistry is the use of chiral host compounds, which bind to the substrate [226]. The direct irradiation of the substrate, which is bound to the host compound, leads to an enantioselective bond formation due to steric hindrance. Since this approach does not imply a true photosensitization step from a photo-excited catalyst to the substrate, this reaction is not considered as photocatalytic according to the definition (Chapter 1).

The study, presented in this thesis, is based on a system in which the chiral catalyst and the photocatalyst are combined within one molecular assembly. In the group of Thorsten Bach (Technical University Munich) the organic chromophores benzophenone (compare

---

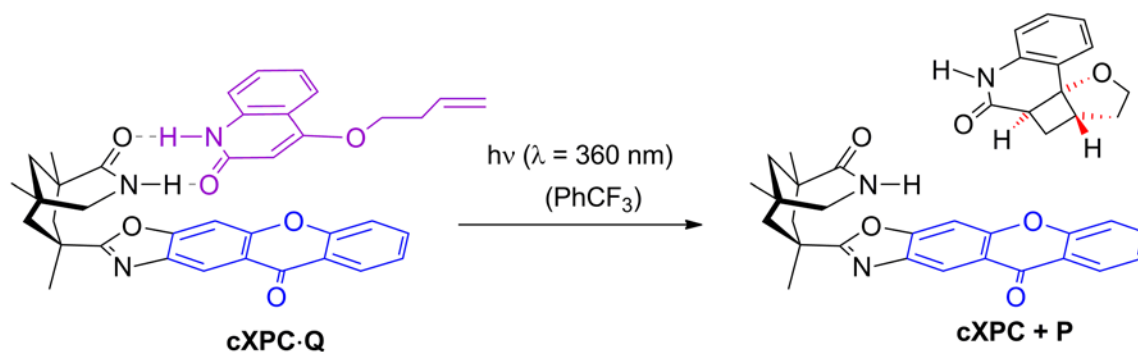
<sup>19</sup>  $\alpha$ -alkylation: transfer of an alkyl group (e.g. methyl- or ethyl-group) next to a carbonyl group ( $\alpha$ -position)

<sup>20</sup> aldehydes are compounds in which a carbonyl group is bonded to one hydrogen atom : -CHO

<sup>21</sup>  $\alpha$ -trifluoromethylation: transfer of a  $\text{CF}_3$ -group next to a carbonyl group ( $\alpha$ -position)

<sup>22</sup>  $\alpha$ -benzylation: transfer of a benzyl group next to a carbonyl group ( $\alpha$ -position)

Chapter 3.4) and xanthone, substituted by a chiral hydrogen-bonding motif, are applied as enantioselective light-driven organocatalysts [5, 156, 227, 228]. Since the intramolecular [2+2] photocycloaddition of substituted quinolones implies a triplet mechanism, the organic chromophore xanthone, which undergoes efficient inter-system crossing (ISC) [229, 230], seems to be perfectly suited as photocatalyst. The mechanistic details of the non-catalyzed intramolecular [2+2] photocycloaddition of substituted quinolones after direct photoexcitation have been described in detail in Chapter 4.1. Chemical yields up to 90% and a rather high enantioselectivity of 94% *ee*<sup>23</sup> can be achieved using the chiral xanthone-based photocatalyst **cXPC** under optimum reaction conditions [156]. The structures of the photocatalyst-substrate complex **cXPC·Q**, comprising the chiral xanthone-based photocatalyst **cXPC** and the pro-chiral quinolone substrate **Q** (equal to **4** in Chapter 4.1), and the enantioselectively formed product **P** (equal to **P4<sub>s</sub>** in Chapter 4.1) are depicted in Scheme 4.5. According to the scheme, it is easily conceivable, that the presence of the rigid xanthone chromophore sterically hinders the formation of one stereoisomer of the product **P** and therefore provides enantioselective bond formation.



**Scheme 4.5** Catalyst-substrate complex **cXPC·Q**: xanthone moiety (blue), chiral binding site (black) and 4-(but-3-enyl)oxyquinolone **Q** (purple) as prochiral target for enantioselective photocatalysis. Under various reaction conditions at low temperatures ( $T = -25\text{ }^{\circ}\text{C}$ ) the straight product **P** is predominantly formed with an enantioselectivity of up to 94% *ee* [156].

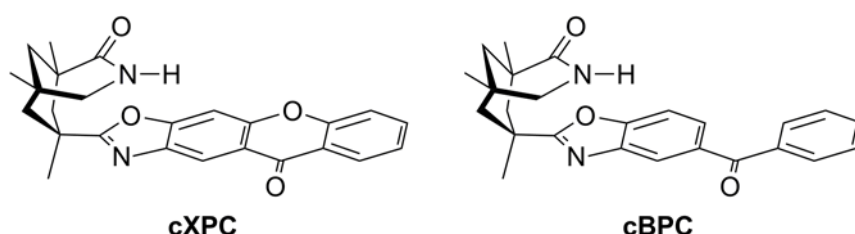
The triplet energy levels of **cXPC** ( $E_T \cong 2.95\text{ eV}$ ) and **Q** ( $E_T \cong 3.07\text{ eV}$ ) [231], which are comparable and shown in Table 4.2, suggest a triplet-triplet energy transfer mechanism [30] as the sensitization mechanism for the subsequent [2+2] photocycloaddition [156]. The ultrafast ISC of xanthone [230], which makes a competing singlet reaction less efficient, corroborates this picture. However the results presented in this chapter will reveal an unexpected, new picture of the reaction mechanism, which actually accounts for sensitization of the enantioselective photocatalytic reaction.

<sup>23</sup> the enantiomeric excess (% *ee*) describes the composition of a sample with regard to the occurrence of different enantiomers and is defined by the mole or weight fractions  $F_{(+)}$  and  $F_{(-)}$  of both enantiomers [219]:

$$\% ee = \frac{F_{(+)} - F_{(-)}}{F_{(+)} + F_{(-)}} \times 100\%$$

### Triplet-Triplet Energy Transfer and Photo-Induced Electron Transfer: Sensitization Experiments with Xanthone and Benzophenone

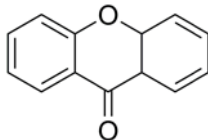
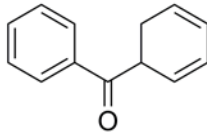
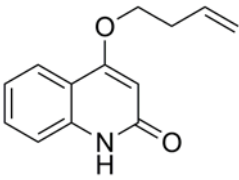
In the group of Thorsten Bach two different chiral photocatalysts based on common organic chromophores are applied for enantioselective photocatalysis: one utilizes benzophenone, the other xanthone as photocatalytic active moiety. The structures of the chiral xanthone-based photocatalyst **cXPC** and the chiral benzophenone-based photocatalyst **cBPC** are shown in Scheme 4.6



**Scheme 4.6** Chiral xanthone-based photocatalyst **cXPC** and chiral benzophenone-based photocatalyst **cBPC** applied for enantioselective photocatalysis.

Whereas a triplet-triplet energy transfer (TTET) seems to account for the sensitization process of the xanthone-based photocatalyst **cXPC** [156] a photo-induced electron transfer, in which benzophenone acts as electron acceptor, is assumed to account for the sensitization process of the benzophenone-based photocatalyst **cBPC** [227]. This differentiation gives evidence that depending on the photocatalyst, different reaction mechanisms are leading to an analogous conversion of the substrate. Whereas the TTET mechanism involves an intermediate triplet state of quinolone  $^3[\mathbf{Q}]$  as the parent state of the subsequent [2+2] photocycloaddition, the photo-induced oxidation involves a quinolone radical cation. However, it is reported in the literature that not only the triplet state but also the radical cation state represents a parent state of the [2+2] photocycloaddition [194]. The comparison of the triplet energies of all relevant compounds in Table 4.2 clearly reveals that the triplet energy of pure xanthone is sufficient to allow for sensitization of the pro-chiral quinolone **Q** via TTET.

**Table 4.2** Triplet energies  $E_T$  of different compounds: xanthone and benzophenone from Ref. [165], quinolone from Ref. [231]

			
	xanthone	benzophenone	quinolone ( <b>Q</b> )
$E_T$	310 kJ/mol 3.2 eV	287 kJ/mol 3.0 eV	297 kJ/mol 3.1 eV



As proof of concept and to ensure that both xanthone and benzophenone are suited for the sensitization of the [2+2] photocycloaddition of **Q**, pure xanthone and pure benzophenone were used as photosensitizer in irradiation experiments. The diffusion-controlled sensitization of **Q** shows both with xanthone and with benzophenone a significant increase of reaction efficiency in comparison to pure quinolone under equal irradiation conditions. Both sensitization experiments lead to a near unity product yield [5].

However, the situation looks completely different going from the diffusion-limited triplet sensitization, which is intrinsically not a stereoselective process, to the stereoselective photocatalytic process, where catalyst and substrate form a complex. For the stereoselective conversion of quinolone **Q**, the chiral xanthone-based photocatalyst **cXPC** and the chiral benzophenone-based photocatalyst **cBPC** were applied. The most significant difference can be seen by comparing the enantiomeric excess (% *ee*) of both reactions: whereas the use of **cXPC** as chiral photocatalyst leads to an enantioselectivity of 92% *ee*, the use of **cBPC** yields only 39% *ee* under the same experimental conditions [5]. This observation stands in strong contrast to the previous results, where benzophenone showed even a slightly better photocatalytic performance.

These results provide first evidence that the intrinsic photophysical properties of xanthone and benzophenone do not remain unaffected in the photocatalytic complex. It seems that within the catalyst-substrate complex comprising the xanthone-based photocatalyst **cXPC**, new properties arise, which do not appear in the complex comprising the benzophenone-based photocatalyst **cBPC**. This effect would explain the significant difference in enantioselectivity. Both the attached chiral binding site and the close stacking of catalyst and substrate which leads to an overlap of the  $\pi$ -orbitals of both constituents are suited to affect the photophysical properties of xanthone and quinolone within the complex. The fundamental investigation of the photocatalytic system based on the chiral xanthone-based photocatalyst **cXPC** with the help of transient absorption spectroscopy on multiple time scales finds answers to this substantial question.

### Outline

The argumentation presented to explain the reaction mechanism of the enantioselective photocatalyzed [2+2] photocycloaddition is rather complex and relies on a large number of experimental results originating from different experimental techniques. This outline therefore provides a brief overview of the fundamental steps of the following argumentation:

- 4.2.2 Experimental Section

This chapter basically describes the preparation of the sample solutions containing the photocatalyst and different substrates applied for steady state and time resolved spectroscopic measurements. Also the experimental conditions of the performed TA measurements on different time scales and the achievable temporal resolution in the fs-ps TA measurements are discussed. In order to allow the quantitative comparison of different TA measurements, a reasonable scaling factor is introduced which accounts for deviations in signal intensity caused by a

differing composition of the sample solutions and a varying excitation energy density. Furthermore the method of spectroelectrochemistry and the related experimental details are introduced.

- 4.2.3 For a Basic Understanding: Diffusion Controlled Sensitization of the [2+2] Photocycloaddition with Pure Xanthone as Sensitizer

Preliminary studies from the group of Thorsten Bach referred to the diffusion-controlled sensitization of the [2+2] photocycloaddition by unsubstituted xanthone and benzophenone as reference system for the enantioselective photocatalysis. Therefore the diffusion-controlled sensitization process of quinolone by unsubstituted xanthone is quantified with the help of ns- $\mu$ s TA spectroscopy. These results are perfectly suited to introduce the approach of combining synthesis and TA spectroscopy to gain a basic understanding of a photocatalytic process. In a first measurement, the photophysical properties of pure xanthone, in particular its triplet spectrum and its triplet life time in the solvent environment of PhCF<sub>3</sub> are determined. For the investigation of the early steps of the sensitized reaction, in a second measurement, the chemical rather simple reference substrate **MQ** which cannot react in a [2+2] photocycloaddition is applied as reference target. In a third measurement, the actual substrate **Q** provides insight into the subsequent steps of the reaction. Combining the results of all measurements provides a coherent picture of the full reaction mechanism.

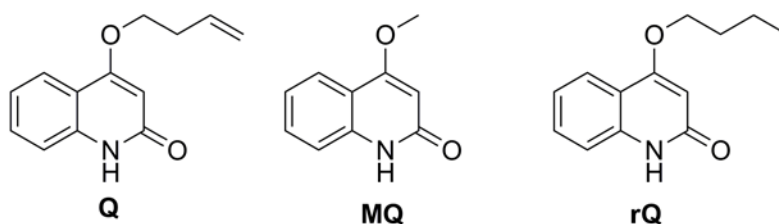
- 4.2.4 Accessing the Mechanistic Details with Transient Absorption Spectroscopy on Multiple Time Scales and Quantum Chemistry

Performing both fs-ps and ns- $\mu$ s TA spectroscopy on the photocatalytic molecular system comprising the xanthone-based photocatalyst **cXPC** with chiral binding site and the pro-chiral substrate **Q** reveals unexpected results. To understand the observed behavior, at first, the underlying association processes of catalyst and substrate in the solvent environment of PhCF<sub>3</sub> are quantified. This allows the calculation of the actual absorption spectrum of the associated catalyst-substrate complex **cXPC·Q**. It turns out, that the spectrum of the complex is not only the sum spectrum of its constituents. The observed deviations of the absorption spectrum are discussed with the help of ab initio calculations. For the spectroscopic investigation of the whole process, in a first measurement series the photophysical properties of the pure chiral xanthone-based photocatalyst **cXPC** on the fs-ps and on the ns- $\mu$ s time scale are determined. In a second measurement series, a reference substrate **rQ**, which cannot react in a [2+2] photocycloaddition serves as target for the investigation of the early steps of the reaction. For the analysis of unknown transient signatures it is referred to spectroelectrochemistry as appropriate tool, which helps to identify an intermolecular charge transfer process. The combination of these measurements resolves the initially unexpected behavior of the catalyst-substrate system and reveals the full reaction mechanism of the enantioselective photocatalytic process.

## 4.2.2 Experimental Section

### Preparation of the Samples

The quantification of a complex reaction mechanism, which comprises many subsequent reaction steps, requires the detailed understanding of each partial reaction. Therefore, the discussion of the photocatalytic process is based on a very similar approach as already introduced in Chapter 4.1: different reference compounds, quinolones **MQ** and **rQ**, which cannot react in a [2+2] photocycloaddition serve as target to study the intrinsic sensitization process, the suggested TTET between catalyst and substrate. Overlying photochemical processes, which would make the data analysis more difficult, do not occur in the reference quinolones. The light-absorbing chromophore, which determines the photophysical properties, is identical in all quinolones **MQ**, **rQ** and **Q**. The only difference can be found in the covalently bound side chain, which does not significantly affect the electronic properties of the light absorbing chromophore. The structures of all investigated quinolones are shown in Scheme 4.7.



**Scheme 4.7** Quinolones synthesized in the framework of the present study: quinolone **Q**, which is able to undergo the [2+2] photocycloaddition and methoxy quinolone **MQ** and reference quinolone **rQ**, which cannot react in a [2+2] photocycloaddition.

All sample solutions for TA spectroscopy and for UV/Vis absorption spectroscopy were prepared by Mark Maturi (Group of Thorsten Bach) in the chemistry laboratories at the Technical University of Munich (TUM). A first series of compounds was prepared for TA measurements in March 2013 and a second series was prepared in October 2013 for the measurement of the UV/Vis absorption spectra. To resolve inconsistencies with previously published data, an exact quantification of the absorption coefficients of all compounds was performed in December 2013 in the chemistry laboratories at the TUM. The resulting spectra are shown in Figure 4.1.

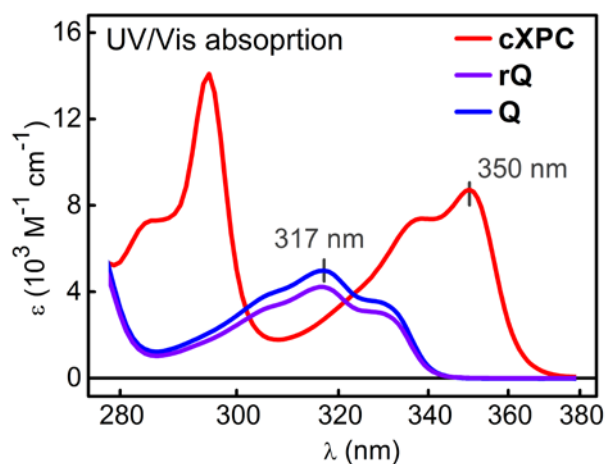


**Figure 4.1** UV/Vis absorption spectra of the chiral xanthone-based photocatalyst **cXPC** and quinolones **rQ** and **Q**.

The absorption properties reveal, that irradiation in the spectral region between 345 and 360 nm provides selective excitation of the photocatalyst **cXPC**. In comparison to pure xanthone, which has its absorption maximum around 337 nm, the absorption maximum around 350 nm of **cXPC** is redshifted. This bathochromic shift is most probably caused by the attached oxazole<sup>24</sup> ring, which expands the  $\pi$ -electron system of the light absorbing xanthone chromophore.

The absorption properties of quinolones **rQ** and **Q** are nearly identical. The only difference is a slight decrease in absorption strength of **rQ**. The fully saturated side chain of **rQ** and the side chain comprising a carbon-carbon double bond of **Q** might exhibit slightly different strengths of electronic interaction with the quinolone chromophore. This potentially affects the absorption properties of the light absorbing chromophore and leads to a minor decrease in absorption strength of **rQ** compared to **Q**.

<sup>24</sup> oxazole is a five-membered ring composed of three carbon atoms, one oxygen atom, and one nitrogen atom with one carbon atom between the oxygen and nitrogen atoms

In a previous study, characteristic absorption coefficients of **cXPC** and **Q** in PhCF<sub>3</sub> for selected wavelengths were published [5]. The more accurately determined values of the absorption coefficients, which were measured in the framework of the present study, are summarized in Table 4.3.

**Table 4.3** Characteristic absorption coefficients of **cXPC**, **rQ** and **Q** determined in PhCF<sub>3</sub> in a 1-mm cuvette (type: Hellma 110-QS) at given reference points: 350 nm for **cXPC** and 317 nm for **rQ** and **Q**.

compound	characteristic absorption coefficient
<b>cXPC</b> in PhCF <sub>3</sub>	$\epsilon(350 \text{ nm}) = 8805 \text{ M}^{-1} \text{ cm}^{-1}$
<b>rQ</b> in PhCF <sub>3</sub>	$\epsilon(317 \text{ nm}) = 4268 \text{ M}^{-1} \text{ cm}^{-1}$
<b>Q</b> in PhCF <sub>3</sub>	$\epsilon(317 \text{ nm}) = 5003 \text{ M}^{-1} \text{ cm}^{-1}$

### Transient Absorption Spectroscopy on the fs-ps Time Scale: Experimental Details

The fs-ps broadband pump-probe setup has been introduced in Chapter 2.1 and is discussed in detail in Ref. [33]. Briefly, a Ti:sapphire amplifier system (CPA 2001, Clark-MXR) with a repetition rate of 1 kHz was used to pump a noncollinear optical parametric amplifier (NOPA) which provides pulses with a center wavelength of ~710 nm. After compression and frequency doubling in a BBO-crystal (100  $\mu\text{m}$  nominal thickness) pump pulses with a center wavelength of ~355 nm were achieved. The beam with a pulse energy of about 400 nJ was focused with a spot size of ~150  $\mu\text{m}$  (FWHM) into a  $d = 0.5$  mm flow cell containing the sample solution with an optical density below 1 within the probed spectrum. A flow cell with fused silica windows with a thickness of just 0.2 mm was used for TA measurements both on the fs-ps and the ns- $\mu\text{s}$  time scale to allow direct comparability. A supercontinuum (285–720 nm) was generated and used as probe by focusing another part of the Ti:sapphire laser into a CaF<sub>2</sub> (4 mm thickness) disk executing a circular translatory motion to avoid degradation of the crystal due to cumulative effects of the high laser intensity. The relative polarization of pump and probe pulses was set to the magic angle ( $\theta = 54.78^\circ$ ) to avoid contributions from the rotational relaxation to the observed kinetics. A computer controlled delay line was used to set pump-probe delays up to  $\Delta t = 2$  ns. After the interaction in the sample, the probe light was dispersed with a fused silica prism and detected with a 524 pixel CCD.

### Spectral and Temporal Characterization of the Excitation Pulse

The excitation pulse applied in fs-ps TA was spectrally characterized with the help of a fiber coupled spectrometer (Ocean Optics USB2000+). The measured spectrum is exemplarily shown in Figure 4.2.

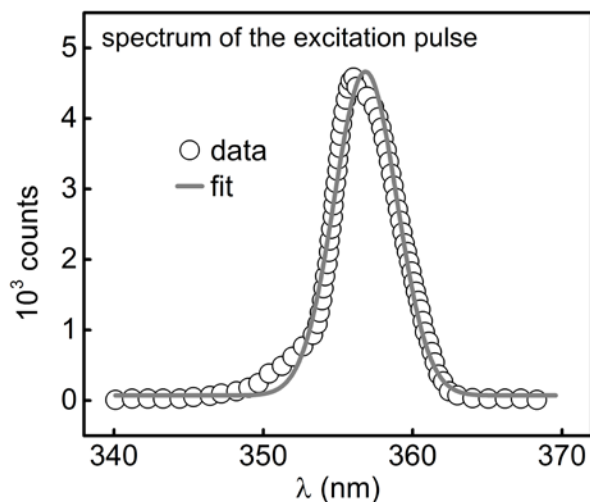


**Figure 4.2** Spectrum of the typical excitation pulse used in the fs-ps TA measurements: data and fit with Gaussian with parameters  $\lambda_0 = 356.8$  nm, FWHM = 4.9 nm ( $= 770$  cm<sup>-1</sup>). The corresponding Fourier limit is  $\Delta t = 40$  fs.

The depicted excitation spectrum was measured in an early TA measurement series in March 2011. All presented fs-ps TA measurements with an excitation wavelength of  $\lambda_{\text{EXC}} = 355$  nm were conducted with comparable spectral characteristics of the excitation pulse. Relying on the spectral shape of the pump pulse, the physical limit of the temporal pulse width is  $\Delta t = 40$  ps.

However, due to the poor solubility of the components and due to the complex association processes of catalyst and substrate it was required to deviate slightly from well established measurement conditions, which are typically applied in fs-ps TA spectroscopy to achieve a high temporal resolution. Therefore limitations regarding the temporal resolution had to be accepted. To achieve a sufficient signal intensity and a high relative contribution of transient signal originating from catalyst-quinolone complexes **cXPC·rQ** and **cXPC·Q**, the TA measurements with an excitation wavelength of  $\lambda_{\text{EXC}} = 355$  nm were performed in a rather thick flow cell with 0.5 mm optical path length and a relatively high excitation energy density of up to  $\sim 2.3$  mJ/cm<sup>2</sup> ( $E_{\text{EXC}} = 400$  nJ,  $D_{\text{FWHM}} = 150$  μm). Therefore the TA setup was optimized toward a rather high excitation energy which not necessarily coincides with the highest temporal resolution. The effective temporal width of the excitation pulse was in the order of  $\Delta t = 80$  fs in all fs-ps measurements, which was experimentally confirmed in an autocorrelation measurement [232].

### Effective Temporal Resolution in fs-ps Transient Absorption Spectroscopy

The achievable temporal resolution of a fs-ps TA measurement is not only determined by the temporal width of the excitation pulse. In the present study, the rather thick flow cell negatively affected the achievable temporal resolution. Due to the 0.2 mm fused silica windows and the 0.5 mm solvent layer, the laser pulse propagated effectively through 0.9 mm of bulk material. In particular, the temporal broadening of the excitation pulse caused by dispersion within the bulk material and the group velocity mismatch [233] between the excitation wavelength and each spectral component of the probe pulse lead to a decrease in temporal resolution.

Within the course of the present study an estimation of the temporal resolution is required to understand the underlying process. Therefore the achieved temporal resolution has to be determined. For an accurate quantification, the temporal width of the coherent artifact, which is caused by interaction of pump and probe pulse within the bulk material of the glass windows and the solvent, represents a meaningful estimate [234]. Therefore the coherent artifact was measured in pure solvent to avoid signals caused by overlying molecular dynamics. The profile plot of the coherent artifact of a fs-ps TA measurement of pure PhCF<sub>3</sub> after  $\lambda_{\text{EXC}} = 355$  nm excitation in a 1 mm flow cell is shown in Figure 4.3.

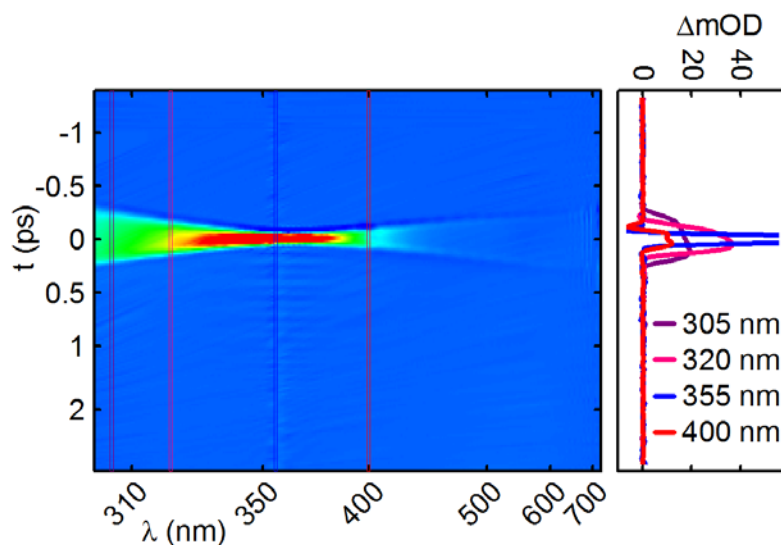


**Figure 4.3** Profile plot of fs-ps TA of pure PhCF<sub>3</sub> ( $\lambda_{\text{EXC}} = 355$  nm,  $E_{\text{EXC}} = 400$  nJ,  $D_{\text{FWHM}} = 150$   $\mu\text{m}$ ,  $d = 1.0$  mm,  $\Delta\text{OD} > 0$  in red,  $\Delta\text{OD} < 0$  in blue).

The symmetric double conical shape of the coherent artifact in the profile plot impressively demonstrates the effect of group velocity mismatch (GVM) between pump pulse ( $\lambda_{\text{EXC}} = 355$  nm) and each spectral component of the probe spectrum. Whereas the artifact is relatively narrow in the spectral region around the excitation wavelength, it significantly broadens with increasing spectral distance. For a more accurate view on the coherent artifact, Figure 4.4 shows the sub-ps signal of selected spectral traces of the transient data matrix.

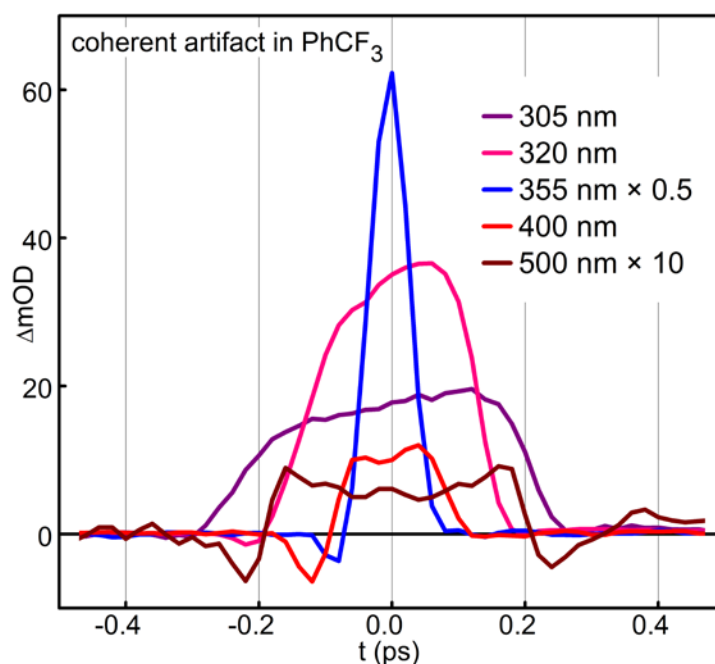


**Figure 4.4** Coherent artifact in pure PhCF<sub>3</sub> of selected spectral traces ( $\lambda_{\text{EXC}} = 355$  nm,  $E_{\text{EXC}} = 400$  nJ,  $D_{\text{FWHM}} = 150$   $\mu\text{m}$ ), measured in a 1.0 mm flow cell.

The temporal width of the coherent artifact of approximately  $\Delta t = 400$  fs at a probe wavelength of 305 nm (purple line, Figure 4.4) represents the limit of the achievable temporal resolution in this measurement. Although the coherent artifact was measured in a 1 mm flow cell whereas the presented fs-ps TA measurements of the photocatalytic system were performed in a 0.5 mm flow cell, this measurement can provide a valid estimate of the achievable temporal resolution in the 0.5 mm flow cell. As the artifact is caused by interaction of pump and probe pulse both within the solvent and the glass windows of the flow cell, the temporal width of the coherent artifact in a 0.5 mm flow cell roughly scales with the factor 0.64 compared to the temporal width in a 1.0 mm flow cell, as shown in Equation 4.1:

$$\frac{2 \cdot 0.2 \text{ mm} + 0.5 \text{ mm}}{2 \cdot 0.2 \text{ mm} + 1.0 \text{ mm}} = 0.64 \quad (4.1)$$

Hence, the limit of the effective temporal resolution in a 0.5 mm flow cell under comparable measurement conditions is  $0.64 \cdot 400$  fs = 240 fs at the edges of the probe spectrum.

### Transient Absorption Spectroscopy on the ns- $\mu\text{s}$ time scale: Experimental Details

For transient absorption measurements on the ns- $\mu\text{s}$  time scale, a pulsed ns laser system (EKSPLA NT242) with 1 kHz repetition rate and integrated OPO for spectral tunability was used as pump. The ns laser is electronically synchronized with the Ti:sapphire amplifier system, running at 1 kHz repetition rate as well. The supercontinuum, generated by the fs laser system as described above was used for spectrally resolved probing. This setup for fs-ps TA spectroscopy, combining two electronically connected laser sources, provides a temporal resolution better than 2.5 ns and allows recording transient absorption spectra up to



temporal delays of some hundred  $\mu\text{s}$ . The details have been described in detail elsewhere [App A.1].

The sample solution is permanently pumped through a degasser (Knauer Smartline Online Degasser) to keep the oxygen concentration low in order to decrease effects of oxygen mediated triplet quenching. In order to ensure comparability between all TA measurements, the ns- $\mu\text{s}$  measurements were conducted in the same flow cell, which was already used for fs-ps TA spectroscopy. Only the diffusion-controlled sensitization experiments with pure xanthone (Chapter 4.2.3) with an excitation wavelength of  $\lambda_{\text{EXC}} = 348.5 \text{ nm}$  were conducted in a commercially available flow cell (Hellma 137-QS) with thicker glass windows.

In all measurements with an excitation wavelength of  $\lambda_{\text{EXC}} = 355 \text{ nm}$ , the energy of the pump pulse was  $E \cong 3 \mu\text{J}$  at the place of the sample. Applying a Gaussian fit function on the strongly inhomogeneous beam profile resulted in a full width half maximum of the beam profile of  $\text{FWHM} \cong 400 \mu\text{m}$ . These parameters ( $E \cong 3 \mu\text{J}$ ,  $\text{FWHM} \cong 400 \mu\text{m}$ ) would lead to a medium excitation energy density of  $0.6 \text{ mJ/cm}^2$  in the focus of the pump pulse assuming a homogenous, Gaussian-shaped beam profile (compare  $2.3 \text{ mJ/cm}^2$  in the fs-ps TA measurements). However, an exact comparability of both values is not given due to the strongly inhomogeneous beam profile in the ns- $\mu\text{s}$  TA measurements. Relying on the absolute signal strength at early times after excitation, the excitation energy density in the ns- $\mu\text{s}$  TA measurements in the probe focus ( $\text{FWHM} \cong 25\text{-}30 \mu\text{m}$ ) was generally 2-3 times higher compared to the excitation energy density in the fs-ps TA measurements. A small factor of 2-3 in excitation energy density still provides an adequate comparability of the reaction dynamics for both types of TA spectroscopy and does not represent a fundamental change in reaction conditions.

### Measurement Protocol and Data Processing

In this section, the measurement protocol, which ensures constant conditions and therefore comparability of the individual measurements, is defined. Although the laser setup applied for fs-ps TA spectroscopy provides relatively stable measurement conditions, some essential physical parameters, particularly regarding the energy, the spectrum and the beam profile of the excitation pulse are required to be checked and potentially realigned from day to day.

The excitation pulse was spectrally characterized after passing a diffusing plate using a miniature fiber optic spectrometer (Ocean Optics USB200+). The averaged intensity of the laser beam was measured using a high sensitivity thermopile sensor device (Coherent FieldMaxII with Coherent PS10Q sensor). The medium pulse energy was calculated from the averaged laser power assuming a repetition rate of exactly 1 kHz. Usually pump and probe beam were overlapped at the z-position where the focused probe beam has its minimum diameter (FWHM). During the TA measurements, the sample flow cell was placed at this position. This ensures a high degree of homogeneity of the beam profile and a high excitation energy density within the probed sample volume. Prior to each measurement the spatial profiles of pump and probe beam were characterized at this position using a laser beam camera (Photon Inc. USBeamPro, Model 2323).

#### 4. Beyond Photoredox Catalysis: [2+2] Cycloaddition Reactions

---

All TA measurements performed in the framework of this study were conducted at room temperature. The following measurement routine was performed each day before starting the fs-ps TA measurements. Deviations exceeding the tolerance limits were corrected.

1. Excitation energy equals  $E = 400 \text{ nJ} (\pm 10\%)$ ?
2. Spectrum of the excitation pulse symmetric, approximately Gaussian-shaped and centered around  $\lambda = 355 \text{ nm} (\pm 1 \text{ nm})$ ?
3. Beam profile approximately Gaussian-shaped with  $\text{FWHM} = 150 \mu\text{m} (\pm 20 \mu\text{m})$ ?
4. Stability of the beam profile during movement of the delay line from  $t = 0 \text{ ps}$  to  $t = 1800 \text{ ps}$ :
  - a. FWHM of beam profile constant ( $\pm 10\%$ )?
  - b. Centroid position of Gauss fit of beam profile constant within  $5 \mu\text{m}$  in x-and in y-direction?

Each scan was performed using the LabVIEW-based measurement acquisition software<sup>25</sup> with the following parameters:

- Time scale: “poly-lin-log” or “riedle\_mini”
- Number of linear points: 80 or 100
- Averages per point: 1200-2000
- Number of scans: 3

These parameters resulted in a data matrix with 358 to 448 measured spectra for different pump-probe delays and lead to a measurement time typically between 60 to 90 minutes. At least 2 of the 3 scans were selected and averaged for the further data processing. The chirp correction was manually conducted for each measurement on the basis of the coherent artifact. All measurements performed within one day are based on the same wavelength calibration, which assigns a wavelength scale to the data matrix. The wavelength calibration is based on the characteristic absorption spectra of selected optical filter [33].

---

<sup>25</sup> program path at the Chair for BioMolecular Optics (Ludwig Maximilian University):  
\\johann\agriedle\Software\_und\_Treiber\Labview\messprogramme\Z22\_Breitband\CCD-Kamera\_v2plus\_2012\_06\_26 (2013-11-30)

Another aspect that has to be considered is the stability of the sample solution during the measurement. Consumption of the substrate or photo-degradation of the photocatalyst would significantly distort the result of a TA measurement. Therefore the ratio of the photons absorbed during the measurement ( $n_\gamma$ ) and the amount of substance of the photocatalyst **cXPC** in the sample solution ( $n_{\text{cXPC}}$ ) provides a good estimate of the average number of excitation cycles of one photocatalyst molecule. During a TA measurement, which can last up to 2 hours, with an averaged excitation energy of 400 nJ, an excitation repetition rate of  $500 \text{ s}^{-1}$  and an excitation wavelength of  $\lambda_{\text{EXC}} = 355 \text{ nm}$ , approximately  $4.3 \mu\text{E}^{26}$  photons are absorbed by the photocatalyst assuming an infinity optical density of the sample solution, as calculated in Equation 4.2:

$$n_\gamma = \frac{400 \text{ nJ} \cdot 500 \text{ s}^{-1} \cdot 7200 \text{ s}}{E_\gamma(\lambda = 355 \text{ nm})} = 2.6 \cdot 10^{18} = 4.3 \mu\text{E} \quad (4.2)$$

The amount of substance was  $n_{\text{cXPC}} = 4 \mu\text{mol}$  of the photocatalyst and  $n_{\text{Q}} = 10 \mu\text{mol}$  of the substrate in a typical sample solution ( $V = 4 \text{ ml}$ ,  $[\text{cXPC}] = 1 \text{ mM}$ ,  $[\text{Q}] = 2.5 \text{ mM}$ ). Hence, a photocatalyst molecule undergoes statistically approximately one excitation cycle within a measurement. Considering that not every excited photocatalyst is bound to a substrate and that excitation of a bound catalyst-substrate complex not necessarily leads to product formation, consumption of the substrate does not cause any significant change in measurement conditions. Furthermore, the estimated quantities in Equation 4.2. of the measurement time and the amount of absorbed photons represent upper limits of the actual values.

### Overlaying Transient Signals from the Solvent and from Quinolone?

The presented TA measurements comprise overlying signals of different origin and therefore show rather complex dynamics. To allow for an accurate decomposition of these signals, it is required to identify background signals originating from the solvent. Therefore, in this section the results of a fs-ps TA measurement of the pure solvent  $\text{PhCF}_3$  are discussed.

A basic concept of photocatalysis is, that exclusively photo-excitation of the photocatalyst leads to the conversion of the substrate – and not the direct excitation of the substrate. In particular in the present approach for enantioselective photocatalysis, direct excitation of the substrate would lead to a competing, racemic product formation, which lowers the enantiomeric excess (% *ee*). Hence, it is required to ensure that no overlying photochemical processes are caused by direct photo-excitation of the substrate. Therefore a reference measurement with an excitation wavelength of  $\lambda_{\text{EXC}} = 355 \text{ nm}$  on a sample solution just containing **Q** in  $\text{PhCF}_3$  was performed. To fulfill the requirements of a true photocatalytic reaction, the TA spectrum of this measurement should not deviate from the TA signal of the pure solvent  $\text{PhCF}_3$  measured under the same experimental conditions. Figure 4.5 shows

<sup>26</sup> the rarely used unit einstein (E) is defined as  $1 \text{ E} = 1 \text{ Mol}$  of photons

selected transient spectra of the fs-ps TA measurements of pure PhCF<sub>3</sub> (a) and the substrate **Q** in PhCF<sub>3</sub> (b) after  $\lambda_{\text{EXC}} = 355$  nm excitation.

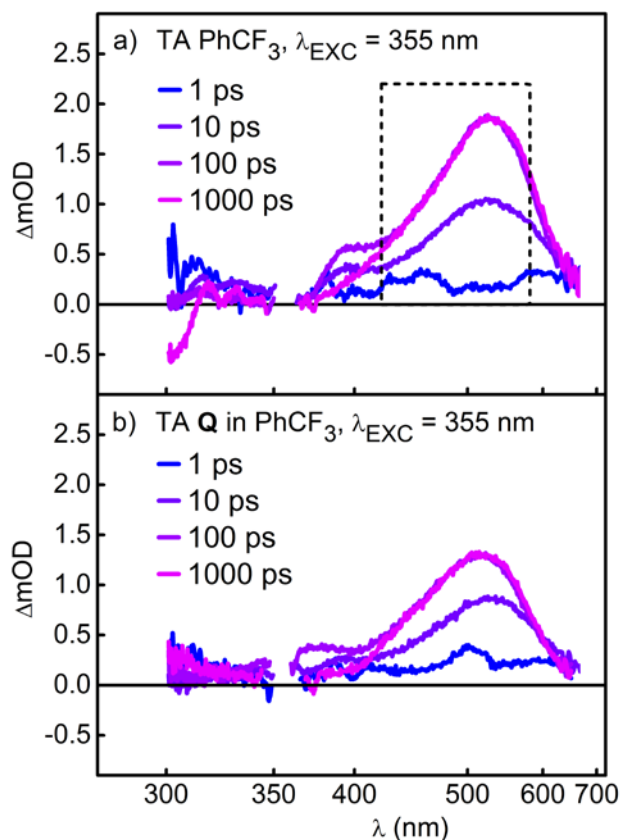


**Figure 4.5** a) Selected transient spectra of pure PhCF<sub>3</sub> after excitation. b) Selected transient spectra of **Q** after excitation. Both measurements conducted under the same experimental conditions ( $\lambda_{\text{EXC}} = 355$  nm,  $E_{\text{EXC}} = 400$  nJ,  $D_{\text{FWHM}} = 150$   $\mu\text{m}$ ,  $d = 1$  mm).

Although the solvent PhCF<sub>3</sub> does not absorb in the spectral region around the excitation wavelength, an upcoming and long lasting transient absorption between 420 and 600 nm is observed (boxed region, Figure 4.5 a). This effect can be readily explained by the generation of a solvated electron, which typically shows a broad unstructured absorption in the visible and near-infrared spectral region [235], depending on the solvent.

The fs-ps TA measurement of the sample solution containing the substrate **Q** diluted in PhCF<sub>3</sub> (Figure 4.5 b), which theoretically does not absorb at the excitation wavelength, shows qualitatively the same behavior. As there are no significant deviations between the TA signal of the pure solvent and the signal of the sample solution containing the substrate **Q**, direct photo-excitation of the substrate at an excitation wavelength of  $\lambda_{\text{EXC}} = 355$  nm can be definitely negated. This is an important prerequisite for the spectroscopic investigation of the present catalyst-substrate system. To quantify the excited state dynamics of the solvated electron, the temporal evolution of the integrated TA signal between 420 and 600 nm (boxed region, Figure 4.5 a) is shown in Figure 4.6.

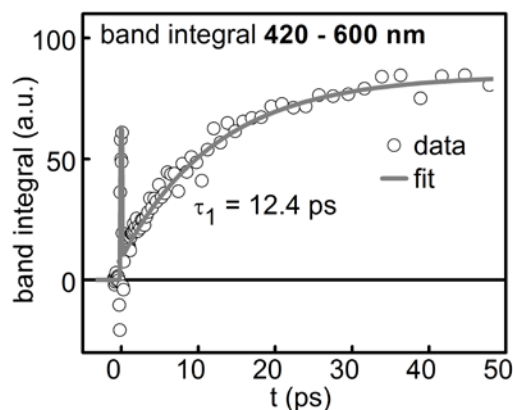


**Figure 4.6** Temporal evolution of the integrated transient absorption signal of pure  $\text{PhCF}_3$  in the wavelength region from 420 – 600 nm (boxed region, Figure 4.5 a).

Whereas the life time of the solvated electron exceeds the accessible pump-probe delay of this measurement, its exponential increase is described by a time constant of  $\tau_1 = 12.4$  ps, which is comparable to values published in literature [235]. The observed signal is up to ten times lower in intensity compared to the TA signal of the photocatalytic system. Therefore its contribution to the TA signal of the photocatalytic system can be safely neglected. Particularly the absorption of the photocatalyst in these measurements again lowers the contribution of the signal of the solvated electron to the total signal intensity. As both in the TA measurements and in the irradiation experiments no reasonable amount of degradation of the photocatalyst could be observed, potential reactions between the solvated electron and the photocatalyst can be neglected.

### Comparability of the Individual fs-ps TA Measurements

The later discussion requires the subtraction of selected transient spectra of different measurements. Particularly the TA signal of the pure photocatalyst **cXPC** will be subtracted from the signal of a measurement of a sample solution containing both the photocatalyst **cXPC** and quinolone **rQ** or **Q**. Although the measurement protocol (vide supra) ensures approximately constant measurement conditions, the exact subtraction requires a more accurate quantification of the measurement conditions to account for small deviations in excitation energy density between the measurements. Therefore in this section, a meaningful scaling factor is introduced and discussed.

In the framework of the present study, not only direct measurement data, which represent physical properties of a given sample solution, containing both **cXPC** and **Q**, are shown. Also processed measurement data, which explicitly characterize the physical properties of the catalyst-quinolone complexes **cXPC·rQ** and **cXPC·Q** are discussed. Therefore, the distinction between a solution containing certain amounts of catalyst **cXPC** and substrate **Q** and the actual catalyst-quinolone complex **cXPC·rQ** or **cXPC·Q** is essential for the interpretation of the measurement data. Also quinolone-quinolone dimerization has to be considered. A quantitative description of the complexation and dimerization processes between **cXPC**, **Q** and **rQ** is given in Chapter 4.2.4. Hence, an unambiguous nomenclature is introduced and shown in Table 4.3.

**Table 4.3** Applied nomenclature:  $\mathbf{cXPC \cdot Q}$  refers explicitly to the catalyst-substrate complex, whereas  $\mathbf{cXPC + Q}$  refers to a sample solution in which the catalyst  $\mathbf{cXPC}$  and the substrate  $\mathbf{Q}$  are diluted in  $\text{PhCF}_3$ .

	symbol	sample
a)	$\mathbf{Q, rQ}$	unbound quinolone
b)	$\mathbf{rQ \cdot rQ, Q \cdot Q}$	dimerized quinolone
c)	$\mathbf{cXPC}$	uncomplexed chiral xanthone-based photocatalyst
d)	$\mathbf{cXPC \cdot rQ, cXPC \cdot Q}$	catalyst-quinolone complexes
e)	$\mathbf{cXPC + rQ, cXPC + Q}$	sample solution containing entries a) - d) with initial concentrations: $[\mathbf{cXPC}]_0 = 1.0 \text{ mM}$ , $[\mathbf{rQ}]_0 = [\mathbf{Q}]_0 = 2.5 \text{ mM}$

Generally, after  $\lambda_{\text{EXC}} = 355 \text{ nm}$  excitation, the transient absorption signal  $\text{TA}(\mathbf{cXPC + Q})$  of sample solution  $\mathbf{cXPC + Q}$  contains overlaying transient signatures both of uncomplexed  $\mathbf{cXPC}$  and of catalyst-substrate complexes  $\mathbf{cXPC \cdot Q}$ :

$$\text{TA}(\mathbf{cXPC + Q}) = \text{TA}(\mathbf{cXPC \cdot Q}) + \text{TA}(\mathbf{cXPC}) \quad (4.3)$$

$\mathbf{Q}$  is not directly optically excited in this type of measurement and therefore it does not contribute to the excited state spectrum. To calculate the transient signal  $\text{TA}(\mathbf{cXPC \cdot Q})$  of the pure catalyst-substrate complex on the basis of this measurement, it is required to subtract  $\text{TA}(\mathbf{cXPC})$ , the overlying transient signal of  $\mathbf{cXPC}$  from  $\text{TA}(\mathbf{cXPC + Q})$ , which was measured in an independent measurement. Therefore a scaling factor  $\alpha$ , which accounts for the contribution of uncomplexed photocatalyst  $\mathbf{cXPC}$  to the total signal intensity in  $\text{TA}(\mathbf{cXPC + Q})$  has to be introduced:

$$\text{TA}(\mathbf{cXPC \cdot Q}) = \text{TA}(\mathbf{cXPC + Q}) - \alpha \cdot \text{TA}(\mathbf{cXPC}) \quad (4.4)$$

The easiest approach is to calculate the scaling factor  $\alpha$  on the basis of the ratio of uncomplexed photocatalyst under consideration of the absorption coefficient of complexed and uncomplexed photocatalyst at the excitation wavelength:

$$\alpha = \frac{[\mathbf{cXPC}]}{[\mathbf{cXPC \cdot Q}] + [\mathbf{cXPC}]} \cdot \frac{\epsilon_{355 \text{ nm}}(\mathbf{cXPC})}{\epsilon_{355 \text{ nm}}(\mathbf{cXPC \cdot Q})} \quad (4.5)$$

However, this simplification is only valid if both measurements were performed under exactly the same conditions – particularly regarding the excitation energy density. Since the excitation energy density slightly differed between the measurements, these deviations are to take into account for an accurate signal analysis.

The measurement data reveal significant differences in the fs-ps TA signal of **cXPC** and of **cXPC + Q**, but not in the wavelength region between 400 and 450 nm. The signal intensity in this spectral region can be used as probe for the relative excitation energy density. Figure 4.7 shows transient spectra at pump-probe delays of  $\Delta t = 0.35, 1, 10$  and  $100$  ps of **cXPC** and of the sample solutions **cXPC + rQ** and **cXPC + Q**.

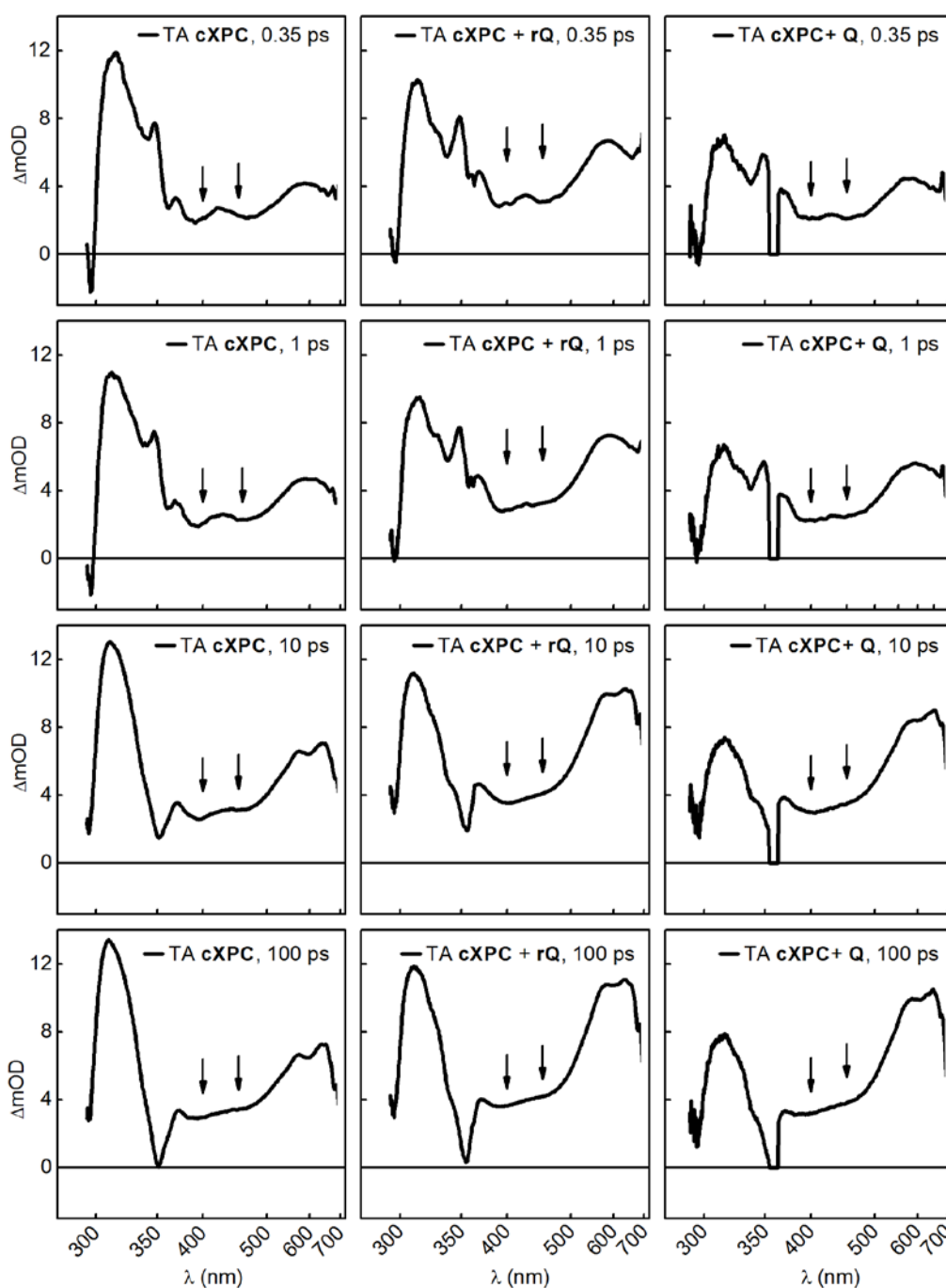


**Figure 4.7** Selected transient spectra of fs-ps TA of **cXPC** (left), **cXPC + rQ** (middle) and **cXPC + Q** (right) after  $\lambda_{\text{EXC}} = 355$  nm excitation. The signal intensities at 400 and at 450 nm (black arrows) were used as probe for the actual excitation energy density in each measurement ( $\lambda_{\text{EXC}} = 355$  nm,  $E_{\text{EXC}} = 400$  nJ,  $D_{\text{FWHM}} = 150$   $\mu\text{m}$ ,  $d = 0.5$  mm).

#### 4. Beyond Photoredox Catalysis: [2+2] Cycloaddition Reactions

The determination of an averaged signal intensity at 400 and 450 nm for different pump-probe delays allows the calculation of a meaningful scaling factor, which accounts for differences in excitation energy density between the individual measurements. Table 4.4 and Table 4.5 therefore show the values of the TA signal intensity of the selected data points.

**Table 4.4** Signal intensity at 400 and 450 nm: the excitation energy density in the fs-ps TA of sample solution **cXPC + rQ** ( $[rQ] = 2.5$  mM,  $[cXPC] = 1.0$  mM) is 1.34-fold higher compared to the measurement of **cXPC** ( $[cXPC] = 1.0$  mM).

	TA(cXPC)	TA(cXPC + rQ)	$\frac{TA(cXPC + rQ)}{TA(cXPC)}$
400 nm, 0.35 ps	2.14 mOD	3.02 mOD	1.41
400 nm, 1 ps	2.06 mOD	2.89 mOD	1.40
400 nm, 10 ps	2.67 mOD	3.56 mOD	1.33
400 nm, 100 ps	2.99 mOD	3.64 mOD	1.22
450 nm, 0.35 ps	2.28 mOD	3.10 mOD	1.36
450 nm, 1 ps	2.28 mOD	3.28 mOD	1.44
450 nm, 10 ps	3.12 mOD	4.10 mOD	1.31
450 nm, 100 ps	3.4 mOD	4.19 mOD	1.23
<b>averaged value</b>			<b>1.34</b>

**Table 4.5** Signal intensity at 400 and 450 nm: the excitation energy density in the fs-ps TA of sample solution **cXPC + Q** ( $[Q] = 2.5$  mM,  $[cXPC] = 1.0$  mM) is 1.07-fold higher compared to the measurement of **cXPC** ( $[cXPC] = 1.0$  mM).

	TA(cXPC)	TA(cXPC + Q)	$\frac{TA(cXPC + Q)}{TA(cXPC)}$
400 nm, 0.35 ps	2.14 mOD	2.11 mOD	0.99
400 nm, 1 ps	2.06 mOD	2.28 mOD	1.11
400 nm, 10 ps	2.67 mOD	3.01 mOD	1.13
400 nm, 100 ps	2.99 mOD	3.20 mOD	1.07
450 nm, 0.35 ps	2.28 mOD	2.11 mOD	0.93
450 nm, 1 ps	2.28 mOD	2.48 mOD	1.09
450 nm, 10 ps	3.12 mOD	3.52 mOD	1.13
450 nm, 100 ps	3.40 mOD	3.83 mOD	1.13
<b>averaged value</b>			<b>1.07</b>



These results show, that the excitation energy density in the fs-ps TA measurements of sample solution **cXPC** + **rQ** and sample solution **cXPC** + **Q** were slightly higher compared to the fs-ps TA measurement of the pure photocatalyst **cXPC** in PhCF<sub>3</sub>. Moreover, these results in combination with the amount of uncomplexed photocatalyst (Table 4.7) and the absorption coefficients of **cXPC** and **cXPC·Q** (Figure 4.13) allow for the exact determination of the scaling factor  $\alpha$ . This factor allows a quantitative subtraction of the TA signal of **cXPC** from the measurement of sample solution containing **cXPC** and **Q** or **rQ** to obtain the TA signal of **cXPC·Q** without overlaying signal from uncomplexed photocatalyst.

$$\alpha_{\text{cXPC+rQ}} = 1.34 \cdot \frac{[\text{cXPC}]}{[\text{cXPC} \cdot \text{rQ}] + [\text{cXPC}]} \cdot \frac{\epsilon_{355\text{nm}}(\text{cXPC})}{\epsilon_{355\text{nm}}(\text{cXPC} \cdot \text{rQ})} \quad (4.6)$$

$$\alpha_{\text{cXPC+Q}} = 1.07 \cdot \frac{[\text{cXPC}]}{[\text{cXPC} \cdot \text{Q}] + [\text{cXPC}]} \cdot \frac{\epsilon_{355\text{nm}}(\text{cXPC})}{\epsilon_{355\text{nm}}(\text{cXPC} \cdot \text{Q})} \quad (4.7)$$

The first factor in this equation accounts for the different excitation energy density in each measurement (Tables 4.4 and 4.5), the second factor displays the fraction of uncomplexed **cXPC** in the sample solution (Table 4.7) and the last factor is required due to a different absorption coefficient of **cXPC** and **cXPC·Q** at the excitation wavelength of  $\lambda_{\text{EXC}} = 355 \text{ nm}$  (Figure 4.13). Insertion of all quantities leads to a value of the scaling factor  $\alpha$ :

$$\alpha_{\text{cXPC+rQ}} = 1.34 \cdot \frac{0.269}{0.731 + 0.269} \cdot \frac{6638}{6465} = 1.34 \cdot 0.27 \cdot 1.03 = 0.37 \quad (4.8)$$

$$\alpha_{\text{cXPC+Q}} = 1.07 \cdot \frac{0.269}{0.731 + 0.269} \cdot \frac{6638}{6465} = 1.07 \cdot 0.27 \cdot 1.03 = 0.30 \quad (4.9)$$

To determine the TA signal of the pure complex **cXPC·rQ** from the measurement of sample solution **cXPC** + **rQ**, the TA signal of pure **cXPC** is to subtract after multiplication with 0.37. To determine the TA signal of the pure complex **cXPC·Q** from the measurement of sample solution **cXPC** + **Q**, the TA signal of pure **cXPC** is to subtract after multiplication with 0.30. It should be noted that this approach is only valid on the ps time scale, where overlying diffusion-controlled processes between catalyst and substrate can be neglected, which typically occur on the time scale of tens and hundreds of ns, when both compounds are diluted in the few mM range.

##### **Spectroelectrochemistry**

Spectroelectrochemistry was carried out in water-free acetonitrile (MeCN) with 150 mM tetrabutylammonium tetrafluoroborate ( $\text{Bu}_4\text{N}^+ \text{BF}_4^-$ ) as the supporting electrolyte. Bulk electrolysis was performed using a computer controlled potentiostat (Gamry Interface 100) and a three-electrode arrangement in a 0.2 mm glass cuvette utilizing a platinum wire mesh working electrode, a platinum wire mesh auxiliary electrode, and a silver wire pseudoreference electrode (Optically Transparent Thin Layer Electrochemical Cell, Frantisek Hartl, University of Reading). The cuvette was placed in a computer controlled diode array spectrophotometer (Jenoptik Specord S 100) to measure the full optical spectral range at once. Spectra of the electrochemically generated anions and cations were recorded by passing the light from the spectrophotometer through the platinum mesh working electrode. A blank spectrum consisting of the cuvette filled with solvent and supporting electrolyte was subtracted from each data set. A detailed description of the applied experimental setup can be found in Ref. [236].

### 4.2.3 For a Basic Understanding: Diffusion Controlled Sensitization of the [2+2] Photocycloaddition with Pure Xanthone as Sensitizer

#### The Triplet State of Xanthone

The design of the chiral photocatalyst **cXPC** is based on the idea that the covalently bound chiral binding site does not significantly affect the photophysical properties of the xanthone chromophore, which contributes the photocatalytic activity. Xanthone, which has a strong ( $\epsilon \cong 10,000 \text{ M}^{-1} \text{ cm}^{-1}$ ) absorption band in the ultraviolet spectral region around 337 nm, is an organic chromophore which is versatilely applied in different fields of photochemistry. In particular the triplet state properties have attracted major scientific interest. The ultrafast ISC within 1.5 ps [230], the strong dependency of the triplet energy on the solvent environment [237, 238, 239, 240, 241] and its relatively high triplet energy of  $E_T = 310 \text{ kJ/mol}$  (3.2 eV) [165] make xanthone an interesting candidate for the sensitization of many different chemical reactions. Referring to the idea of triplet sensitization, the diffusive sensitization of the [2+2] photocycloaddition of quinolone **Q**, in which diluted xanthone acts as photosensitizer, depicts a well suited reference system. The understanding and quantification of the reaction dynamics within this reference system provides a basis for the understanding of the more complex reaction dynamics within the catalytic active system.

A ns- $\mu\text{s}$  TA measurement series was performed to investigate the intrinsic reaction dynamics of the diffusion-controlled xanthone sensitized [2+2] photocycloaddition of substituted quinolones. The excitation wavelength was  $\lambda_{\text{EXC}} = 348.5 \text{ nm}$  in all measurements, which provides selective excitation of the xanthone chromophore. Although the absorption of quinolones **MQ** and **Q** extends weakly beyond 348.5 nm, the contribution of TA signal of directly excited quinolone can be neglected. Its contribution after  $\lambda_{\text{EXC}} = 348.5 \text{ nm}$  excitation is more than 100 times lower in intensity compared to the strength of the TA signal originating from directly excited xanthone. A list of all prepared and measured samples is given in Table 4.6. All sample solutions were prepared by Mark Maturi (Group of Thorsten Bach) in the chemistry laboratories at the TUM.

**Table 4.6** Samples prepared for ns- $\mu\text{s}$  TA.

sample	description	concentration	reaction of interest
1	xanthone	[xanthone] = 1 mM in PhCF <sub>3</sub>	intrinsic triplet dynamics of xanthone
2	xanthone + <b>MQ</b>	[xanthone] = 1 mM [ <b>MQ</b> ] = 4.3 mM in PhCF <sub>3</sub>	TTET from xanthone to <b>MQ</b> $E_T(\text{MQ}) < E_T(\text{xanthone})$
3	xanthone + <b>Q</b>	[xanthone] = 1 mM [ <b>Q</b> ] = 5.0 mM in hCF <sub>3</sub>	triplet sensitized [2+2] photocycloaddition of <b>Q</b> $E_T(\text{Q}) < E_T(\text{xanthone})$

On the ns- $\mu$ s time scale, after excitation, pure xanthone in PhCF<sub>3</sub> shows a sharp, intense transient absorption band centered around 640 nm and a weaker one around 294 nm. According to the literature [238], this spectrum can be unambiguously identified with the absorption of the xanthone T<sub>1</sub> state. The ultrafast ISC ( $\tau_{\text{ISC}} = 1.5$  ps) [230] cannot be resolved in this measurement as the instrument response function within this type of setup has a full width half maximum of  $\sim 2.5$  ns. For this reason, the T<sub>1</sub> spectrum seems to appear instantaneously after excitation. The resulting profile plot is shown in Figure 4.8.

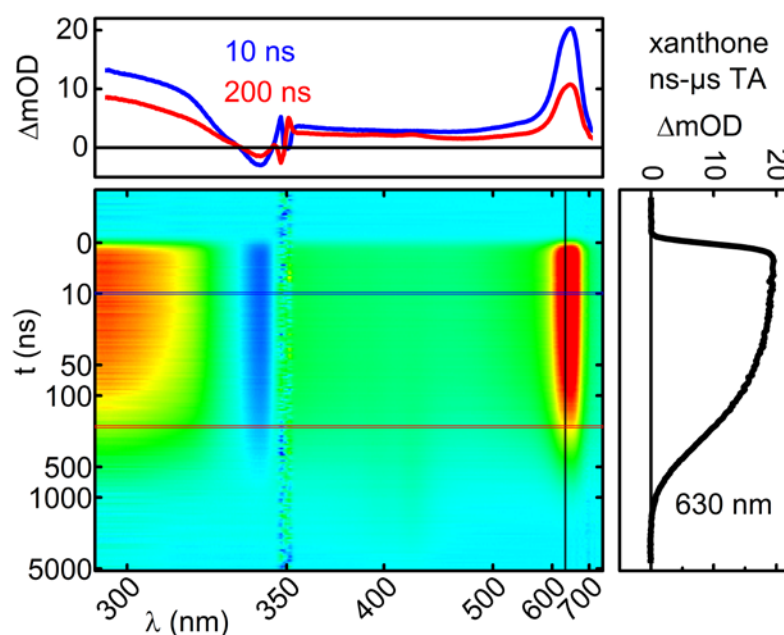


**Figure 4.8** Profile plot of ns- $\mu$ s TA of pure xanthone in partially degassed PhCF<sub>3</sub> after  $\lambda_{\text{EXC}} = 348.5$  nm excitation ( $d = 1$  mm,  $\Delta\text{OD} > 0$  in red,  $\Delta\text{OD} < 0$  in blue).

Fitting exponential decay curves to the transient data matrix only provides limited information of the temporal evolution of a selected spectral region. For a more meaningful interpretation of the transient data and in particular to reveal the spectral changes caused by the corresponding process, a more sophisticated data analysis is required. Therefore the transient data set is analyzed with the help of global fit analysis<sup>27</sup>, which provides the exact signature of the spectral changes caused by a certain process. The data analysis presented in this chapter will primarily rely on global fit analysis. Detailed information about this method can be found in Appendix A.1. The global fit analysis of the ns- $\mu$ s TA measurement of pure xanthone in PhCF<sub>3</sub> (Figure 4.8) results in decay associated difference spectra (DADS), which are shown in Figure 4.9.

<sup>27</sup> program path at the Chair for BioMolecular Optics (Ludwig Maximilian University):  
\\johann\agriedle\Software\_und\_Treiber\Labview\Global-Fit-Programm (2014-03-01)

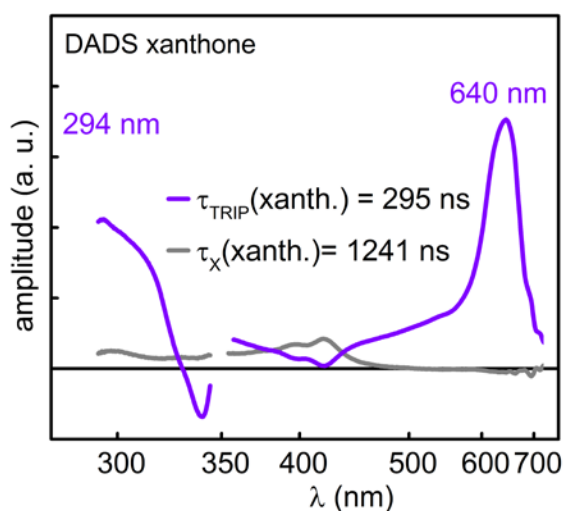
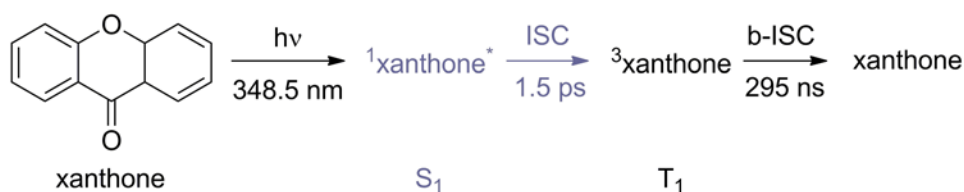


**Figure 4.9** DADS analysis of the ns- $\mu$ s TA data: the decay of the  $T_1$  spectrum (violet line) is described by a time constant of  $t_{\text{TRIP}} = 295$  ns. An additional decay component (grey line) is described by a time constant of  $\tau_X = 1241$  ns.

The temporal evolution of the transient spectrum is dominated by a  $\tau_1 = 295$  ns process. This process describes the decay of the  $T_1$  specific absorption bands around 294 and 640 nm. The negative amplitude of the corresponding DADS (violet line, Figure 4.9) around 337 nm, the spectral position of the xanthone ground state absorption maximum, indicates the repopulation of the xanthone ground state within this process. A second DADS is associated with a time constant of  $\tau_2 = 1241$  ns (grey line, Figure 4.9). Since its relative amplitude is low and the spectrum cannot be clearly identified with any known spectral signature, it is not discussed in detail. This intermediate state, which decays within 1241 ns is populated from the  $T_1$  state, which can be clearly seen in the wavelength region around 400 nm, where both DADS are mirror images of each other. Hence, the xanthone  $T_1$  state not only decays back to the ground state but also to a 1241 ns lived intermediate state. Photochemical triplet reactions of xanthone upon collision with a ground state xanthone or oxygen or intrinsic photochemical triplet processes can explain this behavior. The photophysical processes of xanthone after  $\lambda_{\text{EXC}} = 348.5$  nm excitation are schematically shown in Scheme 4.8.



**Scheme 4.8** Photophysics of xanthone in  $\text{PhCF}_3$ : the time constants represent the life time of the parent state—not the inverse rate of the underlying process. States displayed in grey were spectroscopically not accessible in this type of measurement.

The xanthone triplet life time of  $\tau_{\text{TRIP}} = 295$  ns, which is limited both by inter-system crossing to the singlet ground state, by oxygen-mediated triplet quenching and by a further unspecified photochemical process, determines the temporal window for photocatalytic

processes. The observed xanthone triplet life time in partially degassed PhCF<sub>3</sub> is significantly smaller than published values in completely degassed solvent in the range of tens of  $\mu\text{s}$  [237]. To observe a reasonable amount of triplet sensitization in ns- $\mu\text{s}$  TA, the diffusion-controlled TTET process needs to be triggered to occur not significantly slower than 295 ns but not faster than 2.5 ns, the temporal resolution of the TA setup. Common quenching constants for diffusion limited TTET processes are in the order of  $K_Q = 10^9 \text{ M}^{-1} \text{ s}^{-1}$ . Hence, to obtain a diffusion limited triplet sensitization process which is described by a rate of  $k_Q \cong (295 \text{ ns})^{-1}$ , a quencher concentration of  $\sim 3.4 \text{ mM}$  is required. Although quinolones **MQ** and **Q** are not soluble at high concentrations, a concentration in the few mM range can be readily achieved. The subsequent sensitization experiments were conducted under quinolone concentrations of  $[\text{MQ}] = 4.3 \text{ mM}$  and  $[\text{Q}] = 5.0 \text{ mM}$ .

### Evidence of Triplet-Triplet Energy Transfer from Xanthone to Quinolone

The triplet state dynamics of pure xanthone in partially degassed PhCF<sub>3</sub> were sufficiently characterized in the previous section. In this section, the intrinsic TTET process from xanthone to **MQ** is discussed. In comparison to quinolone **Q**, quinolone **MQ** cannot undergo a [2+2] photocycloaddition from its triplet state due to the absent side chain (compare Scheme 4.7). Therefore **MQ** serves as reference compound to study the TTET process without overlaying reaction dynamics, which make an accurate data analysis more difficult.

The global fit analysis of the ns- $\mu\text{s}$  TA measurement of sample solution xanthone + **MQ** after  $\lambda_{\text{EXC}} = 348.5 \text{ nm}$  excitation is shown in Figure 4.10. For comparison, the triplet-triplet absorption of **MQ** (black line) from [App A.6] is also plotted in Figure 4.10. Due to the relatively high concentration of **MQ** in combination with an optical path length of 1 mm, the wavelength region below 390 nm was spectroscopically not accessible in this type of experiment.

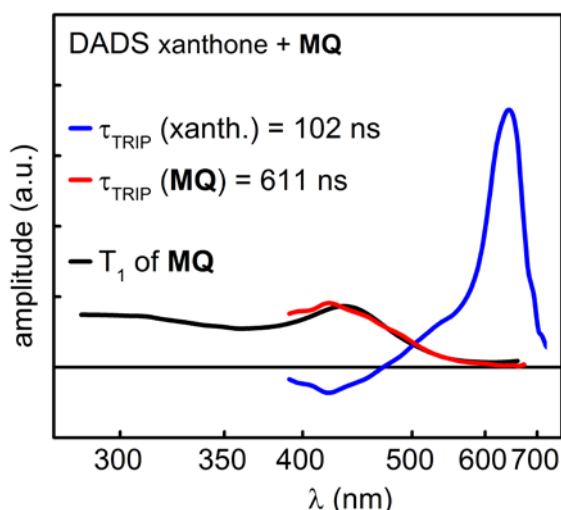
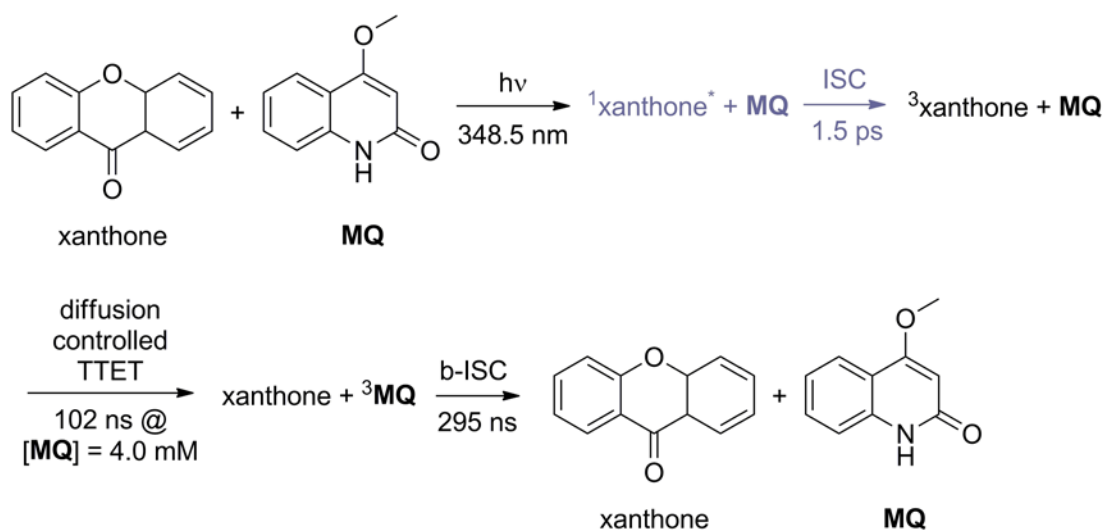


**Figure 4.10** DADS of the ns- $\mu\text{s}$  TA of sample solution xanthone + **MQ** ( $[\text{MQ}] = 4.3 \text{ mM}$ ) in partially degassed PhCF<sub>3</sub> after  $\lambda_{\text{EXC}} = 348.5 \text{ nm}$  excitation, measured in a flow cell with 1 mm thickness: decay of the xanthone  $T_1$  state (blue), decay of the quinolone  $T_1$  state (red) and comparison to the  $T_1$  absorption of **MQ** (black) from [App A.6].

The temporal evolution of the transient spectrum is dominated by two processes: one process described by a time constant of  $\tau_1 = 102$  ns and a second process with a characteristic time constant of  $\tau_2 = 611$  ns. The  $\tau_1 = 102$  ns DADS (blue line, Figure 4.10) shows the decay of a sharp and intense absorption band around 640 nm, which is characteristic for the xanthone triplet state (vide supra). The negative amplitude of the  $\tau_1 = 102$  ns DADS around 430 nm is characteristic for the population of a new state. In contrast, the  $\tau_2 = 611$  ns DADS (red line, Figure 4.10) with a positive amplitude in this spectral region exactly renders the decay of this previously populated intermediate state back to the ground state. The comparison of the spectral features of this transient state with the triplet absorption of **MQ** (black line, Figure 4.10) unambiguously identifies this state with the quinolone triplet state  $^3[\text{MQ}]$ . In summary, the xanthone triplet state decays and simultaneously the quinolone triplet state is populated, which is characteristic for a TTET process. The quinolone located triplet state  $^3[\text{MQ}]$  itself decays by inter-system crossing back to the ground state. The observed increase of the quinolone  $T_1$  life time in partially degassed  $\text{PhCF}_3$  ( $\tau_{\text{TRIP}} = 611$  ns) in comparison to the life time measured in air equilibrated MeCN ( $\tau_{\text{TRIP}} = 116$  ns [App A.6]) can be readily explained with the lower oxygen concentration in  $\text{PhCF}_3$ . A scheme depicting the diffusion controlled TTET process from xanthone to quinolone **MQ** in  $\text{PhCF}_3$  and the subsequent decay of the quinolone  $T_1$  state  $^3[\text{MQ}]$  is shown in Scheme 4.9.



**Scheme 4.9** TTET from xanthone to **MQ**: the time constants represent the life time of the parent state — not the inverse rate of the underlying process. States displayed in grey are spectroscopically not accessible in this type of measurement.

This measurement proves the TTET process from xanthone to quinolone. Reference quinolone **MQ** is not able to undergo further chemical transformations from its  $T_1$  state, and therefore this experiment allows the quantification of the reaction dynamics of the energy transfer process. Since the xanthone triplet life time both in pure solvent and in the environment of quinolone **MQ** was accurately measured,  $k_Q$ , the effective rate of the diffusion controlled TTET, can be easily calculated as shown in Equation 4.10. The rate  $k_Q$  is the difference of the rate, displaying the xanthone  $T_1$  life time in the environment of

quinolone **MQ** ( $\tau_{\text{TRIP}}^{-1} = 1/102 \text{ ns}$ ) and the rate displaying the intrinsic  $T_1$  life time of xanthone in the environment of partially degassed  $\text{PhCF}_3$  ( $\tau_{\text{TRIP}}^{-1} = 1/295 \text{ ns}$ ).

$$k_Q = (102 \text{ ns})^{-1} - (295 \text{ ns})^{-1} = 6.4 \cdot 10^6 \text{ s}^{-1} \quad (4.10)$$

With an effective concentration of  $[\text{MQ}] = 4.3 \text{ mM}$ , the quenching constant  $K_Q$ , which describes the linear dependence between the rate of diffusion controlled quenching  $k_Q$  and the quencher concentration  $[\text{MQ}]$ , can be calculated according to Equation 4.11:

$$K_Q(\text{MQ}) = \frac{k_Q}{[\text{MQ}]} = \frac{6.4 \cdot 10^6 \text{ s}^{-1}}{4.3 \text{ mM}} = 1.5 \cdot 10^9 \text{ s}^{-1} \text{ M}^{-1} \quad (4.11)$$

The determined quenching constant of  $K_Q = 1.5 \cdot 10^9 \text{ s}^{-1} \text{ M}^{-1}$  characterizes the system of triplet donor xanthone and triplet acceptor **MQ** in the environment of  $\text{PhCF}_3$  as solvent. The determined value corresponds very well with values reported in literature for related TTET processes [165]. The decay of the xanthone triplet signatures and the simultaneous population of the **MQ** triplet state in combination with a reasonable value of the quenching constant clearly identifies the underlying process as a TTET process.

### Sensitization of the [2+2] Cycloaddition of Substituted Quinolones by Triplet-Triplet Energy Transfer

Both the intrinsic triplet decay of xanthone and the dynamics of the TTET from xanthone to quinolone were quantified. In this section, the [2+2] photocycloaddition of quinolone **Q** sensitized by TTET from xanthone is discussed. In Chapter 4.1 the [2+2] photocycloaddition of **Q** after direct photo-excitation was fundamentally investigated. It has been shown that the formation of the cyclobutane ring occurs via a triplet mechanism in which a quinolone triplet 1,4-diradical  $^3[\text{Q-dirad}]$  represents the key intermediate state. The quinolone diradical  $^3[\text{Q-dirad}]$  is formed from the quinolone triplet state  $^3[\text{Q}]$  within 0.651 ns and decays within 29 ns either to the ground state of the product or back to the starting material.

The global fit analysis of the data matrix of the ns- $\mu\text{s}$  TA measurement of sample solution xanthone + **Q** is shown in Figure 4.11. Again, the wavelength region below 390 nm was spectroscopically not accessible due to the relatively high concentration of **Q** in combination with an optical path length of 1 mm. For comparison, the absorption of  $^3[\text{Q-dirad}]$  (black line) from [App A.6] is plotted in Figure 4.11.



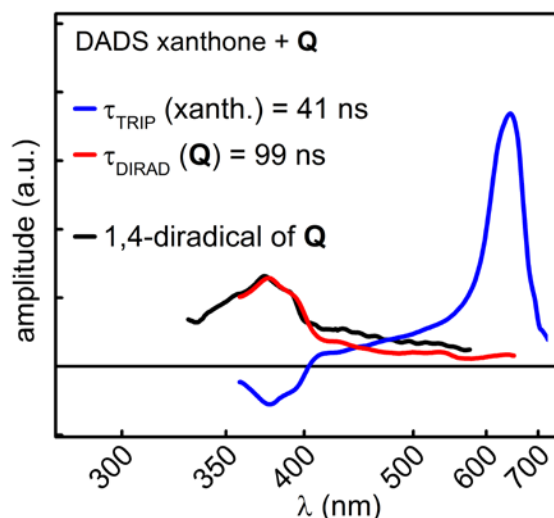
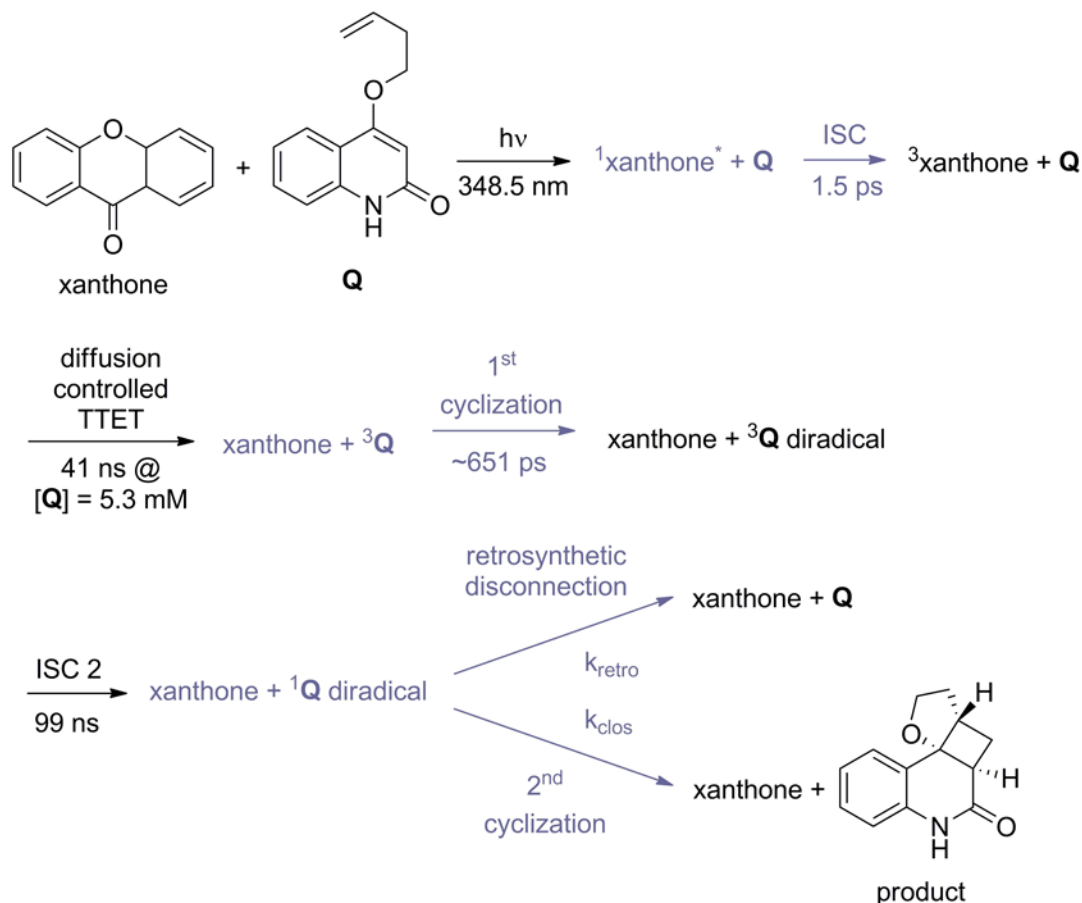


**Figure 4.11** DADS of the ns- $\mu$ s TA of sample solution xanthone + **Q** ( $[\mathbf{Q}] = 5.0$  mM) in partially degassed  $\text{PhCF}_3$  after  $\lambda_{\text{EXC}} = 348.5$  nm excitation, measured in a flow cell with 1 mm thickness: decay of the xanthone  $T_1$  state (blue), decay of the quinolone diradical  $^3[\mathbf{Q}\text{-dirad}]$  (red) and comparison to the absorption spectrum of  $^3[\mathbf{Q}\text{-dirad}]$  measured after direct photo-excitation (black) from [App A.6].

The temporal evolution of the transient spectrum is dominated by two processes: one process, described by a time constant of  $\tau_1 = 41$  ns, and a second process with a characteristic time constant of  $\tau_2 = 99$  ns. Due to the relatively high signal intensity of  $\Delta\text{OD} \leq 50$  mOD and the clearly exponential decay dynamics both observed time constants, which are rather close to each other, were easily distinguishable in the data analysis. The  $\tau_1 = 41$  ns DADS (blue line Figure 4.11) shows the decay of the sharp and intense xanthone triplet absorption band around 640 nm. The negative amplitude of this DADS around 370 nm is characteristic for the population of a new state. However, not the quinolone triplet  $^3[\mathbf{Q}]$  state which exhibits its characteristic absorption band around 430 nm, but a new state with a characteristic absorption around 370 nm is populated within this process. The  $\tau_2 = 99$  ns DADS (red line, Figure 4.11) with a positive amplitude in this spectral region exactly renders the decay of this intermediate state. The comparison of the spectral features of this transient state with the absorption spectrum of the quinolone diradical  $^3[\mathbf{Q}\text{-dirad}]$  from [App A.6] (black line, Figure 4.11) unambiguously identifies this transient state with the quinolone triplet 1,4-diradical state  $^3[\mathbf{Q}\text{-dirad}]$ .

It seems that the quinolone diradical  $^3[\mathbf{Q}\text{-dirad}]$  is directly populated from the xanthone  $T_1$  state. However, it has been shown (Chapter 4.1), that after direct photo-excitation of quinolone **Q**, the triplet state  $^3[\mathbf{Q}]$  decays within 0.651 ns to  $^3[\mathbf{Q}\text{-dirad}]$ . Since the diffusion limited TTET process occurs on the time scale of tens of nanoseconds, the quinolone located triplet state  $^3[\mathbf{Q}]$  is actually not populated in this type of diffusion-limited sensitization experiment. The depopulating process of  $^3[\mathbf{Q}]$ , the formation of  $^3[\mathbf{Q}\text{-dirad}]$  is considerably faster than the populating process, the TTET from xanthone to **Q**. Furthermore, the observed life time  $\tau_{\text{DIRAD}}$  of  $^3[\mathbf{Q}\text{-dirad}]$  in the sensitization experiments ( $\tau_{\text{DIRAD}} = 99$  ns) is significantly longer than observed in acetonitrile after direct photo-excitation ( $\tau_{\text{DIRAD}} = 29$  ns). Since

$^3[\text{Q-dirad}]$  exhibits triplet character, this observation can be again explained with a lower oxygen concentration in the present measurement. A scheme depicting the diffusion controlled TTET process from xanthone to **Q** in  $\text{PhCF}_3$ , the cyclization forming the triplet 1,4-diradical, the second ISC to the singlet 1,4-diradical and the subsequent decay either to the product or to the starting material is shown in Scheme 4.10. The structure of  $^3[\text{Q-dirad}]$  is shown in Scheme 4.4 in Chapter 4.1.



**Scheme 4.10** TTET from xanthone to quinolone **Q** and subsequent [2+2] photocycloaddition: the time constants represent the life time of the parent state — not the inverse rate of the underlying process. States displayed in grey are spectroscopically not accessible in the ns/ $\mu\text{s}$  measurement.

This measurement proves the sensitization of the [2+2] photocycloaddition of **Q** by TTET from xanthone. Since the xanthone  $T_1$  life time both in absence and in presence of **Q** was measured,  $k_{\text{Q}}$ , the effective rate of the diffusion controlled TTET, can be easily calculated as shown in Equation 4.12. The rate  $k_{\text{Q}}$  is the difference of the rate displaying the life time of the xanthone triplet state in the environment of **Q** ( $\tau_{\text{TRIP}}^{-1} = 1/41 \text{ ns}$ ) and the rate displaying the intrinsic life time of the xanthone triplet state in the environment of partially degassed  $\text{PhCF}_3$  ( $\tau_{\text{TRIP}}^{-1} = 1/295 \text{ ns}$ ).

$$k_{\text{Q}} = (41 \text{ ns})^{-1} - (295 \text{ ns})^{-1} = 20.4 \cdot 10^6 \text{ s}^{-1} \quad (4.12)$$

With a concentration of  $[\mathbf{Q}] = 5.0 \text{ mM}$ , the quenching constant  $K_Q$ , which describes the linear dependence between the rate of diffusion controlled quenching  $k_Q$  and the quencher concentration  $[\mathbf{Q}]$ , can be calculated according to Equation 4.13:

$$K_Q(\mathbf{rQ}) = \frac{k_Q}{[\mathbf{Q}]} = \frac{20.4 \cdot 10^6 \text{ s}^{-1}}{5.0 \text{ mM}} = 4.1 \cdot 10^9 \text{ s}^{-1} \text{ M}^{-1} \quad (4.13)$$

The determined quenching constant of  $K_Q = 4.1 \cdot 10^9 \text{ s}^{-1} \text{ M}^{-1}$  characterizes the system of triplet donor xanthone and triplet acceptor  $\mathbf{Q}$  in the environment of  $\text{PhCF}_3$  as solvent. The determined value is higher than observed for  $\mathbf{MQ}$  ( $K_Q = 1.5 \cdot 10^9 \text{ s}^{-1} \text{ M}^{-1}$ ) but still corresponds very well with values reported in literature for related TTET processes [165]. The deviation between  $\mathbf{MQ}$  and  $\mathbf{Q}$  can be explained with a change in diffusional motion of the quinolone. Potentially the non-polar side chain of  $\mathbf{Q}$  in the rather low-polar solvent environment of  $\text{PhCF}_3$  improves the diffusional motion of the quinolone chromophore. Another explanation would be that the side chain operates as antenna and positively affects the efficiency of the TTET process between xanthone and  $\mathbf{Q}$ .



#### 4.2.4 Accessing the Mechanistic Details of Enantioselective Photocatalysis with Transient Absorption Spectroscopy on Multiple Time Scales and Quantum Chemistry

##### Unexpected Observations on the fs-ps Time Scale

The design of the catalyst-substrate system is based on the idea of sensitization by TTET. Particularly the energy levels of the involved triplet states seem to allow for TTET from the xanthone-based photocatalyst **cXPC** to the substrate **Q**. Since the  $^3[\mathbf{Q}]$  spectrum is already known (Chapter 4.1) and the  $^1[\mathbf{cXPC}]^*$  and  $^3[\mathbf{cXPC}]$  spectra are easy to measure with the help of transient absorption spectroscopy on the fs-ps time scale, a clear picture about the expected excited state dynamics both in fs-ps TA and in the ns- $\mu$ s time domain evolved. The only uncertainty in this experimental framework is the actual rate of the TTET process. However, the comparison with related systems clearly suggests a rather fast energy transfer between both closely stacked chromophores on the 10 ps time scale [242, 243, 244, 245, 246, 247, 248, 249]. The following reaction steps are therefore expected to be observed consecutively in the TA measurements:

- Selective photo-excitation of **cXPC**: instantaneous absorption signal of the xanthone photocatalyst  $S_1$  state  $^1[\mathbf{cXPC}]$
- Ultrafast ISC of **cXPC** within  $\sim 1.5$  ps after excitation: depletion of the  $^1[\mathbf{cXPC}]^*$  absorption and simultaneous increase of the  $^3[\mathbf{cXPC}]$  absorption
- TTET from the **cXPC** to **Q** within tens of picoseconds: depletion of the  $^3[\mathbf{cXPC}]$  absorption and simultaneous increase of the  $^3[\mathbf{Q}]$  absorption around 430 nm
- First and second cyclization of quinolone: depletion of the  $^3[\mathbf{Q}]$  spectrum within 0.651 ns and simultaneous increase of the  $^3[\mathbf{Q-dirad}]$  absorption spectrum around 370 nm with subsequent product formation within 29 ns

However, already on the fs-ps time scale the actually observed excited state dynamics of the sample solution **cXPC** + **Q** heavily deviate from the expected behavior. The profile plot of the corresponding fs-ps TA measurement is shown in Figure 4.12.

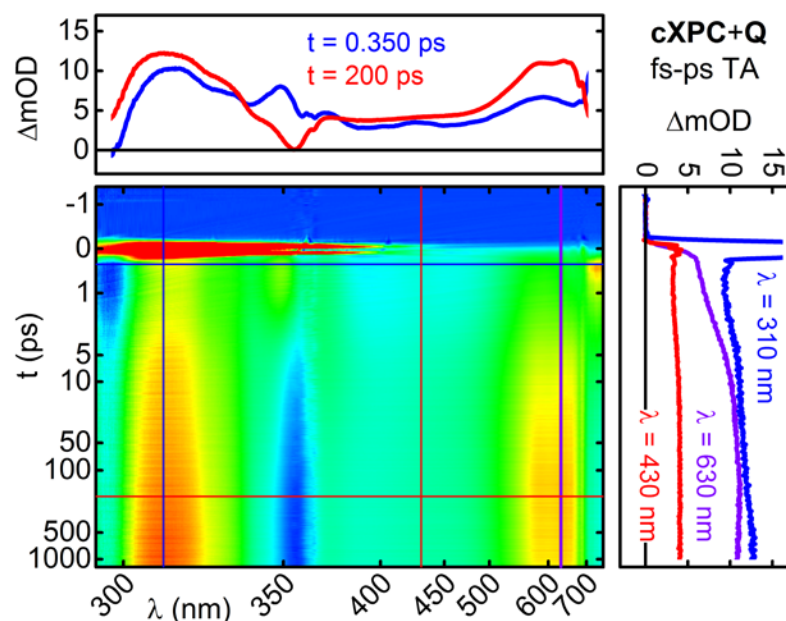


**Figure 4.12** Profile plot of fs-ps TA of sample solution **cXPC + Q** ( $[\text{cXPC}] = 1.0 \text{ mM}$ ,  $[\text{Q}] = 2.5 \text{ mM}$ ) in partially degassed  $\text{PhCF}_3$  ( $\lambda_{\text{EXC}} = 355 \text{ nm}$ ,  $E_{\text{EXC}} = 400 \text{ nJ}$ ,  $D_{\text{FWHM}} = 150 \mu\text{m}$ ) measured in a 0.5 mm flow cell.

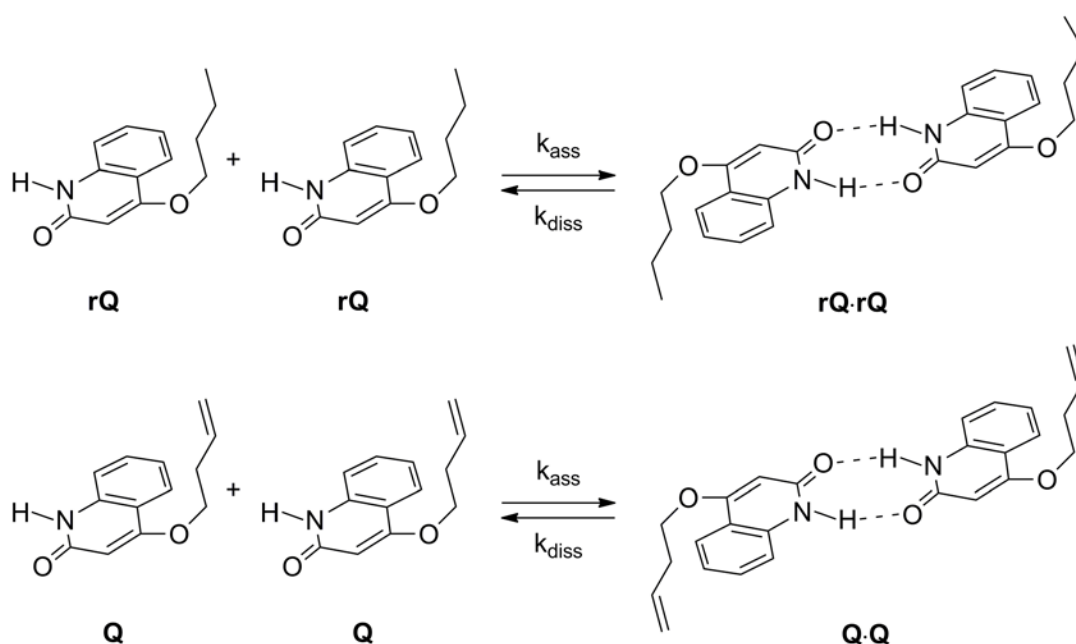
On a first view it can be seen, that the transient spectrum only shows dynamics on the time scale up to 10 ps. After 10 ps the TA signal remains nearly constant. ISC of xanthone within 1.5 ps and internal conversion processes between  $n\pi^*$  and  $\pi\pi^*$  states of the singlet and the triplet state on the few ps time scale [230] might readily explain the observed behavior. Slight spectral changes on the time scale of  $\sim 1000$  ps, which can be particularly seen in the 310 nm time trace (blue line, Figure 4.12) are due to a change of pump-probe overlap within the measurement, which was verified by further measurements. However, the expected processes, the TTET on the 10 ps time scale, and the formation of the quinolone triplet 1,4-diradical  $^3[\text{Q-dirad}]$  on the sub-ns time scale can be definitely not observed in this measurement. These observations and the related fundamental questions gave the starting signal for a deeper and more detailed analysis of the present photocatalytic system, which lead to unexpected results and to the postulation of a new sensitizing mechanism in organic photocatalysis.

### Quantifying the Association Processes

For an enantioselective chemical process, generally the interaction between a chiral host compound and a pro-chiral target is required. In the present catalyst-substrate system the interaction between the chiral catalyst **cXPC** and the pro-chiral substrate **Q** is mediated through a hydrogen binding motif. **cXPC** comprises a hydrogen binding site which is adapted to bind a substrate molecule **Q** in a defined geometric orientation. The pro-chiral substrate **Q** comprises a complementary hydrogen bonding motif. The complexation of the rigid photocatalyst **cXPC** and the pro-chiral substrate **Q** sterically hinders the formation of one enantiomer of both possible product enantiomers, depending on the actual chirality of

**cXPC**. Therefore, photo-excitation of a stacked catalyst-substrate complex **cXPC·Q** provides enantioselective product formation.

However, the hydrogen bonding motif not only leads to the expected complexation of **cXPC** and **Q**, it also allows for the dimerization of quinolones forming quinolone dimers **rQ·rQ** and **Q·Q**. The quinolone-quinolone dimerization is shown in Scheme 4.11. Whereas the dimerization of the photocatalyst in an enantiomerically pure solution of **cXPC** is negligible [250], the dimerization of **rQ** and **Q** causes a significant effect on the actual equilibrium between uncomplexed and complexed **cXPC**: quinolone-quinolone dimerization competes with catalyst-substrate complexation. Therefore the association equilibrium of all components in a given sample solution containing **cXPC** and **Q** has to be thoughtfully considered and quantified.



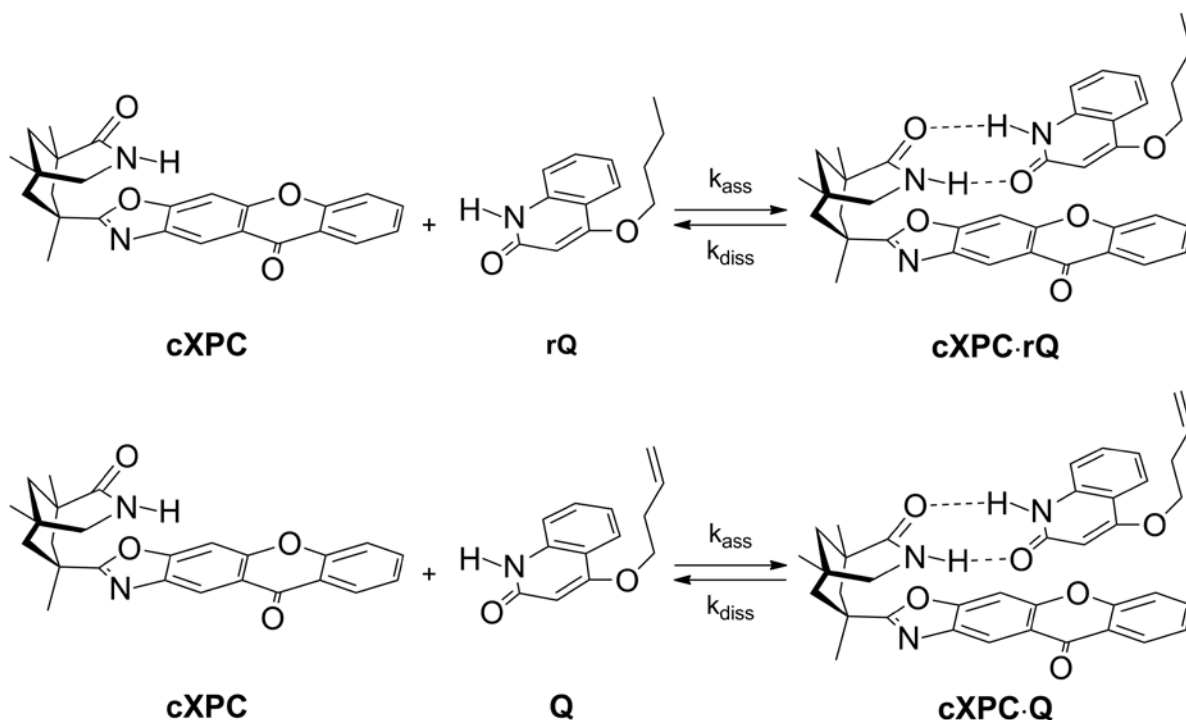
**Scheme 4.11** Dimerization of **rQ** and **Q**: depending on the initial concentration of **rQ** and **Q**, an equilibrium of association ( $k_{\text{ass}}$ ) and dissociation ( $k_{\text{diss}}$ ) is established.

The amount of quinolone monomers and dimers in a given sample solution depends on the rates of association ( $k_{\text{ass}}$ ) and dissociation ( $k_{\text{diss}}$ ). The actual rates are experimentally not accessible, but the ratio of both rates, the binding constant  $K_{\text{QQ}}$ , describing the equilibrium concentration of monomers and dimers can be experimentally determined. With the help of a NMR titration series, performed by Mark Maturi and Andreas Bauer in the group of Thorsten Bach, a value for the binding constant in toluene at room temperature was determined:

$$K_{\text{QQ}} = \frac{k_{\text{ass}}}{k_{\text{diss}}} = \frac{[\text{Q} \cdot \text{Q}]}{[\text{Q}] \cdot [\text{Q}]} = 3027 \text{ M}^{-1} \quad (4.14)$$

According to this value, in a solution with an initial quinolone concentration of  $[\text{Q}]_0 = 1.0 \text{ mM}$ , the effective concentration of non-dimerized quinolones is  $[\text{Q}] = 0.332 \text{ mM}$  whereas the concentration of quinolone-quinolone dimers is  $[\text{Q} \cdot \text{Q}] = 0.334 \text{ mM}$ . However,

not only the binding constant for quinolone-quinolone dimerization, but also the binding constant for catalyst-substrate complexation was determined in this measurement series. The catalyst-substrate complexation is schematically shown in Scheme 4.12.



**Scheme 4.12** Complexation of quinolones **rQ** and **Q** and the photocatalyst **cXPC** to **cXPC·rQ** (top) and **cXPC·Q** (bottom), the photocatalytic active complex.

Hence, a value of  $K_{\text{cXPCQ}}$ , which quantifies the complexation of **cXPC** and **Q**, was determined:

$$K_{\text{cXPCQ}} = \frac{k_{\text{ass}}}{k_{\text{diss}}} = \frac{[\text{cXPC} \cdot \text{Q}]}{[\text{cXPC}] \cdot [\text{Q}]} = 5865 \text{ M}^{-1} \quad (4.15)$$

Since quinolone-quinolone dimerization is competing with catalyst-substrate complexation, the calculation of an effective equilibrium concentrations requires to take both processes into account. Therefore, Equation System 4.16 describes both association processes and allows for the calculation of the effective equilibrium concentration at given initial concentrations of  $[\text{Q}]_0$  and  $[\text{cXPC}]_0$ .

The dimerization of quinolone is described by the binding constant  $K_{\text{QQ}}$  (Equation 4.14):

$$K_{\text{QQ}} = \frac{[\text{Q} \cdot \text{Q}]}{[\text{Q}] \cdot [\text{Q}]} \quad (4.16 \text{ a})$$



The complexation of **Q** and **cXPC** to the catalyst-substrate complex is described by the binding constant  $K_{\text{cXPCQ}}$ :

$$K_{\text{cXPCQ}} = \frac{[\text{cXPC} \cdot \text{Q}]}{[\text{cXPC}] \cdot [\text{Q}]} \quad (4.16 \text{ b})$$

The initial concentration  $[\text{cXPC}]_0$  can be divided into complexed **cXPC·Q** and unbound **cXPC**:

$$[\text{cXPC}]_0 = [\text{cXPC} \cdot \text{Q}] + [\text{cXPC}] \quad (4.16 \text{ c})$$

The initial concentration  $[\text{Q}]_0$  can be divided into catalyst-substrate complexes **cXPC·Q**, unbound **Q** and **Q·Q** dimers:

$$[\text{Q}]_0 = [\text{cXPC} \cdot \text{Q}] + [\text{Q}] + 2 \cdot [\text{Q} \cdot \text{Q}] \quad (4.16 \text{ d})$$

Solutions of Equation System 4.16 for typical applied initial concentrations  $[\text{Q}]_0$  and  $[\text{cXPC}]_0$  are listed in Table 4.7. At conditions, which were used for TA measurements (Table 4.7, d), 27% of **cXPC** is uncomplexed, whereas 73% of **cXPC** is complexed to **cXPC·Q**. However, at concentrations, which were used for photocatalytic experiments [5, 156] (Table 4.7, e), 18% of **cXPC** is unbound whereas 82% is complexed to **cXPC·Q**. The photocatalytic experiments were usually conducted at a temperature of  $T = -25^\circ\text{C}$  [5, 156], whereas the binding constants were determined at room temperature, which drives the equilibrium in the photocatalytic experiments even more to the complex **cXPC·Q**.

**Table 4.7** Effective concentrations (in mM) of quinolone monomers (**Q**), quinolone dimers (**Q·Q**), unbound photocatalyst (**cXPC**) and catalyst-substrate complexes (**cXPC·Q**) in  $\text{PhCF}_3$  at room temperature, calculated with the binding constants  $K_{\text{QQ}} = 3027 \text{ M}^{-1}$  and  $K_{\text{cXPCQ}} = 5865 \text{ M}^{-1}$  solving Equation System 4.16. The TA measurements discussed in this thesis were conducted under conditions (d) whereas the photocatalytic experiments in Ref. [5] and [156] were conducted under conditions (e).

	$[\text{Q}]_0$	$[\text{cXPC}]_0$	$[\text{Q}]$	$[\text{Q} \cdot \text{Q}]$	$[\text{cXPC}]$	$[\text{cXPC} \cdot \text{Q}]$
a)	0.1	0.1	0.056	0.010	0.075	0.025
b)	1.0	0.1	0.319	0.308	0.035	0.065
c)	1.0	1.0	0.204	0.126	0.455	0.545
<b>d)</b>	<b>2.5</b>	<b>1.0</b>	<b>0.464</b>	<b>0.652</b>	<b>0.269</b>	<b>0.731</b>
e)	5.0	0.5	0.792	1.898	0.089	0.411

### The Ground State Absorption Properties of the Photocatalytic Active Complex

In the previous section the dimerization of **Q** to the dimer **Q·Q** and the complexation of **cXPC** and **Q** to the catalyst-substrate complex **cXPC·Q** was quantified on the basis of experimental data. Due to both association processes, the absorption spectrum of the sample solution containing both **cXPC** and **Q** always comprises contributions from the dimer **Q·Q** and the complex **cXPC·Q**. Since the relative concentration of all contributing compounds can be calculated on the basis of the binding constants, the actual absorption spectrum of the complex **cXPC·Q** and furthermore its wavelength dependent absorption coefficient  $\epsilon(\mathbf{cXPC}\cdot\mathbf{Q})$  can be determined according to the Beer-Lambert law:

$$\epsilon(\mathbf{cXPC}\cdot\mathbf{Q}) = \frac{1}{[\mathbf{cXPC}\cdot\mathbf{Q}]} \left\{ \frac{\text{OD}(\mathbf{cXPC} + \mathbf{Q})}{d} - \epsilon(\mathbf{cXPC}) \cdot [\mathbf{cXPC}] \right\} \left\{ -\epsilon(\mathbf{Q}) \cdot ([\mathbf{Q}] + 2 \cdot [\mathbf{Q}\cdot\mathbf{Q}]) \right\} \quad (4.17)$$

The dimerization of quinolone proceeds via hydrogen bonding, which is generally a weak interaction and does not largely affect the optical properties of the quinolone chromophore. Hence, the absorption coefficient of the dimer **Q·Q** is assumed to be twice the absorption coefficient of the monomer **Q**. Insertion of the calculated concentrations of each compound from Table 4.7 leads to Equation 4.18 and provides the quantitative description of the absorption spectrum of the complex **cXPC·Q**.

$$\epsilon(\mathbf{cXPC}\cdot\mathbf{Q}) = \frac{1}{0.731 \text{ mM}} \left\{ \frac{\text{OD}(\mathbf{cXPC} + \mathbf{Q})}{1 \text{ mm}} - \epsilon(\mathbf{cXPC}) \cdot 0.269 \text{ mM} \right\} \left\{ -\epsilon(\mathbf{Q}) \cdot (0.464 \text{ mM} + 2 \times 0.652 \text{ mM}) \right\} \quad (4.18)$$

The resulting UV/Vis absorption spectrum of the complex  $\epsilon(\mathbf{cXPC}\cdot\mathbf{Q})$  compared to the spectra  $\epsilon(\mathbf{cXPC})$ ,  $\epsilon(\mathbf{Q})$  and its sum spectrum  $\epsilon(\mathbf{cXPC}) + \epsilon(\mathbf{Q})$  is shown in Figure 4.13.

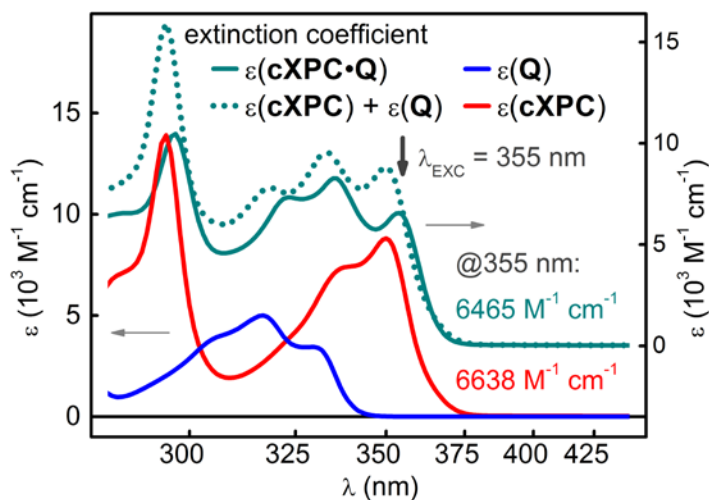


**Figure 4.13** Wavelength dependent absorption coefficients:  $\epsilon(\mathbf{Q})$  (blue line),  $\epsilon(\mathbf{cXPC})$  (red line), and  $\epsilon(\mathbf{cXPC}\cdot\mathbf{Q})$  (cyan line) compared to the expected absorption spectrum of the complex  $\epsilon(\mathbf{cXPC}) + \epsilon(\mathbf{Q})$  (cyan dotted line) in  $\text{PhCF}_3$ , measured in a  $d = 1$  mm cuvette at initial concentrations of  $[\mathbf{Q}]_0 = 2.5$  mM and  $[\mathbf{cXPC}]_0 = 1.0$  mM.

Assuming that the photophysical properties of the light absorbing chromophores remain constant in the closely stacked catalyst-substrate complex  $\mathbf{cXPC}\cdot\mathbf{Q}$ , its absorption spectrum should exactly render the sum of the spectra of  $\mathbf{Q}$  and  $\mathbf{cXPC}$  (cyan dotted line, Figure 4.13). However, although the measured absorption spectrum of its constituents  $\epsilon(\mathbf{cXPC}\cdot\mathbf{Q})$  (cyan line, Figure 4.13) comprises strong contributions of the absorption spectra of its constituents  $\epsilon(\mathbf{cXPC})$  and  $\epsilon(\mathbf{Q})$ , it strongly deviates from the expected sum spectrum  $\epsilon(\mathbf{cXPC}) + \epsilon(\mathbf{Q})$ . The close stacking of catalyst and substrate affects the electronic properties of both chromophores. In particular the shape and the strength of the absorption spectrum of  $\mathbf{cXPC}\cdot\mathbf{Q}$  deviate from the expected behavior. Whereas in a large spectral range the absorption strength of  $\mathbf{cXPC}\cdot\mathbf{Q}$  is lower than expected, between 350 and 370 nm an additional absorption emerges, which overlays with the red edge of the first  $\mathbf{cXPC}$  absorption band. Also the characteristic sharp absorption band of  $\mathbf{cXPC}$  around 295 nm is shifted to longer wavelengths in the complex  $\mathbf{cXPC}\cdot\mathbf{Q}$ .

The absorption strength of  $\mathbf{cXPC}\cdot\mathbf{Q}$ , which is in the order of  $10^4 \text{ M}^{-1} \text{ cm}^{-1}$  is comparable to common organic chromophores. With regard to the TA measurements performed in the framework of this study, in particular the absorption coefficient at the excitation wavelength  $\lambda_{\text{EXC}} = 355$  nm is of major interest. At 355 nm the complex  $\mathbf{cXPC}\cdot\mathbf{Q}$  exhibits nearly the same absorption strength ( $\epsilon_{355 \text{ nm}} = 6465 \text{ M}^{-1} \text{ cm}^{-1}$ ) compared to  $\mathbf{cXPC}$  ( $\epsilon_{355 \text{ nm}} = 6638 \text{ M}^{-1} \text{ cm}^{-1}$ ). However, in order to quantify the relative amounts of optical excitation of the complex  $\mathbf{cXPC}\cdot\mathbf{Q}$  and pure  $\mathbf{cXPC}$  in a sample solution at an excitation wavelength of  $\lambda_{\text{EXC}} = 355$  nm not only the absorption coefficient is of interest. Moreover the contributions of both complexed  $\mathbf{cXPC}\cdot\mathbf{Q}$  and uncomplexed  $\mathbf{cXPC}$  to the total optical density at the excitation wavelength is the determining quantity. By multiplication of the wavelength dependent absorption coefficient  $\epsilon(\lambda)$  with the mole fractions from Table 4.7 and an optical path length of  $d = 0.5$  mm used in the TA measurements, the contribution of each

constituent to the total optical density of the sample solution can be easily calculated. The result is shown in Figure 4.14.

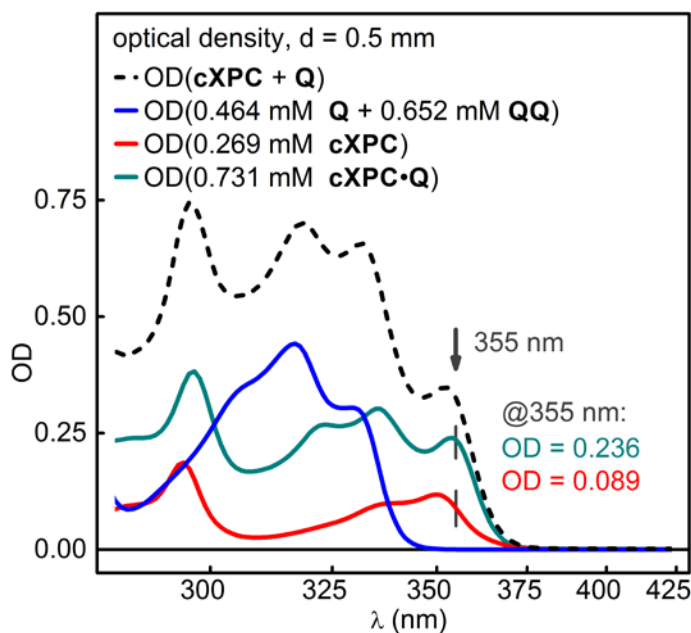


**Figure 4.14** Total optical density (black dotted line) of sample solution **cXPC + Q** and contributions of **Q** (blue line), **cXPC** (red line) and **cXPC·Q** (cyan line) in PhCF<sub>3</sub> at an initial concentration of [Q]<sub>0</sub> = 2.5 mM and [cXPC]<sub>0</sub> = 1.0 mM and d = 0.5 mm optical path length. Relative concentrations of all compounds from Table 4.7.

According to this analysis, excitation at  $\lambda_{\text{EXC}} = 355$  nm leads to a contribution of 73% of **cXPC·Q** and 27% of **cXPC** to the total excited state signal of the sample solution **cXPC + Q**. Under consideration of this distribution, the exact transient signal originating from **cXPC·Q** can be calculated by subtraction of a consistently scaled transient spectrum of **cXPC**. In the next section, the picture that stacking of catalyst and substrate leads to new electronic properties of the complex **cXPC·Q**, which are not present in its constituents **cXPC** and **Q** will be put on solid ground with the help of ab initio calculations.

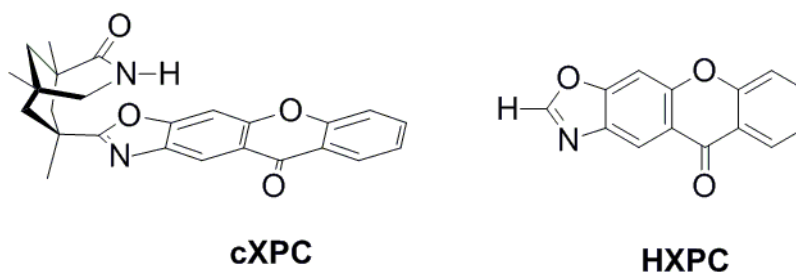
#### Ab Initio Calculations: New Photophysical Properties of the Catalyst-Substrate Complex

For the interpretation of the UV/Vis absorption spectrum of **cXPC·Q** and the observations in the TA measurements, quantum chemical calculations in the gas phase were conducted. The results presented in this section are relying on ab initio calculations performed by Igor Pugliesi (Ludwig Maximilian University).

The singlet ground state geometries of **Q**, **cXPC** and the complex **cXPC·Q** were optimized with the M062X density functional and the double  $\zeta$  basis set 6-31G\*. Frequencies were computed at the equilibrium geometries to verify that the optimized geometries are true minima. For all calculations the Gaussian09 ab initio suite was employed [251]. The xanthone chromophore moiety **cXPC** was found to be planar. Also for **Q** the quinolone

chromophore moiety is planar, while in the gas phase the butenyloxy chain is folded over the chromophore unit with the double bond nearly aligned with the CC double bond next to the C-O functional group. In the **cXPC·Q** ground state geometry **cXPC** and **Q** are parallel and 3.2 Å apart from each other.

To simulate the UV/Vis spectra of **cXPC**, **Q** and **cXPC·Q**, vertical energies were calculated using the M062X/6-31G\* ground state geometries. The resolution of identity coupled cluster method RI-CC2 [252, 253, 254] implemented in Turbomole [255] was used with the Karlsruhe double  $\zeta$  basis set def2-SVP and the triple  $\zeta$  basis set def2-TZVP as auxiliary basis set [256]. To reduce computational costs for the **cXPC·Q** complex, the aliphatic cage carrying the chiral hydrogen binding site of **cXPC** was replaced by a hydrogen atom forming the reduced photocatalyst **HXPC**. For all three species the core electrons were frozen. The reduced xanthone-based photocatalyst **HXPC** compared to the full molecule **cXPC** is shown in Scheme 4.13.



**Scheme 4.13** Chiral xanthone-based photocatalyst **cXPC** and the reduced xanthone-based photocatalyst **HXPC** applied to reduce the computational costs of the ab initio calculations.

The calculated spectra of **Q** and **HXPC** show their first strong transition at 291 and 293 nm and correspond very well to the measured UV/Vis absorption spectra (Figure 4.13) of **Q** and **cXPC** under consideration of the 0.2 eV blue-shift intrinsic to the RI-CC2 method [257] and the absence of the solvent. The calculated transitions can be associated with the measured absorption bands at 317 nm for **Q** and with 350 nm for **cXPC**. The spectral position and the intensity of the calculated transitions are schematically shown in Figure 4.15.

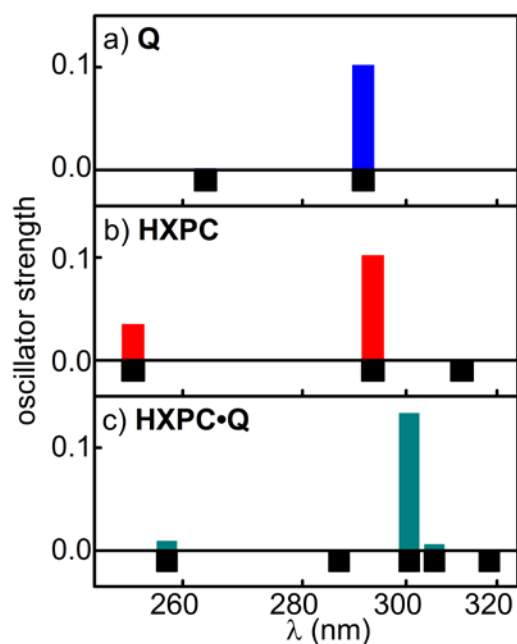


**Figure 4.15** Calculated absorption spectra at the RI-CC2/SVP/TZVP level of theory on M062X/6-31G\* ground state optimized geometries.

The calculated absorption spectrum of **HXPC·Q** (Figure 4.15 c) reveals two new absorption bands at 301 and 306 nm that are red-shifted with respect to the **Q** and **HXPC** spectra. These transitions can be associated with the increased absorption around 355 nm in the UV/Vis absorption spectrum of **cXPC·Q**. In comparison to the calculated transitions of the photocatalyst **HXPC** (Figure 4.15 b) the lowest  $\pi\pi^*$  transition of the complex **cXPC·Q** is red-shifted (Figure 4.15 c), as seen as well in the measured UV/Vis spectrum of **cXPC·Q** and **cXPC** (Figure 4.13). The lowest  $\pi\pi^*$  transitions of **HXPC·Q** involve orbitals, which are delocalized over both the xanthone and the quinolone moiety of the complex. Furthermore a partial CT character of this delocalized excited singlet state in which negative charge is transferred from **Q** to **HXPC** is present. The orbitals involved in both  $\pi\pi^*$  transitions are shown in Figure 4.16. It can be clearly seen, that these transitions are composed of orbitals, located both on the xanthone and the quinolone moiety of the catalyst-quinolone complex, but dominated by the xanthone moiety. However, in comparison to the calculated spectrum, the measured spectrum comprises stronger contributions of **Q** and **cXPC** located transitions. A systematic underestimation of transitions located exclusively on **Q** and **cXPC** in the calculations can explain these deviations between experiment and theory.

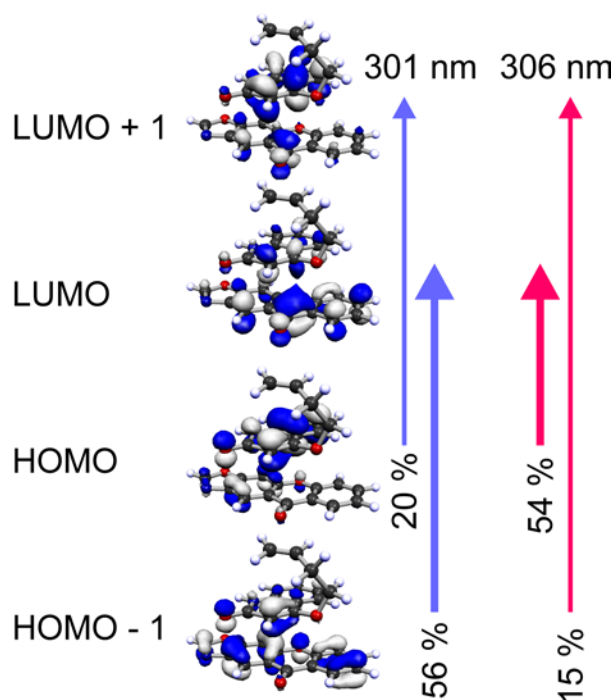


**Figure 4.16** Orbitals involved in the one electron excitations describing the lowest two  $\pi\pi^*$  transitions of **HXPC·Q**.

The weaker transition at 306 nm of the complex **HXPC·Q** is composed to 54% of one electron excitations from a  $\pi$  orbital localized on **Q** to a  $\pi$  orbital on **HXPC**. Additionally there is a transition with 15% from a  $\pi$  orbital localized on **HXPC** to a  $\pi$  orbital on **Q**. This transition is thus of charge transfer character. The stronger band at 301 nm is of locally excited character with a one electron  $\pi\pi^*$  excitation mainly localized on **HXPC** (56%) and a one electron  $\pi\pi^*$  mainly excitation localized on **Q** (20%). This transition is assigned to the increased absorption around 355 nm in the measured spectrum of **cXPC·Q** (Figure 4.13). The calculations show, that the increased absorption in **cXPC·Q** is due to excitonic coupling composed of transitions involving orbitals located both on the xanthone and the quinolone moiety. According to the calculations,  $\lambda_{\text{EXC}} = 355$  nm excitation in the TA measurement directly involves these delocalized excited states.

Furthermore the  $T_1$  state of the complex  $^3[\text{cXPC}\cdot\text{Q}]$  was investigated. The geometry of  $^3[\text{cXPC}\cdot\text{Q}]$  has been optimized at the M062X/6-31G\* level of theory using the Gaussian09 ab initio suite [251]. The obtained equilibrium geometry is very similar to that of the singlet ground state. Also the M062X/6-31G\* lowest triplet state of **cXPC·Q** has a delocalized character: Both singly occupied molecular orbitals (SOMOs) of the  $T_1$  state are  $\pi$  orbitals, one localized on the xanthone moiety and one on the quinolone moiety. Both SOMOs of the  $T_1$  state of the complex **cXPC·Q** are shown in Figure 4.17.

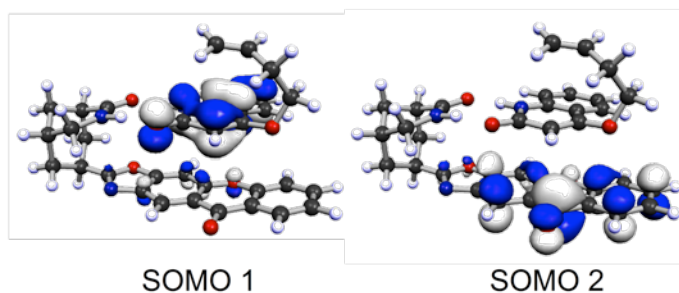


**Figure 4.17** Singly occupied molecular orbitals (SOMOs) of the delocalized  $T_1$  state of  $\mathbf{cXPC}\cdot\mathbf{Q}$ .

The SOMOs describing the triplet state are  $\pi$  orbitals, one localized on the xanthone moiety and one on the quinolone moiety. Thus, the  $T_1$  state is of charge transfer character, in which charge density equivalent to one electron is transferred from the quinolone to the xanthone moiety of the complex. The highest occupied molecular orbital (HOMO) is localized on the quinolone moiety whereas the lowest unoccupied molecular orbital (LUMO) is localized on the xanthone moiety. Hence, the  $T_1$  state is generated by electron transfer from  $\mathbf{Q}$  to  $\mathbf{cXPC}$ .

#### Photophysical Properties of the Photocatalyst $\mathbf{cXPC}$

The TA spectrum of sample solution  $\mathbf{cXPC} + \mathbf{Q}$  is composed of signals originating both from  $\mathbf{cXPC}$  and from  $\mathbf{cXPC}\cdot\mathbf{Q}$ . The relative intensity of both signals depends on the actual concentration of  $\mathbf{cXPC}$  and  $\mathbf{cXPC}\cdot\mathbf{Q}$  in the sample solution and the ratio of the absorption coefficient at the excitation wavelength. To allow for separation of both contributions in the data analysis, the photophysical properties and in particular the excited state dynamics of the xanthone-based photocatalyst  $\mathbf{cXPC}$  have to be reliably quantified. Therefore, TA spectroscopy on the fs-ps and on the ns- $\mu\text{s}$  time scale was performed on  $\mathbf{cXPC}$  in  $\text{PhCF}_3$ .

Comparable to pure xanthone [230], after excitation of the lowest optical accessible transition, the fs-ps TA spectrum of  $\mathbf{cXPC}$  is dominated by ultrafast ISC on the few ps time scale and a long-lived  $T_1$  state. Selected transient spectra of the fs-ps TA measurement after  $\lambda_{\text{EXC}} = 355 \text{ nm}$  excitation are shown in Figure 4.18.



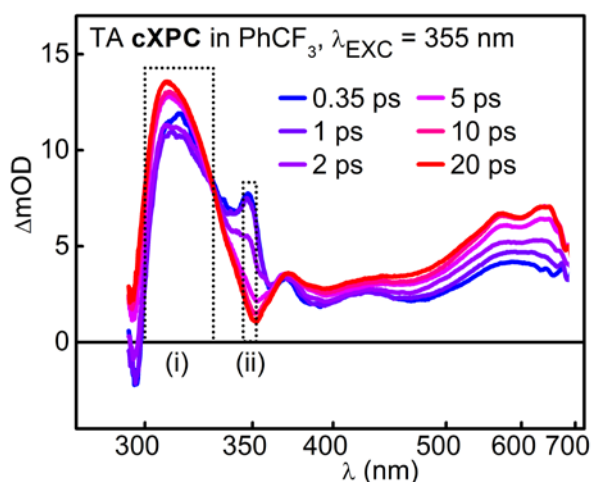


**Figure 4.18** Selected transient spectra from fs-ps TA of **cXPC** ( $[\mathbf{cXPC}] = 1.0 \text{ mM}$ ) in partially degassed  $\text{PhCF}_3$  ( $\lambda_{\text{EXC}} = 355 \text{ nm}$ ,  $E_{\text{EXC}} = 400 \text{ nJ}$ ,  $D_{\text{FWHM}} = 150 \mu\text{m}$ ,  $d = 0.5 \text{ mm}$ ). The temporal evolution of the signal within the boxed spectral regions is shown in Figure 4.20.

Particularly the excited state dynamics on the few ps time scale are overlaid by a multiplicity of processes, such as internal conversion both in the singlet and in the triplet manifold of xanthone [230], vibrational relaxation and solvation. Hence, the exact absorption spectrum of the **cXPC** excited singlet state  $^1[\mathbf{cXPC}]^*$  is not readily accessible. However, the transient absorption signal of the early transient spectra between 345 and 350 nm (boxed region (ii), Figure 4.18) is a  $S_1$  specific absorption and therefore suited to monitor the decay of the  $^1[\mathbf{cXPC}]^*$  state.

The  $T_1$  spectrum of **cXPC** exhibiting an absorption band in the UV, centered around 310 nm, and a broad absorption in the long-wave visible spectral region with two characteristic maxima around 570 and 640 nm is comparable to the  $T_1$  spectrum of pure xanthone with characteristic peaks around 294 and 640 nm (Figure 4.9). The splitting of the long-wave triplet absorption band into two sub-bands can be also observed for pure xanthone in a rather nonpolar solvent environment [240].

The analysis of the transient data matrices of sample solution **cXPC** + **Q**, in which not only **cXPC** contributes to the observed dynamics, requires an accurate quantification of the ISC process of  $^1[\mathbf{cXPC}]^*$ . However, conventional data analysis methods relying on single and multi channel fits (“band integral”) or a global data analysis (“global fit”) do not reveal a coherent picture of the process. Therefore maximum entropy analysis [258], which was developed in the group of Bernhard Dick (University of Regensburg), is applied to reliably quantify the excited state dynamics of **cXPC** on the few ps time scale. In comparison to the maximum entropy analysis, conventional data analysis algorithms generally provide one time constant, which most likely describes the dynamics of the underlying process, usually assuming an exponential decay model. In contrast, maximum entropy analysis describes the probability  $p(\tau)$  of each time constant  $\tau$  within a selected interval to describe the process causing spectral changes on the basis of an exponential function. The resulting probability curves for selected spectral traces are shown in Figure 4.19.

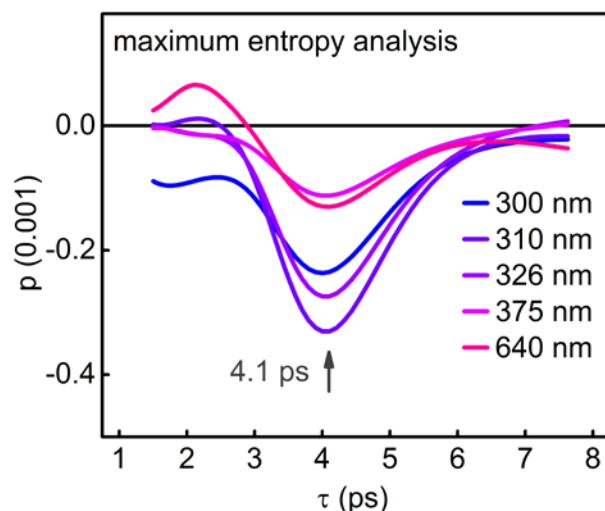


**Figure 4.19** Maximum entropy analysis of selected spectral traces from the fs-ps TA of **cXPC** in  $\text{PhCF}_3$  after  $\lambda_{\text{EXC}} = 355$  nm excitation. Values below 1 ps are clipped, due to the temporally broad coherent artifact in this measurement.

The maximum entropy analysis clearly reveals a time constant of  $\tau_{\text{ISC}} = 4.1$  ps to describe the ISC process of  $^1[\text{cXPC}]^*$ , which is comparable to pure xanthone ( $\tau_{\text{ISC}} = 1.5$  ps [230]). To prove the reliability of the obtained time constant, a sum of exponential functions<sup>28</sup> was fitted to describe the temporal evolution of the integrated transient absorption signal of the selected spectral regions (boxed regions, Figure 4.18). The data points and the resulting fit curves with  $\tau_{\text{ISC}} = 4.1$  ps as fixed parameter are shown in Figure 4.20. The values of the remaining fit parameter  $\tau_{\text{FWHM}}$ ,  $\tau_1$ ,  $\tau_2$  and  $\tau_3$  are given in the figure caption.

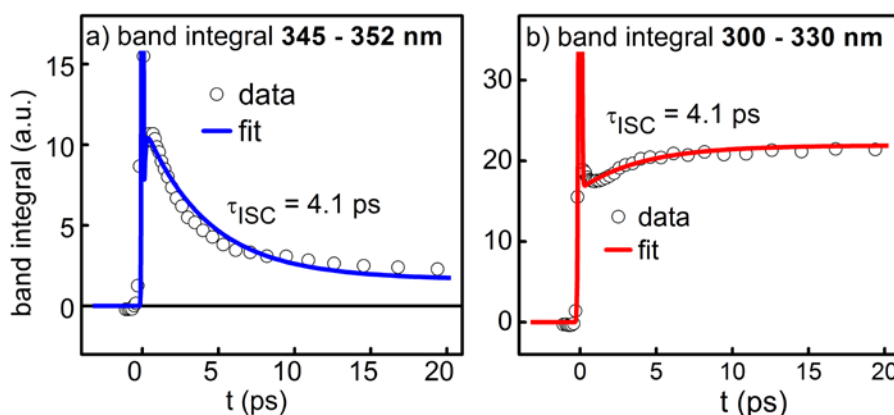


**Figure 4.20** a) Integrated signal of a  $^1[\text{cXPC}]^*$  specific absorption band, fit with  $\tau_{\text{FWHM}} = 94$  fs,  $\tau_1 = 0.08$  ps,  $\tau_{\text{ISC}} = 4.1$  ps (fixed, from maximum entropy analysis),  $\tau_2 = 120$  ps,  $\tau_3 = \text{inf}$ . b) Integrated signal of a  $^3[\text{cXPC}]$  specific absorption band, fit with  $\tau_{\text{FWHM}} = 186$  fs,  $\tau_{\text{ISC}} = 4.1$  ps (fixed, from maximum entropy analysis),  $\tau_3 = \text{inf}$ .

<sup>28</sup> program path at the Chair for BioMolecular Optics (Ludwig Maximilian University):  
 \\johann\agriedle\Software\_und\_Treiber\Labview\Auswertung\_Spektroskopie\band integral (2014-01-25)

The temporal evolution of the selected spectral regions on the few ps time scale is rather complex. Although a sum of up to 4 exponential functions is used to describe the transient signal, there are still minor deviations between fit curve and data points. However, the time constant of  $\tau_{\text{ISC}} = 4.1$  ps seems to be a good compromise to describe the major component of the temporal evolution.

The life time of  $^3[\text{cXPC}]$  clearly exceeds the accessible temporal window of the experimental setup used for fs-ps TA spectroscopy. To quantify the life time of  $^3[\text{cXPC}]$ , TA spectroscopy on the ns- $\mu\text{s}$  time scale was required. The transient spectra of the ns- $\mu\text{s}$  TA measurement of **cXPC** after  $\lambda_{\text{EXC}} = 355$  nm excitation are rather unspectacular and exclusively show the exponential decay of the  $^3[\text{cXPC}]$  specific absorption. Therefore the transient data matrix is not shown in a profile plot. The ISC from singlet to triplet manifold cannot be resolved within this type of measurement. However, the global fit analysis of the data matrix provides the most reliable spectral rendering of the  $^3[\text{cXPC}]$  absorption. The resulting DADS are therefore shown in Figure 4.21.

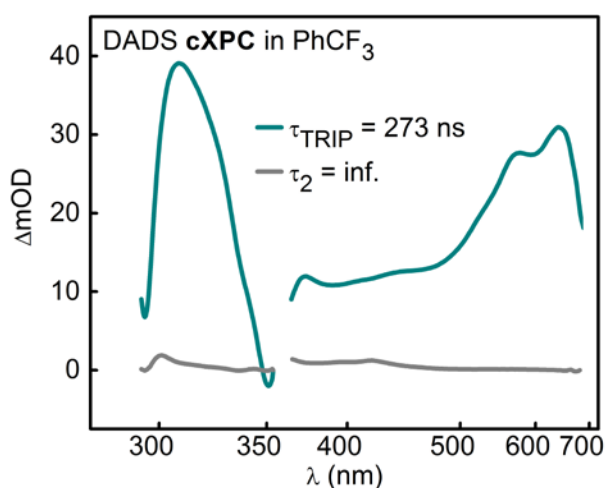


**Figure 4.21** DADS from ns- $\mu\text{s}$  TA of **cXPC** ( $[\text{cXPC}] = 1.0$  mM) in partially degassed  $\text{PhCF}_3$  ( $\lambda_{\text{EXC}} = 355$  nm,  $E_{\text{EXC}} = 400$  nJ,  $D_{\text{FWHM}} = 150$   $\mu\text{m}$ ,  $d = 0.5$  mm).

The  $^3[\text{cXPC}]$  spectrum is dominated by an absorption band in the UV, centered around 310 nm and a broad absorption in the long-wave visible spectral region with two characteristic maxima around 570 and 640 nm (cyan line, Figure 4.21). In the environment of partially degassed  $\text{PhCF}_3$  as solvent the  $^3[\text{cXPC}]$  life time is  $\tau_{\text{TRIP}} = 273$  ns. The DADS associated with  $\tau_2 = \text{inf.}$  renders the base line and therefore proves that the decay of  $^3[\text{cXPC}]$  is not overlaid by competing processes as observed for pure xanthone (vide supra). This indicates that **cXPC** is sufficiently photo-stable in the environment of partially degassed  $\text{PhCF}_3$  at room temperature.

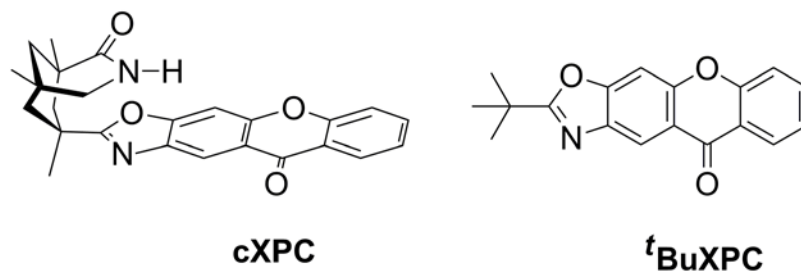
The results presented in this section provide a solid base for the investigation of the more complex dynamics observed in the TA measurements of sample solution **cXPC** + **Q**. Not only the ultrafast ISC of **cXPC**, described by a time constant of  $\tau_{\text{ISC}} = 4.1$  ps, was quantified but also the spectral shape of the  $^3[\text{cXPC}]$  absorption was characterized with high precision,

which will help to identify **cXPC** triplet species occurring in the photocatalytic process of **cXPC** and **Q**.

### Spectroelectrochemistry

To identify a potential charge separation process within the catalyst-quinolone complex, the radical ion spectra of quinolone and the xanthone-based photocatalyst were measured with the help of spectroelectrochemistry.

Spectroelectrochemical measurements usually require a thin optical glass cuvette and therefore a rather dense solution and a high amount of sample for a sufficient signal intensity. Since the chiral xanthone-based photocatalyst **cXPC** requires a laborious synthesis route, the nearly identical, but synthetically cheaper compound **<sup>t</sup>BuXPC** was used for spectroelectrochemistry. The light absorbing xanthone-based chromophore, which determines the photophysical properties is equal in **cXPC** and in **<sup>t</sup>BuXPC**. In comparison to pure xanthone, the chromophores both of **cXPC** and **<sup>t</sup>BuXPC** are complemented by an additional oxazole ring. The structures of **<sup>t</sup>BuXPC** and **cXPC** are shown in Scheme 4.14.



**Scheme 4.14** Structure of **<sup>t</sup>BuXPC** (right), used instead of **cXPC** (left) in the spectroelectrochemistry measurements. The chromophore is identical since both compounds have an oxazole ring attached to the xanthone backbone.

The spectroelectrochemical measurements reveal a very strong ( $\epsilon \cong 18,000 \text{ M}^{-1} \text{ cm}^{-1}$ ) absorption band centered around 390 nm of the radical anion **<sup>t</sup>BuXPC<sup>-•</sup>**.

Since the reference quinolone **rQ** is less reactive compared to the substrate **Q**, **rQ** was employed for the determination of the quinolone radical cation spectrum. However, spectroelectrochemistry measurements performed on **Q** revealed equal absorption properties of the cation **Q<sup>+</sup>** [236]. The quinolone radical cation **rQ<sup>•+</sup>** shows an increased absorption around 300 nm with respect to its ground state absorption spectrum. The spectroelectrochemical reduction and oxidation processes are shown Figure 4.22.

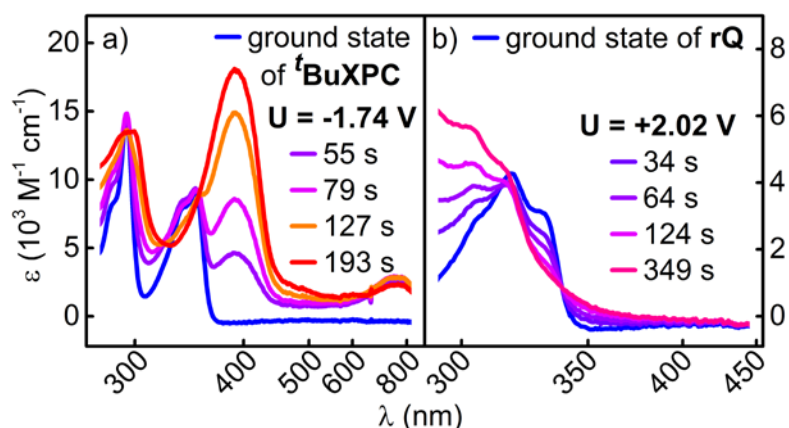


**Figure 4.22** Spectroelectrochemical raw data of the reduction of **tBuXPC** (a) and of **rQ** (b), measured in acetonitrile, voltages against NHE. The ground state absorption spectra (blue lines) were measured without applying any voltage.

### Photo-Induced Charge Separation from the Delocalized Triplet State and Charge Re-combination in the Reference Complex

For an elementary understanding of the rather diverse excited state dynamics of the photocatalytic active complex **cXPC·Q**, the analysis starts with a more simple approach. Therefore, in a first measurement series, the reference complex **cXPC·rQ**, was studied. The use of reference quinolone **rQ**, which cannot react in a [2+2] photocycloaddition, provides insights into the early steps of the reaction, as already shown for the diffusion-controlled sensitization of the [2+2] photocycloaddition of quinolone by xanthone (Chapter 4.2.3).

One major issue that has to be considered is the multiplicity of different transient signals contributing to the transient absorption spectrum of sample solution **cXPC + rQ**. Particularly the signals originating from **cXPC·rQ** and from uncomplexed **cXPC** are required to be separated to provide an accurate analysis of the excited state dynamics of the catalyst-quinolone complex **cXPC·rQ**. As the limit of the temporal resolution was estimated to be approximately 240 fs (Chapter 4.2.2), the investigation of the transient absorption signal at a pump-probe delay of  $\Delta t = 350$  fs seems to be suited as basis for the discussion of the very early steps of the reaction. Therefore, Figure 4.23 a) shows the transient spectrum after  $\lambda_{\text{EXC}} = 355$  nm excitation of sample solution **cXPC + rQ** (red line) compared to the spectrum of the pure photocatalyst **cXPC** (blue line) at a pump-probe delay of  $\Delta t = 350$  fs.

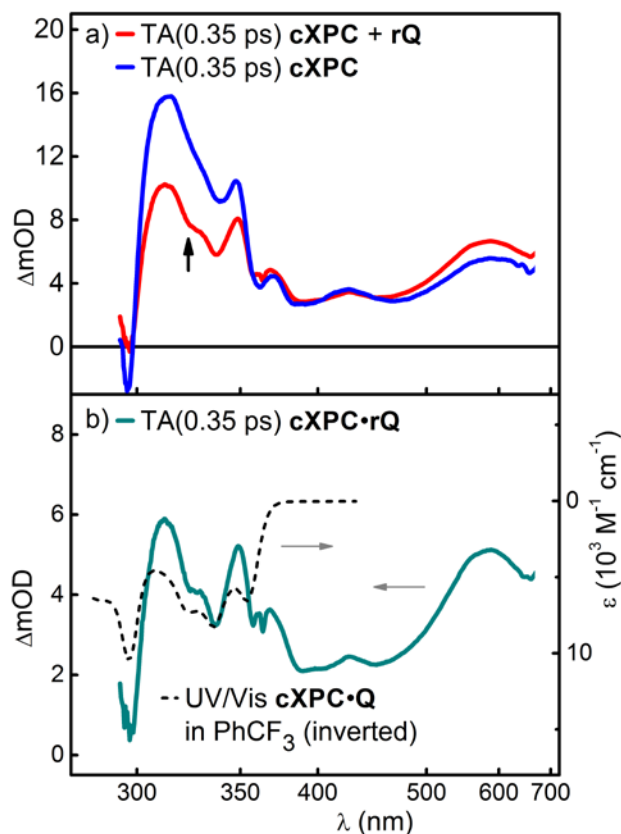


**Figure 4.23** a) TA(0.35 ps) of sample solution **cXPC + rQ** (red line) and of **cXPC** (blue line) ( $\lambda_{\text{EXC}} = 355 \text{ nm}$ ,  $E_{\text{EXC}} = 400 \text{ nJ}$ ,  $D_{\text{FWHM}} = 150 \mu\text{m}$ ,  $d = 0.5 \text{ mm}$ ), b) TA(0.35 ps) of complex **cXPC·rQ** (cyan line) and comparison to the inverse ground state absorption spectrum of **cXPC·Q** (black dotted line)

The transient spectra of the sample solution **cXPC + rQ** and of pure **cXPC** show qualitatively comparable characteristics. Since the spectrum of **cXPC + rQ** (red line, Figure 4.23) comprises a reasonable contribution of the excited state absorption of **cXPC**, the spectral similarity is not too surprising. On a closer view, it can be seen that there are significant deviations between both spectra in the wavelength region between 320 and 340 nm (black arrow, Figure 4.23 a): Whereas the spectrum of **cXPC** is smooth in this region, the spectrum of sample solution **cXPC + rQ** is lower in intensity and shows an overlaying structuring. For an exact quantitative determination of the transient spectrum of **cXPC·rQ** at a pump-probe delay of  $\Delta t = 350 \text{ fs}$ , the spectrum of **cXPC** has to be subtracted from the data, using the scaling factor derived in Chapter 4.2.2. The scaling factor of 0.37 considers both the relative concentration (Table 4.7) and the relative absorption coefficients (Figure 4.13) of uncomplexed **cXPC** and complexed **cXPC·rQ** at the excitation wavelength and takes the specific excitation energy density in each measurement into account.

$$\text{TA}(350 \text{ fs}, \mathbf{cXPC} \cdot \mathbf{Q}) = \text{TA}(350 \text{ fs}, \mathbf{cXPC} + \mathbf{Q}) - 0.37 \cdot \text{TA}(350 \text{ fs}, \mathbf{cXPC}) \quad (4.19)$$

The resulting transient spectrum of the complex **cXPC·rQ** and its comparison to the inverted ground state absorption spectrum of **cXPC·Q** is shown in Figure 4.23 b). It can be clearly seen, that the transient spectrum (cyan line) comprises strong contributions of the ground

state absorption spectrum of the catalyst-quinolone complex **cXPC·Q** (black dotted line), which appears inversely as ground state bleach. Characteristic features both of the xanthone and the quinolone moiety of the complex **cXPC·Q** reappear in this early transient spectrum. Minor deviations can be readily explained by a structured overlaying excited state absorption. The analysis of the early transient absorption spectra give clear evidence, that excitation at  $\lambda_{\text{EXC}} = 355$  nm actually leads to an excited state, which involves both the xanthone and the quinolone moiety of the complex. As this excited state is neither localized on the quinolone nor on the xanthone moiety, it is referred to this state as a delocalized excited state. Hence, the initially proposed picture [156], that photo-excitation leads to a xanthone located excited state, which is transferred by excitation energy transfer to the quinolone, must be reconsidered. As the complexation of both chromophores and particularly the interaction of the  $\pi$ -orbitals lead to new optically accessible electronic states, as shown in the ab initio calculations (vide supra), the observed excited state is considered as the lowest excited singlet state  $^1[\text{cXPC}\cdot\text{rQ}]^*$  of the catalyst-quinolone complex. As the temporal resolution was approximately 240 fs in these measurements, the delocalized excited state  $^1[\text{cXPC}\cdot\text{rQ}]^*$  is either directly populated upon photo-excitation or formed faster than 240 fs from a **cXPC** localized excited state. However, as the ab initio calculations support the picture of an optically accessible delocalized excited state of the catalyst-quinolone complex, the direct photo-excitation of **cXPC·rQ** to  $^1[\text{cXPC}\cdot\text{rQ}]^*$  is more likely.

For an understanding of the photocatalytic reaction, the excited state dynamics of the complex **cXPC·rQ** need to be quantified. As already observed in the initial fs-ps TA measurement of sample solution **cXPC + Q**, the transient spectra do not show significant excited state dynamics on the time scale  $10 \text{ ps} < \Delta t < 2000 \text{ ps}$ , but only on the few ps time scale. The xanthone-based photocatalyst **cXPC**, which undergoes ISC within  $\tau_{\text{ISC}} = 4.1 \text{ ps}$ , presumably affects the excited state properties of **cXPC·rQ** and therefore causes as well a rather fast ISC of the singlet state  $^1[\text{cXPC}\cdot\text{rQ}]^*$  to the triplet state  $^3[\text{cXPC}\cdot\text{rQ}]$  of the complex. However, due to a multiplicity of overlaying dynamics in the transient signal of sample solution **cXPC + Q** on the few ps time scale, conventional analysis methods are not sufficient for an exact quantification of the ISC dynamics. For an accurate data analysis, the following contributing processes, which affect the observed transient absorption signal, have to be taken into account:

- ISC of  $^1[\text{cXPC}\cdot\text{rQ}]^*$
- ISC of  $^1[\text{cXPC}]^*$ :  $\tau_{\text{ISC}} = 4.1 \text{ ps}$  (vide supra)
- Rise of the absorption signal of the solvated electron:  $\tau = 12.4 \text{ ps}$  (vide supra)
- Internal conversion of  $^3[\text{cXPC}]$  within the triplet manifold:  $\sim 10 \text{ ps}$  (for xanthone [230])
- Vibrational relaxation of **cXPC** and **cXPC·rQ**: few ps – tens of ps [259]
- Solvation processes: hundreds of fs – tens of ps [260]

Yet, only the ISC process of  $^1[\text{cXPC}]^*$  within  $\tau_{\text{ISC}} = 4.1 \text{ ps}$  and the rise of the absorption of the transient absorption of the solvated electron within  $\tau = 12.4 \text{ ps}$  have been reliably



quantified. For the quantification of the excited state dynamics and particularly the ISC process of  $^1[\mathbf{cXPC}\cdot\mathbf{rQ}]^*$ , maximum entropy analysis [258] is applied, which was already introduced and applied for the analysis of the TA signal of  $\mathbf{cXPC}$  (vide infra). The resulting probability curves of a selected probe wavelength, which is exemplarily for all other spectral traces, are shown in Figure 4.24. In Figure 4.24 not only the probability curves for  $\mathbf{cXPC}$  and sample solution  $\mathbf{cXPC} + \mathbf{rQ}$ , but also for sample solution  $\mathbf{cXPC} + \mathbf{Q}$ , which is discussed in detail in the next section, are shown.

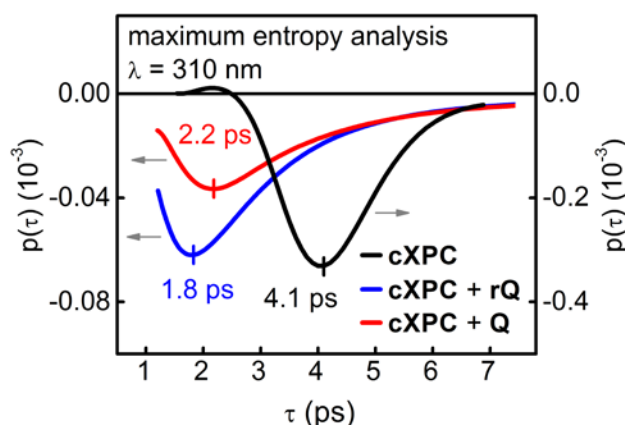


**Figure 4.24** Maximum entropy analysis of the 310 nm spectral trace of the fs-ps TA of  $\mathbf{cXPC}$  (black),  $\mathbf{cXPC} + \mathbf{rQ}$  (blue) and  $\mathbf{cXPC} + \mathbf{Q}$  (red). Remarkable is the asymmetric shape of  $\mathbf{cXPC} + \mathbf{rQ}$  and  $\mathbf{cXPC} + \mathbf{Q}$  which is due to the overlying  $\tau = 4.1$  ps component from uncomplexed  $\mathbf{cXPC}$ . The light grey arrows indicate the ordinate for each graph.

The probability curve of  $\mathbf{cXPC}$  (black line) is of symmetric shape whereas the probability curves of the catalyst-quinolone complexes  $\mathbf{cXPC}\cdot\mathbf{rQ}$  (blue line) and  $\mathbf{cXPC}\cdot\mathbf{Q}$  (red line) are of asymmetric shape. However, this behavior is in agreement with the expectations: the falling edge of the curves indicates that a broader distribution of processes contributes to the observed excited state dynamics. As  $\lambda_{\text{EXC}} = 355$  nm photo-excitation of both sample solutions  $\mathbf{cXPC} + \mathbf{rQ}$  and  $\mathbf{cXPC} + \mathbf{Q}$  leads to a contribution of 28% (Chapter 4.2.2) of uncomplexed  $\mathbf{cXPC}$  to the total number of excited molecules, the intrinsic dynamics of  $\mathbf{cXPC}$  in the transient spectrum cannot be neglected. The falling edges of the probability curves of the catalyst-quinolone complexes reflect the overlaying intrinsic ISC process of uncomplexed  $\mathbf{cXPC}$  within  $\tau_{\text{ISC}} = 4.1$  ps. Hence, the maxima of the probability curves, which are centered around  $\tau = 1.8$  ps ( $\mathbf{cXPC} + \mathbf{rQ}$ ) and  $\tau = 2.2$  ps ( $\mathbf{cXPC} + \mathbf{Q}$ ) reflect the excited state dynamics of the catalyst-quinolone complexes. The fs-ps TA spectra of sample solutions  $\mathbf{cXPC} + \mathbf{rQ}$  and  $\mathbf{cXPC} + \mathbf{Q}$  do not reveal further processes up to a pump-probe delay of  $\Delta t = 2$  ns. As the ISC process of the catalyst-quinolone complexes was already expected to occur on the few ps time scale, the observed time constants of  $\tau = 1.8$  and  $\tau = 2.2$  can be safely identified with the ISC process of  $^1[\mathbf{cXPC}\cdot\mathbf{rQ}]^*$  and  $^1[\mathbf{cXPC}\cdot\mathbf{Q}]^*$ , respectively.

According to this picture, the transient data matrix of sample solution  $\mathbf{cXPC} + \mathbf{rQ}$  for pump-probe delays  $10 \text{ ps} < \Delta t < 2000 \text{ ps}$  is exclusively composed of triplet-triplet absorption signal of  $^3[\mathbf{cXPC}]$  and of  $^3[\mathbf{cXPC}\cdot\mathbf{rQ}]$ . The relative contribution of each component to the total



signal intensity can be deduced from the ratio of complexed and uncomplexed photocatalyst (Table 4.7) and the ratio of the absorption coefficients of both compounds at the excitation wavelength of  $\lambda_{\text{EXC}} = 355 \text{ nm}$  (Figure 4.13). According to these quantities, the spectrum of  $^3[\text{cXPC}]$  has a contribution of 28% to the total signal, whereas the spectrum of  $^3[\text{cXPC}\cdot\text{rQ}]$  accounts for 72% of the signal. This estimation was already used to calculate the excited state absorption of the singlet state  $^1[\text{cXPC}\cdot\text{rQ}]^*$  of the complex (Figure 4.23, Equation 4.19). For a meaningful discussion of the triplet-triplet absorption of  $^3[\text{cXPC}\cdot\text{rQ}]$  a pump-probe delay of  $\Delta t = 100 \text{ ps}$  was chosen. Therefore Figure 4.25 a) shows the TA signal at a pump-probe delay of  $\Delta t = 100 \text{ ps}$  both of sample solution  $\text{cXPC} + \text{rQ}$  (red line) and of  $\text{cXPC}$  (blue line). Figure 4.25 b) shows the triplet-triplet absorption of the complex  $^3[\text{cXPC}\cdot\text{rQ}]$  which was calculated on the basis of the spectra shown in Figure 4.25 a).

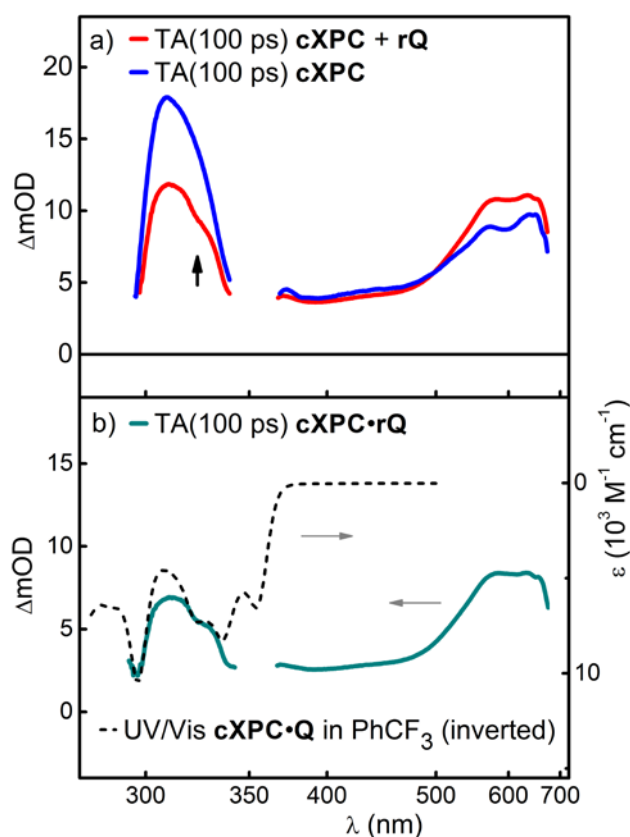


**Figure 4.25** a) TA(100 ps) after  $\lambda_{\text{EXC}} = 355 \text{ nm}$  excitation of sample solution  $\text{cXPC} + \text{rQ}$  (red line) and  $\text{cXPC}$  (blue line) in  $\text{PhCF}_3$ . b) TA(100 ps) of the complex  $\text{cXPC}\cdot\text{rQ}$  (cyan line) and comparison to the inverse ground state absorption spectrum of  $\text{cXPC}\cdot\text{Q}$  (black dotted line)

The  $^3[\text{cXPC}\cdot\text{rQ}]$  spectrum with characteristic absorption maxima around 315 nm and a broad absorption in the long-wave spectral region between 570 and 640 nm (cyan line, Figure 4.25 b) is qualitatively comparable to the triplet-triplet absorption spectrum of  $^3[\text{cXPC}]$  (blue line Figure 4.25 a). However, in the ultraviolet spectral region, the TA spectrum of  $\text{cXPC}\cdot\text{rQ}$  comprises strong contributions of the ground state absorption spectrum of  $\text{cXPC}\cdot\text{Q}$  (black dotted line, Figure 4.25 b), which appear inversely as ground state bleach. This observation again supports the picture, that the whole catalyst-quinolone

complex  $\mathbf{cXPC}\cdot\mathbf{rQ}$  still remains in an excited state. The triplet state  $^3[\mathbf{cXPC}\cdot\mathbf{rQ}]$  involves the whole complex and is neither located on the quinolone nor the xanthone moiety.

To follow the excited state dynamics of  $^3[\mathbf{cXPC}\cdot\mathbf{rQ}]$ , ns- $\mu$ s TA spectroscopy with an excitation wavelength of  $\lambda_{\text{EXC}} = 355$  nm was performed on the sample solution  $\mathbf{cXPC} + \mathbf{rQ}$ . As the reference compound  $\mathbf{rQ}$  is not able to undergo a [2+2] cycloaddition, this measurement might reveal a deeper understanding of the early reaction steps, which lead to product formation in the photocatalytic active complex  $\mathbf{cXPC}\cdot\mathbf{Q}$ . As a profile plot reveals information about the spectral properties of a certain state but provides only limited insights into the spectral changes caused by the underlying processes, the more meaningful DADS analysis of the ns- $\mu$ s TA measurement of sample solution  $\mathbf{cXPC} + \mathbf{rQ}$  is shown in Figure 4.26.

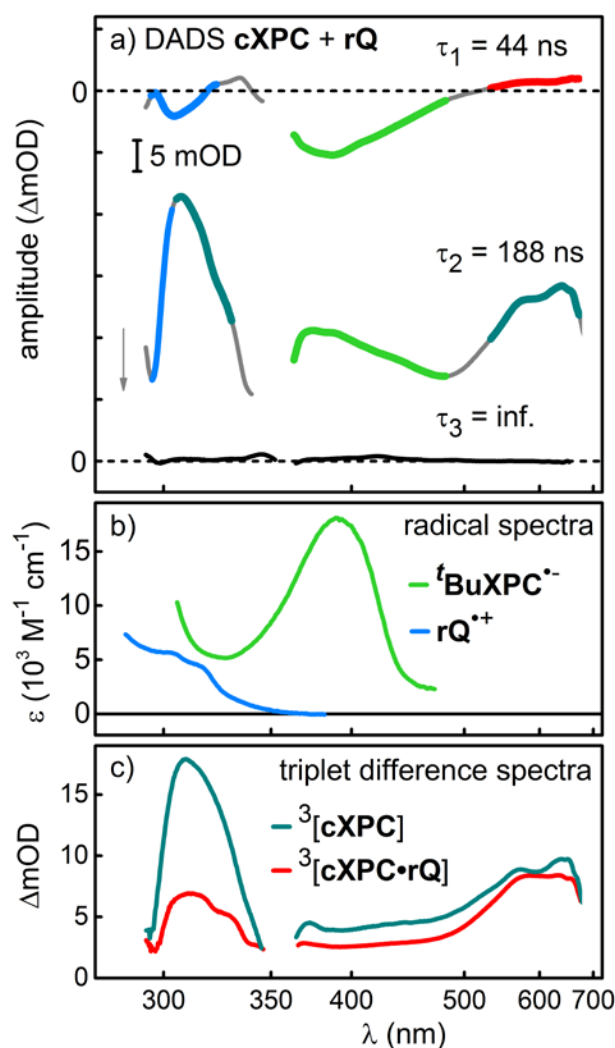


**Figure 4.26** a) DADS of ns- $\mu$ s TA after  $\lambda_{\text{EXC}} = 355$  nm excitation of  $\mathbf{cXPC} + \mathbf{rQ}$ . b) Radical ion spectra of  ${}^t\text{BuXPC}^{\bullet-}$  and  $\mathbf{rQ}^{\bullet+}$ . c) Difference spectra of the triplet states  $^3[\mathbf{cXPC}]$  and  $^3[\mathbf{cXPC}\cdot\mathbf{rQ}]$  with respect to the ground state absorption of  $\mathbf{cXPC}$  and  $\mathbf{cXPC}\cdot\mathbf{rQ}$ .

The spectral changes in the transient spectrum can be described by two processes with characteristic time constants of  $\tau_1 = 44$  ns and  $\tau_2 = 188$  ns. The DADS related with an infinity

time constant (black line, Figure 4.26 a), which renders the base line, indicates that product formation or a reasonable amount of photo-degradation of the photocatalyst do not occur in this type of experiment.

However, it has to be kept in mind, that generally both the ns- $\mu$ s TA spectrum and the DADS comprise contributions both of **cXPC** and **cXPC·rQ**. The life time of the  $T_1$  state  $^3[\text{cXPC}]$  in partially degassed  $\text{PhCF}_3$  is  $\tau_{\text{TRIP}} = 273$  ns (Figure 4.21). Hence, the  $\tau_1 = 44$  ns DADS unambiguously reflects a process, which exclusively involves  $^3[\text{cXPC·rQ}]$ , the triplet state of the catalyst-quinolone complex. This DADS is composed of multiple contributions, which are marked in different colors (Figure 4.26 a). In the ultraviolet spectral region, the absorption around 305 nm slightly increases, which is indicated by a negative amplitude of the DADS (marked in light blue). The major component is a broad upcoming absorption band around 390 nm, appearing as well as signal with negative amplitude in the DADS (marked in light green). In the visible spectral region between 540 and 670 nm, the positive amplitude of the DADS renders the decay of an absorption band (marked in red). As the underlying process exclusively involves the excited state dynamics of the triplet state of the complex  $^3[\text{cXPC·rQ}]$ , this decaying absorption is associated with the depopulation of this state, which can be seen by comparison to the triplet-triplet absorption of  $^3[\text{cXPC·rQ}]$ , which is shown on the same wavelength scale (red line) in Figure 4.26 c). The rather low amplitude of the DADS in this spectral region (red line, Figure 4.26 a) is probably an effect of the global data analysis. As both observed time constants  $\tau_1 = 44$  ns and  $\tau_2 = 188$  ns are of comparable magnitude, the spectral changes cannot always be perfectly assigned to the corresponding DADS in the global fit analysis.

However, the question remains still unanswered, which kind of state is actually populated from the triplet state  $^3[\text{cXPC·rQ}]$ . The upcoming absorption bands (marked in light blue and light green, Figure 4.26 a) so far cannot be associated with any known spectral signatures. A localization or transfer of the triplet state  $^3[\text{cXPC·rQ}]$  on the quinolone moiety of the complex would lead to an upcoming absorption band centered around 430 nm, which represents the maximum of the quinolone triplet-triplet absorption (Figure 4.10), and not around 390 nm as seen in the DADS. The comparison of the upcoming absorption bands with the absorption spectra of the spectroelectrochemically determined radical ion spectra of **'BuXPC<sup>-</sup>**, which is similar to the absorption of **cXPC<sup>-</sup>** (light green line, Figure 4.26 b), and **rQ<sup>+</sup>** (light green line, Figure 4.26 b) provides an answer to the question of the nature of the populated state. According to this, the upcoming absorption bands can be associated with the radical ion spectra of **cXPC<sup>-</sup>** and **rQ<sup>+</sup>**. Whereas the upcoming absorption band around 390 nm can be clearly identified with the spectrum of **cXPC<sup>-</sup>** (light green line, Figure 4.26 b) the increasing absorption around 300 nm can be identified with the spectrum of **rQ<sup>+</sup>** (light green line, Figure 4.26 b). It has to be kept in mind, that the  $^3[\text{cXPC·rQ}]$  spectrum already shows excited state absorption in this spectral region and therefore the related DADS, which only renders the spectral changes caused by the underlying process, is not too high in amplitude in this spectral region.

As the  $\tau_1 = 44$  ns DADS on the one hand is exclusively related with the triplet state of the complex  $^3[\text{cXPC·rQ}]$  and on the other hand all spectral contributions of the DADS were

identified, the data base is sufficient to describe the underlying process. The DADS is composed of spectral signatures, which render both the decay of the complex triplet state  $^3[\mathbf{cXPC}\cdot\mathbf{rQ}]$  and the population of a radical ion pair, comprising the spectra of  $\mathbf{cXPC}^-$ , the radical anion of the photocatalyst and of  $\mathbf{rQ}^+$ , the radical cation of quinolone. Hence, the time constant of  $\tau_1 = 44$  ns can be associated with a charge separation process, in which one electron is transferred from the quinolone moiety to the xanthone moiety of the complex, forming the radical ion pair of  $\mathbf{cXPC}^-/\mathbf{rQ}^+$ . As the ab initio calculations already revealed a charge transfer character of the delocalized  $T_1$  state  $^3[\mathbf{cXPC}\cdot\mathbf{rQ}]$ , in which negative charge density is transferred from the quinolone to the xanthone moiety of the complex, the term “charge localization” instead of “charge transfer” might be better suited for the description of the underlying process. Furthermore, the observed process depicts the transition of the delocalized triplet state  $^3[\mathbf{cXPC}\cdot\mathbf{rQ}]$  into a radical ion pair of  $\mathbf{cXPC}^-/\mathbf{rQ}^+$  in which the individual properties of the components  $\mathbf{cXPC}$  and  $\mathbf{Q}$  of the complex reappear and the electronic states become localized again.

As the DADS related with  $\tau_1 = 44$  ns is fully understood, the DADS related with  $\tau_2 = 188$  ns is discussed in the next section. Since the DADS related with an infinity time constant (black line, Figure 4.26 a) exactly renders the base line of the TA spectrum, the  $\tau_2 = 188$  ns DADS exclusively represents decay processes, which lead back to the ground states of  $\mathbf{cXPC}$  and  $\mathbf{cXPC}\cdot\mathbf{rQ}$ . Whereas a contribution of the decay of the  $T_1$  state  $^3[\mathbf{cXPC}]$  of uncomplexed  $\mathbf{cXPC}$  in the  $\tau_1 = 44$  ns DADS could be definitely negated, its contribution to the  $\tau_2 = 188$  ns DADS has to be considered. The ns- $\mu$ s TA of  $\mathbf{cXPC}$  revealed an intrinsic triplet life time of  $\tau_{\text{TRIP}} = 273$  ns (Figure 4.21). The triplet life time of uncomplexed  $\mathbf{cXPC}$  might vary slightly around this value due to changes in oxygen concentration between the measurements, as the applied degasser does not provide accurately reproducible measurement conditions. Additionally overlaying diffusion controlled triplet state quenching by diluted quinolone decreases the observed triplet life time of  $^3[\mathbf{cXPC}]$  in the sample solution  $\mathbf{cXPC} + \mathbf{rQ}$  compared to pure  $\mathbf{cXPC}$ . Furthermore, the global fit analysis is not perfectly suited to differentiate between two time constants, which are rather comparable. Hence, the DADS related with  $\tau_2 = 188$  ns comprises both the decay of the triplet state of  $^3[\mathbf{cXPC}]$  and the subsequent dynamics of the recently formed radical ion pair of  $\mathbf{cXPC}^-/\mathbf{rQ}^+$ . Therefore, the time constant of  $\tau_2 = 188$  ns represents an averaged value of the time constant of both processes.

The  $\tau_2 = 188$  ns DADS can be divided into different contributions, which are marked in different colors (Figure 4.26). The contributions originating from the decay of  $^3[\mathbf{cXPC}]$ , the triplet state of the uncomplexed photocatalyst, can be identified by comparison of the DADS with the difference spectrum of  $^3[\mathbf{cXPC}]$ , measured after direct excitation of pure  $\mathbf{cXPC}$  (cyan line, Figure 4.26 c). Furthermore, the DADS comprises spectral signatures appearing with positive amplitude of the recently established absorption bands of the radical ion pair  $\mathbf{cXPC}^-/\mathbf{rQ}^+$ , which can be seen by comparison of the DADS to the measured absorption spectra of  $\mathbf{cXPC}^-$  and  $\mathbf{rQ}^+$  (light green line, light blue line, Figure 4.26 b). This behavior indicates an underlying charge recombination process within the radical ion pair  $\mathbf{cXPC}^-/\mathbf{rQ}^+$ , which leads back to the ground state of  $\mathbf{cXPC}\cdot\mathbf{rQ}$ .

In summary, photo-excitation of the complex **cXPC·rQ** leads to a delocalized excited singlet state  $^1[\mathbf{cXPC}\cdot\mathbf{rQ}]^*$ , which undergoes fast ISC within 1.8 ps to a delocalized triplet state  $^3[\mathbf{cXPC}\cdot\mathbf{rQ}]$ . The triplet state  $^3[\mathbf{cXPC}\cdot\mathbf{rQ}]$  has an intrinsic charge transfer character in which electron density is transferred from the quinolone to the xanthone moiety of the complex. This state is relatively stable and decays within 44 ns into a radical ion pair  $\mathbf{cXPC}^-/\mathbf{rQ}^+$  in which the charges become localized on the xanthone and the quinolone moiety of the complex. The charge separated state  $\mathbf{cXPC}^-/\mathbf{rQ}^+$  is relatively long-lived and decays within 188 ns by charge recombination to the ground state of the complex **XPC·rQ**. The relatively long life time of the charge separated state  $\mathbf{cXPC}^-/\mathbf{rQ}^+$  of 188 ns can be readily explained by a persistent spin correlation exhibiting triplet character. Therefore it is referred to the radical ion pair  $\mathbf{cXPC}^-/\mathbf{rQ}^+$  as spin correlated radical ion pair with triplet character  $^3[\mathbf{cXPC}^-/\mathbf{rQ}^+]$ . The spin correlation makes a fast charge recombination process spin-forbidden and therefore less favored [99].

The previous analysis was based on a global fit analysis, which renders the spectral changes caused by a certain process. To confirm the established picture, the discussion in this section refers to transient spectra, which provide the spectral properties of a certain state and not the dynamics of an underlying process. As the focus lies on the charge separated state  $^3[\mathbf{cXPC}^-/\mathbf{rQ}^+]$ , which is populated within 44 ns and depopulated within 188 ns, a transient spectrum at a pump-probe delay of  $\Delta t = 132$  ns is chosen for the further analysis. At a pump-probe delay of  $\Delta t = 132$  ns, the population of the parent state  $^3[\mathbf{cXPC}\cdot\mathbf{rQ}]$  has dropped to less than 5% of the initial population ( $\tau_1 = 44$  ns =  $1/3 \cdot 132$  ns) and the charge separated state  $^3[\mathbf{cXPC}^-/\mathbf{rQ}^+]$  is still sufficiently populated. However, the transient spectrum at a pump-probe delay of  $\Delta t = 132$  ns also comprises contributions of the triplet-triplet absorption of  $^3[\mathbf{cXPC}]$ . Hence, for the preparation of the transient absorption spectrum of **cXPC·rQ** at  $\Delta t = 132$  ns, the overlaying triplet-triplet absorption of  $^3[\mathbf{cXPC}]$  needs to be subtracted from the measured spectrum. The scaling factor derived in Chapter 4.1.2 is only valid on the ps time scale and cannot be applied in this case. Overlaying diffusion controlled TTET processes between uncomplexed **cXPC** and **rQ**, which lower the contribution of transient signal of uncomplexed **cXPC**, have to be taken into account. Therefore the spectrum of  $^3[\mathbf{cXPC}]$  was manually scaled and subtracted from the transient absorption spectrum. The scaling factor was determined by setting the transient absorption in the wavelength region between 480 and 600 nm to zero, since the radical ion spectra both of  $\mathbf{cXPC}^-$  and  $\mathbf{rQ}^+$  do not show significant absorption bands beyond 480 nm (Figure 4.22). The resulting spectrum, which renders the absorption spectrum of the spin correlated radical ion pair  $^3[\mathbf{cXPC}^-/\mathbf{rQ}^+]$  is shown in Figure 4.27 a) and for comparison the absorption spectra of the radical ions  $\mathbf{BuXPC}^-$  (similar to  $\mathbf{cXPC}^-$ ) and  $\mathbf{rQ}^+$  are shown in Figure 4.27 b).

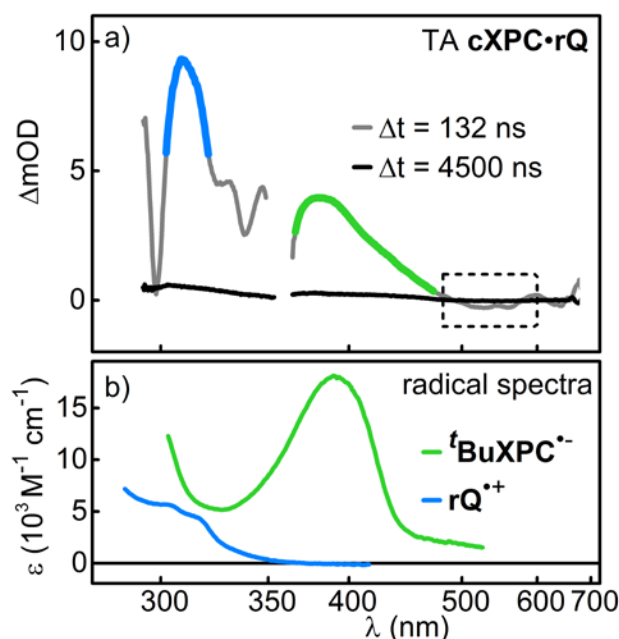
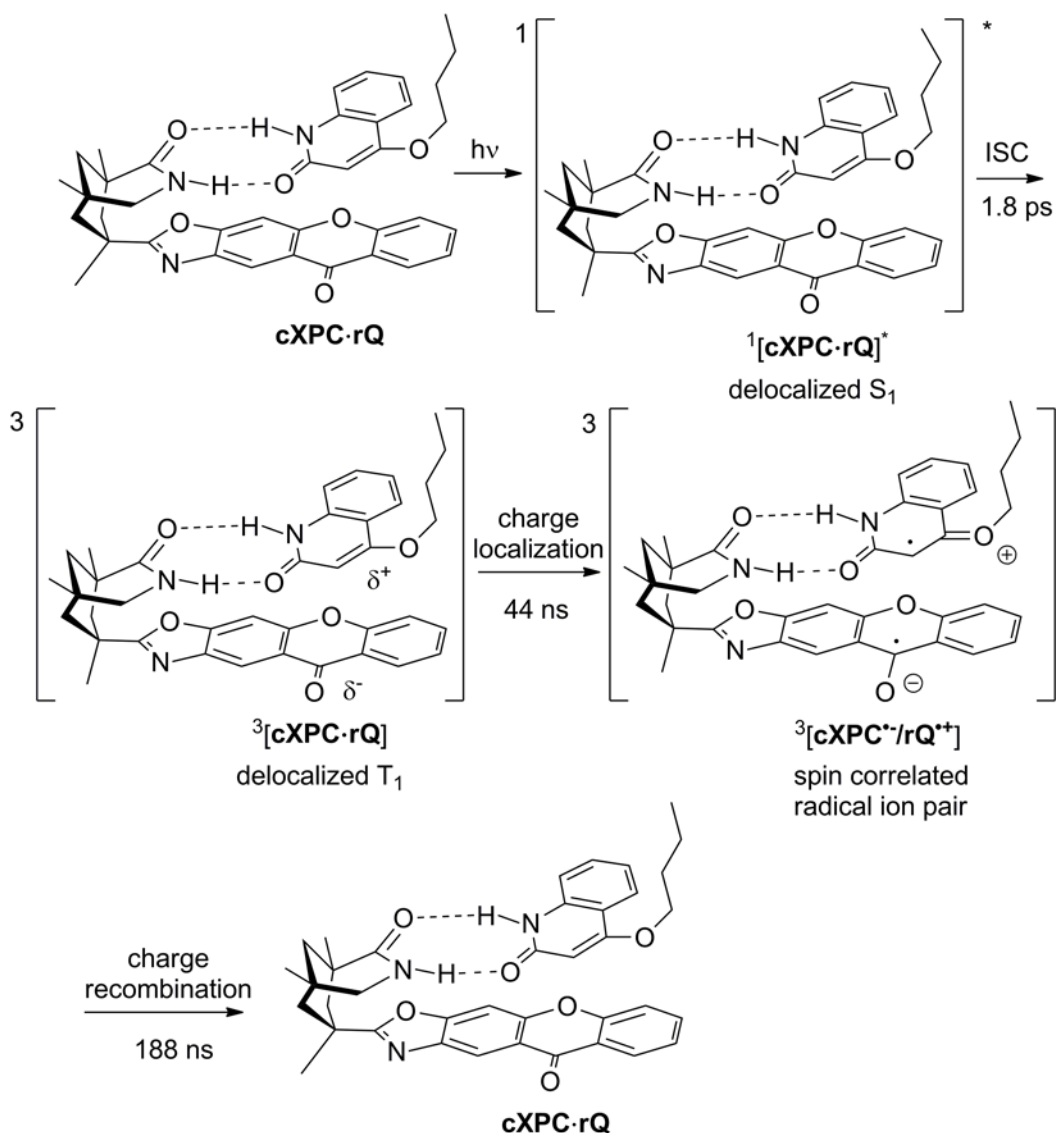


**Figure 4.27** a) TA(132 ns) and TA(4500 ns) after  $\lambda_{\text{EXC}} = 355$  nm excitation of the complex **cXPC·rQ**. The wavelength region between 480 and 600 nm (boxed region) was used to determine of the scaling factor for the spectral subtraction of the triplet spectrum  $^3[\text{cXPC}]$ . b) Radical ion spectra of  $^t\text{BuXPC}^{\bullet-}$  and  $\text{rQ}^{\bullet+}$ .

By comparison of the transient absorption spectrum at a pump-probe delay of  $\Delta t = 132$  ns (grey line, Figure 4.27 a) with the reference spectra in Figure 4.27 b) it can be clearly seen, that the transient spectrum at  $\Delta t = 132$  ns is exclusively composed of the sum of the absorption spectra of the radical ions **cXPC** $^{\bullet-}$  (light green line) and **rQ** $^{\bullet+}$  (light blue line). Slight deviations in intensity in the ultraviolet spectral region can be readily explained by an incomplete oxidation of **rQ** in the spectroelectrochemistry measurements. Furthermore the ground state absorption of **cXPC·rQ** reappears inversely as structured overlaying ground state bleach in the ultraviolet spectral region. In summary, the transient absorption spectrum in combination with the spectroelectrochemistry data strongly support the picture of an intermediate spin correlated charge separated state  $^3[\text{cXPC}^{\bullet-}/\text{rQ}^{\bullet+}]$ , which is formed from the delocalized triplet state of the complex  $^3[\text{cXPC}\cdot\text{rQ}]$ .

The combination of the results of the transient absorption measurements on multiple time scales with the spectroelectrochemical measurements and the ab initio calculations reveal a coherent picture of the photophysical processes within the catalyst-quinolone complex **cXPC·rQ**. A scheme of the full mechanism is shown in detail in Scheme 4.15.



**Scheme 4.15** Mechanism of charge localization and subsequent recombination of the charge separated state.

Although the presented measurements are based on the non-reactive quinolone **rQ**, the results provide a reliable insight into the early reaction steps of the more complex reaction dynamics in the photocatalytic active complex **cXPC·Q**, which comprises the actual quinolone substrate **Q**. As the electronic properties of the chromophores of both quinolones **rQ** and **Q** are identical, a charge separation process on the 44 ns time scale is expected to occur in **cXPC·Q** after photo-excitation as well. The present results indicate a charge transfer mechanism instead of a TTET process to account for the sensitization of the [2+2] photocycloaddition within the photocatalytic active complex **cXPC·Q**. It seems, that the close stacking between catalyst and substrate actually affects the course of the reaction and changes the reaction pathway from a triplet to a radical cation mediated mechanism.

### The Charge Separated State as the Parent State of the [2+2] Photocycloaddition in the Photocatalytic Active Complex

The analysis of the TA measurements both on the fs-ps and on the ns- $\mu$ s time scale of the reference complex **cXPC**·**rQ** in the previous section revealed the excitation of a delocalized singlet state  $^1[\mathbf{cXPC}\cdot\mathbf{rQ}]^*$  which undergoes a rather fast ISC within 1.8 ps to a delocalized triplet state  $^3[\mathbf{cXPC}\cdot\mathbf{rQ}]$ . From the delocalized triplet state  $^3[\mathbf{cXPC}\cdot\mathbf{rQ}]$  a charge separation process forms the spin correlated radical ion pair  $^3[\mathbf{cXPC}^{\cdot-}/\mathbf{rQ}^{\cdot+}]$ . Since reference quinolone **rQ** is not able to undergo further chemical transitions from its radical cation state  $\mathbf{rQ}^{\cdot+}$ , the charge separated state  $^3[\mathbf{cXPC}^{\cdot-}/\mathbf{rQ}^{\cdot+}]$  decays back to the ground state of the complex **cXPC**·**rQ**. However, the photocatalytic complex **cXPC**·**Q** comprising the actual quinolone substrate **Q** is able to undergo chemical transitions from its excited state. As the radical cation state is generally considered as a potential parent state of the [2+2] cycloaddition [194], a radical initiated mechanism becomes likely in the present catalyst-substrate complex **cXPC**·**Q**. The following section finds answers to the question if a radical cation mechanism accounts for the enantioselective formation of the cyclobutane ring.

Analogue to the previous section, the early processes after photo-excitation are discussed first. Comparable to the transient signal of sample solution **cXPC** + **rQ**, the signal of sample solution **cXPC** + **Q** is composed of signals originating both from uncomplexed **cXPC** and from catalyst-substrate complexes **cXPC**·**Q**. The signal of **cXPC** contributes 28% to the total number of excited molecules, whereas the signal of the complex **cXPC**·**Q** has a contribution of 72%. As the excitation of a delocalized excited singlet state was found in the reference complex **cXPC**·**rQ**, a similar process is expected in the photocatalytic active complex **cXPC**·**Q** as well. Therefore Figure 4.28 a) shows the transient spectrum after  $\lambda_{\text{EXC}} = 355$  nm of the sample solution **cXPC** + **Q** (red line) compared to the spectrum of the pure photocatalyst **cXPC** (blue line) at a pump-probe delay of  $\Delta t = 350$  fs. Figure 4.28 b) shows the transient spectrum of the complex **cXPC**·**Q** after  $\lambda_{\text{EXC}} = 355$  nm excitation at a pump-probe delay of  $\Delta t = 350$  fs which was calculated on the basis of the spectra shown in Figure 4.28 a).



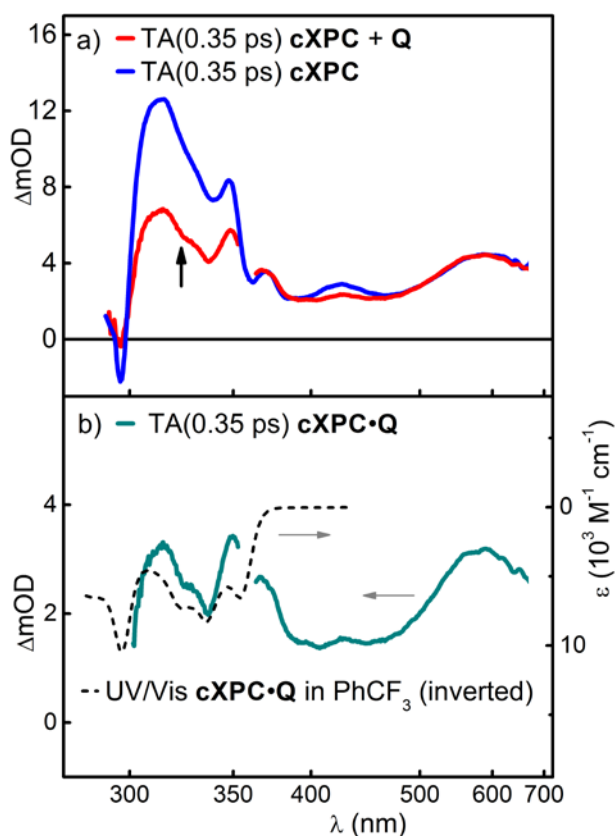


**Figure 4.28** a) TA(0.35 ps) of sample solution **cXPC + Q** (red line) and of **cXPC** (blue line) ( $\lambda_{\text{EXC}} = 355$  nm,  $E_{\text{EXC}} = 400$  nJ,  $D_{\text{FWHM}} = 150$   $\mu\text{m}$ ,  $d = 0.5$  mm), b) TA(0.35 ps) of complex **cXPC·Q** (cyan line) and comparison to the inverse ground state absorption spectrum of **cXPC·Q** (black dotted line)

Comparable to the  $\Delta t = 350$  fs transient absorption spectrum of the sample solution **cXPC + rQ** (Figure 4.23), both transient spectra in Figure 4.28 a) show qualitatively comparable characteristics. On a closer view, it can be seen that there are significant deviations between both spectra in the wavelength region between 320 and 340 nm (black arrow, Figure 4.28 a). Whereas the spectrum of **cXPC** is smooth in this region, the spectrum of sample solution **cXPC + Q** is lower in intensity and shows an overlaying structuring. For an exact quantitative determination of the transient spectrum of **cXPC·Q** at a pump-probe delay of  $\Delta t = 350$  fs, the spectrum of **cXPC** has to be subtracted from the data, using the scaling factor derived in Chapter 4.2.2.

The resulting transient spectrum of the complex **cXPC·Q** and its comparison to the inverted ground state absorption spectrum of **cXPC·Q** is shown in Figure 4.28 b). Comparable to **cXPC + rQ**, it can be clearly seen, that the transient spectrum (cyan line) comprises strong contributions of the ground state absorption spectrum of the catalyst-quinolone complex **cXPC·Q** (black dotted line), which appear inversely as ground state bleach in the transient signal. Minor deviations can be readily explained by a structured overlaying excited state absorption. This result gives clear evidence, that excitation at  $\lambda_{\text{EXC}} = 355$  nm actually leads to an excited state, which involves both the xanthone and the quinolone moiety of the complex, as already observed for the reference complex **cXPC·rQ**.

The ISC process of the delocalized excited singlet state was already quantified in the previous section (Figure 4.24). The slight deviation of both time constants ( $\tau_{\text{ISC}} = 2.2$  ps for **cXPC·rQ** and  $\tau_{\text{ISC}} = 1.8$  ps for **cXPC·Q**) can be both explained by the measurement uncertainty and a slight change in electronic properties of the chromophore due to different side chains in **rQ** and **Q**. Considering the rather fast ISC of **cXPC** within 4.1 ps, the transient data matrix of sample solution **cXPC + Q** for pump-probe delays  $\Delta t > 10$  ps is exclusively composed of triplet-triplet absorption signal of  $^3[\text{cXPC}]$  and  $^3[\text{cXPC}\cdot\text{Q}]$ . Therefore Figure 4.29 a) shows the TA signal at a pump-probe delay of  $\Delta t = 100$  ps both of sample solution **cXPC + Q** (red line) and of **cXPC** (blue line). Figure 4.29 b) shows the triplet-triplet absorption of the complex  $^3[\text{cXPC}\cdot\text{Q}]$  which was calculated on the basis of the spectra shown in Figure 4.29 a).

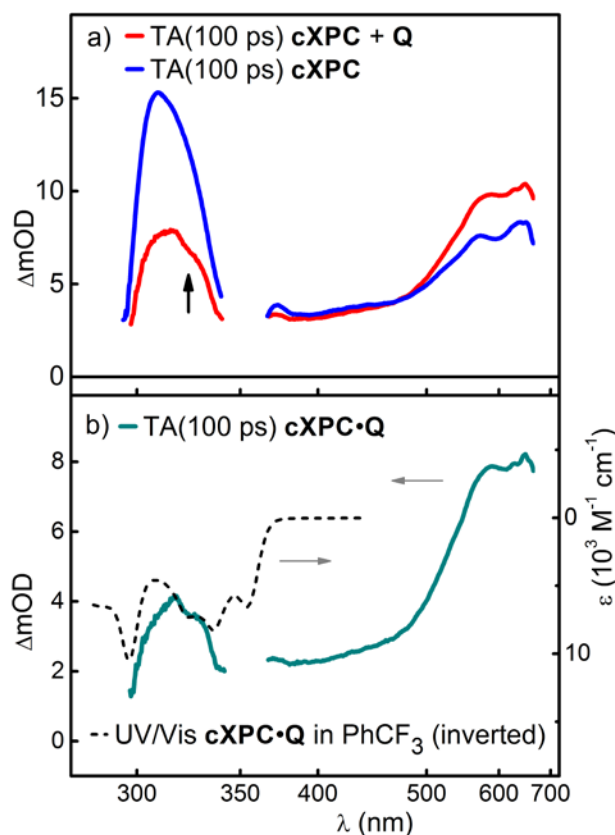


**Figure 4.29** a) Measured TA(100 ps) after  $\lambda_{\text{EXC}} = 355$  nm excitation of **cXPC + Q** (red line) and **cXPC** (blue line) in  $\text{PhCF}_3$ . b) TA(100 ps) of complex **cXPC·Q** (cyan line) and comparison to the inverse ground state absorption spectrum of **cXPC·Q** (black dotted line)

The  $^3[\text{cXPC}\cdot\text{Q}]$  spectrum with characteristic absorption maxima around 315 nm and a broad absorption in the long-wave spectral region between 570 and 640 nm (cyan line, Figure 4.29 b) is qualitatively comparable to the triplet-triplet absorption spectrum of  $^3[\text{cXPC}]$  (blue line, Figure 4.29 a). However, in the ultraviolet spectral region, the TA spectrum of **cXPC·Q** comprises strong contributions of the ground state absorption spectrum of **cXPC·Q** (black dotted line, Figure 4.29 b), which appear inversely as ground state bleach. This observation again supports the picture, that as well the triplet state  $^3[\text{cXPC}\cdot\text{Q}]$  involves

the whole catalyst-substrate complex  $\mathbf{cXPC}\cdot\mathbf{Q}$  and is neither located on the quinolone nor the xanthone moiety.

To follow the excited state dynamics of  $^3[\mathbf{cXPC}\cdot\mathbf{Q}]$ , ns- $\mu\text{s}$  TA spectroscopy with an excitation wavelength of  $\lambda_{\text{EXC}} = 355 \text{ nm}$  was performed on the sample solution  $\mathbf{cXPC} + \mathbf{Q}$ . While the excited state dynamics of sample solution  $\mathbf{cXPC} + \mathbf{Q}$  on the fs-ps time scale are identical to the excited state dynamics of  $\mathbf{cXPC} + \mathbf{rQ}$ , significant deviations are expected to be observed on the ns- $\mu\text{s}$  time scale. As a profile plot reveals information about the spectral properties of a certain state but provides only limited insights into the spectral changes caused by the underlying processes, the more meaningful DADS analysis of the ns- $\mu\text{s}$  TA measurement of sample solution  $\mathbf{cXPC} + \mathbf{Q}$  is shown in Figure 4.30.

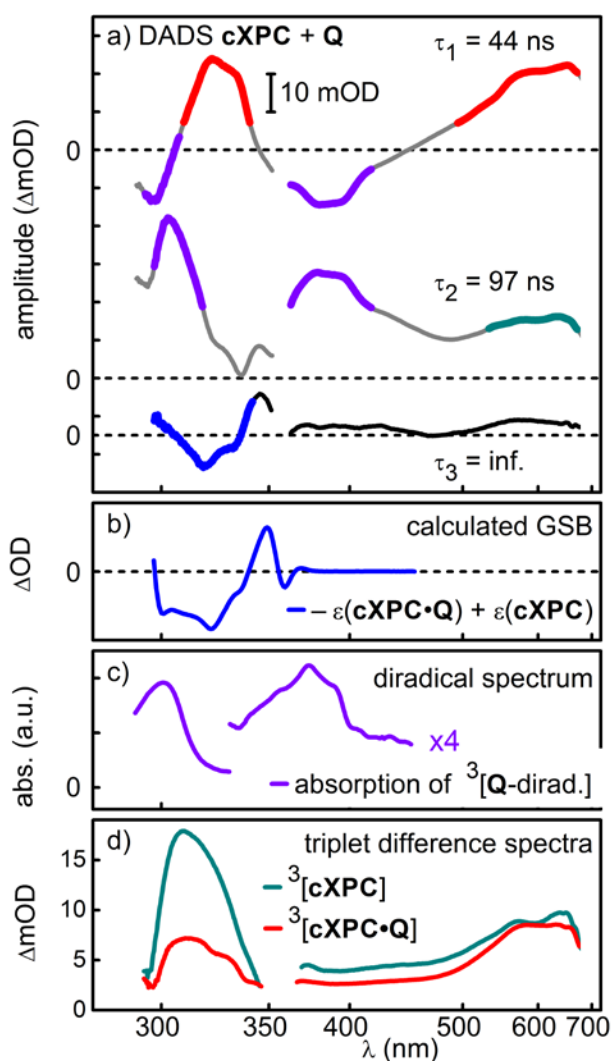


**Figure 4.30** a) DADS of ns- $\mu\text{s}$  TA after  $\lambda_{\text{EXC}} = 355 \text{ nm}$  excitation of  $\mathbf{cXPC} + \mathbf{Q}$ . b) Expected ground-state bleach after product formation, calculated on the basis of the absorption spectra of  $\mathbf{cXPC}\cdot\mathbf{Q}$  and  $\mathbf{Q}$ . c) Absorption spectrum of the quinolone triplet 1,4-diradical  $^3[\mathbf{Q}\text{-dirad}]$  from [App A.6]. d) Difference spectra of the triplet states  $^3[\mathbf{cXPC}]$  and  $^3[\mathbf{cXPC}\cdot\mathbf{Q}]$  with respect to the ground state absorption of  $\mathbf{cXPC}$  and  $\mathbf{cXPC}\cdot\mathbf{Q}$ .

The spectral changes in the transient spectrum can be described by two processes with characteristic time constants of  $\tau_1 = 44$  ns and  $\tau_2 = 97$  ns. The DADS related with an infinity time constant (black line, Figure 4.30 a) rendering the base line overlaid by a ground state bleach (marked in blue), which corresponds very well to the expected spectral signature after product formation (blue line, Figure 4.30 b), proves product formation within this experimental setup. As the enantioselectively formed product **P** does not absorb in the probed spectrum [5] this observation can be clearly assigned to product formation.

It has to be kept in mind, that initially a catalyst-substrate complex **cXPC·Q** was optically excited and therefore the transient spectrum reflects the spectral changes with respect to the ground state absorption of the catalyst-quinolone complex. However, after product formation, the catalyst-substrate complex **cXPC·Q** dissociates to catalyst **cXPC** and product **P**, which does not show significant absorption in the probed spectral range. Therefore, after product formation, the remaining ground state bleach (Figure 4.30 a) renders the inverted absorption spectrum of the catalyst-substrate complex  $\epsilon(\mathbf{cXPC}\cdot\mathbf{Q})$  subtracted by the absorption spectrum of the photocatalyst  $\epsilon(\mathbf{cXPC})$ , as shown in Figure 4.30 b),

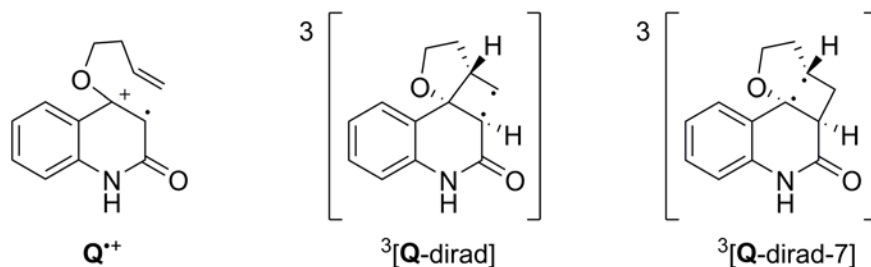
The dynamics of the fastest process, observed in the ns- $\mu$ s transient spectrum of sample solution **cXPC + Q** are comparable to the  $\tau_1 = 44$  ns process in sample solution **cXPC + rQ**. Hence, the time constant of  $\tau_1 = 44$  ns was applied for the description of ns- $\mu$ s dynamics of sample solution **cXPC + Q** and set as fixed parameter in the global fit analysis. A treatment of the time constant as an independent fit parameter would lead to a value of  $\tau = 39$  ns, but reveals inconsistencies in the spectral analysis, as both processes in the transient spectrum proceed on a very similar time scale ( $\tau_1 = 44$  ns and  $\tau_2 = 97$  ns). As the only difference between the complexes **cXPC·rQ** and **cXPC·Q** is in the side chain of the quinolone, which does not affect the electronic properties and the excited state dynamics of the complex, this analogy is justified.

Although the transient spectrum is composed of contributions originating both from uncomplexed **cXPC** and from catalyst-substrate complexes **cXPC·Q**, the  $\tau_1 = 44$  ns DADS is exclusively related with the  $T_1$  dynamics of the complex  $^3[\mathbf{cXPC}\cdot\mathbf{Q}]$ . The DADS is mainly composed of two contributions, which are marked in different colors in Figure 4.30 a). Comparable to the  $\tau_1 = 44$  ns DADS of the reference complex **cXPC·rQ** the DADS of **cXPC·Q** renders the decay of the delocalized triplet state  $^3[\mathbf{cXPC}\cdot\mathbf{Q}]$ , which can be seen by comparison of the spectral segments of the DADS marked in red (Figure 4.30 a) with the triplet-triplet absorption of  $^3[\mathbf{cXPC}\cdot\mathbf{Q}]$  shown on the same wavelength scale (red line) in Figure 4.30 c). However, an upcoming absorption band of a spin correlated radical ion pair  $^3[\mathbf{cXPC}^{\cdot-}/\mathbf{Q}^{\cdot+}]$  cannot be observed in this DADS. In contrast, a well-structured transient absorption band, centered around 375 nm emerges, which appears with negative amplitude in the DADS (marked in violet, Figure 4.30 a). This upcoming absorption band can be neither identified with the triplet-triplet absorption of the quinolone localized  $T_1$  state  $^3[\mathbf{Q}]$ , which is centered around 430 nm (Figure 4.10), nor the absorption of the **cXPC** radical anion **cXPC $^{\cdot-}$**  around 390 nm (Figure 4.22). However, by comparison of the spectral position and shape of the emerging absorption band with the absorption of the triplet quinolone diradical  $^3[\mathbf{Q}\text{-dirad}]$  (Figure 4.30 b), the populated state can be clearly identified with the

quinolone triplet 1,4-diradical state  $^3[\text{Q-dirad}]$ . Particularly the characteristic shape of the absorption around 375 nm and the sharp and intense absorption band around 305 nm (marked in violet, Figure 30 a) support this picture.

Contrary to the excited states dynamics of the reference complex  $\text{cXPC}\cdot\text{rQ}$ , the delocalized triplet state  $^3[\text{cXPC}\cdot\text{Q}]$  seems to decay directly to the quinolone located triplet diradical state  $^3[\text{Q-dirad}]$ . The spin correlated radical ion pair  $^3[\text{cXPC}^{\cdot-}/\text{Q}^{\cdot+}]$  is not sufficiently populated in this experiment and its spectral signatures cannot be detected. As the spin correlated radical ion pair  $^3[\text{cXPC}^{\cdot-}/\text{rQ}^{\cdot+}]$  is formed within 44 ns in the reference complex  $\text{cXPC}\cdot\text{rQ}$ , a charge localization process forming the spin correlated radical ion pair  $^3[\text{cXPC}^{\cdot-}/\text{Q}^{\cdot+}]$  is as well postulated in the catalyst-substrate complex  $\text{cXPC}\cdot\text{Q}$ . As the radical ion pair state  $^3[\text{cXPC}^{\cdot-}/\text{Q}^{\cdot+}]$  is not significantly populated to be detected with transient absorption spectroscopy, the depopulating rate of the radical ion pair  $^3[\text{cXPC}^{\cdot-}/\text{Q}^{\cdot+}]$  must be faster than its populating rate  $k_{\text{CS}} = (44 \text{ ns})^{-1}$ . Therefore, the radical ion pair state  $^3[\text{cXPC}^{\cdot-}/\text{Q}^{\cdot+}]$  is not significantly populated and cannot be detected with transient absorption spectroscopy.

The further discussion requires the differentiation between the triplet and the cation mediated reaction mechanism of the [2+2] photocycloaddition. Therefore, Scheme 4.16 shows the structures of the quinolone radical cation  $\text{Q}^{\cdot+}$  (left), the quinolone triplet 1,4-diradical with a 5-membered ring  $^3[\text{Q-dirad}]$  (middle), which was already introduced and discussed in Chapter 4.1 with respect to the [2+2] photocycloaddition after direct photoexcitation of  $\text{Q}$ , and the hypothetical quinolone triplet 1,4-diradical with a 7-membered ring  $^3[\text{Q-dirad-7}]$  (right).



**Scheme 4.16** Structures of the quinolone radical cation  $\text{Q}^{\cdot+}$  (left), the quinolone triplet 1,4-diradical with a 5-membered ring  $^3[\text{Q-dirad}]$  (middle) and a hypothetical quinolone triplet 1,4-diradical with a 7-membered ring  $^3[\text{Q-dirad-7}]$  (right).

The question has to be answered, which processes actually lead from the spin correlated radical ion pair  $^3[\text{cXPC}^{\cdot-}/\text{Q}^{\cdot+}]$  to the quinolone triplet diradical  $^3[\text{Q-dirad}]$ . The quinolone triplet diradical state  $^3[\text{Q-dirad}]$  is the central intermediate state of the [2+2] photocycloaddition, in which the first of the two newly formed bonds of the cyclobutane ring has been closed (Scheme 4.16). As the rate-limiting step, the formation of the radical ion pair  $^3[\text{cXPC}^{\cdot-}/\text{Q}^{\cdot+}]$  within  $\tau = 44 \text{ ns}$  is rather slow, the intermediate processes are spectroscopically not accessible. Therefore the order of the necessary individual steps, which are formation of the first bond (vide infra) and the back-electron-transfer to reach the neutral diradical, cannot be deduced from spectroscopic experiments. The present reaction

could be potentially explained by the formation of a 7-membered ring (Scheme 4.16), forming the quinolone diradical  $^3[\text{Q-dirad-7}]$ , which is however a very unlikely process. Potentially, the comparison of the results of the product analysis from photocatalytic irradiation measurements using quinolones with a systematically altered substitution pattern of the side-chain as substrate with related systems might provide more details of the actual course of the reaction. Certain substitution patterns could stabilize or exclude the occurrence of certain electronic states with a defined charge and radical density distribution. If the irradiation measurements reveal significantly deviating reaction yields with certain substitution patterns, a more detailed investigation could be supported by time resolved spectroscopic measurements both on the fs-ps and on the ns- $\mu$ s time scale. However, in the framework of the present thesis the question about the mechanistic details of the intermediate steps between the radical ion pair  $^3[\text{cXPC}^-/\text{Q}^+]$  and the triplet diradical  $^3[\text{Q-dirad}]$  remains unanswered, but many thought-provoking impulses could be provided.

Contrary to the observed photochemical processes of quinolone **Q** after direct photo-excitation (Chapter 4.1), where the first bond is formed from the triplet state  $^3[\text{Q}]$ , in the present system, the first bond seems to be formed from the quinolone radical cation state  $\text{Q}^+$ . Generally, an important prerequisite for the first cyclization is a radical character located on one of the carbon atoms, which are involved in the [2+2] photocycloaddition. Both the quinolone triplet state  $^3[\text{Q}]$  and the quinolone radical cation state  $\text{Q}^+$  are suited to exhibit a radical character located on the relevant carbons of the quinolone chromophore (compare Scheme 4.16). According to this, it should cause only a minor effect on the dynamics of the first cyclization reaction, if the parent state is a quinolone triplet state  $^3[\text{Q}]$  or a quinolone radical cation state  $\text{Q}^+$ . The only prerequisite for the reaction seems to be the radical density located on the relevant carbon-carbon double bond of the quinolone chromophore. After direct photo-excitation of quinolone **Q**, the triplet 1,4-diradical state  $^3[\text{Q-dirad}]$  was found to be formed within  $\tau = 651$  ps [App A.6] from the quinolone triplet state  $^3[\text{Q}]$ . A comparable time constant is expected for the formation of the subsequent intermediate state from the quinolone radical cation  $\text{Q}^+$  as well.

In summary, the  $\tau_1 = 44$  ns DADS, which describes the decay of the delocalized triplet state  $^3[\text{cXPC}\cdot\text{Q}]$  to the quinolone located triplet 1,4-diradical  $^3[\text{Q-dirad}]$ , is composed of three different processes. The rate determining process is the charge localization within 44 ns forming the spin correlated radical ion pair  $^3[\text{cXPC}^-/\text{Q}^+]$ . The quinolone located radical cation state  $\text{Q}^+$  then decays to the subsequent intermediate quinolone located state. This reaction is estimated to occur on the sub-ns time scale, with a time constant comparable to  $\tau = 651$  ps, observed for a related process after direct photo-excitation of **Q** [App A.6].

As the  $\tau_1 = 44$  ns DADS allows no deeper insight, the  $\tau_2 = 97$  ns DADS is discussed in the next section. In contrast to the previously discussed DADS, the  $\tau_2 = 97$  ns DADS cannot be exclusively related with the dynamics of the excited state of the complex  $[\text{cXPC}\cdot\text{Q}]$ . Overlaying dynamics originating from uncomplexed **cXPC** have to be taken into account. As diluted quinolone **Q** is a more efficient triplet quencher, compared to quinolone **rQ**, as seen in the diffusion controlled sensitization experiments (Chapter 4.2.3), the intrinsic triplet life time of the uncomplexed photocatalyst **cXPC** is expected to be further decreased in

sample solution  $\mathbf{cXPC} + \mathbf{Q}$  compared to sample solution  $\mathbf{cXPC} + \mathbf{rQ}$ , where a life time in the order of  $\tau = 188$  ns was estimated. Hence, the  $\tau_2 = 97$  ns DADS renders both the excited state dynamics of the complex  $\mathbf{cXPC}\cdot\mathbf{Q}$  and the uncomplexed photocatalyst  $\mathbf{cXPC}$ . The spectral segments of the DADS representing the decay of the photocatalyst  $T_1$  state  $^3[\mathbf{cXPC}]$  are marked in cyan in Figure 4.30 a) and can be identified by comparison with the reference spectrum (cyan line), shown in Figure 4.30 c). Furthermore the DADS comprises the spectral signatures of the decay of the recently established quinolone diradical state  $^3[\mathbf{Q}\text{-dirad}]$ , which are marked in violet (Figure 4.30 a) and can be identified with the reference spectrum of  $^3[\mathbf{Q}\text{-dirad}]$  from [App A.6], shown in Figure 4.30 b).

As the DADS related with an infinity time constant comprises significant contributions of a permanent quinolone ground state bleach, a significant amount of the quinolone diradical  $^3[\mathbf{Q}\text{ dirad}]$  decays by second cyclization to the desired product  $\mathbf{P}$ . However, as already observed after direct excitation of quinolone  $\mathbf{Q}$ , a reasonable amount of the diradical population decays by retrosynthetic disconnection forming the ground state of the catalyst-substrate complex  $\mathbf{cXPC}\cdot\mathbf{Q}$ . According to Scheme 4.5, it is easy conceivable, that the catalyst-product complex  $\mathbf{cXPC}\cdot\mathbf{P}$  tends to dissociate due to steric reasons caused by the rather bulky, newly formed cyclobutane ring, whereas the catalyst-substrate complex  $\mathbf{cXPC}\cdot\mathbf{Q}$  remains stable.

In summary, photo-excitation of the complex  $\mathbf{cXPC}\cdot\mathbf{Q}$  leads to a delocalized excited singlet state  $^1[\mathbf{cXPC}\cdot\mathbf{Q}]^*$ , which undergoes fast ISC within 2.2 ps to the delocalized triplet state  $^3[\mathbf{cXPC}\cdot\mathbf{Q}]$  of the complex. The triplet state  $^3[\mathbf{cXPC}\cdot\mathbf{Q}]$  has an intrinsic charge transfer character in which electron density is transferred from the quinolone to the xanthone moiety of the complex. This state is relatively stable and decays within 44 ns into a spin correlated radical ion pair  $^3[\mathbf{cXPC}^{\cdot-}/\mathbf{Q}^{\cdot+}]$  in which the charges become localized on the xanthone and the quinolone moiety of the complex. According to the picture obtained by transient absorption spectroscopy, the quinolone radical cation  $\mathbf{Q}^{\cdot+}$  within the spin correlated radical ion pair  $^3[\mathbf{cXPC}^{\cdot-}/\mathbf{Q}^{\cdot+}]$  represents the parent state of the subsequent [2+2] photocycloaddition of the quinolone. In this model, the radical cation seems to establish a sufficient radical character located on the relevant carbon atom of the chromophore. This leads to a fast first cyclization process. Subsequent charge recombination within the complex forms the quinolone located triplet diradical  $^3[\mathbf{Q}\text{-dirad}]$ , which decays within 97 ns either to the product  $\mathbf{P}$  or back to the starting material  $\mathbf{Q}$ , which is still bound to the complex.

The previous analysis was based on a global fit analysis, which renders the spectral changes caused by a certain process. To confirm the established picture, the discussion in this section refers to transient spectra, which provide the spectral properties of a certain state and not the dynamics of an underlying process. As the focus lies on the quinolone located triplet diradical  $^3[\mathbf{Q}\text{-dirad}]$  which is populated within 44 ns and depopulated within 97 ns, a transient spectrum at a pump-probe delay of  $\Delta t = 132$  ns is chosen for the further analysis. At a pump-probe delay of  $\Delta t = 132$  ns, the population of the parent state  $^3[\mathbf{cXPC}\cdot\mathbf{Q}]$  has dropped to less than 5% of the initial population ( $\tau_1 = 44$  ns =  $1/3 \cdot 132$  ns) and the quinolone located triplet diradical state  $^3[\mathbf{Q}\text{-dirad}]$  is still sufficiently populated. However, the transient spectrum at a pump-probe delay of  $\Delta t = 132$  ns also comprises contributions of the triplet-

triplet absorption of  $^3[\mathbf{cXPC}]$ . Therefore, as already shown for the reference complex  $\mathbf{cXPC}\cdot\mathbf{rQ}$ , the triplet spectrum  $^3[\mathbf{cXPC}]$  was subtracted with a reasonable scaling (boxed region, Figure 4.31 a). The resulting spectrum, which renders the absorption spectrum of the quinolone located triplet diradical state  $^3[\mathbf{Q}\text{-dirad}]$  is shown in Figure 4.31 a) (grey line). For comparison, the absorption of the quinolone triplet 1,4-diradical  $^3[\mathbf{Q}\text{-dirad}]$ , which was measured after direct photo-excitation of  $\mathbf{Q}$  [App A.6], is shown on the same wavelength scale in Figure 4.31 c). To show product formation in this measurement, the transient spectrum at the very late pump-probe delay of  $\Delta t = 4500$  ns comprising the ground state bleach is shown in Figure 4.31 a) (black line) and for comparison the expected ground-state bleach after product formation, calculated on the basis of the absorption spectra of  $\mathbf{cXPC}\cdot\mathbf{Q}$  and  $\mathbf{Q}$ .

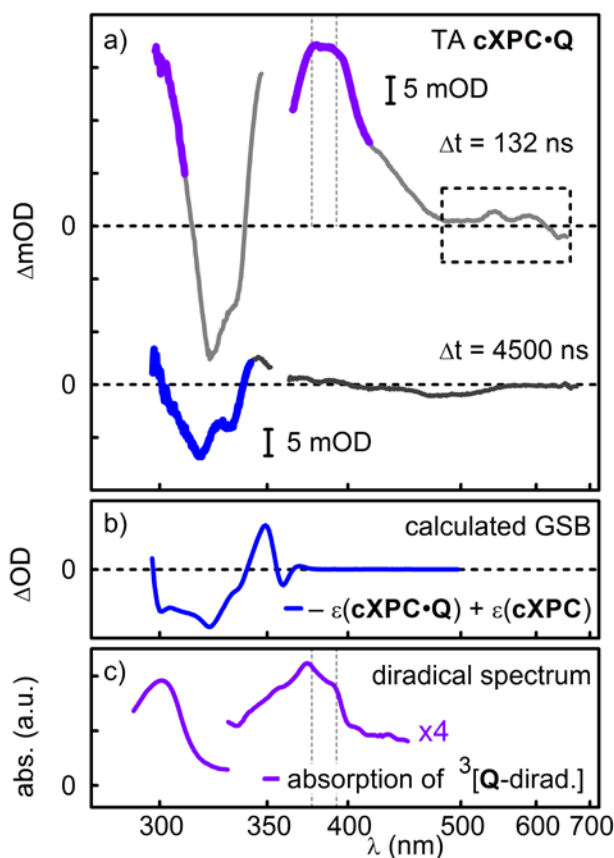


**Figure 4.31** a) TA(132 ns) after  $\lambda_{\text{EXC}} = 355$  nm excitation of the complex  $\mathbf{cXPC}\cdot\mathbf{Q}$ . b) Expected ground-state bleach after product formation, calculated on the basis of the absorption spectra of  $\mathbf{cXPC}\cdot\mathbf{Q}$  and  $\mathbf{Q}$ . c) Absorption spectrum of the quinolone triplet 1,4-diradical  $^3[\mathbf{Q}\text{-dirad}]$  from [App A.6]. The spectral contribution of the quinolone triplet 1,4-diradical can be identified by comparison of the colored segments (violet line) of the TA with the spectrum of  $^3[\mathbf{Q}\text{-dirad}]$  in c).

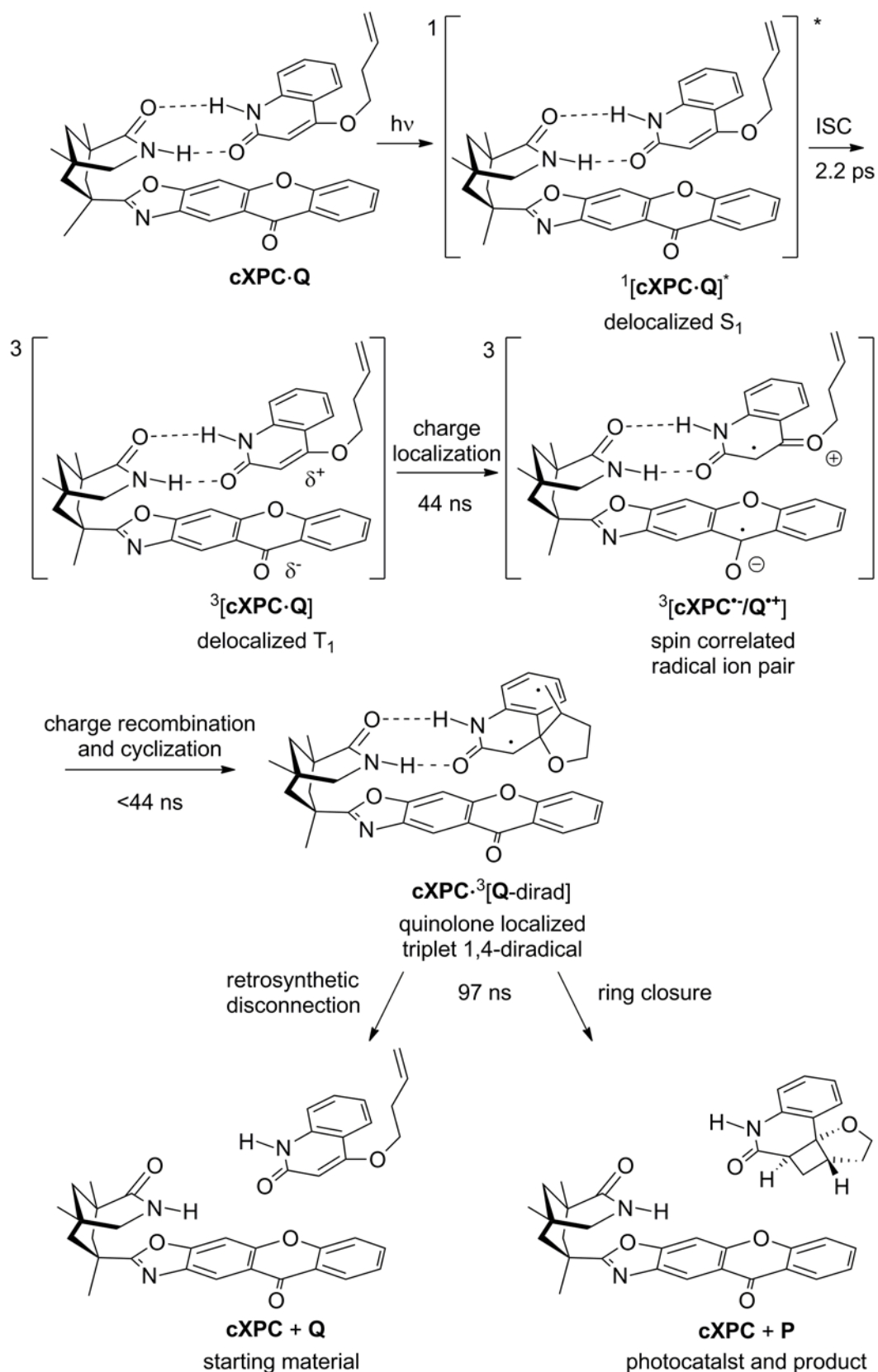
By comparison of the transient absorption spectrum at a pump-probe delay of  $\Delta t = 132$  ns (grey line, Figure 4.31 a) with the reference spectrum in Figure 4.31 c) it can be clearly seen, that the transient spectrum is exclusively composed of the quinolone located 1,4-diradical spectrum of  $^3[\mathbf{Q}\text{-dirad}]$ , overlaid by the ground state bleach of  $\mathbf{cXPC}\cdot\mathbf{Q}$ . The characteristic



spectral regions are marked in violet in Figure 4.31 a). Furthermore the ground state absorption of **cXPC·Q** reappears inversely as structured overlaying ground state bleach in the ultraviolet spectral region. The transient absorption spectrum in combination with the spectroscopic results obtained after direct photo-excitation of the reference complex **cXPC·rQ** and quinolone **Q** [App A.6] clearly support the picture of a quinolone located triplet diradical state  $^3[\text{Q-dirad}]$  as an intermediate state of the [2+2] photocycloaddition in the photocatalytic active complex **cXPC·Q**.

In contrast to direct photo-excitation of **Q**, where a triplet-mechanism accounts for the formation of the cyclobutane ring, the first cyclization in the catalyst-substrate complex **cXPC·Q** occurs from the quinolone radical cation state  $\text{Q}^+$ , as discussed on the basis of the DADS of **cXPC·Q** in combination with the results from the reference complex **cXPC·rQ**. The bond formation is assumed to proceed with a comparable time constant below 1 ns as seen in **Q** after direct photo-excitation [App A.6]. However, after charge recombination within the catalyst-substrate complex, which occurs significantly faster than 44 ns, the subsequent quinolone located diradical state  $^3[\text{Q-dirad}]$  exhibits triplet character. From the diradical  $^3[\text{Q-dirad}]$  either the second cyclization leads to product formation or the recently established bond breaks by retrosynthetic disconnection forming the starting material **Q**.

The combination of the results of the transient absorption measurements on multiple time scales with the spectroelectrochemical measurements and the ab initio calculations reveal a coherent picture of the photophysical processes within the catalyst-substrate complex **cXPC·Q**. A scheme of the full mechanism is shown in detail in Scheme 4.17.



**Scheme 4.17** Full mechanism of the photocatalyzed enantioselective [2+2] cycloaddition.

Photo-excitation of the 355 nm transition of the photocatalyst-substrate complex **cXPC·Q** leads to a delocalized singlet state. The optical properties of this state are still dominated by the xanthone photocatalyst, as can be seen in the ab initio calculations, but also comprise significant spectral contributions of the quinolone (Figure 4.13). Within 2.2 ps, the delocalized singlet state  $^1[\mathbf{cXPC}\cdot\mathbf{Q}]^*$  undergoes ultrafast ISC forming a delocalized triplet state  $^3[\mathbf{cXPC}\cdot\mathbf{Q}]$ . Then, on the time scale of 44 ns, the triplet state, which already has an intramolecular charge transfer character, decays into a spin-correlated radical ion pair  $^3[\mathbf{cXPC}^-/\mathbf{Q}^+]$ , in which the individual properties of the constituents reappear, comprising the radical ions **cXPC<sup>-</sup>** and **Q<sup>+</sup>**. Due to the triplet character of the formed spin correlated radical ion pair, the intermolecular charge recombination is spin-forbidden and therefore the charge separated state is intrinsically long-lived [99]. The radical cation **Q<sup>+</sup>** represents the parent state of the subsequent [2+2] cycloaddition, which decays to the quinolone 1,4-diradical  $^3[\mathbf{Q}\text{-dirad}]$ . The formed quinolone 1,4-diradical  $^3[\mathbf{Q}\text{-dirad}]$  state already contains the full stereoisomeric information for the enantioselectivity of the reaction. The second bond formation of the bound quinolone 1,4-diradical leads to the chiral product **P**, which then dissociates from the complex due to strong steric effects. Within the stacked complex **cXPC·Q** the second cyclization occurs in 97 ns, which is somehow comparable to the time constant of 30 ns observed after direct photo-excitation of **Q** [App A.6].



#### 4.2.5 Exciplex and Excimer States in DNA and Radical Cation Mediated [2+2] Photocycloaddition Reactions

In conclusion, it was demonstrated that in closely stacked organic complexes new electronic properties appear which can be efficiently utilized to drive photocatalytic processes. The observed reaction pathway depicts a new sensitization mechanism which has, to the author's best knowledge, never been described in organic photocatalysis before. The mechanism was not only found to be new, it also has a significant effect on the actual course of the [2+2] photocycloaddition of the substituted quinolone, which is non-covalently bound to the chiral photocatalyst. Whereas after direct photo-excitation of substituted quinolones, a triplet mechanism is clearly evident [App A.6], the [2+2] photocycloaddition within the catalyst-substrate complex occurs by a radical cation mediated mechanism. Through the combination of broadband TA spectroscopy covering time scales from fs to  $\mu$ s with state-of-the-art theoretical methods and spectroelectrochemistry, for the first time a clear picture of the major steps of the complex mechanism behind the catalyzed enantioselective [2+2] photocycloaddition in closely stacked xanthone-quinolone complexes has emerged. However, some questions about the details of the mechanism, particularly regarding the steps leading from the quinolone radical cation to product formation, remain to be elucidated with the help of further measurements.

It is commonly accepted that the photophysical properties of strongly coupled systems, such as closely stacked molecular assemblies, are not always composed of the sum of the properties of the individual constituents. An example, which is very well comparable to the present system and which has been intensively investigated is the stacking of the nucleobases in DNA [119, 261, 262, 263, 264, 265, 266]. Comparable to the present system, the aggregation of the constituents of the DNA occurs both via hydrogen bonding and via  $\pi\pi$ -interaction [267].  $\pi$ -stacking in planar aromatic molecules facilitates the formation of excimer (excited dimer) and exciplex (excited complex) states, in which the excitation is shared between two closely spaced molecules [263]. Mainly the  $\pi\pi$ -interaction determines the fate of excited electronic states in DNA. This leads to formation of intrastrand exciplex states with near unity quantum yields [263, 266]. These exciplex states with a varying life time, ranging from 100 ps to the ns time scale were observed whenever adenine is stacked with itself, with thymine [263] or cytosine [266]. The formation of exciplex states, exhibiting charge transfer character, was observed to be clearly faster than 400 fs [263]. However, not only in DNA the formation of exciplex states can be observed. Also pyrene in solution tends to show abnormal excited state dynamics at high concentration when the stacking of molecules becomes predominant. Moreover, pyrene was the first molecule in which the formation of excimer states was actually observed by Förster and Kaspar in 1955 [268]. The formation of excimer states of pyrene can be directly deduced from the fluorescence properties at varying concentrations [269, 270, 271]. According to the definition, an excimer or exciplex, is a dimer or complex which is associated in its electronically excited state and which is dissociative in its ground state [271, 272]. In contrast, in the present system already the ground state absorption properties of the complex **cXPC**·**Q** are affected by  $\pi\pi$ -interaction of both closely stacked chromophores **cXPC** and **Q**.

This behavior does not strictly match the given definition of the term “exciplex”, which requires a dissociative ground state. Therefore the term “delocalized excited state” was applied in the framework of this study.

The observed reaction mechanism, comprising a delocalized excited state as the key intermediate state of the subsequent reaction is not only highly interesting with respect to organic photocatalysis. Also for damage formation in DNA, where the occurrence of delocalized excited states is observed as well [119, 261, 262, 263, 264, 265, 266], this mechanism has to be seriously considered as a new potential reaction pathway towards the photo-induced formation of pyrimidine dimers [273].

According to literature, Yoon and coworkers already observed a radical-mediated mechanism using a ruthenium-based catalyst for the sensitization of the [2+2] cycloaddition of enones<sup>29</sup> [274, 275]. This type of mechanism was first described by Krische and Bauld [276]. Chiba and coworkers, who are following an electrochemical approach for electron-transfer-induced intermolecular [2+2] cycloaddition reactions, report a cation radical-mediated [2+2] cycloaddition between enol ethers and several unactivated olefins [277, 278, 279].

---

<sup>29</sup> an enone is a functional group consisting of a conjugated system of a ketone (carbonyl group bonded to two other carbon atoms) and an alkene (unsaturated compound containing at least one carbon-to-carbon double bond)

## 5. Conclusion and Outlook

This thesis illustrates how an elaborate combination of different transient absorption techniques covering multiple time scales can lead to a fundamental understanding and unambiguous disentanglement of the role of sensitizing mechanisms, reaction mechanisms and reactive intermediate states in photocatalysis. Photocatalytic reactions, which are currently applied and still improved in chemical synthesis, involving largely different sensitizing mechanisms, were investigated with experimental techniques offering a very high quality. The results were interpreted on the basis of an advanced and complex data analysis to obtain a deep understanding of the underlying molecular processes. The gained mechanistic picture of largely different systems reveal how state-of-the-art transient absorption spectroscopy in the near ultraviolet and visible spectral range covering the whole time scale from sub-ps up to  $\mu\text{s}$  without any gap provides fundamental insights onto the molecular level of photochemistry. In many cases, the analysis of the measurement data, obtained by transient absorption experiments, on the basis of well established standard methods such as fitting a sum of exponential functions to the transient decay curve only slightly scratches the surface of the underlying mechanism and still leaves the whole truth buried. In contrast to that, a suited and well-considered data analysis, which is precisely adapted to the problem, leads to unexpected results and surprising insights, as demonstrated in the present thesis on the basis of many different examples.

Due to the very laborious chemical synthesis of DNA-based molecules, such as flavin capped DNA hairpin structures (Chapter 3.3) or benzophenone dinucleotides (Chapter 3.4), often low amounts of the sample molecule in the 100 nanomole regime are supplied from synthetic chemistry for transient absorption measurements where usually rather dense concentrations in the mM regime are required for a sufficient signal intensity. In case of the flavin capped DNA hairpins, problems related to the low amount of the available sample could be circumvented since the attached flavin chromophore exhibits a suitably high absorption coefficient  $\epsilon$ . In contrast to that, the investigation of the benzophenone dinucleotides required the optical excitation of a  $n\pi^*$  transition of the benzophenone chromophore which usually exhibits a very low absorption coefficient  $\epsilon$  in the order of  $\epsilon \cong 100 \text{ M}^{-1} \text{ cm}^{-1}$ . Hence, reliable time constants describing the excited state dynamics could only be obtained by applying a global data analysis, in which global time constants  $\tau_i$  were used for a mathematical description of the whole transient data matrix including the entire spectral range from the ultraviolet to the red edge of the probe spectrum.

A further result of the present thesis is regarding the approach to utilize DNA as inert environment to study photo-induced processes of covalently linked chromophores. The spectroscopic investigation both of flavin capped DNA hairpins and of benzophenone dinucleotides demonstrated, that even the nucleobases thymine and cytosine, which exhibit the highest one-electron oxidation potential and which therefore should provide a non-reactive environment for an optical excited chromophore, are generally not suited to serve as inert backbone for every kind of photochemical reaction.

A rather complex fit model taking diffusion limited dynamics into account was required for a full interpretation of the time resolved spectroscopic data of flavin photocatalysis (Chapter 3.5). Numerous previous efforts to force the data analysis into a coherent picture based on exponential decay modeling failed. The application of a diffusion fit model, however, based on the Einstein Smoluchowski Theory of diffusion resolved all inconsistencies, which were related with the strictly exponential approach. Moreover, the application of this model surprisingly revealed many microscopic insights onto the reaction mechanism on the molecular level, which were later confirmed by other research groups [189]. Furthermore the decomposition of the transient data matrices into species associated spectra (SAS) of the contributing intermediate states allowed for the comparison of the spectral properties of the transient species with previously published spectra of the different redox and protonation states [146] and therefore provided a reliable assignment of the occurring intermediate states.

The decomposition of the transient data matrices into species associated spectra has been as well applied in the investigation of specific donor-bridge-acceptor (D-B-A) molecules presented in Chapter 3.2 and proved, that during the photo-induced intramolecular electron transfer processes the radical anion state of the fluorenone bridge becomes actually populated and is not tunneled. This observation was on the one hand not directly accessible by just relying on standard fit routines for transient data analysis and on the other hand not expected, as the determined damping coefficient  $\beta$  indicated a coherent tunneling process, in which the bridge state is not populated. This observation was corroborated by further transient absorption measurements in the infrared spectral domain and by femtosecond stimulated Raman spectroscopy (FSRS). This investigation has proven that the damping coefficient  $\beta$  is not always a reliable quantity for assessing the underlying electron transfer mechanism of a given charge transfer reaction to coherent superexchange or incoherent hopping.

The calculation of species associated spectra revealed the spectral properties of all occurring intermediate states within the course of the [2+2] photocycloaddition of substituted quinolones (Chapter 4.1). For the first time, the [2+2] photocycloaddition of substituted quinolones has been fully resolved and quantified by transient absorption spectroscopy in combination with quantum yield measurements. The investigation required time resolved spectroscopy both on the ps and on the ns time scale since the involved processes cover a huge temporal range. For instance the vibrational relaxation processes after excitation and the inter-system crossing to the triplet state were found to occur on the low ps time scale whereas the second inter-system crossing back to the singlet manifold, which is required for the second bond formation, occurs on the ns time scale.

The present thesis also demonstrates, that pre-aggregation of photocatalyst and substrate is generally one essential approach toward a highly efficient utilization of incident photons in homogeneous photocatalysis. A close proximity of catalyst and substrate usually ensures that after photon absorption the catalyst cannot undergo a competing deactivation process with a significant probability. However, as shown in flavin photocatalysis, where a close proximity of catalyst and substrate implies a competing, nonproductive singlet reaction pathway, the



highest achievable quantum yield for product formation was only in the few percent regime. Room for improvement of this reaction cannot only be found by optimizing the triplet reaction pathway, as briefly discussed in Chapter 3.5. Moreover it is conceivable to enhance the singlet reaction pathway by slowing down the charge recombination process within the formed radical ion pair. Applicable tools toward this issue are provided by Marcus Theory. Photo-induced conducting of an electron away from the light absorbing chromophore to a catalytically active center or tweaking the energetic landscape of the reactants in order to drive the charge recombination process in the inverted region are reasonable approaches which can be utilized to stabilize a charge separated state.

More complex chemical reactions, for instance photoredox catalysis involving many consecutive electron and proton transfer steps between photocatalyst and substrate, as observed in flavin photocatalysis, are leading to a significant decrease of the total quantum efficiency since diffusion of the reactants causes the separation of an initially formed catalyst-substrate pair. This leads to an interruption of the reaction pathway and therefore to a waste of absorbed photons. In case that diffusive control of a photocatalytic reaction cannot be avoided, a rather simple sensitization mechanism should be attempted.

A further key element toward efficient photoredox catalysis, which is particularly required when diffusion limited processes cannot be avoided, is to establish long-lived intramolecular charge separated states. As discussed in Chapters 3.1 and 3.2 donor-bridge-acceptor molecules, in which after photo-excitation an electron is conducted away from the light absorbing chromophore to an electron acceptor moiety, can be utilized to establish long-lived charge separated states to provide photoredox capabilities with a sufficiently high quantum efficiency. In this context, DNA represents a well-studied model system for the investigation of long-range intramolecular charge transfer processes and in particular with regard to its distance dependence.

The present thesis for the first time has provided a time resolved spectroscopic investigation of the charge transfer dynamics in flavin capped DNA hairpins. A rather small damping coefficient of  $\beta = 0.2 \text{ \AA}^{-1}$  was roughly estimated on the basis of the time-resolved data to describe the distance dependence of the intramolecular charge transfer processes. It has been shown, that the synthesized flavin DNA hairpins can be utilized to establish long-lived charge separated states with yields up to  $\Phi_{CS} = 0.14$ . A potential approach toward the improvement of flavin photocatalysis might be to link the flavin capped DNA hairpin structure or an analogue flavin-based acceptor-bridge system to a photocatalytic active electron donor site. After photo-induced reduction of the flavin chromophore by electron transfer from the donor site the oxidized electron donor site then serves as redox catalyst for the oxidation of an external substrate molecule. Since flavin is generally capable of two subsequent electron transfer processes, it is conceivable to drive two independent one electron redox processes by absorbing only one photon which would theoretically allow for product quantum yields up to  $\Phi_P = 200\%$ .

A further approach, which is astonishingly little noticed in recent literature, is to drive the charge recombination process within a photo-induced radical ion pair or a covalently linked

donor-bridge-acceptor molecule in the inverted regime [58]. For this approach it is required to tweak the redox properties of the involved reactants very precisely in order to thermodynamically strongly favor the charge separation and to inhibit or to slow down the charge recombination process. Time resolved spectroscopic methods may help to find an adapted catalyst-substrate pair which exhibits suited redox properties.

The intensive research on largely different photocatalytic systems on the basis of time-resolved spectroscopy and the related mechanistic understanding revealed many both interesting and promising ideas for further improvements of existing or the development of new photocatalysts:

For instance, an remarkable improvement toward DNA mediated enantioselective photocatalysis would be to test the discussed approach to replace the benzophenone chromophore by 4-amino-benzophenone, which exhibits more suited excited-state properties both of excited singlet and triplet state in comparison to pure benzophenone (Chapter 3.4). In the environment of a photo-excited 4-amino-benzophenone, relying on the presented estimations and calculations, the nucleobases thymine and cytosine should provide an inert backbone for enantioselective photocatalysis. Therefore, first the photophysical properties – in particular the  $S_1$  life time in environment of the sugar backbone – have to be determined on the basis of ultrafast time resolved spectroscopy. To study the photocatalytic capability, a suited pro-chiral substrate has to be found. Since the reaction mechanism and all occurring intermediate states of the intramolecular [2+2] cycloaddition of substituted quinolones have been intensively investigated by transient absorption spectroscopy, quinolone seems to be a perfectly suited pro-chiral target for the spectroscopic investigation of enantioselective DNA mediated photocatalysis.

In the group of Thorsten Bach (Technical University Munich) new catalysts in particular for enantioselective photocatalytic processes are currently under development. For instance, research is going on to couple a coordination metal complex to a chiral hydrogen bonding motif. Since coordination metal complexes often undergo photo-induced electron transfer reactions, this seems to be a promising approach toward enantioselective photoredox catalysis. The different redox states of coordination metal complexes are usually easily distinguishable by their absorption in the ultraviolet and visible spectral range and therefore this system is well adapted for time resolved spectroscopic investigations.

Also one important question for the future will be, how to transfer the new sensitizing mechanism, which involves delocalized excited states and is found in closely stacked catalyst-substrate complexes (Chapter 4.2), to other photocatalytic systems. Potentially the formation of delocalized excited states in bound catalyst-substrate-systems provides access to new, undiscovered reaction pathways of certain substrate molecules.

Another idea in terms of enantioselective photocatalysis is a further improvement of the existing xanthone-based photocatalyst. Replacing the xanthone moiety by thioxanthone, in which one oxygen atom is replaced by a sulfur atom heavily affects the optical properties of the light absorbing chromophore and therefore leads to a strong redshift of the absorption spectrum. This would provide the possibility of enantioselective photocatalysis in the visible

spectral domain. Transient absorption spectroscopy can provide answers to the question, whether actually the same sensitizing mechanism, which has been already found in the xanthone-catalyzed enantioselective [2+2] photocycloaddition of substituted quinolones, applies here as well.

The present thesis illustrates that on the one hand molecular photocatalysis has become a fully developed technique which is versatily applied in chemical synthesis but on the other hand still leaves room for improvement until it finds broad application both in industry and in energy production. It is still a long way until the forecast of the future of one of the pioneers of photochemistry Giacomo Luigi Ciamician, who was already quoted in the introduction of the present thesis, will become true. The further intensive cooperation between the research fields of physics and chemistry can essentially help to achieve this goal.

At present, one of the leading pioneers who is substantially pushing forward the research on chemical utilization of sun light in the spirit of Giacomo Luigi Ciamician, is the American scientist Daniel G. Nocera from the Massachusetts Institute of Technology. Nocera's "artificial leaf", a heterogeneous photoredox catalytic system based on silicon semiconductors and earth abundant catalysts [2] seems to be a very promising approach for solar hydrogen production on the industrial scale, which is not too far away from series production. The recently increasing global interest on chemical utilization of sunlight – also beyond the scientific community – is strongly corroborated by the fact, that Nocera's efforts to harness solar energy earned him a place in Time magazine's 2009 list of the 100 most influential people, an honor that he shared with US Secretary of Energy Steven Chu [280].

In face of mankind's growing energy demand it cannot yet surely be answered if the incident solar energy will cover a remarkable amount of the global energy requirements in the future. However, there is no doubt that science and engineering cannot circumvent addressing the demand of a secure, carbon-neutral, and plentiful low-cost energy source in pursuing the goal of utilizing the sun as a green, alternative energy [281]. Definitely in the future the contribution of solar energy – also beyond silicon-based photovoltaics – to the worlds energy supply will constantly grow and become more and more important. The present thesis hopefully represents a significant building block in the framework of the development of sustainable and green energy sources for the future of the mankind.



## References

- [1] A. J. Esswein, D. G. Nocera, *Chem. Rev.* **2007**, *107*, 4022-4047.
- [2] S. Y. Reece, J. A. Hamel, K. Sung, T. D. Jarvi, A. J. Esswein, J. J. H. Pijpers, D. G. Nocera, *Science* **2011**, *334*, 645-649.
- [3] G. Ciamician, P. Silber, *Science* **1912**, *36*, 385-394.
- [4] M. Neumann, S. Földner, B. König, K. Zeitler, *Angew. Chem. Int. Ed.* **2011**, *50*, 951-954.
- [5] C. Müller, A. Bauer, M. M. Maturi, M. C. Cuquerella, M. A. Miranda, T. Bach, *J. Am. Chem. Soc.* **2011**, *133*, 16689-16697.
- [6] D. P. Hari, B. König, *Org. Lett.* **2011**, *13*, 3852-3855.
- [7] M. Cherevatskaya, M. Neumann, S. Földner, C. Harlander, S. Kümmel, S. Dankesreiter, A. Pfitzner, K. Zeitler, B. König, *Angew. Chem. Int. Ed.* **2012**, *51*, 4062-4066.
- [8] D. P. Hari, P. Schroll, B. König, *J. Am. Chem. Soc.* **2012**, *134*, 2958-2961.
- [9] S. E. Braslavsky, *Pure Appl. Chem.* **2007**, *79*, 293-465.
- [10] K. J. Laidler, *Pure Appl. Chem.* **1996**, *68*, 149-192.
- [11] A. Fujishima, K. Honda, *Nature* **1972**, *238*, 37-38.
- [12] A. Fujishima, X. Zhangb, D. A. Tryk, *Surf. Sci. Rep.* **2008**, *63*, 515-582.
- [13] F. E. Osterloh, *Chem. Mater.* **2008**, *20*, 35-54.
- [14] X. Chen, S. Shen, L. Guo, S. S. Mao, *Chem. Rev.* **2012**, *110*, 6503-6570.
- [15] B. O'Regan, M. Grätzel, *Nature* **1991**, *353*, 737-740.
- [16] M. Grätzel, *Nature* **2008**, *414*, 338-344.
- [17] N. S. Lewis, D. G. Nocera, *Proc. Natl. Acad. Sci. USA* **2006**, *103*, 15729-15735.
- [18] M. W. Kanan, D. G. Nocera, *Science* **2008**, *321*, 1072-1075.
- [19] Y. Zhao, J. R. Swierk, J. D. Megiatto Jr, B. Sherman, W. J. Youngblood, D. Qin, D. M. Lentz, A. L. Moore, T. A. Moore, D. Gust, T. E. Mallouk, *Proc. Natl. Acad. Sci. USA* **2012**, *109*, 15612-15616.
- [20] J. Brilllet, J.-H. Yum, M. Cornuz, T. Hisatomi, R. Solarska, J. Augustynski, M. Graetzel, K. Sivula, *Nature Photon.* **2012**, *6*, 824-828.
- [21] M. Fagnoni, D. Dondi, D. Ravelli, A. Albini, *Chem. Rev.* **2007**, *107*, 2725-2756.
- [22] D. Ravelli, D. Dondi, M. Fagnonia, A. Albini, *Chem. Soc. Rev.* **2009**, *38*, 1999-2011.
- [23] D. Ravelli, M. Fagnoni, A. Albini, *Chem. Soc. Rev.* **2012**.

- 
- [24] R. G. W. Norrish, G. Porter, *Nature* **1949**, *164*, 658.
- [25] G. Porter, *Proc. Roy. Soc. Lond. Ser. A* **1950**, *200*, 284-300.
- [26] D. E. Spence, P. N. Kean, W. Sibbett, *Opt. Lett.* **1991**, *16*, 42-44.
- [27] U. Keller, *Nature* **2003**, *424*, 831-838.
- [28] R. L. Fork, B. I. Greene, C. V. Shank, *Appl. Phys. Lett.* **1981**, *38*, 671-672.
- [29] T. Förster, *Ann. Phys.* **1948**, *437*, 55-75.
- [30] D. L. Dexter, *J. Chem. Phys.* **1953**, *21*, 836-850.
- [31] K. Zeitler, *Angew. Chem. Int. Ed.* **2009**, *48*, 2-7.
- [32] H.-W. Shih, M. N. Vander Wal, R. L. Grange, D. W. C. MacMillan, *J. Am. Chem. Soc.* **2010**, *132*, 13600-13603.
- [33] U. Megerle, I. Pugliesi, C. Schrieber, C. F. Sailer, E. Riedle, *Appl. Phys. B* **2009**, *96*, 215-231.
- [34] R. R. Alfano, S. L. Shapiro, *Phys. Rev. Lett.* **1970**, *24*, 584-587.
- [35] R. R. Alfano, S. L. Shapiro, *Phys. Rev. Lett.* **1970**, *24*, 592-594.
- [36] M. Bradler, P. Baum, E. Riedle, *Appl. Phys. B* **2009**, *97*, 561-574.
- [37] R. Huber, H. Satzger, W. Zinth, J. Wachtveitl, *Opt. Commun.* **2001**, *194*, 443-448.
- [38] T. Wilhelm, J. Piel, E. Riedle, *Opt. Lett.* **1997**, *22*, 1494-1496.
- [39] E. Riedle, M. Beutter, S. Lochbrunner, J. Piel, S. Schenkl, S. Spörlein, W. Zinth, *Appl. Phys. B* **2000**, *71*, 457-465.
- [40] G. Cerullo, S. De Silvestria, *Rev. Sci. Instrum.* **2003**, *74*, 1-18.
- [41] C. Sailer, *Tracking the short life of highly reactive carbocations: From the ultrafast bimodal photogeneration to bimolecular reactions without diffusion*, Dissertation, Ludwig Maximilian University, Munich, Germany, **2012**.
- [42] C. Ruckebusch, M. Sliwa, P. Pernot, A. de Juan, R. Tauler, *J. Photochem. Photobiol. C* **2012**, *13*, 1-27.
- [43] S. A. Rice, *Comprehensive Chemical Kinetics*, Elsevier, Amsterdam, Netherlands, **1985**.
- [44] S. Murata, M. Nishimura, S. Y. Matsuzaki, M. Tachiya, *Chem. Phys. Lett.* **1994**, *219*, 200-206.
- [45] V. Gladkikh, A. I. Burshtein, G. Angulo, Stéphane Pagés, Bernard Lang, Eric Vauthey, *J. Phys. Chem. A* **2004**, *108*, 6667-6678.
- [46] M. Koch, A. Rosspeintner, G. Angulo, E. Vauthey, *J. Am. Chem. Soc.* **2012**, *134*, 3729-3736.

- 
- [47] M. N. Berberan-Santos, E. N. Bodunov, B. Valeur, *Chem. Phys.* **2005**, *315*, 171-182.
- [48] P. Kaden, E. Mayer-Enthart, A. Trifonov, T. Fiebig, H.-A. Wagenknecht, *Angew. Chem. Int. Ed.* **2005**, *44*, 1636-1639.
- [49] D. C. Johnston, *Phys. Rev. B* **2006**, *74*, 184430.
- [50] Y.-T. Kao, X. Guo, Y. Yang, Z. Liu, A. Hassanali, Q.-H. Song, L. Wang, D. Zhong, *J. Phys. Chem. B* **2012**, *116*, 9130-9140.
- [51] F. C. Grozema, S. Tonzani, Y. A. Berlin, G. C. Schatz, L. D. A. Siebbeles, M. A. Ratner, *J. Am. Chem. Soc.* **2008**, *130*, 5157-5166.
- [52] J. Li, Z. Liu, C. Tan, X. Guo, L. Wang, A. Sancar, D. Zhong, *Nature* **2010**, *466*, 887-891.
- [53] C. F. Sailer, B. P. Fingerhut, S. Thallmair, C. Nolte, J. Ammer, H. Mayr, I. Pugliesi, R. de Vivie-Riedle, E. Riedle, *ChemPhysChem* **2013**, *14*, 1423-1437.
- [54] G. J. Kavarnos, N. J. Turro, *Chem. Rev.* **1986**, *86*, 401-449.
- [55] R. A. Marcus, *J. Chem. Phys.* **1956**, *24*, 966-978.
- [56] R. A. Marcus, *J. Chem. Phys.* **1965**, *43*, 679-701.
- [57] R. A. Marcus, *Angew. Chem. Int. Ed. Engl.* **1993**, *32*, 1111-1121.
- [58] P. F. Barbara, T. J. Meyer, M. A. Ratner, *J. Phys. Chem.* **1996**, *100*, 13148-13168.
- [59] J. R. Miller, L. T. Calcaterra, G. L. Closs, *J. Am. Chem. Soc.* **1984**, *106*, 3047-3049.
- [60] G. L. Closs, J. R. Miller, *Science* **1988**, *240*, 440-447.
- [61] F. D. Lewis, R. S. Kalgutkar, Y. Wu, X. Liu, J. Liu, R. T. Hayes, S. E. Miller, M. R. Wasielewski, *J. Am. Chem. Soc.* **2000**, *122*, 12346-12351.
- [62] A. Rosspeintner, M. Koch, G. Angulo, E. Vauthey, *J. Am. Chem. Soc.* **2012**, *134*, 11396-11399.
- [63] D. Rehm, A. Weller, *Isr. J. Chem.* **1970**, *8*, 259-271.
- [64] R. A. Marcus, N. Sutin, *Biochim. Biophys. Acta* **1985**, *811*, 265-322.
- [65] H. B. Gray, J. R. Winkler, *Annu. Rev. Biochem.* **1996**, *65*, 537-561.
- [66] H. Imahori, K. Tamaki, D. M. Guldi, C. Luo, M. Fujitsuka, O. Ito, Y. Sakata, S. Fukuzumi, *J. Am. Chem. Soc.* **2001**, *123*, 2607-2617.
- [67] H. Heitele, F. Pöllinger, T. Häberle, M. E. Michel-Beyerle, *J. Phys. Chem.* **1994**, *98*, 7402-7410.
- [68] H. Imahori, N. V. Tkachenko, V. Vehmanen, K. Tamaki, H. Lemmetyinen, Y. Sakata, S. Fukuzumi, *J. Phys. Chem A* **2001**, *105*, 1750-1756.
- [69] M. Murakami, K. Ohkubo, S. Fukuzumi, *Chem. Eur. J.* **2010**, *16*, 7820-7832.

- [70] C.-P. Hsu, *Acc. Chem. Res.* **2009**, *42*, 509-518.
- [71] M. Bixon, Joshua Jortner, Jan W. Verhoeven, *J. Am. Chem. Soc.* **1994**, *116*, 7349-7355.
- [72] J. Jortner, *J. Chem. Phys.* **1976**, *64*, 4860-4867.
- [73] M. N. Paddon-Row, *Acc. Chem. Res.* **1994**, *27*, 18-25.
- [74] M. D. Newton, *Chem. Rev.* **1991**, *91*, 767-792.
- [75] B. Giese, *Acc. Chem. Res.* **2000**, *33*, 631-636.
- [76] B. Giese, *Annu. Rev. Biochem.* **2002**, *71*, 51-70.
- [77] T. Fiebig, W. Kühnle, H. Staerk, *Chem. Phys. Lett.* **1998**, *282*, 7-15.
- [78] T. Fiebig, K. Stock, S. Lochbrunner, E. Riedle, *Chem. Phys. Lett.* **2001**, *345*, 81-88.
- [79] M. R. Wasielewski, *Chem. Rev.* **1992**, *92*, 435-461.
- [80] W. B. Davis, Walter A. Svec, M. A. Ratner, M. R. Wasielewski, *Nature* **1998**, *396*, 60-63.
- [81] B. Giese, J. Amaudrut, A.-K. Köhler, M. Spormann, S. Wessely, *Nature* **2001**, *412*, 318-320.
- [82] R. H. Goldsmith, L. E. Sinks, R. F. Kelley, L. J. Betzen, W. Liu, E. A. Weiss, M. A. Ratner, M. R. Wasielewski, *Proc. Natl. Acad. Sci. USA* **2005**, *102*, 3540-3545.
- [83] B. Albinsson, M. P. Eng, K. Pettersson, M. U. Winters, *Phys. Chem. Chem. Phys.* **2007**, *9*, 5847-5864.
- [84] D. Segal, A. Nitzan, W. B. Davis, M. R. Wasielewski, M. A. Ratner, *J. Phys. Chem. B* **2000**, *104*, 3817-3829.
- [85] Y. A. Berlin, A. L. Burin, M. A. Ratner, *J. Phys. Chem. A* **2000**, *104*, 443-445.
- [86] Y. A. Berlin, A. L. Burin, M. A. Ratner, *J. Am. Chem. Soc.* **2001**, *123*, 260-268.
- [87] Y. A. Berlin, G. R. Hutchison, P. Rempala, M. A. Ratner, J. Michl, *J. Phys. Chem. A* **2003**, *107*, 3970-3980.
- [88] Y. A. Berlin, F. C. Grozema, L. D. A. Siebbeles, M. A. Ratner, *J. Phys. Chem. C* **2008**, *112*, 10988-11000.
- [89] F. C. Grozema, Y. A. Berlin, L. D. A. Siebbeles, M. A. Ratner, *J. Phys. Chem. B* **2010**, *114*, 14564-14571.
- [90] J. J. Hopfield, *Proc. Natl. Acad. Sci. USA* **1974**, *71*, 3640-3644.
- [91] F. C. Grozema, Y. A. Berlin, L. D. A. Siebbeles, *J. Am. Chem. Soc.* **2000**, *122*, 10903-10909.
- [92] A. M. Scott, T. Miura, A. B. Ricks, Z. E. X. Dance, E. M. Giacobbe, M. T. Colvin, M. R. Wasielewski, *J. Am. Chem. Soc.* **2009**, *131*, 17655-17666.



- 
- [93] J. M. Nocek, J. S. Zhou, S. De Forest, S. Priyadarshy, D. N. Beratan, J. N. Onuchic, B. M. Hoffman, *Chem. Rev.* **1996**, *96*, 2459-2489.
- [94] P. T. Henderson, D. Jones, G. Hampikian, Y. Kan, G. B. Schuster, *Proc. Natl. Acad. Sci. USA* **1999**, *96*, 8353-8358.
- [95] M. Bixon, B. Giese, S. Wessely, T. Langenbacher, M. E. Michel-Beyerle, J. Jortner, *Proc. Natl. Acad. Sci. USA* **1999**, *96*, 11713-11716.
- [96] R. H. Goldsmith, O. DeLeon, T. M. Wilson, D. Finkelstein-Shapiro, M. A. Ratner, M. R. Wasielewski, *J. Phys. Chem A* **2008**, *112*, 4410-4414.
- [97] O. S. Wenger, *Acc. Chem. Res.* **2011**, *44*, 25-35.
- [98] B. Albinsson, J. Martensson, *J. Photochem. Photobiol. C* **2008**, *9*, 138-155.
- [99] J. W. Verhoeven, *J. Photochem. Photobiol. C* **2006**, *7*, 40-60.
- [100] H. B. Gray, J. R. Winkler, *Proc. Natl. Acad. Sci. USA* **2005**, *102*, 3534-3539.
- [101] F. D. Lewis, T. F. Wu, Y. F. Zhang, R. L. Letsinger, S. R. Greenfield, M. R. Wasielewski, *Science* **1997**, *277*, 673-676.
- [102] A. M. Scott, A. B. Ricks, M. T. Colvin, M. R. Wasielewski, *Angew. Chem. Int. Ed.* **2010**, *49*, 2010.
- [103] H. M. McConnell, *J. Chem. Phys.* **1961**, *35*, 508-515.
- [104] G. S. M. Tong, I. V. Kurnikov, D. N. Beratan, *J. Phys. Chem. B* **2002**, *106*, 2381-2392.
- [105] F. D. Lewis, J. Liu, W. Weigel, W. Rettig, I. V. Kurnikov, D. N. Beratan, *Proc. Natl. Acad. Sci.* **2002**, *99*, 12536-12541.
- [106] Z. E. X. Dance, M. J. Ahrens, A. M. Vega, A. B. Ricks, D. W. McCamant, M. A. Ratner, M. R. Wasielewski, *J. Am. Chem. Soc.* **2008**, *130*, 830-832.
- [107] A. B. Ricks, G. C. Solomon, M. T. Colvin, A. M. Scott, K. Chen, M. A. Ratner, M. R. Wasielewski, *J. Am. Chem. Soc.* **2010**, *132*, 15427-15434.
- [108] J. V. Lockard, A. B. Ricks, D. T. Co, M. R. Wasielewski, *J. Phys. Chem. Lett.* **2010**, *1*, 215-218.
- [109] T. Watanabe, T. Shida, S. Iwata, *Chem. Phys.* **1967**, *13*, 65-72.
- [110] J.-M. Lü, S. V. Rosokha, J. K. Kochi, *J. Am. Chem. Soc.* **2003**, *125*, 12161-12171.
- [111] J.-F. Penneau, B. J. Stallman, P. H. Kasai, L. L. Miller, *Chem. Mater.* **1991**, *3*, 791-796.
- [112] S. F. Nelsen, A. E. Konradsson, M. N. Weaver, J. P. Telo, *J. Am. Chem. Soc.* **2003**, *125*, 12493-12501.
- [113] M. Fujitsuka, S. Tojo, T. Shinmyozub, T. Majima, *Chem. Commun.* **2009**, 1553-1555.

- [114] D. Gosztola, M. P. Niemczyk, W. Svec, A. S. Lukas, M. R. Wasielewski, *J. Phys. Chem. A* **2000**, *104*, 6545-6551.
- [115] S. Tanaka, C. Kato, K. Horie, H. Hamaguchi, *Chem. Phys. Lett.* **2003**, *381*, 385-391.
- [116] O. D. Schärer, *Angew. Chem. Int. Ed.* **2003**, *42*, 1946-2974.
- [117] J. H. J. Hoeijmakers, *Nature* **2001**, *411*, 366-374.
- [118] J.-M. L. Pecourt, J. Peon, B. Kohler, *J. Am. Chem. Soc.* **2001**, *123*, 10370-10378.
- [119] C. T. Middleton, K. de La Harpe, C. Su, Y. K. Law, C. E. Crespo-Hernandez, B. Kohler, *Annu. Rev. Phys. Chem.* **2009**, *60*, 217-239.
- [120] C. E. Crespo-Hernández, B. Cohen, P. M. Hare, B. Kohler, *Chem. Rev.* **2004**, *104*, 1977-2019.
- [121] D. B. Bucher, B. M. Pilles, T. Carell, W. Zinth, *Proc. Natl. Acad. Sci.* **2014**, *111*, 4369-4374.
- [122] M. C. Cuquerella, V. Lhiaubet-Vallet, J. Cadet, M. A. Miranda, *Acc. Chem. Res.* **2012**, *45*, 1558-1570.
- [123] H. Görner, *J. Photochem. Photobiol. B: Biol.* **1994**, *26*, 117-139.
- [124] A. Banyasz, I. Vaya, P. Changenet-Barret, T. Gustavsson, T. Douki, D. Markovitsi, *J. Am. Chem. Soc.* **2011**, *133*, 5163-6165.
- [125] A. Besaratinia, J. Yoon, C. Schroeder, S. E. Bradforth, M. Cockburn, G. P. Pfeifer, *FASEB J.* **2011**, *25*, 3079-3091.
- [126] S. V. Jovanovic, M. G. Simic, *J. Phys. Chem.* **1986**, *90*, 974-978.
- [127] C. A. M. Seidel, A. Schulz, M. H. M. Sauer, *J. Phys. Chem.* **1996**, *100*, 5541-5553.
- [128] S. Steenken, S. V. Jovanovic, *J. Am. Chem. Soc.* **1997**, *119*, 617-618.
- [129] P. Wolf, G. D. D. Jones, L. P. Candeias, P O'Neill, *Int. J. Radiat. Biol.* **1993**, *64*, 7-18.
- [130] H. Sies, W. A. Schulz, S. Steenken, *J. Photochem. Photobiol. B: Biol.* **1996**, *32*, 97-102.
- [131] H. Sugiyama, Isao Saito, *J. Am. Chem. Soc.* **1996**, *118*, 7063-7068.
- [132] I. Saito, M. Takayama, H. Sugiyama, K. Nakatani, *J. Am. Chem. Soc.* **1995**, *117*, 6406-6407.
- [133] W. L. Neeley, J. M. Essigmann, *Chem. Res. Toxicol.* **2006**, *19*, 491-505.
- [134] D. D. Eley, D. I. Spivey, *Trans. Faraday Soc.* **1962**, *58*, 411-415.
- [135] J. D. Watson, F. H. C. Crick, *Nature* **1953**, *171*, 737-738.

- [136] C. J. Murphy, M. R. Arkin, Y. Jenkins, N. D. Ghatlia, S. H. Bossmann, N. J. Turro, J. K. Barton, *Science* **1993**, *262*, 1025-1029.
- [137] M. G. Debije, M. T. Milano, W. A. Bernhard, *Angew. Chem. Int. Ed.* **1999**, *38*, 2752-2756.
- [138] J. Jortner, M. Bixon, T. Langenbacher, M. E. Michel-Beyerle, *Proc. Natl. Acad. Sci. USA* **1998**, *95*, 12759-12765.
- [139] B. Giese, S. Wessely, M. Spormann, U. Lindemann, E. Meggers, M. E. Michel-Beyerle, *Angew. Chem. Int. Ed.* **1999**, *7*, 996-998.
- [140] E. Meggers, M. E. Michel-Beyerle, B. Giese, *J. Am. Chem. Soc.* **1998**, *120*, 12950-12955.
- [141] F. D. Lewis, H. Zhu, P. Daublain, B. Cohen, M. R. Wasielewski, *Angew. Chem. Int. Ed.* **2006**, *45*, 7982-7985.
- [142] G. B. Schuster, *Acc. Chem. Res.* **2000**, *33*, 253-260.
- [143] K. Kawai, T. Takada, T. Nagai, X. Cai, A. Sugimoto, M. Fujitsuka, T. Majima, *J. Am. Chem. Soc.* **2003**, *125*, 16198-16199.
- [144] C. Behrens, M. Ober, T. Carell, *Eur. J. Org. Chem.* **2002**, 3281-3289.
- [145] D. Meisel, P. Neta, *J. Phys. Chem.* **1975**, *79*, 2459-2461.
- [146] M. Sakai and H. Takahashi, *J. Mol. Struct.* **1996**, *379*, 9-18.
- [147] C. N. Pace, F. Vajdos, L. Fee, G. Grimsley, T. Gray, *Prot. Sci.* **1995**, *4*, 2411-2423.
- [148] H. Sugiyama, I. Saito, *J. Am. Chem. Soc.* **1996**, *118*, 7063-7068.
- [149] I. Saito, T. Nakamura, K. Nakatani, Y. Yoshioka, K. Yamaguchi, H. Sugiyama, *J. Am. Chem. Soc.* **1998**, *120*, 12686-12687.
- [150] C. Behrens, T. Carell, *Chem. Commun.* **2003**, 1632-1633.
- [151] M. R. Arkin, E. D. A. Stemp, R. E. Holmlin, J. K. Barton, A. Hörmann, E. J. C. Olson, P. F. Barbara, *Science* **1996**, *273*, 475-480.
- [152] P. W. K. Rothmund, *Nature* **2006**, *440*, 297-302.
- [153] G. P. Acuna, M. Bucher, I. H. Stein, C. Steinhauer, A. Kuzyk, P. Holzmeister, R. Schreiber, A. Moroz, F. D. Stefani, T. Liedl, F. C. Simmel, P. Tinnefeld, *ACS Nano* **2012**, *6*, 3189-3195.
- [154] G. Roelfes, A. J. Boersma, B. L. Feringa, *Chem. Commun.* **2006**, 635-637.
- [155] T. E. Lehmann, A. Berkessel, *J. Org. Chem.* **1997**, *62*, 302-309.
- [156] C. Müller, A. Bauer, T. Bach, *Angew. Chem. Int. Ed.* **2009**, *48*, 6640-6642.
- [157] S. Steenken, *Chem. Rev.* **1989**, *89*, 503-520.
- [158] D. F. Cauble, V. Lynch, M. J. Krische, *J. Org. Chem.* **2003**, *68*, 15-21.

- 
- [159] D. M. Cai, M. J. Li, D. L. Li, T. P. You, *Chin. Chem. Lett.* **2004**, *15*, 163-166.
- [160] M. Weinberger, H.-A. Wagenknecht, *Synthesis-Stuttgart* **2012**, *44*, 648-652.
- [161] G. S. Hammond, P. A. Leermakers, *J. Phys. Chem.* **1962**, *66*, 1148-1150.
- [162] V. Lhiaubet, N. Paillous, N. Chouini-Lalanne, *Photochem. Photobiol.* **2001**, *74*, 670-678.
- [163] P. S. Rao, E. Hayon, *J. Am. Chem. Soc.* **1974**, *96*, 1295-1300.
- [164] N. A. Borisevich, D. V. Kazberuk, N. A. Lysak, G. B. Tolstorozhev, *J. Appl. Spectros.* **1994**, *60*, 193-195.
- [165] M. Montalti, A. Credi, L. Prodi, M. T. Gandolfi, *Handbook of Photochemistry, Third Edition*, CRC Press, Boca Raton, FL, USA, **2006**.
- [166] M. J. Lowe, J. A. Schellman, *J. Mol. Biol.* **1972**, *65*, 91-109.
- [167] S. Aloise, C. Ruckebusch, L. Blanchet, J. Réhault, G. Buntinx, J.-P. Huvenne, *J. Phys. Chem. A* **2008**, *112*, 224-231.
- [168] A. Bondi, *J. Phys. Chem.* **1964**, *68*, 441-451.
- [169] A. Amini, A. Harriman, *J. Photochem. Photobiol. C* **2003**, *4*, 155-177.
- [170] C. Walsh, *Acc. Chem. Res.* **1980**, *13*, 148-155.
- [171] S. Fukuzumi, S. Kuroda, T. Tanaka, *J. Am. Chem. Soc.* **1985**, *107*, 3020-3027.
- [172] S. Fukuzumi, K. Yasui, T. Suenobu, K. Ohkubo, M. Fujitsuka, O. Ito, *J. Phys. Chem. A* **2001**, *105*, 10501-10510.
- [173] J. Svoboda, H. Schmaderer, B. König, *Chem. Eur. J.* **2008**, *14*, 1854-1865.
- [174] R. Lechner, S. Kümmel, B. König, *Photochem. Photobiol. Sci.* **2010**, *9*, 1367-1377.
- [175] V. M. Berezovskii, T. A. Zhilina, *Chem. Nat. Compd.* **1979**, *15*, 219-235.
- [176] A. Wynter Blyt, *J. Chem. Soc.* **1879**, *35*, 530-539.
- [177] M. Wenninger, *Spektroskopische Charakterisierung der ultraschnellen Reaktionsmechanismen flavinbasierter Photochemie*, Diploma thesis, Ludwig Maximilian University, **2010**.
- [178] Nobel Lectures, *Chemistry 1922-1941*, Elsevier Publishing Company, Amsterdam, **1966**.
- [179] R. Kuhn, P. György, T. Wagner-Jauregg, *Chem. Ber.* **1933**, *66*, 576-580.
- [180] R. Kuhn, H. Rudy, T. Wagner-Jauregg, *Chem. Ber.* **1933**, *66*, 1950-1956.
- [181] Y.-T. Kao, C. Saxena, T.-F. He, L. Guo, L. Wang, A. Sancar, D. Zhong, *J. Am. Chem. Soc.* **2008**, *130*, 13132-13139.
- [182] P. F. Heelis, *Chem. Soc. Rev.* **1982**, *11*, 15-39.

- [183] U. Megerle, *Photoinduced molecular dynamics in increasingly complex systems: From ultrafast transient absorption spectroscopy to nanoscopic models*, Dissertation, Ludwig Maximilian University, Munich, Germany, **2011**.
- [184] M. Insinska-Rak, E. Sikorska, J. L. Bourdelande, I. V. Khmelinskii, W. Prukala, K. Dobek, J. Karolczak, I. F. Machado, L. F. V. Ferreira, A. Komasa, D. R. Worrall and M. Sikorski, *J. Mol. Struct.* **2006**, *783*, 184–190.
- [185] S. Salzmann, J. Tatchen and C. M. Marian, *J. Photochem. Photobiol. A* **2008**, *198*, 221–231.
- [186] G. G. Giachino, D. R. Kearns, *J. Chem. Phys.* **1970**, *52*, 2964-2974.
- [187] E. Baciocchi, M. Bietti, M. Mattioli, *J. Org. Chem.* **1993**, *58*, 7106-7110.
- [188] M. Fabbrini, C. Galli, P. Gentili, *J. Mol. Catal. B: Enzym.* **2002**, *16*, 231-240.
- [189] J. Dadova, S. Kümmel, C. Feldmeier, J. Cibulkov, R. Pazout, J. Maixner, R. M. Gschwind, B. König, R. Cibulka, *Chem. Eur. J.* **2013**, *19*, 1066-1075.
- [190] E. C. Breinlinger, C. J. Keenan, V. M. Rotello, *J. Am. Chem. Soc.* **1998**, *120*, 8606-8609.
- [191] C. B. Martin, M.-L. Tsao, C. M. Hadad, M. S. Platz, *J. Am. Chem. Soc.* **2002**, *124*, 7226-7234.
- [192] R. Cibulka, R. Vasold, B. König, *Chem. Eur. J.* **2004**, *10*, 6223-6231.
- [193] M. A. Ischay, Z. Lu, T. P. Yoon, *J. Am. Chem. Soc.* **2010**, *132*, 8572-8574.
- [194] F. Müller, J. Mattay, *Chem. Rev.* **1993**, *93*, 99-117.
- [195] A. Albini, M. Fagnoni, *Handbook of Synthetic Photochemistry*, Wiley-VCH, Weinheim, Germany, **2010**.
- [196] M. T. Crimmins, *Chem. Rev.* **1988**, *88*, 1453-1473.
- [197] G. Ciamician, P. Silber, *Chem. Ber.* **1908**, *41*, 1928-1935.
- [198] E. J. Corey, J. D. Bass, R. LeMahieu, R. B. Mitra, *J. Am. Chem. Soc.* **1964**, *86*, 5570-5583.
- [199] G. Büchi, I. M. Goldman, *J. Am. Chem. Soc.* **1957**, *79*, 4741-4748.
- [200] L. K. Montgomery, K. Schueller, P. D. Bartlett, *J. Am. Chem. Soc.* **1963**, *86*, 622-628.
- [201] P. de Mayo, A. A. Nicholson, M. F. Tchir, *Can. J. Chem.* **1969**, *47*, 711-712.
- [202] R. Y. Brogaard, A. E. Boguslavskiy, O. Schalk, G. D. Enright, H. Hopf, V. A. Raev, P. G. Jones, D. L. Thomsen, T. I. Sølling, A. Stolow, *Chem. Eur. J.* **2011**, *17*, 2922-2931.
- [203] D. Becker, N. Haddad, *Tetrahedron Lett.* **1986**, *27*, 6393-6396.

- [204] A. R. Matlin, C. F. George, S. Wolff, W. C. Agosta, *J. Am. Chem. Soc.* **1986**, *108*, 3385-3394.
- [205] C. Schroder, S. Wolff, W. C. Agost, *J. Am. Chem. Soc.* **1987**, *109*, 5941-5947.
- [206] D. Becker, M. Nagler, Y. Sahali, N. Haddad, *J. Org. Chem.* **1991**, *56*, 4537-4543.
- [207] T. Bach, *Synthesis-Stuttgart* **1998**, *5*, 683-703.
- [208] C. Kaneko, T. Suzuki, M. Sato, T. Naito, *Chem. Pharm. Bull.* **1987**, *35*, 112-123.
- [209] D. I. Schuster, G. Lem, N. A. Kaprinidis, *Chem. Rev.* **1993**, *93*, 3-22.
- [210] T. Yamamuro, I. Tanaka, N. Hata, *Bull. Chem. Soc. Jpn.* **1971**, *44*, 667-671.
- [211] T. Yamamuro, N. Hata, I. Tanaka, *Bull. Chem. Soc. Jpn.* **1973**, *46*, 29-34.
- [212] R. S. H. Liu, G. D. Hammind, *J. Am. Chem. Soc.* **1967**, *89*, 4936-4944.
- [213] R. Srinivasan, Karen Hill Carlough, *J. Am. Chem. Soc.* **1967**, *89*, 4932-4936.
- [214] S. J. Strickler, Robert A. Berg, *J. Chem. Phys.* **1962**, *37*, 814-822.
- [215] X. Cai, P. Cygon, B. Goldfuss, A. G. Griesbeck, H. Heckroth, M. Fujitsuka, T. Majima, *Chem. Eur. J.* **2006**, *12*, 4662-4667.
- [216] R. D. Small, J. C. Scaiano, *J. Phys. Chem.* **1977**, *81*, 2126-2131.
- [217] N. A. Kaprinidis, G. Lem, S. H. Courtney, D. I. Schuster, *J. Am. Chem. Soc.* **1993**, *115*, 3324-3325.
- [218] U. Megerle, R. Lechner, B. König, E. Riedle, *Photochem. Photobiol. Sci.* **2010**, *9*, 1400-1406.
- [219] G. P. Moss, *Pure Appl. Chem.* **1996**, *68*, 2193-2222.
- [220] L. Friedman, J. G. Miller, *Science* **1971**, *172*, 1044-1046.
- [221] E. Varesio, J.-L. Veuthey, *J. Chromatogr. A* **1995**, *717*, 219-228.
- [222] C.-S. Chen, W.-R. Shieh, P.-H. Lu, S. Harriman, C.-Y. Chen, *Biochim. Biophys. Acta* **1991**, *1078*, 411-417.
- [223] N. M. Maier, P. Franco, W. Lindner, *J. Chromatogr.* **2001**, *906*, 3-33.
- [224] D. A. Nicewicz, D. W. C. MacMillan, *Science* **2008**, *322*, 77-80.
- [225] D. A. Nagib, M. E. Scott, D. W. C. MacMillan, *J. Am. Chem. Soc.* **2009**, *131*, 10875-10877.
- [226] T. Bach, H. Bergmann, K. Harms, *Angew. Chem. Int. Ed.* **2000**, *112*, 2391-2393.
- [227] A. Bauer, F. Westkämper, S. Grimme, T. Bach, *Nature* **2005**, *436*, 1139-1140.
- [228] A. Bakowski, M. Dressel, A. Bauer, T. Bach, *Org. Biomol. Chem.* **2011**, *9*, 3516-3529.
- [229] R. E. Connors, W. R. Christian, *J. Phys. Chem.* **1982**, *86*, 1524-1528.

- [230] H. Satzger, B. Schmidt, C. Root, W. Zinth, B. Fierz, F. Krieger, T. Kiefhaber, P. Gilch, *J. Phys. Chem. A* **2004**, *108*, 10072-10079.
- [231] C. Müller, *Enantioselektive katalytische [2+2]-Photocycloadditionen von 2-Chinolonen*, Dissertation, Technical University Munich, Germany, **2010**.
- [232] A. Waritschlager, *Entwicklung und Erprobung der direkten Autokorrelationsmessung von 20 fs Pulsen im tiefen UV*, Bachelor Thesis, Ludwig Maximilian University, Munich, Germany, **2010**.
- [233] I. Z. Kozma, P. Krok, E. Riedle, *J. Opt. Soc. Am. B* **2005**, *22*, 1479-1485.
- [234] M. Lorenc, M. Ziolk, R. Naskrecki, J. Karolczak, J. Kubicki, A. Maciejewski, *Appl. Phys. B* **2002**, *74*, 19-27.
- [235] X. Chen, D. S. Larsen, S. E. Bradforth, *J. Phys. Chem. A* **2011**, *115*, 3807-3819.
- [236] N. A. Maierhofer, L. Wildgruber, *Elektrochemisch induzierte Ladungstransferprozesse: Spektroskopische Charakterisierung von Radikationen als Intermediate in chemischen Reaktionen*, Ludwig Maximilian University, Munich, Germany, **2013**.
- [237] H. J. Pownall, J. R. Huber, *J. Am. Chem. Soc.* **1971**, *93*, 6429-6436.
- [238] J. C. Scaiano, *J. Am. Chem. Soc.* **1980**, *102*, 7747-7753.
- [239] J. J. Cavaleri, K. Prater, R. M. Bowman, *Chem. Phys. Lett.* **1996**, *259*, 495-502.
- [240] C. Ley, F. Morlet-Savary, J.P. Fouassier, P. Jacques, *J. Photochem. Photobiol. A* **2000**, *137*, 87-92.
- [241] B. Heinz, B. Schmidt, C. Root, H. Satzger, F. Milota, B. Fierz, T. Kiefhaber, W. Zinth, P. Gilch, *Phys. Chem. Chem. Phys.* **2006**, *8*, 3432-3439.
- [242] R. W. Anderson, R. M. Hochstrasser, H. Lutz, and G. W. Scott, *J. Chem. Phys.* **1974**, *61*, 2500-2506.
- [243] G. L. Closs, P. Piotrowiak, J. M. MacInnis, G. R. Fleming, *J. Am. Chem. Soc.* **1988**, *110*, 2652-2653.
- [244] T. Tanaka, M. Yamaji, H. Shizuka, *J. Chem. Soc., Faraday Trans.* **1998**, *94*, 1179-1187.
- [245] C. Luo, D. M. Guldi, H. Imahori, K. Tamaki, Y. Sakata, *J. Am. Chem. Soc.* **2000**, *122*, 6535-6551.
- [246] X. Cai, M. Sakamoto, M. Fujitsuka, T. Majima, *Chem. Eur. J.* **2005**, *11*, 6471-6477.
- [247] P. B. Merkel, J. P. Dinnocenzo, *J. Phys. Chem. A* **2008**, *112*, 10790-10800.
- [248] J. Vura-Weis, S. H. Abdelwahed, R. Shukla, R. Rathore, Mark A. Ratner, M. R. Wasielewski, *Science* **2010**, *328*, 1547-1550.
- [249] C. Curutchet, A. A. Voityuk, *Angew. Chem. Int. Ed.* **2011**, *50*, 1820-1822.

- [250] A. Bauer, T. Bach, *Tetrahedron: Asymmetry* **2004**, *15*, 3799-3803.
- [251] Gaussian 09, Revision A.02, M. J. Frisch, G. W. Trucks, H. B. Schlegel, G. E. Scuseria, M. A. Robb, J. R. Cheeseman, G. Scalmani, V. Barone, B. Mennucci, G. A. Petersson, H. Nakatsuji, M. Caricato, X. Li, H. P. Hratchian, A. F. Izmaylov, J. Bloino, G. Zheng, J. L. Sonnenberg, M. Hada, M. Ehara, K. Toyota, R. Fukuda, J. Hasegawa, M. Ishida, T. Nakajima, Y. Honda, O. Kitao, H. Nakai, T. Vreven, J. A. Montgomery, Jr., J. E. Peralta, F. Ogliaro, M. Bearpark, J. J. Heyd, E. Brothers, K. N. Kudin, V. N. Staroverov, R. Kobayashi, J. Normand, K. Raghavachari, A. Rendell, J. C. Burant, S. S. Iyengar, J. Tomasi, M. Cossi, N. Rega, J. M. Millam, M. Klene, J. E. Knox, J. B. Cross, V. Bakken, C. Adamo, J. Jaramillo, R. Gomperts, R. E. Stratmann, O. Yazyev, A. J. Austin, R. Cammi, C. Pomelli, J. W. Ochterski, R. L. Martin, K. Morokuma, V. G. Zakrzewski, G. A. Voth, P. Salvador, J. J. Dannenberg, S. Dapprich, A. D. Daniels, O. Farkas, J. B. Foresman, J. V. Ortiz, J. Cioslowski, and D. J. Fox, *Gaussian, Inc., Wallingford CT*, **2009**.
- [252] O. Christiansen, H. Koch, P. Jørgensen, *Chem. Phys. Lett.* **1995**, *243*, 409-418.
- [253] F. Weigend, A. Köhn, C. Hättig, *J. Chem. Phys.* **2002**, *116*, 3175-3183.
- [254] C. Hättig, A. Köhn, *J. Chem. Phys.* **2002**, *117*, 6939-6951.
- [255] R. Ahlrichs, M. Bär, M. Häser, H. Horn, C. Kölmel, *Chem. Phys. Lett.* **1989**, *162*, 165-169.
- [256] A. Schäfer, C. Huber, R. Ahlrichs, *J. Chem. Phys.* **1994**, *100*, 5829-5835.
- [257] I. Borges, M. Barbatti, A. J. A. Aquino, H. Lischka, *Int. J. Quant. Chem.* **2012**, *112*, 1225-1232.
- [258] R.-J. Kutta, T. Langenbacher, U. Kensy, B. Dick, *Appl. Phys. B* **2013**, *111*, 203-216.
- [259] R. M. Stratt, M. Maroncelli, *J. Phys. Chem.* **1996**, *100*, 12981-12996.
- [260] M. Maroncelli, J. MacInnis, G. R. Fleming, *Science* **1989**, *243*, 1681-1989.
- [261] J. Eisinger, M. Gueron, R. G. Shulman, T. Yamane, *Proc. Natl. Acad. Sci. USA* **1966**, *55*, 1015-1020.
- [262] J. Eisinger, R. G. Shulman, *Science* **1968**, *161*, 1311-1319.
- [263] C. E. Crespo-Hernández, B. Cohen, B. Kohler, *Nature* **2005**, *436*, 1141-1144.
- [264] D. Markovitsi, F. Talbot, T. Gustavsson, D. Onidas, E. Lazzarotto, S. Marguet, *Nature* **2006**, *441*, E7.
- [265] D. Markovitsi, T. Gustavsson, F. Talbot, *Photochem. Photobiol. Sci.* **2007**, *6*, 717-724.
- [266] T. Takaya, C. Su, K. de La Harpe, C. E. Crespo-Hernández, B. Kohler, *Proc. Natl. Acad. Sci. USA* **2008**, *105*, 10285-10290.



- 
- [267] E. T. Kool, *Chem. Rev.* **1997**, *97*, 1473-1487.
- [268] T. Förster, K. Kasper, *Z. Elektrochem.* **1955**, *59*, 976-980.
- [269] J. B. Birks, D. J. Dyson, I. H. Munro, *Proc. Roy. Soc. Lond. A* **1963**, *275*, 575-588.
- [270] J. M. G. Martinho, M. A. Winnik, *J. Phys. Chem.* **1987**, *91*, 3640-3644.
- [271] F. M. Winnik, *Chem. Rev.* **1993**, *93*, 587-614.
- [272] J. B. Birks, *Rep. Prog. Phys.* **1975**, *38*, 903-974.
- [273] W. J. Schreier, T. E. Schrader, F. O. Koller, P. Gilch, C. E. Crespo-Hernández, V. N. Swaminathan, T. Carell, W. Zinth, B. Kohler, *Science* **2007**, *315*, 625-629.
- [274] J. Du, T. P. Yoon, *J. Am. Chem. Soc.* **2009**, *131*, 14604-14605.
- [275] M. A. Ischay, M. E. Anzovino, J. Du, T. P. Yoon, *J. Am. Chem. Soc.* **2008**, *130*, 12886-12887.
- [276] J. Yang, G. A. N. Felton, N. L. Bauld, M. J. Krische, *J. Am. Chem. Soc.* **2004**, *126*, 1634-1635.
- [277] K. Chiba, T. Miura, S. Kim, Y. Kitano, M. Tada, *J. Am. Chem. Soc.* **2001**, *123*, 11314-11315.
- [278] T. Miura, S. Kim, Y. Kitano, M. Tada, K. Chiba, *Angew. Chem. Int. Ed.* **2006**, *45*, 1461-1563.
- [279] Y. Okada, A. Nishimoto, R. Akaba, K. Chiba, *J. Org. Chem.* **2011**, *76*, 3470-3476.
- [280] P. Nair, *Proc. Natl. Acad. Sci.* **2012**, *109*, 15-17.
- [281] D. G. Nocera, *ChemSusChem* **2009**, *2*, 387-390.



## **Appendix A1**

### **Time Resolved Spectroscopy in Photocatalysis**

*Eberhard Riedle, Matthias Wenninger*

Burkhard König (Editor), *Chemical Photocatalysis*, 2013, 319-378

Reproduced by permission of Walter De Gruyter GmbH, Berlin



Eberhard Riedle, Matthias Wenninger

## 16 Time resolved spectroscopy in photocatalysis

### 16.1 UV/Vis absorption spectroscopy: More than just $\epsilon$ !

The basic principles of optical spectroscopy were discovered in the nineteenth century. The German optician Joseph von Fraunhofer (1787–1826) was the first one, who observed effects of atomic absorption processes in the spectrum of the sun. Narrow black absorption lines, which are now named Fraunhofer lines, correspond to optical transitions of the elements in the solar atmosphere. The spectral position of these lines allows conclusions on the composition of the atmosphere. Later, in the middle of the nineteenth century, the physicist Gustav Robert Kirchhoff and the chemist Robert Wilhelm Bunsen were the first who discovered previously unknown elements (Caesium and Rubidium) with the help of optical spectroscopy. The significant development of spectroscopic techniques since then has pushed spectroscopy to become one of the most important scientific tools. As a recent example, the Curiosity rover, which was landed by NASA on Mars in 2012, carries a spectrometer for the visible and UV spectral range for the optical analysis of matter.

Since there are a huge number of different spectroscopic techniques which are already described in detail elsewhere, we will only give a brief introduction on UV/Vis absorption spectroscopy in the context of time-resolved spectroscopy and photocatalysis. In general, UV/Vis absorption spectroscopy provides a wavelength dependent optical density  $OD(\lambda)$ . The Beer–Lambert-Law

$$T(\lambda) = \frac{I}{I_0} = 10^{-\epsilon(\lambda)cd} = 10^{-OD(\lambda)} \quad (16.1)$$

allows calculating the molar absorption coefficient  $\epsilon(\lambda)$ , a quantity describing molecular properties, from the measured optical density  $OD(\lambda)$ , the concentration  $c$  of the sample and the optical path length  $d$ . However, the UV/Vis absorption spectrum can provide much more information than just  $\epsilon$  values, which arise from the spectral distribution of possible optical absorption and thereby the energy differences. In particular, effects caused either by self aggregation or by the complexation of catalyst and substrate are often well distinguishable in UV/Vis spectroscopy by encountering additional absorption bands with increasing concentration. Also a change of the dipole moment of the excited chromophore between the ground state and its excited state can be often seen with the help of absorption spectroscopy in a variety of polar solvents.

Two different types of self-aggregation of dyes in solution are discussed in the literature: H-aggregates and J-aggregates. J-aggregates, named after their inventor Jelley and H-aggregates, are named for the hypsochromic shift (to shorter wave-

lengths) of their UV/Vis absorption spectrum when they are aggregated. In the 1930s Günter Scheibe from the Technical University of Munich and Edwin E. Jelley from the Kodak Research Laboratory in Harrow, UK observed independently an unusual behavior of pseudoisocyanine (PIC) chloride in aqueous solution and in ethanol. The absorption maximum was shifted to higher wavelengths and became more intense and sharp upon increasing the dye concentration. Dye aggregates with an absorption band that is bathochromically shifted (to longer wavelengths) with respect to the monomer absorption band are generally termed Scheibe aggregates or J-aggregates. [1–3] Substituted perylene diimides which are also used as a light absorbing chromophore in photocatalysis [4] show – depending on their substituents – very strong effects due to J-aggregation in their absorption spectrum. [5, 6]

Self-aggregation does not necessarily need to affect the energy levels of electronic states but it still can result in changes of the vibronic structure of the electronic absorption. Figure 16.1 shows for instance how self-aggregation of 4-(3'-butenyloxy)quinolone, a pro-chiral target in enantioselective photocatalysis [7, 8], changes the shape of the UV/Vis absorption properties with increasing concentration. It can be clearly seen, that the spectral position of the absorption band is not influenced by aggregation whereas the shape of the absorption band broadens with increasing concentration.

The ability of a chromophore to change its absorption and fluorescence properties due to a change in solvent polarity is called solvatochromism. A hypsochromic shift (to shorter wavelengths) of a transition with increasing solvent polarity corresponds to negative solvatochromism whereas a bathochromic shift (to longer wavelengths) with increasing solvent polarity corresponds to positive solvatochromism. Since polar solvents energetically stabilize states with larger dipole moment, the sign of the solvatochromism generally depends on the change in dipole moment

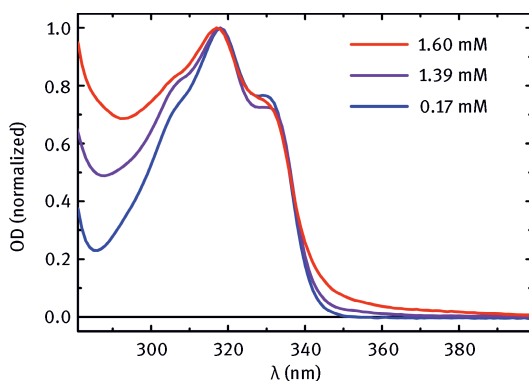


**Figure 16.1:** Normalized absorption of 4-(3'-butenyloxy)quinolone in trifluorotoluene at different concentrations.

between the ground state and the excited state. The effects of solvatochromism do not necessarily have to affect all ground state transitions of the chromophore. For example, only the second optical accessible transition of riboflavin tetraacetate (RFTA) shows solvatochromism whereas the first accessible transition is nearly unaffected by a change of solvent polarity (Figure 16.2, right panel). The solvatochromism of RFTA is not only caused by a change of polarity. A major part of the solvatochromism of RFTA originates from a change in hydrogen bonding between solvent and chromophore. [9, 10]

The second example to demonstrate the effects of solvatochromism we chose from the group of fluorescein dyes. The dianion of eosin Y (2',4',5',7'-tetrabromo-fluorescein), which has now been reported to provide photocatalytic capability [11], shows a strong negative solvatochromism of its energetically lowest absorption band (Figure 16.2, left panel). A solvent dependent change of the hydrogen bonding is suggested to strongly affect the ground state absorption properties. [12] Also the monomeric and the dimeric form of eosin Y are distinguishable by their absorption properties. [13] It is reported in the literature that the solvent polarity not only affects the ground state absorption spectra but also the excited state dynamics and absorption properties of eosin dyes. The lifetime of the  $S_1$  state, for instance, strongly decreases when diluted in water and in other protic solvents. The occurrence of hydrogen-bond assisted non-radiative deactivation competes with fluorescence and, therefore, leads to an ultrafast relaxation of the excited singlet state back to the ground state. [14]

Intramolecular charge transfer states play a major role in photoredox catalysis. Excitation of these states generally leads to a strong change in the dipole moment of the chromophore with respect to its ground state. Especially coordination complexes, which are often used as photoredox catalysts, exhibit intramolecular charge

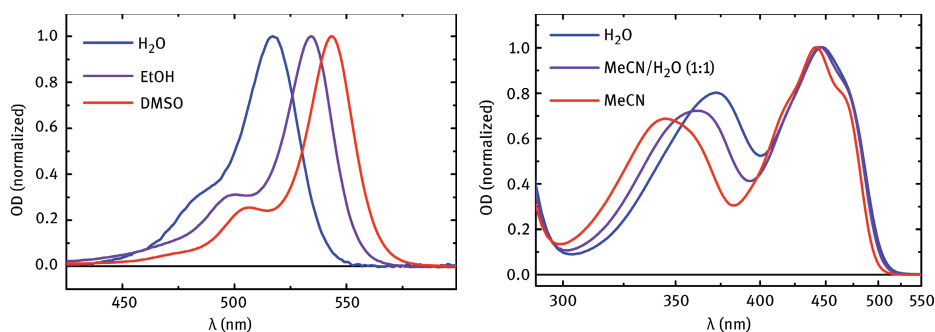


**Figure 16.2:** Negative solvatochromism of eosin Y (2',4',5',7'-tetrabromo-fluorescein-dianion, left) and positive solvatochromism of riboflavin tetraacetate (right). The empiric values of the polarity of the solvents on the Reichardt scale are 1.00 for H<sub>2</sub>O, 0.65 for ethanol (EtOH), 0.46 for acetonitrile (MeCN), and 0.44 for dimethyl sulfoxide (DMSO) [15].

transfer states, so-called metal-to-ligand charge transfer states (MLCT). The excitation of a MLCT transition causes a significant charge rearrangement within the coordination complex in its excited state and, hence, strongly affects the ground state absorption properties with increasing solvent polarity.

Ruthenium centered metal complexes are a well investigated group of coordination complexes due to their versatile application in photoredox catalysis. In reference [16] and reference [17] the solvatochromism of different ruthenium centered coordination complexes is described and a hypsochromic shift of the ground state absorption spectrum with increasing solvent polarity was found which corresponds to a negative solvatochromism. According to reference [17] the excitation of a MLCT transition of the ruthenium centered coordination complex leads to a decrease in dipole moment of the investigated asymmetric coordination complex. The polar solvent environment stabilizes the polar ground state of the chromophore and, hence, enlarges the energetic gap between the ground state and the excited state. This causes the blue shift of the ground state absorption spectrum.

When considering the influence of polar solvent molecules on excited states, it has to be mentioned that immediately after excitation both the nuclear configuration of the chromophore and the solvent environment remain in the ground state configuration. Then, on the time scale of hundreds of femtoseconds to a few ps, the energy is redistributed among intrachromophore modes. The fastest solvation processes take place on the same sub-ps time scale, with a strong dependence on the particular solvent, and diffusive solvent motion occurs on a somewhat longer ps time scale. [18–20] The similarity in time scale for vibrational relaxation and solvation makes their interplay highly complicated. After the two processes have concluded, the excited chromophore and the solvent environment are in equilibrium. This causes, at the same time, an increase of the energy of the electronic ground state. As a consequence, a rather large shift of the emission spectrum to longer wavelengths is found.

To describe the effects of the solvent polarity on optical properties and chemical reactivity as well in a simple model is not sufficient. The effective polarity of a solvent is influenced by a huge number of effects: On the one hand the dielectric constant ( $\epsilon$ ) and the permanent dipole moment ( $\mu$ ) are contributing to the intensity of the solvent polarity. On the other hand, effects between solvent and solute caused, for instance, by nonspecific Coulombic, directional, inductive and dispersion interactions are contributing to the effective solvent polarity as well as hydrogen bond, electron pair donor/acceptor and solvophobic interactions. [21] The empiric scale of Christian Reichardt reduces all contributing effects on a one-dimensional scale describing the effective polarity of a solvent and can be found in reference [15]. On this scale the highest empiric value of polarity of one is assigned to water whereas the lowest value of 0.006 is attributed to cyclohexane. A fundamental overview of solvatochromism, solvatochromic dyes and their use as solvent polarity indicator is presented by Reichardt in reference [22].



## 16.2 Time-Resolved spectroscopic methods from fs to $\mu$ s to elucidate photocatalytic processes

### 16.2.1 Transient absorption spectroscopy: Signals, time scales, and data processing

In the previous section, an introduction to UV/Vis absorption spectroscopy was given and it was exemplified how optical spectroscopy is able to provide more than only static information of the ground state absorption properties of a molecule. However, to understand the mechanism of a photocatalytic reaction, it is not sufficient only to rely on steady state spectra. Even bimolecular photocatalytic reactions include multiple intermediate steps, which may occur on a huge range of different time scales. Whereas intramolecular electron transfer processes, and the closure or breaking of covalent bonds occur on time scales down to the fs regime ( $10^{-15}$ s), diffusion limited bimolecular reactions or triplet chemistry happen on time scales up to the  $\mu$ s regime ( $10^{-6}$ s) or even beyond. For this reason it would be a great benefit for the understanding of photocatalysis to observe the individual steps of the photocatalytic reaction in slow motion.

Since many of these processes cause changes in the optical properties of the sample, time resolved spectroscopic methods come into play. There are numerous different spectroscopic techniques, which can be used for the investigation of excited state dynamics. The most common methods provide time resolved emission or absorption properties from the near UV to the IR range of the electromagnetic spectrum. Common methods for the time resolved observation of emission are streak lifetime imaging, time-correlated single-photon counting (TCSPC) and fluorescence upconversion, to mention only the most common ones. Since these techniques only allow the investigation of electronic states which emit photons, the accessible insight into the excited state dynamics is quite limited. Much more information is provided by time resolved absorption spectroscopy. There are also various spectroscopic techniques to access largely different time scales and spectral windows: laser flash photolysis, time resolved infrared spectroscopy, femtosecond stimulated Raman spectroscopy [25], multi-photon absorption spectroscopy and 2D spectroscopy to mention again only a few of them.

The modern version of ultrafast transient absorption (TA) spectroscopy is a direct successor of the flash photolysis technique developed by R. G. W. Norrish and G. Porter around 1950. [23, 24] In their experiments, which earned them the Nobel prize in chemistry in 1967, they used light bursts with millisecond duration from discharge lamps to trigger fast chemical reactions. The course of the reaction was monitored by taking photographs of the absorption of the sample at different delay times after the excitation. Thereby, the sample was exposed to a second light flash with a continuous spectrum that was dispersed in a polychromator before illuminating the photo plates. The basic idea behind this is that

different intermediate states of the photoinduced reaction have different absorption properties.

Here we will only focus on time resolved absorption spectroscopy which covers the visible, the near UV and near IR spectral region. The following chapter describes how transient absorption (TA) spectroscopy on largely different time scales can be applied to photocatalytic reactions to gain deep insights into the underlying reaction mechanism and to obtain a fundamental understanding of the intermediate steps. In combination with a suitable data analysis, one is enabled to cover a huge field of questions. With regards to the investigation of photocatalytic processes, especially the following questions are of specific interest:

Which are the intermediate steps of the photocatalytic reaction?

Is the catalytic reaction singlet or triplet chemistry?

How does diffusion contribute to the reaction dynamics?

Are intramolecular charge transfer processes involved?

Are catalyst-substrate-complexes formed and which impact has the complex formation on the electronic properties of a molecule?

Time resolved spectroscopic methods provide the quantitative and qualitative determination of the kinetics of intermediate states in light-induced chemical reactions within the experimental limits such as time resolution, maximum pump-probe delay and spectral probe detection bandwidth. Since the fastest molecular electronic processes occur on the fs time scale, ultrafast spectroscopic techniques are necessary to resolve these processes. There are many different approaches for the measurement of photo-induced reaction kinetics. In this chapter we present two spectroscopic techniques allowing the determination of time resolved absorption spectra on timescales from tens of fs to hundreds of  $\mu$ s when they are combined.

In general, time resolved absorption spectroscopy is a pump-probe technique: The sample is first optically excited by a spectrally defined pump pulse tuned into resonance with a selected electronic transition or vibronic feature and then probed with a broadband white light pulse after a chosen delay time  $\Delta t$ . This procedure is repeated for selected values of  $\Delta t$  until the whole temporal window is covered with the desired temporal resolution. The chosen method which determines the pump probe delay  $\Delta t$  depends on the observed time window: On the one hand, for  $\Delta t$  values from tens of fs to few ns, a computer controlled mechanical delay stage to control the optical path length of pump- or probe-pulse is reasonable. An increase of the optical pathway by  $3\ \mu\text{m}$  corresponds to a temporal delay of  $\sim 10$  fs between pump and probe pulse whereas an increase of 30 cm corresponds to a  $\sim 1$  ns delay. To resolve ultrashort processes on this time scale, it is necessary that the duration of pump and probe pulse also have to match these temporal conditions. On the other hand, to cover time scales larger than some ns or even in the  $\mu$ s or ms range, a mechanical delay is no longer feasible. Here electronic delay triggering provides the desired temporal accuracy and time window.

One aspect which all methods of transient absorption spectroscopy have in common is the kind of signals that contribute to the observed transient spectrum. Since all common pump-probe techniques measure the change of absorption with respect to the ground state absorption and not the pure absorption spectrum of the excited state or product states, the more correct term for the presented methods would be “transient differential absorption spectroscopy”, which is sometimes used. In general there are four major contributions to the transient absorption spectrum. The change of absorption of the excited state with respect to the ground state absorption can be either positive ( $\Delta OD > 0$ ) or negative ( $\Delta OD < 0$ ):

Excited state absorption (ESA),  $\Delta OD > 0$

Absorption of excited state > absorption of ground state

Ground state bleach (GSB),  $\Delta OD < 0$

Absorption of excited state < absorption of ground state

Stimulated emission (SE),  $\Delta OD < 0$

Stimulated emission amplifies probe light within the spectral region of the fluorescence

Product absorption (PA),  $\Delta OD > 0$

Newly formed species will absorb in general and their absorption will differ from the absorption spectra of the reactants

The signal of the stimulated emission can be clearly assigned to an excited singlet state – usually the  $S_1$  state. Stimulated phosphorescence of the triplet state is generally not often observable in transient absorption spectroscopy since it usually involves a spin forbidden transition from the triplet state back to the ground state, which has singlet character. The ground state bleach corresponds to a lack of ground state absorption due to the excitation of a fraction of molecules within the probed sample volume. The ground state bleach is specifically suited to quantify the fraction of molecules which populate an intermediate or product state of the photochemical reaction: Its persistence indicates that not all of the excited molecules have relaxed back to the ground state. Figure 16.3 a) shows the ground state absorption spectrum and the fluorescence spectrum of riboflavin tetraacetate (RFTA), a versatile investigated organic photocatalyst. The transient differential absorption spectrum of RFTA immediately after excitation at 450 nm is shown in Figure 16.3. b) Since the majority of common pure organic chromophores does not exhibit sup-ps excited state dynamics after excitation into the  $S_1$  state, only the signal of the first excited singlet state is contributing to the measured overall differential transient absorption spectrum at a pump-probe delay of 1 ps. One exception for instance is the organic chromophore xanthone, which undergoes inter-system crossing on the time scale of 1.5 ps. [26] The comparison of Figure 16.3 a) and Figure 16.3 b) clearly shows how the signals of ground state bleach and stimulated emission in the transient differential absorption spectrum correspond to ground state absorption and emission spectra.

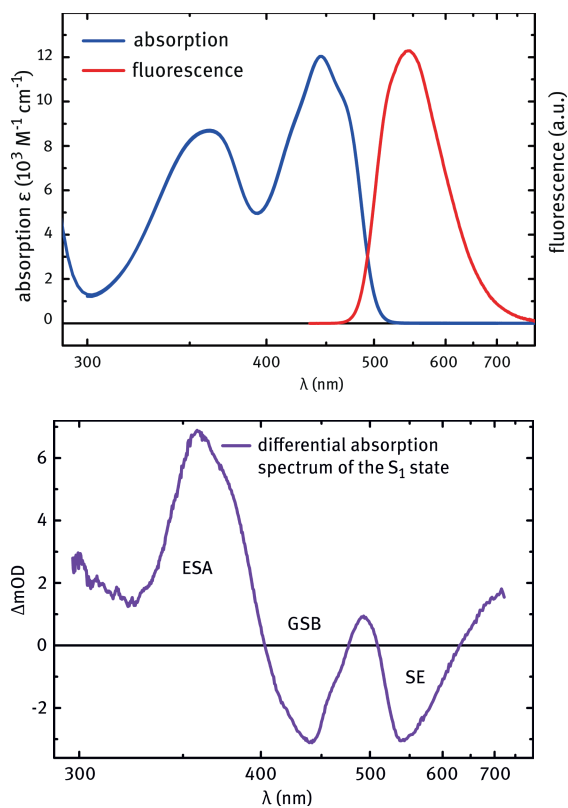


**Figure 16.3:** UV/Vis absorption and fluorescence spectra of riboflavin tetraacetate (top). Difference spectrum of the  $S_1$  state of riboflavin tetraacetate (bottom) 1 ps after excitation at  $\lambda = 480 \text{ nm}$ .

### 16.2.2 Spectroscopy on the fs to ps time scale

Several technical approaches for time resolved absorption spectroscopy are available to cover a huge range of time scales. The speed of light is the determining physical quantity when choosing the adequate experimental technique for the measurement of time resolved absorption spectra on different time scales. In the 1980s of the last century the first femtosecond lasers based on dye technology became available and allowed seminal investigation into fundamental dynamical processes. Only with the discovery of the modelocked Ti:sapphire, utilizing a solid-state laser material with the necessary broad gain bandwidth, laser pulses with fs duration became readily and reliably accessible. [27, 28] This discovery made the investigation of complex chemical reaction dynamics on the fs time scale possible for many laboratories. The initial work that was relying on the more complex CPM technology was rewarded with a Nobel Prize in chemistry for Prof. Ahmed Zewail in 1999.

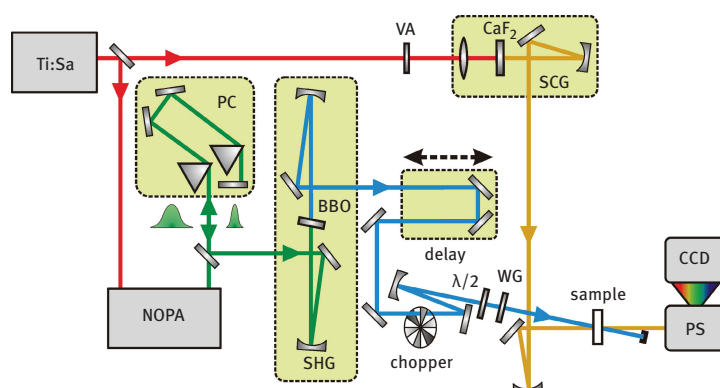


**Figure 16.4:** Scheme of a state-of-the-art ultrafast pump-probe spectrometer. [29] Tunability of the pump pulse is provided by a noncollinear optical parametric amplifier (NOPA) and second harmonic generation (SHG) in a BBO crystal. The prism compressor (PC) compresses the NOPA output pulse in the time domain. The variable attenuator (VA) adjusts the energy for the supercontinuum generation (SCG) in the calcium fluoride crystal ( $\text{CaF}_2$ ). The prism spectrometer (PS) detects the spectrally dispersed probe pulse after passing the sample with the help of a CCD array. The combined half-wave plate ( $\lambda/2$ ) and wire-grid polarizer (WG) allow adjusting of the intensity of the pump beam.

As mentioned before, time resolved absorption spectroscopy is a pump-probe technique. It does not only require ultrashort laser pulses, also an accurate control of the temporal delay between pump and probe pulse within the sample cell is essential. For the measurement of reaction kinetics on time scales from tens of fs ( $10^{-15}$ s) up to a couple of ns ( $10^{-9}$ s) the temporal delay can be easily adjusted by changing the optical pathway of pump or probe beam by moving a reflector on a mechanical delay stage. Mechanical delay stages provide accuracy on the  $\mu\text{m}$  scale, which is sufficient ( $c \cdot 10 \text{ fs} = 3 \mu\text{m}$ ) to obtain a time resolution of tens of fs. At the other end, mainly the limitations given by diffractive optics inhibit continuously tunable temporal delays, which are larger than a couple of ns ( $c \cdot 10 \text{ ns} = 3 \text{ m}$ ).

Megerle et al. [29] provide an overview over a state-of-the-art setup for an accurate measurement of transient absorption (TA) spectra on time scales of fs to ns, which is schematically drawn in Figure 16.4. This section only gives a brief introduction into the ultrafast TA spectroscopy.

Modern amplified femtosecond laser sources, which are applied in femtosecond transient absorption spectroscopy, provide ultra short laser pulses centered around 800 nm with a duration of 35–150 fs and pulse energies of about 1 mJ at a repetition rate of a few kHz. Due to the very short duration of the laser pulses, the peak intensities are in the gigawatt regime. By focusing a small part of the pulses into a transparent solid – usually a crystal – a supercontinuum is generated. [31, 32, 39] The spectral shape and the stability of the generated supercontinuum strongly depend on the crystal material. The parametric amplification of a selected region of this supercontinuum allows the direct generation of ultrashort pulses with new wave-

lengths in the spectral range between 450 nm and the central wavelength of the laser source. Further mixing processes such as second harmonic generation (SHG), sum frequency generation (SFG) and difference frequency generation (DFG) even enlarge the accessible wavelength region down to 189 nm. [33–35] These pulses usually have durations down to below 20 fs, a spectral bandwidth of tenths of THz and a pulse energy of hundreds of nJ to many  $\mu\text{J}$ . They can be used for excitation of a photocatalytic active chromophore at any desired spectral region.

Another part of the laser is focused into a further crystal for supercontinuum generation. This second supercontinuum is used for probing the transient response of the sample. Therefore, an extremely broad and stable white light is desired to gain detailed spectral information within the complete spectral window at once. White light generated in a high quality calcium fluoride ( $\text{CaF}_2$ ) crystal provides a stable probe spectrum within the wavelength region from 290 to 720 nm, when pumped with the fundamental of a Ti:Sa laser at 775 nm. [36] To prevent damage during supercontinuum generation, the crystal has to be kept constantly in motion. Care has to be taken to not negatively affect the shot-to-shot stability of the generated white light by the permanent movement. A translation motion of the  $\text{CaF}_2$  crystal within the focal plane provides the best supercontinuum properties for transient absorption spectroscopy. This motion avoids detrimental effects that would be caused by rotation of the crystal. Using a sapphire crystal instead of the  $\text{CaF}_2$  crystal provides the advantage that the sapphire crystal is more stable against photo damage and does not need to be translated. However, the generated supercontinuum extends only weakly into the blue ( $\sim 440$  nm).

The spectral position of the  $\text{CaF}_2$  white light can be shifted to adjacent spectral regions when pumping the supercontinuum generation with the second harmonic or even with an arbitrary chosen wavelength, which is generated by an additional optical parametric amplifier, instead of the fundamental. [32] Figure 16.5 shows

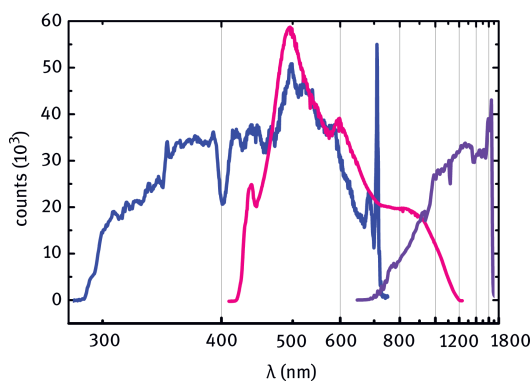


**Figure 16.5:** Supercontinuum, generated with 775 nm (blue line), with 1100 nm (purple line), and with 2200 nm (violet line) pump pulse in  $\text{CaF}_2$ . The long wavelength cutoffs are given by spectral filters that suppress the pump pulses.

supercontinua, which are generated in a  $\text{CaF}_2$  crystal pumped with femtosecond pulses of different wavelengths. As an alternative to the supercontinuum generation, also a second tunable parametric amplifier can be used for probing the excited sample. The probe pulses, which are generated by a parametric amplifier, are spectrally much narrower than a supercontinuum and, hence, provide less spectral information of the excited state. But in terms of pulse-to-pulse stability and achievable time resolution, this method provides advantages. For recording of broadband transient spectra with this method, it is necessary to repeat the measurement several times with different probe wavelengths to cover the whole spectral range of interest.

Usually in photocatalysis the excited state dynamics in the sub-ps regime only play a minor role, since photocatalysis is a bimolecular reaction and diffusion processes usually occur on the time scale of hundreds of picoseconds or slower. But for the characterization of the underlying sensitizing mechanism, sometimes it becomes inevitable to understand the ultrafast dynamics on the fs time scale. Especially if there is pre-association of catalyst and substrate, dynamics on the femtosecond time scale may be interesting. For instance, electron transfer between the excited state of the photocatalyst flavin and the amino acid tryptophane, both covalently bound to DNA and, hence, in close proximity, occurs on the 100 fs time scale. [38] The achievable time resolution of a transient absorption measurement strongly depends on the duration of the pump pulse, which is used for excitation. The duration of the probe pulse is not significantly affecting the achievable time resolution if the spectral resolution of the detection is accurate enough. [39] Hence, a compressed pump pulse is desired for a high time resolution. The output of a parametric amplifier can be easily compressed by passing a prism compressor, which allows pulse durations in the sub-20-fs regime in the visible and even in the near UV spectral range. To keep the pulse duration short, the use of reflective optics instead of bulk glass material is recommended to avoid additional chirp due to effects of dispersion. [29] Also the use of ultrathin windows for the sample cell minimizes the effect of additional chirp on the pump pulse. Furthermore, effects caused by overlap of pump and probe pulse within the window material, which also negatively affect the achievable time resolution, are minimized.

Time resolved spectroscopic pump-probe techniques require multiple excitation cycles of the probed sample volume to obtain a low-noise transient absorption spectrum with a sufficient density of data points to obtain a high time resolution. When using laser sources with a kHz repetition rate, the duration of a reasonable standard measurement ranges from 20 minutes to 2 hours depending on the averaging and the desired density of data points. Even if the quantum yield of the photocatalytic conversion of the substrate is in the low percent regime, the use of a flow cell is inevitable to keep the reaction conditions constant during the measurement. In addition, effects of the photo degradation of the photocatalyst can be avoided when measuring in a flow cell. A flow cell, which fulfills both the issues of a thin sample size and thin windows of the cell is depicted in Figure 16.6. [29]

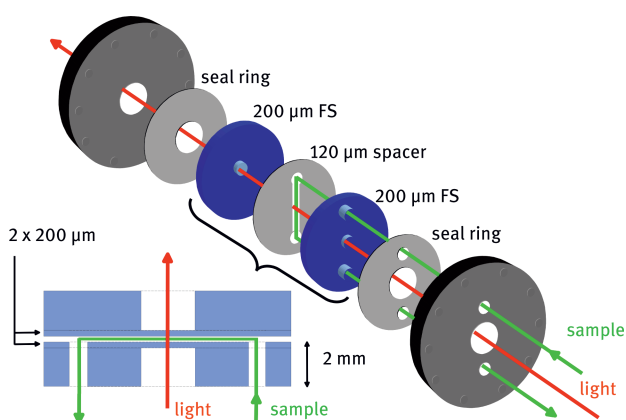


**Figure 16.6:** Scheme of the custom-made flow cell designed for low dispersion and a small optical path length. Reprinted from reference [29] with permission from Springer.

Another aspect that has to be covered especially when investigating photocatalytic reactions is the total amount of the sample and the effective concentration of the photocatalyst and substrate within the sample solution which is available for the spectroscopic measurement. Due to a limited length of pump-probe overlap within the sample cell, which usually does not exceed  $\sim 1$  mm, the optical density and; hence, the concentration of the sample solution needs to be sufficiently high. On the one hand, depending on the energy density of the pump pulse, the optical density at the excitation wavelength has to be high enough to generate a reasonable signal of the excited state within the probed spectral region. Also, the optical density within the probed spectrum has to be low enough not to completely absorb any part of the probe spectrum. An optical density of about 0.5 but not higher than 1 is recommended. Especially when product formation or photo degradation of the catalyst plays a major role, one has to be aware of the number of total excitation cycles of one molecule in the sample solution. Performing a transient absorption measurement of a common chromophore ( $\epsilon = 10 \cdot 10^3 \text{ M}^{-1} \text{ cm}^{-1}$ ) under standard conditions of ultrafast transient absorption spectroscopy ( $d = 120 \mu\text{m}$ ; signal = 10 mOD, spot size of pump pulse:  $\sim 100 \mu\text{m}$ ), the amount of excited molecules within a measurement time of one hour is in the range of hundreds of nanomoles. Considering a sample volume in the milliliter regime and a concentration of the chromophore in the mM and sub-mM regime, the excitation probability of one chromophore already comes close to unity.

### 16.2.3 Spectroscopy on the ns to $\mu\text{s}$ time scale

In the previous section an experimental method for the measurement of photo-induced reaction kinetics on time scales from tens of fs up to a couple of nanosec-



onds was presented. Since particularly in bimolecular reactions, the relevant intermediate steps may occur on much longer time scales, ultrafast transient absorption spectroscopy on this time scale is no longer sufficient and new experimental approaches are needed. Laser flash photolysis has become the standard tool to gain time resolved spectroscopic data on the ns and  $\mu\text{s}$  time scale. But in comparison to the presented ultrafast spectroscopic techniques, it brings some drawbacks: First to our knowledge, common commercially available systems provide a temporal resolution not below 7 ns. Although it is possible to cover the time scale up to  $\sim 10$  ns using a pump-probe setup with a sufficiently long mechanical delay stage, the obtained time constants on the ns time scale are not reliable due to a possible change of overlap of pump and probe beam within the sample cell while moving the delay mirrors. Only a very accurate beam alignment gives access to reliable time constants in the few ns region. Second, in comparison to the presented ultrafast transient absorption setup, the measurement conditions are completely different in classical laser flash photolysis. For instance, the Laser Flash Photolysis Spectrometer LP920 from Edinburgh Photonics [37] works with excitation pulse energies in the millijoule regime whereas the excitation energies in ultrafast transient absorption spectroscopy are many magnitudes smaller and remain in the hundred nanojoule regime. The need for much higher pump energies is due to the lack of spatial coherence of the probe light generated in a pulsed discharge. Therefore a sample volume of about 5 mm diameter and 10 mm length is typically used. The high energy density of the pump pulse and the large optical path length for the probe means the concentration of the chromophore has to be much lower in laser flash photolysis. The concentration is also much lower than typically used for the synthetic investigations. These issues make the transient kinetics obtained by laser flash photolysis difficult to compare directly with transient data measured in ultrafast transient absorption spectroscopy. To avoid all these problems, a transient absorption setup is desirable, which allows the measurement of time resolved reaction kinetics from time scales of femtoseconds up to microseconds within one measurement. In the following chapter an experimental approach is presented which covers all these requirements.

It has been shown that the key element for the access of different time scales is an accurate control of the temporal delay between pump and probe pulse. Whereas an electronic control of the pump-probe delay on time scales below the 100-ps regime is not practical due to physical limitations, in contrast for time scales in the ns regime or moreover in the  $\mu\text{s}$  regime, an electronic control of the temporal pump probe delay is easily accessible. An experimental technique for TA spectroscopy on the ns- $\mu\text{s}$  time scale which can be easily integrated into an existing setup for transient absorption measurements on the fs-ps time scale will be presented here.

The basic idea of this approach is to combine two pulsed laser sources. The existing fs laser source is complemented by a second pulsed laser source. To perform pump-probe spectroscopy and to control the temporal delay between pump and probe pulse accurately, both laser sources need to be triggered by a common clock.

Since a mode-locked Ti:sapphire or fiber oscillator cannot be easily triggered, we use the fiber seed laser of our amplified Ti:sapphire system as a master clock. This allows delaying the electronic trigger signal for the second laser source and controlling the temporal delay between the two laser pulses with the help of an electronic delay generator. This is always possible if the

repetition rates  $f_1$  and  $f_2$  of the two lasers are identical or an integral multiple, and Q-switching of at least one laser source can be externally triggered to high precision.

It is also possible to perform pump-probe spectroscopy with two independent pulsed laser sources without synchronization. In this approach the two laser sources, which have to be triggered with slightly different repetition rates, are combined to one pump-probe setup: The first laser generates the pump pulse, the second laser delivers the probe pulses. Depending on the frequency difference  $\Delta f = f_1 - f_2$ , the pump-probe delay changes from pulse to pulse. Now the pump-probe delay  $\Delta t$  only has to be measured for every excitation cycle and the obtained value has to be assigned to the corresponding measured spectrum. [40] Sorting the recorded spectra according to their assigned pump-probe  $\Delta t$  results in a full transient spectrum of the investigated photo-induced reaction. We will not expand on this method, but would like to point out, that it is pursued by others. [41] In this section we will only focus on transient absorption techniques where the temporal pump-probe delay can be directly controlled. In terms of time resolution and duration of a single measurement, this method is clearly favorable.

To allow probing the excited sample over a broad spectral range at once, a fs laser system is suggested for the generation of a spectrally broad white light continuum, which can be used as a probe pulse. Such a femtosecond continuum is spatially coherent and has a sub-ps duration. It is therefore superior to any other broadband light source for transient absorption spectroscopy in our opinion. It allows measurements in an extremely small sample volume and with very low optical load of the sample. Since amplified fs laser sources are anyway available in many laser laboratories due to their use as a fs-ps pump probe spectroscopy and in view of the superior continuum generation with fs laser pulses in bulk materials, the astonishing situation arises, that the femtosecond system is better used for the detection than for the pump, i. e. the triggering of the reaction cycle.

It is highly desirable that the temporal window of the ns- $\mu$ s transient absorption setup directly attaches to the end of the time windows of the fs-ps pump setup without any gap. This requires two things. The temporal duration of the additional laser source has to be in the low ns-regime and the electronic jitter of the second laser should be sub-ns. Further advantages of the application of a ns laser source are the comparatively low investment costs – as compared to a second fs system – and the availability of easy to handle optical parametric oscillators (OPO) for ns pulses. This provides an easy tunability of the excitation wavelength within a huge spectral

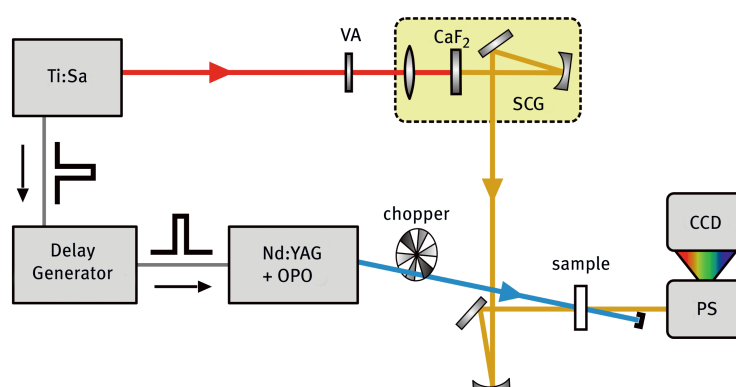


**Figure 16.7:** Simplified scheme of pump-probe setup for the measurement of TA spectra on time scales from ns to hundreds of  $\mu\text{s}$ . The fs pulse from the Ti:Sa system is still used for super continuum generation (SCG) in the calcium fluoride crystal ( $\text{CaF}_2$ ). The Nd:YAG laser provides ns pump pulses and is electronically synchronized with the Ti:Sa laser. Parametric amplification in an optical parametric oscillator (OPO) provides tunability of the pump wavelength. The prism spectrometer (PS) detects the spectrally dispersed probe pulse after passing the sample.

range. The diode pumped solid state laser NT242 from the Lithuanian manufacturer EKSPILA [37], which has an easy to handle OPO integrated within the laser housing, fulfills all the above requirements. The following discussion of a suggested setup for ns- $\mu\text{s}$  TA spectroscopy is mainly based on this laser.

By the use of the fs seed laser as a master clock, only the precision of the delay generator and the trigger jitter of the ns system contribute to the achievable stability. Up-to-date electronic delay generators, e.g. the DG535 from Stanford Research Systems [37] provide temporal accuracy of better than 100 ps. The NT242 has a measured trigger jitter of below 200 ps. Both values are well below the measured pulse length of the ns OPO of about 2.5 ns. Since the DG645 delay generator provides an Ethernet and a RS232 interface, it can be controlled by the computer used for data recording. This also allows a simple implementation of the communication software into the existing LabVIEW routines, which are already in use for the acquisition of transient spectra. [29] A simplified scheme of the combined setup is given in Figure 16.7.

The combination of these components allows the measurement of transient absorption spectra up to pump-probe delays of some hundreds of  $\mu\text{s}$  with a time resolution below 3 ns. A good estimate of the over-all time resolution, which was achieved during a measurement, is provided by the full width half maximum (FWHM) of the instrument response function. The width of the instrument response function (IRF) can be obtained from fitting the convolution of a Gaussian with the sum of the exponential functions on the measured decay kinetics. If the slowest kinetics of a sample are well below 1 ns, as this is often found for excited state

quenching by forward and back electron transfer [42], the IRF can be directly read off the raw data.

Within the presented setup, the fs laser source, which generates the probe continuum, is triggered by the signal of its own seed laser. The ns laser source, which is used for excitation, is triggered by the same laser clock, but the trigger signal first passes the delay generator, which delays the signal for a variable delay time. However, for pump probe spectroscopy, a reversed pulse sequence is needed: The sample first has to be excited and then to be probed. To fix this issue, one has to consider some details regarding the trigger sequence. Consequently, the measurement of one transient spectrum requires two cycles of the laser clock. After passing the delay generator, the first trigger signal releases the ns pump pulse whereas the fs probe pulse is released not until the next trigger pulse. Since two cycles of the laser clock are necessary to generate one transient spectrum, both the jitter of the seed laser and the jitter of the electronic control of the ns laser system contribute to the achievable over-all time resolution. In practice we find that the seed laser stability is so high that it actually does not contribute.

Another issue regarding the triggering sequence has to be solved: When measuring transient absorption spectra, usually transient spectra with pump-probe delays smaller than zero are recorded to obtain a flat base line, which serves as reference. For the measurement of transient spectra with negative pump-probe delays  $\Delta t < 0$ , the delay generator would need to generate a delay  $\Delta t_{DG}$  of the trigger signal, which is larger than the inverse repetition rate  $1/f$  of the signal, since the probe pulse has to be released first. However, the used delay generator does not provide this functionality. To solve this problem and to access negative pump-probe delays, a second delay generator is introduced, which generates a fixed pre-delay  $\Delta t_0$ . This then allows the measurement of transient spectra of negative pump-probe delays at the expense of clipping the temporal pre-delay  $\Delta t_0$  at the end of the observable time window.

The final issue, which limits the window of accessible pump-probe delays is that the EKSPLA NT 242 requires two trigger pulses: the first one for triggering the Nd:YAG rods for pumping the laser cavity and the second one for Q-switching and outcoupling the laser pulse. For an efficient amplification within the laser medium of the EKSPLA NT 242, a temporal delay of  $\sim 200 \mu\text{s}$  between the first and second trigger pulse is required. This presently leads to a clipping of the observable time window by  $200 \mu\text{s}$ . It would also be possible to circumvent this problem by a further computer controlled delay generator.

A more fundamental issue that should be noted is the exchange of the sample solution within the sample cell. Since the primary aim of photocatalysis is the conversion of a substrate into a product, every excitation pulse leads to a certain amount of product formation, as discussed in the previous section. However, the measurement of reliable transient absorption spectra, which requires the acquisition of a huge number of data points, is only feasible under stable conditions within the probed sample volume. Therefore a constant exchange of the excited sample is

inevitable. Since the flow cells with ultrathin glass windows, which are necessary to achieve a high time resolution in fs measurements, are not always easy to handle, the use of commercially available flow cells (e.g. Hellma 137-QS [37]) with path lengths of 1 mm or 2 mm are suggested for TA measurements on the ns- $\mu$ s time scale. This also allows the measurement at somewhat reduced concentrations that are comparable to the ones used in synthetic work.

For recording a transient spectrum of a selected pump-probe delay  $\Delta t$ , at least some hundred excitation cycles are necessary to obtain a low-noise difference absorption spectrum. Due to a shot-to-shot referencing combined with the repetition rate of  $f = 1$  kHz of both the fs and the ns laser source, the temporal delay between two consecutive excitation pulses is  $\Delta t = 2$  ms. The typical volume current within the circuit of the sample solution, which is pumped by a micro annular gear pump (HNP Mikrosysteme GmbH, model mzs-2921 [37]), is 18 ml/min. Considering the dimensions of the cross-sectional area of the applied flow cell (1 mm  $\times$  10 mm) and the volume current, the flow speed of the sample solution within the flow cell can be estimated to be 30  $\mu$ m/ms. With a spot size of the excitation pulse of  $\sim 300$   $\mu$ m, roughly 20% of the excited sample volume is replaced between two consecutive excitation pulses. Assuming a model reaction in which a substrate is converted into an equally absorbing product with a reaction quantum yield of 50%, the ratio of the signal contribution of the formed product molecules to the over-all signal is 5% when neglecting diffusion processes, which would lead to a further decrease of the product contribution. The excitation probability was assumed to be 10%, considering the usual excitation energy densities combined with a typical extinction coefficient of  $\sim 10,000$  M<sup>-1</sup>cm<sup>-1</sup> of the chromophore. Our experience is that in the particular flow conditions, pump light focus diameter and possibly a reduced laser repetition rate have to be carefully considered for any measurement that pushes the limits of detection window and sensitivity.

To summarize: For reliable time resolved spectroscopic measurements of photocatalytic processes, performing the measurements in a flow cell is inevitable. If the presented prerequisites are met, commercially available standard components are sufficient for the measurement of time resolved absorption spectra. But if, for example, highly absorbing products in large amounts are produced within the observed photochemical reaction, the presented system has to be modified. One possibility is the use of flow cells with a small cross-section area, either obtained by using a thin optical path length or a narrow flow channel, to increase the flow speed within the flow cell.

To demonstrate the versatility of the presented setup for application in photocatalysis, the flavin sensitized photo-oxidation of methoxy benzyl alcohol to its corresponding aldehyde is chosen as a model reaction. [43] Figure 16.8 shows that the photocatalytic process comprises several intermediate processes and species, which occur on largely different time scales. The time constants, which are applied to perfectly describe the decay dynamics, span five magnitudes of time and range from

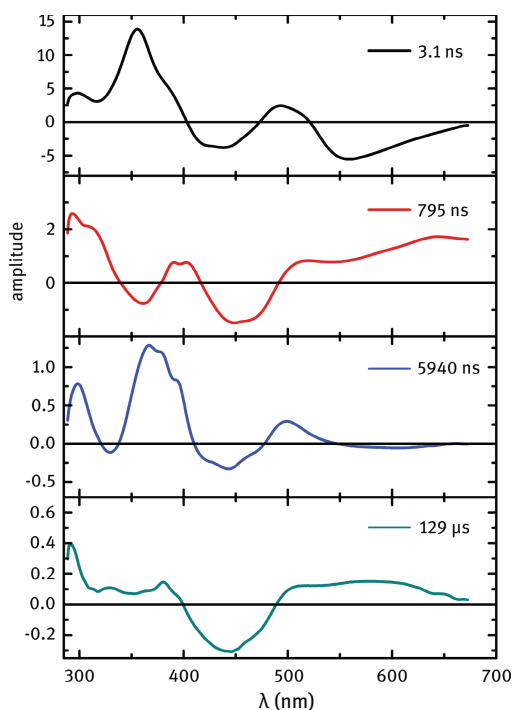


**Figure 16.8:** Decay associated difference spectra  $A_i(\lambda)$  (DADS), obtained from a single TA measurement, which was performed with the presented ns- $\mu$ s setup of the flavin sensitized oxidation of methoxy benzyl alcohol to the corresponding aldehyde.

few ns to hundreds of  $\mu$ s. All occurring time constants can be obtained within just one measurement. A detailed description of the spectroscopic investigation of flavin catalysis and the underlying intermediate steps can be found in reference [43].

#### 16.2.4 Rate models and the determination of the species associated spectra of the intermediate states

Time resolved differential absorption spectroscopy both on the fs-ps and on the ns- $\mu$ s time scale generally provides data matrices which describe the change of optical density  $\Delta OD$  with respect to the ground state, depending on pump-probe delay  $\Delta t$  and spectral position  $\lambda$ . These data matrices  $\Delta OD(\lambda, \Delta t)$  contain spectral information of the intermediate states and species. But generally this spectral information is not directly accessible. Data processing is required to gain this spectral information. The species associated spectrum  $\epsilon_i(\lambda)$  (SAS) of an intermediate state or a species allows their identification and the temporal evolution renders the kinetics of the process.

After the measurement the obtained data matrix has to be chirp-corrected in the case of sub-ps time resolution. The chirp correction is necessary since the different colors in the probe pulse arrive at slightly different times in the sample due to group velocity dispersion. This chirp of the broadband probe pulse generates a wavelength dependent time-zero. After chirp correction a sum of time dependent exponential fit functions can be applied to describe the decay dynamics of each individual spectral trace.

$$\Delta OD(\lambda, t) = \sum_i A_i(\lambda) \cdot \exp\left(-\frac{t}{\tau_i(\lambda)}\right) \quad (16.2)$$

Usually the amplitudes  $A_i(\lambda)$  and the time constants  $\tau_i(\lambda)$ , which are both wavelength dependent, are the fit parameters. More sophisticated fit functions can be used to describe more complex processes such as diffusion, which will be discussed in the following section. The data evaluation on the basis of single spectral traces has a number of disadvantages:

Inferior signal to noise ratio

Effects of spectral diffusion, e.g. caused by solvation or vibrational cooling result in additional non-exponential contributions to the decay signal

Contributions of similar time constants cannot be clearly distinguished

No complete spectral information of intermediate states is obtained

A more powerful method of data evaluation, which avoids these drawbacks, is the so-called global data analysis or global fit. No longer a set of wavelength dependent, individual time constants  $\lambda\tau_i(\lambda)$  is applied to the data matrix  $\Delta OD(\lambda, t)$  to describe the decay dynamics of each single time trace independently from each other. Moreover, global data analysis tries to apply exponential terms with global wavelength independent time constants  $\tau_i$  with a wavelength dependent amplitude  $A_i(\lambda)$  to describe the decay dynamics of the full spectral window of the data matrix  $\Delta OD(\lambda, t)$ :

$$\Delta OD(\lambda, t) = \sum_i A_i(\lambda) \cdot \exp\left(-\frac{t}{\tau_i}\right). \quad (16.3)$$

Since the amplitudes  $A_i(\lambda)$  describe the spectral composition of each decay with the time constant  $\tau_i$ , the obtained  $A_i(\lambda)$  are called decay associated difference spectra (DADS). Fita et al. [44] suggest a formalism for this kind of data analysis. But before applying the global fit routine on transient data, it is recommended to rescale the wavelength scale from a scale linear in  $\Delta\lambda$  to a scale linear in  $\Delta E$  to avoid the enhancement of the weight of the long-wave components. The number of the applied time constants  $\tau_i$  is directly linked to the number of processes which occur within the observed time window. Every process which populates an intermediate or final product state leads to an additional time constant  $\tau_i$  in the global fit. Intermediate states which are not significantly populated, e.g. if the depopulating rate  $k_{out}$  of the



corresponding state is much higher than the populating rate  $k_{in}$ , do not contribute significantly to the global fit. But these states are generally not accessible in TA spectroscopy as well.

Now the challenge is to extract the species associated spectra (SAS) or the species associated difference spectra (SADS) from the DADS. But first, the difference between SADS and SAS has to become clear. The SAS describe the true absorption spectrum of a certain intermediate state or species whereas the SADS only describe the spectral changes of this intermediate state with respect to the ground state absorption spectrum and the fluorescence spectrum of the chromophore. But the calculation of the SAS first requires the extraction of the SADS from the DADS, which are directly obtained as a result of the global fit routine. The conversion from SADS to SAS is very easy: It just requires adding the wavelength dependent absorption spectrum  $abs(\lambda)$  and the wavelength dependent fluorescence spectrum  $fluo(\lambda)$  of the excited chromophore to the SADS as shown in Equation 16.4, where  $\alpha$  and  $\beta$  are scaling factors.

$$\varepsilon_1(\lambda) = SAS_1(\lambda) = SADS_1(\lambda) + \alpha \cdot abs(\lambda) + \beta \cdot fluo(\lambda) \cdot \lambda^4 \quad (16.4)$$

The multiplication of the wavelength dependent fluorescence intensity by  $\lambda^4$  is required due to the conversion factor of the Einstein coefficient between spontaneous and stimulated emission and due to rescaling the fluorescence intensity per wavelength interval  $\Delta\lambda$  to the corresponding quantity per frequency interval  $\Delta\nu$ . [45] One has to keep in mind that in a fluorometer, the spectral shape of the spontaneous emission is measured whereas in TA spectroscopy the spectral shape of the stimulated emission is detected.

The difference between DADS  $A_i(\lambda)$ , SADS and SAS  $\varepsilon_i(\lambda)$  can be well explained with the following simplified example: A spectrally well characterized chromophore is optically excited. The well confined absorption spectra  $\varepsilon_i(\lambda)$  of the ground state, the first excited singlet state ( $S_1$ ) and the lowest triplet state ( $T_1$ ) are assumed to be known and are depicted in Figure 16.9. Fluorescence does not play a role for the sake of simplicity.

After excitation of the chromophore into the  $S_1$  state, let there be two competing processes, which depopulate this state: internal conversion with a rate of  $k_{IC} = (100 \text{ ps})^{-1}$  and inter-system crossing with a rate of  $k_{ISC} = (100 \text{ ps})^{-1}$  as well. The internal conversion process converts the population from the  $S_1$  state back to the ground state and the inter-system crossing process converts the population from the  $S_1$  state to a third state, the triplet state  $T_1$ . Due to both processes depopulating the  $S_1$  state, the overall rate  $k_{S_1}$  which describes the depopulation of the  $S_1$  state can be written as the sum of  $k_{IC}$  and  $k_{ISC}$ . Therefore, the life time of the  $S_1$  state is  $\tau_{S_1} = 50 \text{ ps}$ .

$$k_{S_1} = (\tau_{S_1})^{-1} = k_{IC} + k_{ISC} = (50 \text{ ps})^{-1} \quad (16.5)$$



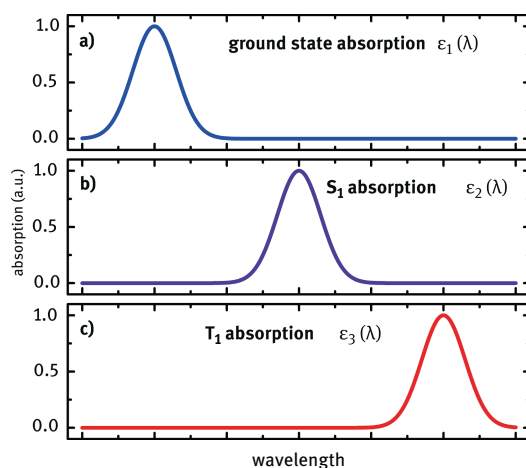


**Figure 16.9:** Optical absorption spectra of ground state (a), excited singlet state (b) and lowest triplet state (c) of an example chromophore. Since the spectra  $\epsilon(\lambda)$  describe the wavelength dependent absorption properties of each state they are named species associates spectra (SAS).

Since  $k_{IC}$  and  $k_{ISC}$  are equal, the branching ratio between internal conversion and inter-system crossing is 1:1. This means that for each excited chromophore in the  $S_1$  state both the probability to decay back to the ground state and the probability to decay into the long-lived triplet state  $T_1$  are 50%. The Jablonski diagram in Figure 16.10 provides a schematic overview of the excited state dynamics.

The species spectra of all populated excited states are contributing in different ways to the transient difference absorption spectrum, and generally, the spectra of these states do not directly appear in the measured data set. Immediately after excitation of the model chromophore, there are only two signal contributions: The depopulation of the ground state leads to the negative signal of the ground state

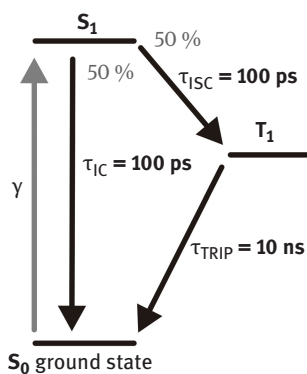


**Figure 16.10:** Jablonski diagram of the example chromophore

bleach (GSB) whereas the population of the  $S_1$  state results in a positive signal of excited state absorption (ESA) due to the possible excitation into a higher state. The simulated transient signal directly after excitation is shown in Figure 16.11 a).

With the beginning of the inter-system crossing (ISC) process on the time scale of 100 ps, the transient signal now contains contributions of all three states and the spectra of the contributing individual states are no longer directly accessible. Applying the global fit to the full data matrix provides a fit described by two time constants:  $\tau_1 = 50$  ps, the life time of the  $S_1$  state and  $\tau_2 = 10$  ns, the life time of the  $T_1$  state with the corresponding amplitude spectra  $A_1(\lambda)$  and  $A_2(\lambda)$ . These spectra  $A_1(\lambda)$  and  $A_2(\lambda)$  are the so-called DADS and are shown in Figure 11 b) and c), respectively. The amplitude spectrum  $A_1(\lambda)$  shows, that the  $S_1$  absorption in the middle decays and simultaneously both the ground state and the  $T_1$  state are populated. Since the quantum yield for the triplet state  $T_1$  is only 50 %, its contribution to  $A_2(\lambda)$  is only half as intense as the amplitude of the  $S_1$  decay in  $A_1(\lambda)$ .

The whole population of the  $T_1$  state decays back to the ground state, which can be seen, by comparing the contributions of the amplitudes of the decay of the  $T_1$  ESA and the recovery of the GSB in  $A_2(\lambda)$ . The full spectral information of the intermediate states now can be extracted from these DADS.

When understanding the relation between DADS, SADS and SAS of the previously presented model reaction, now a more formal treatment can be introduced. It can be seen by comparison of Figure 16.9 and Figure 16.11, that the DADS  $A_i(\lambda)$  are composed of a linear combination of the SAS  $\varepsilon_i(\lambda)$ , including the ground state absorption spectrum  $\varepsilon_{S_0}(\lambda)$ . Consequently, the SAS can be obtained as linear combinations of the DADS. The inverse of the relative yield of the corresponding state deter-

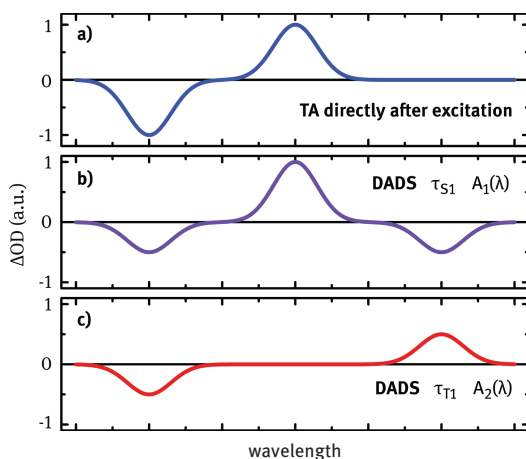


**Figure 16.11:** Transient difference absorption spectrum directly after excitation (a),  $A_1(\lambda)$ , DADS of the  $\tau = 50$  ps component, that describes the decay of the  $S_1$  state and the population of the  $T_1$  state (b) and  $A_2(\lambda)$ , DADS of the  $\tau = 10$  ns decay of the triplet state (c)

mines the weighting coefficient of the DADS. It can be written as fraction of the involved rates  $k_i$ .

$$\varepsilon_{S1}(\lambda) = A_{50ps}(\lambda) + A_{10ns}(\lambda) + \varepsilon_{S0}(\lambda) \quad (16.6)$$

$$\varepsilon_{T1}(\lambda) = \frac{k_{ISC} + k_{IC}}{k_{ISC}} A_{10ns}(\lambda) + \varepsilon_{S0}(\lambda) = 2 \cdot A_{10ns}(\lambda) + \varepsilon_{S0}(\lambda) \quad (16.7)$$

A more general treatment of the data analysis is given in the following section. To introduce a mathematical description the use of a rate model is recommended. A rate model is based on the assumption, that an arbitrarily chosen intermediate state  $i$  is populated from a state  $i-1$  with rate  $k_i$  and decays with rate  $k_2$  into subsequent intermediate states or the final product state. This allows describing the temporal behavior of the population of the observed state  $n_i(t)$  by the following differential equation:

$$\frac{dn_i}{dt} = \dot{n}_i = +k_1 \cdot n_{i-1}(t) - k_2 \cdot n_i(t). \quad (16.8)$$

For the full description of a rate model, involving more than one state, the differential equations for each state, which are no longer independent from each other, can be written in matrix formalism, as shown in Equation 16.9.

$$\begin{pmatrix} \dot{n}_1 \\ \dot{n}_2 \\ \dot{n}_3 \\ \vdots \end{pmatrix} = \begin{pmatrix} -k_{11} & 0 & 0 & \dots \\ +k_{21} & -k_{22} & 0 & \dots \\ +k_{31} & +k_{32} & -k_{33} & \dots \\ \vdots & \vdots & \vdots & \ddots \end{pmatrix} \cdot \begin{pmatrix} n_1 \\ n_2 \\ n_3 \\ \vdots \end{pmatrix}. \quad (16.9)$$

If there is no repopulation from lower to higher states, which means that the matrix  $A$  is a lower triangular matrix, the diagonal elements  $k_{ii} = (\tau_i)^{-1}$  represent the decay rate of state  $i$  and are directly obtained as the inverse of the time constants from the global fit. By solving the differential equation system 16.9 one can obtain mathematical terms for  $n_i(t)$  which describe the population dynamics of each state  $i$ .

How to solve such a differential equation system is demonstrated by the following example of a sequential model involving three states. A scheme of the process is provided in Figure 16.12.

The population dynamics  $n_i(t)$  of each state are described by a differential equation, which relates the temporal behavior of state  $i$   $\dot{n}_i(t)$  with its current population  $n_i(t)$ .

$$\begin{aligned} \dot{n}_1 &= -k_1 \cdot n_1 \\ \dot{n}_2 &= +k_1 \cdot n_1 - k_2 \cdot n_2 \\ \dot{n}_3 &= +k_2 \cdot n_2 \end{aligned} \quad (16.10)$$

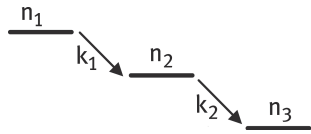


**Figure 16.12:** Sequential three state model: State 1 with population  $n_1(t)$  decays with rate  $k_1$  to state 2. State 2 with population  $n_2(t)$  decays back to the ground state with rate  $k_2$ .

Now, according to Equation 16.9, a matrix can be introduced for an easier treatment of the differential equation system:

$$\begin{pmatrix} \dot{n}_1 \\ \dot{n}_2 \\ \dot{n}_3 \end{pmatrix} = A \cdot \mathbf{n} = \begin{pmatrix} -k_1 & 0 & 0 \\ +k_1 & -k_2 & 0 \\ 0 & +k_2 & 0 \end{pmatrix} \cdot \begin{pmatrix} n_1 \\ n_2 \\ n_3 \end{pmatrix}. \quad (16.11)$$

Since the introduced matrix  $A$  is a triangular matrix, the diagonal entries of  $A$  give the multiset of eigenvalues of  $A$ .

$$\lambda_1 = -k_1 \quad \lambda_2 = -k_2 \quad \lambda_3 = 0 \quad (16.12)$$

The eigenvector  $\mathbf{x}_i$  of each eigenvalue  $\lambda_i$  is required for the further treatment and solving of the differential equation system:

$$\mathbf{x}_1 = \begin{pmatrix} 1 \\ k_1 \\ \frac{-k_1 + k_2}{-k_1 + k_2} \\ \frac{-k_2}{-k_1 + k_2} \\ \frac{-k_1 + k_2}{-k_1 + k_2} \end{pmatrix} \quad \mathbf{x}_2 = \begin{pmatrix} 0 \\ 1 \\ 1 \end{pmatrix} \quad \mathbf{x}_3 = \begin{pmatrix} 0 \\ 0 \\ 1 \end{pmatrix}. \quad (16.13)$$

Finally, the information, which is needed to solve the differential equation system, is complete. An exponential approach with free parameters  $c_i$  solves the differential equation system.

$$\mathbf{n}(t) = c_1 \cdot \mathbf{x}_1 \cdot \exp(\lambda_1 \cdot t) + c_2 \cdot \mathbf{x}_2 \cdot \exp(\lambda_2 \cdot t) + c_3 \cdot \mathbf{x}_3 \cdot \exp(\lambda_3 \cdot t) \quad (16.14)$$

The parameters  $c_i$  now only have to be adapted to the boundary conditions. Reasonable boundary conditions for the temporal behavior of the intermediate states of a sequential three state model in transient absorption spectroscopy are:

$$n_1(0) = n_0 \quad n_2(0) = 0 \quad n_3(0) = 0 \quad n_i(t > 0) \geq 0 \quad n_3(t \rightarrow \infty) = n_0. \quad (16.15)$$

The solution for the excited state dynamics of the presented sequential three state model, which matches the given boundary conditions, is given in Equation 16.16.

$$\begin{aligned}
n_1(t) &= n_0 \cdot \exp(-k_1 \cdot t) \\
n_2(t) &= n_0 \cdot \left[ \frac{k_1}{-k_1 + k_2} \exp(-k_1 \cdot t) - \frac{k_1}{-k_1 + k_2} \exp(-k_2 \cdot t) \right] \\
n_3(t) &= n_0 \cdot \left[ \frac{-k_2}{-k_1 + k_2} \exp(-k_1 \cdot t) + \frac{k_1}{-k_1 + k_2} \exp(-k_2 \cdot t) + 1 \right]
\end{aligned} \tag{16.16}$$

One sees readily that the population of the initially excited state 1 decays with a single exponential rate as assumed. State 2 gets populated with  $k_1$  and depopulated with  $k_2$ . For the final state 3 both rates are important again, even though there is no direct path from state 1 to state 3. This is only mediated by state 2, but by its involvement, the rate  $k_1$  also becomes important for the population of the final state.

For processes with more than three contributing excited states, which have to be described by a more complex system of rate equations, applying a numeric solution might be more practical to gain reasonable results. Since it now should be clear how to obtain solutions for a rate equation system, the functions  $n_i(t)$  describing the excited state dynamics can be used for the interpretation of the results of the global fit. The transient data matrix  $\Delta OD(\lambda, t)$  can be written as the time dependent population dynamics  $n_i(t)$  of state  $i$  multiplied by the corresponding SAS  $\varepsilon_i(\lambda)$ , which describes the wavelength dependency.

$$\Delta OD(\lambda, t) = n_1(t) \cdot \varepsilon_1(\lambda) + n_2(t) \cdot \varepsilon_2(\lambda) + n_3(t) \cdot \varepsilon_3(\lambda) + \dots + n_0(t) \cdot \varepsilon_{s_0}(\lambda) \tag{16.17}$$

Equation 16.17 contains the population dynamics of the intermediate states  $n_i(t)$ . The next step towards obtaining the SAS  $\varepsilon_i(\lambda)$  of state  $i$ , is equalizing the whole expression with the result of the global fit (Equation 16.3).

$$n_1(t) \cdot \varepsilon_1(\lambda) + n_2(t) \cdot \varepsilon_2(\lambda) + \dots + \varepsilon_{s_0}(\lambda) = A_1(\lambda) \cdot e^{-t/\tau_1} + A_2(\lambda) \cdot e^{-t/\tau_2} + \dots \tag{16.18}$$

Now, the population dynamics  $n_i(t)$  of each state, which can be calculated by solving the differential equation system, given in Equation 16.9, has to be inserted into Equation 16.18. The independent population dynamics  $n_i(t)$  are written as a sum of exponential terms with individual time constants  $\tau_i$ . The last step is to sort the different time dependent exponential terms on the left side of Equation 16.18. Now the relation between SAS  $\varepsilon_i(\lambda)$  and DADS  $A_i(\lambda)$  can be directly seen by comparison of the wavelength dependent pre-factors of the individual time dependent exponential terms of both sides of the equation.

The global fit is one of the most powerful evaluation methods of transient absorption dynamics. But, nevertheless, before it provides confidential results, it requires either a detailed knowledge of the spectra of all occurring intermediate states or a detailed knowledge of the reaction kinetics of each intermediate state. It is not sufficient just to know the decay dynamics of each state – also a majority of

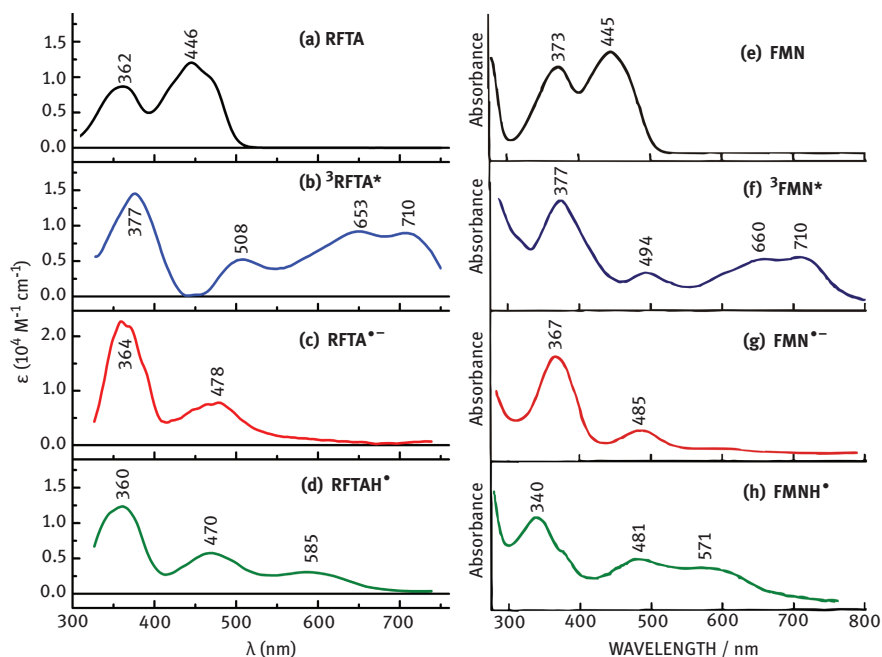


**Figure 16.13:** Absorption spectra of the ground state RFTA (a) and (e), the triplet state  ${}^3\text{RFTA}^*$  (b) and (f), the radical anion state  $\text{RFTA}^{\bullet-}$  (c) and (g) and the neutral protonated state  $\text{RFTA H}^{\bullet}$  (d) and (h) of riboflavin tetraacetate. The spectra on the right side are reprinted from reference [47] with permission from Elsevier, the spectra on the left side are extracted from the DADS, which were obtained by applying a global fit on the data matrices  $\Delta\text{OD}(\lambda, t)$  of the time-resolved spectroscopic investigation of the photocatalytic oxidation of methoxy benzyl alcohol. [43, 48]

the off-diagonal elements of the matrix in Equation 16.9 has to be identified. Estimating the quantum yield of the intermediate states, for instance with the help of the time dependent intensity of the ground state bleach, may help determining the off-diagonal elements.

Since there have been various further approaches developed over the years to interpret the outcome of the transient spectroscopy, and since the investigated problems vary widely, the interested reader is referred to a more general treatment of data analysis given in a recent review. [46] There it is nicely explained, whichever model assumption is made or not made, one has to input into the various data treatments.

To demonstrate the application of the global fit, the spectroscopic investigation of the flavin sensitized photo-oxidation of methoxy benzyl alcohol (MBA) is used as a model reaction. After excitation and inter-system crossing (ISC) of the riboflavin tetraacetate (RFTA) chromophore, a first electron transfer from the MBA to the triplet state  ${}^3\text{RFTA}$  leads to the radical anion  $\text{RFTA}^{\bullet-}$ . The MBA is only a weak chromophore and renders no contribution to the transient absorption signal within the probed

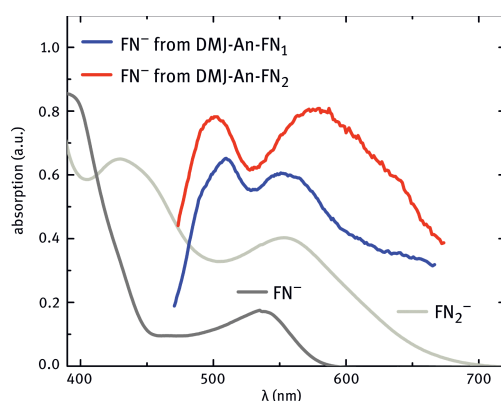


**Figure 16.14:** Spectra of the fluorenone anion (dark grey line), the anion of two covalently linked fluorenones (bright grey line), and the SAS of an intramolecular charge transfer state of a complex donor-bridge-acceptor molecule (blue and red line), where the electron is temporarily located on the fluorenone moiety of the molecule. [10]

spectral range. The next step of the reaction is the protonation of the radical. [47] The extracted SAS of the occurring intermediate states of the flavin photocatalyst and their assignment to known spectra [47] of the different redox and protonation states of flavin are shown in Figure 16.4.

Another field of application is the combination of global fit analysis with the methods of spectroelectrochemistry. Especially when charge transfer processes between two chromophores, either of intermolecular or intramolecular character, are suspected to occur within the investigated reaction, the combination of these experimental techniques can help to recognize and allocate these intermediate states. One example of the successful combined application of the presented data analysis and spectroelectrochemistry is given in reference [49]. Here, the intramolecular charge transfer of a donor-bridge-acceptor molecule was investigated. The main aspect of the study was to proof an incoherent hopping mechanism, which transports an electron from the donor site of the molecule to its acceptor site. Incoherent hopping includes that the charge transfer state is temporarily located on the bridge molecules, which link electron donor and acceptor. The bridge consists of alternatively one, two or three covalently linked fluorenone molecules. The spectra of the radical anion of a single fluorenone and of two covalently linked fluorenone molecules were determined with the help of spectroelectrochemistry. The spectra of the radical anions exhibit a strong absorption band centered around 550 nm and 575 nm, respectively. The decomposition of the transient spectra with the help of the global data analysis clearly showed a significant spectral contribution of the fluorenone radical anion absorption to the intermediate spectra and proved the proposed reaction mechanism via incoherent hopping. The spectra are shown in Figure 16.14.

## 16.3 Diffusion limited reactions

### 16.3.1 Diffusion limited excited state quenching with time dependent reaction rate

For intermolecular photo-sensitization processes, a close proximity between donor and acceptor molecule is inevitable due to a strong distance dependence of the common sensitizing mechanisms. In general, there are two different mechanical approaches to allow photo-induced sensitization: diffusive sensitization after photo-excitation and complex formation before photo-excitation. This chapter will describe the challenges in transient absorption spectroscopy which are related to the investigation of diffusion controlled sensitizing mechanisms.

A very widely accepted principle of the data analysis in transient absorption spectroscopy is the exponential decay modeling. It is based on the assumption, that the number of excited molecules which decay to a lower state within an infinitesimal time period  $dt$  is proportional to the total number of molecules which are momentarily in the observed excited state. However, to describe the ultrafast population dynamics on the ps ( $10^{-12}$ s) time scale of diffusion limited reactions, the exponential decay modeling is inappropriate and a more sophisticated model is required. The reaction rate  $k$ , which is a constant in exponential decay modeling, turns into a time dependent quantity  $k(t)$  when describing diffusion limited dynamics. The time dependency of  $k(t)$  is usually negligible for reaction dynamics on the ns time scale but causes major deviations from strongly monoexponential decay dynamics on the low ps time scale.

The time dependency of the reaction rate can be justified qualitatively: Directly after excitation, there is a certain average distance  $d_0$  between excited sensitizer molecule and quencher molecule, which only depends on the initial quencher concentration  $[Q_0]$ . The quencher molecules are randomly distributed around the sensitizer molecules if there are no effects of attracting or repulsive forces. This average distance  $d_0$  is the determining quantity of the reaction rate  $k$  since, due to the laws of diffusion, the average distance is related to the average time until collision between two molecules occurs. The values of  $d_0$  are typically between 1 and 5 nanometers when using quencher (substrate) concentrations between 10 and 1000 mM which are common for photocatalytic processes. Electron transfer reactions and energy transfer mechanisms require a sub-nm distance to work efficiently.

To quantitatively model the time dependency of the reaction rate  $k(t)$  the following ideas are used: After excitation the sensitizer molecules with a quencher molecule in close proximity are quenched first whereas excited sensitizer molecules without a quencher molecule in close proximity remain in the excited state. These excited chromophores are able to decay spontaneously back to the ground state within the life time  $\tau$  of the excited state. These effects lead to an increase in the average distance  $d_0$  between excited sensitizer molecules and quencher and, hence, to a decrease in reaction rate  $k$ . A detailed derivation of an applicable mathematical



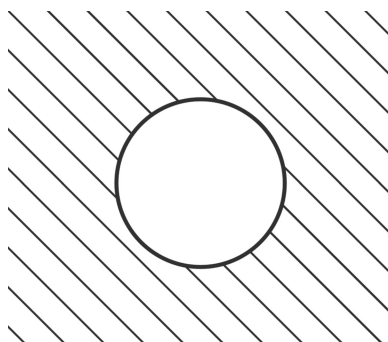


**Figure 16.15:** Spherical sensitizer with radius  $R$  surrounded by the quencher  $Q$  which is described as scalar field in spherical coordinates  $[Q(r)]$

model can be found in the book of S. A. Rice, who provides an excellent overview of diffusion limited reaction kinetics. [50] A short summary is presented in the following section.

For the derivation of a mathematical model which describes diffusion limited bimolecular processes, some simplifications are inevitable. The model is based on the Einstein–Smoluchowski-Theory of diffusion and assumes a spherical chromophore with radius  $R$  located at the origin of a spherical coordinate system as shown in Figure 16.15. The sensitizer is enclosed by the quencher molecules, which are described as a scalar field instead of discrete molecules. This means that at least in first approximation the distribution function of the quencher is continuous. The concentration  $[Q]$  of the quencher is much higher than  $[S]$ , the concentration of the sensitizer. Inside the spherical chromophore, the quencher concentration equals zero for  $t \leq 0$ .

The homogeneous initial concentration of the quencher is  $[Q_0]$ . The following discussion is based on the assumption that the excited chromophore is separated far enough from the next excited chromophore that competing processes can be neglected. For an easy mathematical description, a normalized quencher density  $\rho(r)$  which depends on the distance  $r$  with respect to the coordinate origin is introduced.

$$\rho(r) = \frac{[Q(r)]}{[Q_0]} \quad (16.19)$$

The assumption, which was applied with the introduction of the model, can be expressed by the following boundary conditions:

$$\begin{aligned} \rho(r,t) &= 0 & (t=0 \quad r \leq R) \\ \rho(r,t) &= 1 & (t=0 \quad r > R) \\ \rho(r,t) &= 1 & (t \geq 0 \quad r \rightarrow \infty) \end{aligned} \quad (16.20)$$

This model assumes that the excited chromophore is quenched when the quencher molecule Q is at an encounter distance R. Hence, the quencher concentration at encounter distance R equals zero independently of t, which can be expressed by a fourth boundary condition.

$$\rho(r,t)=0 \quad (t \geq 0 \quad r=R) \quad (16.21)$$

Due to Fick's laws of diffusion the concentration gradient at an arbitrarily chosen distance  $r = r_0$  with  $r_0 > R$  leads to a particle current density  $J(r_0)$  crossing the spherical surface. The particle current density can be written as the product of the diffusion constant D and the concentration gradient at  $r = r_0$ .

$$J(r_0) = D \left. \frac{\partial c}{\partial r} \right|_{r=r_0} \quad (16.22)$$

The particle current  $I(r_0)$  of quencher molecules Q crossing this spherical surface is obtained by multiplication of the particle current density J by the area of the spherical surface.

$$I(r_0) = 4 \pi r_0^2 D \left. \frac{\partial c}{\partial r} \right|_{r=r_0} \quad (16.23)$$

Now we have to calculate the net loss of quencher Q within a spherical shell with radius  $r_0$  and an infinitesimal thickness  $dr$ . First of all, the particle current  $I(r_0 + dr)$  through the external spherical surface with radius  $r_0 + dr$  has to be formulated.

$$I(r_0 + dr) = 4 \pi (r_0 + dr)^2 D \left. \frac{\partial c}{\partial r} \right|_{r=r_0+dr} \quad (16.24)$$

The net loss of quencher Q within this spherical shell now can be calculated by subtraction of the particle current, which is flowing into the shell, by the particle current, which is flowing out.

$$I(r_0) - I(r_0 + dr) = 4 \pi r_0^2 D \left. \frac{\partial c}{\partial r} \right|_{r=r_0} - 4 \pi (r_0 + dr)^2 D \left. \frac{\partial c}{\partial r} \right|_{r=r_0+dr} \quad (16.25)$$

To obtain the rate of loss of concentration of Q per unit time within this spherical shell of infinitesimal thickness one has to divide the net particle loss of this spherical shell by its volume  $4 \pi r_0^2 dr$ .

$$\begin{aligned}
\frac{\partial c}{\partial t} &= \frac{4\pi D}{4\pi r_0^2 dr} \left[ r_0^2 \frac{\partial c}{\partial r} \Big|_{r=r_0} - (r_0 + dr)^2 \frac{\partial c}{\partial r} \Big|_{r=r_0+dr} \right] \\
\frac{\partial c}{\partial t} &= \frac{D}{dr} \left[ \frac{\partial c}{\partial r} \Big|_{r=r_0} - \left( 1 + \frac{2dr}{r_0} \right) \cdot \left( \frac{\partial c}{\partial r} \Big|_{r=r_0} + \frac{\partial^2 c}{\partial r^2} \Big|_{r=r_0} dr \right) \right] \\
\frac{\partial c}{\partial t} &= \frac{D}{dr} \left[ -\frac{\partial^2 c}{\partial r^2} \Big|_{r=r_0} dr - \frac{2dr}{r_0} \cdot \frac{\partial c}{\partial r} \Big|_{r=r_0} - \frac{2dr}{r_0} \cdot \frac{\partial^2 c}{\partial r^2} \Big|_{r=r_0} dr \right] \\
\frac{\partial c}{\partial t} &= -D \left[ \frac{\partial^2 c}{\partial r^2} \Big|_{r=r_0} + \frac{2}{r_0} \frac{\partial c}{\partial r} \Big|_{r=r_0} \right]
\end{aligned} \tag{16.26}$$

The concentration  $c$  in Equation 16.26 now can be expressed with the normalized quencher density  $\rho(r)$  according to Equation 16.19:

$$\frac{\partial \rho}{\partial t} = D \left( \frac{\partial^2 \rho}{\partial r^2} + \frac{2}{r_0} \frac{\partial \rho}{\partial r} \right) \tag{16.27}$$

The right hand side of Equation 16.27 contains two spherically symmetric derivatives of  $\rho(r, t)$  which can be replaced by the Laplace operator.

$$\frac{\partial \rho}{\partial t} = D \nabla^2 \rho \tag{16.28}$$

This equation describes the diffusion of matter as well as the diffusion of heat and its solution has been already studied. In consideration of the boundary conditions in Equations 16.20 and 16.21 the complementary error function  $\text{erfc}(x)$  solves the differential equation.

$$\rho(r, t) = 1 - \frac{R}{r} \text{erfc} \left\{ \frac{r-R}{\sqrt{4Dt}} \right\} \tag{16.29}$$

The time dependent particle current  $I(t)$  of quencher  $Q$  diffusing towards the excited chromophore at encounter distance  $R$  per infinitesimal time interval represents the time dependent reaction rate  $k(t)$  of excited state quenching. The particle current at encounter distance  $R$  can be obtained by insertion of  $\rho(R, t)$  into Fick's law of diffusion, which is formulated in Equation 16.30. The obtained rate  $k(t)$  describes the dynamics of the non-stationary quenching process assuming, that the excited state life time is infinite. The quencher concentration  $[Q_0]$  is given in units of particles per unit volume, e.g.,  $\text{m}^{-3}$ .

$$k(t) = I(R, t) = 4\pi R^2 D \left. \frac{\partial \rho}{\partial r} \right|_{r=R} [Q_0] = 4\pi R^2 D \left[ \frac{1}{R} + \frac{1}{\sqrt{\pi D t}} \right] [Q_0] \quad (16.30)$$

It can be seen that the rate starts at very large values at early times  $t$ . However, when we insert the rate into the decay function, and include the intrinsic life time  $\tau$  of the excited state which is quenched, we see immediately that the  $t$ -term in the denominator is more than balanced by the multiplication of the rate by  $t$ .

$$n(t) = n_{\text{diff}} \cdot \exp(-k(t)t) = n_{\text{diff}} \cdot \exp \left\{ -\frac{t}{\tau} - 4\pi R D \cdot [Q_0] \cdot \left[ 1 + \frac{2R}{\sqrt{4Dt}} \right] \cdot t \right\} \quad (16.31)$$

The result can also be written as a product of an exponential term with  $t$  in the exponent and an exponential term with the square root of  $t$  in the exponent:

$$n(t) = n_{\text{diff}} \cdot \exp \left( -\frac{t}{\tau} \right) \cdot \exp(-4\pi R D \cdot [Q_0] \cdot t) \cdot \exp \left\{ -4\pi R D \cdot [Q_0] \cdot \frac{2R\sqrt{t}}{\sqrt{4D}} \right\}. \quad (16.32)$$

This means that the temporal evolution is given by i) the spontaneous decay of the sensitizer excitation, ii) a classical rate term, and iii) a stretched exponential. The last term is the result of the non-equilibrium situation caused by the ultrafast excitation. It deviates strongly from the widely used multi-exponential modeling and can only be poorly compensated in an exponential model by adding ever more time constants.

For  $t \rightarrow \infty$  the reaction rate  $k(t)$  becomes time independent. This time independent rate  $k_\infty$  linearly depends on the initial quencher concentration  $[Q_0]$  and describes the dynamics of the stationary quenching process.

$$k_\infty = 4\pi R D \cdot [Q_0] \quad (16.33)$$

The proportionality constants have to be multiplied by the product of the Avogadro constant  $N_A$  and  $1000 \text{ l mol}^{-1} \text{ m}^{-3}$  to allow inserting the quencher concentration in units of  $\text{mol l}^{-1}$  instead of  $\text{m}^{-3}$ , which was used until now.

$$k_\infty = 4\pi R D \cdot N_A \cdot 10^3 \cdot [Q_0^{\text{mol}}] \quad (16.34)$$

Typically all proportionality constants in Equation 16.34 are put together into one factor, usually named  $K_q$ , which describes the dependence of the time constant  $k_\infty$  of the stationary quenching process on the quencher concentration  $[Q_0^{\text{mol}}]$ . A huge number of quenching constants  $K_q$  for different sensitizer quencher combinations

**Table 16.1:** Rate constants  $K_q$  for the stationary regime of diffusive quenching at room temperature for selected sensitizer-quencher pairs.

sensitizer	quencher	solvent	$K_q$ [ $10^9 \text{ M}^{-1} \text{ s}^{-1}$ ]	sensitizing mechanism
eosin Y	2-phenyl-1,2,3,4-tetrahydroisoquinoline	DMSO	0.8	not known
riboflavin tetraacetate	4-methoxybenzylalcohol	98 % MeCN	1.9	singlet
riboflavin tetraacetate	4-methoxybenzylalcohol	2 % DMSO		photo-oxidation
riboflavin tetraacetate	4-methoxybenzylalcohol	50 % MeCN	4.0	singlet
riboflavin tetraacetate	4-methoxybenzylalcohol	50 % H <sub>2</sub> O		photo-oxidation
riboflavin tetraacetate	4-methoxybenzylalcohol	50 % MeCN	0.02	triplet
xanthone (derivative)	1,3-pentadiene	50 % H <sub>2</sub> O		photo-oxidation
		trifluorotoluene	2.6	triplet-triplet energy transfer

and a variety of sensitizing mechanisms in different solvents can be found in Montali et. al., “Handbook of Photochemistry”. [51] Typical values for  $K_q$  range from  $K_q = 10^5 \text{ l mol}^{-1} \text{ s}^{-1}$  for slow triplet quenching processes up to  $K_q = 10^{10} \text{ l mol}^{-1} \text{ s}^{-1}$  for fast singlet quenching processes.

The last step toward applying the model of diffusion limited reaction kinetics on transient absorption spectra is the derivation of a suitable diffusion fit function, which can be applied to the measured data set. Since signals in TA spectroscopy are generally proportional to the number of molecules  $n(t)$  which are momentarily in the observed state, a quantity proportional to Equations 16.31 and 16.32 results. Note that the diffusion fit function includes the intrinsic life time  $\tau$  of the excited state, which is quenched. Diffusion terms only become significant, if this time is long. However, this just corresponds to the requirement of a long intrinsic excited state lifetime of the sensitizer for efficient catalysis.

### 16.3.2 Application of the diffusion fit function to experimental data

In the last section the derivation of a fit function, which describes the diffusion controlled reaction kinetics of a photo-sensitizer and a quencher molecule, was shown. The derivation of the model was based on the Einstein–Smoluchowski-Theory of diffusion. It should be noted that we are actually interested in the time dependence of the electron transfer from or toward the substrate, but this is just a different way of looking at the fluorescence quenching of the sensitizer. As the optical signature of the sensitizer is typically more accessible, this focus on the sensitizer is actually closely related with the time resolved spectroscopy. From the synthetic viewpoint of photocatalysis, the substrate is obviously more in the focus.

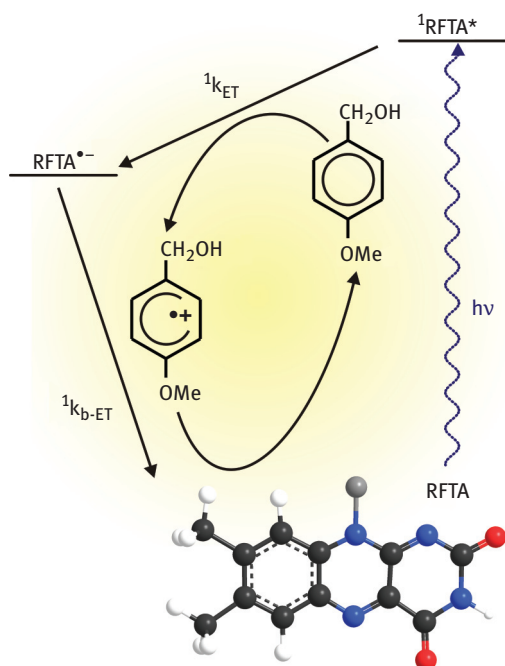


**Figure 16.16:** Jablonski diagram of the reductive quenching of the  $S_1$  state of riboflavin tetraacetate (RFTA). The rate  $^1k_{\text{ET}}$  is controlled by diffusion of RFTA and methoxybenzyl alcohol (MBA).

We now apply and test the derived function on photoinduced reaction kinetics, which are controlled by diffusion. As a model reaction the diffusive quenching process of the  $S_1$  state of riboflavin tetraacetate (RFTA) by methoxybenzyl alcohol (MBA) was chosen. The reductive quenching process produces a radical pair comprising the flavin radical anion and the radical cation of the benzyl alcohol. After formation of the radical pair, typically a fast electron back-transfer tends to offset the oxidation of the alcohol. Two neutral ground state molecules result and the energy of the absorbed photon is converted to heat. Since the rate of the charge recombination process  $^1k_{\text{b-ET}}$  at common substrate concentrations below 1 mol/l is much faster than the diffusion limited rate of the initial electron transfer step  $^1k_{\text{ET}}$ , no considerable population of the charge separated radical pair state occurs. Hence, the only visible process is the reductive  $S_1$  quenching. Signals of the involved intermediate radicals won't be observable due to the fast charge recombination process. A Jablonski diagram of the model reaction is shown in Figure 16.16.

The transient signal of stimulated emission is a unique sign for excited sensitizers. It clearly shows diffusion limited decay dynamics, signaled by non-exponential kinetics and is therefore chosen for the application of the diffusion fit function. Instead of using the signal of only one individual spectral trace within the spectral

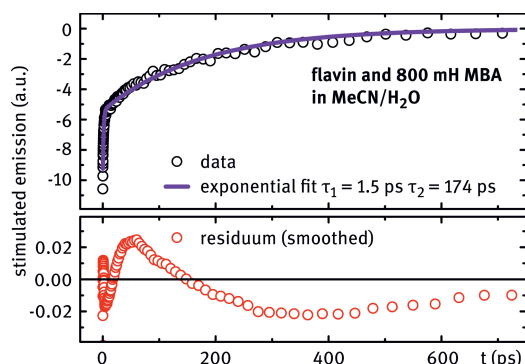


**Figure 16.17:** Exponential fit applied to the transient signal of the stimulated emission. The main time range of hundreds of ps is augmented by a 1.5 ps component discussed below. Upper panel: experimental data and fit. Lower panel: residuum on an expanded scale.

region of the stimulated emission, the integrated signal of all spectral traces containing major signal contributions of the stimulated emission was selected for the further data processing. This minimizes the influence of spectral diffusion caused for instance by solvation or vibrational cooling and decreases the statistic error of the measurement.

Figure 16.17 shows, that diffusive decay dynamics are not accurately enough described by an exponential fit function. The residuum, i. e. the difference between the data and the fit function, deviates systematically from the measured decay data. In contrast, the application of the diffusion fit function, given in Equation 16.31, results in a very good fit in the range of tens to hundreds of ps (see Figure 16.18 and 16.19). Still, the fit to the measured data points (red line, Figure 16.18) is not yet perfect in the first few ps.

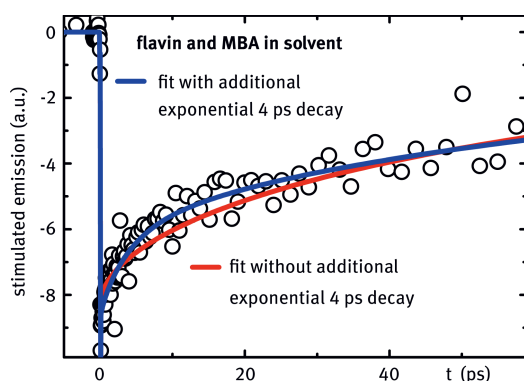


**Figure 16.18:** Diffusion fit function (Equation 16.34, red line) and extended diffusion fit function (Equation 16.35, blue line) applied to the transient signal of the stimulated emission.

For a full description of the decay dynamics of the observed model reaction an additional term has to be added (blue line, Figure 16.18) to the diffusion fit function in Equation 16.31. From another TA measurement which was performed without using any solvent by diluting RFTA directly in the highly viscous MBA, the intrinsic rate  $k_{\text{ET}}^0$  of the electron transfer from MBA to RFTA could be determined to  $k_{\text{ET}}^0 = (4 \text{ ps})^{-1}$ . Adding an exponential term, describing the quenching processes with this intrinsic rate  $k_{\text{ET}}^0$ , to the diffusion fit function leads to an extended fit function shown in Equation 16.35. Applying this fit function to the transient data leads to a perfect description of the measured  $S_1$  decay dynamics. The fit parameters are the radius of the chromophore  $R$ , the diffusion constant  $D$  and the relative amplitudes  $n_{\text{nondiff}}$  and  $n_{\text{diff}}$  of both exponential terms.

$$n(t) = n_{\text{nondiff}} \cdot \exp\{-k_{\text{ET}}^0 \cdot t\} + n_{\text{diff}} \cdot \exp\left\{-\frac{t}{\tau_{S_1}} - 4 \pi R D \cdot [Q]_0 \cdot \left[1 + \frac{2R}{\sqrt{4Dt}}\right] \cdot t\right\} \quad (16.35)$$

The additional term has to be added due to apparent pre-association of chromophore and quencher. The reductive quenching of pre-associated pairs of RFTA and MBA is not a diffusion limited process. It occurs with the constant reaction rate  $k_{\text{ET}}^0$  which was already obtained when both reactants are in closest proximity. The contribution of the constant reaction rate  $k_{\text{ET}}^0$  to the overall decay dynamics becomes more dominant with increasing the quencher concentration. This is in line with a statistical association.

The detailed investigation of flavin photocatalysis has shown that the addition of water to the solvent improves the reaction quantum yield for product formation. For this reason, Figure 16.19 shows the diffusion limited decay dynamics of the integrated

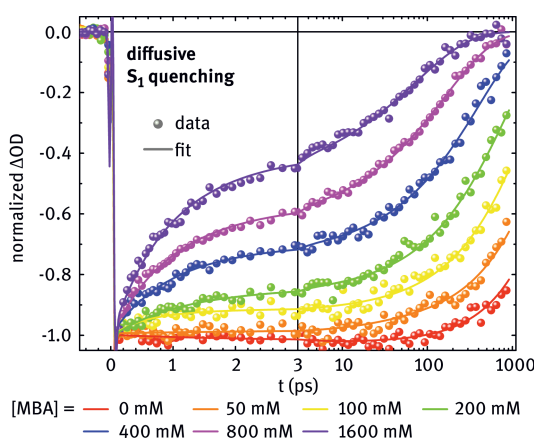


**Figure 16.19:** Diffusion fit function with an additional exponential decay according to Equation 16.35 applied on TA data of the reductive quenching of excited RFTA by MBA. [43]



stimulated emission of RFTA in a solvent mixture of acetonitrile and water at different MBA concentrations. The extended diffusion fit function from Equation 16.35 has been applied to describe the measured data points. It has to be noted, that in water, the intrinsic time constant for electron transfer changes from  $k_{\text{ET}}^0 = (4 \text{ ps})^{-1}$  in pure acetonitrile to  $k_{\text{ET}}^0 = (0.9 \text{ ps})^{-1}$  in a mixture of acetonitrile and water.

The simultaneous application of the diffusion fit function to the transient absorption data at varied MBA concentration not only provides an excellent modeling of the diffusion limited kinetics. It provides moreover a detailed microscopic insight into the molecular processes:

For instance, the encounter distance  $R$  is a fit constant, which is directly obtained from applying the fit function to the transient data. It provides a rough estimate of the distance at which an electron transfer between substrate and excited photocatalyst becomes efficient. It has to be noted that the underlying assumption that electron transfer occurs at a certain encounter distance is a heavy simplification of the theory of electron transfer. But this simplification seems to be justified due to a strong exponential distance dependency of the common theoretical models of electron transfer dynamics. Usually, exponential damping coefficients for distance dependent electron transfer processes are on the scale of  $1 \text{ \AA}^{-1}$ . [10] In contrast, the average distance between photocatalyst and quencher is on the scale of some nm, when working under substrate concentrations, which are usually used in photocatalysis and are in the mM range. Hence, the assumption of instantaneous electron transfer, which occurs at a certain encounter distance  $R$ , is legitimate. The resulting interaction radius was determined to  $R = 3.8 \text{ \AA}$  for the observed model reaction in a 1:1 solvent mixture of acetonitrile and water.

Another insight into molecular processes is provided by the fit of the relative amplitudes of diffusion fit function  $n_{\text{diff}}$  and of the exponential term  $n_{\text{nondiff}}$ , which describes the non-diffusive quenching of pre-associated sensitizer-quencher pairs. In particular, the interesting quantity is the ratio of both amplitudes since its dependency on the substrate concentration allows the direct determination of the association constant of catalyst and substrate. For the model reaction an association constant of  $K = 0.63 \text{ M}^{-1}$  in a solvent mixture of acetonitrile and water was determined, as shown in Figure 16.20.

Also the last fit parameter, the diffusion constant  $D$ , has to be discussed. The Stokes–Einstein equation relates the diffusion constant  $D$  to macroscopic accessible physical quantities such as temperature  $T$ , viscosity  $\eta$  of the solvent and the effective radius  $R_{\text{eff}}$  of the diffusing molecule, which is supposed to be spherical.

$$D = \frac{k_B T}{6 \pi \eta R_{\text{eff}}} \quad (16.36)$$

It has to be mentioned that  $R_{\text{eff}}$  in the denominator of Equation 16.36 is not directly related with the encounter distance  $R$  for electron transfer between photo-sensitizer

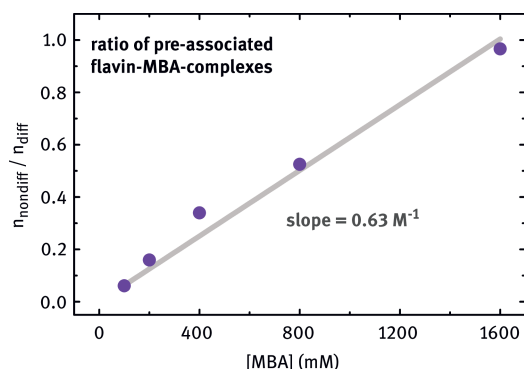


**Figure 16.20:** Ratio of relative amplitudes of diffusion fit function and of the exponential term, which describes the non-diffusive quenching of pre-associated sensitizer-quencher pairs according to Equation 16.35.

and quencher. The  $R_{\text{eff}}$  is the effective radius of the molecule, which is relevant for diffusion. Not only the size of a spherical model of the diffusing molecules determines  $R_{\text{eff}}$  but rather the size of the molecule including the shell of associated solvent molecules can be directly linked to  $R_{\text{eff}}$ . Since not only the quencher molecules but also the photo-sensitizer are contributing to the diffusion process,  $R_{\text{eff}}$  gives a description of an effective intermediate radius of both molecules, which is relevant for diffusion.

Figure 16.21 shows the concentration dependency of the fit parameter  $D$  resulting from applying the extended fit function from Equation 16.35 to the observed  $S_1$  decay dynamics. The slight decrease of  $D$  with higher concentrations of the substrate can be explained by the increase of the solvent viscosity due to adding large amounts of the highly viscous methoxy benzyl alcohol to the solvent with a low viscosity.

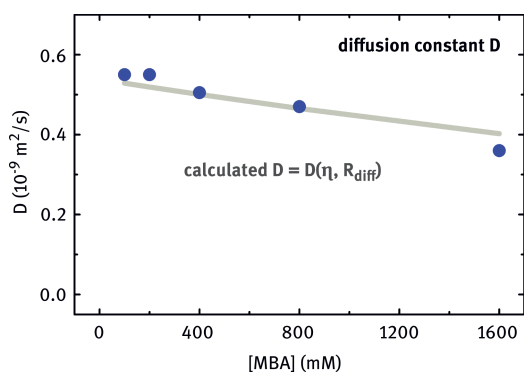


**Figure 16.21:** Diffusion constant  $D$  derived from the diffusion limited  $S_1$  decay dynamics at different concentrations of the highly viscous substrate MBA.  $D$  was obtained from applying the fit function, given in Equation 16.35, on the diffusion limited decay dynamics of the  $S_1$  state of RFTA.

For the observed model reaction, which was performed in different solvents, the analysis of the fit of the diffusion constant  $D$  offers the following results:  $R_{\text{eff}}$  increases from  $R_{\text{eff}}=4.5 \text{ \AA}$  in pure acetonitrile to  $R_{\text{eff}}=8.0 \text{ \AA}$  in the solvent mixture of acetonitrile and water. This result suggests that a solvent shell of associated water molecules is able to slow down the diffusive movement of the interacting particles.

In summary, it has been shown that the presented model of diffusion limited excitation quenching applied to experimental data provides much more data than only a perfect description of the decay curve. It offers deep insights into molecular processes and extends the previous model of diffusion limited reaction kinetics, which still divides the diffusion limited decay of a signal into three contributions: static quenching, non-stationary quenching and stationary quenching dynamics. [52] Especially for the investigation of photocatalytic processes, a more sophisticated model seems to be a great help to obtain a deep knowledge of the underlying reaction mechanisms.

The literature provides only very few examples where diffusion limited excited state dynamics obtained by time resolved spectroscopic techniques are quantitatively described with the help of suitable fit functions. The application of a very similar model of diffusion controlled decay modelling, which is also based on Einstein–Smoluchowski-Theory, including a Coulomb potential between the reactants, is presented in reference [53]. The model can well describe the diffusion influenced fluorescence quenching reaction of rhodamine B and ferrocyanide. A more general discussion of the model, which describes diffusion controlled fluorescence quenching by electron transfer based on Marcus Theory can be found in reference [54]. It has to be mentioned, that the temporal resolution of the transient spectroscopic techniques, which were applied in this work, was 60 ps. This is somewhat critical, since the decay curves at earlier times are very important for the correct modelling. Some theoretical considerations on distance distribution and photo-induced electron transfer between diluted reactants in solution regarding Marcus theory are presented in reference [55]. Diffusion controlled fluorescence quenching by long range electron transfer in highly viscous non-polar solvents was investigated in reference [56].

## 16.4 Costs of photocatalysis: The reaction quantum yield

### 16.4.1 Requirements for an accurate definition of the quantum yield

In photochemistry, the term “quantum yield” has been used for many different quantities over the years. From a physical point of view and in the context of photocatalysis it should describe the ratio of the number of product molecules formed to the number of absorbed photons. Usually a high quantum yield  $\Phi$  is desired for an efficient photocatalytic process. At this point efficiency is focused onto the best

possible use of the available light. As early investigations on the fundamentals of photocatalysis are not so much concerned yet about the use of the photons but rather worry about the endurance of the photocatalyst and the ability to quantitatively convert a substrate, it becomes understandable why other usages have surfaced.

This section will provide a rigid definition of the term “quantum yield” and suggest an easy and cheap method for the accurate determination in homogeneous catalysis. A detailed discussion of the difficulty to properly report photonic efficiencies and quantum yields in heterogeneous photocatalysis can be found in Nick Serpone, “Relative photonic efficiencies and quantum yields in heterogeneous photocatalysis”. [57] One of the main aspects for an accurate usage is that the quantum yield  $\Phi$  has to describe the properties of a molecular reaction independently of the experimental boundary conditions. It is not sufficient to report a quantity which strongly depends on the measurement setup since the result is not reproducible. Whereas the number of incident photons impinging on the external reactor walls is relatively easy to measure, it is more sophisticated to determine the number of the photons actually absorbed by a photocatalyst molecule.

Depending on the sensitizing mechanism and the subsequent reaction mechanism of the photocatalytic reaction, the quantum yield  $\Phi$  can be affected by a huge number of physical quantities. The solvent environment causes the largest influence on the photo-induced reaction. But also temperature, irradiation wavelength and its bandwidth, and the concentration of catalyst and substrate may affect the efficiency of the catalytic reaction. In particular when intermediate steps of the photocatalytic reaction are limited by diffusion, the concentration of the substrate plays a major role on reaction dynamics and, hence, on the total efficiency of the reaction. [43] Usually the temperature strongly affects the viscosity of the solvent and, therefore, also changes the diffusion dynamics on the microscopic scale. But a change of temperature can also cause major effects in template photocatalysis, where complexation of the catalyst and substrate is required for the photocatalytic reaction. If the catalyst-substrate binding is mediated through hydrogen bonding, where binding energies are close to  $k_B \cdot T$ , a change of temperature dramatically changes the equilibrium of associated and non-associated catalyst-substrate complexes and therefore affects the quantum yield  $\Phi$  of the desired template mediated photocatalytic process. [7, 8, 58] Also, the oxygen concentration in the solvent has to be taken into account. Oxygen is known to efficiently quench triplet states and for this reason strongly reduces the life time of intermediate states with triplet character, which may affect the over-all reaction quantum yield  $\Phi$ . Another aspect which has to be considered is a wavelength dependent definition of  $\Phi$ . For example, in organometallic coordination complexes, which are used for photocatalysis, there are examples where it is possible to excite different states depending on the excitation wavelength. [59–61] Only the excitation of metal-to-ligand-charge-transfer transitions (MLCT) directly leads to photocatalytic active states. Also competing absorption of the substrate or the formed product has to be considered when discussing the wave-

length dependency of the quantum yield. For the determination of the optimal environment for an efficient photocatalytic reaction, it can be essential to measure  $\Phi$  under a variety of conditions. Therefore,  $\Phi$  needs to be easy to measure.

A seminal contribution to this debate is given by Nick Serpone in “Suggested terms and definitions in photocatalysis and radiocatalysis” discussing a large number of terms and definitions for the application in photocatalysis. [62] The following definition of the quantum yield  $\Phi$  strongly relies on this work. Generally, in chemistry, the quantum yield can be determined for lots of processes such as reactant disappearance, light emission, product formation and various other events occurring as a result of a photochemical process. Since generally in catalysis the disappearance of a substrate molecule does not necessarily lead to formation of the desired product molecule, determining the quantum yield by taking the number of disappearing reactant molecules into account is not appropriate. Rather considering the actually formed product molecules results in a meaningful definition of the quantum yield  $\Phi$ . Whereas in heterogeneous photochemistry the term quantum yield  $\Phi$  describes the ratio of the total number of photons incident on the reactor walls and the number of product molecules formed [57, 62], in homogeneous catalysis a more accurate definition is required to describe the actual efficiency of a molecular process.

The definition, given in Equation 16.37, fulfills all the previously discussed conditions. The quantum yield  $\Phi$  is directly defined as the ratio of the number of photons which are actually absorbed by the photocatalyst  $N_{\text{abs}}$  and the number of formed product molecules  $N_{\text{product}}$ . In Equation 16.37 the amount of substance  $n_{\text{product}}$  can be inserted instead of the total number  $N_{\text{product}}$  of molecules, which were formed within the catalytic process. The corresponding quantity  $n_{\text{abs}}$  describing the number of moles of absorbed photons can be expressed by the occasionally used physical unit einstein, which is equivalent to one mole of photons.

$$\Phi_{\lambda} = \frac{N_{\text{abs}}}{N_{\text{product}}} = \frac{n_{\text{abs}}}{n_{\text{product}}} \quad (16.37)$$

It should be noted that this definition of the wavelength dependent reaction quantum yield is most precise, if quasi-monochromatic light is used. This can either originate from a laser source, e.g. in basic studies, or from high power light emitting diodes (LEDs) with a spectrum narrower than the typical width of molecular absorption bands. [63] On the other hand, Maschmeyer and Che have argued for the solar spectrum as proper reference. [64] While this is eventually the proper measure for an industrial process, much greater insight can be gained from wavelength selective determinations. If a range of wavelengths has been used, the convolution of the spectrum of a broad light with the catalyst absorption spectrum and the wavelength dependent intrinsic yield will give the overall efficiency.

In terms of efficient photocatalysis, typically the formation of a product molecule is the desired process to occur with a high quantum yield. In enantioselective

photocatalysis for instance not only the formation of a product molecule is essential. Only product molecules which exhibit the proper chirality contribute to the number of desired product molecules formed.

Another aspect which has to be considered when determining the quantum yield  $\Phi$  is the change of reaction environment during photocatalysis since product molecules are formed and substrate molecules are consumed. Upcoming product absorption within the spectral region of irradiance may lead to completely new photochemical processes within the solution. The primary, desired photocatalytic process will be overlaid by another competing photochemical process with unknown products formed. A further contribution to the change of the reaction environment involves the catalytic cycle of the light absorbing photocatalyst. Particularly in photoredox catalysis, the oxidation state of the catalyst has changed after the primary photocatalytic process. Typically the reacted photocatalyst is catalytically inactive and needs to be regenerated in order to retrieve its full photocatalytic capability and to complete the catalytic cycle. The regeneration of the photocatalyst with the help of sacrificial electron donor and acceptor molecules in solution may impact the reaction conditions, since they are consumed with catalyst regeneration. [65] Therefore monitoring the photon absorption for a long period of the photocatalytic reaction is not beneficial for the determination of a meaningful product quantum yield  $\Phi$  which solely has to describe the yield of the primary photocatalytic reaction. This problem is normally overcome by determination of the quantum yield  $\Phi_\lambda$  at small conversions of the reactants, usually less than 10%, a point not often respected in heterogeneous photocatalysis, where the focus is usually complete transformation of the substrate. [62]

With the discussed requirements on an accurate definition of the product quantum yield  $\Phi$  and an unambiguous definition, we now focus on experimental techniques which readily allow for the determination of the required quantities. Whereas the denominator in Equation 16.37, the product yield, is relatively easy to measure in a chemistry lab using standard analytical methods, more sophisticated methods are required for the determination of an exact value of the numerator, the amount of the actually absorbed photons. The following summary is based on the article “Laboratory apparatus for the accurate, facile and rapid determination of visible light photoreaction quantum yields”. [66] The classical chemical actinometric procedures for the determination of the quantum yield, which are standardized by IUPAC [51, 67, 68] are often too laborious and newly developed ones are in most cases only suitable within the UV spectral region [69, 60, 71]. Efficient solar harvesting does, however, require primarily absorption in the visible.

Our experimental approach for an easy determination of the number of photons, which are actually absorbed by the photocatalyst, is shown in Figure 16.22. The homogeneous photochemical reaction of interest is performed in a standard cuvette with 10 mm optical path length. Since photochemical or photocatalytic active chromophores generally only absorb selected parts of the electromagnetic spec-

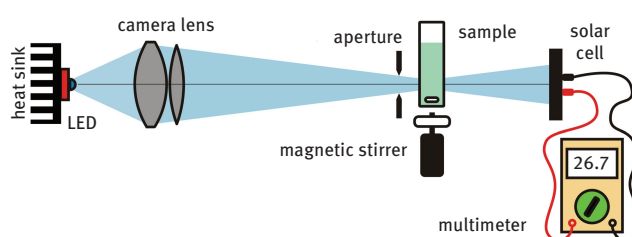


**Figure 16.22:** Setup for the easy and cheap determination of the product quantum yield  $\Phi$  of a photo-induced reaction: A camera lens images a high power LED into the sample solution, which is constantly stirred. The power of the transmitted light is measured with the help of a commercially available solar cell as a power meter. Reprinted from reference [66] with permission from the Royal Society of Chemistry.

trum, the illumination spectrum has to be adapted to the absorption properties. Modern high power light emitting diodes (LEDs) provide high photon fluxes at a variety of well defined spectral regions which allows the choice of the optimized light source for a given photocatalytic chromophore. [72, 73] The emitted light from the LED is imaged with the help of a commercially available camera lens into the sample solution to drive the photocatalytic process. In order to facilitate the measurement of the absorbed illumination power and to provide stable conditions to the photo-induced process, the optical density of the sample solution within the illumination spectrum has to be set to values between 0.3 and 1.0. This provides, on the one hand, a reasonable amount of absorption of the irradiating photons but, on the other hand, the absorption takes place within the whole cuvette volume and not in a thin solvent layer at the front side of the cuvette. This would be the case when performing the irradiation under very high optical densities. The transmitted residual light, which passes through the cuvette with the sample solution, is continuously measured by a dedicated and calibrated solar cell. The illumination dependent output current of the solar cell is converted with the help of a low Ohm resistor into a illumination dependent voltage which can be easily measured with a multimeter. The comparison of illumination levels, which were detected with the solar cell, and the values of illumination power, which were measured with a calibrated thermopile powermeter, results in a nearly perfect linearity between output voltage and effective incident illumination power. The use of a solar cell instead of a laser powermeter provides an easy and inexpensive measurement method of the transmitted illumination power.

Finally, for the determination of the number of actually absorbed photons within the sample cell, first the transmitted illumination power has to be measured once with and once without the sample solution within the beam path of the focused LED light. Not only absorption by the photocatalytic chromophore leads to a decrease in illumination power. The back reflection at the terminal air glass interface accounts for a sizable contribution to the illumination power decline as well, which is still in



the few percent regime and has to be considered when calculating the absorbed illumination power. A more detailed description of all these issues can be found in reference [66]. With the absorbed power determined, the duration of illumination immediately gives the number of absorbed photons  $N_{\text{abs}}$ . Together with the total volume of the solution and the independently determined concentration of products, finally the desired value for the yield is found.

We do not want to undervalue the importance to determine other quantum yields like the triplet or photoluminescence yields. They can greatly contribute to the full characterization of photocatalysts or photocatalytic processes. Therefore, we briefly refer to related techniques in the following section.

A completely different technical approach for the determination of the triplet quantum yield of some organic dyes with the help of picosecond laser double-pulse fluorescence excitation and time resolved fluorescence detection [74] is presented in reference [75]. In this two-pulse excitation technique a sequence of picosecond laser pulses is used to determine the yield of triplet state population after photoexcitation. The first pulse strongly excites the molecules to the excited singlet state. From there they decay either back to the ground state or to the triplet state. The second pulse probes the fluorescence reduction by triplet formation, since the fluorescence signal is proportional to the population of the excited singlet state, which has – in contrast to the triplet state – the ability to fluoresce. A modified version of this technique that decouples the triplet yield and cross section determination has been presented recently. [76]

The determination of photoluminescence quantum yields can readily be performed with a commercial spectrofluorometer. A suitable standard, usually a well fluorescing dye solution is needed for absolute values. Relative values and the change with experimental parameters can be determined even more easily. Finally, we want to point the interested reader to a very informative review on light intensity distribution in photocatalytic reactors with some comments on the reaction quantum yield within the focus of heterogeneous photocatalysis in reference [77].

#### 16.4.2 Determination of the quantity of excited molecules in transient absorption measurements

Transient absorption spectroscopy on multiple time scales is in itself a powerful tool for the determination of quantum yields either of the population of an intermediate state or of the formation of a product molecule. Deactivation processes of electronically excited states and recombination of charge separated states are the most important processes which are competing with product formation and, therefore lower the over-all product quantum yield  $\Phi$  in homogeneous photocatalysis. Both processes result in the formation of ground state molecules of catalyst and substrate. Therefore, the analysis of the ground state bleach (GSB) recovery in transient



absorption measurement allows the determination of the number of molecules which are still in an intermediate state or the final product state at selected points of time after excitation. [78] However, the determination of the quantum yield of intermediate or final states using this method requires that the GSB is not significantly overlaid by absorption of the state of interest, which is a prerequisite rather of a purely theoretical nature. If either GSB or the overlaying absorption spectrum of the intermediate state are well structured or exhibit significant characteristic spectral features, the linear combination of spectra can be easily deconvoluted to obtain the contribution of each spectrum and thereby the population of the intermediate states. If in fact the GSB and the excited state absorption of all intermediate states of a photochemical reaction are spectrally sufficiently separated from each other, the quantum yield of each intermediate state and the final product state can be determined readily. For this procedure the intensity of the ground state bleach immediately after excitation of the light absorbing chromophore has to be scaled to 100% to account for the degree of optical excitation. Then the ratio of the GSB intensity at a certain pump-probe delay  $\Delta t$  to the intensity of the initial GSB directly provides the quantum yield of the observed excited intermediate state of the system. Often transient absorption spectroscopy in the visible and near UV spectral region is reported in the literature, where GSB and excited state absorption are not well enough separated from each other. To still utilize the introduced technique for the direct calculation of the quantum yield for all intermediate states, an extended range of observation and the highest possible fidelity [79] has to be sought. This is the reason why we continuously try to improve the femtosecond spectrometer.

Sometimes, at the beginning of an investigation, only the wavelength dependent extinction coefficient  $\varepsilon_i(\lambda)$  of just one intermediate state or of the final product is known beyond the spectrum of the catalyst and substrate. In this case methods of spectroelectrochemistry can provide in addition the wavelength dependent extinction coefficient  $\varepsilon_i(\lambda)$  of radical anion and radical cation states of the participating molecules. In case of photoredox catalysis these spectra may directly appear in the transient absorption spectrum. Since transient absorption spectroscopy provides the wavelength dependent change of absorption  $OD(\lambda)$  in units of optical density, the application of the Beer–Lambert-Law reveals the effective concentration of molecules, which are momentarily in the observed intermediate state. Now, only the information of the concentration of the initially excited photocatalyst molecules is missing for the calculation of the quantum yield of the observed radical state. Since the extinction coefficient of the ground state absorption spectrum is accessible with UV/Vis absorption spectroscopy and also the excitation energy, focal size and the optical path length within the sample cell is straightforward to measure, the excitation probability of each molecule within the excited sample volume can be easily determined.

A relatively accurate estimation of the excitation probability  $P_{\text{exc}}$  in transient absorption measurements is shown in Equation 16.38. [28] The  $P_{\text{exc}}$  usually depends on

the excitation energy of the pump pulse  $E_{\text{pump}}$ , the central excitation wavelength  $\lambda$ , the full width half maximum (FWHM) of the excitation pulse diameter  $D$  within the sample cell and the absorption coefficient of the excited molecule at the excitation wavelength  $\epsilon$ . The factor  $\ln(2)$  results from the conversion from a Gaussian beam profile with a FWHM  $D$  of the beam diameter to a homogeneous circular beam profile with diameter  $D$ . To avoid effects of multi photon excitation it is reasonable to keep the excitation probability below 10% in transient absorption measurements. An excitation probability of 10% will typically lead to a contribution of two photon processes of less than 1% to the transient signal.

$$P_{\text{exc}} = n_{\text{ph}} \cdot \sigma = \frac{E_{\text{pump}}}{(hc/\lambda) \cdot \pi \cdot (D/2)^2} \cdot \epsilon \cdot \frac{\ln(10)}{N_A} \cdot \ln(2) \quad (16.38)$$

This estimate assumes that the ESA strength is similar to the ground state absorption. Since photocatalysts are expected to be good absorbers, this assumption is most often justified.

Multiplication of the excitation probability  $P_{\text{exc}}$  with the effective concentration of the photocatalyst in the sample solution results in the concentration of the initially excited molecules and the quantum yield of an observed intermediate state can be easily calculated, if its extinction coefficient  $\epsilon(\lambda)$  is known. Since Equation 16.38 provides an average excitation probability for the whole cross-section area of the excitation beam but usually only a small fraction of this volume – usually the centre area – is within the probed sample volume, there are minor deviations to the actual excitation probability which have to be explicitly modeled if very quantitative results are needed.

### 16.4.3 Example of the spectroscopic determination of reaction quantum yields: Flavin photocatalysis

The riboflavin tetraacetate (RFTA) sensitized photo-oxidation of methoxy benzyl alcohol (MBA) is a well suited example for the determination of the reaction quantum yield  $\Phi$ . It allows to prove the picture of the underlying reaction mechanism, which was obtained with the help of time resolved absorption spectroscopy on a large range of time scales. The spectroscopic details of the investigation of the reaction have been described in detail elsewhere. [43] In brief summary: The first electron transfer from MBA to the photo-excited catalyst RFTA is the determining step for the subsequent processes of the photocatalytic reaction. If the singlet state of RFTA is quenched by electron transfer from MBA, fast charge recombination occurs within the formed spin-correlated radical pair on the time scale of 50 ps. This process is fast in comparison to the subsequent processes of product formation and does not significantly contribute to the photocatalytic product formation since it leads back to the

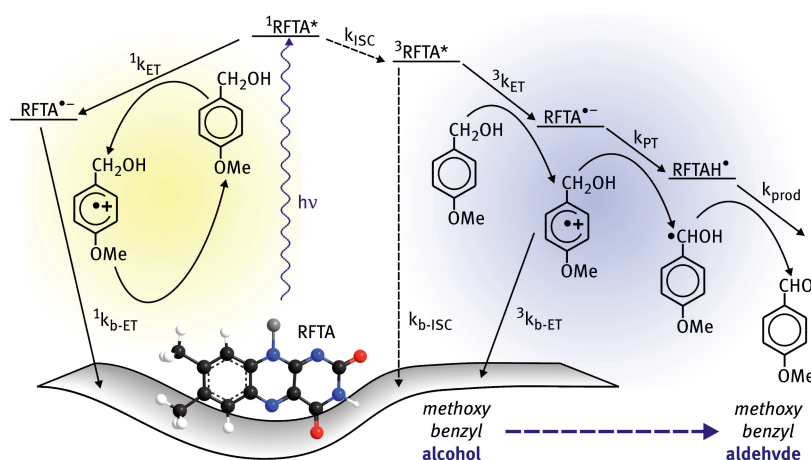


**Figure 16.23:** Reaction mechanism of flavin sensitized photo-oxidation of methoxy benzyl alcohol to the corresponding aldehyde. [43, 48]

ground state of photocatalyst and substrate. However, the situation is completely different, when the first electron transfer occurs after inter-system crossing of the photocatalyst, i. e. when the RFTA is allowed to reach its triplet state. Charge recombination within a formed spin-correlated radical pair with triplet character is a spin-forbidden process and; therefore, it is significantly slowed down in comparison to the spin-correlated ion pair with singlet character. [80, 81] Now the subsequent reaction steps, which begin with the protonation of the formed radical anion of RFTA, may occur with reasonable yield since competing processes take place on a very slow time scale. A scheme of the full mechanism is depicted in Figure 16.23.

In order to achieve a high reaction quantum yield, the main task is to drive the reaction in the triplet manifold of the photocatalyst. The inter-system crossing of RFTA occurs on the 10 ns time scale with quantum yields up to more than 70 % if there are no competing processes deactivating the excited singlet state. [82, 83, 84] Since diffusive quenching processes of excited states in solvents take place on a comparable time scale and this time scale strongly depends on the quencher concentration, a change of the concentration of the substrate allows an easy and effective control of the reaction pathway. At high concentrations of the substrate, the diffusive quenching of the excited state of RFTA is fast in comparison to the inter-system crossing dynamics and the reaction is driven to the non-productive electron transfer in the singlet manifold with immediately subsequent charge recombination. In contrast, at very low MBA concentrations, the excited singlet state quenching dynamics are slow in comparison to the intersystem-crossing process. From now on the triplet yield of the photocatalyst comes closer to the intrinsic triplet quantum yield since the yield of the singlet radical pair formation has significantly dropped. This provides an

effective population of the triplet state of RFTA, from where the productive steps of the photocatalytic reaction start with the drawback that low substrate concentrations include slow diffusive triplet quenching. However, an effective and relatively fast quenching of the RFTA triplet state is required for the next reaction step, the generation of a spin-correlated radical ion pair with triplet character via electron transfer from MBA to the RFTA in its triplet state. But when the substrate concentration is too low, the diffusion limited electron transfer becomes slower than the intrinsic lifetime of the RFTA triplet state and the majority of the RFTA triplet population decays back to the ground state or is quenched by diluted oxygen.

From the point of view of a chemist, a very basic idea to increase the triplet lifetime of RFTA would be to conduct the photocatalysis under oxygen free conditions. However, diluted oxygen is required for this type of reaction since it thermally re-oxidizes the photocatalyst which remains in its fully reduced form as a result of the catalytic aldehyde production. So the only remaining parameter to drive the photocatalytic reaction into its efficiency maximum is to adjust the substrate concentration: On the one hand, the concentration has to be low enough for an efficient population of the triplet state but, on the other hand, it has to be high enough for a reasonable generation of the spin-correlated triplet radical pairs, which is a diffusive process. With the help of the time resolved spectroscopic methods, it was possible to quantify each intermediate step of the flavin-sensitized photo-oxidation and especially to understand and to predict the diffusion limited reaction dynamics. Since the data analysis was based on a very complex model describing diffusion controlled reaction dynamics, which was presented in the last section, verification by another independent measurement strongly supports the credibility of the developed model.

Often time resolved spectroscopic methods do not directly give access to the total reaction quantum yield of a photo-induced reaction. This is due to the fact that typically not all intermediate states and species are observed reliably and more importantly, that the reaction quantum yield might be small. In this case the product would have to be detected with very high sensitivity in a sea of other species. But transient absorption spectroscopy reveals a lot of information which can be used to calculate quantum yields of the contributing intermediate steps. The quantum yield of an intermediate step can be determined either, if all contributing reaction rates  $k_i$  are known, or if the relative quantum yields of competing reaction pathways can be determined by analyzing the time dependent intensities of the ground state bleach or of other transient signatures with known extinction coefficients. How to calculate quantum yields on the basis of the underlying rate model is shown as follows: For instance, after photo-excitation, an intermediate parent-state is depopulated by three different processes, described by the rate constants  $k_1$ ,  $k_2$  and  $k_3$  resulting in three different sub-states, named state 1, 2 and 3. The yield for the population of state 1, which leads to the product formation, is given by dividing rate  $k_1$ , which populates this state, by the sum of rates  $k_1 + k_2 + k_3$ , which depopulate

the parent-state. This results in the following equation, describing the quantum yield of this intermediate step:

$$\Phi_1 = \frac{k_1}{k_1 + k_2 + k_3}. \quad (16.39)$$

The total reaction quantum yield  $\Phi$  of a photocatalytic reaction, in case of a sequential reaction, can be written as product of the quantum yields  $\Phi_i$  of the intermediate steps which are contributing to the product formation.

$$\Phi = \Phi_1 \cdot \Phi_2 \cdot \Phi_3 \cdot \dots \quad (16.40)$$

Since the flavin sensitized MBA oxidation involves two redox steps, the catalysis comprises two reduction processes of the photocatalyst. Taking the inter-system crossing and the competing non-productive electron transfer in the singlet state of RFTA into account, the product quantum yield is given by Equation 16.41. Since the non-productive singlet quenching and the productive triplet quenching process via electron transfer are both diffusion controlled processes, and, hence, both rates depend on the substrate concentration, also the over-all reaction quantum  $\Phi$  yield depends on the substrate concentration.

$$\Phi = \Phi([\text{MBA}]) = \Phi_T([\text{MBA}]) \cdot \Phi_{ETI}([\text{MBA}]) \cdot \Phi_{PTI} \cdot \Phi_{ETII} \cdot \Phi_{PTII} \quad (16.41)$$

We find that the first proton transfer process and both the second electron and proton transfer do not depend on the substrate concentration. A possible explanation for this finding is the presence of large amounts of water that greatly increases the overall efficiency. As water is dissociated to a sizable degree, protons and eventually the extra electron can be buffered by this reservoir and the yield become independent of the catalyst and substrate concentration. Many rates of the competing processes are known from additional transient absorption measurements which we performed, and we can now write the over-all reaction quantum yield by inserting these rates into Equation 16.41.

$$\Phi = \frac{k_{ISC}}{k_{ISC} + {}^1k_{IC} + k_{RAD} + {}^1k_{ET}([\text{MBA}])} \cdot \frac{{}^3k_{ET}([\text{MBA}])}{{}^3k_{IC} + {}^3k_{ET}([\text{MBA}])} \cdot \Phi_{PTI} \cdot \Phi_{ETII} \cdot \Phi_{PTII} \quad (16.42)$$

Whereas the first factor, which describes the triplet quantum yield, contains the substrate concentration only in the denominator, the second factor, which describes the yield of the formation of the spin-correlated triplet radical pair, contains the substrate concentration both in the numerator and in the denominator. Since the rate of the diffusive triplet quenching by electron transfer  ${}^3k_{ET}$  is much slower in comparison to the singlet quenching process  ${}^1k_{ET}$ , not necessarily the full kinetic diffusion model

has to be applied to describe the triplet quenching process. Here a linear dependency between substrate concentration and diffusive reaction rate seems to be sufficient for modeling the quenching process. However, for the calculation of a rate describing diffusion controlled dynamics on the ultrafast time scale, a linear dependency between concentration and reaction rate is not longer sufficient. In the last section we introduced a mathematical model for diffusive decay modeling on the ultrafast time scale, which is used here. According to Equation 16.30 the diffusive singlet quenching rate  ${}^1k_{ET}$ , which depends on the substrate concentration as well, can be written as

$${}^1k_{ET}(t, [MBA]) = 4 \pi R^2 D \left[ \frac{1}{R} + \frac{1}{\sqrt{\pi D t}} \right] [MBA]. \quad (16.43)$$

Comparable to the diffusive triplet quenching process, which was approximated by a linear correlation, Equation 16.43 also exhibits a strictly monotonic increasing relation between substrate concentration and reaction rate. Under consideration of the monotonic behavior of both singlet and triplet quenching with increasing substrate concentration, Equations 16.41 and 16.42 exhibit an efficiency maximum at a certain substrate concentration with trailing edges both with increasing and decreasing concentration.

For the calculation of the over-all reaction quantum yield, which is generally time independent, the time dependent reaction rate has to be converted into a time independent quantity. By integration from time zero to infinity of an exponential function describing the decay of an excited state by diffusion, an average, time independent reaction rate can be determined.

$${}^1k_{ET}^0([MBA]) = \int_{t=0}^{\infty} dt \exp(-{}^1k_{ET}(t, [MBA]) \cdot t) \quad (16.44)$$

As shown in the previous section, both diffusive and non-diffusive quenching, caused by pre-association of catalyst and substrate, are contributing to the over-all singlet quenching process and have to be considered when calculating the effective, time independent electron transfer rate. Integration of an exponential function, describing the decay of the excited singlet state only considering the diffusive quenching process, from time zero to infinity results in a time independent average quenching rate, which still depends on the substrate concentration.

$${}^1k_{ET}([MBA]) = \int_{t=0}^{\infty} dt \frac{n_{\text{nondiff}}}{n_{\text{nondiff}} + n_{\text{diff}}} \cdot \exp\{-{}^1k_{ET}^0 \cdot t\} + \frac{n_{\text{diff}}}{n_{\text{nondiff}} + n_{\text{diff}}} \cdot \exp\left\{-4 \pi R D \cdot [MBA] \cdot \left[1 + \frac{2 R}{\sqrt{4 D t}}\right] \cdot t\right\} \quad (16.45)$$

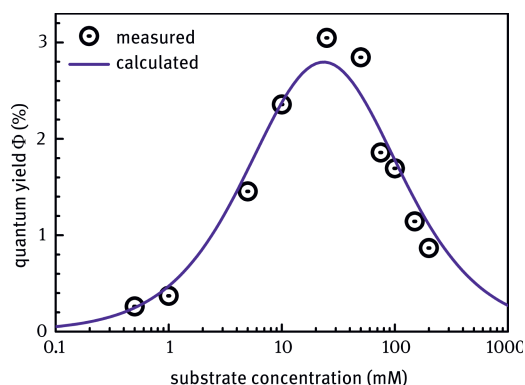


**Figure 16.24:** Concentration dependent reaction quantum yield of flavin sensitized photo oxidation of methoxy benzyl alcohol on a logarithmic x-coordinate. [43]

Now all contributing contributions of Equation 16.41 are known and the over-all concentration dependent reaction quantum yield can be expressed by quantities which were all determined by time resolved absorption spectroscopy. The result is given as solid line in Figure 16.24. Since the data analysis and especially the diffusive decay modeling is based to some degree on simplifications and assumptions, verification of the predicted substrate concentration dependent reaction quantum yield will strongly support the credibility of the understanding of the photocatalytic reaction.

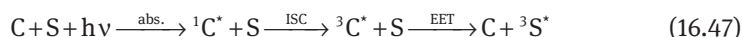
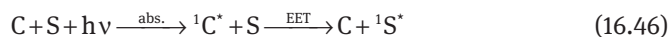
The comparison of predicted over-all reaction quantum yield in Figure 16.24, which was calculated with the help of the diffusion-based model, and the actual over-all reaction quantum yield determined with the help of the presented setup for the measurement of reaction quantum yields and UV/Vis steady state spectroscopy perfectly confirms the understanding of the photocatalytic process obtained by time resolved spectroscopy. The reaction can be driven in its efficiency maximum, which corresponds to a product quantum yield of 3%, by adjusting the substrate concentration in the 25 mM range.

## 16.5 From light absorption to chemistry: Sensitizing mechanisms in homogeneous photocatalysis

### 16.5.1 Sensitization by excitation energy transfer

Sensitization by excitation energy transfer (EET) processes is sometimes considered for photocatalysis but only plays a minor role in homogeneous photocatalysis. Therefore, we will only comment very briefly on some basic considerations.

Generally there are two different mechanisms to distinguish: Singlet excitation energy transfer via Förster resonance energy transfer (FRET) [85] and triplet triplet energy transfer (TTET) via Dexter [86]. A scheme of both processes is given in Equation 16.46 and 16.47.



Since excited singlet states and triplet states of organic chromophores are usually easily distinguishable with the help of their optical absorption properties, time resolved absorption spectroscopy in the visible is a well suited tool for the investigation of EET sensitization processes both in the singlet and triplet manifold. Whereas triplet sensitization mechanisms are often applied meaningfully, applications for singlet sensitization processes are hardly imaginable in photocatalysis, since the EET usually occurs between two optical accessible excited states. Then in terms of efficient photocatalysis a direct excitation of the substrate is more convenient. A senseful exception might be the case where the lowest optical transition of the substrate leads to the  $n\pi^*$  state and consequently the absorption strength is very low. Furthermore, the lifetime of excited singlet states is usually limited by fluorescence decay and inter-system crossing and does commonly not exceed a couple of nanoseconds and; therefore, diffusion limited sensitizing becomes inefficient. If there is no catalyst-substrate pre-association, the expected time scale for triplet EET sensitization is in the ns and  $\mu$ s range, when the reaction dynamics are controlled by diffusion of the reactants. Therefore, long lived triplet states are better suited for photo-sensitization. Especially when the following requirements are matched, applications of TTET can improve the efficiency of a photocatalytic process:

Triplet sensitization with a photo-sensitizer with high triplet quantum yield  $\Phi_T$  to substrate with low intrinsic  $\Phi_T$  to increase the total reaction quantum yield for a triplet reaction

Triplet sensitization with a photo-sensitizer, which has a lower energy gap between the optically accessible singlet and the triplet state to allow irradiation at longer wavelengths to expand the usable irradiation spectrum far into the visible

Triplet sensitization of weakly bound catalyst-substrate complexes to allow selective sensitization to provide stereoselective photochemistry. [7, 87]

### 16.5.2 Photoredox catalysis: Requirements on catalyst and substrate

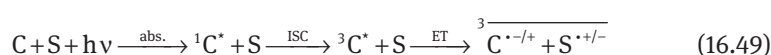
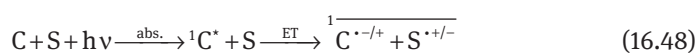
The general mechanism of a photocatalytic reaction comprises two initial steps: The excitation of the chromophore and the sensitization of the substrate. The sensitiza-



tion is the use of the excitation energy from the photocatalyst in its excited state for the suitable modification of the substrate in its ground state to start a chemical conversion. The minor importance of the genuine energy transfer processes such as singlet energy transfer via Förster resonance energy transfer [85] or triplet energy transfer via the Dexter mechanism [86] is discussed in the preceding section. The more important sensitization process is photo-induced electron transfer where light serves as energy source for intra- and intermolecular electron transport. Depending on the catalytic system and the sensitizing mechanism, the temporal delay between photo-excitation and sensitization can cover the time range from  $1 \cdot 10^{-13}$  s, e.g. for intramolecular charge transfer reactions in electronically strongly interacting systems, to  $1 \cdot 10^{-6}$  s, e. g. for slow diffusion limited intermolecular charge transfer reactions. [43, 51, 88] This section will provide examples of different photo-induced sensitization mechanisms in photocatalysis with strong connection to the application of time resolved spectroscopic methods. The examples are chosen from photoredox catalysis, which is one of the most important sensitizing mechanisms in photocatalysis. [89, 90] Photoredox catalysis relies on the general property of excited states that they are usually more easily reduced or more easily oxidized than the ground state. Therefore, the excited photocatalyst can serve either as highly reactive electron donor or electron acceptor. [90]

From the perspective of time resolved spectroscopy it causes a major difference if the excited state quenching of the photocatalyst occurs in its excited singlet or triplet state. Since charge recombination within the formed spin correlated radical ion pair (RIP) with triplet character is a spin forbidden process, the charge separated state within the triplet RIP is more stable. [80] This allows the subsequent reaction steps to take place with significant yields. In terms of efficient photocatalysis it is, therefore, often advantageous to drive the electron transfer process in the triplet state of the photocatalyst. [43] A lifetime of the charge separated radical ion pair in the microsecond range is considered to be sufficient for efficient catalysis and this has been achieved in many artificial systems as reviewed in various review papers and chapters, although only in a limited number of cases this has been combined with a close to unity total reaction quantum yield. [80, 91, 92]

The sensitization by electron transfer, either photo-induced oxidation or reduction of the substrate by the excited photocatalyst, comprises two spectroscopically accessible steps in the singlet manifold and three steps in the triplet manifold, respectively. All contributing intermediate steps are shown in Equations 16.48 and 16.49, where C is the photocatalyst and S is the substrate and  $h\nu$  stands for the incident photon, which is absorbed by the photocatalyst.



From Equation 16.48 and 16.49 it can be seen, that the photocatalyst remains in its reduced or oxidized state after the photo-induced radical ion pair formation and, therefore, needs to be regenerated in order to retrieve its full photocatalytic capability and to complete the catalytic cycle. On the other hand it can be seen, that the electron transfer process between excited photocatalyst and substrate needs to be thermodynamically allowed.

First we will comment on the latter: The actual sensitizing mechanism of a photocatalytic reaction strongly depends on the electrochemical and photophysical properties of catalyst and substrate. Calculating the change of Gibbs energy  $\Delta G^0$  according to Rehm and Weller [94], which is shown in Equation 16.50, helps to predict the sensitizing mechanism or to find a suitable photocatalyst for the desired reaction. The standard oxidation potential of the electron donor in its ground state is  $E^0(D^{+\cdot}/D)$ , the standard reduction potential of the electron acceptor in its ground state is  $E^0(A/A^{-\cdot})$ . These can be easily measured by cyclovoltametry. The quantity  $r$  stands for the electron donor-acceptor distance which can be deduced from quantum chemical calculations or knowledge of the molecular structure. The quantity  $\Delta E_{00}$  represents the energy with respect to the ground state of the excited state, which is quenched by ET. For the excited singlet state  $\Delta E_{00}$  can be readily read off the absorption spectrum. The change of  $\Delta G^0$  serves as driving force for the ET reaction between donor and acceptor and has to be below zero, to thermodynamically allow the ET process.

$$\Delta G^0 = e \left[ E^0(D^{+\cdot}/D) - E^0(A/A^{-\cdot}) \right] - \frac{e^2}{4\pi\epsilon_0\epsilon r} - \Delta E_{00} \quad (16.50)$$

The corresponding data of common organic photo-sensitizers, which are applied in homogeneous photocatalysis, and of the very useful  $\text{Ru}(\text{bpy})_3^{2+}$  are listed in Table 16.2. [95] Although these data provide a first idea of the underlying mechanism, an experimental proof of the actual sensitizing mechanism is crucial for a full understanding of the photo-catalytic reaction. Especially time-resolved spectroscopic methods on multiple time scales provide detailed insights into the photo-induced sensitization processes.

The re-oxidation or re-reduction of the photocatalyst after the photo-induced primary ET to its ground state is generally a required process in terms of catalysis. Otherwise the total photo-induced charge transfer process should be discussed as photochemistry, since the light-absorbing chromophore is consumed with the conversion of one substrate molecule. However, the second ET step might seem useless for the desired reaction, but it is necessary for the total catalytic cycle. It is also possible to drive the desired conversion of the substrate with the regeneration step of the photo-formed radical ion of the catalyst. [98] But in this situation, time resolved spectroscopy is not the perfect tool for the investigation of the actual sensitization process of the substrate since the starting point of the reaction is not anymore de-

**Table 16.2:** Electrochemical and photophysical data of selected organic sensitizers in comparison with the photoredox catalyst Ru(bpy)<sub>3</sub><sup>2+</sup>

sensitizer	E <sup>0</sup> (D <sup>+</sup> ·/D) vs. SCE [V]	E <sup>0</sup> (A/A <sup>-·</sup> ) vs. SCE [V]	λ <sub>00</sub> [nm]	E <sub>S1</sub> [eV]	E <sub>T1</sub> [eV]	Φ <sub>T</sub>
anthracene <sup>a</sup>	1.09 (MeCN)	-1.95 (DMF)	375	3.31	1.84	0.7
benzophenone <sup>a</sup>		-1.83 (MeCN)	384	3.23	3.00	1
eosin Y <sup>a,b</sup>		-1.38 (MeCN)	571	2.17	1.83	0.3
riboflavin <sup>a,c</sup>		-0.29 <sup>e</sup> (H <sub>2</sub> O)	495	2.50	2.17	0.7
xanthone <sup>a</sup>		-1.77 (DMF)	370	3.35	3.21	1
Ru(bpy) <sub>3</sub> <sup>2+</sup> <sup>d</sup>	1.29	-1.33	452	2.74		

(a) reference [51] (b) 2',4',5',7'-tetrabromo-fluorescein-dianion (c) reference 96 (d) reference [97] (e) vs. NHE

fined by the pump pulse. It is the photo-induced generation of the reactive radical ion species of the photocatalyst that is easily and directly accessible. Tracing the second ET step with methods of time resolved spectroscopy is much more challenging, especially if both ET steps are limited by diffusion of the reactants. Then, if both the sacrificial reactant and the substrate are diluted with comparable concentration, the diffusion limited quenching process occurs on equal time scales and, therefore, both processes are difficult to distinguish with the help of time-resolved spectroscopy. The intermediate species might even not be present in high enough concentration for a secure detection.

Another aspect, which has to be considered when comparing photoredox chemistry in the singlet and in the triplet manifold, is the achievable reaction rate for the ET step. It has been found that quenching of excited singlet states by electron transfer is usually fast in comparison to the quenching of a triplet state of the same chromophore by electron transfer. [43, 99] Also the listed diffusive, concentration dependent quenching rates  $K_q$  of excited photo-sensitizers by suitable quencher molecules in Montali et al. "Handbook of Photochemistry" [51] strongly support this picture. When discussing rates of inter- and intramolecular ET processes, the Marcus Theory is indispensable for an accurate explanation of the involved processes. [100, 101] The Marcus Equation relates the electron transfer rate  $k_{ET}$  to the electronic coupling  $H_{if}$  between initial and final state, the reorganization energy  $\lambda$  and the change of Gibbs energy  $\Delta G^0$ .

$$k_{et} = \frac{2\pi}{\hbar} |H_{if}|^2 \frac{1}{\sqrt{4\pi\lambda k_B T}} \exp\left\{-\frac{(\lambda + \Delta G^0)^2}{4\lambda k_B T}\right\} \quad (16.51)$$

A well suited example for this effect is the diffusion limited quenching of excited riboflavin by intermolecular electron transfer from 4-methoxybenzylalcohol, which is 200-fold slower when quenching the triplet state in comparison when quenching the excited singlet state (Table 16.1 and Ref. [43]). Also the quenching of excited

states of benzophenone from a covalently bound DNA nucleobase occurs roughly 20 times faster in the excited singlet state than in the triplet state. [102] The Marcus theory provides two explanations for this behavior: Due to the usually energetically lower lying triplet state in comparison to the optical accessible excited singlet states in organic chromophores (Table 16.2), the absolute value of the change of Gibbs energy  $\Delta G^0$  is smaller when the excited state quenching by electron transfer occurs in the triplet regime. This leads to a decrease in the electron transfer rate  $k_{et}$  and therefore to a decrease in reactivity [99] and clearly can be seen by calculating the  $\Delta G^0$  values according to Rehm and Weller (Equation 16.47) and inserting the result into the Marcus equation (Equation 16.51). Another explanation for the decrease in the rate of electron transfer  $k_{et}$  can be a change in the coupling term  $|H_{if}|^2$  which describes the electronic coupling between initial state and final state of the charge transfer reaction. Generally speaking, on the one hand, in photocatalyst's triplet chemistry provides the advantage of spin-forbidden charge recombination but, on the other hand, it has the disadvantage of a slow electron transfer process in comparison to singlet chemistry.

As a further example, irradiation of organometallic coordination complexes such as  $\text{Ru}(\text{bpy})_3^{2+}$  which are often used as redox photocatalysts, due to their versatile optical and electrochemical capabilities [91, 103, 104], leads to a species which exhibits catalytic activity. [104] This is a convenient and often used method for the photo-induced activation of a catalyst [105], also adsorbed on a solid [65, 107–109]. Covalently bound to a platinum or palladium centered catalytic active site forming a donor-bridge-acceptor-system, ruthenium organometallic coordination complexes can also serve as intramolecular electron donor sites and, therefore, provide photo-induced water splitting capability. [110]

For further information on photosensitization by reversible electron transfer the early but still informative review article from Kavarnos and Turro [111] is strongly recommended.

## 16.6 Epilogue

In this final chapter we have described, how modern transient spectroscopy can contribute decisively to the understanding of the mechanisms governing chemical photocatalysis. The methods developed in our laboratories over the last years allow the excitation of the catalyst at any selected wavelength. This is important to ensure that indeed the catalyst and not the substrate is excited. In addition it allows one to investigate whether higher electronic states or vibrational excess energy influences the outcome and efficiency of the processes.

We now have a detection range from the UV, as low as 250 nm, and out to NIR, as high as 1700 nm available at a temporal resolution of better than 50 fs. With the help of an auxiliary tunable nanosecond laser we can measure without gaps out to

the high  $\mu\text{s}$  range. This enormous detection range allows one to identify many of the reaction intermediates. As a consequence, the transient optical spectroscopy does not restrict itself anymore to the determination of specific rates, but it renders a complete picture of a multistep reaction chain.

For this analysis it is far from sufficient to fit exponential models to the signal at an individual wavelength. Such an approach has been used many times in the past, since early experiments only had single detection wavelengths available and the investigators relied on their a priori knowledge where a specific chemical species could be detected. Instead, a global analysis of the whole spectral range has to be performed to arrive at an unambiguous interpretation.

From such an analysis it can readily be determined whether a reaction proceeds via singlet or triplet states. For singlet schemes a pre-association is desired, as the short singlet lifetime does not allow efficient diffusional encounters. We showed, however, that such an approach can easily lead to rapid charge recombination after the initial electron transfer that starts the catalysis. Pre-association is, however, highly desired for stereoselective reactions.

When the initial dynamics is intersystem crossing in the catalyst, the aim has to be to generate a high triplet yield. As this takes typically some nanoseconds, the subsequent step of charge transfer to the substrate cannot be boosted by pre-association but has to be enabled by diffusion. The time resolved spectroscopy should then be repeated for a number of substrate concentrations. What is most important is that the analysis of the resulting set of data has to be performed comprehensively in order to obtain the true system behavior and not just effective values for each value of the concentration. The final set of parameters which truly describes the reaction has to model the complete spectrum and all concentrations simultaneously. From such a comprehensive analysis, a clear picture of the diffusional encounter and separation results. Such information has previously only been used very rarely and as a matter of fact the community of ultrafast spectroscopists has not considered it possible to analyze these rather complex situations. On the other hand, the chemists working on chemical photocatalysis have not dared to apply transient spectroscopy from the femtosecond to the microsecond range to their complex problems.

We hope that the present account and the evolving original work by our efforts will encourage more researchers to use the new methods and capabilities. Not only chemical photocatalysis, but also the sustainable energy source water splitting [112] and a wide range of issues in green chemistry should be able to profit. The detailed understanding of the reaction mechanisms is not only of academic interest, but it can readily lead to strategies for improving the efficiency of the use of the photons. Even so, the solar photons are free of direct cost, and they should be used diligently to keep the demand on collection space low. Only with high reaction quantum yields new routes to solar energy harvesting, in particular the solar backed production of fuels, will gain the necessary technical and industrial acceptance.

## 16.7 References

- [1] Würthner, F.; Kaiser, T. E.; Saha-Müller, C. R. (2011). *Angew. Chem. Int. Ed.*, 50, 3376–3410.
- [2] Scheibe, G. (1937). *Angew. Chem.*, 50, 212–219.
- [3] Jelley, E. E. (1936). *Nature*, 138, 1009–1010.
- [4] Icli, S.; Demića, S.; Dindar, B.; Doroshenko, A. O.; Timur, C. (2000). *J. Photochem. Photobiol. A*, 136, 15–24.
- [5] Würthner, F.; Thalacker, C.; Diele S.; Tschierske, C. (2001). *Chem. Eur. J.*, 7, 2245–2253.
- [6] Würthner, F. (2004). *Chem. Commun.*, 1564–1579.
- [7] Müller, C.; Bauer, A.; Bach, T. (2009). *Angew. Chem Int. Ed.*, 48, 6640–6642.
- [8] Müller, C.; Bauer, A.; Maturi, M. M.; Cuquerella, M. C.; Miranda, M. A.; Bach, T. (2011). *J. Am. Chem. Soc.*, 133, 16689–16697.
- [9] Sikorska, E.; Khmelinskii, I.; Komasa, A.; Koput, J.; Ferreira, L. F. V.; Herance, J. R.; Bourdelande, J.L.; Williams, S. L.; Worrall, D. R.; Insinska-Rak, M.; Sikorski M. (2005). *Chem. Phys.*, 314, 239–247.
- [10] Salzmann, S.; Tatchen, J.; Marian, C. M. (2008). *J. Photochem. Photobiol. A*, 198, 221–231.
- [11] Hari, D. P.; Schroll, P.; König, B. (2012). *J. Am. Chem. Soc.*, 134, 2958–2961.
- [12] Klönis, N.; Clayton, A. H. A.; Voss Jr., E. W.; Sawyer, W. H. (1998). *Photochem. Photobiol.*, 67, 500–510.
- [13] Chakraborty, M.; Panda, A. K. (2011). *Spectrochim. Acta A*, 81, 458–465.
- [14] Fita, P.; Fedoseeva, M.; Vauthey, E. (2011). *J. Phys. Chem A*, 115, 2465–2470.
- [15] Reichardt, C. (2003). *Solvents and Solvent Effects in Organic Chemistry*, 3<sup>rd</sup> edition (Wiley-VCH, Weinheim)
- [16] Curtis, J. C.; Sullican, B. P.; Meyer, T. J. (1983). *Inorg. Chem.*, 22, 224–236.
- [17] Fantacci, S.; De Angelis, F.; Selloni, A. (2003). *J. Am. Chem. Soc.*, 125, 4381–4387.
- [18] Stratton, R. M.; Maroncelli, M. (1996). *J. Phys. Chem.*, 100, 12981–12996.
- [19] Fleming, G. R.; Cho, M. (1996). *Annu. Rev. Phys. Chem.*, 47, 109–134.
- [20] de Boeij, W. P.; Pshenichnikov, M.S.; Wiersma, D. A. (1998). *Annu. Rev. Phys. Chem.*, 49, 99–123.
- [21] Reichardt, C. (1979). *Angew. Chem. Int. Ed.*, 18, 98–110.
- [22] Reichardt R. (1994). *Chem. Rev.*, 94, 2319–2358.
- [23] Norrish, R. G. W.; Porter, G. (1949). *Nature*, 164, 658–658.
- [24] Porter, G. (1950). *Proc. Roy. Soc. Lond. Ser. A*, 200, 284–300.
- [25] Kukura, P.; McCamant, D. W.; Mathies, R. A. (2007). *Annu. Rev. Phys. Chem.*, 58, 461–488.
- [26] Satzger, H.; Schmidt, B.; Root, C.; Zinth, W.; Fierz, B.; Krieger, F.; Kiefhaber, T.; Gilch, P. (2004). *J. Phys. Chem A*, 108, 10072–10079.
- [27] Keller, U. (2003). *Nature*, 424, 831–838.
- [28] Spence, D. E.; Kean, P. N.; Sibbett, W. (1991). *Opt. Lett.*, 16, 42–44.
- [29] Megerle, U.; Pugliesi, I.; Schrieffer, C.; Sailer, C.; Riedle, E. (2009). *Appl. Phys. B*, 96, 215–231.
- [30] Alfano, R. R.; Shapiro, S. L. (1970). *Phys. Rev. Lett.*, 24, 584–587.
- [31] Alfano, R. R.; Shapiro, S. L. (1970). *Phys. Rev. Lett.*, 24, 592–594.
- [32] Bradler, M.; Baum, P.; Riedle, E. (2009). *Appl. Phys. B*, 97, 561–574.
- [33] Kozma, I. Z.; Baum, P.; Lochbrunner, S.; Riedle, E. (2003). *Opt. Express*, 11, 3110–3115.
- [34] Homann, C.; Lang, P.; Riedle, E. (2012). *J. Opt. Soc. Am. B*, 29, 2765–2769.
- [35] Bradler, M.; Homann, C.; Riedle, E. (2011). *Opt. Lett.*, 36, 4212–4214.
- [36] Huber, R.; Satzger, H.; Zinth, W.; Wachtveitl, J. (2001). *Opt. Commun.*, 194, 443–448.
- [37] Mention of vendor names and model numbers is for technical communication purposes only and does not necessarily imply recommendation of these units, nor does it imply that comparable units from another vendor would be any less suitable for this application.
- [38] Wenninger, M.; Fazio, D.; Megerle, U.; Trindler, C.; Schiesser, S.; Riedle, E.; Carell, T. (2011). *ChemBioChem*, 12, 703–706.

- [39] Polli, D.; Brida, D.; Mukamel, S.; Lanzani, G.; Cerullo, G. (2010). *Phys. Rev. A*, 82, 053809.
- [40] Schrieber, C.; Pugliesi, I.; Riedle, E. (2009). *Appl. Phys. B*, 96, 247–250.
- [41] Ganz, T.; von Ribbeck, H. G.; Brehm, M.; Keilmann, F. (2008). *Opt. Commun.*, 281, 3827–3830.
- [42] Pugliesi, I.; Krok, P.; Lochbrunner, S.; Blaszczyk, A.; von Hänisch, C.; Mayor, M.; Riedle, E. (2010). *J. Phys. Chem. A*, 114, 12555–12560.
- [43] Megerle, U.; Wenninger, M.; Kutta, R.-J.; Lechner, R.; König, B.; Riedle, E. (2011). *Phys. Chem. Chem. Phys.*, 13, 8869–8880.
- [44] Fita, P.; Luzina, E.; Dziembowska, T.; Radzewicz, C.; Grabowska, A. (2006). *J. Chem. Phys.*, 125, 184508.
- [45] Birks, J. B. (1970). *Photophysics of Aromatic Molecules* (Wiley-Interscience, London)
- [46] Ruckebusch, C.; Sliwa, M.; Pernot, P.; de Juan, A.; Tauler, R. (2012). *J. Photochem. Photobiol. C*, 13, 1–27.
- [47] Sakai, M.; Takahashi, H. (1996). *J. Mol. Struct.*, 379, 9–18.
- [48] Megerle, U. (2011). *Photoinduced molecular dynamics in increasingly complex systems: From ultrafast transient absorption spectroscopy to nanoscopic models*. (Dissertation, Ludwig-Maximilians-Universität, Fakultät für Physik. München)
- [49] Ricks, A. B.; Brown, K. E.; Wenninger, M.; Karlen, S. D.; Berlin, Y. A.; Co, D. T.; Wasielewski, M. R. (2012). *J. Am. Chem. Soc.*, 134, 4581–4588.
- [50] Rice, S. A. (1985). *Diffusion-limited reactions*, (Elsevier Science Publishers B.V., Amsterdam)
- [51] Murov, S. L.; Carmichael, I.; Hug, G. L. (1993). *Handbook of Photochemistry*, 2<sup>nd</sup> edition (M. Decker, New York)
- [52] Koch, M.; Rosspeintner, A.; Angulo, G.; Vauthey, E. (2012). *J. Am. Chem. Soc.*, 134, 3729–3736.
- [53] Eads, D. D.; Dismar, S. G.; Fleming, G. R. (1990). *J. Chem. Phys.*, 93, 1136–1148.
- [54] Murata, S.; Matsuzaki, S. Y.; Tachiya, M. (1995). *J. Phys. Chem.*, 99, 5354–5358.
- [55] Murata, S.; Tachiya, M. (1996). *J. Phys. Chem.*, 100, 4064–4070.
- [56] Burel, L.; Mostafavi, M.; Murata, S.; Tachiya, M. (1999). *J. Phys. Chem. A*, 103, 5882–5888.
- [57] Serpone, N. J. (1997). *Photochem. Photobiol. A*, 104, 1–12.
- [58] Bakowski, A.; Dressel, M.; Bauer, A.; Bach, T. (2011). *Org. Biomol. Chem.*, 9, 3526–3529.
- [59] Vichova, J.; Hartl, F.; Vlcek, A. (1992). *J. Am. Chem. Soc.*, 114, 10903–10910.
- [60] Tfouni, E. (2000). *Coord. Chem. Rev.*, 196, 281–305.
- [61] Xia, H.-L.; Liu, F.; Ardo, S.; Sarjeant, A. A. N.; Meyer, G. J. (2010). *J. Photochem. Photobiol. A*, 216, 94–103.
- [62] Serpone, N.; Emeline, A. V. (2002). *Int. J. Photoenergy*, 4, 91–131.
- [63] Cherevatskaya, M.; Neumann, M. Földner, S.; Harlander, C.; Kümmel, S.; Dankesreiter, S.; Pfitzner, A.; Zeitler, K.; König, B. (2012). *Angew. Chem.*, 124, 4138–4142
- [64] Maschmeyer, T.; Che, M. (2010). *Angew. Chem. Int. Ed.*, 49, 1536–1539.
- [65] Fagnoni, M.; Dondi, D.; Ravelli, D.; Albin, A. (2007). *Chem. Rev.*, 107, 2725–2756.
- [66] Megerle, U.; Lechner, R.; König, B.; Riedle, E. (2010). *Photochem. Photobiol. Sci.*, 9, 1400–1406.
- [67] Parker, C. A. (1953). *Proc. R. Soc. London, Ser. A*, 220, 104–116.
- [68] Kuhn, H. J.; Braslavsky, S. E.; Schmidt, R. (2004). *Pure Appl. Chem.*, 76, 2105–2146.
- [69] Jankowski, J. J.; Kieber, D. J.; Mopper, K. (1999). *Photochem. Photobiol.*, 70, 319–328.
- [70] Rahn, R. O. (1997). *Photochem. Photobiol.*, 66, 450–455.
- [71] Zepp, R. G.; Gumz, M. M.; Miller, W. L.; Gao, H. (1998). *J. Phys. Chem. A*, 102, 5716–5723.
- [72] Ghosh, J. P.; Sui, R.; Langford, C. H.; Achari, G.; Berlinguette, C. P. (2009). *Water Res.*, 43, 4499–4506.
- [73] Schmidhammer, U.; Roth, S.; Riedle, E.; Tishkov, A. A.; H. Mayr, H. (2005). *Rev. Sci. Instrum.*, 76, 093111
- [74] Reindl, S.; Penzkofer, A. (1996). *Chem. Phys.*, 211, 431–439.
- [75] Reindl, S.; Penzkofer, A. (1996). *Chem. Phys.*, 213, 429–438.



- [76] Peceli, D.; Webster, S.; Fishman, D. A.; Cirloganu, C. M.; Hu, H.; Przhonska, O. V.; Kurdyukov, V. V.; Slominsky, Y. L.; Tolmachev, A. I.; Kachkovski, A. D.; Dasari, R. R.; Barlow, S.; Marder, S. R.; Hagan, D. J.; Van Stryland E. W. (2012). *J. Phys. Chem. A*, 116, 4833–4841.
- [77] Pareek, V.; Chong, S.; Tade, M.; Adesina, A. A. (2008). *Asia Pac. J. Chem. Eng.*, 3, 171–201.
- [78] Middleton, C. T.; de La Harpe, K.; Su, C.; Law, Y. K.; Crespo-Hernandez, C. E.; Kohler, B. (2009). *Annu. Rev. Phys. Chem.*, 60, 217–239.
- [79] Dobryakov, A. L.; Kovalenko, S. A.; Weigel, A.; Pérez-Lustres, J. L.; Lange, J.; Müller, A.; Ernsting, N. P. (2010). *Rev. Sci. Instrum.*, 81, 113106.
- [80] Verhoeven, J. W. (2006). *J. Photochem. Photobiol. C*, 7, 40–60.
- [81] Hore, P. J.; Broadhurst, R. W. (1993). *Prog. Nucl. Mag. Res. Sp.*, 25, 345–402.
- [82] Heelis, P. F. (1982). *Chem. Soc. Rev.*, 11, 15–39.
- [83] Insinska-Rak, M.; Sikorska, E.; Bourdelande, J. L.; Khmelinskii, I. V.; Prukala, W.; Dobek, K.; Karolczak, J.; Machado, I. F.; Ferreira, L. F. V.; Komasa, A.; Worrall, D. R. and Sikorski, M. (2006). *J. Mol. Struct.*, 783, 184–190.
- [84] Salzmann, S.; Tatchen, J.; Marian, C. M. (2008). *J. Photochem. Photobiol. A*, 198, 221–231.
- [85] Förster, T. (1948). *Ann. Phys.*, 437, 55–75.
- [86] Dexter, D. L. (1953). *J. Chem. Phys.*, 21, 836–850.
- [87] Cauble, D. F.; Lynch, V.; Krische, M. J. (2003). *J. Org. Chem.*, 68, 15–21.
- [88] Zewail, A. H. J. (2000). *Phys. Chem. A*, 104, 5660–5694.
- [89] Hsu, C.-P. (2009). *Acc. Chem. Res.*, 42, 509–518.
- [90] Zeitler, K. (2009). *Angew. Chem. Int. Ed.*, 48, 9785–9789.
- [91] Wasielewski, M. R. (1992). *Chem. Rev.*, 92, 435–461.
- [92] Gust, D.; Moore, T. A.; Moore, A. L. (2001). *Acc. Chem. Res.*, 34, 40–48.
- [93] Lhiaubet, V.; Paillous, N.; Chouini-Lalanne, N. (2001). *Photochem. Photobiol.*, 74, 670–678.
- [94] Rehm, D.; Weller, A. (1970). *Isr. J. Chem.*, 8, 259–271.
- [95] Ravelli, D.; Fagnoni, M.; Albin, A. (2012). *Chem. Soc. Rev.*
- [96] Meisel, D.; Neta, P. (1975). *J. Phys. Chem.*, 79, 2459–2461.
- [97] Narayanam, J. M. R.; Stephenson, C. (2011). *Chem. Soc. Rev.*, 40, 102–113.
- [98] Ischay, M. A.; Anzovino, M. E.; Du, J.; Yoon, T. P. (2008). *J. Am. Chem. Soc.*, 130, 12886–12887.
- [99] Steiner, U.; Winter, G.; Kramer, H. E. A. (1977). *J. Phys. Chem.*, 81, 1104–1110.
- [100] Marcus, R. A. (1956). *J. Chem. Phys.*, 24, 966–978.
- [101] Marcus, R. A.; Sutin, N. (1985). *Biochim. Biophys. Acta*, 811, 265–322.
- [102] März, T.; Wenninger, M.; Weinberger, M.; Wagenknecht, H.-A.; Riedle, E.; Schütz, M. in preparation
- [103] Campagna, S.; Puntoriero, F.; Nastasi, F.; Bergamini, G.; Balzani, V. (2007). *Top. Curr. Chem.*, 280, 117–214.
- [104] Juris, A.; Balzani, V.; Barigelletti, F.; Campagna, S.; Belser, P.; von Zelewsky, A. (1988). *Coord. Chem. Rev.*, 84, 85–277.
- [105] Hennig, H.; Dietze, F.; Thomas, P.; Rehorek, D. (1978). *Z. Chem.*, 18, 458–460.
- [106] Hennig, H. (1999). *Coord. Chem. Rev.*, 182, 101–123.
- [107] Wada, Y.; Nakaoka, C.; Morikawa, A. (1988). *Chem. Lett.*, 25–26.
- [108] Ballinger, T. H.; Yates Jr., J. T. (1992). *J. Phys. Chem.*, 96, 9979–9983.
- [109] Ichikawa, M.; Pan, W.; Imada, Y.; Yamaguchi, M.; Isobe, K.; Shido, T. (1996). *J. Mol. Catal. A: Chem.*, 107, 23.
- [110] Tschierlei, S.; Presselt, M.; Kuhnt, C.; Yartsev, A.; Pascher, T.; Sundström, V.; Karnahl, M.; Schwalbe, M.; Schäfer, B.; Rau, S.; Schmitt, M.; Dietzek, B.; Popp, J. (2009). *Chem. Eur. J.*, 15, 7678–7688.
- [111] Kavarnos, G. J.; Turro, N. J. (1986). *Chem. Rev.*, 86, 401–449.
- [112] Nocera, D. G. (2009). *ChemSusChem*, 2, 387–390.



## **Appendix A2**

### **Exponential Distance Dependence of Photoinitiated Stepwise Electron Transfer in Donor-Bridge-Acceptor Molecules: Implications for Wire-like Behaviour**

Annie Butler Ricks, Kristen E. Brown, Matthias Wenninger, Steven D. Karlen,  
Yuri A. Berlin, Dick T. Co, Michael R. Wasielewski

*Journal of the American Chemical Society* **2012**, *134*, 4581-4588



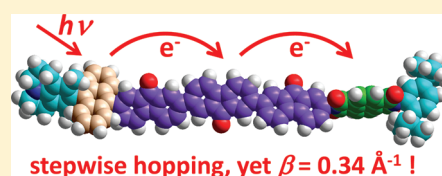
# Exponential Distance Dependence of Photoinitiated Stepwise Electron Transfer in Donor–Bridge–Acceptor Molecules: Implications for Wirelike Behavior

Annie Butler Ricks, Kristen E. Brown, Matthias Wenninger, Steven D. Karlen, Yuri A. Berlin, Dick T. Co,\* and Michael R. Wasielewski\*

Department of Chemistry and Argonne–Northwestern Solar Energy Research (ANSER) Center, Northwestern University, Evanston, Illinois 60208-3113, United States

**S** Supporting Information

**ABSTRACT:** Donor–bridge–acceptor (D–B–A) systems in which a 3,5-dimethyl-4-(9-anthracenyl)julolidine (DMJ-An) chromophore and a naphthalene-1,8:4,5-bis(dicarboximide) (NI) acceptor are linked by oligomeric 2,7-fluorenone (FN<sub>n</sub>) bridges (*n* = 1–3) have been synthesized. Selective photoexcitation of DMJ-An quantitatively produces DMJ<sup>+</sup>•-An<sup>-</sup>•, and An<sup>-</sup>• acts as a high-potential electron donor. Femtosecond transient absorption spectroscopy in the visible and mid-IR regions showed that electron transfer occurs quantitatively in the sequence: DMJ<sup>+</sup>•-An<sup>-</sup>•-FN<sub>n</sub>-NI → DMJ<sup>+</sup>•-An-FN<sub>n</sub>•-NI → DMJ<sup>+</sup>•-An-FN<sub>n</sub>-NI<sup>-</sup>•. The charge-shift reaction from An<sup>-</sup>• to NI<sup>-</sup>• exhibits an exponential distance dependence in the nonpolar solvent toluene with an attenuation factor ( $\beta$ ) of 0.34 Å<sup>-1</sup>, which would normally be attributed to electron tunneling by the superexchange mechanism. However, the FN<sub>n</sub>• radical anion was directly observed spectroscopically as an intermediate in the charge-separation mechanism, thereby demonstrating conclusively that the overall charge separation involves the incoherent hopping (stepwise) mechanism. Kinetic modeling of the data showed that the observed exponential distance dependence is largely due to electron injection onto the first FN unit followed by charge hopping between the FN units of the bridge biased by the distance-dependent electrostatic attraction of the two charges in D<sup>+</sup>•-B<sup>-</sup>•-A. This work shows that wirelike behavior does not necessarily result from building a stepwise, energetically downhill redox gradient into a D–B–A molecule.



## INTRODUCTION

Achieving distance-independent “wirelike” electron transfer in molecular donor–bridge–acceptor (D–B–A) systems requires a detailed understanding of how electron transfer depends on molecular structure.<sup>1</sup> Systematic studies of electron transfer involving covalently linked D–B–A systems have examined a variety of bridge molecules, including DNA base pairs;<sup>2</sup> peptides in proteins;<sup>3</sup> porphyrins;<sup>4</sup> saturated alkane  $\sigma$  systems;<sup>5</sup> and unsaturated alkene, alkyne, and aromatic  $\pi$ -conjugated spacers.<sup>6</sup> In most of these D–B–A systems, electron transfer from D to A occurs by the coherent superexchange mechanism, which involves mixing of virtual states having charge formally on the bridge with the initial donor state and requires the virtual bridge states to be energetically much higher in energy than the donor state. McConnell used second-order perturbation theory to derive an expression for the bridge-mediated electronic coupling  $V_{DA}$  between D and A with identical B units that mediate the electronic coupling:<sup>7</sup>

$$V_{DA} = \frac{V_{DB}V_{BA}}{\Delta E_{DB}} \left( \frac{V_{BB}}{\Delta E_{DB}} \right)^{n-1} \quad (1)$$

where  $V_{DB}$  and  $V_{BA}$  are the matrix elements that couple D to B and B to A, respectively,  $n$  is the number of identical B units,  $V_{BB}$  is the electronic coupling between B units, and  $\Delta E_{DB}$  is the

energy gap between the donor and bridge states. When  $V_{BB} \ll \Delta E_{DB}$ , the distance dependence of the electronic coupling is described by

$$V_{DA} = V_0 e^{-\beta(R-R_0)/2} \quad (2)$$

where  $V_0$  is the coupling at the van der Waals contact distance  $R_0$ ,  $R$  is the D–A distance, and  $\beta$  is the attenuation factor, given by eq 3:

$$\beta = \frac{2}{r} \ln \left| \frac{\Delta E_{DB}}{V_{BB}} \right| \quad (3)$$

in which  $r$  is the length of one bridge segment. Since theory shows that the electron-transfer rate constant  $k_{DA}$  is proportional to  $V_{DA}$ ,<sup>2,8</sup> the distance dependence of  $k_{DA}$  via the coherent superexchange mechanism is exponential and is given by<sup>2a,9</sup>

$$k_{DA} = k_0 e^{-\beta(R-R_0)} \quad (4)$$

When the energies of the virtual states having charge on the bridge become resonant with that of the initial state or drop below it, the bridge states become real, and incoherent charge hopping from one distinct redox site to the next can occur.<sup>10</sup>

Received: June 24, 2011

Published: February 15, 2012

Under these conditions, the perturbation theory assumptions inherent in the superexchange mechanism break down, and the observed small  $\beta$  values are strictly phenomenological. Thus, depending on the energies of the charge-separated states involving the bridge molecules, the incoherent hopping mechanism should become more efficient than the coherent superexchange process at long distances, so measurements of the distance dependence of the electron-transfer rate are often employed to differentiate between these mechanisms. Charge transport within  $\pi$ -linked D–B–A molecules has been studied under a variety of conditions<sup>2–4,5b,6d,11</sup> to identify the molecular properties that determine the crossover from superexchange to hopping when molecular systems exhibit a combination of these mechanisms.<sup>7,12</sup> However, lengthening the bridge often changes other system parameters, such as bridge redox potentials and molecular conformations.<sup>6c</sup> Nevertheless, the shallow distance dependence of the charge-hopping mechanism should be favorable for constructing a molecular wire that allows efficient electron transfer over long distances.

While determining  $\beta$  has been the object of many experimental<sup>6d,11b,13</sup> and theoretical<sup>14</sup> studies, concerns have been raised as to the reliability of  $\beta$  in assessing the role of superexchange in a given electron-transfer reaction.<sup>15</sup> The observed  $\beta$  values for  $\pi$ -conjugated bridges range from those characteristic of fully conducting bridges ( $\beta$  close to zero) to those of nearly insulating ones ( $\beta > 0.5 \text{ \AA}^{-1}$ ), while  $\sigma$  bridges have very high  $\beta$  values near unity.<sup>15b</sup> By convention,  $\beta = 0.2\text{--}0.3 \text{ \AA}^{-1}$  is considered to be the lower limit of the superexchange regime, with lower values attributed to a significant contribution from the incoherent hopping mechanism.<sup>14a,b</sup> For D–B–A systems in which the charge-hopping mechanism is operative, it is difficult to assign an upper limit to the observed phenomenological  $\beta$  value because several potential mechanisms can result in such behavior, which is the principal focus of this paper.

For sufficiently long bridges, theory has identified three conditions under which the incoherent hopping mechanism can exhibit an exponential distance dependence with a  $\beta$  value similar to that for the single-step coherent superexchange mechanism.<sup>14</sup> In general, these conditions all reflect an asymmetry in the hopping rates between bridge sites in the forward (toward A) and backward (toward D) directions and/or the competition of hopping with different channels for charge depopulation of the bridge.<sup>14</sup> First, if the charge-hopping rates between independent bridge sites are the same, a significant difference in the rates of charge recombination from the bridge to the donor and charge trapping by the terminal acceptor can lead to a large  $\beta$  value. Second, the distance-dependent electrostatic attraction of the two charges in  $D^{+\bullet}\text{--}B^{-\bullet}\text{--}A$  can provide asymmetries in the rate constants that lead to significant  $\beta$  values.<sup>14a</sup> Third, injection of the electron onto the bridge may result in polaron formation resulting from significant charge delocalization over multiple bridge sites along with the structural and solvent distortions that accompany it, which may result in significant  $\beta$  values.<sup>16</sup>

We now report on a series of D–B–A molecules for which we have experimentally shown the electron transfer to proceed solely by stepwise, incoherent hopping yet exhibit a significant  $\beta$  value in a nonpolar solvent. Previous studies of D–B–A systems with reported  $\beta$  values as high as  $1.47 \text{ \AA}^{-1}$ , which were attributed to the hopping mechanism, mostly involved charge transport in DNA, where the polar solvent (water) and counterions provided a means for polaron-like hopping.<sup>17</sup>

Utilizing femtosecond visible pump/visible probe and visible pump/mid-IR probe transient absorption spectroscopies, we have unequivocally identified the reduced bridge as an intermediate in the charge-transfer process and determined the charge separation time as a function of the D–A distance using distinctive spectroscopic tags for the electron arrival at the acceptor. The D–B–A system that we employed consists of an anthracene radical anion electron donor produced by photoexcitation of 3,5-dimethyl-4-(9-anthracenyl)julolidine (DMJ-An) to its charge-transfer state,  $DMJ^{+\bullet}\text{--}An^{-\bullet}$ ; a series of fluorenone oligomers  $FN_n$  ( $n = 1\text{--}3$ ) as the bridges; and naphthalene-1,8:4,5-bis(dicarboximide) (NI) as the electron acceptor (Figure 1). Photoexcitation of DMJ-An produces

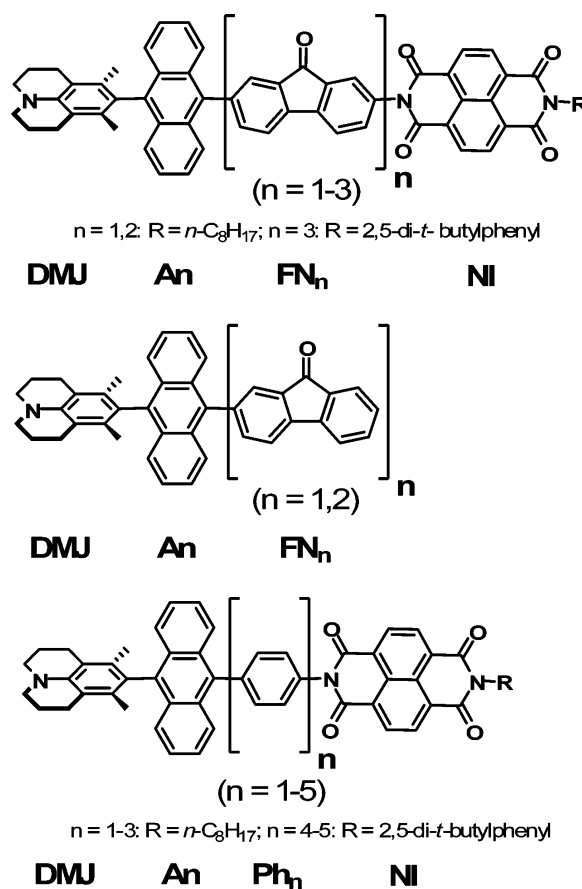


**Figure 1.** (top) D–B–A molecules and (center) model compounds used in this study. Results were compared to the (bottom) analogous molecules studied previously.<sup>25</sup>

$DMJ^{+\bullet}\text{--}An^{-\bullet}$  quantitatively,<sup>17</sup> and  $An^{-\bullet}$  acts as a high-potential electron donor. The  $FN_n$  bridges are advantageous because their reduction potentials change only modestly as  $n$  increases ( $-1.27, -1.14,$  and  $-1.08 \text{ V vs SCE}$  for  $n = 1\text{--}3$ , respectively; see the Supporting Information). The aforementioned hopping mechanisms are discussed below along with comparisons with the coherent superexchange mechanism.

## EXPERIMENTAL SECTION

**Synthesis.** The synthesis and characterization of  $DMJ\text{--}An\text{--}FN_n\text{--}NI$  ( $n = 1\text{--}3$ ) were reported earlier,<sup>18</sup> while those of  $DMJ\text{--}An\text{--}FN_n$  ( $n = 1, 2$ ) are described in the Supporting Information. All reagents were purchased from Sigma-Aldrich and used as received. All final products were purified by normal-phase preparative thin-layer chromatography prior to characterization. All solvents were spectrophotometric grade

or distilled prior to use. Intermediates and the resulting products were characterized by  $^1\text{H}$  NMR and UV–vis spectroscopy and high-resolution mass spectrometry.

**Optical Spectroscopy.** Steady-state absorption spectroscopy was performed using a Shimadzu UV-1800 spectrophotometer. All solvents were spectroscopic grade and used as received, except for tetrahydrofuran (THF) and toluene, which were further purified through a GlassContour solvent system immediately prior to use. Spectroelectrochemistry was carried out in argon-purged  $N,N$ -dimethylformamide (DMF) with 0.1 M  $\text{Bu}_4\text{NPF}_6$  as the supporting electrolyte. Bulk electrolysis was performed using a computer-controlled potentiostat (CH Instruments) and a three-electrode arrangement in a 2 mm glass cuvette utilizing a platinum wire mesh working electrode, a platinum wire auxiliary electrode, and a silver wire pseudoreference electrode. The cuvette was placed in a computer-controlled spectrophotometer (Shimadzu UV-1800). Spectra of the electrochemically generated anions were recorded by passing the light from the spectrophotometer through the platinum mesh and sweeping from 800 to 350 nm every 2 min. A blank spectrum consisting of the cuvette filled with solvent and supporting electrolyte was subtracted from each data set.

Femtosecond visible pump/visible probe transient absorption measurements were made using the 416 nm frequency-doubled output from a 2 kHz regeneratively amplified Ti:sapphire laser system as the pump.<sup>6a</sup> A white-light-continuum probe pulse was generated by focusing the IR fundamental into a 1 mm sapphire disk.<sup>19</sup> Detection with a charge-coupled device (CCD) spectrograph has been described previously.<sup>19</sup> The optical density of all samples was maintained between 0.3 and 0.5 at 416 nm. The samples were placed in a 2 mm path length quartz cuvette equipped with a vacuum adapter and subjected to five freeze–pump–thaw degassing cycles prior to transient absorption measurements. The samples were irradiated with 1.0  $\mu\text{J}$ , 416 nm laser pulses focused to a 200  $\mu\text{m}$  spot. Typically, 5–7 s of averaging was used to obtain the transient spectrum at a given delay time. The total instrument response function (IRF) for the pump–probe experiments was 150 fs. The transient absorption kinetics at a given wavelength was determined by using a nonlinear least-squares fit to a general sum of exponentials (Levenberg–Marquardt algorithm) convolved with a Gaussian function to account for the finite instrument response. The three-dimensional (3D) data set ( $\Delta A$  vs time and wavelength) was analyzed using global fitting to obtain decay-associated difference spectra (DADS) (see the Supporting Information).

Femtosecond visible pump/mid-IR probe transient absorption spectroscopy was performed on DMJ-An– $\text{FN}_n$ –NI ( $n = 1, 2$ ) and DMJ-An– $\text{FN}_2$ –NI. The data were obtained in THF because toluene is too absorptive in the 1500–1800  $\text{cm}^{-1}$  spectral region. Complementary femtosecond visible transient absorption data in THF were also obtained for direct comparison with the transient IR results. The femtosecond IR transient absorption setup was based on a 1 kHz Ti:sapphire regenerative amplifier (Spitfire Pro, Spectra-Physics) seeded by a Ti:sapphire oscillator (Tsunami, Spectra-Physics). The 1 mJ, 45 fs output of the amplifier was split into two beams of equal energy that were used to pump two separate optical parametric amplifiers (TOPAS-C, Light Conversion) to generate the tunable visible pump (290–2600 nm) and mid-IR probe (1000–4000  $\text{cm}^{-1}$ ) pulses. A gradient neutral-density filter wheel was used as the first turning mirror in the mid-IR beam path. By adjustment of the amount of reflectance, the intensity of the mid-IR probe pulse could be attenuated to a level below the detector saturation limit. The mid-IR beam was then split into vertically displaced probe and reference beams before the sample with a wedged ZnSe window, and multichannel detection of the  $\sim 400$   $\text{cm}^{-1}$  bandwidth IR probe light was achieved using a dual-array,  $2 \times 64$ -element mercury cadmium telluride (MCT) detector (InfraRed Associates, Inc.). The 400 nm pump pulse was produced from the 800 nm fundamental by second-harmonic generation, chopped at 500 Hz, and sent down an optical delay line before being focused at the sample with a 10 cm off-axis silver parabolic mirror along with the probe and reference beams. The probe beam was horizontally polarized, and the pump beam

polarization was set to the magic angle ( $54.7^\circ$ ) to eliminate contributions from rotational motion of the molecule in solution. The IRF was  $\sim 300$  fs. The sample cell consisted of a 2 mm Teflon spacer between two 2 mm thick  $\text{CaF}_2$  windows (Harrick Scientific Products, Inc.). The pump beam was rejected with an iris after passing through the sample, and the probe and reference beams were dispersed by an imaging spectrometer (Triax 190, HORIBA Jobin Yvon) equipped with a 75 groove/mm grating. Typically  $\sim 250$   $\text{cm}^{-1}$  of mid-IR light was imaged onto the 64 pixels of the MCT detector. However, our data in the same spectral window had three times the density of pixels as a result of interleaving of the spectra obtained at three grating positions and reconstitution of the recorded spectrum. Each time point was the sum of three spectra, each of which was obtained after 4 s of averaging.

## RESULTS

**Steady-State Spectroscopy.** The ground-state absorption spectrum of DMJ-An in toluene exhibits a broad charge-transfer absorption maximum at 367 nm with a broad emission maximum at 519 nm, resulting in an excited singlet charge-transfer state with an energy of 2.89 eV.<sup>17,20</sup> The ground-state absorption spectra of DMJ-An– $\text{FN}_n$ –NI and DMJ-An– $\text{FN}_n$  have absorption maxima at 360 and 380 nm and a shoulder at 398 nm, with the prominent vibronic structure coming from overlapping contributions of the DMJ-An charge-transfer absorption and the NI acceptor Franck–Condon progression (Figure 2). As the bridge length increases, additional broad

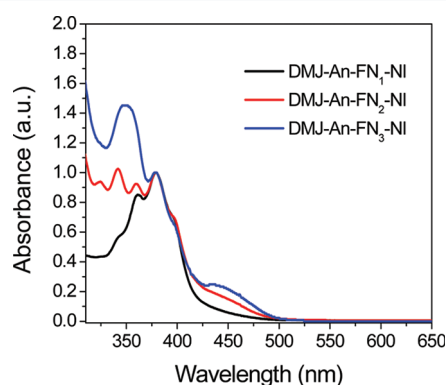


**Figure 2.** Ground-state absorption spectra of DMJ-An– $\text{FN}_n$ –NI ( $n = 1$ –3) normalized at 380 nm.

features resulting from the increased conjugation of the FN bridging units appear between 300 and 360 nm, along with a weak band at 450 nm whose intensity grows in proportion to the length of the bridge, which is assigned to  $\text{FN}_n$ .<sup>21</sup>

**Ion-Pair Distances and Energies.** Given that photoexcitation of DMJ-An results in quantitative subpicosecond charge separation to produce  $\text{DMJ}^{+\bullet}\text{-An}^{-\bullet}$  with a spectroscopically determined energy of 2.89 eV in toluene,<sup>17,20</sup> the energy levels for the charge-separated states  $\text{DMJ}^{+\bullet}\text{-An-FN}_n^{-\bullet}\text{-NI}$  and  $\text{DMJ}^{+\bullet}\text{-An-FN}_n\text{-NI}^{-\bullet}$  were determined in toluene using eq 5:

$$\Delta G_{\text{F}} = \Delta G_{\text{I}} + \text{sign}(E_{\text{I}} - E_{\text{F}}) + \frac{e^2}{\epsilon_{\text{S}}} \left( \frac{1}{r_{\text{I}}} - \frac{1}{r_{\text{F}}} \right) \quad (5)$$

where  $\Delta G_{\text{I}}$  and  $\Delta G_{\text{F}}$  are the energies above ground state for the initial and final ion pairs, respectively,  $E_{\text{I}}$  and  $E_{\text{F}}$  are the redox potentials for the initial and final ions between which the electron is transferred, respectively,  $r_{\text{I}}$  and  $r_{\text{F}}$  are the initial and final ion-pair distances, respectively,  $e$  is the electron charge,  $\epsilon_{\text{S}}$



is the static dielectric constant of the solvent (2.38 for toluene), and  $\text{sign}(E_1 - E_F)$  is negative when  $E_F > E_1$  and positive when  $E_1 > E_F$ . The parameters used in eq 5 are listed in Table S1 in the Supporting Information, and the energy levels of the relevant states are illustrated in Figure 3 and listed in Table S2.

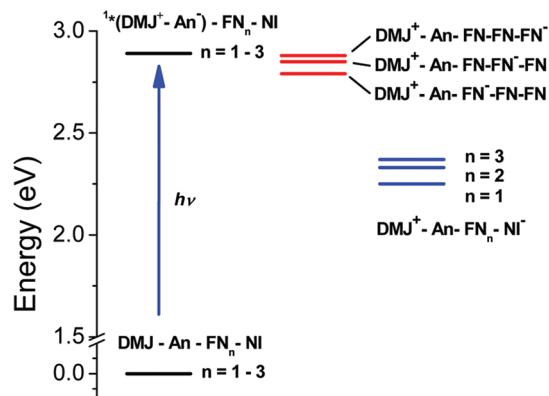


**Figure 3.** Energy levels for the electronic states relevant to the electron-transfer pathways for DMJ-An-FN<sub>n</sub>-NI ( $n = 1-3$ ), as determined by eq 5.

**Visible Transient Absorption Spectroscopy.** The data in Figure 3 show that the reaction  $\text{DMJ}^+\text{-An}^{\bullet-}\text{-FN}_n\text{-NI} \rightarrow \text{DMJ}^+\text{-An-FN}_n\text{-NI}$  leading to the reduction of the FN<sub>n</sub> bridge is exergonic for  $n = 1-3$ . To test this result, model compounds DMJ-An-FN<sub>n</sub> ( $n = 1, 2$ ) consisting of only the donor and bridge were studied. Their ground-state absorption spectra are shown in Figure S1 in the Supporting Information. DMJ-An-FN<sub>3</sub> proved to be very insoluble and was not examined. Femtosecond transient absorption spectra in toluene were recorded using 416 nm pulses to excite the charge-transfer band of DMJ-An.<sup>18</sup> The relative extinction coefficients of FN<sub>n</sub> ( $n = 1-3$ ) versus DMJ-An at 416 nm result in  $\sim 70\%$  selective excitation of DMJ-An. Since the energy of the lowest excited singlet state of DMJ-An is lower than those of FN<sub>n</sub> ( $n = 1-3$ ), energy transfer from FN<sub>n</sub> to DMJ-An likely occurred within the 150 fs IRF, as the transient spectra at the earliest time points strongly resemble that of  $\text{DMJ}^+\text{-An}^{\bullet-}$ , with a more intense band in the red ( $\lambda > 600$  nm) than in the blue ( $\lambda < 500$  nm).<sup>22</sup> The 3D data sets ( $\Delta A$  vs time and wavelength) were analyzed using global fitting to obtain the DADS that are shown in Figure 4 along with the spectroelectrochemical spectra for FN<sub>1</sub><sup>•-</sup> and FN<sub>2</sub><sup>•-</sup>. The DADS for DMJ-An-FN<sub>1</sub> shows two bands at  $\sim 485$  and 572 nm, while that for DMJ-An-FN<sub>2</sub> shows two bands at  $\sim 485$  and 606 nm. The band near 485 nm is assigned to  $\text{DMJ}^{\bullet+}$ ,<sup>22</sup> while the 572 and 606 nm bands are assigned to FN<sub>1</sub><sup>•-</sup> and FN<sub>2</sub><sup>•-</sup>, respectively, on the basis of the spectra of FN<sub>1</sub><sup>•-</sup> (560 nm) and FN<sub>2</sub><sup>•-</sup> (579 nm) determined by spectroelectrochemistry in DMF (Figure 4). The modest red shift of the transient absorption maximum of FN<sub>2</sub><sup>•-</sup> relative to that of FN<sub>1</sub><sup>•-</sup> (34 nm for the transient spectra in toluene and 19 nm for the spectroelectrochemical data in DMF) is consistent with the presence of an electronic interaction between the two FN bridge units within FN<sub>2</sub><sup>•-</sup>. The global fits yielded a charge-separation time constant ( $\tau_{\text{CS}}$ ) of 21 ps and a charge-recombination lifetime ( $\tau_{\text{CR}}$ ) of 6.0 ns for DMJ-An-FN<sub>1</sub> and gave  $\tau_{\text{CS}} = 30$  ps and  $\tau_{\text{CR}} = 3.9$  ns for DMJ-An-FN<sub>2</sub>.

Transient absorption measurements on DMJ-An-FN<sub>n</sub>-NI ( $n = 1-3$ ) were performed under the same conditions (Figure 5). The transient spectra show the formation of 480 nm ( $\epsilon =$

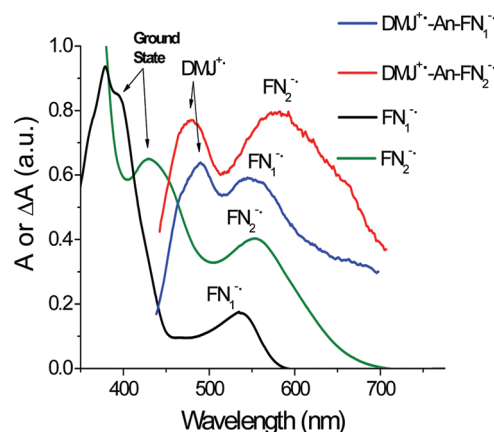


**Figure 4.** Spectroelectrochemical data of partially reduced FN<sub>1</sub> (black) and FN<sub>2</sub> (green) in DMF/0.1 M TBAPF<sub>6</sub> compared with the decay-associated difference spectra (DADS) obtained by singular value decomposition of the 3D transient absorption data sets ( $\Delta A$  vs time and wavelength) for DMJ-An-FN<sub>1</sub> (blue) and DMJ-An-FN<sub>2</sub> (red) in toluene.

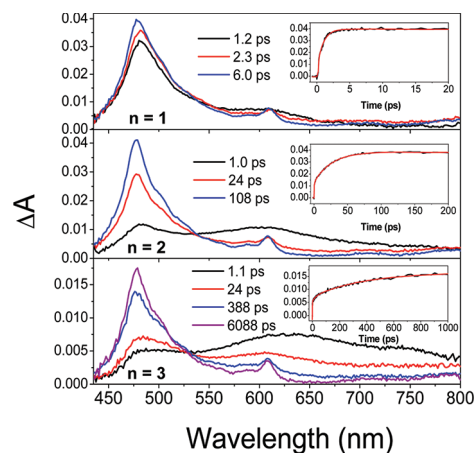


**Figure 5.** Transient absorption spectra of DMJ-An-FN<sub>n</sub>-NI ( $n = 1-3$ ) in toluene at 293 K at the indicated times following a 150 fs, 416 nm laser pulse. Insets: transient kinetics at 480 nm (black) and fits to the data (red).

$26\,000\text{ M}^{-1}\text{ cm}^{-1}$ ) and 610 nm ( $\epsilon = 7200\text{ M}^{-1}\text{ cm}^{-1}$ ) absorption bands characteristic of  $\text{NI}^{\bullet-}$ .<sup>23</sup> In comparison, the  $\text{DMJ}^{\bullet+}$  absorption at 485 nm is weak ( $\epsilon_{\text{max}} = 4500\text{ M}^{-1}\text{ cm}^{-1}$ )<sup>22</sup> and overlaps with that of  $\text{NI}^{\bullet-}$ , and therefore, it could not be observed distinctly. Additional broad features were observed at early times at wavelengths consistent with the formation of FN<sub>n</sub><sup>•-</sup> as determined by spectroelectrochemistry and femtosecond transient absorption spectroscopy of the model compounds without the NI acceptor. Once again, the 3D data sets were analyzed using global fitting to obtain the DADS (Figures S2 and S3 in the Supporting Information). The kinetic data associated with these spectra are given in Table 1. For DMJ-An-FN<sub>1</sub>-NI, the first charge-separation step (CS1) from  $\text{An}^{\bullet-}$  to FN<sub>1</sub> was too rapid to be resolved with our IRF.

Monitoring the appearance and decay of the  $\text{NI}^{\bullet-}$  absorption bands yielded the time constants for the second charge-separation step (CS2) from FN<sub>1</sub><sup>•-</sup> to NI (the defined effective charge-separation time) and charge recombination back to the ground state as  $\tau_{\text{CS2}} = 0.9$  ps and  $\tau_{\text{CR}} = 54$  ns, respectively. The charge-recombination time constants for all of the full D-B-A

Table 1. Electron-Transfer Time Constants

compound	$\tau_{CS1}$ (ps)	$\tau_{CS2}$ (ps)	$\tau_{CR}$ (ns)
DMJ-An-FN <sub>1</sub> -NI	–	0.9 ± 0.3	54 ± 1
DMJ-An-FN <sub>2</sub> -NI	5.6 ± 1.4	24 ± 3	420 ± 20
DMJ-An-FN <sub>3</sub> -NI	13 ± 1	334 ± 40	5000 ± 400
DMJ-An-FN <sub>1</sub>	21 ± 3	–	6.0 ± 0.2
DMJ-An-FN <sub>2</sub>	30 ± 3	–	3.9 ± 0.2

systems were determined using nanosecond transient absorption spectroscopy, as they are significantly longer than 3 ns.<sup>18</sup> For DMJ-An-FN<sub>n</sub>-NI ( $n = 2, 3$ ), CS1 could be resolved, giving  $\tau_{CS1} = 5.6$  ps for  $n = 2$  and 13 ps for  $n = 3$ . It should be noted here that  $\tau_{CS1}$  for DMJ-An-FN<sub>2</sub>-NI is faster than that for DMJ-An-FN<sub>2</sub>. Since the transient absorption maximum of FN<sub>2</sub><sup>•-</sup> is red-shifted relative to that of FN<sub>1</sub><sup>•-</sup>, there is some conjugation between the two FN bridge units within FN<sub>2</sub><sup>•-</sup>. Thus, attaching the NI acceptor to the second FN bridge unit can plausibly affect the electronic coupling between the FN units and the donor, thereby increasing the initial charge-separation rate in DMJ-An-FN<sub>2</sub>-NI. Kinetic analysis of the NI<sup>•-</sup> absorption bands showed that  $\tau_{CS2} = 24$  ps and  $\tau_{CR} = 420$  ns for DMJ-An-FN<sub>2</sub>-NI and  $\tau_{CS2} = 334$  ps and  $\tau_{CR} = 5$   $\mu$ s for DMJ-An-FN<sub>3</sub>-NI. Additionally, transient absorption measurements on DMJ-An-FN<sub>n</sub> ( $n = 1, 2$ ) and DMJ-An-FN<sub>n</sub>-NI ( $n = 1, 2$ ) were performed in THF under the same conditions as discussed above. The transient absorption spectra and kinetic analyses are shown in Figure S4 in the Supporting Information.

#### Femtosecond IR Transient Absorption Spectroscopy.

Visible pump/mid-IR probe spectroscopy was performed on DMJ-An-FN<sub>n</sub> ( $n = 1, 2$ ) and DMJ-An-FN<sub>2</sub>-NI as an additional check on whether bridge reduction occurs in these molecules. The data were obtained in THF because toluene is too absorptive in the 1500–1800 cm<sup>-1</sup> region. The data for DMJ-An-FN<sub>n</sub> ( $n = 1$  shown in Figure 6 and  $n = 2$  shown in

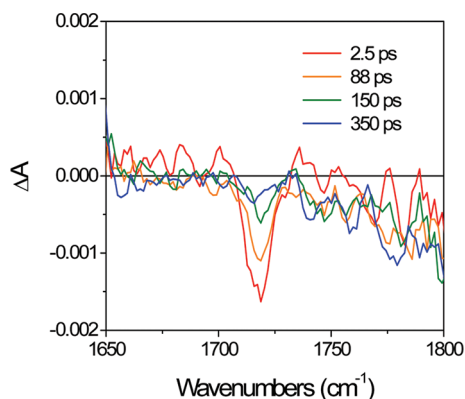


Figure 6. Femtosecond IR transient absorption spectra for DMJ-An-FN<sub>1</sub> in THF as a function of time following a 40 fs, 400 nm laser pulse.

Figure S5 in the Supporting Information) indicate that the 1720 cm<sup>-1</sup> carbonyl stretching band<sup>24</sup> of FN<sub>n</sub> is bleached with a time constant  $\tau = 1.3$  ps, which is longer than the 300 fs IRF of the apparatus. Therefore, the bleaching results from FN<sub>n</sub><sup>•-</sup> formation rather than <sup>1</sup>\*FN or <sup>1</sup>\*FN<sub>2</sub> formation. Charge recombination in DMJ<sup>+</sup>-An-FN<sub>n</sub><sup>•-</sup> occurs with  $\tau_{CR} = 120$  ps ( $n = 1$ ) and 170 ps ( $n = 2$ ). The transient IR data for DMJ-An-FN<sub>2</sub>-NI are shown in Figure 7 and the kinetics is presented in Figure S5. The 1720 cm<sup>-1</sup> bleaching appears with  $\tau_{CS1} = 1.1 \pm 0.5$  ps and decays with  $\tau_{CS2} = 19 \pm 4$  ps, which agrees to within

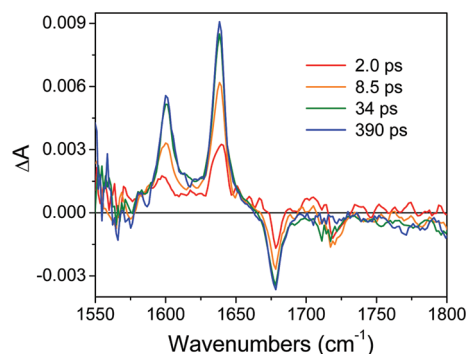


Figure 7. Femtosecond IR transient absorption spectra for DMJ-An-FN<sub>2</sub>-NI in THF as a function of time following a 40 fs, 400 nm laser pulse.

experimental error with the appearance of the absorption changes at 1600, 1640, and 1677 cm<sup>-1</sup> ( $\tau_{CS2} = 16.2 \pm 0.5$  ps) resulting from NI<sup>•-</sup> formation. The charge-separation rate constants in more polar THF are somewhat larger than those observed in less polar toluene and are in excellent agreement with the corresponding visible transient absorption spectra and kinetics in THF (Figure S4 in the Supporting Information).

## DISCUSSION

**Determining the  $\beta$  Value.** Femtosecond transient absorption measurements on DMJ-An-FN<sub>n</sub>-NI ( $n = 1-3$ ) at early times showed broad spectra consistent with the formation of FN<sub>n</sub><sup>•-</sup> followed by formation of the characteristic NI<sup>•-</sup> peaks. The DADS data (Figure S3 in the Supporting Information) revealed the sequence DMJ<sup>+</sup>-An<sup>-</sup>-FN<sub>n</sub>-NI → DMJ<sup>+</sup>-An-FN<sub>n</sub><sup>•-</sup>-NI → DMJ<sup>+</sup>-An-FN<sub>n</sub>-NI<sup>•-</sup> for  $n = 2$  and 3 but could not clearly separate a distinct FN<sup>•-</sup> spectrum for  $n = 1$ , although the early-time spectra for  $n = 1$  (Figure 5) suggested that FN<sup>•-</sup> may have been present in very low concentrations. Complementary femtosecond transient IR data confirmed that the FN<sub>n</sub><sup>•-</sup> bridge was reduced prior to NI reduction. A logarithmic plot of  $\tau_{CS2}$  versus the donor-acceptor distance ( $r_{D-A}$ ) is shown in Figure 8. The rate constant for electron arrival on NI decays exponentially with  $r_{D-A}$  with  $\beta = 0.34 \text{ \AA}^{-1}$ . This phenomenological  $\beta$  value cannot be attributed to the usual superexchange mechanism because the transient spectra show that stepwise electron transfer occurs in DMJ-An-FN<sub>n</sub>-NI ( $n = 2, 3$ , and most likely also  $n = 1$ ). In Figure 8 these data are compared with those obtained previously for the analogous

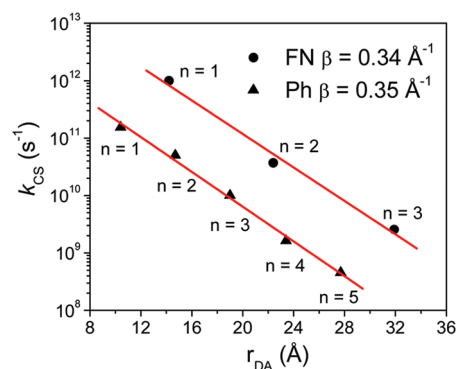


Figure 8. Plots of  $\ln k_{CS2}$  vs  $r_{DA}$  for DMJ-An-FN<sub>n</sub>-NI ( $n = 1-3$ ) and DMJ-An-Ph<sub>n</sub>-NI ( $n = 1-5$ ). The red lines are the linear fits to the data.

molecules having *p*-phenylene (Ph<sub>*n*</sub>) bridges.<sup>25</sup> The DMJ<sup>•+</sup>-An-Ph<sub>*n*</sub><sup>-•</sup>-NI states are all virtual, so electron transfer to NI occurs strictly by the coherent superexchange mechanism. Interestingly, the  $\beta$  value for the FN<sub>*n*</sub> bridge series is coincidentally nearly identical to that for the Ph<sub>*n*</sub> bridge series, even though experiment shows that the charge-separation mechanisms differ.

Since there is clear spectroscopic evidence of bridge reduction prior to electron arrival at the terminal acceptor in the DMJ-An-FN<sub>*n*</sub>-NI systems, it is logical to deduce that the electron is initially transferred from An<sup>-•</sup> to the nearest FN unit. While the demonstrated red shifts in the FN<sub>2</sub><sup>-•</sup> and FN<sub>3</sub><sup>-•</sup> transient spectra relative to that of FN<sup>-•</sup> indicate that the electron may be delocalized to a small degree beyond the first bridge unit, the delocalization is most likely modest because of the electrostatic attraction by DMJ<sup>•+</sup>. Since the individual bridge units are identical, we cannot experimentally differentiate between different FN sites. Nevertheless, by examining the data within the framework of several charge-hopping models, we can ascertain which of these models best describes the data.

As noted above, theory indicates that a significant phenomenological  $\beta$  value is possible for stepwise electron transfer if one or more of the following conditions is true: (1) the rates of charge hopping between independent bridge sites are the same but the rates of recombination to the donor and separation to the acceptor are significantly different; (2) the distance-dependent electrostatic attraction of the charges provides asymmetries in the forward and backward electron-hopping rates; and (3) significant electronic coupling between the bridge sites exists, which may cause injection of the electron onto the bridge to result in polaron formation.<sup>16</sup> For the molecules presented here, the modest red shift of the transient absorption maximum of FN<sub>2</sub><sup>-•</sup> relative to that of FN<sub>1</sub><sup>-•</sup> is consistent with some electronic interaction between the two FN bridge units within FN<sub>2</sub><sup>-•</sup>; however, the observed spectral changes are far smaller than those expected for a fully delocalized radical anion.<sup>26</sup> In addition,  $|\Delta G| \leq 0.06$  eV for electron transfer between FN bridge sites (Figure 3 and Table S2 in the Supporting Information), and the total reorganization energy  $\lambda = \lambda_s + \lambda_1$  is  $\sim 0.2$  eV because the solvent reorganization energy ( $\lambda_s$ ) for nonpolar toluene is approximately zero and the internal reorganization energy for electron transfer between FN bridge sites ( $\lambda_1$ ) is  $\sim 0.2$  eV (Table S3 in the Supporting Information). The resultant height of the activation barrier for electron transfer between FN bridge sites precludes substantial delocalization at room temperature. Thus, it is unlikely that polaron formation plays a significant role in the charge-transfer dynamics within DMJ-An-FN<sub>*n*</sub>-NI, so we will focus on unbiased and biased charge hopping between discrete FN sites to model the data.

**Unbiased Charge Hopping.** If bidirectional electron hopping between each pair of FN units occurs at the same rate ( $k_h$ ) and there is a substantial difference between the rates of charge removal from the bridge by recombination from the FN unit closest to the oxidized donor ( $k_{1,D}$ ) and charge transfer to the acceptor from the FN unit adjacent to it ( $k_{N,A}$ ) (Figure 9,  $k_1 = k_2 = k_h$ ), kinetic modeling<sup>14b</sup> predicts that

$$k_{ET} = \frac{k_h e^{-\Delta E_{DB}/k_B T}}{\frac{k_h}{k_{N,A}} + \frac{k_h}{k_{1,D}} + N - 1} \quad (6)$$

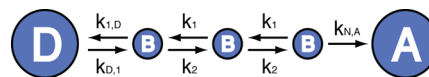


**Figure 9.** Kinetic schemes for the unbiased ( $k_1 = k_2 = k_h$ ) and biased ( $k_1 \gg k_2$ ) charge-hopping mechanisms following electron injection onto the bridge.  $k_h$  is the rate constant for electron hopping between adjacent bridge (B) units, while  $k_1$  and  $k_2$  are the electron-hopping rates toward the donor (D) and the acceptor (A), respectively.  $k_{1,D}$  is the rate constant for charge transfer to the donor from the bridge unit adjacent to it,  $k_{D,1}$  is the rate constant for charge transfer from the donor to the first bridge unit, and  $k_{N,A}$  is the rate constant for charge transfer to the acceptor from the bridge unit adjacent to it.

where  $\Delta E_{DB}$  is the energy change for charge injection from the donor to the first bridge site,  $k_B$  is Boltzmann's constant,  $T$  is the absolute temperature, and  $N$  is the number of bridge sites. The derivation of eq 6 using the conservation of flux can be found in the Supporting Information, eq 6 can be simplified to

$$k_{ET} = \frac{k_d e^{-\Delta E_{DB}/k_B T}}{1 + \frac{k_d}{k_h}(N - 1)} \quad (7)$$

where  $k_d = k_{1,D}k_{N,A}/(k_{1,D} + k_{N,A})$ . The numerator of eq 7 does not depend on distance, but the denominator does; therefore, when  $k_d(N-1)/k_h \ll 1$ , the standard series expansion of the exponential function gives

$$\frac{1}{1 + \frac{k_d}{k_h}(N - 1)} \approx e^{-k_d(N-1)/k_h} \quad (8)$$

Since  $N = 1 + R/r$ , where  $r$  is the distance between FN units and  $R$  is the overall distance over which the electron is transferred, eq 7 can be written as

$$k_{ET} = k_d e^{-\Delta E_{DB}/k_B T} e^{-k_d R/k_h r} \quad (9)$$

which gives  $\beta = k_d/k_h r$  and  $k_h = k_d/\beta r$ . The data for DMJ-An-FN<sub>1</sub> and DMJ-An-FN<sub>1</sub>-NI give  $1/\tau_{CR} = k_{1,D} = 1.7 \times 10^8$  s<sup>-1</sup> and  $1/\tau_{CS2} = k_{N,A} = 1.1 \times 10^{12}$  s<sup>-1</sup>, respectively, which in turn yield  $k_d = 1.7 \times 10^8$  s<sup>-1</sup>. Since the FN-FN distance is  $r = 8$  Å and the measured value of  $\beta$  is  $0.34$  Å<sup>-1</sup>, this model predicts that  $k_h = 6.3 \times 10^7$  s<sup>-1</sup>. However, the observed rates of electron arrival on NI ( $1/\tau_{CS2}$ ) in DMJ-An-FN<sub>2</sub>-NI and DMJ-An-FN<sub>3</sub>-NI far exceed this predicted charge-hopping rate. Since the electron removal rates at the two ends of the bridge are substantially different, the failure of this simple kinetic model to describe the data indicates that the assumption of equal forward and backward hopping rates between the bridge sites is not fulfilled.

**Biased Charge Hopping.** As a result of the electrostatic attraction of DMJ<sup>•+</sup> during electron transfer from An<sup>-•</sup> to individual FN<sub>*n*</sub> bridge units and ultimately to NI, the system can be described in terms of an asymmetric random walk.<sup>27</sup> The kinetic scheme is illustrated in Figure 9 ( $k_1 \neq k_2$ ) and involves a treatment similar to that of the unbiased hopping model given above except that the rates of site-to-site hopping toward ( $k_1$ ) and away ( $k_2$ ) from the donor are assumed to be different. In this case,  $k_{ET}$  is given by

$$k_{ET} = \frac{k_1 e^{(-\Delta E_{DB}/k_B T)}}{\alpha} \xi^{R/r} = \frac{k_1 e^{(-\Delta E_{DB}/k_B T)}}{\alpha} e^{(R/r \ln \xi)} \quad (10)$$



where  $\alpha = k_1/k_{N,A} - 1/(\xi - 1)$  and  $\xi = k_2/k_1$  and it is assumed that  $k_1 \gg k_2$  because in the case of electrostatic attraction, the rate of electron hopping toward the positively charged donor ( $k_1$ ) is usually larger than that for hopping toward the neutral acceptor ( $k_2$ ) (see the Supporting Information for the derivation). Comparison of eq 10 with the standard exponential distance dependence in eq 4 yields

$$\beta = -\frac{1}{r} \ln\left(\frac{k_2}{k_1}\right) \quad (11)$$

In this case, the rate constant for the electron-transfer process is also characterized by an exponential distance dependence. Using eq 11 with  $r = 8 \text{ \AA}$  and  $\beta = 0.34 \text{ \AA}^{-1}$ , one calculates  $k_1/k_2 \approx 15$ . The free energy changes for moving the electron from the first FN<sup>•-</sup> to the other two FN sites in the presence of DMJ<sup>•+</sup> for the series DMJ<sup>•+</sup>-An-FN<sup>•-</sup>-FN-FN  $\rightarrow$  DMJ<sup>•+</sup>-An-FN-FN<sup>•-</sup>-FN  $\rightarrow$  DMJ<sup>•+</sup>-An-FN-FN-FN<sup>•-</sup> are  $\Delta G = 0.06$  and  $0.03$  eV, respectively (Table S2 in the Supporting Information). Thus, at room temperature, the expected values of  $k_1/k_2 \approx e^{-\Delta G/k_B T}$  are 11 and 3.3, which are within an order of magnitude of the charge-hopping rate ratio predicted using the observed  $\beta$  value and the biased hopping model.

## CONCLUSIONS

With the use of femtosecond transient absorption spectroscopy in the visible and mid-IR regions, the D-B-A systems studied here allowed us unequivocally to observe stepwise electron transfer while measuring an exponential distance dependence of the rate for the overall charge-separation reaction. The observed exponential distance dependence is attributed to electron injection onto the first FN unit followed by subsequent charge hopping within the FN<sub>n</sub> bridge biased by the electrostatic attraction of the charge on DMJ<sup>•+</sup>, with ultimate trapping at NI. This unusually high  $\beta$  value is likely a result of DMJ-An being a push-pull donor, where the charge-transfer excited state that is populated upon photoexcitation is dominated by a fully charge-separated radical ion pair state, DMJ<sup>•+</sup>-An<sup>•-</sup>.<sup>17</sup> The ultrafast formation of DMJ<sup>•+</sup> provides an electrostatic attraction that slows electron injection from An<sup>•-</sup> to the bridge and the subsequent electron hopping along the FN units to the NI trap site. These results show that D-B-A molecules designed to have stepwise, energetically downhill redox gradients do not necessarily exhibit wirelike behavior. Moreover, they highlight the need for a thorough knowledge of the mechanistic details of charge transport in D-B-A molecules that are utilized in systems for solar energy conversion and organic electronics, where wirelike properties are targeted.

## ASSOCIATED CONTENT

### Supporting Information

Details regarding the synthesis and characterization of DMJ-An-FN<sub>n</sub>, redox potentials, absorption spectra, visible and IR transient absorption data, and derivations of eqs 6 and 10. This material is available free of charge via the Internet at <http://pubs.acs.org>.

## AUTHOR INFORMATION

### Corresponding Author

m-wasielewski@northwestern.edu; co@northwestern.edu

### Notes

The authors declare no competing financial interest.

## ACKNOWLEDGMENTS

This work was supported by the Chemical Sciences, Geosciences, and Biosciences Division, Office of Basic Energy Sciences, U.S. Department of Energy, under Grant DE-FG02-99ER14999. The authors thank Dr. Anton Trifonov for his help in assembling the femtosecond transient IR instrument.

## REFERENCES

- Weiss, E. A.; Wasielewski, M. R.; Ratner, M. A. *Top. Curr. Chem.* **2005**, *257*, 103–133.
- (a) Jortner, J.; Bixon, M.; Langenbacher, T.; Michel-Beyerle, M. E. *Proc. Natl. Acad. Sci. U.S.A.* **1998**, *95*, 12759–12765. (b) Lewis, F. D.; Wu, T.; Zhang, Y.; Letsinger, R. L.; Greenfield, S. R.; Wasielewski, M. R. *Science* **1997**, *277*, 673–676.
- Gray, H. B.; Winkler, J. R. *Proc. Natl. Acad. Sci. U.S.A.* **2005**, *102*, 3534–3539.
- Kobori, Y.; Yamauchi, S.; Akiyama, K.; Tero-Kubota, S.; Imahori, H.; Fukuzumi, S.; Norris, J. R. Jr. *Proc. Natl. Acad. Sci. U.S.A.* **2005**, *102*, 10017–10022.
- (a) Hush, N. S.; Paddon-Row, M. N.; Cotsaris, E.; Oevering, H.; Verhoeven, J. W.; Heppener, M. *Chem. Phys. Lett.* **1985**, *117*, 8–11. (b) Paulson, B. P.; Miller, J. R.; Gan, W. X.; Closs, G. J. *Am. Chem. Soc.* **2005**, *127*, 4860–4868.
- (a) Weiss, E. A.; Ahrens, M. J.; Sinks, L. E.; Gusev, A. V.; Ratner, M. A.; Wasielewski, M. R. *J. Am. Chem. Soc.* **2004**, *126*, 5577–5584. (b) Goldsmith, R. H.; Sinks, L. E.; Kelley, R. F.; Betzen, L. J.; Liu, W.; Weiss, E. A.; Ratner, M. A.; Wasielewski, M. R. *Proc. Natl. Acad. Sci. U.S.A.* **2005**, *102*, 3540–3545. (c) Davis, W. B.; Svec, W. A.; Ratner, M. A.; Wasielewski, M. R. *Nature* **1998**, *396*, 60–63. (d) Albinsson, B.; Eng, M. P.; Pettersson, K.; Winters, M. U. *Phys. Chem. Chem. Phys.* **2007**, *9*, 5847–5864. (e) Winters, M. U.; Dahlstedt, E.; Blades, H. E.; Wilson, C. J.; Frampton, M. J.; Anderson, H. L.; Albinsson, B. *J. Am. Chem. Soc.* **2007**, *129*, 4291–4297.
- McConnell, H. M. *J. Chem. Phys.* **1961**, *35*, 508–515.
- (a) Marcus, R. A. *J. Chem. Phys.* **1965**, *43*, 679–701. (b) Jortner, J. *J. Chem. Phys.* **1976**, *64*, 4860–4867. (c) Hopfield, J. J. *Proc. Natl. Acad. Sci. U.S.A.* **1974**, *71*, 3640–3644.
- Bixon, M.; Jortner, J. *Adv. Chem. Phys.* **1999**, *106*, 3.
- Berlin, Y. A.; Hutchison, G. R.; Rempala, P.; Ratner, M. A.; Michl, J. *J. Phys. Chem. A* **2003**, *107*, 3970–3980.
- (a) Lembo, A.; Tagliatesta, P.; Guldi, D. M.; Wielopolski, M.; Nuccetelli, M. *J. Phys. Chem. A* **2009**, *113*, 1779–1793. (b) Wielopolski, M.; Atienza, C.; Clark, T.; Guldi, D. M.; Martin, N. *Chem.—Eur. J.* **2008**, *14*, 6379–6390. (c) Eng, M. P.; Martensson, J.; Albinsson, B. *Chem.—Eur. J.* **2008**, *14*, 2819–2826.
- (a) Paddon-Row, M. N.; Oliver, A. M.; Warman, J. M.; Smit, K. J.; de Haas, M. P.; Oevering, H.; Verhoeven, J. W. *J. Phys. Chem.* **1988**, *92*, 6958–6962. (b) Roest, M. R.; Oliver, A. M.; Paddon-Row, M. N.; Verhoeven, J. W. *J. Phys. Chem. A* **1997**, *101*, 4867–4871. (c) Lafalet, F.; Welter, S.; Popovic, Z.; De Cola, L. *J. Mater. Chem.* **2005**, *15*, 2820–2828.
- (a) Atienza-Castellanos, C.; Wielopolski, M.; Guldi, D. M.; van der Pol, C.; Bryce, M. R.; Filippone, S.; Martin, N. *Chem. Commun.* **2007**, 5164–5166. (b) Eng, M. P.; Albinsson, B. *Angew. Chem., Int. Ed.* **2006**, *45*, 5626–5629. (c) Giacalone, F.; Segura, J. L.; Martin, N.; Ramey, J.; Guldi, D. M. *Chem.—Eur. J.* **2005**, *11*, 4819–4834.
- (a) Grozema, F. C.; Tonzani, S.; Berlin, Y. A.; Schatz, G. C.; Siebbeles, L. D. A.; Ratner, M. A. *J. Am. Chem. Soc.* **2008**, *130*, 5157–5166. (b) Berlin, Y. A.; Grozema, F. C.; Siebbeles, L. D. A.; Ratner, M. A. *J. Phys. Chem. C* **2008**, *112*, 10988–11000. (c) Grozema, F. C.; Berlin, Y. A.; Siebbeles, L. D. A.; Ratner, M. A. *J. Phys. Chem. B* **2010**, *114*, 14564–14571.
- (a) Goldsmith, R. H.; DeLeon, O.; Wilson, T. M.; Finkelstein-Shapiro, D.; Ratner, M. A.; Wasielewski, M. R. *J. Phys. Chem. A* **2008**, *112*, 4410–4414. (b) Albinsson, B.; Martensson, J. *J. Photochem. Photobiol., C* **2008**, *9*, 138–155.
- (a) Henderson, P. T.; Jones, D.; Hampikian, G.; Kan, Y.; Schuster, G. B. *Proc. Natl. Acad. Sci. U.S.A.* **1999**, *96*, 8353–8358.

- (b) Conwell, E. M. *Proc. Natl. Acad. Sci. U.S.A.* **2005**, *102*, 8795–8799.
- (c) Conwell, E. M.; Rakhmanova, S. V. *Proc. Natl. Acad. Sci. U.S.A.* **2000**, *97*, 4556–4560. (d) Kucherov, V. M.; Kinz-Thompson, C. D.; Conwell, E. M. *J. Phys. Chem. C* **2010**, *114*, 1663–1666.
- (17) Lockard, J. V.; Ricks, A. B.; Co, D. T.; Wasielewski, M. R. *J. Phys. Chem. Lett.* **2010**, *1*, 215–218.
- (18) Scott, A. M.; Ricks, A. B.; Colvin, M. T.; Wasielewski, M. R. *Angew. Chem., Int. Ed.* **2010**, *49*, 2904–2908.
- (19) Giaimo, J. M.; Gusev, A. V.; Wasielewski, M. R. *J. Am. Chem. Soc.* **2002**, *124*, 8530–8531.
- (20) Dance, Z. E. X.; Ahrens, M. J.; Vega, A. M.; Ricks, A. B.; McCamant, D. W.; Ratner, M. A.; Wasielewski, M. R. *J. Am. Chem. Soc.* **2008**, *130*, 830–832.
- (21) Uckert, F.; Setayesh, S.; Müllen, K. *Macromolecules* **1999**, *32*, 4519–4524.
- (22) Okada, T.; Fujita, T.; Kubota, M.; Masaki, S.; Mataga, N.; Ide, R.; Sakata, Y.; Misumi, S. *Chem. Phys. Lett.* **1972**, *14*, 563–568.
- (23) Gosztola, D.; Niemczyk, M. P.; Svec, W.; Lukas, A. S.; Wasielewski, M. R. *J. Phys. Chem. A* **2000**, *104*, 6545–6551.
- (24) Tanaka, S.; Kato, C.; Horie, K.; Hamaguchi, H. *Chem. Phys. Lett.* **2003**, *381*, 385–391.
- (25) Scott, A. M.; Miura, T.; Ricks, A. B.; Dance, Z. E. X.; Giacobbe, E. M.; Colvin, M. T.; Wasielewski, M. R. *J. Am. Chem. Soc.* **2009**, *131*, 17655–17666.
- (26) (a) Fujitsuka, M.; Tojo, S.; Shinmyozu, T.; Majima, T. *Chem. Commun.* **2009**, 1553–1555. (b) Lue, J.-M.; Rosokha, S. V.; Kochi, J. K. *J. Am. Chem. Soc.* **2003**, *125*, 12161–12171. (c) Nelsen, S. F.; Konradsson, A. E.; Weaver, M. N.; Telo, J. P. *J. Am. Chem. Soc.* **2003**, *125*, 12493–12501. (d) Penneau, J. F.; Stallman, B. J.; Kasai, P. H.; Miller, L. L. *Chem. Mater.* **1991**, *3*, 791–796. (e) Shida, T.; Iwata, S. *J. Chem. Phys.* **1972**, *56*, 2858–2864.
- (27) Bar-Haim, A.; Klafter, J. *J. Chem. Phys.* **1998**, *109*, 5187–5193.

## Appendix A3

### **Flavin-induced DNA photooxidation and charge movement probed by ultrafast transient absorption spectroscopy**

*Matthias Wenninger\*, Danila Fazio\*, Uwe Megerle, Christian Trindler,  
Stefan Schiesser, Eberhard Riedle, Thomas Carell*

ChemBioChem 2011, 12, 703-706

\* these authors contributed equally to the work



DOI: 10.1002/cbic.201000730

## Flavin-Induced DNA Photooxidation and Charge Movement Probed by Ultrafast Transient Absorption Spectroscopy

 Matthias Wenninger,<sup>[a]</sup> Danila Fazio,<sup>[b]</sup> Uwe Megerle,<sup>[a]</sup> Christian Trindler,<sup>[b]</sup> Stefan Schiesser,<sup>[b]</sup> Eberhard Riedle,<sup>[a]</sup> and Thomas Carell<sup>\*[b]</sup>

Charge-transfer processes through DNA have been intensively investigated over recent years with the aid of a variety of methods and model systems.<sup>[1–6]</sup> It is now well established that a positive charge moves through the duplex by a hopping mechanism, using the purine bases—and here particularly dG—as stepping stones.<sup>[7]</sup> Under ideal conditions a positive charge can hop over more than 200 bp before it is trapped.<sup>[8]</sup> In contrast, an excess electron, which introduces a negative charge into the duplex, hops through the double strand only over about 10–20 bp, with the pyrimidine bases acting as stepping stones in this case.<sup>[9–16]</sup>

In nature, FAD and FMN cofactors, in the oxidized state, are known to photooxidize duplex DNA, which leads to severe oxidative DNA damage, particularly at guanine sites.<sup>[17–18]</sup> The fact that UV-A or visible light causes mutations<sup>[19]</sup> even though DNA features no absorption in this wavelength region is thought to be the result of such flavin-cofactor-mediated DNA photooxidation processes.<sup>[20]</sup>

Detailed information on the dynamics and lifetime of flavin-dependent photooxidation of DNA as the basis for UV-A photocarcinogenesis can be obtained from ultrafast UV/Vis spectroscopy.<sup>[21]</sup> We therefore synthesized and investigated a series of DNA hairpins to gain insight into the flavin-triggered photooxidation of selected DNA sequences. For the study the DNA hairpins depicted in Figure 1 were prepared. All feature the flavin derivative **1** as a capping structure stacking on top of the hairpins.<sup>[22]</sup>

Melting point measurements were performed to ensure that the hairpins (**H1–H7** and **HT1**) are fully closed at room temperature (see the Supporting Information). CD spectra show that the hairpins each adopt a B-type DNA double-helix structure (Supporting Information). The hairpins each feature a strong absorption below 280 nm due to the absorption of the DNA bases. The absorption maxima at 360 nm and 450 nm correspond to flavin transitions and allow the selective excitation of the covalently bound chromophore. The intensity of the flavin fluorescence at 550 nm is sequence-dependent.

[a] M. Wenninger,<sup>\*</sup> U. Megerle, Prof. Dr. E. Riedle  
Fakultät für Physik, Lehrstuhl für BioMolekulare Optik  
Ludwigs-Maximilians-Universität München  
Oettingenstrasse 67, 80538 München (Germany)  
Fax: (+49) 89-2180-9202

[b] D. Fazio,<sup>\*</sup> C. Trindler, S. Schiesser, Prof. Dr. T. Carell  
Department of Chemistry, Ludwigs-Maximilians-Universität München  
Butenandtstrasse 5–13, 81377 München (Germany)  
Fax: (+49) 89-2189-77756  
E-mail: thomas.carell@cup.uni-muenchen.de

[\*] These authors contributed equally to this work.

Supporting information for this article is available on the WWW under <http://dx.doi.org/10.1002/cbic.201000730>.

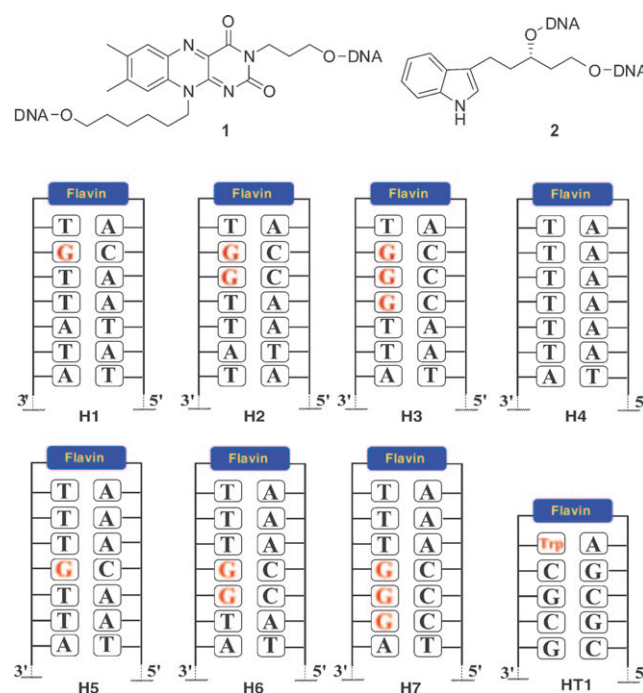


**Figure 1.** Structures of the DNA hairpins **H1–H7**, of the flavin derivative **1** used as cap, and of the tryptophan derivative **2** introduced into hairpin **HT1**.

In the first hairpin series **H1–H3** we introduced one AT base pair between the dG electron donors and the flavin acceptor cap. In addition we used either a (dG)<sub>2</sub> (**H2**) or even a (dG)<sub>3</sub> (**H3**) sequence rather than a single dG as the electron-donating unit. It is known that the electron donation capabilities of adenines<sup>[23–24]</sup> are lower than those of guanines and that for guanines they increase with the number of dG bases in a row.<sup>[25–30]</sup> As a reference duplex we synthesized **H4**, containing a flavin cap and no dG base. Relative to the fluorescence intensity measured for compound **1**, the fluorescence was found to be quenched in all hairpins. The strongest flavin fluorescence was measured for the reference duplex **H4**, but even here the detected fluorescence is significantly lower than that of the free flavin **1**. This suggests that the oxidation potential of the excited-state flavin is high enough to oxidize both dG and dA bases, yielding the flavin radical anion and the dA and dG radical cations.<sup>[31]</sup>

The photoinduced dynamics of the hairpin structures with the flavin cap were measured with a femtosecond broadband pump-probe setup.<sup>[32]</sup> The sample solutions were irradiated with a sub-50 fs pulse at 480 nm to excite the flavin selectively and were probed with a white light pulse to obtain the transi-

ent absorption in the spectral region between 300 and 750 nm up to delay times of 1 ns. The transient spectra of all hairpins each consist of three major contributions that can be assigned to flavin transitions (Figure 2A). Two bands with negative tran-

signal of the stimulated emission has decayed to 1/e of the initial value at  $\Delta t=0$ . The 1/e time constants that are compiled in Table 1 were found to be suitable for a consistent classification of the ET dynamics.

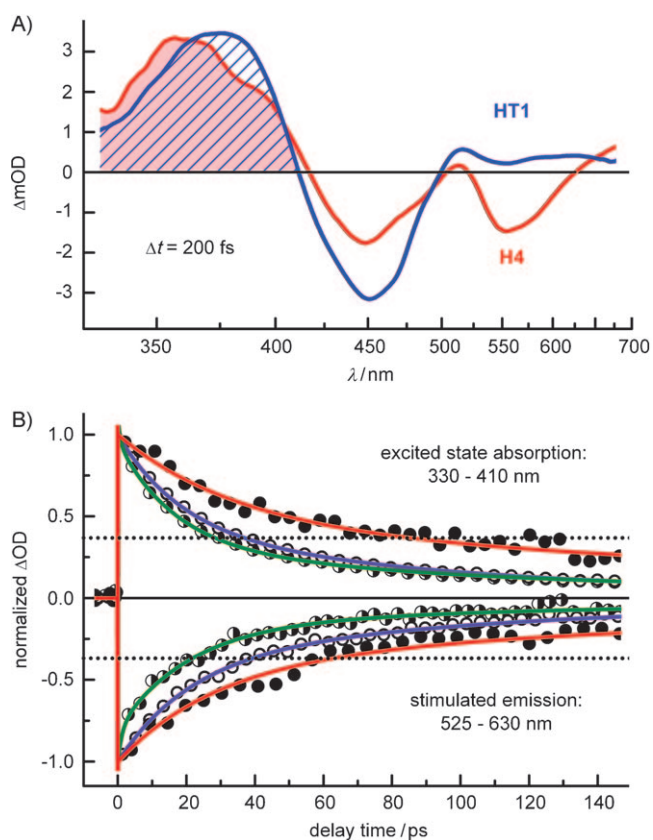


**Figure 2.** A) Transient absorption spectrum at  $\Delta t=200$  fs of the hairpins **H4** ( $S_1$  state of flavin) and **HT1** (flavin radical anion). B) Decay of the transient signal integrated over the spectral region of the excited state absorption (top) and of the stimulated emission (bottom). Red: **H4**, violet: **H1**, green: **H2**; dotted lines: 1/e level of the initial amplitude.

sient absorption indicate the ground-state bleach (around 450 nm) and the stimulated emission (around 550 nm) of the flavin. These bands are partially overlaid with the excited state absorption, which contributes a positive absorption change and has a prominent maximum around 370 nm.

For the free flavin compound **1**, the transient signatures decay monoexponentially with a fluorescence lifetime of  $\tau=2$  ns (Supporting Information). The decay dynamics of the flavin cap in the hairpin structures are governed by the ultrafast electron transfer (ET) from the bases, which quenches the singlet excited state of flavin. The observed dynamics are more complex and require multiexponential fits.<sup>[33]</sup> Typically, two to three exponential terms and one constant signal lasting beyond the measurement range were necessary for a good parametrization of the data (Supporting Information). The complexity of the quenching dynamics prohibits the full and direct interpretation of the obtained time constants. Instead, we used the fit curves to determine the delay times when the

Sample	$\tau_{1/e}$ [ps]	$\Phi_{cs}$ [%]	Sample	$\tau_{1/e}$ [ps]	$\Phi_{cs}$ [%]
<b>H1</b>	$38 \pm 2$	$< 0.5$	<b>H2</b>	$26 \pm 4$	$< 0.5$
<b>H3</b>	$26 \pm 1$	$< 0.5$	<b>H4</b>	$63 \pm 3$	$< 0.5$
<b>H5</b>	$49 \pm 3$	$3 \pm 1$	<b>H6</b>	$50 \pm 3$	$7 \pm 1$
<b>H7</b>	$52 \pm 3$	$14 \pm 1$	<b>HT1</b>	$0.10 \pm 0.05$	0

The hairpins **H1–H7** show very similar dynamics, both in the stimulated emission and in the absorption band (see Figure 2B). The first result of this study is therefore that the charge recombination, which takes place in the Coulomb field established by the  $Fl^-$  and  $dA^+/dG^+$  ions, is faster than the initial forward ET process. In order to measure the hidden charge recombination rate we replaced the electron-donating dG unit by a more strongly donating tryptophan unit.<sup>[34]</sup> To ensure proper closing of the hairpin, which we found to be too unstable otherwise, we had to insert additional dG:dC base pairs in the stem. In the hairpin **HT1**, we indeed measured an extremely fast forward ET within 100 fs, allowing us to determine the rate of charge recombination as about 1 ps. This experiment also allowed us to identify the spectral signature of the flavin radical anion (see Figure 2A). The main difference from the flavin  $S_1$  spectrum is the missing stimulated emission around 550 nm. The excited state absorption of the radical around 370 nm is similar to the  $S_1$  absorption in strength but appears slightly red-shifted.

In the hairpin structure **H1**, the ET leads to the decay of the flavin excited state on a timescale of 38 ps. If we replace the single dG base by a  $(dG)_2$  or  $(dG)_3$  sequence, the decay time is shorter (26 ps), indicating that the ET is now slightly faster, in agreement with the fact that dG bases stacked in homo-dG sequences possess a reduced oxidation potential.

As with the steady-state fluorescence experiments, we observe that the flavin excited singlet state still decays rather quickly even in the dG-free reference hairpin **H4**. Here, the electron is donated by the dA base. The time constant for this process is 63 ps, and hence only slightly longer than in the dG-containing hairpins (26 ps), showing that dA photooxidation by the excited flavin is slower only by a factor of two to three.

From the short flavin–donor distances we can safely assume that the ET process in the first hairpin series is governed by a direct superexchange-based mechanism, in which the charges do not hop over intermediate charge carriers but are directly transferred from the dG nucleobases to the excited flavin and back.<sup>[35–36]</sup> This direct-ET-based situation changes totally in the hairpin series **H5–H7**, in which a  $(dA:dT)_3$  cassette is situated between the hairpin cap and one, two, or three dG electron donors.<sup>[25]</sup> Over the rather large distance of 13.5 Å between the flavin and the first dG base, electron donation is now dominat-



ed by a hopping mechanism.<sup>[35,37]</sup> For all three hairpins we find identical  $S_1$  decay timescales of 50 ps, not affected by the number of dG bases. We believe that in these systems the charges hop through the spacing dA:dT sequence and that this hopping rate is now governing the rate of flavin photo-reduction. The rate of electron donation from the (dG)<sub>n</sub> bases to a putative dA<sup>+</sup> hopping intermediate is clearly slower. The data therefore show that the charge-hopping reaction is slower than electron donation from a dG to a close dA<sup>+</sup>.

The (dA:dT)<sub>3</sub> cassette used as a spacer has another important consequence: in the hairpins **H5–H7** we do not observe a complete charge recombination but a partial escape of the injected positive charge. The positive charge in the (dA:dT)<sub>3</sub> cassette hops to the adjacent (dG:dC)<sub>n</sub> cassette. From there, charge recombination is substantially slower because the electron has moved out of the Coulomb field of the flavin radical anion. This process leads to the formation of a long-lived, charge-separated state. Most interestingly, the yield of formation of the charge-separated state is influenced by the number of stacking dG bases. To determine the quantum yield of the long-lived charge separation we decomposed the transient absorption spectra at  $\Delta t = 1$  ns into a residual contribution from the flavin  $S_1$  state and the flavin radical anion spectrum known from **HT1**. The integral of the flavin radical signature between 330 nm and 410 nm (Figure 3, shaded area) was used to quantify the quantum yield of the long-lived charge separation. In the hairpin **H5**, with just one dG electron donor, about 3% of the flavin is still in the radical anion state at  $\Delta t = 1$  ns. In **H6**, with a (dG:dC)<sub>2</sub> sequence, the amount has increased to 7% and in hairpin **H7**, possessing a (dG:dC)<sub>3</sub> sequence, we even find a fivefold increase to 14% (Table 1).

In summary, by using short-time spectroscopy we were able to decipher the dynamics of flavin-induced photooxidation of DNA, which is one factor contributing to UV-A-induced photocarcinogenesis.<sup>[38–39]</sup> We were able to show that long-lived, charge-separated states can be created in particular sequences by using flavin as photooxidant.<sup>[25]</sup> This requires fast forward electron transfer by hopping through dA:dT sequences followed by charge trapping in dG:dC sequences.

## Experimental Section

**DNA synthesis and purification:** The synthesis of the oligonucleotides containing the flavin *H*-phosphonate was performed with an Expedite 8900 DNA synthesizer and use of a mixed phosphoramidite/*H*-phosphonate/phosphoramidite coupling protocol. For full oxidation of the flavin an additional oxidation step was necessary at the end of the synthesis: I<sub>2</sub> in MeCN and *N*-methylmorpholine in water were used as the first oxidation solution and I<sub>2</sub> in MeCN and NEt<sub>3</sub> in water as the second one. Oligonucleotides were cleaved from the solid support and deprotected by use of conc. ammonia/ethanol 3:1 for 20 h at room temperature. Analytical and preparative HPLC were performed on C<sub>18</sub> reversed-phase columns (Macherey–Nagel) with NH<sub>4</sub>Et<sub>3</sub>OAc (0.1 M) in water/acetonitrile as eluent. The strands were further characterized by MALDI-TOF-MS. MALDI spectra were recorded with a Bruker Autoflex mass spectrometer with 3-hydroxypicolinic acid as matrix substance and measurement in negative polarity mode.

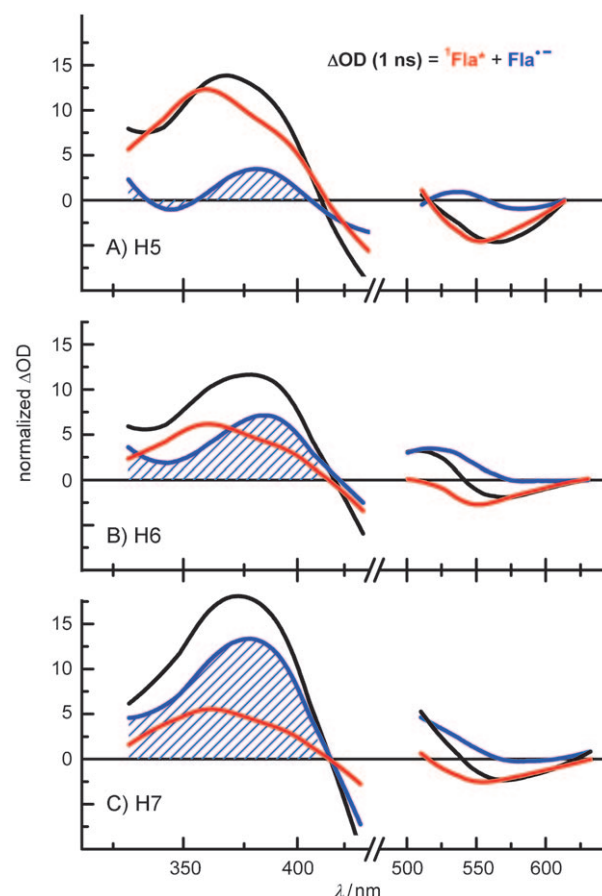


**Figure 3.** Decomposition of the transient absorption spectrum at  $\Delta t = 1$  ns (black line): the residual contribution from the  $S_1$  state of flavin (from  $\Delta t < 200$  fs, red line) is subtracted to obtain the contribution from the long-lived radical anion of flavin (blue line). The spectra were normalized to the initial amplitude directly after excitation.

**Melting point experiments:** Melting temperatures ( $T_m$ ) were measured with a Cary 100 UV/Vis spectrometer and 1 mL quartz cuvettes with 1 cm pathlength. Absorptions of equimolar DNA complements [3  $\mu$ M in NaCl (150 mM), Tris-HCl (10 mM, pH 7.4)] were measured at 260 nm. For every strand four temperature cycles from 5 to 90 °C were recorded; the average melting points are depicted in the Supporting Information.

**CD experiments:** CD spectra were recorded at room temperature with a Jasco J-810 spectropolarimeter fitted with a Peltier temperature controller and with 1 mL quartz cuvettes with 1 cm pathlength. The samples contained NaCl (150 mM), Tris-HCl (10 mM, pH 7.4), and the hairpin structures (3  $\mu$ M).

**Femtosecond transient absorption:** The femtosecond broadband pump-probe setup has been described in detail elsewhere.<sup>[32]</sup> Briefly, a Ti:sapphire amplifier system (CPA 2001, Clark-MXR) with a repetition rate of 1 kHz was used to pump a noncollinear optical parametric amplifier delivering pump pulses at  $\lambda = 480$  nm with a length of 40 fs. The pump pulses were focused into a 250  $\mu$ m flow cell containing the cooled sample (10 °C) with a spot size of 150  $\mu$ m. The pump energy was limited to  $< 1$   $\mu$ J to avoid nonlinear effects. A supercontinuum (300–750 nm) was generated and used as probe by focusing another part of the Ti:sapphire laser into a rotating CaF<sub>2</sub> disk. The polarizations of the pump and probe pulses were set to the magic angle (54.7°). After the interaction in the

sample, the probe light was dispersed with a fused silica prism and detected with a 512 pixel photodiode array. The chirp of the white light was corrected for prior to data analysis, and the resulting temporal resolution was better than 100 fs.

## Acknowledgements

We thank the SFB 749 and the Excellence Cluster NIM (Nano Initiative Munich). M.W. thanks the GRK 1626 Chemical Photocatalysis for a fellowship.

**Keywords:** charge transfer · DNA · flavins · oxidative damage · photomutagenesis

- [1] J. C. Genereux, J. K. Barton, *Chem. Rev.* **2010**, *110*, 1642–1662.
- [2] B. Giese, *Annu. Rev. Biochem.* **2002**, *71*, 51–70.
- [3] G. B. Schuster, *Acc. Chem. Res.* **2000**, *33*, 253–260.
- [4] F. D. Lewis, R. L. Letsinger, M. R. Wasielewski, *Acc. Chem. Res.* **2000**, *33*, 159–170.
- [5] M. Pavanello, L. Adamowicz, M. Volobuyev, B. Mennucci, *J. Phys. Chem. B* **2010**, *114*, 4416–4423.
- [6] T. Takada, M. Fujitsuka, T. Majima, *Proc. Natl. Acad. Sci. USA* **2007**, *104*, 11179–11183.
- [7] B. Giese, J. Amaudrut, A.-K. Kohler, M. Spormann, S. Wessely, *Nature* **2001**, *412*, 318–320.
- [8] M. E. Núñez, D. B. Hall, J. K. Barton, *Chem. Biol.* **1999**, *6*, 85–97.
- [9] C. Behrens, T. Carell, *Chem. Commun.* **2003**, 1632–1633.
- [10] S. Breeger, U. Hennecke, T. Carell, *J. Am. Chem. Soc.* **2004**, *126*, 1302–1303.
- [11] H. A. Wagenknecht, *Angew. Chem.* **2003**, *115*, 2558–2565; *Angew. Chem. Int. Ed.* **2003**, *42*, 2454–2460.
- [12] P. Daublain, A. K. Thazhathveetil, Q. Wang, A. Trifonov, T. Fiebig, F. D. Lewis, *J. Am. Chem. Soc.* **2009**, *131*, 16790–16797.
- [13] K. Siegmund, P. Daublain, Q. Wang, A. Trifonov, T. Fiebig, F. D. Lewis, *J. Phys. Chem. B* **2009**, *113*, 16276–16284.
- [14] C. Wagner, H. A. Wagenknecht, *Chem. Eur. J.* **2005**, *11*, 1871–1876.
- [15] T. Ito, S. E. Rokita, *J. Am. Chem. Soc.* **2004**, *126*, 15552–15559.
- [16] C. Behrens, L. T. Burgdorf, A. Schwögler, T. Carell, *Angew. Chem.* **2002**, *114*, 1841–1844; *Angew. Chem. Int. Ed.* **2002**, *41*, 1763–1766.
- [17] C.-Y. Lu, S.-D. Yao, N.-Y. Lin, *Chem. Phys. Lett.* **2000**, *330*, 389–396.
- [18] W. L. Neeley, J. M. Essigmann, *Chem. Res. Toxicol.* **2006**, *19*, 491–505.
- [19] L. D. McGinty, R. G. Fowler, *Mutat. Res.* **1982**, *95*, 171–181.
- [20] R. B. Webb, M. M. Malina, *Photochem. Photobiol.* **1970**, *12*, 457–468.
- [21] A. Weigel, A. L. Dobryakov, M. Veiga, J. L. Pérez Lustres, *J. Phys. Chem. A* **2008**, *112*, 12054–12065.
- [22] C. Behrens, M. Ober, T. Carell, *Eur. J. Org. Chem.* **2002**, 3281–3289.
- [23] K. Kawai, Y. Osakada, M. Fujitsuka, T. Majima, *Chem. Eur. J.* **2008**, *14*, 3721–3726.
- [24] S. Fukuzumi, H. Miyao, K. Ohkubo, T. Suenobu, *J. Phys. Chem. A* **2005**, *109*, 3285–3294.
- [25] K. Kawai, Y. Osakada, T. Takada, M. Fujitsuka, T. Majima, *J. Am. Chem. Soc.* **2004**, *126*, 12843–12846.
- [26] S. Kanvah, J. Joseph, G. B. Schuster, R. N. Barnett, C. L. Cleveland, U. Landman, *Acc. Chem. Res.* **2010**, *43*, 280–287.
- [27] Y. A. Lee, A. Durandin, P. C. Dedon, N. E. Geacintov, V. Shafirovich, *J. Phys. Chem. B* **2008**, *112*, 1834–1844.
- [28] I. Saito, T. Nakamura, K. Nakatani, Y. Yoshioka, K. Yamaguchi, H. Sugiyama, *J. Am. Chem. Soc.* **1998**, *120*, 12686–12687.
- [29] F. D. Lewis, X. Liu, J. Liu, S. E. Miller, R. T. Hayes, M. R. Wasielewski, *Nature* **2000**, *406*, 51–53.
- [30] Y. A. Lee, B. H. Yun, S. K. Kim, Y. Margolin, P. C. Dedon, N. E. Geacintov, V. Shafirovich, *Chem. Eur. J.* **2007**, *13*, 4571–4581.
- [31] C. E. Crespo-Hernández, D. M. Close, L. Gorb, J. Leszczynski, *J. Phys. Chem. B* **2007**, *111*, 5386–5395.
- [32] U. Megerle, I. Pugliesi, C. Schriever, C. F. Sailer, E. Riedle, *Appl. Phys. B* **2009**, *96*, 215–231.
- [33] F. D. Lewis, T. Wu, Y. Zhang, R. L. Letsinger, S. R. Greenfield, M. R. Wasielewski, *Science* **1997**, *277*, 673–676.
- [34] A. Harriman, *J. Phys. Chem.* **1987**, *91*, 6102–6104.
- [35] K. Kawai, T. Takada, T. Nagai, X. Cai, A. Sugimoto, M. Fujitsuka, T. Majima, *J. Am. Chem. Soc.* **2003**, *125*, 16198–16199.
- [36] F. D. Lewis, P. Daublain, B. Cohen, J. Vura-Weis, M. R. Wasielewski, *Angew. Chem.* **2008**, *120*, 3858–3860; *Angew. Chem. Int. Ed.* **2008**, *47*, 3798–3800.
- [37] K. Kawai, T. Takada, S. Tojo, T. Majima, *J. Am. Chem. Soc.* **2003**, *125*, 6842–6843.
- [38] A. J. Ridley, J. R. Whiteside, T. J. McMillan, S. L. Allinson, *Int. J. Radiat. Biol.* **2009**, *85*, 177–195.
- [39] M. C. Skala, K. M. Ricking, A. Gendron-Fitzpatrick, J. Eickhoff, K. W. Elieiri, J. G. White, N. Ramanujam, *Proc. Natl. Acad. Sci. USA* **2007**, *104*, 19494–19499.

Received: December 8, 2010

Published online on February 18, 2011



## **Appendix A4**

### **Conformational control of benzophenone-sensitized charge transfer in dinucleotides**

*Thomas Merz\*, Matthias Wenninger\*, Michael Weinberger,  
Eberhard Riedle, Hans-Achim Wagenknecht, Martin Schütz*

accepted for publication in Physical Chemistry Chemical Physisc

\* these authors contributed equally to the work



## Conformational control of benzophenone-sensitized charge transfer in dinucleotides†

Cite this: *Phys. Chem. Chem. Phys.*, 2013, **15**, 18607

Thomas Merz,<sup>†a</sup> Matthias Wenninger,<sup>†b</sup> Michael Weinberger,<sup>c</sup> Eberhard Riedle,<sup>\*b</sup> Hans-Achim Wagenknecht<sup>\*c</sup> and Martin Schütz<sup>\*a</sup>

Charge transfer in DNA cannot be understood without addressing the complex conformational flexibility, which occurs on a wide range of timescales. In order to reduce this complexity four dinucleotide models **1X** consisting of benzophenone linked by a phosphodiester to one of the natural nucleosides **X = A, G, T, C** were studied in water and methanol. The theoretical work focuses on the dynamics and electronic structure of **1G**. Predominant conformations in the two solvents were obtained by molecular dynamics simulations. **1G** in MeOH adopts mainly an open geometry with a distance of 12–16 Å between the two aromatic parts. In H<sub>2</sub>O the two parts of **1G** form primarily a stacked conformation yielding a distance of 5–6 Å. The low lying excited states were investigated by electronic structure theory in a QM/MM environment for representative snapshots of the trajectories. Photo induced intramolecular charge transfer in the S<sub>1</sub> state occurs exclusively in the stacked conformation. Ultrafast transient absorption spectroscopy with **1X** reveals fast charge transfer from S<sub>1</sub> in both solvents with varying yields. Significant charge transfer from the T<sub>1</sub> state is only found for the nucleobases with the lowest oxidation potential: in H<sub>2</sub>O, charge transfer occurs with 3.2 × 10<sup>9</sup> s<sup>-1</sup> for **1A** and 6.0 × 10<sup>9</sup> s<sup>-1</sup> for **1G**. The reorganization energy remains nearly unchanged going from MeOH to the more polar H<sub>2</sub>O. The electronic coupling is rather low even for the stacked conformation with H<sub>AB</sub> = 3 meV and explains the moderate charge transfer rates. The solvent controls the conformational distribution and therefore gates the charge transfer due to differences in distance and stacking.

Received 5th June 2013,  
Accepted 11th September 2013

DOI: 10.1039/c3cp52344f

www.rsc.org/pccp

### Introduction

Charge transfer in DNA is a phenomenon with two opposing “faces”. On the one hand, charge transfer has been intensively studied over the last twenty years.<sup>1</sup> Yet on the other hand it has become obvious that charge transfer processes in DNA cannot be understood without explicitly addressing the manifold of conformational states present in DNA.<sup>2</sup> The concept of “conformational gating” has been presented to describe the influence of DNA conformations and conformational flexibility on charge transfer.<sup>3</sup> The main problem is that the conformational flexibility of double

helical DNA is very complex and occurs on multiple timescales. Since charge transfer rates strongly depend on the DNA base environment we expect not to observe single kinetic rate constants for DNA-mediated charge transfer, but rather a distribution of rates.<sup>4</sup> Hence, the central question is how the issue of conformational influence on charge transfer can be addressed properly by the combination of time-resolved measurements and theory. For this purpose, we designed the dinucleotides **1X** as the smallest possible models for photoinduced charge transfer in DNA. They consist of benzophenone as an artificial C-nucleoside linked by a phosphodiester bridge to one of the natural nucleosides (X = A, G, T or C). These dinucleotides are soluble both in water and in polar organic solvents like MeOH. It is expected that the conformational scenario changes significantly between water and MeOH and, therefore, the conformational influence on photoinduced singlet and triplet charge transfer<sup>5</sup> can be studied in full detail by both time-resolved transient absorption spectroscopy and theory, including molecular dynamics and quantum chemical calculations to describe the charge transfer states.

Using benzophenone as the photo-induced electron acceptor has the advantage that the dinucleotides **1X** represent both

<sup>a</sup> Institute of Physical and Theoretical Chemistry, University of Regensburg, Universitätsstraße 31, D 93040 Regensburg, Germany.

E-mail: martin.schuetz@chemie.uni-regensburg.de

<sup>b</sup> Lehrstuhl für BioMolekulare Optik, Ludwig Maximilians Universität München, Oettingenstraße 67, 80538 Munich, Germany

<sup>c</sup> Karlsruhe Institute of Technology, Department of Chemistry, Fritz Haber Weg 6, Campus Süd, Geb. 30.42, 76131 Karlsruhe, Germany

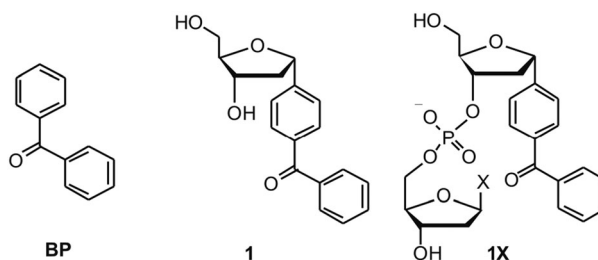
† Electronic supplementary information (ESI) available: Details of (1) preparation of dinucleotides, (2) transient spectroscopic methods and raw data, (3) modeling of the ET dynamics with Marcus theory and (4) computational work. See DOI: 10.1039/c3cp52344f

‡ These authors contributed equally.

interesting biologically relevant systems with respect to DNA damage<sup>6</sup> and the starting point for future applications in chemical biology and photocatalysis. Benzophenone (BP) is a well characterized organic chromophore for biological photochemistry and chemical photocatalysis due to the very efficient inter-system crossing (ISC) to the triplet ( $T_1$ ) state.<sup>7–17</sup> With respect to photoaffinity labeling there are several other advantages:<sup>8</sup> (i) benzophenone is chemically more stable than azides and diazirines, especially under the special or harsh conditions of peptide and nucleic acid synthesis. (ii) The  $T_1$  state of BP is able to extract hydrogen atoms from unreactive C–H bonds in biopolymers, *e.g.*,  $\alpha$ -hydrogen from amino acids.<sup>9</sup> (iii) The absorption of BP in the UV-A region allows selective excitation outside the typical absorption range of biopolymers including tryptophan in proteins and DNA/RNA bases. On the other hand, BP plays an increasingly important role as an excitation antenna collecting the light and thereby initiating substrate conversion in photochemical reactions.<sup>10,11</sup> Molecular BP architectures can be considered as chemical photocatalysts if they bear a substrate binding site, and substrate conversion occurs initiated by energy or electron transfer.<sup>12</sup> In fact, both processes have been applied successfully for the development of BP- and xanthone-based photoorganocatalysts.<sup>13</sup> Template-assisted photocatalysis yields enantioselective [2+2] cycloaddition<sup>14–16</sup> and, more importantly, templated photoinduced electron transfer can be applied to enantioselective aminocyclizations.<sup>17</sup> With respect to the mentioned properties of BP and its derivatives, covalent conjugates with nucleosides and nucleic acids could be of significant interest.<sup>18–23</sup> New photoaffinity labels based on BP-modified nucleic acids could help to identify DNA- and RNA-binding proteins. On the other hand, BP as an artificial nucleoside provides the molecular basis to develop photocatalytically active DNazymes. Among the few examples found in the literature, BP-substituted nucleosides have been prepared as models for ribonucleotide reductases<sup>18,19</sup> and as photoreactive dyads.<sup>20</sup> BP has been attached to phosphothioates in RNA<sup>21</sup> and to 2'-deoxyuridine in DNA<sup>22</sup> to form interstrand crosslinks. 4-Cyanobenzophenone-substituted 2'-deoxyuridines have been extensively used for photoinduced charge transfer studies with DNA.<sup>23,24</sup>

We recently presented the synthesis of a novel C-nucleoside consisting of BP directly attached to the anomeric center of 2'-deoxyribofuranoside.<sup>25</sup> Thereby, the chromophore is placed as an artificial DNA base and can be incorporated synthetically into oligonucleotides by automated phosphoramidite chemistry. In the present study, we furnish a complete characterization of the optical properties of **1** as an artificial nucleoside and in the context of four different dinucleotides (**1G**, **1A**, **1C** and **1T**, Scheme 1) to evaluate the influence of the neighboring DNA base on the BP properties. The photophysical properties of **1** can be influenced by two different protic solvents, water and methanol. Time-resolved measurements of singlet and triplet lifetimes elucidate how conformational changes control the photophysical properties of BP and gate the charge transfer in the dinucleotides.

The theoretical part of our work focuses on the dynamics and electronic structure of the dinucleotide **1G**, which is the most interesting dinucleotide based on the knowledge that BP-initiated



**Scheme 1** BP nucleoside **1** and dinucleotides **1X** with BP as an artificial DNA base (X = G, T, A, C).

charge transfer could lead to oxidation of guanine,<sup>23,26,27</sup> and the results from the time resolved studies (*vide infra*) that will be described. At first, the isolated **1G** (and for comparison **1T**) dinucleotides were investigated. Geometry optimizations were performed for the electronic ground state, and excitation energies were computed at the resulting minimum energy geometry. Second, **1G** was also investigated in two different solvent environments ( $H_2O$  and MeOH) *via* Molecular Dynamics (MD) simulations and subsequent hybrid Quantum Mechanics/Molecular Mechanics (QM/MM) calculations. Representative snapshots from related MD production trajectories were selected, and the individual geometries reoptimized at the QM/MM level. At the resulting geometries, excitation energies and other properties of the relevant low-lying excited states were calculated in the QM/MM framework. In the following sections we present the detailed results of these calculations.

## Theoretical elucidation of conformations and molecular dynamics in water and methanol

First, DFT geometry optimizations (BP functional,<sup>28</sup> def-SVP basis set<sup>29</sup>) were performed for the isolated **1G** and **1T** molecules. For simplicity, **1G** and **1T** were considered as neutral molecules with a proton added to the phosphate in all calculations presented here. Two strongly differing basic geometries of **1G** and **1T** were found; (i) a compact, folded structure for **1G** as displayed in Fig. 1(b), with the G and one of the phenyl rings undergoing  $\pi$ -stacking, and (ii) a stretched, unfolded structure as shown in Fig. 1(a) (analog figures for the folded and unfolded structure of **1T** can be found in Fig. SI-19, ESI†).

The latter constitutes in both cases a local minimum on the potential energy surface. At the Coupled Cluster level (CC2 model)<sup>30</sup> in the same basis the unfolded structure is not stable and folds to the geometry given in Fig. 1(a). The absence of long-range van der Waals dispersion in the pure DFT/BP description is mainly responsible for the existence of the unfolded structure, which can be repaired to some extent, by *e.g.* the inclusion of Grimme's-D2 correction,<sup>31</sup> which is employed in the subsequent DFT QM/MM calculations. Nevertheless, the unfolded structure reappears again if we perform the calculations not *in vacuo* but in a methanol environment (*vide infra*). Hence, both folded and unfolded structures were further investigated.

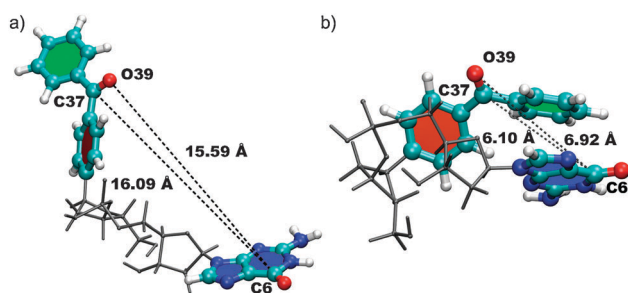


**Fig. 1** Optimized structures of **1G** in the gas phase. The five- and six-membered rings are colored in red/green and blue for better recognition. Also the distances  $d(\text{C6 O39})$  and  $d(\text{C6 C37})$  are given. (a) Unfolded structure computed with DFT/BP in the def SVP basis;  $d(\text{C6 O39}) = 15.59 \text{ \AA}$  and  $d(\text{C6 C37}) = 16.09 \text{ \AA}$ . (b) Folded structure computed with CC2/def SVP;  $d(\text{C6 O39}) = 6.92 \text{ \AA}$  and  $d(\text{C6 C37}) = 6.10 \text{ \AA}$ .

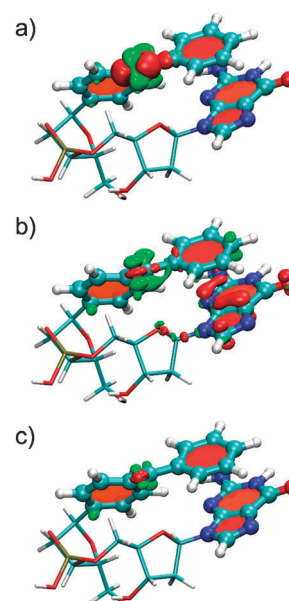
Next, for the isolated dinucleotides, excitation energies, density differences between excited and ground state, and related dipole moment differences of the three lowest singlet states were calculated at the respective ground state minima. To this end, TD-DFT (B3LYP functional<sup>32,33</sup>), as well as TD-CC2 response<sup>30,34–36</sup> (often casually termed as just CC2) were applied. The def-SVP and aug-cc-pVDZ basis<sup>37</sup> sets were used for these calculations (for the latter basis set excitation energies were computed only). The resulting excitation energies of the three lowest excited singlet states are compiled in Table 1 for the unfolded and folded geometries of **1G** and **1T** (triplet excitation energies for **1G** can be found in the ESI† cf. Table SI-2, for comparison).

Fig. 2 depicts the related electron density differences for the case of the folded geometry of **1G** (related electron density differences of the folded geometry of **1T** are displayed in Fig. SI-20 (ESI†)); for the relevant molecular orbitals for **1G** and **1T** cf. Fig. SI-21 and SI-22 (ESI†).

For the folded geometry of **1G** the  $S_1$ ,  $S_2$ , and  $S_3$  states are of ( $n\pi^*$ ), charge transfer (CT), and ( $\pi\pi^*$ ) type. The CT state features depletion of electron density on G, and increase of electron density on the BP part. Comparison of the TD-DFT vs. TD-CC2 results shows a substantial increase in the energy gap between the  $S_1$  and  $S_2$  from 0.18 eV (TD-DFT) to 0.85 eV (TD-CC2, def SVP) and 0.70 eV (TD-CC2, aug-cc-pVDZ). CT states are notoriously underestimated by TD-DFT with local, or semi-local functionals

**Table 1** Results for folded and unfolded molecules of **1G** and **1T**; optimized ground state; TD B3LYP/def SVP TD CC2/def SVP and TD CC2/aug cc pVDZ

Method	Folded geometry				Unfolded geometry				
	<b>1G</b>		<b>1T</b>		<b>1G</b>		<b>1T</b>		
	Type	$\omega$ [eV]	Type	$\omega$ [eV]	Type	$\omega$ [eV]	Type	$\omega$ [eV]	
TD B3LYP	$S_1$	( $n\pi^*$ )	3.36	( $n\pi^*$ )	3.53	( $n\pi^*$ )	3.50	( $n\pi^*$ )	3.50
	$S_2$	CT	3.54	CT	4.16	CT	3.56	CT	4.42
	$S_3$	( $\pi\pi^*$ )	4.42	( $\pi\pi^*$ )	4.46	( $\pi\pi^*$ )	4.45	( $\pi\pi^*$ )	4.46
TD CC2 def SVP	$S_1$	( $n\pi^*$ )	3.74	( $n\pi^*$ )	3.74	( $n\pi^*$ )	3.82	( $n\pi^*$ )	3.76
	$S_2$	CT	4.59	( $\pi\pi^*$ )	4.79	( $\pi\pi^*$ )	4.88	( $\pi\pi^*$ )	4.82
	$S_3$	( $\pi\pi^*$ )	4.78	( $\pi\pi^*$ )	4.83	( $\pi\pi^*$ )	4.96	( $\pi\pi^*$ )	4.90
TD CC2 a VDZ	$S_1$	( $n\pi^*$ )	3.63	( $n\pi^*$ )	3.61	( $n\pi^*$ )	3.63	( $n\pi^*$ )	3.63
	$S_2$	CT	4.33	( $\pi\pi^*$ )	4.65	( $\pi\pi^*$ )	4.69	( $\pi\pi^*$ )	4.69
	$S_3$	( $\pi\pi^*$ )	4.66	( $\pi\pi^*$ )	4.68	( $\pi\pi^*$ )	4.78	( $\pi\pi^*$ )	4.76



**Fig. 2** Electron density difference plots for the first three excited states of the folded geometry of **1G**, calculated with TD CC2 in def SVP basis. Isosurfaces are plotted for  $\pm 0.005$  a.u., red refers to a decrease, green to an increase in the density upon excitation. (a)  $S_1$ : ( $n\pi^*$ ) state;  $|\Delta\mu| = 1.72 \text{ D}$  (b)  $S_2$ : CT state;  $|\Delta\mu| = 10.58 \text{ D}$  (c)  $S_3$ : ( $\pi\pi^*$ ) type state;  $|\Delta\mu| = 1.32 \text{ D}$ .

due to the electronic self-interaction problem inherent in DFT.<sup>38,39</sup> For isolated folded **1T**, on the other hand, only the TD-DFT calculation features a CT state among the three lowest states. The order and type of characters are similar to **1G**. However, the gap between the  $S_1$  and the CT states is significantly increased, compared to **1G** (0.63 vs. 0.18 eV). For TD-CC2, the CT state disappears among the three lowest excitations, and the  $S_1$ ,  $S_2$  and  $S_3$  states correspond to a ( $n\pi^*$ ), ( $\pi\pi^*$ ) and ( $\pi\pi^*$ ) types, respectively. Hence, the CT state in the TD-DFT calculation for **1T** is just an artifact, caused by the abovementioned electronic self-interaction problem. Adding diffuse functions has the usual effect of decreasing the TD-CC2 excitation energies by 0.1–0.2 eV, which is seen in both cases.

For the unfolded geometry the  $S_1$ ,  $S_2$ , and  $S_3$  states calculated by TD-CC2 are of ( $n\pi^*$ ), ( $\pi\pi^*$ ), and ( $\pi\pi^*$ ) type for both **1G** and **1T**. The CT state for **1G** is clearly absent, which is not too surprising since the distance between donor (G) and acceptor (BP) is much larger than in the folded geometry. For TD-DFT, on the other hand, the CT state is clearly present (as the  $S_2$  state) and features about the same excitation energy as in the folded geometry. This is the typical irregular behavior of TD-DFT, since CT states described by that method do not reflect the proper distance dependence between donor and acceptor (according to the Coulomb law).

Based on the gas phase results presented so far we conclude that (i) the distance between the BP and the G subsystems intimately affects the character of the three relevant, lowest excited states. In particular there is a low-lying CT state present for the folded geometry, which is absent for the unfolded one. (ii) All these excitations are either localized on G, or BP, or both for the CT state, as is evident from Fig. 2. The sugar and phosphate

groups linking these two subunits do not play a role and can therefore be safely omitted from the QM part in the subsequent QM/MM studies of the system in solvent environments. (iii) A CT state in **1T** cannot be observed, neither in the unfolded, nor the folded geometry.

In order to generate proper starting structures for a subsequent QM/MM treatment of **1G** in water and methanol solvent environments, classical molecular dynamics (MD) simulations were carried out first. Similar MD simulations were also carried out for **1T**, which however will not be further discussed. For the latter we refer to Fig. SI-26 and SI-27 in the ESI† (Section 4). Also the technical details of these simulations are described in the ESI† (Section 4). MD simulations in water and methanol were performed by starting from either the folded or the unfolded gas phase structure of **1G** (overall four MD simulations). It turns out that the resulting trajectories are rather independent of the starting geometry: **1G** solvated in water primarily exists in the folded form, while **1G** solvated in methanol primarily exists in the unfolded form.

The trajectories of the MD simulation of **1G** in methanol (starting from the folded geometry) and of the MD simulation of **1G** in water (starting from the unfolded geometry) are displayed in Fig. 3(a) and (b). The trajectories of the two other MD simulations with converse starting geometries are included in Fig. SI-25 (ESI†). The degree of folding is measured by the distances  $d(\text{C6}-\text{C37})$  and  $d(\text{C6}-\text{O39})$  (cf. Fig. SI-18, ESI†), which reflect the spatial separation of the BP and G subunits. For the isolated molecule these distances amount to 5–6 Å for the folded, and 15–16 Å for the unfolded form. Thus, in our MD simulations we consider

geometries with distances of above 10 Å as unfolded (grey shaded area in Fig. 3), and geometries with distances of below 10 Å as folded forms. Evidently, unfolded **1G** in water folds and stays folded most of the time. In contrast, folded **1G** in methanol unfolds and stays in that form most of the time. Obviously, in the polar water solvent, the two hydrophobic ring systems BP and G stick together and undergo  $\pi$ -stacking, while in the less polar methanol they are individually solvated by methanol molecules.

For the subsequent QM/MM study we have selected five representative snapshots: from each of the four trajectories, as indicated in Fig. 3 and in Fig. SI-25 (ESI†), there are two snapshots related to the water environment,  ${}^a\mathbf{1G}_{\text{H}_2\text{O}}$  and  ${}^b\mathbf{1G}_{\text{H}_2\text{O}}$ , corresponding to the folded form, and two related to the methanol environment,  ${}^a\mathbf{1G}_{\text{MeOH}}$ , and  ${}^b\mathbf{1G}_{\text{MeOH}}$ , corresponding to the unfolded form; additionally, a fifth snapshot  ${}^c\mathbf{1G}_{\text{MeOH}}$ , which represents the rather rare event of a folded form in the methanol environment, was also considered.

## Spectroscopic results

For the time resolved measurements and their interpretation the optical properties of the artificial nucleoside **1** and the dinucleotides **1X** were characterized. The spectra of compound **1** in MeOH (Fig. 4a and b) are typical for all other compounds. One prominent strong absorption band is centered at 259 nm (4.79 eV) that corresponds to a  ${}^1(\pi\pi^*)$  transition located on BP. A much weaker band is centered at 329 nm (3.77 eV) and corresponds to the  ${}^1(n\pi^*)$  transition of BP.<sup>40</sup> The assignment of the bands to transitions located on BP is corroborated by the high similarity to the spectrum of BP (Fig. 4a). Furthermore, the band positions are in good agreement with the TD-CC2 excitation energies

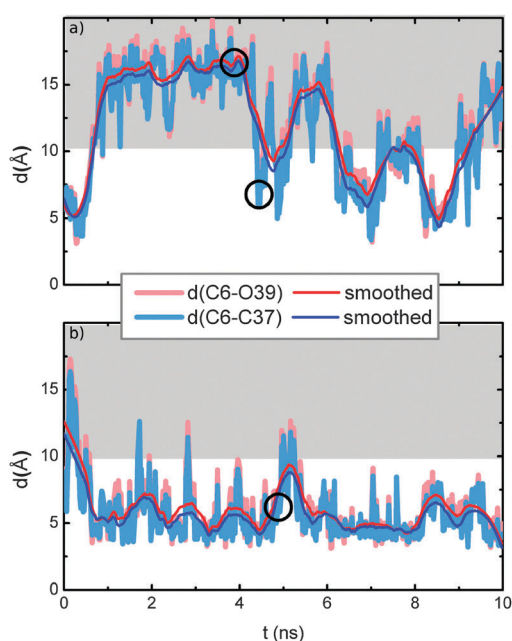


**Fig. 3** Trajectories of MD run; (a) shows **1G** in methanol environment and (b) **1G** in water; the distances  $d(\text{C6}-\text{C37})$  and  $d(\text{C6}-\text{O39})$  in Å are plotted against the simulation time in ns. The grey area is the region in which the molecule is unfolded. The cycles depict the chosen snapshots. (a) MD of **1G** MeOH, folded (4.2 ns;  ${}^c\mathbf{1G}_{\text{MeOH}}$ ) and unfolded (4.0 ns;  ${}^a\mathbf{1G}_{\text{MeOH}}$ ) starting geometry. (b) MD of **1G** water, folded (4.5 ns;  ${}^a\mathbf{1G}_{\text{H}_2\text{O}}$ ) starting geometry.

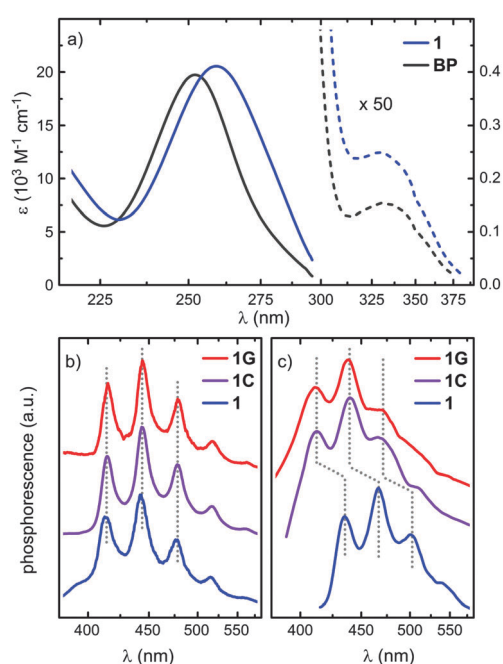


**Fig. 4** (a) Absorption of BP and **1** in MeOH at r.t. (b) Phosphorescence of **1**, **1C** and **1G** at 77 K in MeOH. (c) Phosphorescence of **1**, **1C** and **1G** at 77 K in  $\text{H}_2\text{O}$ .



reported in Table 1. The latter transition allows selective excitation of the BP chromophore outside the nucleic acid absorption range. This is an important prerequisite for the photochemical and photobiological applications. Both electronic transitions are broad and structureless at r.t. due to the thermal population of low frequency vibrational levels and the interaction with the environment.

Upon excitation at 355 nm, nucleoside **1** in MeOH shows a well structured phosphorescence at 77 K. This structure becomes visible due to the lack of thermal vibrational excitation and the long lifetime of the  $T_1$  state. The first vibronic peak corresponding to the 0–0 vibrationless electronic transition is found at 413 nm. The shape and the energetic positions are very similar for all dinucleotides **1X** (compare spectra for **1G** and **1C** in Fig. 4b). This observation differs from the phosphorescence in aqueous buffer solution (Fig. 4c). **1** dissolved in  $H_2O$  exhibits the 0–0 peak at 435 nm. Due to the characteristic intensity pattern we can be sure that we observe a shift and not a disappearance of the 0–0 subband. The shift compared to the MeOH solution is interpreted as the exposure of the chromophore to water. The 0–0 phosphorescence peak of the dinucleotides in  $H_2O$  is found to be very similar to MeOH. This shows that the DNA base adjacent to the BP in the dinucleotides is able to shield the chromophore from the electrostatic influence of the water molecules. We therefore expect that the photochemical reactivity of the BP derivative **1** as part of the synthesized dinucleotides **1X** is more similar to **1** in organic solvents (like MeOH) than **1** in water. We can confirm the presence of a preferred stacked (folded) conformation of **1X** in water as suggested by the molecular dynamics simulations.

Electron transfer (ET) between nucleobases and an excited organic chromophore is well established and usually occurs on time scales of 10–100 ps when the two moieties are in close proximity.<sup>41,42</sup> We used femtosecond transient absorption (TA) spectroscopy<sup>43</sup> to measure the kinetics of the various compounds. Directly after excitation of the lowest  $^1(n\pi^*)$  transition, pure BP in MeOH shows the spectrum of the  $S_1$  state with prominent absorption maxima at 340 and 580 nm (Fig. SI-9, ESI†). BP in MeOH serves as reference according to the results obtained with the steady state spectroscopy. The decay of the singlet spectral signatures is dominated by very fast ISC.<sup>40</sup> Upcoming absorption bands at 320 and 530 nm can be uniquely assigned to the BP triplet state  $T_1$ . We find a lifetime of  $\tau_{S_1} = 12.5$  ps for the  $S_1$  state. Assuming a quantum yield of  $\Phi_T = 100\%$  for the population of the BP  $T_1$  state in agreement with the literature<sup>44</sup> the rate of ISC is determined as  $k_{ISC} = (\tau_{S_1})^{-1}$ . An analogous modeling will also be used in the analysis of the more complex TA data of the BP dinucleotides **1X**.

A first measurement series of the BP nucleosides **1X** and reference compound **1** was performed in MeOH (Fig. 5 and Fig. SI-10 to SI-13, ESI†). Directly after excitation we observe transient spectra which are very similar to those of pure BP showing the absorption features of the BP  $S_1$  state. The covalently bound 2'-deoxyribofuranoside does not significantly affect the excited state spectral features. The ultrafast ISC is also found for the nucleosides **1X** and reference **1**, the lifetime of **1** in MeOH is  $\tau_{S_1} = 9.4$  ps.

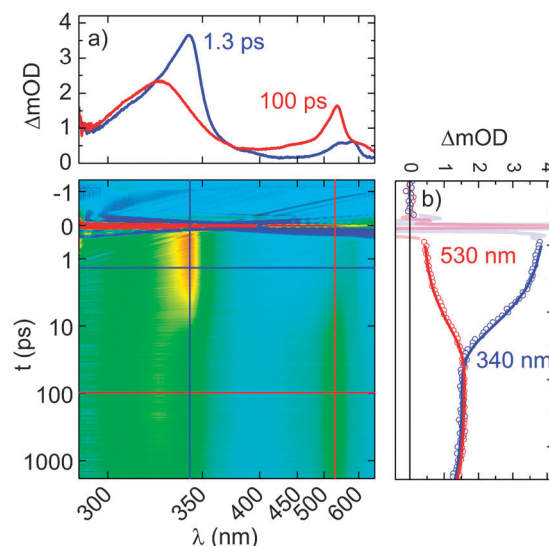


**Fig. 5** Transient absorption spectra of **1C** in MeOH after 358 nm excitation (a) selected spectra (b) temporal evolution at selected wavelengths (dots) with corresponding traces from the global fit (lines).

The slightly faster ISC compared to BP is reasonable in view of the covalently bound substituent. In comparison to **1** all nucleosides **1X** show a further reduced lifetime of the  $S_1$  state and a dependence on the adjacent nucleobase. Especially the lifetime of compound **1G**, where BP is linked to guanine (the nucleobase with the lowest standard oxidation potential  $E^0$ ) is considerably reduced: we find  $\tau_{S_1} = 7.6$  ps in MeOH. All obtained time constants are summarized in Table 2. The lifetime of the triplet states in MeOH cannot be determined by the ultrafast TA spectroscopy, since it exceeds the maximum pump–probe delay of 2 ns. We therefore set it to infinity for the analysis.

It is interesting to compare the variation of the  $S_1$  lifetimes  $\tau_{S_1}$  with the variation of the standard oxidation potential  $E^0$  of the corresponding nucleobase.<sup>45</sup> In **1G**, which contains the nucleobase with the lowest  $E^0$  and hence is the most easily oxidized,  $\tau_{S_1}$  is significantly reduced in comparison to all other compounds. This indicates that ET from the covalently bound nucleobase to the excited singlet state of BP can compete with the ISC process, which explains the reduced  $\tau_{S_1}$  of all **1X** in comparison to **1**. The transient signature of the intermediate BP radical anion expected at 333 and 720 nm<sup>46</sup> is not visible. A charge recombination process, which is fast in comparison to the ET process, can readily explain the absence of the spectral signatures of the intermediate charge separated state.

From the inhomogeneous distribution of conformations it could be expected that the  $S_1$  decay time does not conform to a simple exponential behavior.<sup>47</sup> We fitted the curves with a stretched exponential and obtained somewhat unexpected exponents around 1.1 and not the expected values below 1. A rational can be that we have a highly nonstatistical distribution as we find indeed from the trajectories in Fig. 3. Since this precludes any reasonable analytical modeling, we decided to use the single-exponential fit values for further interpretation.

The ET time constant  $^1\tau_{ET}$  determined from the measured lifetime  $\tau_{S_1}$  for all dinucleotides **1X** is depicted in Table 2.

**Table 2** Time constants of excited state dynamics in MeOH and H<sub>2</sub>O: standard oxidation potential  $E^0$  of the nucleobase from ref. 45,  $\tau_{S_1}$  obtained from a global fit,  ${}^1\tau_{ET}$  was calculated by using the  $S_1$  lifetime of compound **1** in MeOH as intrinsic lifetime of the  $S_1$  state and  ${}^3\tau_{ET}$  from the dynamics of the integrated transient absorption at 300–400 nm. The triplet yield  $\Phi_T$  was determined by inserting the quantities into a rate model based on eqn (3) ( $\Phi_T$  theor.) and also experimentally by integration of the triplet specific transient absorption ( $\Phi_T$  exp.)

Sample	$E^0$ [V]	MeOH				H <sub>2</sub> O				
		$\tau_{S_1}$ [ps]	${}^1\tau_{ET}$ [ps]	${}^1\Phi_1$ theo.	${}^1\Phi_1$ exp.	${}^3\tau_{ET}$ [ns]	$\tau_{S_1}$ [ps]	${}^1\tau_{ET}$ [ps]	${}^1\Phi_1$ theo.	${}^3\tau_{ET}$ [ns]
<b>BP</b>		12.5 ± 0.5								
<b>1</b>		9.4 ± 0.5								
<b>1C</b>	2.14	8.8 ± 0.5	140 ± 50	0.94	0.92	>2	9.0 ± 0.8	210 ± 70	0.96	>2
<b>1T</b>	2.11	9.1 ± 0.5	290 ± 100	0.97	0.97	>2	8.4 ± 0.8	80 ± 25	0.89	>2
<b>1A</b>	1.96	8.9 ± 0.5	170 ± 50	0.95	0.89	>2	8.2 ± 0.8	65 ± 15	0.87	0.310 ± 0.040
<b>1G</b>	1.49	7.6 ± 0.5	40 ± 10	0.81	0.87	~1	4.6 ± 0.5	9 ± 2	0.49	0.166 ± 0.020

The ET time constant  ${}^1\tau_{ET}$  was calculated using  $k_{ISC}$  from compound **1** as the intrinsic lifetime of the  $S_1$  state of BP in the dinucleotide environment as

$$({}^1\tau_{ET})^{-1} = {}^1k_{ET} = \frac{1}{\tau_{S_1}} k_{ISC} \quad (1)$$

We interpret the dependence of the ET rate on the standard oxidation potential  $E^0$  of the nucleobase with the help of standard Marcus theory.<sup>48</sup> For details see the ESI† (Section 3). We calculate  $\Delta G^0$ , which serves as the driving force for the ET reaction between the nucleobase and the BP  $S_1$  or  $T_1$  according to Rehm–Weller:<sup>49</sup>

$$\Delta G^0 = e[E^0(D^{\bullet+}/D) - E^0(A/A^{\bullet-})] - \frac{e^2}{4\pi\epsilon_0\epsilon r} \Delta E_{00} \quad (2)$$

where  $E^0$  is the one-electron oxidation/reduction potential,  $\epsilon$  is the permittivity of the solvent,  $r$  is the average donor–acceptor distance, and  $\Delta E_{00}$  is the energy of the excited state relative to the ground state. For the lowest BP  ${}^1(n\pi^*)$  singlet state,  ${}^1\Delta E_{00}$  equals 318 kJ mol<sup>-1</sup> (3.30 eV, 376 nm) and for the lowest triplet state  ${}^3\Delta E_{00}$  is 293 kJ mol<sup>-1</sup> (3.04 eV).<sup>49</sup> The standard potential  $E^0$  for the reduction of BP is  $E^0 = -1.00$  V against the normal hydrogen electrode (NHE).<sup>50</sup> The average distance  $r$  between the donor and acceptor was found from the molecular dynamics calculations to be  ${}^1r_{MeOH} = {}^3r_{MeOH} = 12$  Å for the  $S_1$  and  $T_1$  states of all **1X** in MeOH, and  ${}^1r_{H_2O} = {}^3r_{H_2O} = 6$  Å in H<sub>2</sub>O. The use of an average value instead of the distance distribution is justified since the distance dependence in eqn (2) only causes minor variations of  $\Delta G^0$ . The values of the permittivity of the solvents are  $\epsilon_{MeOH} = 32.66 \cdot \epsilon_0$  and  $\epsilon_{H_2O} = 78.36 \cdot \epsilon_0$ .<sup>51</sup> The results of the calculated  $\Delta G^0$  values are listed in Table 3 for BP in its  $S_1$  and  $T_1$  states in MeOH and in H<sub>2</sub>O.

**Table 3** Change of free energy  $\Delta G^0$  corresponding to the oxidation of DNA nucleobases by the  $S_1$  ( ${}^1\Delta G^0$ ) and  $T_1$  state ( ${}^3\Delta G^0$ ) of BP in MeOH and in H<sub>2</sub>O

Sample	$E^0$ <sup>44</sup> [V]	MeOH		H <sub>2</sub> O	
		${}^1\Delta G^0$ [kJ mol <sup>-1</sup> ]	${}^3\Delta G^0$ [kJ mol <sup>-1</sup> ]	${}^1\Delta G^0$ [kJ mol <sup>-1</sup> ]	${}^3\Delta G^0$ [kJ mol <sup>-1</sup> ]
<b>1C</b>	2.14	20	6	20	5
<b>1T</b>	2.11	22	3	23	2
<b>1A</b>	1.96	37	12	38	12
<b>1G</b>	1.49	82	57	83	58

The Marcus equation is highly nonlinear and an intuitive prediction of the dependence of  ${}^1k_{ET}$  on  $\Delta G^0$  is difficult. From a detailed consideration we conclude that only  $\lambda$  values around 62 kJ mol<sup>-1</sup> and  $H_{AB} = 1.49$  meV (12 cm<sup>-1</sup>) allow a good reproduction of the experimental observations. We find that the ET process already seems to be in the Marcus inverted regime for **1G**, in agreement with the reported behaviour in DNA hairpin structures.<sup>52</sup>

Another approach to verify an ET process between the nucleobase and BP in its  $S_1$  state is the spectroscopic determination and analysis of the triplet yield  $\Phi_T$  for each compound. If a deactivation pathway of the BP  $S_1$  state competes with ISC, the triplet quantum yield  $\Phi_T$  of BP should be reduced. For the measurements in MeOH we are indeed able to quantify  $\Phi_T$ . By dividing the integrated transient absorption of an  $S_1$  specific absorption band (303–350 nm, blue shaded area in Fig. 6) directly after excitation ( $t = 0.5$  ps) by the integrated transient absorption of a  $T_1$  specific absorption band (450–600 nm, red shaded area) at a pump–probe delay of  $\Delta t = 100$  ps we calculate  $\Phi_T$  for each compound. The yield  $\Phi_T$  determined in this way (see Table 2) is in good agreement with the triplet yield calculated from the values of  ${}^1k_{ET}$  and  $k_{ISC}$  determined above according to eqn (3)

$$\Phi_T = \frac{k_{ISC}}{{}^1k_{ET} + k_{ISC}} \quad (3)$$

Turning to the triplet manifold, we note that in MeOH there are seemingly no charge transfer processes between the BP moiety and the attached nucleobase which are faster than a nanosecond. This stands in contrast to the results in water (see below) and

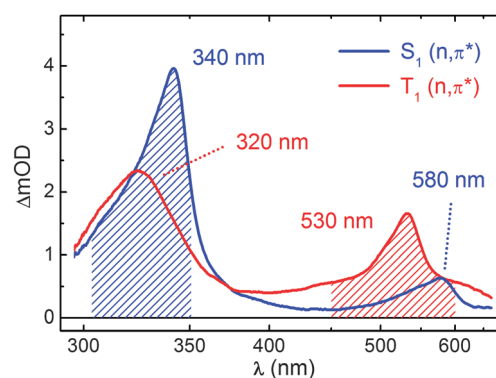


**Fig. 6** SAS of BP  $S_1$  (blue) and  $T_1$  state (red) after 358 nm excitation of **1C** in MeOH. The shaded integrals were used to determine the relative triplet yield.



implies gating of electron transfer by conformational changes, as discussed later in the theoretical part. The calculated  $\Delta G^0$  values for **1A**, and particularly **1C** and **1T** for the BP  $T_1$  state are close to zero or even positive in MeOH and effectively prohibit an ET process. This is in agreement with our measurements. For **1G** we see a weak signature of the BP anion around 333 nm toward the end of the probe range that might well be due to slow and inefficient ET between guanine and the BP triplet state.

The species associated spectra (SAS) of compound **1C** in MeOH (Fig. 6) are determined from the decay associated difference spectra (DADS) directly obtained from a global fit. The species decaying with 9 ps is assigned as the  $S_1$  state, the species with the long lasting spectral contribution as the  $T_1$  state. The corresponding spectra of all other compounds are identical within experimental precision to these two spectra. The SAS corroborate our qualitative discussion given above that the early spectral features are due to the initially populated  $S_1$  state, and the later ones to the  $T_1$  state. The lack of sizable anion signatures in the transient spectra indicates that the back ET is considerably faster than the forward rates of  $3 \times 10^9$  to  $2.5 \times 10^{10} \text{ s}^{-1}$ .

It was shown above that the phosphorescence spectrum of the BP chromophore in **1** is affected by water as a solvent (Fig. 4). This influence is, however, not observed for the nucleosides **1X**. To clarify the kinetics behind this observation, a second series of measurements was performed in  $\text{H}_2\text{O}$ , the natural environment for DNA. Directly after excitation of compounds **1X** we observe the transient signatures of the BP  $S_1$  state as already observed in MeOH. The lifetime of the  $S_1$  state reduces with decreasing standard oxidation potential  $E^0$  of the adjacent nucleobase, similar to what is observed in MeOH. In contrast to the measurements in MeOH, we also find changes in the transient spectra for **1G** and **1A** at delay times in the 100 ps regime (Fig. 7). They have to be interpreted as a significantly reduced lifetime of the  $T_1$  state due to ET from the adjacent nucleobase. The spin multiplicity of the dinucleotide is conserved in this process and the formed intramolecular radical ion pair still exhibits triplet character.<sup>53</sup> All determined time constants are summarized in Table 2.

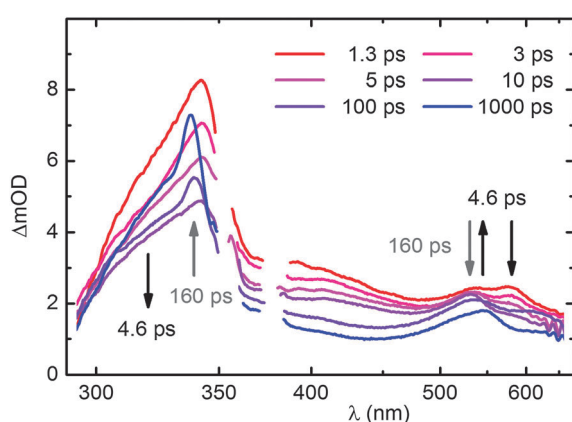


**Fig. 7** TA spectra of compound **1G** in  $\text{H}_2\text{O}$  for selected pump-probe delays after 358 nm excitation. The wavelength region containing scattered light of the pump pulse was clipped.

The dominant influence of the nucleobases in compounds **1X** dissolved in  $\text{H}_2\text{O}$  is the singlet ET. A plot of  $^1k_{\text{ET}}$  vs.  $^1\Delta G^0$  (see Fig. SI-17, ESI†) confirms the picture which we already obtained from the measurements in MeOH. We also applied the Marcus equation for evaluation of the dependence of  $^1k_{\text{ET}}$  on  $^1\Delta G^0$  in  $\text{H}_2\text{O}$ . The reorganization energy of  $\lambda = 67 \text{ kJ mol}^{-1}$  (0.70 eV) is close to the value found for MeOH, while the fitted electronic coupling strength is  $H_{\text{AB}} = 2.64 \text{ meV}$  ( $21 \text{ cm}^{-1}$ ). Again, the parameter  $H_{\text{AB}}$  is just an effective value and will be later discussed in connection with the distribution of donor-acceptor distances.

Due to the decay dynamics of the triplet state, *i.e.* the significant ET in the triplet state, we were not able to quantify the triplet yield in the same fashion as for MeOH. The transient spectra of samples **1G** and **1A** in  $\text{H}_2\text{O}$  show a decay of the triplet spectrum with simultaneously upcoming sharp spectral signatures of the BP radical anion at 335 nm (Fig. 7 and 8). The assignment of the spectral features to the spectrum of the BP radical anion is done in accord with the literature.<sup>46</sup> The spectra in Fig. 7 for compound **1G** are exemplary also for compound **1A** with the exception of the precise values of the time constants.

To further clarify the charge transfer dynamics between the nucleobase and the BP  $T_1$  state it seems reasonable to analyze the dynamics of the integrated transient absorption between 300 and 340 nm due to well distinguishable absorption characteristics of the excited singlet, triplet, and radical anion state in this spectral region. A multi-exponential fit provides within experimental error the same time constants as already obtained from the global data analysis. The data points and the corresponding multi-exponential fit curves are depicted in Fig. 8. All data have a sizable offset, *i.e.* the integral signal does not decay to zero within the observation window. This is due to the lasting charge separation in the triplet state. Such a long living CT state is not unexpected, due to the remaining spin correlation in the intramolecular radical ion pair.<sup>53</sup>

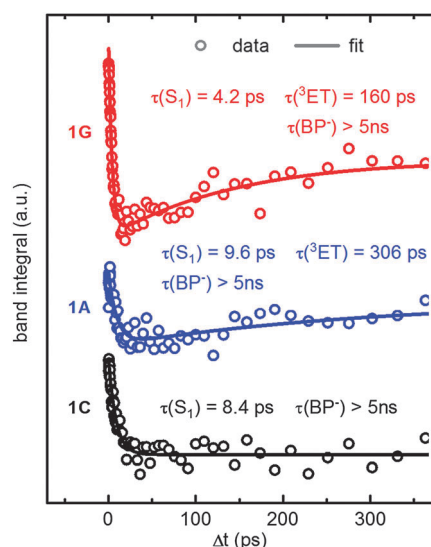


**Fig. 8** Integrated transient absorption from 300 to 340 nm of samples **1G**, **1A**, and **1C** in  $\text{H}_2\text{O}$  after 358 nm excitation. The time constants are obtained from multi-exponential fits.

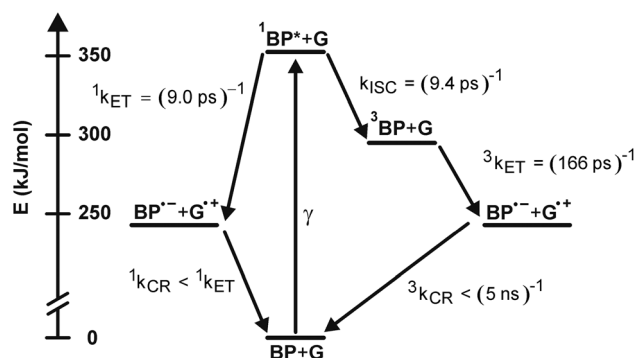


Fig. 9 Excited state energetics and kinetics of **1G** in H<sub>2</sub>O.

Despite differing sample concentrations and experimental conditions, the differing temporal behavior can be well seen from the displayed curves. Note in particular that the signal for **1C** is settled after 100 ps while the signals for **1G** and **1A** keep increasing due to the triplet charge transfer.

All processes and the energetics of the involved levels are summarized for **1G** in H<sub>2</sub>O in Fig. 9. ET is found both in the singlet and the triplet system, but the charge separation is only persistent for the triplet system. These observations are similar to the recent reports on anthraquinone–DNA conjugates.<sup>5a</sup> From the experimental data no solid reasoning for this striking observation can be deduced. The only argument to be invoked would be spin correlation between the radical ions and the forbidden character of the back transfer involving spin flip. It should also be remembered that ET in the triplet system is not found for MeOH. For an explanation of these observations we turn to quantum chemical calculations.

## QM/MM studies for the energy landscape of **1G**

In the following, the discussion of the results is divided into two parts discussing **1G** solvated in water, and in methanol, respectively.

According to our MD simulations reported in Fig. 3, **1G** in water almost exclusively exists in the folded form. We therefore have selected two snapshots <sup>a</sup>**1G**<sub>H<sub>2</sub>O</sub>, and <sup>b</sup>**1G**<sub>H<sub>2</sub>O</sub> which represent the folded configuration. The calculated singlet excitation energies for these two snapshots are compiled in Table 4 (for triplet energies at the optimised ground state see Table SI-7, ESI†).

First we concentrate on the results for the optimized ground state. The folded snapshots feature a distance between C7 and O39 of about 3.3 Å. As is evident from Table 4, the excitation energies of the three lowest excited states are very similar for the two individual snapshots. For all snapshots the S<sub>1</sub>, S<sub>2</sub>, and S<sub>3</sub> states are of (nπ\*), (ππ\*) and (ππ\*) types. Hence, in contrast to the isolated molecule, there is no low-lying CT state in the Franck–Condon region for the folded form of **1G** in water. Apparently, the solvent shell relaxed for the ground state destabilizes the CT state. Presumably, primarily the BP subunit

**Table 4** TD CC2 QM/MM excitation energies  $\omega$  at the respective TD DFT minima, calculated in aug cc pVDZ basis, respectively.  $\Delta E$  corresponds to the total energy difference of the optimised (nπ\*) state and the (nπ\*) state at the ground state geometry ( ${}^a\Delta E = E_{\text{tot}}(\text{n}\pi^*)_{\text{opt}} - E_{\text{tot}}(\text{n}\pi^*)_{\text{FC}}$ ), or of the optimised CT state and the (nπ\*) state at the ground state geometry ( ${}^b\Delta E = E_{\text{tot}}(\text{CT})_{\text{opt}} - E_{\text{tot}}(\text{n}\pi^*)_{\text{FC}}$ ); solvent: H<sub>2</sub>O

Structure	State	FC point		(nπ*) state		CT state		$\Delta E$ [eV]
		Type	$\omega$ [eV]	Type	$\omega$ [eV]	Type	$\omega$ [eV]	
<sup>a</sup> <b>1G</b> <sub>H<sub>2</sub>O</sub>	S <sub>1</sub>	(nπ*)	3.85	(nπ*)	3.02	CT	2.83	0.08 <sup>a</sup>
	S <sub>2</sub>	(ππ*)	4.62	(ππ*)	4.57	(nπ*)	3.38	
	S <sub>3</sub>	(ππ*)	4.75	(ππ*)	4.71	(ππ*)	4.18	0.36 <sup>b</sup>
	S <sub>4</sub>			CT	4.74			
<sup>b</sup> <b>1G</b> <sub>H<sub>2</sub>O</sub>	S <sub>1</sub>	(nπ*)	3.80	(nπ*)	3.12	CT	2.58	0.18 <sup>a</sup>
	S <sub>2</sub>	(ππ*)	4.57	(ππ*)	4.51	(nπ*)	3.34	
	S <sub>3</sub>	(ππ*)	4.61	(ππ*)	4.57	(ππ*)	4.14	0.20 <sup>b</sup>
	S <sub>4</sub>			CT	4.76			

is responsible for this effect (BP is not soluble in water); the solvent shell around BP changes considerably when optimizing the geometry on the potential energy surface of the CT state.

The density difference plots and dipole differences (relative to the ground state) corresponding to <sup>a</sup>**1G**<sub>H<sub>2</sub>O</sub> are displayed in Fig. 10 (for the relevant molecular orbital contributions cf. Fig. SI-29-a, ESI†). The density difference of the S<sub>1</sub> state looks similar to that of the S<sub>1</sub> state of the isolated system (Fig. 2).

It has the character of a (nπ\*) transition with a dipole moment difference of about 1.9 D. The S<sub>1</sub> ← S<sub>0</sub> excitation energies of the two snapshots amount to 320–330 nm, which fits the experimental value of 329 nm quite well. Relative to the gas phase values, the solvated molecules appear to be blue shifted by 10–20 nm.

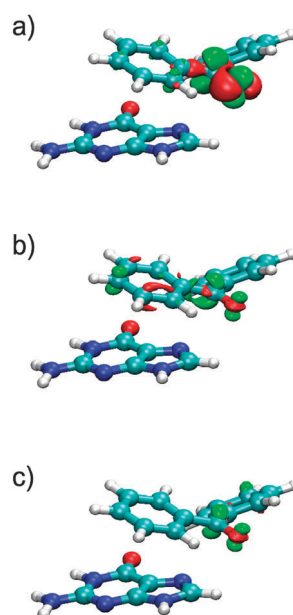


**Fig. 10** Electron density difference plots for the first three excited singlet states of <sup>a</sup>**1G**<sub>H<sub>2</sub>O</sub>, calculated with TD CC2 in the aug cc pVDZ basis in the QM/MM framework at the Franck–Condon point. Isosurfaces are plotted for  $\pm 0.005$  a.u., red refers to a decrease, green to an increase in the density upon excitation. (a) S<sub>1</sub>: (nπ\*) state,  $|\Delta\mu| = 1.86$  D (b) S<sub>2</sub>: (ππ\*) state,  $|\Delta\mu| = 2.43$  D (c) S<sub>3</sub>: (ππ\*) state,  $|\Delta\mu| = 2.46$  D.

$S_2$  and  $S_3$  are quite well separated from  $S_1$ , but the gap between  $S_2$  and  $S_3$  is very small. These are ( $\pi\pi^*$ ) states with dipole differences of 2.4–2.5 D.

Geometry optimization on the  $S_1$  state surface, which was done in order to check if on the route downhill to the  $S_1$  state minimum a crossing with a CT state occurs, showed that the above mentioned distances  $d(C7-O39)$  compared to the ground state optimized ones (see Table SI-5, ESI†), do not alter much. Relative to the FC point the total energy drops slightly by 0.1 eV ( ${}^a\mathbf{1G}_{H_2O}$ ) and 0.2 eV ( ${}^b\mathbf{1G}_{H_2O}$ ). Similarly as at the Franck–Condon point the  $S_1$ ,  $S_2$ , and  $S_3$  states are again of ( $n\pi^*$ ), ( $\pi\pi^*$ ), and ( $\pi\pi^*$ ) type, respectively. Again,  $S_2$  and  $S_3$  are energetically rather close, while the gap between  $S_1$  on the one hand, and  $S_2$ ,  $S_3$  on the other hand, is fairly large. However, a CT state now comes into play as the  $S_4$  state.

Therefore, for  ${}^a\mathbf{1G}_{H_2O}$  and  ${}^b\mathbf{1G}_{H_2O}$  further geometry optimizations on this CT state surface were performed. The relevant density difference plots and dipole moment differences related to  ${}^a\mathbf{1G}_{H_2O}$  are given in Fig. 11. The CT state minimum for the  ${}^a\mathbf{1G}_{H_2O}$  and  ${}^b\mathbf{1G}_{H_2O}$  snapshots is  $\Delta E = 0.4$  and  $\Delta E = 0.2$  eV below the FC point (cf. Table 4), hence at about the same energy as the  $S_1$  state minimum ( ${}^b\mathbf{1G}_{H_2O}$ ), or slightly below ( ${}^a\mathbf{1G}_{H_2O}$ ). This allows population transfer from the excited  $S_1$  state to the dark CT state with reasonable efficiency.

Interestingly, the  $S_3$  ( $\pi\pi^*$ ) state at the CT state minimum now corresponds to a local excitation on the G subunit with a relatively large dipole moment difference (relative to the ground state at that geometry) of more than 10 D.

In the course of the optimization on the CT state surface, the distance between the oxygen O39 of the carbonyl group of BP

and the C7 atom of the G decreases substantially from 3.22 Å ( ${}^a\mathbf{1G}_{H_2O}$ ) or 3.39 Å ( ${}^b\mathbf{1G}_{H_2O}$ ) for the ground state minimum to 2.73 Å ( ${}^a\mathbf{1G}_{H_2O}$ ) or 2.93 Å ( ${}^b\mathbf{1G}_{H_2O}$ ) for the optimized CT state. The shortening of this distance might indicate a possible subsequent proton transfer, equalizing the charge separation induced by the preceding electron transfer (cf. Fig. 11).

From the MD trajectory in methanol three individual snapshots were taken, i.e. two snapshots  ${}^a\mathbf{1G}_{MeOH}$  and  ${}^b\mathbf{1G}_{MeOH}$ , which represent the characteristic unfolded conformation, and a representative snapshot  ${}^c\mathbf{1G}_{MeOH}$  for a folded conformation in methanol. As already discussed,  $\mathbf{1G}$  exists in the methanol environment predominantly in the unfolded conformation. The folded conformation was selected to check if in such a geometry a transition to the charge transfer state is also possible in the methanol environment. For the optimized ground state geometries, the distance  $d(C7-O39)$  of the unfolded conformers ranges between 14 and 17 Å, while that of the folded conformer amounts to about 3.1 Å (see Fig. SI-28, ESI†). This is comparable to the folded snapshots in water. The excitation energies of the three lowest excited singlet states obtained by the QM/MM calculations are compiled in Table 5 (for triplet energies at the optimised ground state see Table SI-7, ESI†).

Evidently, the excitation energies of the two unfolded snapshots are very similar: the first excitation corresponds to a ( $n\pi^*$ ) state. As is the case also in water, the calculated first excitation energies fit the experimental value of 329 nm quite well. Again, similar to the spectrum in water, the ( $n\pi^*$ ) state is well separated from the  $S_2$  and  $S_3$  states, which in turn are rather close together.  $S_2$  and  $S_3$  are ( $\pi\pi^*$ ) states. In contrast to  $\mathbf{1G}$  solvated in water the  $S_3$  state now corresponds to a local excitation on the G, rather than on the BP subunit.

The  $S_1$  state of the folded snapshot also has ( $n\pi^*$ ) character with similar excitation energy as the  $S_1$  states of the two unfolded snapshots, and similar also to the  $S_1$  state excitation energies of the two folded snapshots in water (*vide supra*). It thus appears that the  $S_1$  state is hardly affected by the different solvent environments and the dynamics of folding and unfolding. The  $S_2$  state of the folded snapshot on the other hand has CT character: in contrast to the case of the water environment and

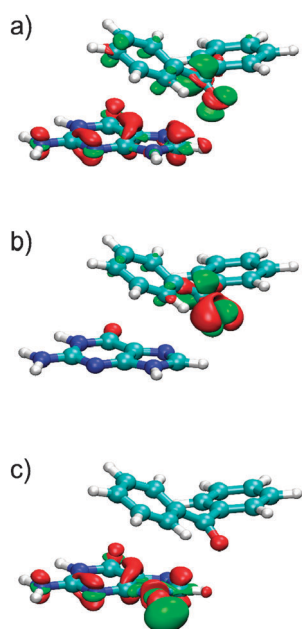


**Fig. 11** Electron density difference plots for the first three excited singlet states of  ${}^a\mathbf{1G}_{H_2O}$ , calculated with TD CC2 in the aug cc pVDZ basis in the QM/MM framework, at the TD DFT/BHLYP CT minimum. Isosurfaces are plotted for  $\pm 0.005$  a.u., red refers to a decrease, green to an increase in the density upon excitation. (a)  $S_1$ : CT state;  $|\Delta\mu| = 15.59$  D (b)  $S_2$ : ( $n\pi^*$ ) state;  $|\Delta\mu| = 2.34$  D (c)  $S_3$ : ( $\pi\pi^*$ ) type state;  $|\Delta\mu| = 14.24$  D.

**Table 5** TD CC2 QM/MM excitation energies  $\omega$  at the respective TD DFT minima, calculated in aug cc pVDZ basis, respectively.  $\Delta E$  ( $\Delta E = E_{\text{tot}}(\text{CT})_{\text{opt}} - E_{\text{tot}}(n\pi^*)_{\text{FC}}$ ) corresponds to the total energy difference of the optimised CT state and the ( $n\pi^*$ ) at the FC point; solvent: MeOH

Structure	State	FC point		(n $\pi^*$ ) state		CT state		$\Delta E$ [eV]
		Type	$\omega$ [eV]	Type	$\omega$ [eV]	Type	$\omega$ [eV]	
${}^a\mathbf{1G}_{MeOH}$	$S_1$	( $n\pi^*$ )	3.78	( $n\pi^*$ )	3.15			
	$S_2$	( $\pi\pi^*$ )	4.70	( $\pi\pi^*$ )	4.66			
	$S_3$	( $\pi\pi^*$ )	4.82	( $\pi\pi^*$ )	4.71			
${}^b\mathbf{1G}_{MeOH}$	$S_1$	( $n\pi^*$ )	3.84	( $n\pi^*$ )	3.13			
	$S_2$	( $\pi\pi^*$ )	4.58	( $\pi\pi^*$ )	4.43			
	$S_3$	( $\pi\pi^*$ )	4.65	( $\pi\pi^*$ )	4.61			
${}^c\mathbf{1G}_{MeOH}$	$S_1$	( $n\pi^*$ )	3.96			CT	2.28	0.84
	$S_2$					( $n\pi^*$ )	3.48	
	$S_3$	( $\pi\pi^*$ )	4.61			( $\pi\pi^*$ )	3.75	

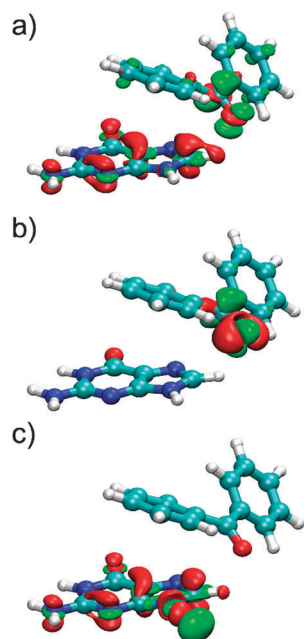


**Fig. 12** Electron density difference plots for the first three excited singlet states of  ${}^c\mathbf{1G}_{\text{MeOH}}$ , calculated with TD CC2 in the aug cc pVDZ basis in the QM/MM framework, at the TD DFT/BHLYP CT minimum. Isosurfaces are plotted for  $\pm 0.005$  a.u., red refers to a decrease, green to an increase in the density upon excitation. (a)  $S_1$ : CT state;  $|\Delta\mu| = 19.75$  D (b)  $S_2$ :  $(n\pi^*)$  state;  $|\Delta\mu| = 2.04$  D (c)  $S_3$ :  $(\pi\pi^*)$  type state;  $|\Delta\mu| = 11.11$  D.

similar to the case of the isolated system, we find a low-lying CT state already at the FC point, only 0.32 eV above the  $S_1$  state. Here, in contrast to the water environment, the solvent shell relaxed for the electronic ground state also stabilizes the CT state (note that BP is soluble in MeOH, but not in water). The density difference plots, dipole differences and relevant molecular orbitals related to  ${}^a\mathbf{1G}_{\text{MeOH}}$  and  ${}^c\mathbf{1G}_{\text{MeOH}}$  are given in the ESI† (Fig. SI-29-b, SI-29-c and SI-30).

In analogy to the calculations performed for  $\mathbf{1G}$  in water geometry optimizations on the  $S_1$  state surface were also performed. For the two unfolded conformers the resulting geometries overall look quite similar to those of the ground state. The distance  $d(\text{C7-O39})$  measuring the degree of unfolding does not alter much.

The  $S_1$  state excitation energy decreases by about 0.7 eV on going from the ground state to the  $S_1$  state minimum, which is very similar to the situation of  $\mathbf{1G}$  in water. The characters of the three lowest excited states at the  $S_1$  state minimum geometry are  $(n\pi^*)$ ,  $(\pi\pi^*)$ , and  $(\pi\pi^*)$ , respectively, with the  $S_3$  state corresponding to a local excitation on the BP, rather than on the G subunit. No CT state occurs.

The situation is entirely different for the folded snapshot: during optimization on the  $S_1$  state surface, the  $S_1$  state switches character from  $(n\pi^*)$  to CT. An optimization of the respective state with  $(n\pi^*)$  character was not possible. The CT state minimum energy geometry definitely constitutes the deepest minimum; the total energy drops by about 0.8 eV on going from the FC point to the CT state minimum (*cf.* Table 5). Furthermore, the  $d(\text{C7-O39})$  distance contracts from 3.1 to 2.85 Å.

Population transfer from the excited  $(n\pi^*)$  to the CT state thus appears to be rather efficient.

The  $S_2$  state at the CT state minimum geometry has now  $(n\pi^*)$  character. It is similar to the  $S_1$  state at the Franck–Condon point with a dipole moment difference of  $|\Delta\mu| = 2.04$  D. The  $S_3$  state now corresponds to a  $(\pi\pi^*)$  state localized on the G subunit with a very high dipole moment difference of  $|\Delta\mu| = 11.11$  D, which looks quite similar to the  $S_3$  state at the CT minimum of  $\mathbf{1G}$  in water (*cf.* Fig. 10c). The density difference plots and dipole moment differences related to the  $S_1$  (CT) state minimum of  ${}^c\mathbf{1G}_{\text{MeOH}}$  are given in Fig. 12.

From the QM/MM results discussed in this section the following conclusions, independent of the solvent environment, can be drawn: (i) for  $\mathbf{1G}$  in the unfolded form no low-lying CT state is found, which could quench the excited  $(n\pi^*)$  singlet state. Here, the lifetime of the excited  $(n\pi^*)$  state is primarily determined by intersystem crossing to the triplet state. (ii) For  $\mathbf{1G}$  in the folded form, on the other hand, there indeed exists a low-lying CT state in some regions of the configuration space, which could quench the excited  $(n\pi^*)$  singlet state. In the methanol environment, provided that  $\mathbf{1G}$  adopts the folded form, the transition from the  $(n\pi^*)$  to the CT state should be more efficient than in the water environment, where the conical intersection apparently does not cross the downhill path from the FC to the  $S_1$  state minimum point. However, in the methanol environment  $\mathbf{1G}$  predominantly exists in the unfolded form, hence transition from the  $(n\pi^*)$  to the CT state is overall not very frequent. On the other hand, in water,  $\mathbf{1G}$  predominantly exists in the folded form, but the state transition itself is less efficient. We conclude that in both environments quenching of the  $S_1$  state due to population transfer to the dark CT state can occur, but with rather low efficiency due to different reasons. Nevertheless, the calculations predict that the lifetime of the  $(n\pi^*)$  singlet state is not solely governed by ISC, as is also seen in the experiments.

## Discussion

The major goal of this study is to elucidate the conformational influence on photoinduced charge transfer in four different dinucleotides that were designed and synthesized as models to reduce the complexity of the conformational manifold present in double-stranded DNA. The first advantage of the models is that the influence of each of the four different DNA bases on the photo-physical behavior of BP can be studied exclusively. Therefore this approach provides the best chance to get a profound understanding of BP interactions in nucleic acids. The second advantage is that two different solvents can be chosen since the dinucleotides are soluble in  $\text{H}_2\text{O}$  and MeOH.  $\text{H}_2\text{O}$  represents the typical solvent for oligonucleotides in a pH-controlled buffer, whereas MeOH mimics a protic solvent<sup>54</sup> approximately the polarity of the inner part of double stranded DNA (DNA base stack). BP as an artificial nucleoside, allows selective excitation of its photochemically important  ${}^1(n\pi^*)$  transition outside the typical nucleic acid absorption range ( $>300$  nm), which is an important prerequisite to use the chromophore in photochemistry and photobiology.



By employing ultrafast transient absorption spectroscopy it was found that the lifetime of the excited ( $n\pi^*$ ) singlet state is primarily determined by fast intersystem crossing (ISC) to the lowest triplet state. In MeOH the reference compound **1** features a somewhat reduced  $S_1$  ( $n\pi^*$ ) singlet lifetime of 9.4 ps relative to the BP monomer (12.5 ps). Relative to the reference **1**, the  $S_1$  lifetimes of the dinucleotides **1X** are further decreased. This effect is most pronounced for **1G** ( $7.6 \pm 0.5$  ps). These observations indicate a singlet electron transfer in **1X**, and indeed ET from a DNA nucleobase to the  $S_1$  state of BP in MeOH occurs at a rate between  $3 \times 10^9$  and  $25 \times 10^9 \text{ s}^{-1}$ , which competes with the ISC process. In  $\text{H}_2\text{O}$  the lifetime of the  $S_1$  state reduces with decreasing standard oxidation potential  $E^0$  of the adjacent nucleobase similar to what is observed in MeOH. Changing the solvent from MeOH to  $\text{H}_2\text{O}$  has the most dramatic effect in **1G**: the ( $n\pi^*$ ) state lifetime of **1G** now drops to 4.6 ps, while the lifetimes of the other dinucleotides **1X** with  $X = \text{T, A}$  or  $\text{C}$  are much less affected. This can again be attributed to a transition from the  $S_1$  ( $n\pi^*$ ) to a singlet charge transfer (CT) state. The interpretation of the  $S_1$  lifetime shortening is strongly supported by the calculations that find indeed an energetically low lying CT state for **1G** in both solvents. For **1A** and **1G** in  $\text{H}_2\text{O}$  we even find clear spectroscopic signatures for the BP anion moiety. As the triplet energy is well below the singlet one, an ET from the  $S_1$  state must have a large driving force.

The population transfer to the CT state is competitive with the ISC for the **1G** dinucleotide in  $\text{H}_2\text{O}$ , with a 51% yield. The reorganization energy was determined to be  $\lambda = 0.62$  eV in MeOH and is nearly identical ( $\lambda = 0.67$  eV) in the more polar  $\text{H}_2\text{O}$ . Considering the conformational distribution, we find a value for the electronic coupling of  $H_{AB} = 3$  meV. In comparison to previously reported values for electronic coupling<sup>52</sup> the presented value appears to be rather small. It became clear that the solvent controls the conformational distribution and thereby gates the charge transfer due to differences in distance and stacking. Therefore our results represent a full account of the photophysical properties of the singlet and triplet states of the BP chromophore in the context of each of the four different DNA bases.

The theoretical work focuses on the dynamics and electronic structure of the dinucleotide **1G**, which is the most interesting dinucleotide. Extensive molecular mechanics (MM) and hybrid quantum mechanics/molecular mechanics (QM/MM) calculations were carried out for **1G** solvated in MeOH and water. It turns out that **1G** solvated in water predominantly exists in a folded form with the G ring system undergoing  $\pi$ -stacking with one of the rings of BP. The distance between the two ring systems amounts to 5–6 Å. Furthermore, there indeed exists a low-lying CT state, corresponding to the lowest-lying excited singlet state in some part of configuration space. This CT state shifts electron density from the G to the BP subsystem. No conical intersection seam between CT and  $S_1$  ( $n\pi^*$ ) state is found in the vicinity of the Franck–Condon point, or on the path downhill on the potential energy surface towards the  $S_1$  state minimum. This speaks for a possible additional singlet to singlet decay channel for the  $S_1$  ( $n\pi^*$ ) state, which however is not so efficient to outperform ISC, as is indeed observed experimentally. For **1G** solvated in MeOH,

on the other hand, the unfolded form, with the G and the BP subunits being separated by about 15 Å, is the favored arrangement, for which no such decay channel to a CT state exists. However, there are some rather rare occurrences of also a folded form of **1G** in methanol in the MD trajectory. For these a CT state can indeed be observed. The decay channel for the ( $n\pi^*$ ) state *via* this CT state appears to be much more efficient than in the water environment, since the conical intersection is encountered directly on the downhill path from the Franck–Condon point on the ( $n\pi^*$ ) state surface. Nevertheless, since the **1G** predominantly exists in an unfolded form, population transfer from the ( $n\pi^*$ ) to the CT state surface remains inefficient in the methanol environment.

By combining these theoretical results with the experimental work now a complete picture emerges. The almost twice as large lifetime  $\tau_{S_1}$  of **1G** in MeOH *vs.* water (*cf.* Table 2) can thus be explained by the different distances between the donor and the acceptor, which are controlled by the solvent: CT in closed geometry of **1G** ( $\text{H}_2\text{O}$ ) on a time scale of 9 ps against CT in the open geometry of **1G** (MeOH) on a 40 ps time scale. Of course, some smaller fraction of the solvated molecules in MeOH assumes the folded form where the channel to the CT state is open. This explains the somewhat reduced  $S_1$  ( $n\pi^*$ ) state lifetime of  $7.6 \pm 0.5$  ps of **1G** in MeOH compared to that of **1**.

Finally, the photophysical behavior of the triplet state of the BP moiety in **1X** is explored, since the triplet state is predominantly applied in photochemical and photobiological reactions. As already discussed in the previous section, singlet CT processes between the DNA base and the BP chromophore of dinucleotides **1X** solvated in MeOH occur on a time scale of tens of ps, which is comparable to the rate of ISC. In contrast, the lifetimes of the BP  $T_1$  state of the dinucleotides **1X** in MeOH remain unaffected on the ps time-scale by the adjacent nucleobase. There seems to be no charge transfer taking place between the BP  $T_1$  state and the attached nucleobase which is faster than a couple of nanoseconds. And again, the situation in  $\text{H}_2\text{O}$  looks significantly different from MeOH. The lifetimes of the  $T_1$  state of **1C** and **1T** remain unaffected while the  $T_1$  lifetimes of **1G** and **1A** are significantly reduced due to CT from the adjacent nucleobase. In fact, the transient absorption of **1G** and **1A** shows the decay of the triplet spectrum concomitantly with the upcoming spectral signature of the BP radical anion. Charge transfer from the  $T_1$  state occurs in  $\text{H}_2\text{O}$  with  $3.2 \times 10^9$  to  $6.0 \times 10^9 \text{ s}^{-1}$ . In contrast to the fast recombination in the singlet manifold the CT state, which is populated from the BP  $T_1$  state, is long-lived due to spin-forbidden charge recombination. The difference of the triplet photophysics of **1X** in  $\text{H}_2\text{O}$  *vs.* MeOH, once again, can be rationalized by the different geometries. In the predominantly unfolded conformation in MeOH, CT from the triplet state is very unlikely due to a large distance between the chromophore and the DNA bases (15 Å). In the primarily stacked conformation in  $\text{H}_2\text{O}$ , CT becomes principally possible. The photochemistry of the  $T_1$  state that lies energetically lower than the  $S_1$  state is decisive: G and A can clearly be photooxidized, whereas C and T are silent with respect to CT.

## Conclusion and outlook

The central problem that currently emerges from experimental work on photoinduced charge transfer in DNA is that the conformational flexibility of double helical DNA is very complex and occurs on a wide range of time scales. In order to reduce this complexity we designed and synthesized four different dinucleotides **1X** as models to study the conformational influence on photoinduced charge transfer in DNA. The major advantage of such small model compounds is that they are soluble both in water and MeOH. The latter solvent was used to mimic the polarity in the interior of DNA. Using these dinucleotides the conformational influence on photoinduced singlet and triplet charge transfer was studied in full detail by both time-resolved transient absorption spectroscopy and theory. It turned out that the concept of controlling the conformational distribution by the solvent works well.<sup>55</sup> The dinucleotide **1G** in MeOH adopts mainly an open and unfolded geometry, and in H<sub>2</sub>O primarily a stacked conformation. Charge transfer occurs only in the stacked conformation due to the significantly larger distance between BP and the nucleobase in the unfolded geometry. It became clear that the solvents not only control the conformational distribution, they actually gate the charge transfer due to differences in distance and degree of stacking. Therefore, our results give a full understanding of the photophysical properties of the singlet and triplet states of the BP chromophore in the context of each of the four different DNA bases. Since BP was chosen as the photoinduced electron acceptor the dinucleotides represent not only interesting biologically relevant models with respect to charge transfer and DNA damage but also the starting point for future applications in chemical biology, like photoaffinity labeling, and chemical photocatalysis.

## Abbreviations

r.t.	Room temperature
ISC	Intersystem crossing
ET	Electron transfer
DADS	Decay associated difference spectra
SADS	Species associated difference spectra
TA	Transient absorption
NHE	Normal hydrogen electrode

## Acknowledgements

T.M., M.W., and M.W. thank the DFG research training group 1626 “Chemical Photocatalysis” gratefully for funding.

## Notes and references

- (a) Y. A. Berlin, I. V. Kurnikov, D. Baratan, M. A. Ratner and A. L. Burin, *Top. Curr. Chem.*, 2004, **237**, 1; (b) F. D. Lewis, H. Zhu, P. Daublain, T. Fiebig, M. Raytchev, Q. Wang and S. J. Vladimir, *J. Am. Chem. Soc.*, 2005, **128**, 791; (c) B. Giese, *Bioorg. Med. Chem. Lett.*, 2006, **14**, 6139; (d) T. Takada, K. Kawai, M. Fujitsuka and T. Majima, *J. Am. Chem. Soc.*, 2006, **128**, 11012; (e) S. Kanvah, J. Joseph, G. B. Schuster, R. N. Barnett, C. L. Cleveland and U. Landman, *Acc. Chem. Res.*, 2010, **43**, 280; (f) J. Genereux and J. K. Barton, *Chem. Rev.*, 2010, **110**, 1642.
- F. C. Grozema, S. Tonzani, Y. A. Berlin, G. C. Schatz, L. D. A. Siebbeles and M. A. Ratner, *J. Am. Chem. Soc.*, 2008, **130**, 5157.
- (a) M. A. O'Neill and J. K. Barton, *J. Am. Chem. Soc.*, 2004, **126**, 11471; (b) M. A. O'Neill and J. K. Barton, *J. Am. Chem. Soc.*, 2004, **126**, 13234.
- P. Kaden, E. Mayer-Enthart, A. Trifonov, T. Fiebig and H.-A. Wagenknecht, *Angew. Chem., Int. Ed.*, 2005, **44**, 1636.
- (a) F. D. Lewis, A. K. Thazathveetil, T. A. Zeidan, J. Vura-Weis and M. R. Wasielewski, *J. Am. Chem. Soc.*, 2010, **132**, 444; (b) R. Carmieli, A. L. Semigh, S. M. M. Conron, A. K. Thazhaveetil, M. Fuki, Y. Kobori, F. D. Lewis and M. R. Wasielewski, *J. Am. Chem. Soc.*, 2012, **134**, 11251.
- (a) M. C. Cuquerella, V. Lhiaubet-Vallet, J. Cadet and M. A. Miranda, *Acc. Chem. Res.*, 2012, **45**, 1558; (b) B. Kohler, *J. Phys. Chem. Lett.*, 2010, **1**, 2047.
- S. A. Fleming, *Tetrahedron*, 1995, **51**, 12479.
- G. Dorman and G. D. Prestwich, *Biochemistry*, 1994, **33**, 5661.
- R. E. Galaray, L. C. Craig, J. D. Jamieson and M. P. Printz, *J. Biol. Chem.*, 1974, **249**, 3510.
- M. Fagnoni, D. Dondi, D. Ravelli and A. Albini, *Chem. Rev.*, 2007, **107**, 2725.
- D. Ravelli, D. Dondi, M. Fagnoni and A. Albini, *Chem. Soc. Rev.*, 2009, **38**, 1999.
- J. Svoboda and B. König, *Chem. Rev.*, 2006, **106**, 5413.
- P. Wessig, *Angew. Chem., Int. Ed.*, 2006, **45**, 2168.
- C. Müller, A. Bauer and T. Bach, *Angew. Chem., Int. Ed.*, 2009, **48**, 6640.
- C. Müller, A. Bauer, M. M. Maturi, M. C. Cuquerella, M. A. Miranda and T. Bach, *J. Am. Chem. Soc.*, 2011, **133**, 16689.
- D. F. Kauble, V. Lynch and M. J. Krische, *J. Org. Chem.*, 2003, **68**, 15.
- A. Bauer, F. Westkamper, S. Grimme and T. Bach, *Nature*, 2005, **436**, 1139.
- T. E. Lehmann and A. Berkessel, *J. Org. Chem.*, 1997, **62**, 302.
- T. E. Lehmann, G. Müller and A. Berkessel, *J. Org. Chem.*, 2000, **65**, 2508.
- C. Paris, S. Encinas, N. Belmadoui, M. J. Climent and M. A. Miranda, *Org. Lett.*, 2008, **10**, 4409.
- K. Musier-Forsyth and P. Schimmel, *Biochemistry*, 1994, **33**, 773.
- K. Nakatani, T. Yoshida and I. Saito, *J. Am. Chem. Soc.*, 2002, **124**, 2118.
- K. Nakatani and I. Saito, *Top. Curr. Chem.*, 2004, **236**, 163.
- W. Adam, M. A. Arnold, W. M. Nau, U. Pischel and C. R. Saha-Möller, *J. Am. Chem. Soc.*, 2002, **124**, 3893.
- M. Weinberger and H.-A. Wagenknecht, *Synthesis*, 2012, 648.
- T. Douki and J. Cadet, *Int. J. Radiat. Biol.*, 1999, **75**, 571.
- B. Morin and J. Cadet, *Photochem. Photobiol.*, 1994, **60**, 102.
- J. Perdew, *Phys. Rev. B: Condens. Matter Mater. Phys.*, 1986, **33**, 8822.

- 29 A. Schäfer, H. Horn and R. Ahlrichs, *J. Chem. Phys.*, 1992, **97**, 2571.
- 30 O. Christiansen, H. Koch and P. Jørgensen, *Chem. Phys. Lett.*, 1995, **243**, 409.
- 31 (a) T. Schwabe and S. Grimme, *Phys. Chem. Chem. Phys.*, 2007, **9**, 3397; (b) S. Grimme and M. Waletzke, *J. Chem. Phys.*, 1999, **111**, 5645.
- 32 A. D. Becke, *J. Chem. Phys.*, 1993, **98**, 5648.
- 33 F. Furche and R. Ahlrichs, *J. Chem. Phys.*, 2002, **117**, 7433.
- 34 C. Hättig and F. Weigend, *J. Chem. Phys.*, 2000, **113**, 5154.
- 35 C. Hättig and A. Kohn, *J. Chem. Phys.*, 2002, **117**, 6939.
- 36 C. Hättig, *J. Chem. Phys.*, 2003, **118**, 7751.
- 37 D. E. Woon and T. H. Dunning Jr., *J. Chem. Phys.*, 1993, **98**, 1358.
- 38 A. Dreuw, J. L. W. Worth and M. J. Head-Gordon, *Chem. Phys.*, 2003, **119**, 2943.
- 39 D. Tozer, *J. Chem. Phys.*, 2003, **119**, 12697.
- 40 S. Aloise, C. Ruckebusch, L. Blanchet, J. Réhault, G. Buntix and J.-P. Huvenne, *J. Phys. Chem. A*, 2008, **112**, 224.
- 41 M. Wenninger, D. Fazio, U. Megerle, C. Trindler and S. S. Schiesser, *ChemBioChem*, 2011, **12**, 703.
- 42 (a) F. Lewis, T. Wu, Y. Zang, R. Letsinger, S. Greenfield and M. Wasielewski, *Science*, 1997, **277**, 673; (b) T. Fiebig, C. Wan and A. H. Zewail, *ChemPhysChem*, 2002, **3**, 781.
- 43 U. Megerle, I. Pugliesi, C. Schrieffer, C. F. Sailer and E. Riedle, *Appl. Phys. B: Lasers Opt.*, 2009, **96**, 215.
- 44 R. V. Bensasson and J. C. D. Gramain, *Faraday Trans. I*, 1980, **76**, 1801.
- 45 C. A. M. Seidel, A. Schulz and M. H. M. Sauer, *J. Phys. Chem.*, 1996, **100**, 5541.
- 46 K. R. Walczyk, G. S. Popkirov and R. N. Schindler, *Ber. Bunsenges. Phys. Chem.*, 1995, **99**, 1028.
- 47 (a) Y.-T. Kao, X. Guo, Y. Yang, Z. Liu, A. Hassanali, Q.-H. Song, L. Wang and D. Zhong, *J. Am. Chem. Soc.*, 2012, **116**, 9130; (b) J. Li, Z. Liu, C. Tan, X. Guo, L. Wang, A. Sancar and D. Zhong, *Nature*, 2010, **466**, 887.
- 48 R. A. Marcus, *J. Chem. Phys.*, 1956, **24**, 966.
- 49 (a) D. Rehm and A. Weller, *Isr. J. Chem.*, 1970, **8**, 259; (b) V. Lhiaubet, N. Paillous and N. Chouini-Lalanne, *Photochem. Photobiol.*, 2001, **74**, 670; (c) N. A. Borisevich, D. V. Kazberuk, N. A. Lysak and G. B. Tolstotozhev, *J. Appl. Spectrosc.*, 1994, **60**, 193.
- 50 P. S. Rao and E. Hayon, *J. Am. Chem. Soc.*, 1974, **96**, 1295.
- 51 C. Reichardt, *Solvent and Solvent Effects in Organic Chemistry*, Wiley-VCH, Weinheim, 2003.
- 52 F. D. Lewis, R. S. Kalgutkar, Y. Wu, X. Liu, J. Liu, R. T. Hayes, S. E. Miller and M. R. Wasielewski, *J. Am. Chem. Soc.*, 2000, **122**, 12346.
- 53 J. W. Verhoeven, *J. Photochem. Photobiol., C*, 2006, **7**, 40.
- 54 M. Weinberger, F. Berndt, R. Mahrwald, N. P. Ernsting and H.-A. Wagenknecht, *J. Org. Chem.*, 2013, **78**, 2589.
- 55 M. J. Lowe and J. A. Shellman, *J. Mol. Biol.*, 1972, **65**, 91.





## **Appendix A5**

### **Unraveling the flavin-catalyzed photooxidation of benzylic alcohol with transient absorption spectroscopy from sub-pico- to microseconds**

*Uwe Megerle, Matthias Wenninger, Roger-Jan Kutta, Robert Lechner,  
Burkhard König, Bernhard Dick, Eberhard Riedle*

Physical Chemistry Chemical Physics 2011, 13, 8869-8880



Cite this: *Phys. Chem. Chem. Phys.*, 2011, **13**, 8869–8880

www.rsc.org/pccp

PAPER

# Unraveling the flavin-catalyzed photooxidation of benzylic alcohol with transient absorption spectroscopy from sub-pico- to microseconds

Uwe Megerle,<sup>a</sup> Matthias Wenninger,<sup>a</sup> Roger-Jan Kutta,<sup>b</sup> Robert Lechner,<sup>c</sup> Burkhard König,<sup>c</sup> Bernhard Dick<sup>b</sup> and Eberhard Riedle<sup>\*a</sup>

Received 21st January 2011, Accepted 23rd February 2011

DOI: 10.1039/c1cp20190e

Flavin-mediated photooxidations have been described for applications in synthetic organic chemistry for some time and are claimed to be a route to the use of solar energy. We present a detailed investigation of the involved photophysical and photochemical steps in methoxybenzyl alcohol oxidation on a timescale ranging from sub-picoseconds to tens of microseconds. The results establish the flavin triplet state as the key intermediate for the photooxidation. The initial step is an electron transfer from the alcohol to the triplet state of the flavin catalyst with  ${}^3k_{\text{ET}} \approx 2 \times 10^7 \text{ M}^{-1} \text{ s}^{-1}$ , followed by a proton transfer in  $\sim 6 \mu\text{s}$ . In contrast, the electron transfer involving the singlet state of flavin is a loss channel. It is followed by rapid charge recombination ( $\tau = 50 \text{ ps}$ ) without significant product formation as seen when flavin is dissolved in pure benzylic alcohol. In dilute acetonitrile/water solutions of flavin and alcohol the electron transfer is mostly controlled by diffusion, though at high substrate concentrations  $> 100 \text{ mM}$  we also find a considerable contribution from preassociated flavin–alcohol-aggregates. The model including a productive triplet channel and a competing singlet loss channel is confirmed by the course of the photooxidation quantum yield as a function of substrate concentration: We find a maximum quantum yield of 3% at 25 mM of benzylic alcohol and significantly smaller values for both higher and lower alcohol concentrations. The observations indicate the importance to perform flavin photooxidations at optimized substrate concentrations to achieve high quantum efficiencies and provide directions for the design of flavin photocatalysts with improved performance.

## 1. Introduction

Riboflavin, vitamin B<sub>2</sub>, is an important biological redox cofactor capable of two subsequent one electron transfers.<sup>1</sup> Due to its reasonably strong absorption up to 500 nm and the redox properties of its excited states it has been used as a chemical photocatalyst operating with visible light. Flavin-based photoredox systems were inspired by the biological model of photolyase, a light driven bacterial enzyme repairing thymine dimer DNA lesions by photoinduced single electron transfer. Its mode of action has been investigated and mimicked by several model systems. The studies revealed the photocatalytic one electron repair mechanism and the dependence of the efficiency on the distance of the reduced flavin and additional sensitizing chromophores.

Preparative flavin-mediated photooxidations<sup>2,3</sup> were investigated by Shinkai,<sup>4,5</sup> Fukuzumi<sup>6–8</sup> and others.<sup>9–12</sup> To enhance the photocatalytic efficiency and photocatalyst stability, heterocyclic substrate binding sites or flavin transition metal complexes have been used. The redox properties of flavin were modulated by hydrogen bonding and transition metal complexation.<sup>13–16</sup> Scandium complexes of flavin without a detailed described structure were used by Fukuzumi to investigate photophysical parameters and propose a mechanistic scheme of the process. Some of us have used zinc-cyclen appended flavins for the photooxidation of benzyl alcohols<sup>17</sup> and recently extended the synthetic scope to photocatalytic cleavage of benzyl protection groups and photooxidation of activated hydrocarbons by flavin tetraacetate and blue light.<sup>18</sup>

Flavin photocatalysts reported so far were designed on the assumption that close proximity of the substrate and flavin chromophore will enhance the efficiency and selectivity of the photooxidation process. This assumption is based on the well known distance dependence of electron transfer as described by the Marcus theory and successful examples from template photochemistry.<sup>19</sup> However, our preliminary quantum yield determinations of the flavin photooxidation at different substrate

<sup>a</sup> Lehrstuhl für BioMolekulare Optik, Ludwig-Maximilians-Universität München, 80538 München, Germany. E-mail: riedle@physik.lmu.de; Fax: +49 89 2180 9202; Tel: +49 89 2180 9210

<sup>b</sup> Institut für Physikalische und Theoretische Chemie, Universität Regensburg, D-93040 Regensburg, Germany

<sup>c</sup> Institut für Organische Chemie, Universität Regensburg, D-93040 Regensburg, Germany

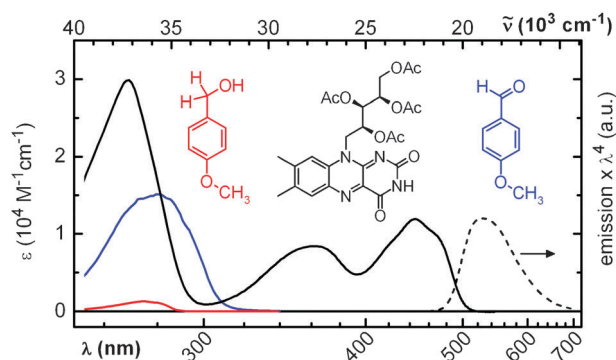


**Fig. 1** Steady state absorption spectra of the oxidized form of riboflavin tetraacetate (RFTA, black), 4-methoxybenzyl alcohol (MBA, red) and 4-methoxy-benzaldehyde (blue) dissolved in MeCN/H<sub>2</sub>O (50 : 50, v/v). The emission spectrum of RFTA is shown as a dashed line. The wavelength scale is reciprocal to render a linear energy scale shown at the top.

concentrations indicated that this assumption is not generally valid.<sup>20</sup> Therefore it seems necessary to reinvestigate the flavin mediated benzyl alcohol photooxidation with state-of-the-art time resolved spectroscopic methods.

The photophysical properties of flavins have been studied for almost a century.<sup>21,22</sup> In the past decade, transient absorption studies with picosecond to microsecond resolution have been carried out in solution<sup>23–26</sup> and in protein environment<sup>27–33</sup> to gain insight into the excited state dynamics of flavin-based systems. The experimental studies have been assisted by various *ab initio* calculations.<sup>34–40</sup> In many cases, the first step of the photo-initiated dynamics consists of an ultrafast electron transfer from a donor to the excited flavin.

In the present paper we aimed at gaining a complete understanding of the photooxidation mechanism of 4-methoxybenzyl alcohol (MBA) to the corresponding aldehyde using riboflavin tetraacetate (RFTA) as catalyst (Fig. 1). We found that relevant processes during the reaction occur both in the singlet and triplet manifold of RFTA states. Therefore, the timescales for the productive reactions and loss channels range from sub-picoseconds to several microseconds. To measure the fast singlet dynamics we used a setup based on a femtosecond white light pulse as a probe, while the slower triplet dynamics were monitored with a Streak camera using a pulsed Xe-flashlamp to generate the probe light. This unique combination of state-of-the-art spectrometers renders a detailed picture of the flavin photoreaction and thereby helps to derive structural design guidelines for photocatalysts with improved performance.

## 2. Experimental section

Riboflavin tetraacetate (RFTA) was synthesized as previously reported.<sup>12</sup> 4-methoxybenzyl alcohol (MBA) was obtained from Acros and distilled before use. The solvents acetonitrile (MeCN), water and DMSO were of spectroscopic quality. The steady state spectra were recorded with a Perkin-Elmer Lambda 19 spectrophotometer and a Spex Fluorolog 2 spectrofluorometer at room temperature. For the fluorescence measurements, the optical density of the sample in a 1 cm cuvette was 0.05 at the excitation wavelength of 420 nm. The fluorescence

spectrum was corrected for the instrument response and multiplied by a factor of  $\lambda^4$  to obtain the spectral shape of the stimulated emission in the time resolved absorption spectra.<sup>41</sup>

### Femtosecond transient absorption measurements

The femtosecond spectrometer has been described in detail.<sup>42</sup> A Ti:sapphire amplifier system (CPA 2001; Clark MXR) was used to pump a noncollinear optical parametric amplifier tuned to 480 nm. The pulses were compressed to  $\sim 50$  fs and attenuated to 400 nJ at the sample position. By focusing another part of the Ti:sapphire laser into a moving CaF<sub>2</sub> disk (4 mm thickness), a probe white light was generated ranging from below 300 nm to 750 nm. A computer controlled delay line was used to set pump-probe delays up to 1 ns. The pump and probe pulses were focused into the sample to spot sizes of 120  $\mu\text{m}$  and 30  $\mu\text{m}$  FWHM using spherical mirrors. After the interaction in the sample, the probe beam was dispersed with a fused silica prism and detected with a photodiode array of 512 pixels. The relative polarizations between the pump and probe were set to the magic angle (54.7°) by a half-wave plate in the pump-beam path. The  $\sim 1.5$  ps chirp of the white light was corrected for prior to the data analysis using the coherent artifact as an indicator for time zero at each wavelength. Throughout the probe range, the spectral resolution was better than 100  $\text{cm}^{-1}$  and the temporal resolution was better than 150 fs. For the experiments in MeCN/H<sub>2</sub>O (50 : 50, v/v) solution, the temperature of the sample was set to 300 K. A flow cell with 1 mm thickness was used and the flavin concentration was 0.5 mM. The measurements in pure MBA and in MeCN/DMSO (98 : 2, v/v) were performed with a flow cell of 120  $\mu\text{m}$  thickness at ambient temperature. Here, the flavin concentration was 2 mM.

### Microsecond transient absorption measurements

To measure transient spectra in the range from nanoseconds to 20  $\mu\text{s}$  the sample was excited with 8–10 ns pulses at 450 nm from a 10 Hz Optical Parametric Oscillator (OPO, Continuum) pumped by the third harmonic of a Nd:YAG laser (Surelite II, Continuum). A pulsed 150 W Xe flashlamp (MSP-05, Müller Elektronik-Optik) was used as probe light and the full time range was monitored at once with a streak camera (C7700, Hamamatsu Photonics).<sup>32</sup> RFTA was dissolved in MeCN/H<sub>2</sub>O (50 : 50, v/v) at a concentration of 40.9  $\mu\text{M}$ , which gave an optical density of about 0.5 at 450 nm with a path length of 10 mm. A fused silica flow cuvette with 10 mm of optical path length for excitation and 10 mm for probe light was used. Including the storage vessel and the peristaltic pump, the overall volume was 10 mL. The excitation light was focused into the sample with a cylindrical lens ( $f = 150$  mm), and the pulse energy was adjusted to about 8 mJ per pulse at the sample. Mechanical shutters were used to select pump and probe pulses. The probe light with a very flat intensity profile of 2 ms duration was refocused three times by a series of toric mirrors: on a mechanical shutter to block the continuous light from the Xe flashlamp, on the sample cell, and on the entrance slit of the imaging spectrograph (Bruker 200is, grating 100 grooves per mm) in front of the streak camera.

The streak camera converts the coupled spectral and temporal information into two-dimensional images of the intensity distribution of the probe white light. Each transient absorption data set was calculated from four images taken with a frequency of 0.5 Hz: an image ( $D_{\text{FL}}$ ) with both flash lamp and laser, an image ( $D_0$ ) without any incoming light, an image ( $D_{\text{F}}$ ) only with the flash lamp, and an image ( $D_{\text{L}}$ ) only with the laser. Results represent the average of 100 individual measurement sequences with a time window of 10  $\mu\text{s}$  and a time resolution of 20 ns. The transient absorption is calculated from these data as  $\log[(D_{\text{F}} - D_0)/(D_{\text{FL}} - D_{\text{L}})]$ . The fluorescence of RFTA can be very strong, much brighter than the white light pulse. In this case the fluorescence is not cancelled well in the difference  $D_{\text{FL}} - D_{\text{L}}$  and we used  $D_0$  instead of  $D_{\text{L}}$  as the background for the data  $D_{\text{FL}}$ . The data analysis then yields the fluorescence spectrum as an additional component with unresolved decay time. All described measurements were performed at ambient temperature.

## Data analysis

Data were analyzed with homemade software to obtain decay associated difference spectra (DADS). This analysis corresponds to the least-squares fit:

$$|\Delta\text{OD}(t, \lambda) - \sum_k^N f_k(t) \text{DADS}_k(\lambda)|^2 = \min, \quad (1)$$

where  $\Delta\text{OD}(t, \lambda)$  is the measured data matrix and the  $f_k(t)$  are exponential (or more complex) decay functions convoluted with a Gaussian function as the apparatus response function  $g(t)$

$$f_k(t) = g(t) \otimes \exp(-(t - t_0)/\tau_k). \quad (2)$$

For each manifold  $\{f_k\}$  the DADS display the spectral changes associated with the particular decay times  $\tau_k$ . This procedure does not assume a specific kinetic model assigning the rates to reaction steps, but is compatible with all models that involve only unimolecular reaction steps. The DADS are in turn linear combinations of the species spectra. The linear coefficients depend on the particular kinetic model, *e.g.*, a linear decay sequence or models involving parallel reactions and branching. After a kinetic model has been chosen, the system of linear equations can be solved for the species spectra.

## Quantum yields

Relative product quantum yields (QY) for different MBA concentrations in MeCN/H<sub>2</sub>O (50 : 50, v/v) were determined by the change in the absorbance in the region of 305 to 325 nm. In this region the absorbance of the product 4-methoxybenzaldehyde is much larger than that of MBA, and the contribution of RFTA is constant (compare Fig. 1). Photoexcitation was performed in fused silica cuvettes with a 2 mm by 10 mm cross section. Two high-power LEDs (Luxeon III Emitter LXHL-PBO9, Philips, 150 mW at 460 nm) were mounted at 1 cm distance to each other on opposite sides of the cuvette. The path length for monitoring the changing absorption was 10 mm, for photoexcitation 2 mm. A custom-designed power supply was used to apply light pulses of reproducible length and intensity. Absorption spectra were

measured with a Perkin Elmer Lambda-9 spectrometer. The temperature of the cuvette was held at 20 °C by a thermostat.

Absolute values for the product QYs were obtained by calibration of the maximum value at 25 mM MBA using an LED-based apparatus described in detail elsewhere.<sup>20</sup> Here, the RFTA concentration was set to 2 mM as in the femtosecond experiments. After a defined irradiation time with 20.2 mW of 443 nm light, the chemical yield of 4-methoxybenzaldehyde was determined by quantitative gas chromatography. From the number of absorbed photons and the resulting chemical conversion, the absolute reaction quantum yield was determined.

## 3. Results and discussion

The spectroscopic study of the flavin-catalyzed photooxidation of benzylic alcohol relies on the differing spectra of the various redox and protonation states of flavin. All existing models assume that essentially only the catalyst and the substrate contribute to the reaction steps. Consequently we can deduce the oxidation mechanism from the time resolved observation of the evolving flavin transformation.

### 3.1 Femtosecond dynamics of riboflavin tetraacetate in pure methoxybenzyl alcohol

The simplest and seemingly clearest approach to study the photocatalytic oxidation is to bring the substrate MBA and the catalyst RFTA in direct contact. Typically, one would assume that this system shows the most effective conversion of alcohol to aldehyde since the reactants are inevitably in close proximity. However, we find that the experimental results contradict this assumption.

Even so MBA solidifies at room temperature, the lowering of the melting point by the solute is already sufficient to turn it into a highly viscous liquid that easily dissolves RFTA in mM concentrations. Thus, we could perform transient absorption measurements at ambient temperature in a flow cell without any additional solvent. Fig. 2a shows the transient absorption spectra of RFTA dissolved in pure MBA between -1 and 1000 ps after excitation at 480 nm, the first absorption maximum of flavin. The spectra consist of three major contributions that can all be assigned to RFTA transitions. Two bands with negative changes of the optical density indicate the ground state bleach (GSB) of RFTA around 450 nm and the stimulated emission (SE) around 560 nm. These bands are partially overlaid with the excited state absorption (ESA) that contributes a positive absorption change and has its maximum around 370 nm. All of these signatures decay to the baseline within the observed time window indicating a complete deactivation back to the ground state of RFTA on the timescale of several tens of picoseconds.

A closer inspection of the data reveals a significantly faster decay of the SE around 560 nm than of the ESA or GSB bands. This is clearly seen in Fig. 2b. The few ps decay of the stimulated emission goes along with an apparent redshift of the ESA band by  $\sim 10$  nm. The GSB, however, shows no significant dynamics on this timescale. Except for minor shifts and the missing SE band, the transient spectrum after the fluorescence quenching (at a delay time  $\Delta t = 10$  ps) is similar



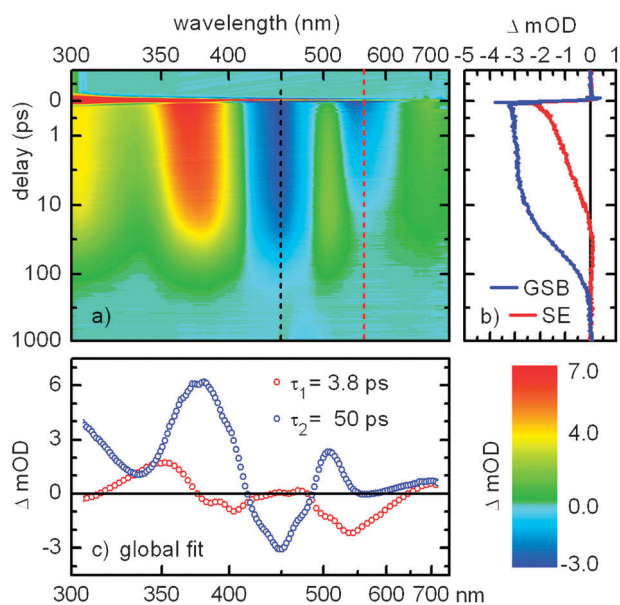


**Fig. 2** (a) Transient absorption of RFTA dissolved in pure methoxybenzyl alcohol after excitation at 480 nm. The delay time axis is linear between  $-1$  and  $1$  ps and logarithmic between  $1$  and  $1000$  ps. (b) Kinetic traces show a faster decay in the band of the stimulated emission (SE,  $560$  nm, red line) than in the ground state bleach (GSB,  $450$  nm, blue line). (c) Decay associated difference spectra from a biexponential global fit.

to the transient spectrum of the  $S_1$  state ( $\Delta t = 0$  ps). This situation is frequently found when the quenching mechanism is an electron transfer to the excited chromophore. Typically, the low energy transitions from the  $S_1$  state involve the promotion of the electron from the highest SOMO (corresponding to the LUMO of the equilibrium molecule) to higher unoccupied orbitals. In first approximation, these transitions are not affected when an additional electron is transferred to the lower lying SOMO of the  $S_1$  state (corresponding to the HOMO). Consistently, the observed spectral features agree well with the absorption spectrum of the flavin radical anion.<sup>43</sup>

This proves that the first step of the photoinduced dynamics is an electron transfer (ET) from one of the surrounding MBA molecules to  $^1\text{RFTA}^*$  yielding the radical anion  $\text{RFTA}^{\bullet-}$  and the radical cation  $\text{MBA}^{\bullet+}$ . The weak signature of the radical cation expected around  $440$  nm<sup>44–46</sup> is not observed spectroscopically as it is masked by the much stronger ground state bleach of flavin. The absence of any residual signals at long delay times indicates a full charge recombination by back electron transfer from  $\text{RFTA}^{\bullet-}$  to  $\text{MBA}^{\bullet+}$ .

In a precise description, the ET process described above changes the ESA band of  $^1\text{RFTA}^*$  into a very similar product absorption of  $\text{RFTA}^{\bullet-}$ . Due to the spectral similarity and the nearly identical intensity, we choose to use the term “ESA band” for the denomination of both.

To quantify the dynamics of the ET processes, we perform a least square global analysis using a biexponential fit function. We find that the spectral evolution can be well reproduced with two decay time constants of  $3.8$  and  $50$  ps. The decay associated difference spectra shown in Fig. 2c underline the qualitative description given above. The fast time constant is

negligible in the region of the GSB, but forms the strongest contribution in the SE band. The dispersive shape of the amplitude spectrum around  $370$  nm again shows the fast spectral shift of the ESA band. In contrast, the decay associated difference spectrum of the  $50$  ps component has a very low amplitude in the SE band, but reflects the concerted decay of ESA and GSB.

Thus, after photoexcitation, the system of RFTA in pure MBA performs a nonproductive cycle of fast forward ET ( $\sim 4$  ps), but also rapid back-ET ( $50$  ps) that restores the reactants RFTA and MBA to the ground state. It is noteworthy that the triplet state  $^3\text{RFTA}$  does not play a role under these conditions as the known rate of intersystem crossing<sup>39,47</sup> is about three orders of magnitude smaller than the competing  $S_1$  quenching rate of  $\sim (4 \text{ ps})^{-1}$ . The fast back-reaction essentially rules out any further electron or proton transfer steps from MBA to RFTA needed to convert the alcohol to aldehyde. From the photocatalytic point of view, dissolving RFTA directly in the substrate MBA inhibits an effective utilization of photons, *i.e.* a good photoreaction quantum yield. The results from the ultrafast spectroscopic analysis explain why practically no conversion of MB-alcohol to MB-aldehyde can be observed even under long-time irradiation. To reach traceable aldehyde concentrations in an alcohol environment requires so many excitations per RFTA molecule that the flavin will likely degrade before.

### 3.2 Femtosecond dynamics in a dilute solution of MeCN/DMSO

As shown in the previous section, a direct contact between MBA and RFTA is not desirable for efficient photocatalysis. To circumvent this we used the “inert” solvent acetonitrile (MeCN) to dissolve RFTA and MBA in chosen concentrations. For better solubility of RFTA (up to  $2$  mM), we added  $2$  vol.% of DMSO to MeCN. By changing the MBA concentration one can then tune the average distance between the reactants. Based on the strong distance dependence of electron transfer one can also expect the rates to decrease significantly.

The transient absorption spectra of RFTA in solution are very similar to the ones in pure MBA. As shown in Fig. 3a, they consist of the same signatures, most prominently a strong ESA band around  $360$  nm, the negative GSB around  $440$  nm and the negative SE band around  $550$  nm. Small differences in the shape and position of these bands with respect to the ones observed in pure MBA can be explained by the lower polarity of the MeCN/DMSO mixture.<sup>48</sup>

In the absence of MBA, our time window of  $1$  ns allows for the observation of only the onset of a slow decay of all signals. This decay reflects the photophysical lifetime of the  $S_1$  state of flavin. With time correlated single photon counting we can determine the fluorescence lifetime of RFTA with higher accuracy and find a value of  $6.0$  ns, very similar to other flavins in solution.<sup>26</sup> Upon addition of MBA in concentrations of several hundred mM, one observes an increasingly faster decay of all signatures. For example, at  $300$  ps delay and  $400$  mM MBA, the amplitude of the RFTA signals has dropped to  $50\%$  of the initial value directly after excitation (Fig. 3a).

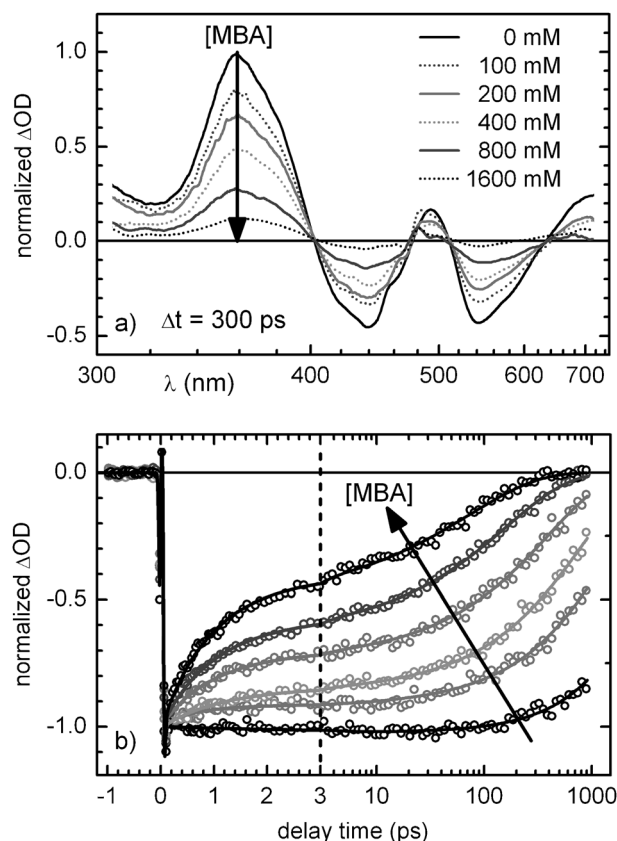


**Fig. 3** (a) TA spectra of RFTA in MeCN/DMSO (98 : 2, v/v) for different MBA concentrations at 300 ps delay. The spectra have been normalized to the initial amplitude of the ESA band after photo-excitation. (b) Decay of the SE of RFTA in MeCN/H<sub>2</sub>O (50 : 50, v/v) for the same MBA concentrations as in (a). The kinetic traces are obtained from band integrals (525–625 nm, circles). The fit functions according to the diffusion model described in the text are shown as solid lines. The delay time axis is linear between –1 and 3 ps and logarithmic between 3 and 1000 ps.

In contrast to the situation in pure MBA, the SE now decays on the same timescale as the other signatures. The reason for this is that the reaction of <sup>1</sup>RFTA\* with MBA is now a two-stage process: first, the reactants have to approach from a large separation distance to close proximity by diffusion and then the ET and all subsequent steps occur in this close configuration. If the concentration of MBA is not extremely high (< 1 M), the rate to form an encounter pair of <sup>1</sup>RFTA\* and MBA is much smaller than the first-order rate coefficient <sup>1</sup>k<sub>ET</sub> = (4 ps)<sup>–1</sup> of the ET and also smaller than the back reaction rate <sup>1</sup>k<sub>b–ET</sub> = (50 ps)<sup>–1</sup> (see Section 3.1). Hence, the observed dynamics are governed by the diffusion limited formation of <sup>1</sup>RFTA\*–MBA-encounter pairs that lead to a non-productive deactivation of <sup>1</sup>RFTA\* by an ET cycle like in pure MBA. Again, this model is qualitatively confirmed by the absence of any product signals at long delays for the highest MBA concentrations.

For a quantitative modeling of the diffusion dynamics, the use of single or multi-exponential fit functions is generally not justified. In the case of diffusive quenching, the intensity decay becomes non-exponential due to a time dependence of the reaction rate.<sup>49,50</sup> The transient effect originates from a changing concentration of MBA quenchers around the excited RFTA molecules.

The concentration is directly related to the average distance between the reactants and thereby to the time needed for an encounter after a random walk. Following excitation, the RFTA chromophores with nearby quenchers from the statistical distribution will react first. At later times, the ensemble of left over excited flavins faces a smaller effective MBA concentration and reacts with a smaller rate. At some point, the depletion of the MBA density around the remaining RFTA\* molecules is balanced by the diffusion of bulk MBA molecules towards RFTA\*. Thus, the reaction rate decreases from an initially high value to a constant that depends on the mutual diffusion coefficient *D* and the interaction distance *R*<sub>int</sub> of the molecules.

The derivation of the mathematical description of this model follows ref. 49. It starts from Fick's law of diffusion for the MBA quencher molecules:

$$\frac{\partial \rho_{\text{MBA}}(r, t)}{\partial t} = D \nabla^2 \rho_{\text{MBA}}(r, t) \quad (3)$$

The concentration of MBA quencher molecules is described by the normalized density distribution  $\rho_{\text{MBA}}$  around a spherical RFTA\* molecule at  $r = 0$ . The diffusion equation contains three partial derivatives, the general solution therefore requires one initial condition at fixed time and two boundary conditions for fixed space coordinates. In the Smoluchowski theory, the initial condition is used that at the moment of excitation  $\rho_{\text{MBA}}$  is homogeneous around any RFTA molecule, *i.e.*  $\rho_{\text{MBA}}(r, t = 0) = 1$  for  $r > R_{\text{int}}$ , but no reactant separation smaller than the interaction distance  $R_{\text{int}}$  is possible, *i.e.*  $\rho_{\text{MBA}}(r, t = 0) = 0$  for  $r \leq R_{\text{int}}$ . One boundary condition is obtained by assuming that the bulk concentration of quenchers far away from the excited chromophore is not affected by the reaction, *i.e.*  $\rho_{\text{MBA}}(r \rightarrow \infty, t) = 1$ . The second boundary condition follows from the fact that no quencher molecules are found at a distance  $R_{\text{int}}$  from the excited chromophores at any time, *i.e.*  $\rho_{\text{MBA}}(R_{\text{int}}, t) = 0$ .

Solving eqn (3) under these conditions and substituting the result into the particle current of MBA molecules through a surface of area  $4\pi R_{\text{int}}^2$  yields the reaction rate of MBA quenchers with the excited RFTA\* molecules:<sup>49</sup>

$$\begin{aligned} -\frac{d[\text{RFTA}^*]}{dt} &= 10^3 N_A 4\pi R_{\text{int}} D \left( 1 + \frac{R_{\text{int}}}{\sqrt{\pi D t}} \right) [\text{MBA}]_0 [\text{RFTA}^*] \\ &= k_{\text{diff}}(t) [\text{MBA}]_0 [\text{RFTA}^*] \end{aligned} \quad (4)$$

$[\text{MBA}]_0$  and  $[\text{RFTA}^*]$  are the initial concentrations of MBA and excited RFTA molecules in the solution. The multiplication with  $10^3 N_A$  where  $N_A$  is Avogadro's number is needed to convert  $k_{\text{diff}}(t)$  to units of  $\text{M}^{-1} \text{s}^{-1}$ .

The change in optical density  $\Delta\text{OD}(t)$  observed in our transient experiments is proportional to  $[\text{RFTA}^*](t)$ . Integrating eqn (4) therefore yields an expression that can be used directly to model the diffusion controlled fluorescence quenching:

$$\begin{aligned} \Delta\text{OD}(t) &= \Delta\text{OD}(0) \exp \left\{ -\frac{t}{\tau_{\text{fl}}} - 10^3 N_A 4\pi R_{\text{int}} D [\text{MBA}]_0 \left( 1 + \frac{2R_{\text{int}}}{\sqrt{\pi D t}} \right) t \right\}. \end{aligned} \quad (5)$$

**Table 1** Results of the fit to the femtosecond TA data for varying MBA concentrations in two solvent mixtures using the diffusion model. The exponential contribution from pre-associated aggregates yielded  $\tau_{\text{fast}}(\text{SE}) = 4.5$  ps and  $\tau_{\text{fast}}(\text{ESA}) = 36$  ps in MeCN/DMSO and  $\tau_{\text{fast}}(\text{SE}) = 0.9$  ps and  $\tau_{\text{fast}}(\text{ESA}) = 6.4$  ps in MeCN/H<sub>2</sub>O. The resulting interaction radii were 3.8 Å and 6.0 Å, respectively.

[MBA]/mM	100	200	400	800	1600
	MeCN/DMSO (98 : 2)				
$A_{\text{fast}}/A_{\text{diff}}$	0.05	0.06	0.09	0.16	0.25
$D/\text{Å}^2 \text{ ns}^{-1}$	160	130	110	100	90
$\tau_{\text{fl,eff}}/\text{ps}$	1100	740	420	230	87
$\Phi_{\text{ISC}}/\Phi_{\text{ISC},0}$ (%)	18	12	7.0	3.8	1.5
	MeCN/H <sub>2</sub> O (50 : 50)				
$A_{\text{fast}}/A_{\text{diff}}$	0.07	0.17	0.32	0.57	0.95
$D/\text{Å}^2 \text{ ns}^{-1}$	59	60	56	52	42
$\tau_{\text{fl,eff}}/\text{ps}$	1400	700	310	120	45
$\Phi_{\text{ISC}}/\Phi_{\text{ISC},0}$ (%)	23	12	5.2	2.0	0.75

Here,  $\tau_{\text{fl}}$  is the fluorescence lifetime of RFTA, and  $D = D_{\text{RFTA}} + D_{\text{MBA}}$  is the mutual diffusion constant.

The Smoluchowski diffusion model provides a consistent description of the predominant contribution to the dynamics for all MBA concentrations and over the whole spectral range. For the quantitative modeling, we preferred band integrals over transients at individual wavelengths. This minimizes the influence of spectral diffusion caused for instance by solvation or vibrational cooling. For a given MBA concentration, the diffusion dynamics in all three major bands (ESA, GSB and SE) could be described by one common set of parameters. The obtained values are given in Table 1.

In MeCN/DMSO solution, the mutual diffusion constant  $D$  of RFTA and MBA was found to lie between 90 and 160 Å<sup>2</sup> ns<sup>-1</sup>. This is in good agreement with the values estimated from the Stokes–Einstein relationship for spherical particles with radius  $R$  in a solution of viscosity  $\eta$  at the absolute temperature  $T$ :

$$D = \frac{k_{\text{B}}T}{6\pi\eta} \left( \frac{1}{R_{\text{RFTA}}} + \frac{1}{R_{\text{MBA}}} \right) \geq \frac{k_{\text{B}}T}{6\pi\eta R_{\text{MBA}}}. \quad (6)$$

From its bulk properties,  $R_{\text{MBA}}$  can be estimated to 3.7 Å, while  $\eta$  of pure MeCN at room temperature is 0.34 mPa s<sup>51</sup> yielding  $D \geq 170$  Å<sup>2</sup> ns<sup>-1</sup>. In the presence of DMSO and upon addition of MBA, the viscosity of the solution rises and  $D$  decreases accordingly (see Table 1).

As expected, the interaction distance  $R_{\text{int}}$  was not found to change for different MBA concentrations within the accuracy of our experiment. Interestingly, the obtained value of 3.8 Å is significantly smaller than the sum of the molecular radii of RFTA and MBA. This indicates that a specific orientation, most likely a face-to-face geometry, is required for an efficient electron transfer.<sup>52,53</sup>

For low MBA concentrations, the agreement between the diffusion model and our transient data is quite satisfactory. However, at higher MBA concentrations we observe an additional very fast component in the flavin kinetics. Since the Smoluchowski theory already poses an upper bound for the reaction rate at contact,<sup>54</sup> this cannot be due to the simplifying assumptions of the diffusion fit function. For a consistent modeling at all MBA concentrations, we therefore added an exponential term with a ps decay time to the fit function.

As shown in Table 1, the relative amplitude  $A_{\text{fast}}$  of this component rises with the MBA concentration. It can therefore be assigned to preassociated RFTA–MBA aggregates<sup>54,55</sup> which are not subject to diffusion control.

This assignment is supported by the characteristic decay time  $\tau_{\text{fast}}$  obtained from the fit: it is not dependent on the MBA concentration and it is smaller in the spectral region of the SE (4.5 ps) than in the ESA band (36 ps). This reflects the forward and backward electron transfer times in the aggregates, in agreement to the situation of RFTA dissolved in pure MBA. From the relative aggregate contribution at different MBA concentrations, one can calculate an association constant of  $K = 0.2 \text{ M}^{-1}$  for RFTA–MBA-complexes in MeCN/DMSO solution. This value is even smaller than the weak association constants around  $1 \text{ M}^{-1}$  found for other aromatic molecules of similar size in MeCN solution.<sup>56</sup> We assume that the aggregates consist of a  $\pi$ -stacked configuration of RFTA and MBA whose driving force is the hydrophobicity of the chromophores.

A careful check of the steady state absorption spectrum at varying MBA concentration in the RFTA solution did not render significant changes relative to the variation induced by changes in the polarity of the solvent. This is not unexpected considering the weak association constant and the large energy difference between the lowest RFTA excitation and the lowest MBA excitation.

Overall, the Smoluchowski diffusion model extended by the contribution from preassociated aggregates completely describes the observed dynamics of RFTA and MBA in dilute solution. Thus, no indications for a significant catalytic photooxidation of MBA to the aldehyde can be found, at least not for the MBA concentrations that are compatible with ultrafast spectroscopy. The higher this concentration, the faster the quenching of the S<sub>1</sub> state of RFTA by ET from MBA, which is then followed by rapid charge recombination.

### 3.3 Changes to the femtosecond dynamics upon the addition of water

From earlier studies<sup>17</sup> it is known that the quantum yield of flavin-catalyzed photooxidation of benzylic alcohol can rise significantly in the presence of water. We therefore performed a series of additional measurements in MeCN/H<sub>2</sub>O (50 : 50, v/v) solution. Overall, we find similar spectral signatures and dynamics as in MeCN/DMSO. Again, an increase of the MBA concentration leads to a faster quenching of the RFTA fluorescence and an essentially concerted decay of all other transient signatures. The same diffusion model with an additional contribution from preassociated RFTA–MBA aggregates could be used to reach a consistent quantitative description of the dynamics (see Fig. 3b). However, the set of parameters had to be altered in comparison to the MeCN/DMSO solution.

First, the contribution of preassociated RFTA–MBA aggregates is now considerably higher. At 1600 mM MBA, the ratio of RFTA molecules in aggregates to free ones approaches 1 : 1 (see Table 1). The obtained association constant of  $K' = 0.6 \text{ M}^{-1}$  is three times higher than in the absence of water. This confirms the hydrophobic effect as a driving force for the aggregation: this effect is of course stronger in the protic and



more polar solvent mixture including water.<sup>56</sup> The characteristic times for the forward (0.9 ps, SE band) and backward ET (6.4 ps, ESA band) inside the aggregates are smaller than in the MeCN/DMSO solution. This might be due to an interaction with the water molecules, *e.g.*, *via* hydrogen bonds that induce a favorable orientation of MBA and RFTA in the aggregates.

Secondly, the parameters of the Smoluchowski diffusion model are also slightly different in the presence of water. We find smaller mutual diffusion constants that indicate a larger effective radius of the moving particles (see eqn (6)). This means that RFTA and MBA probably diffuse together with their solvent shell. A slowed down diffusion of MBA through the last solvent layer around RFTA might add to the effect.<sup>55</sup> The increased amount of “bound” solvent molecules is also supported by the larger interaction distance of 6 Å.<sup>52</sup>

Whereas the obtained parameters from the diffusion model give rich insight into the processes on the molecular level, they are difficult to be interpreted in terms of relevant timescales. To obtain a graspable measure for the reaction dynamics at the different MBA concentrations in both solvent mixtures, we determined an effective fluorescence lifetime  $\tau_{\text{fl,eff}}$  from the normalized integral over the change in signal  $\Delta\text{OD}(\text{SE}; t)$  in the range of the stimulated emission:<sup>57</sup>

$$\tau_{\text{fl,eff}} = \frac{1}{\Delta\text{OD}(\text{SE}; 0)} \int_{t=0}^{\infty} \Delta\text{OD}(\text{SE}; t) dt. \quad (7)$$

This measure is meaningful, as it recovers the decay time for a simple exponential decay as well as the weighted average for a multi-exponential and increases monotonically for longer complex decays. The results are given in Table 1. For technical reasons the values are most reliable for the high MBA concentrations. Their faster dynamics can be observed better within our fixed time window and therefore less extrapolation is required. Nevertheless, the comparison of MeCN/DMSO with MeCN/H<sub>2</sub>O shows that the difference of the reaction speed decreases towards smaller MBA concentrations and eventually changes sign. At 1600 mM, the higher amount of aggregation in the presence of water outweighs the slower diffusion dynamics resulting in half the effective fluorescence lifetime. In contrast, at 100 mM MBA (and below), the contribution from RFTA–MBA-aggregates can be neglected and the speed of the diffusion is the only relevant parameter. Then, the smaller diffusion constants in the aqueous environment lead to a larger fluorescence lifetime than in MeCN/DMSO.

### 3.4 Dynamics involving the triplet state of RFTA

The findings presented above show no photooxidation of MBA as long as the forward and backward ET happen in the singlet manifold. As shown explicitly for RFTA in three different environments (pure MBA, MeCN/DMSO and MeCN/H<sub>2</sub>O), the ET reaction of MBA with <sup>1</sup>RFTA\* is followed by rapid charge recombination. The relevance of this loss channel is lowered when the MBA concentration is decreased. Indeed the chemical conversion was reported at 2 mM,<sup>11</sup> much lower than the concentrations used in the femtosecond measurements. With lower MBA concentration, the probability for intersystem crossing of the excited RFTA rises.

A measure of the quantum yield of triplet formation  $\Phi_{\text{ISC}}$  relative to the intrinsic yield  $\Phi_{\text{ISC},0}$  in the absence of MBA is given by the ratio between  $\tau_{\text{fl,eff}}$  and the native fluorescence lifetime of RFTA of 6.0 ns. As shown in Table 1,  $\Phi_{\text{ISC}}$  is higher in the presence of water for MBA concentrations below 100 mM which could contribute to the increased reaction quantum yield in buffer solution found at low substrate concentrations.<sup>17</sup>

To accentuate the spectral signature of <sup>3</sup>RFTA with our femtosecond setup, we redirected the pump light and omitted the prism compressor and the delay stage. The shortened optical path of the pump pulses resulted in a fixed delay of 12 ns for the white light probe, twice the fluorescence lifetime of flavin. As shown in Fig. 4, the transient spectrum of RFTA in pure MeCN/H<sub>2</sub>O solution measured in this way (dotted line) differs significantly from the S<sub>1</sub> spectrum obtained shortly after excitation ( $\Delta t = 300$  fs, dashed line). On the short wavelength side, the absorption maximum shifts by 2200 cm<sup>-1</sup> from 358 nm to 388 nm. A comparison with the GSB band shows that the extinction coefficient of the ESA band has dropped by roughly a factor of three.

On the long wavelength side above 500 nm, the negative signature from the stimulated emission is largely missing in the 12 ns transient. Instead, a broad absorption is observed with a double peak around 650 and 710 nm and a smaller peak at 510 nm. This is in good agreement with published triplet spectra of similar flavin compounds.<sup>43,58</sup> When MBA is added to the solution (solid line), the amplitude of all signatures decreases, in analogy to the situation at 300 ps delay shown in Fig. 3a. A normalization to the GSB minimum shows that even at 12 ns delay the transient of RFTA without MBA has the expected weak contribution from <sup>1</sup>RFTA\* as seen from the higher absorption around 360 nm and the lower one in the SE region (see Fig. 4) compared to the spectrum with 50 mM MBA.

The dynamics of the triplet state proceed on a nano- to microsecond timescale. This range cannot be covered with the femtosecond setup and transient data were therefore measured with the Streak-camera setup. The obtained spectra at short delay times < 1 μs are identical with the 12 ns spectra

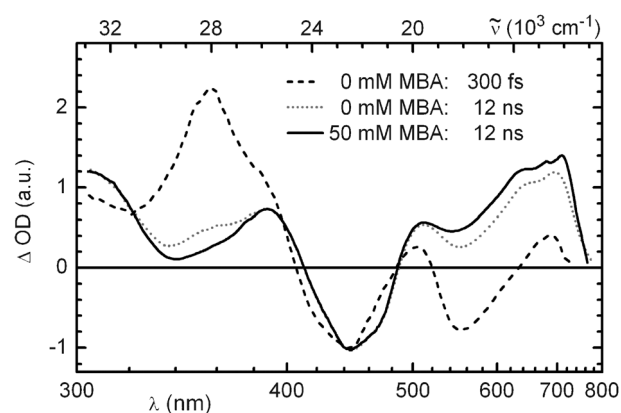


**Fig. 4** Transient absorption spectra of RFTA in MeCN/H<sub>2</sub>O (50 : 50, v/v) directly after excitation (singlet state; dashed line) and after 12 ns delay (triplet state; dotted and solid lines). The spectra have been normalized to the ground state absorption minimum.

from the fs-setup. However, in striking contrast to the unproductive singlet reaction observed in the ultrafast experiments, the  $\mu\text{s}$  measurements reveal a productive reaction between MBA and  $^3\text{RFTA}$  beyond the forward and back-ET. This is most clearly seen as a persistent signature on the 10  $\mu\text{s}$  scale that agrees well with the neutral protonated flavin radical  $\text{RFTA}\cdot^+$  (for details see below).

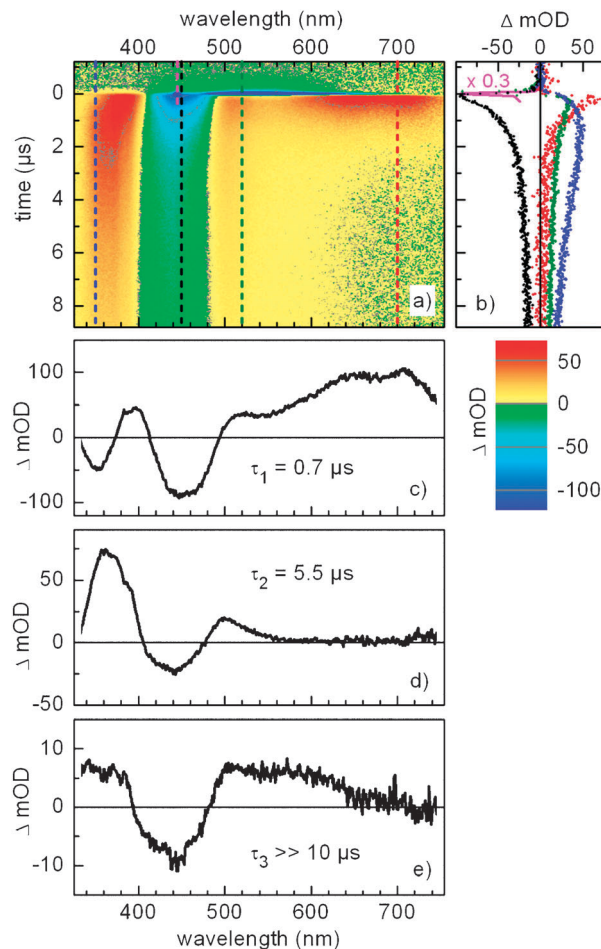
Without MBA in the solution, the TA signal from  $^3\text{RFTA}$  decays monoexponentially with  $\tau = 1.3 \mu\text{s}$  (data not shown). The corresponding rate of  $7.7 \times 10^5 \text{ s}^{-1}$  reflects the diffusional triplet quenching by oxygen in the solution and compares well to similar systems reported in the literature.<sup>24,59,60</sup> Upon addition of MBA, the observed dynamics show significant changes.

Fig. 5 shows the data obtained with 40.9  $\mu\text{M}$  RFTA and 50 mM MBA in MeCN/H<sub>2</sub>O (50 : 50, v/v) solution after excitation at 445 nm. Panel a shows a false colour map of the 2D-transient absorption data matrix. Panel b shows time traces at various wavelengths: the line in magenta represents the time profile of the pump pulse corresponding to the instrument response function. The red dots (700 nm) can be assigned to absorption of the triplet state, decaying with a lifetime of 700 ns. Bleaching at 450 nm (black dots) only recovers partially on this scale. The rise and decay of the green dots (520) and the blue dots (350 nm) indicate the presence of transient intermediates.

A model which contains, in addition to the instrument response function, two exponential functions and one constant term was found suitable to fit the data (Table 2). The fit yields the fluorescence spectrum (associated with the instrument response, not shown) and three decay associated difference spectra (DADS) shown in panels c–e. From the fastest time constant and the intrinsic triplet lifetime in the presence of oxygen we calculated a quenching constant of  $^3k_{\text{ET}} = 1.3 \times 10^7 \text{ M}^{-1} \text{ s}^{-1}$  corresponding to an ET from MBA to  $^3\text{RFTA}$ . The corresponding DADS reflects the conversion of  $^3\text{RFTA}$  to  $\text{RFTA}\cdot^-$  (see Fig. 5c) as seen from the disappearance of the broad long-wavelength absorption and a blueshift of the maximum at  $\sim 370 \text{ nm}$ .<sup>43</sup> The radical ion pair  $\text{RFTA}\cdot^-$  and  $\text{MBA}\cdot^+$  has two deactivation pathways: back-ET to the ground state of the system and the productive proton transfer from MBA to flavin yielding a neutral radical pair. The sum of these two rates was fitted to  $1.8 \times 10^5 \text{ s}^{-1}$ , corresponding to a lifetime of the ion pair of 5.5  $\mu\text{s}$  in accordance with previous studies.<sup>46,61</sup> According to our model, flavin and MBA are in contact—or at least close proximity—after the initial ET. Therefore, the decay of the ion pair should not depend on the substrate concentration. We find a small increase of the effective ion pair lifetime by a factor of 2 when the MBA concentration is increased by a factor of 10 from 50 mM to 500 mM.

In our detection window of up to 20  $\mu\text{s}$ , we observe the signature of a non-decaying species displaying a broad absorption between 500 and 600 nm and a maximum around 350 nm (see Fig. 5e). The signature can be assigned to the neutral protonated flavin radical  $\text{RFTA}\cdot\text{H}^+$ .<sup>43,58,62</sup> This confirms the proposed mechanism of ET followed by a proton transfer between MBA and flavin in the triplet state.

We thus propose that the measurement in the 10  $\mu\text{s}$  range reflects the following reaction steps: The initially populated



**Fig. 5** (a) False colour map of the 2D-transient absorption data matrix measured with 40.9  $\mu\text{M}$  RFTA and 50 mM MBA in MeCN/H<sub>2</sub>O (50 : 50, v/v) solution after excitation at 445 nm. (b) Time traces at various wavelengths. (c–e) Decay associated difference spectra from the global fit.

**Table 2** Results of the global fit to the streak camera measurements for varying MBA concentrations.  $\tau_1 = (k_{\text{b-ISC}} + ^3k_{\text{ET}}[\text{MBA}])^{-1}$ ;  $\tau_2 = (k_{\text{PT}} + ^3k_{\text{b-ET}})^{-1}$ ;  $\tau_3 = (k_{\text{prod}})^{-1}$ . For  $[\text{MBA}] = 0 \text{ mM}$ :  $\tau_1 = (k_{\text{b-ISC}})^{-1} = (7.7 \times 10^5 \text{ s}^{-1})^{-1}$

[MBA]/mM	$\tau_1/\mu\text{s}$	$^3k_{\text{ET}}/\text{M}^{-1} \text{ s}^{-1}$	$\tau_2/\mu\text{s}$	$\tau_3/\mu\text{s}$
0	1.3	—	—	—
2	1.2	$3.2 \times 10^7$	—	—
20	0.92	$1.6 \times 10^7$	4.1	$\gg 10$
50	0.70	$1.3 \times 10^7$	5.5	$\gg 10$
100	0.57	$0.99 \times 10^7$	6.3	$\gg 10$
200	0.31	$1.2 \times 10^7$	8.0	$\gg 10$
500	0.09	$2.1 \times 10^7$	11	$\gg 10$

triplet state decays with a total rate constant  $k_1$ . A fraction  $\alpha$  of this decays into the radical anion  $\text{RFTA}\cdot^-$ , whereas a fraction  $(1 - \alpha)$  decays back to the ground state. Similarly, the total decay of  $\text{RFTA}\cdot^-$  occurs with rate constant  $k_2$  with a fraction  $\beta$  forming the neutral radical  $\text{RFTA}\cdot\text{H}^+$  and a fraction  $(1 - \beta)$  falling back to the ground state. The decay associated difference spectra  $\text{DADS}_1$ ,  $\text{DADS}_2$ , and  $\text{DADS}_3$  (see Fig. 5) corresponding to the three rate constants  $k_1$ ,  $k_2$ , and  $k_3 \approx 0$  are then

expressed in terms of the species associated difference spectra  $SADS_{\text{triplet}}$ ,  $SADS_{\text{neutral radical}}$  and  $SADS_{\text{radical anion}}$  by:

$$DADS_1 = SADS_{\text{triplet}} + \frac{\alpha}{k_1 - k_2} (k_2 \beta \cdot SADS_{\text{neutral radical}} - k_1 \cdot SADS_{\text{radical anion}})$$

$$DADS_2 = \frac{\alpha k_1}{k_1 - k_2} (SADS_{\text{radical anion}} - \beta \cdot SADS_{\text{neutral radical}})$$

$$DADS_3 = \alpha \beta \cdot SADS_{\text{neutral radical}} \quad (8)$$

This system of linear equations can be inverted to yield the SADS but the inversion requires knowledge of the fractions  $\alpha$  and  $\beta$ , which cannot be determined by a fit to the data:

$$\begin{aligned} SADS_{\text{triplet}} &= DADS_1 + DADS_2 + DADS_3 \\ SADS_{\text{radical anion}} &= (DADS_3 + DADS_2 (1 - k_2/k_1))/\alpha \end{aligned} \quad (9)$$

$$SADS_{\text{neutral anion}} = DADS_3/(\alpha\beta)$$

The fraction  $\alpha$ , however, can be calculated from the total decay rate constants of the triplet in the absence ( $k_0$ ) and in the presence ( $k_1$ ) of MBA as  $\alpha = 1 - k_0/k_1$ . For an MBA concentration of 50 mM we find  $\alpha = 0.46$ . The fraction  $\beta$  only enters in the expression for  $S_{\text{neutral radical}}$  as a scaling parameter. The true species associated spectra (SAS) can be obtained from the SADS by adding the ground state spectrum in an appropriate amount depending on the excitation conditions. Fig. 6 shows the SAS of the three intermediate flavin states obtained from the data at 50 mM MBA and assuming  $\beta = 0.3$ . The SAS are in very good agreement with previously reported absorption spectra of flavin in the triplet state, the semi-quinone radical anion and the protonated neutral radical state.<sup>43</sup>

The proposed sequential electron and proton transfer is also confirmed by experiments at different pH values. Under acidic conditions (addition of 1 mM HCl to the sample solution), we observed no radical anion anymore, but immediately ( $\Delta t \approx 50$  ns) the formation of the neutral radical out of the triplet state. In contrast, under alkaline conditions (addition of 1 mM NaOH to the sample solution) no neutral radical could be seen, but only the radical anion form of RFTA.

In our experiments we cannot yet observe the final step of the reaction yielding the fully reduced flavin and the MB-aldehyde. The required hydrogen atom transfer or disproportionation reactions likely occur on slower timescales up to the ms regime.<sup>63</sup>

### 3.5 Mechanism of the photocatalytic MBA oxidation

From the spectroscopic studies on the various timescales we can compile a detailed scheme of the photooxidation mechanism of MBA in the presence of RFTA (Fig. 7). The rapid, non-productive forward and back-ET from the singlet state of flavin is opposed by the productive stepwise redox reaction involving the triplet state of flavin. The complete picture is confirmed by the non-trivial dependence of the reaction quantum yield (QY) on the substrate concentration shown in Fig. 8. The relative QY for the various concentrations was measured by illumination with a high power LED, the absolute

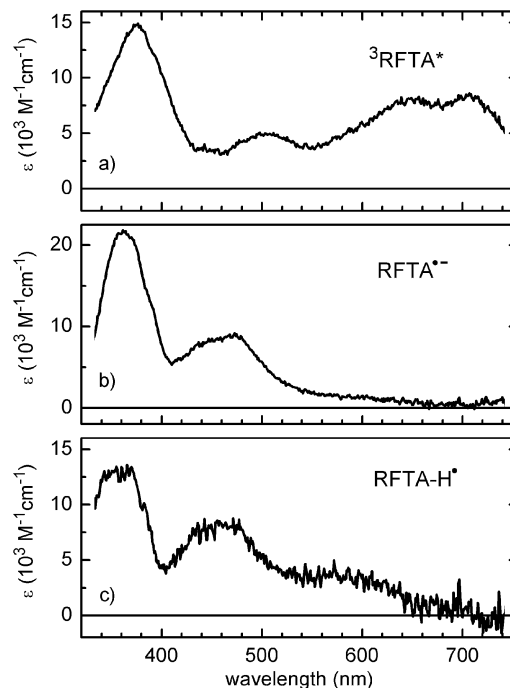


**Fig. 6** Species Associated Spectra (SAS) resulting from the proposed model using the Decay Associated Difference Spectra (DADS) from the global fit analysis. The used parameters were:  $\alpha = 0.46$ ,  $\beta = 0.3$  and  $SAS_{\text{ground state}} = 0.3 S_0$  as the fraction of ground state which was added.

QY by subsequent gas chromatographic detection of the chemical conversion.<sup>20</sup> For a productive singlet channel, one would expect that the QY increases monotonically with the MBA concentration and reaches a constant value at some point.<sup>6–8</sup> However, we find a completely different behavior with a maximum QY of 3% at 25 mM MBA. For both lower and higher MBA concentrations we observe a significant drop of the QY. This can be well understood with our model. At high MBA concentrations, the required ISC to <sup>3</sup>RFTA cannot occur due to fast and non-productive  $S_1$  quenching by MBA. At concentrations below 25 mM, the diffusional approach of MBA and RFTA is becoming slow compared to the intrinsic triplet lifetime. Thus, a balance of the diffusion timescale—*via* the MBA concentration—and the ISC rate is necessary in order to have an encounter of the reactants at the right time: when RFTA is not in the singlet state any more but has not yet relaxed from the triplet state either.

To model quantitatively the dependence of the reaction quantum yield  $\Phi_{\text{tot}}$  on the MBA concentration we use the fit results from the spectroscopic experiments to deduce the QYs of the individual productive steps, *i.e.* intersystem crossing, electron transfer and proton transfer:

$$\begin{aligned} \Phi_{\text{tot}} &\leq \Phi_{\text{ISC}} \Phi_{\text{ET}} \Phi_{\text{PT}} \\ &\leq \frac{k_{\text{ISC}}}{\tau_{\text{fl}}^{-1} + {}^1k_{\text{ET}}[\text{MBA}]} \frac{{}^3k_{\text{ET}}[\text{MBA}]}{{}^3k_{\text{ET}}[\text{MBA}] + k_{\text{b-ISC}}} \frac{k_{\text{PT}}}{{}^3k_{\text{b-ET}} + k_{\text{PT}}} \end{aligned} \quad (10)$$

The less than or equal sign in eqn (10) refers to the fact that the last step of the reaction, which at the moment lies beyond our

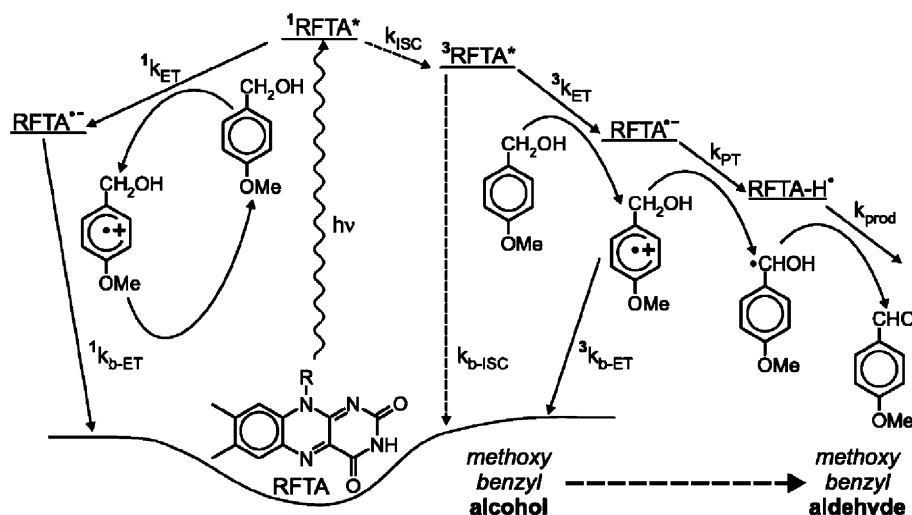


**Fig. 7** Scheme of the oxidation mechanism of MBA. The non-productive singlet channel (left hand side) brings the excited RFTA back to the ground state after diffusion controlled electron transfer from MBA ( $^1k_{ET}$ ) and fast charge recombination ( $^1k_{b-ET}$ ). The encounter of MBA with a triplet flavin (right hand side) can eventually lead to product formation *via* a sequence of electron and proton transfer events. Details see text.

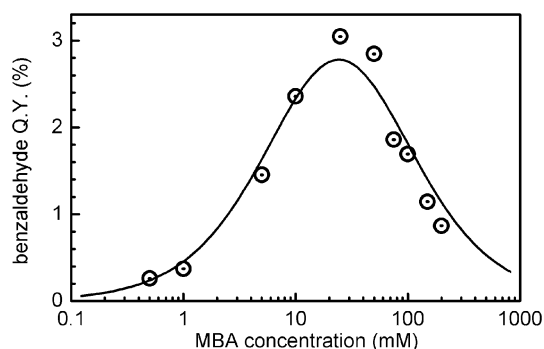


**Fig. 8** Circles: Quantum yield of benzaldehyde production in MeCN/H<sub>2</sub>O (50 : 50, v/v) solution. Solid line: Simulation using the spectroscopically determined reaction rates.

spectroscopically accessible timescale, could further reduce the total QY. The QYs of intersystem crossing  $\Phi_{ISC}$  and electron transfer in the triplet state  $\Phi_{ET}$  depend on the following known rates:

$(\tau_{fl})^{-1} = (6.0 \text{ ns})^{-1} = 1.7 \times 10^8 \text{ s}^{-1}$  (from a TCSPC measurement of the  $^1RFTA^*$  fluorescence)

$^1k_{ET} = 1.3 \times 10^{10} \text{ M}^{-1} \text{ s}^{-1}$  (from a linear fit to  $\tau_{fl,eff}$  at different MBA concentrations)

$^3k_{ET} = 1.7 \times 10^7 \text{ M}^{-1} \text{ s}^{-1}$  (from the  $\mu\text{s}$  decay dynamics at different MBA concentrations)

$k_{b-ISC} = 7.7 \times 10^5 \text{ s}^{-1}$  (from the decay of  $^3RFTA^*$  in the absence of MBA)

The QY of proton transfer  $\Phi_{PT}$  corresponds to the parameter  $\beta = 0.3$  that was used to obtain the SAS (see Section 3.4). Thus,  $k_{ISC}$  is the only free parameter that is not *a priori* known from the spectroscopic analysis. Since it only affects the amplitude of the QY function, the course of  $\Phi_{tot}$  vs. MBA is fixed by the known parameters listed above. As shown in Fig. 8, the derived model (solid line) agrees very well with the measured QYs (circles). This confirms qualitatively and quantitatively the triplet reaction mechanism shown in Fig. 7.

From a least-square fit to the experimental QY data we obtain  $k_{ISC} \geq 1.3 \times 10^8 \text{ s}^{-1}$ . This corresponds to an intrinsic triplet yield of RFTA of 76% in the absence of MBA, which is among the highest values reported for other flavin compounds.<sup>22,37,39</sup> This implies that almost no losses occur in the photooxidation reaction after the first proton transfer step.

For the MeCN/DMSO solvent, *i.e.* in the absence of water, we reported a nearly hundred times lower reaction quantum yield.<sup>20</sup> In the light of the present discussion, we could interpret this as a dramatically reduced probability for proton transfer. It does not seem unlikely that the RFTA radical anion and the MBA radical cation separate by a few solvent molecules between their generation and the proton transfer. In the aqueous environment the hydrogen bond network could still give a good transfer yield, whereas the absence of proton mediators would make this step much more inefficient. One could even speculate that an increased MBA concentration leads to rather far reaching disturbance of the hydrogen network<sup>64</sup> and thereby explains the observed decrease of the proton transfer rate with the rising MBA concentration.

#### 4. Conclusion and outlook

In this work we investigated the flavin-catalyzed photooxidation mechanism of MBA with transient absorption spectroscopy on a timescale ranging from sub-picoseconds to tens of microseconds. The results show that the productive reaction proceeds *via* the triplet state of RFTA and starts with a sequence of an electron and a proton transfer step from MBA to RFTA within 0.1 to 10  $\mu\text{s}$ . In contrast, electron transfer to the singlet excited state of RFTA leads to rapid charge recombination within 50 ps and therefore constitutes a loss channel. Its relevance increases with substrate concentration since diffusion then allows for an encounter of MBA and the excited RFTA before ISC has occurred. In addition, we find a considerable contribution from preassociated RFTA–MBA-aggregates for high MBA concentrations of several 100 mM that also undergo a fast and unproductive



charge separation and recombination cycle. Thus, at high substrate concentrations and especially in pure MBA solution, no significant product formation is observed.

However, if the first ET proceeds after the ISC of RFTA, the charge recombination in the spin correlated radical ion pair is spin forbidden and therefore significantly slowed down.<sup>65</sup> This allows for a higher efficiency of the second reaction step, *i.e.* the proton transfer from  $\text{MBA}^{\bullet+}$  to  $\text{RFTA}^{\bullet-}$ . For a high product QY, the average distance between MBA and RFTA has to be large enough to prevent the likely diffusional encounter within the singlet state lifetime of RFTA which can be achieved by using lower substrate concentrations.

The detailed mechanistic study reveals that the design of a photocatalyst based on the assumption of close proximity of the redox active chromophore and the substrate binding site is not valid for flavins. Instead, other approaches are conceivable to obtain new photocatalysts with improved performance. One possibility is to try to increase the triplet yield by acceleration of the ISC. This might be achieved by exploiting the heavy atom effect through suitable substitution on the flavin chromophore, for instance with sulfur containing groups.<sup>66</sup> Additional substitution of flavin with bulky side chains might impede the aggregation with the substrate by steric hindrance. This would also lead to a higher fraction of excited flavin molecules that can access the triplet state. Another possibility is to use triplet sensitizers<sup>67</sup> that undergo rapid ISC and then transfer their triplet energy to flavin. Thus, the singlet loss channel could be completely circumvented, however with the likely drawback of a higher excitation energy, *i.e.* with the need for UV illumination instead of the desired visible light for the photocatalysis. Performance of the reaction under anaerobic conditions seems tempting, since it would prolong the triplet lifetime. However, oxygen is needed for the reoxidation of RFTA to restore the catalyst. A nearly anaerobic situation might increase the QY at low MBA concentrations, but it would only allow for a very slow overall chemical conversion.

A more promising approach might be to work at high substrate concentrations and render the singlet channel productive. This implies the inhibition of the unproductive back-ET and/or the acceleration of the further productive reaction steps. A concept for this can be found in the general architecture of natural proteins that are involved in redox reactions.<sup>68</sup> There, one frequently finds multiple redox centers in close proximity to each other. By efficient separation of the induced charges along a chain of reaction centers, the charge recombination as well as other deactivation pathways is outpaced. For the flavin photocatalysis, this could imply the attachment of an intermediate electron acceptor unit to the chromophore that also acts as a substrate binding site. After the initial electron transfer from MBA to the intermediate redox center, the negative charge could then be transferred to the flavin. This might slow down the unproductive back electron transfer in favor of subsequent proton and electron transfer events from MBA to the catalyst. Indeed, ten times higher product quantum yields up to 40% were found for the photooxidation of benzylic alcohol using a flavin compound with a covalently linked zinc(II)-cyclen binding site.<sup>17</sup> Further investigations on the details of the reaction mechanism with

this catalyst are needed, as well as an improvement of its photostability. However, the insights from the reaction mechanism of RFTA with MBA described in this work encourage further research along this line to reach higher efficiencies for photocatalytic chemical conversions.

## Acknowledgements

We thank the Deutsche Forschungsgemeinschaft (GRK 1626, SFB 749 and GRK 640) for support of our research. We gratefully acknowledge financial support from the International Max Planck Research School on Advanced Photon Science (U.M.). Discussions with B. Fingerhut and C. F. Sailer were stimulating.

## References

- 1 *Flavins: Photochemistry and Photobiology*, ed. E. Silva and A. M. Edwards, Royal Society of Chemistry, Cambridge, 2006.
- 2 W. Tong, H. P. Ye, H. H. Zhu and V. T. D'Souza, *THEOCHEM*, 1995, **333**, 19–27.
- 3 Y. Yano, *Rev. Heteroat. Chem.*, 2000, **22**, 151–179.
- 4 S. Shinkai, K. Kameoka, K. Ueda, O. Manabe and M. Onishi, *Bioorg. Chem.*, 1987, **15**, 269–282.
- 5 S. Shinkai, K. Kameoka, K. Ueda and O. Manabe, *J. Am. Chem. Soc.*, 1987, **109**, 923–924.
- 6 S. Fukuzumi, S. Kuroda and T. Tanaka, *J. Am. Chem. Soc.*, 1985, **107**, 3020–3027.
- 7 S. Fukuzumi and S. Kuroda, *Res. Chem. Intermed.*, 1999, **25**, 789–811.
- 8 S. Fukuzumi, K. Yasui, T. Suenobu, K. Ohkubo, M. Fujitsuka and O. Ito, *J. Phys. Chem. A*, 2001, **105**, 10501–10510.
- 9 E. Silva, A. M. Edwards and D. Pacheco, *J. Nutr. Biochem.*, 1999, **10**, 181–185.
- 10 A. Mees, C. Behrens, A. Schwögler, M. Ober and T. Carell, *Eur. J. Org. Chem.*, 2003, 2670–2677.
- 11 J. Svoboda, H. Schmaderer and B. König, *Chem.–Eur. J.*, 2008, **14**, 1854–1865.
- 12 H. Schmaderer, P. Hilgers, R. Lechner and B. König, *Adv. Synth. Catal.*, 2009, **351**, 163–174.
- 13 S. Shinkai, G. X. He, T. Matsuda, A. D. Hamilton and H. S. Rosenzweig, *Tetrahedron Lett.*, 1989, **30**, 5895–5898.
- 14 B. König, M. Pelka, R. Reichenbach-Klinke, J. Schelter and J. Daub, *Eur. J. Org. Chem.*, 2001, 2297–2303.
- 15 M. Gray, A. J. Goodman, J. B. Carroll, K. Bardson, M. Markey, G. Cooke and V. M. Rotello, *Org. Lett.*, 2004, **6**, 385–388.
- 16 A. S. F. Boyd, J. B. Carroll, G. Cooke, J. F. Garety, B. J. Jordan, S. Mabruk, G. Rosair and V. M. Rotello, *Chem. Commun.*, 2005, 2468–2470.
- 17 R. Cibulka, R. Vasold and B. König, *Chem.–Eur. J.*, 2004, **10**, 6223–6231.
- 18 R. Lechner and B. König, *Synthesis*, 2010, 1712–1718.
- 19 J. Svoboda and B. König, *Chem. Rev.*, 2006, **106**, 5413–5430.
- 20 U. Megerle, R. Lechner, B. König and E. Riedle, *Photochem. Photobiol. Sci.*, 2010, **9**, 1400–1406.
- 21 R. Kuhn, P. Gyorgy and T. Wagner-Jauregg, *Ber. Dtsch. Chem. Ges. B*, 1933, **66**, 576–580.
- 22 P. F. Heelis, *Chem. Soc. Rev.*, 1982, **11**, 15–39.
- 23 R. J. Stanley and A. W. MacFarlane, *J. Phys. Chem. A*, 2000, **104**, 6899–6906.
- 24 C. Y. Lu, G. Bucher and W. Sander, *ChemPhysChem*, 2004, **5**, 47–56.
- 25 Y. T. Kao, C. Saxena, T. F. He, L. J. Guo, L. J. Wang, A. Sancar and D. P. Zhong, *J. Am. Chem. Soc.*, 2008, **130**, 13132–13139.
- 26 A. Weigel, A. L. Dobryakov, M. Veiga and J. L. P. Lustres, *J. Phys. Chem. A*, 2008, **112**, 12054–12065.
- 27 C. Aubert, M. H. Vos, P. Mathis, A. P. M. Eker and K. Brettel, *Nature*, 2000, **405**, 586–590.
- 28 D. P. Zhong and A. H. Zewail, *Proc. Natl. Acad. Sci. U. S. A.*, 2001, **98**, 11867–11872.

- 29 T. Kottke, J. Heberle, D. Hehn, B. Dick and P. Hegemann, *Biophys. J.*, 2003, **84**, 1192–1201.
- 30 M. Gauden, I. H. M. van Stokkum, J. M. Key, D. C. Lührs, R. Van Grondelle, P. Hegemann and J. T. M. Kennis, *Proc. Natl. Acad. Sci. U. S. A.*, 2006, **103**, 10895–10900.
- 31 A. Lukacs, A. P. M. Eker, M. Byrdin, K. Brettel and M. H. Vos, *J. Am. Chem. Soc.*, 2008, **130**, 14394–14395.
- 32 T. Langenbacher, D. Immeln, B. Dick and T. Kottke, *J. Am. Chem. Soc.*, 2009, **131**, 14274–14280.
- 33 K. Lanzl, M. von Sanden-Flohe, R. J. Kutta and B. Dick, *Phys. Chem. Chem. Phys.*, 2010, **12**, 6594–6604.
- 34 C. B. Martin, M. L. Tsao, C. M. Hadad and M. S. Platz, *J. Am. Chem. Soc.*, 2002, **124**, 7226–7234.
- 35 C. Neiss, P. Saalfrank, M. Parac and S. Grimme, *J. Phys. Chem. A*, 2003, **107**, 140–147.
- 36 E. Sikorska, I. Khmelinskii, A. Komasa, J. Koput, L. F. V. Ferreira, J. R. Herance, J. L. Bourdelande, S. L. Williams, D. R. Worrall, M. Insińska-Rak and M. Sikorski, *Chem. Phys.*, 2005, **314**, 239–247.
- 37 M. Insińska-Rak, E. Sikorska, J. L. Bourdelande, I. V. Khmelinskii, W. Prukała, K. Dobek, J. Karolczak, I. F. Machado, L. F. V. Ferreira, A. Komasa, D. R. Worrall and M. Sikorski, *J. Mol. Struct.*, 2006, **783**, 184–190.
- 38 K. Sadeghian, M. Bocola and M. Schütz, *J. Am. Chem. Soc.*, 2008, **130**, 12501–12513.
- 39 S. Salzmann, J. Tatchen and C. M. Marian, *J. Photochem. Photobiol., A*, 2008, **198**, 221–231.
- 40 S. Salzmann and C. M. Marian, *Photochem. Photobiol. Sci.*, 2009, **8**, 1655–1666.
- 41 G. Angulo, G. Grampp and A. Rosspeintner, *Spectrochim. Acta, Part A*, 2006, **65**, 727–731.
- 42 U. Megerle, I. Pugliesi, C. Schriever, C. F. Sailer and E. Riedle, *Appl. Phys. B: Lasers Opt.*, 2009, **96**, 215–231.
- 43 M. Sakai and H. Takahashi, *J. Mol. Struct.*, 1996, **379**, 9–18.
- 44 E. Baciocchi, M. Bietti, L. Putignani and S. Steenken, *J. Am. Chem. Soc.*, 1996, **118**, 5952–5960.
- 45 M. Bietti, E. Baciocchi and S. Steenken, *J. Phys. Chem. A*, 1998, **102**, 7337–7342.
- 46 E. Baciocchi, M. Bietti and S. Steenken, *Chem.–Eur. J.*, 1999, **5**, 1785–1793.
- 47 S. D. M. Islam, A. Penzkofer and P. Hegemann, *Chem. Phys.*, 2003, **291**, 97–114.
- 48 C. Reichardt, *Solvents and Solvent Effects in Organic Chemistry*, Wiley-VCH, Weinheim, 3rd edn, 2004.
- 49 S. A. Rice, *Diffusion-limited reactions*, Elsevier Science Publishers B.V., Amsterdam, 1985.
- 50 J. R. Lakowicz, *Principles of fluorescence spectroscopy*, Springer Science + Business Media, New York, 3rd edn, 2006.
- 51 J. H. Dymond, M. A. Awan, N. F. Glen and J. D. Isdale, *Int. J. Thermophys.*, 1991, **12**, 443–477.
- 52 S. G. Ballard and D. C. Mauzerall, *J. Chem. Phys.*, 1980, **72**, 933–947.
- 53 X. Allonas, P. Jacques, A. Accary, M. Kessler and F. Heisel, *J. Fluoresc.*, 2000, **10**, 237–245.
- 54 P. Sreearunothai, S. Asaoka, A. R. Cook and J. R. Miller, *J. Phys. Chem. A*, 2009, **113**, 2786–2795.
- 55 S. Pant, H. Ohtaka-Saiki, M. Takezaki, A. D. Scully, S. Hirayama and T. Tominaga, *J. Phys. Chem. A*, 2008, **112**, 5378–5384.
- 56 M. S. Cubberley and B. L. Iverson, *J. Am. Chem. Soc.*, 2001, **123**, 7560–7563.
- 57 M. N. Berberan-Santos, E. N. Bodunov and B. Valeur, *Chem. Phys.*, 2005, **315**, 171–182.
- 58 T. B. Melø, M. A. Ionescu, G. W. Haggquist and K. R. Naqvi, *Spectrochim. Acta, Part A*, 1999, **55**, 2299–2307.
- 59 C. B. Martin, X. F. Shi, M. L. Tsao, D. Karweik, J. Brooke, C. M. Hadad and M. S. Platz, *J. Phys. Chem. B*, 2002, **106**, 10263–10271.
- 60 B. Branchi, M. Bietti, G. Ercolani, M. A. Izquierdo, M. A. Miranda and L. Stella, *J. Org. Chem.*, 2004, **69**, 8874–8885.
- 61 E. Baciocchi, M. Bietti and S. Steenken, *J. Am. Chem. Soc.*, 1997, **119**, 4078–4079.
- 62 F. Müller, M. Brüstlein, P. Hemmerich, V. Massey and W. H. Walker, *Eur. J. Biochem.*, 1972, **25**, 573–580.
- 63 P. F. Heelis, B. J. Parsons, G. O. Phillips and J. F. McKellar, *Photochem. Photobiol.*, 1981, **33**, 7–13.
- 64 M. Heyden, E. Bründermann, U. Heugen, G. Niehues, D. M. Leitner and M. Havenith, *J. Am. Chem. Soc.*, 2008, **130**, 5773–5779.
- 65 J. W. Verhoeven, *J. Photochem. Photobiol., C*, 2006, **7**, 40–60.
- 66 P. Drössler, W. Holzer, A. Penzkofer and P. Hegemann, *Chem. Phys.*, 2003, **286**, 409–420.
- 67 L. Hviid, W. G. Bouwman, M. N. Paddon-Row, H. J. van Ramesdonk, J. W. Verhoeven and A. M. Brouwer, *Photochem. Photobiol. Sci.*, 2003, **2**, 995–1001.
- 68 C. C. Page, C. C. Moser, X. X. Chen and P. L. Dutton, *Nature*, 1999, **402**, 47–52.

## Appendix A6

### **Flavin-induced DNA photooxidation and charge movement probed by ultrafast transient absorption spectroscopy**

*Mark M. Maturi\*, Matthias Wenninger\*, Rafael Alonso\*, Andreas Bauer,  
Alexander Pöthig, Eberhard Riedle, Thorsten Bach*

Chemistry – A European Journal 2013, 19, 7461-7472

\* these authors contributed equally to the work





# Intramolecular [2+2] Photocycloaddition of 3- and 4-(But-3-enyl)oxyquinolones: Influence of the Alkene Substitution Pattern, Photophysical Studies, and Enantioselective Catalysis by a Chiral Sensitizer

Mark M. Maturi,<sup>[a]</sup> Matthias Wenninger,<sup>[b]</sup> Rafael Alonso,<sup>[a]</sup> Andreas Bauer,<sup>[a]</sup>  
Alexander Pöthig,<sup>[a]</sup> Eberhard Riedle,<sup>\*,[b]</sup> and Thorsten Bach<sup>\*,[a]</sup>

**Abstract:** The intramolecular [2+2] photocycloaddition of four 4-(but-3-enyl)oxyquinolones (substitution pattern at the terminal alkene carbon atom: CH<sub>2</sub>, *Z*-CH<sub>2</sub>Et, *E*-CH<sub>2</sub>Et, CMe<sub>2</sub>) and two 3-(but-3-enyl)oxyquinolones (substitution pattern: CH<sub>2</sub>, CMe<sub>2</sub>) was studied. Upon direct irradiation at  $\lambda = 300$  nm, the respective cyclobutane products were formed in high yields (83–95%) and for symmetrically substituted substrates with complete diastereoselectivity. Substrates with a *Z*- or *E*-substituted terminal double bond showed a stereoconvergent reaction course leading to mixtures of regio- and diastereomers with almost identi-

cal composition. The mechanistic course of the photocycloaddition was elucidated by transient absorption spectroscopy. A triplet intermediate was detected for the title compounds, which—in contrast to simple alkoxyquinolones such as 3-butyloxyquinolone and 4-methoxyquinolone—decayed rapidly ( $\tau \approx 1$  ns) through cyclization to a triplet 1,4-diradical. The diradical can evolve through two reaction channels, one leading to the photoproduct and

the other leading back to the starting material. When the photocycloaddition was performed in the presence of a chiral sensitizer (10 mol%) upon irradiation at  $\lambda = 366$  nm in trifluorotoluene as the solvent, moderate to high enantioselectivities were achieved. The two 3-(but-3-enyl)oxyquinolones gave enantiomeric excesses (*ees*) of 60 and 64% at  $-25^\circ\text{C}$ , presumably because a significant racemic background reaction occurred. The 4-substituted quinolones showed higher enantioselectivities (92–96% *ee* at  $-25^\circ\text{C}$ ) and, for the terminally *Z*- and *E*-substituted substrates, an improved regio- and diastereoselectivity.

**Keywords:** cycloaddition • enantioselectivity • photochemistry • sensitizers • time-resolved spectroscopy

## Introduction

Quinolone [2+2] photocycloaddition reactions<sup>[1]</sup> are known since the late 1960s when Evanega and Fabiny reported on the intermolecular reaction of the parent compound (carbostyryl) with various alkenes.<sup>[2]</sup> These studies were preceded by work of Taylor et al.,<sup>[3a]</sup> Elliott,<sup>[3b]</sup> and Buchardt<sup>[3c]</sup> on the [2+2] photodimerization of quinolones. The initial

report by Evanega and Fabiny<sup>[2a]</sup> was followed in rapid succession by several significant contributions from other research groups, most notably from the group of Naito and Kaneko in the 1980s.<sup>[4]</sup> Intramolecular [2+2] photocycloaddition reactions were first reported in 1979<sup>[4d]</sup> and a few reactions of this type were subsequently studied more closely.<sup>[4g,s,5]</sup> The synthetic importance of quinolone [2+2] photocycloaddition is mainly due to further ring-opening reactions at the cyclobutane ring,<sup>[1a,e,6]</sup> which enable access to highly substituted quinolone derivatives (see below).

Mechanistic work on the quinolone [2+2] photodimerization and [2+2] photocycloaddition has revealed that the reactions proceed through the respective triplet excited state ( $T_1$ ), which is populated by direct excitation at  $\lambda = 300$ – $350$  nm to the first excited singlet state ( $S_1$ ) and subsequent rapid intersystem crossing.<sup>[4d,7]</sup> The triplet state can also be populated by sensitization employing compounds with high triplet energy states, for example, benzophenone. The triplet state energy of the parent quinolone has been reported as  $E(T_1) = 276$  kJ mol<sup>-1</sup> corresponding to the energy of a 434 nm photon.<sup>[7a]</sup> The photodimerization of quinolones has been studied by laser flash photolysis,<sup>[7a,b,8]</sup> however, to the best of our knowledge, the course of the intramolecular [2+2] photocycloaddition of quinolones has until recently

[a] M. M. Maturi,<sup>+</sup> Dr. R. Alonso,<sup>+</sup> Dr. A. Bauer, Dr. A. Pöthig, Prof. Dr. T. Bach  
Department Chemie und  
Catalysis Research Center (CRC)  
Technische Universität München  
Lichtenbergstrasse 4  
85747 Garching (Germany)  
Fax: (+49) 89-289-13315  
E-mail: thorsten.bach@ch.tum.de

[b] M. Wenninger,<sup>+</sup> Prof. Dr. E. Riedle  
Lehrstuhl für BioMolekulare Optik  
Ludwig-Maximilians-Universität  
Oettingenstrasse 67, 80538 München (Germany)  
E-mail: riedle@physik.uni-muenchen.de

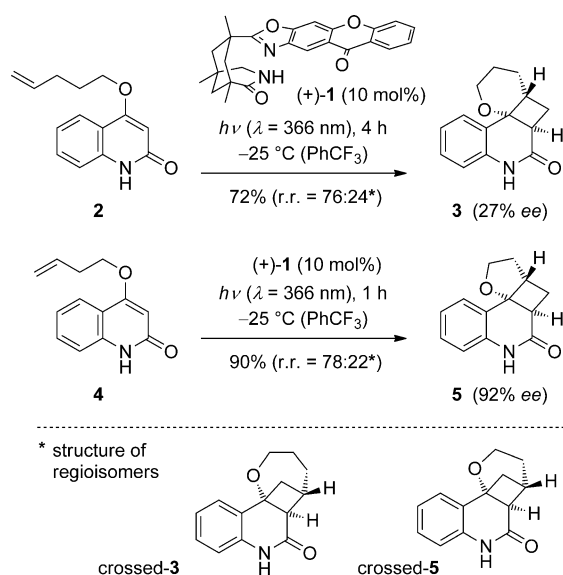
[<sup>+</sup>] These authors contributed equally to this work.

Supporting information for this article is available on the WWW under <http://dx.doi.org/10.1002/chem.201300203>.

(see below)<sup>[9]</sup> not been investigated by transient absorption spectroscopy.

[2+2] Photocycloaddition reactions of quinolones were initially studied in our group<sup>[5b,10]</sup> in the context of enantioselective photochemical reactions mediated by a chiral template.<sup>[11]</sup> Two-point hydrogen-bonding of the quinolone lactam to the lactam part of a chiral bicyclic skeleton<sup>[12]</sup> derived from Kemp's triacid<sup>[13]</sup> led to an efficient enantioface differentiation. An intermolecular reaction of this type was implemented as key step in the first enantioselective total synthesis of the *Melodinus* alkaloid (+)-meloscine. In this case, a ring expansion of the cyclobutane to a cyclopentanone was achieved by a retro-benzilic acid rearrangement.<sup>[14]</sup>

When searching for catalytic enantioselective photochemical reactions,<sup>[15]</sup> we discovered that dextrorotatory xanthone (+)-**1** and its levorotatory enantiomer (–)-**1** exhibit superior catalytic activity in intramolecular quinolone [2+2] photocycloaddition reactions provided that the reacting quinolone was appropriately chosen (Scheme 1).<sup>[9,16]</sup> It was found that



Scheme 1. Major differences in the enantioselectivity (*ee*) of the intramolecular [2+2] photocycloaddition of 4-(pent-4-enyl)oxyquinolone (**2**) and 4-(but-3-enyl)oxyquinolone (**4**) upon sensitization with xanthone (+)-**1**; structure of crossed regioisomers crossed-**3** and crossed-**5** (r.r. = regioisomeric ratio).

the reaction of 4-(but-3-enyl)oxyquinolone (**4**) proceeded under identical conditions with a significantly higher enantioselectivity than the reaction of 4-(pent-4-enyl)oxyquinolone (**2**), the alkyl tether of which is longer by one methylene group than the tether of the former substrate.

The binding properties of both substrates **2** versus **4** and products **3** versus **5** to lactam (+)-**1** should be almost identical. Indeed, it had been previously shown that the reactions **2**→**3** and **4**→**5** proceed with high enantioselectivity in the presence of a stoichiometrically employed template,<sup>[9,10c]</sup> which bears the same 1,5,7-trimethyl-3-azabicyclo-[3.3.1]nonan-2-one skeleton as catalyst **1**. Consequently, the

different behavior in the catalytic reaction seemed to arise from the different kinetic parameters involved in the respective [2+2] photocycloaddition. It was speculated that upon triplet sensitization within a substrate–catalyst complex the subsequent cyclization to an intermediate 1,4-biradical should be faster for substrate **4** (five-membered ring formation) than for substrate **2** (six-membered ring formation). The rate of dissociation from the chiral lactam (+)-**1** competes efficiently with the cyclization rate in the latter case, causing this reaction to occur with lower enantioselectivity. Indeed, it was experimentally shown that the triplet lifetime of compound **4** is significantly shorter than the triplet lifetime of compound **2**. The lifetime of compound **2** in deaerated trifluorotoluene at ambient temperature could be determined by laser flash photolysis as  $\tau [T_1(\mathbf{2})] = 57$  ns. However, the detection limit of the laser setup did not allow for an accurate determination of  $\tau [T_1(\mathbf{4})]$ , which was estimated to be at least by a factor of 0.4 shorter than  $\tau [T_1(\mathbf{2})]$ .<sup>[9]</sup>

In the present study we have largely broadened the scope of quinolone substrates and investigated the reaction behavior of differently substituted 3- and 4-(but-3-enyl)oxyquinolones **6–9** (Figure 1) in the absence and the presence of a chiral sensitizer.

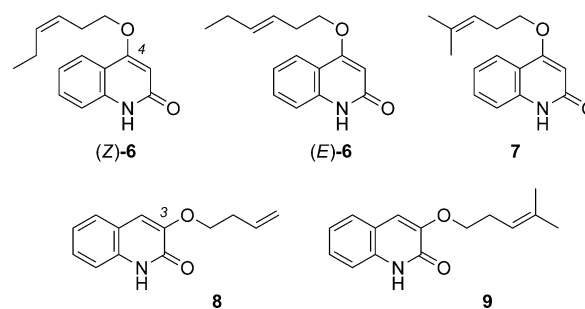
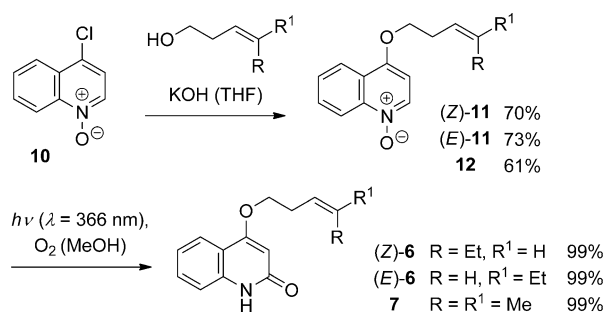


Figure 1. Quinolone substrates **6–9** employed in this study.

The key objective of the study was to prove for 4-(but-3-enyl)oxyquinolones that a higher cyclization rate consistently leads to high enantioselectivity. By using the diastereomerically pure substrates (Z)-**6** and (E)-**6**, conclusions regarding the stereospecificity of the reaction were expected to be drawn. Data for the enantioselective reactions were collected at three different temperatures ( $-25^\circ\text{C}$ ,  $0^\circ\text{C}$ , and RT). The yet completely unexplored 3-(but-3-enyl)oxyquinolones were studied for comparison. The reaction kinetics of the photocycloaddition was followed by transient absorption spectroscopy both on the fs–ps and on the ns– $\mu\text{s}$  time-scale to provide a comprehensive picture of the reaction course through the respective singlet- and triplet state lifetimes.

## Results and Discussion

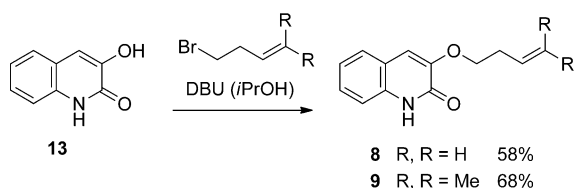
**Synthesis of the quinolone substrates:** The synthesis of 4-(but-3-enyl)oxyquinolones **6** and **7** (Scheme 2) commenced



Scheme 2. Synthesis of 4-(alk-3-enyl)oxyquinolones **6** and **7** from 4-chloroquinolin-*N*-oxide (**10**) by nucleophilic substitution and subsequent photochemical rearrangement.

with an aromatic nucleophilic substitution reaction at 4-chloroquinolin-*N*-oxide<sup>[17]</sup> (**10**). The respective alcohols, which were required to produce the substitution products **11** and **12**, are commercially available. The subsequent rearrangement of the *N*-oxides to the desired products was performed according to a previously reported method,<sup>[18]</sup> which we have optimized in recent years.<sup>[19]</sup> Two modifications are crucial. Firstly, the reaction, which proceeds at the singlet hypersurface, is performed in an oxygen-saturated methanol solution, which avoids reactions of the products from the triplet state (see below). Secondly, a continuous flow system is being used for irradiation, which allows one to optimize the exposure time of the substrates to the light source. It was gratifying to note that this optimization has led to a high level of reproducibility and generality. Product formation was essentially quantitative in all cases and side products were not detected (Scheme 2).

The preparation of 3-(but-3-enyl)oxyquinolones **8** and **9** was straightforward based on literature precedence (Scheme 3). Known 3-hydroxyquinolone (**13**)<sup>[20]</sup> was treated

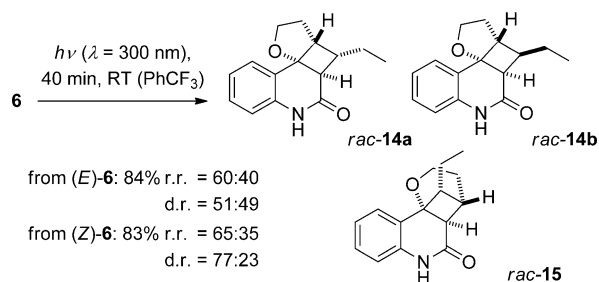


Scheme 3. Synthesis of 3-(alk-3-enyl)oxyquinolones **8** and **9** from the respective bromides by nucleophilic substitution with 3-hydroxyquinolone (**13**).

with the respective alkenyl bromides and 1,8-diazabicyclo[5.4.0]undec-7-ene (DBU) in isopropanol<sup>[21]</sup> to deliver the desired products by nucleophilic substitution. In an analogous fashion, 3-butoxyquinolone was prepared from **13** and butyl bromide.

**[2+2] Photocycloaddition reactions in the absence of a sensitizer at λ = 300 nm:** To check the general feasibility of the photocycloaddition and to secure racemic material for analytical purposes, reactions were performed at λ = 300 nm

(light source: RPR-3000 Å, emission spectrum, see the Supporting Information; *c* = 5 mm). Since the quinolone absorption is relatively high at this wavelength, [2+2] photocycloaddition reactions tend to proceed smoothly without addition of a sensitizer. Indeed, 4-(hex-3-enyl)oxyquinolones (**6**) were converted within 40 min into the respective products. Surprisingly, the regioselectivity was relatively low and, besides the straight products *rac*-**14**, significant amounts of the crossed product *rac*-**15** were obtained (Scheme 4). The



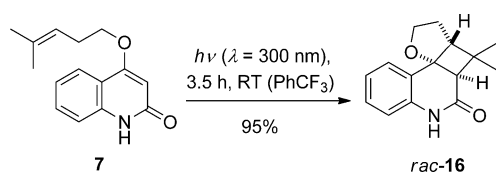
Scheme 4. Intramolecular [2+2] photocycloaddition of 4-(hex-3-enyl)oxyquinolones (**6**) to straight products *rac*-**14** and crossed product *rac*-**15** (r.r. = **14:15**; d.r. = **14a:14b**); light source: RPR-3000 Å (emission spectrum, see the Supporting Information).

straight products *rac*-**14** were formed as two diastereoisomers with *rac*-**14a** prevailing over *rac*-**14b**. A second crossed diastereoisomer apart from *rac*-**15** was not observed. The relative configuration of the products was proven by extensive one- and two-dimensional <sup>1</sup>H NMR studies (see the Supporting Information for further details). Although it is not apparent from the two-dimensional drawings, the preference for the respective diastereoisomer *rac*-**14a** in the straight series and *rac*-**15** in the crossed series can be readily understood from three-dimensional molecular models. In the minor straight diastereoisomer *rac*-**14b**, the ethyl group shows a major steric interaction with the dihydroquinolone ring, which makes the formation of this diastereoisomer less favorable. The situation, that is, the interaction of the ethyl group with the dihydroquinolone ring, would be even worse in the diastereoisomer of *rac*-**15**, which is consequently not formed at all. The photocycloaddition was not stereospecific as expected from a reaction occurring mainly in the triplet manifold.<sup>[22,23]</sup>

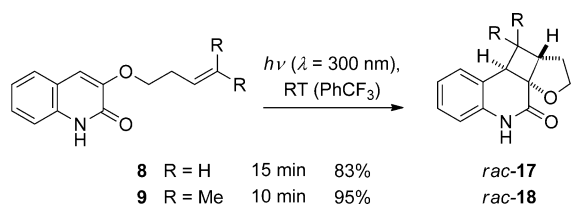
Even the *E* isomer (*E*)-**6**, with the ethyl group and the alkyl chain in a relative *trans*-configuration, gave predominantly products *rac*-**14a** and *rac*-**15**, in which these substituents are *cis*-positioned. The fact that the relative product ratios (regioisomeric ratio (r.r.) and diastereomeric ratio (d.r.)) are not completely identical for (*Z*)-**6** and (*E*)-**6** seems to indicate a minor contribution of the singlet excited state (*S*<sub>1</sub>) to the net reaction. Based on the transient spectroscopy data (see below), however, it is more likely that differences in the first bond formation and in the subsequent reaction branching within the triplet manifold are responsible for this result. The *Z* isomer (*Z*)-**6** exhibits more than a two-fold product efficiency relative to (*E*)-**6**. If the irradiation

experiments were stopped before the conversion was complete, the re-isolated starting material **6** showed epimerization around the double bond. At 0 °C the reactions ( $c = 5 \text{ mM}$  in  $\text{PhCF}_3$ ) were interrupted after five minutes of irradiation. If *Z*-**6** was employed as starting material, the conversion was 60% and the re-isolated substrate showed an *E/Z* ratio of 31/69. If *E*-**6** was used, the conversion was 44% and starting material **6** was recovered in an *E/Z* ratio of 51/49.

The outcome of the [2+2] photocycloaddition of substrate **7** was less complex than that of substrates **6**. Indeed, a single reaction product *rac*-**16** was obtained in high yield (Scheme 5). Complete conversion was achieved after 3.5 h ( $c = 5 \text{ mM}$ ).



Scheme 5. Selective intramolecular [2+2] photocycloaddition of 4-(4-methylpent-3-enyl)oxyquinolone (**7**) to straight product *rac*-**16**.



Scheme 6. Selective intramolecular [2+2] photocycloaddition of 3-(alk-3-enyl)oxyquinolones **8** and **9** to straight products *rac*-**17** and *rac*-**18**.

Similarly, the reaction of 3-(alk-3-enyl)oxyquinolones **8** and **9** ( $c = 2.5 \text{ mM}$ ) proceeded smoothly providing single products *rac*-**16** and *rac*-**17** in high yields (Scheme 6). It is notable that the crossed regioisomer was not observed in the photocycloaddition of 3-(but-3-enyl)oxyquinolone (**8**). The reaction of the 4-substituted analogue **4** delivers under identical conditions the cycloaddition products in a regioisomeric ratio of 86:14.<sup>[9]</sup> The regioselective outcome of the reaction of substrate **9** is in accord with the above-mentioned reaction of the 4-substituted analogue **7**. The reaction times required for complete conversion were relatively short for the 3-alkenyloxy-substituted quinolones **8** and **9** reflecting in part their higher absorption at  $\lambda = 300 \text{ nm}$  (see below).

#### Transient absorption spectroscopy on multiple timescales:

Time-resolved spectroscopic studies, both on the fs–ps and on the ns– $\mu\text{s}$  timescale, were performed with all newly prepared quinolones **6–9** as well as with the previously reported substrate **4**. Two major goals were associated with this study. The first goal was to obtain precise data about the lifetimes  $\tau [T_1]$  of the triplet intermediates derived from substrates **4** and **6–9**. Given the previously mentioned assumption of a

rapid five-membered ring cyclization it was expected that these lifetimes are significantly shorter than the 57 ns determined for  $\tau [T_1(\mathbf{2})]$ .<sup>[9]</sup> A second goal was to substantiate the mechanistic course of the intramolecular quinolone [2+2] photocycloaddition in an extended time interval (fs– $\mu\text{s}$ ) with detection of all relevant intermediates. Time-resolved spectroscopic data covering a sufficient temporal and spectral range for quinolone [2+2] photocycloaddition reaction are scarce<sup>[7–9]</sup> and it was required to obtain a solid database for future studies.

All decay rates and species-associated spectra (SAS) of the occurring intermediate states discussed below were determined by applying a global data analysis on the measured data matrices (see the Experimental Section). 4-Methoxyquinolone (**19**) and 3-butoxyquinolone (**20**), which cannot react in an intramolecular [2+2] photocycloaddition, served as reference to study the intrinsic photophysical properties such as lifetime and spectral properties of the  $S_1$  and  $T_1$  state (Figure 2).

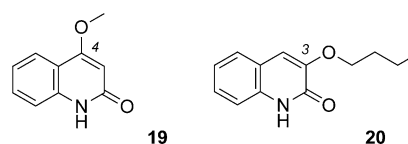


Figure 2. Structures of 4-methoxyquinolone (**19**) and 3-butoxyquinolone (**20**), which were used in the present study as reference compounds.

The excitation wavelength was  $\lambda = 270\text{--}275 \text{ nm}$  in all transient spectroscopy measurements. A reference measurement for **4** at  $\lambda = 330 \text{ nm}$  showed that the observed dynamics are not changed by the excitation to the  $S_2$  state instead of the  $S_1$  state. Since the influence of pump stray light can be dramatically reduced by the shorter wavelength, this choice was preferred. To secure optical transparency in the UV range and due to solubility reasons, acetonitrile was employed as the solvent in all experiments ensuring a homogeneous solution of equal concentration ( $c \approx 0.5 \text{ mM}$ , optical density [318 nm, 1 mm]  $\approx 0.5$ ) for all substrates. The studies were performed under aerobic conditions at room temperature. The solubility of oxygen in air-equilibrated acetonitrile is known to be  $2.4 \text{ mM}$ <sup>[24]</sup> and at this oxygen concentration an interference with intramolecular reaction processes (displaying rate constants larger than  $10^7 \text{ s}^{-1}$ ) was not to be expected.<sup>[25]</sup>

For the time-resolved measurements and their interpretation the steady-state absorption and emission spectra of all compounds were determined. As expected, the spectral properties were equal within the measurement error for all 4-substituted quinolones (**19**, **4**, (*Z*)-**6**, (*E*)-**6**, **7**) and for all 3-substituted quinolones (**20**, **8**, **9**), since the electronic properties of the absorbing chromophore remain constant within each substrate series. The measured spectra are exemplarily shown for both chromophores **19** and **20** in Figure 3. Although the shape of the spectra is very similar for the two compounds, it should be noted that the absorption of the 3-

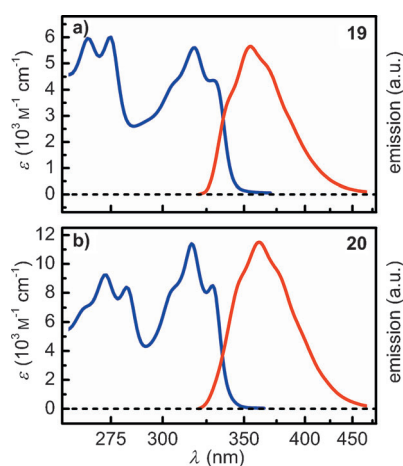


Figure 3. UV/Vis absorption spectra ( $c \approx 0.1$  mM) and normalized emission ( $c \approx 0.01$  mM) after 315 nm excitation of a) 4-methoxyquinolone (**19**) and b) 3-butoxyquinolone (**20**) in MeCN, which are typical for all other studied quinolones.

substituted quinolone, that is, compound **20**, is by a factor 2 more intense than the absorption of **19**. The steady-state spectra allow estimating the radiative decay rate  $k_{\text{rad}}$  of the  $S_1$  state according to Strickler and Berg.<sup>[26]</sup> We calculated the values of  $k_{\text{rad}} = (14 \text{ ns})^{-1}$  for **19** and  $k_{\text{rad}} = (9 \text{ ns})^{-1}$  for **20**.

The photophysical properties of reference compounds **19** and **20** were studied by transient absorption spectroscopy. A very broad, weakly structured excited state absorption of the  $S_1$  state was found, which is overlaid by signals of ground state bleach (310–340 nm) and stimulated emission (370–450 nm) both for **19** (compare  $\Delta t = 1$  ps in Figure 4a) and **20**. The lifetime of the  $S_1$  state is dominated by a relatively fast intersystem crossing (ISC) into the triplet manifold on the 250 ps timescale. Exact values for the  $S_1$  lifetime of the various compounds are given in Table 1. Since the competing radiative deactivation of the  $S_1$  state occurs on

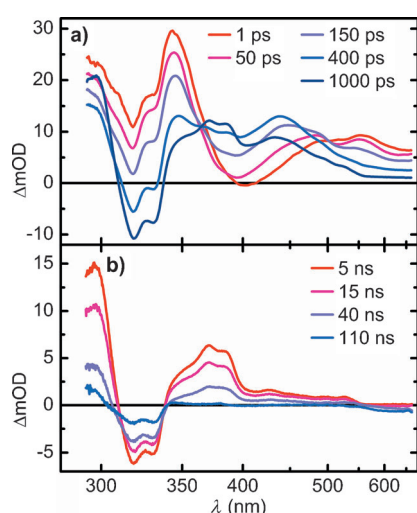


Figure 4. Transient absorption from measurements on the ps (a) and on the ns (b) timescale of quinolone **4** in MeCN at selected pump-probe delays  $\Delta t$  after 270 nm excitation.

Table 1. Parametrization of the excited state dynamics of all synthesized quinolones: The  $S_1$  lifetime  $\tau [S_1]$ , the triplet lifetime  $\tau [T_1]$  and the triplet 1,4-diradical lifetime  $\tau [T\text{-DR}]$  were directly obtained from transient absorption spectroscopy. The quantum yield for product formation  $\Phi_{\text{p}}$  was determined by actinometric measurements. The quantum yields for triplet formation  $\Phi_{\text{T}_1}$ , population of the triplet 1,4-diradical  $\Phi_{\text{D}}$  and the ratio  $k_{\text{clos}}/k_{\text{retro}}$  of the rates for second bond-formation and retrosynthetic disconnection were calculated on the basis of a sequential rate model.<sup>[a]</sup>

Entry	$\tau (S_1)$ [ps]	$\tau (T_1)$ [ns]	$\tau (T\text{-DR})$ [ns]	$\Phi_{\text{p}}$	$\Phi_{\text{T}_1}$	$\Phi_{\text{D}}$	$k_{\text{clos}}/k_{\text{retro}}$
1 <b>19</b>	229	116	–	–	0.98	–	–
2 <b>4</b>	237	0.651	29	0.30	0.98	0.98	31:69
3 ( <i>Z</i> )- <b>6</b>	199	1.319	30	0.72	0.99	0.97	74:26
4 ( <i>E</i> )- <b>6</b>	202	0.934	32	0.32	0.99	0.98	33:67
5 <b>7</b>	176	0.647	34	0.26	0.99	0.98	26:74
6 <b>20</b>	296	81	–	–	0.97	–	–
7 <b>8</b>	362	$\approx 1.5$ <sup>[b]</sup>	23	0.73	0.96	0.95	77:23
8 <b>9</b>	301	0.957	25	0.54	0.97	0.96	57:43

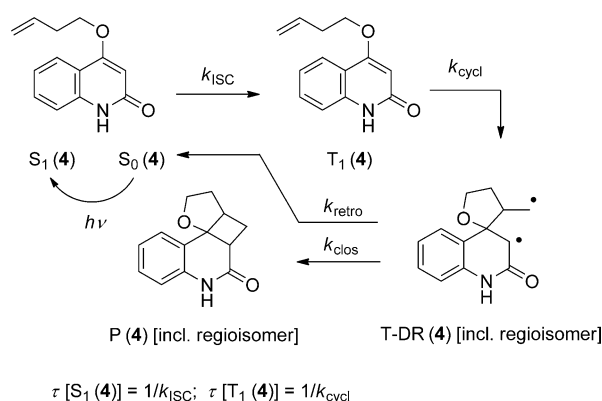
[a] The excitation wavelength was  $\lambda = 270\text{--}275$  nm in all transient spectroscopy measurements. Acetonitrile was employed as the solvent ensuring a homogeneous solution of equal concentration ( $c \approx 0.5$  mM, optical density [318 nm, 1 mm]  $\approx 0.5$ ) for all substrates. [b] The lifetime is in a time window that is not well-covered with the fs–ps (too slow) or with the ns– $\mu$ s (too fast) setup.

the 10 ns timescale (see above), a triplet yield close to unity can be assumed (see Table 1). A direct return to the electronic ground state by internal conversion can be excluded due to the lack of any significant ground state bleach component in the spectrum associated with the 250 ps decay (see the Supporting Information). The lowest triplet state exhibits a clear absorption band centered at 450 (**19**) and 400 nm (**20**), respectively, which is in agreement with reported triplet spectra of related compounds.<sup>[7a,b]</sup> According to previous data,<sup>[9]</sup> the triplet state lifetime of **19** in degassed trifluorotoluene is in the  $\mu$ s range. Due to oxygen-mediated triplet quenching we observe a significantly reduced lifetime in the 100 ns domain both for **19** and **20** in air-equilibrated MeCN. The exact values are summarized in Table 1.

Since all synthesized quinolones **4** and **6–9**, which can undergo intramolecular [2+2] photocycloaddition, qualitatively show the same photochemical behavior and only differ quantitatively, the following discussion of the reaction kinetics is based on quinolone **4** (Figure 4). Compound **4** exhibits after excitation the same spectral properties of the  $S_1$  state as already observed for the reference compound **19** (see Figure 3a). ISC occurs on the 100 ps timescale, whereas the lifetime  $\tau [T_1]$  of the triplet state is significantly reduced compared with reference **19**. We find a lifetime of  $\tau [T_1(\mathbf{4})] = 651$  ps as compared to  $\tau [T_1(\mathbf{19})] = 116$  ns (Table 1). However, in contrast to **19**, the  $T_1$  state of **4** does not decay to the ground state, but a third state with a significant remaining ground state bleach signature is populated. Since the competing decay of the  $T_1$  state by oxygen-mediated triplet quenching occurs on a much longer timescale (as measured for **19**) a close to unity quantum yield for the population of this newly formed state can be safely assumed. This transient state decays with a time constant of  $\tau [T\text{-DR}(\mathbf{4})] = 29$  ns. The remaining spectral signature is perma-

ment within the observed temporal window of several  $\mu\text{s}$  and significantly lower in ground state bleach intensity than its parent state. This observation strongly indicates that the parent state is depopulated by two competing processes: one leading back to the starting material and another one leading to the formation of a stable product, which does not absorb in the spectral range above 300 nm (see Figure 4b).

The transient absorption spectra are fully in line with the mechanistic course previously suggested for related enone [2+2] photocycloaddition reactions,<sup>[23,27]</sup> in which a triplet 1,4-diradical state (T-DR) is proposed to be the key intermediate of the reaction. Adapted to the reaction of quinolones, a picture evolves as drawn in Scheme 7 for the proto-



Scheme 7. Mechanistic scheme for the intramolecular [2+2] photocycloaddition of substrate **4** serving as a general scheme for the discussion of all other quinolone substrates (for nomenclature and abbreviations, see narrative). For the structure of the crossed regioisomer, see Scheme 1.

typical substrate **4**. The triplet 1,4-diradical is formed from the  $T_1$  state, which in turn is populated from the respective singlet excited state with the ISC rate constant  $k_{ISC}$ . For all substrates **4**, **6–9**, which can undergo an intramolecular [2+2] photocycloaddition, the triplet state lifetime  $\tau [T_1]$  is limited by the cyclization to the triplet 1,4-diradical T-DR. The cyclization occurs between the photoactivated double bond and the adjacent carbon–carbon double bond of the side chain, which is not part of the absorbing chromophore. In agreement with previously reported rate constants for  $k_{cycl}$  in enone [2+2] photocycloaddition reactions<sup>[28]</sup> this process is rapid and occurs on the timescale of  $\tau [T_1] \approx 1$  ns (Table 1).

The observed lifetimes  $\tau$  [T-DR], which fit very well to previously reported triplet 1,4-diradical lifetimes,<sup>[29]</sup> strongly support the assignment of the spectral signatures of the occurring intermediates to the respective triplet 1,4-diradicals. Although the determined reaction kinetics suggest a close to unity quantum yield for the population of the triplet 1,4-diradical state, the actinometrically determined quantum yields  $\Phi_p$  for product formation are clearly below unity (see Table 1). Therefore branching reaction kinetics, in which one state is depopulated by two competing processes with comparable probabilities, can be assumed. The ring-closure

( $k_{clos}$ ) and the retrocleavage ( $k_{retro}$ ) are likely to be responsible for the branching leading to the product in one reaction channel and to the starting material in the other reaction channel. A putative singlet 1,4-diradical (S-DR; not shown in Scheme 7) is spectroscopically inaccessible, since its population rate is presumably much lower than the sum of depopulation rates  $k_{retro}$  and  $k_{clos}$ . Still, since the lifetime  $\tau$  [T-DR] of the triplet 1,4-diradical stays constant within the measurement error for both chromophores, the branching between product formation and retrocleavage likely occurs not in the triplet 1,4-diradical state but happens in the singlet 1,4-diradical.

The ratio of  $k_{clos}$  and  $k_{retro}$  is to some extent influenced by the substitution pattern of the side chain. The *cis* configuration of the ethyl group in (*Z*)-**6** for instance favors the second bond formation (Table 1) leading to a higher product quantum yield  $\Phi_p$  for (*Z*)-**6** (0.72) than for (*E*)-**6** (0.32). The higher quantum yield is qualitatively reflected by the previously mentioned higher conversion of (*Z*)-**6** (60%) as compared with (*E*)-**6** (44%) after five minutes of irradiation. A terminal dimethyl substitution favors the retrocleavage over the ring-closure as evident when comparing these substrates to the respective unsubstituted alkenyloxyquinolones (cf., **4** vs. **7** and **8** vs. **9** in Table 1).

Based on a sequential rate model, taking the determined rates, spectra, and states into account, the species-associated absorption spectra (SAS) of the  $T_1$  and the triplet 1,4-diradical state can be extracted from the transient data matrices. The obtained spectrum for the  $T_1$  state of **4** is in agreement with the previously published  $T_1$  absorption spectra of related compounds<sup>[7a,b,8]</sup> and shown in Figure 5. The maximum of

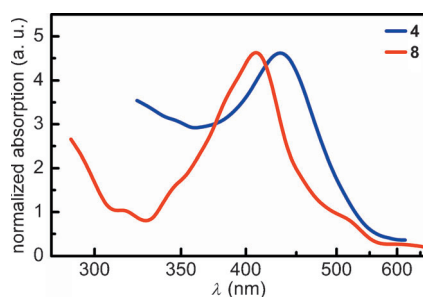


Figure 5. Species-associated absorption spectra (SAS) of the  $T_1$  state of the representative quinolones 4-(but-3-enyl)oxyquinolone (**4**) and 3-(but-3-enyl)oxyquinolone (**8**) after 270 nm excitation in MeCN.

the T–T absorption is observed at  $\lambda \approx 450$  nm for **4**, whereas the T–T absorption of the 3-substituted quinolone **8** is blue-shifted to  $\lambda \approx 400$  nm.

The calculated SAS of the triplet 1,4-diradical state of both chromophores exhibit a strong, characteristic absorption band centered at around 300 nm (**4**, (*Z*)-**6**, (*E*)-**6**, **7**) and at approximately 350 nm (**8**, **9**) as shown for the 1,4-diradicals derived from **7** and **9** in Figure 6. Interestingly, the triplet 1,4-diradicals of **4**, (*Z*)-**6**, (*E*)-**6** and **7** show an additional, less-intense absorption band centered around 380 nm



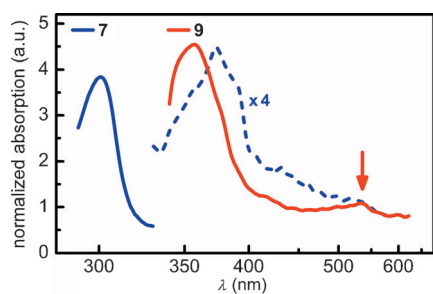


Figure 6. Species-associated absorption spectra (SAS) of the triplet 1,4-diradical (T-DR) states of selected quinolones **7** and **9**.

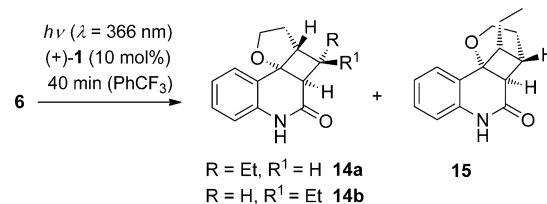
(dotted blue line, Figure 6), which exhibits a Franck-Condon progression, which is very similar to the  $S_1 \leftarrow S_0$  transition (Figure 3a). Also, the triplet 1,4-diradicals derived from compounds **8** and **9** exhibit an additional, redshifted, less-intense absorption band, which could not be well resolved due to a low signal intensity (arrow, Figure 6). Since the spectra of the 1,4-diradical states are well separated from the triplet spectra, transient absorption spectroscopy can be used to differentiate between the two species and follow the course of the [2+2] photocycloaddition reaction.

**Enantioselective [2+2] photocycloaddition reactions in the presence of a sensitizer at  $\lambda = 366$  nm:** Enantioselective reactions were performed in the presence of the chiral sensitizer (+)-**1** or its enantiomer (–)-**1**. The sensitizer is complexed to the substrate with a high association constant and serves two purposes.<sup>[16]</sup> First, it provides enantioselectivity due to steric hindrance (see below). Second, it ensures at the chosen wavelength a selective excitation only within the substrate-sensitizer complex. The excitation of uncomplexed sensitizer leads to a loss of photons as diffusional activation is kept low by the choice of concentrations. If optical excitation of the substrate is possible within the chosen wavelength a racemic background reaction must be expected due to the large number of uncomplexed substrate molecules.

The reactions were performed at three different temperatures, that is,  $-25^\circ\text{C}$ ,  $0^\circ\text{C}$  and ambient temperature (RT) employing 10 mol% of the catalyst. For the reactions of the 4-alkenyloxyquinolones the substrate concentration was consistently 5 mM in trifluorotoluene as the solvent. Since the enantioselective reactions of substrate **4** (Scheme 1) had so far been only performed at  $-25^\circ\text{C}$ , the reactions were also conducted at higher temperature. Complete conversion was achieved after a reaction time of 50 min. At  $0^\circ\text{C}$  the yield was 84% with a regioselectivity of r.r. = 76:24, the major regioisomer **5** showing an enantiomeric excess of 91%. At ambient temperature the total yield was 82% with an r.r. of 81:19 and 88% ee for the straight product **5**. In previous work the enantioselectivity for the reaction of substrate **2** (Scheme 1) had been determined to be 11% ee at  $30^\circ\text{C}$  and 15% ee at  $0^\circ\text{C}$ .

Due to the occurrence of three isomers, the [2+2] photocycloaddition of substrates **6** was (among all reactions studied) the most complex to analyze and the results are com-

Table 2. Enantioselective intramolecular [2+2] photocycloaddition of quinolones **6** at  $\lambda = 366$  nm to provide enantiomerically enriched products **14** and **15**.<sup>[a]</sup>



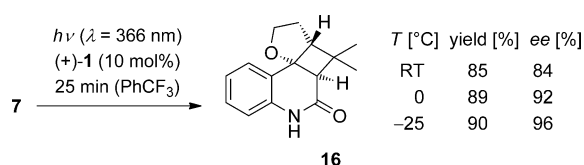
Entry	<i>T</i> [°C]	Yield <sup>[b]</sup> [%]	r.r. <sup>[c]</sup>		d.r. <sup>[c]</sup>		<i>ee</i> <sup>[d]</sup> [%] ( <b>14a</b> )	<i>ee</i> [%] ( <b>14b</b> )	<i>ee</i> [%] ( <b>15</b> )
			<b>14:15</b>	<b>14a:14b</b>					
1	( <i>E</i> )- <b>6</b>	RT	93	76/24	76/24	78	72	68	
2	( <i>E</i> )- <b>6</b>	0	89	82/18	82/18	90	82	74	
3 <sup>[e]</sup>	( <i>E</i> )- <b>6</b>	$-25^\circ\text{C}$	91	82/18	85/15	92	84	74	
4	( <i>Z</i> )- <b>6</b>	RT	91	86/14	85/15	80	70	66	
5	( <i>Z</i> )- <b>6</b>	0	89	88/12	88/12	88	78	68	
6 <sup>[e]</sup>	( <i>Z</i> )- <b>6</b>	$-25^\circ\text{C}$	90	88/12	88/12	92	84	70	

[a] All reactions were conducted at the indicated temperature *T* by using a RPR-100 reactor with sixteen 366 nm, 8 W fluorescent lamps (e.g., Philips black light blue; emission spectrum, see the Supporting Information) as the irradiation source in dry, deaerated trifluorotoluene (*c* = 5 mM) as the solvent. [b] Yield of isolated product. [c] The ratio of regioisomers (r.r.) and diastereoisomers (d.r.) ratio was determined by HPLC. [d] The enantiomeric excess (*ee*) was determined by chiral HPLC after separation of the individual isomers **14a**, **14b**, and **15**. [e] The irradiation time was 45 min.

prehensively provided in Table 2. The reaction yields were high for either starting diastereoisomer (*E*)-**6** (Table 2, entries 1–3) or (*Z*)-**6** (Table 2, entries 4–6). As observed in the racemic series, the influence of the starting olefin configuration was minimal. The *Z* isomer delivered slightly higher selectivities regarding the formation of regioisomers and diastereoisomers, the effect being most pronounced at room temperature (Table 2, entries 1 and 4). In this category, however, the most remarkable effect is exerted by the catalyst. If compared under otherwise identical conditions to the racemic series (Scheme 4), the r.r. increased from 60:40 to 76:24 (Table 2, entry 1) for (*E*)-**6** and from 65:35 to 86:14 (Table 2, entry 4) for (*Z*)-**6**. The d.r. increased from 51:49 to 76:24 (entry 1) for (*E*)-**6** and from 77:23 to 85:15 (entry 4) for (*Z*)-**6**.

The enantiomeric excess was measured for the individual products after having completely separated the three isomers **14a**, **14b**, and **15** by preparative HPLC. The absolute configuration was assigned based on analogy to the known configuration of compound **3** and of a crossed product related to **15**. The assignment is supported by specific rotation data.<sup>[9]</sup> In general, the enantiomeric excesses decreased in the order **14a** > **14b** > **15**. By comparing Table 2 entries 1 versus 4, 2 versus 5, and 3 versus 6 it is obvious that the influence of the starting olefin geometry does not significantly influence the *ee* value. However, there is a temperature influence, which has also been observed for substrate **4**. Lower reaction temperatures favor an enantioselective product formation.

The temperature effect was slightly more pronounced for substrate **7** compared with substrate **4**. The former quino-

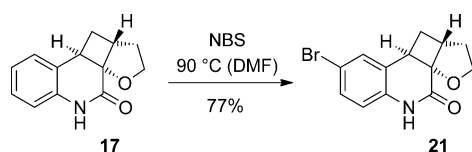


Scheme 8. Highly enantioselective intramolecular [2+2] photocycloaddition of 4-(4-methylpent-3-enyl)oxyquinolone (**7**) to product **16**.

lone reacted with excellent, so far unprecedented enantioselectivity at  $-25^{\circ}\text{C}$  (96%  $ee$ ) and at  $0^{\circ}\text{C}$  (92%  $ee$ ) but showed a lower selectivity (84%  $ee$ ) at room temperature (Scheme 8). Yields of the [2+2] photocycloaddition product **16** were consistently high and the enantioselectivities are remarkable given that only 10 mol% of the catalyst was used (Scheme 8). In particular, the reaction outcome at  $-25^{\circ}\text{C}$  (90% yield, 96%  $ee$ ) powerfully demonstrates that enantioselective catalytic photochemistry is getting competitive with other areas of enantioselective organocatalysis.

Compared with the high enantioselectivities achieved with 4-alkenyloxyquinolones **4** and **7**, the results obtained with their 3-substituted analogues **8** and **9** were somewhat disappointing. Due to a lower solubility, these reactions were performed at a substrate concentration of  $c=2.5$  mM in trifluorotoluene. The enantiomer (–)-**1** of catalyst (+)-**1** was employed for reasons of supply. Compound **1** is prepared racemically<sup>[16]</sup> and subsequently separated by chiral HPLC delivering equal amounts of (–)-**1** and (+)-**1**. To keep the nomenclature consistent the major enantiomers obtained from (–)-**1**, which is the enantiomer *ent-1* of (+)-**1**, are named *ent-17* and *ent-18*. The [2+2] photocycloaddition reactions proceeded rapidly and delivered the respective products in high yields of 83–88%. The enantioselectivity increased with a decrease of the reaction temperature (Table 3; entries 1–3, entries 4–6) but did not exceed 64%  $ee$ .

Since enantioselective [2+2] photocycloaddition reactions of 3-substituted quinolones have not yet been studied, it was desirable to prove the absolute configuration of the products, when produced in the presence of a chiral 1,5,7-trimethyl-3-azabicyclo[3.3.1]nonan-2-one. To this end, the minor enantiomer **17** of the reactions discussed above was separated by chiral HPLC and converted into the respective bromo compound **21** (Scheme 9) by treatment with *N*-bromosuccinimide (NBS). The absolute configuration of this product was unambiguously determined by anomalous X-ray diffraction (see the Supporting Information for further details).



Scheme 9. Preparation of the bromo compound **21**, the absolute configuration of which was elucidated by anomalous X-ray diffraction.

Table 3. Enantioselective intramolecular [2+2] photocycloaddition of quinolones **8** and **9** at  $\lambda=366$  nm to provide enantiomerically enriched products *ent-17* and *ent-18*, respectively.<sup>[a]</sup>

Entry	R	$T$ [°C]	Yield <sup>[b]</sup> [%]	$ee$ <sup>[c]</sup> [%]	
1	<b>8</b>	H	RT	85	46
2	<b>8</b>	H	0	83	54
3 <sup>[d]</sup>	<b>8</b>	H	-25	85	64
4	<b>9</b>	Me	RT	86	58
5	<b>9</b>	Me	0	88	60
6	<b>9</b>	Me	-25	85	60

[a] All reactions were conducted at the indicated temperature  $T$  by using a RPR-100 reactor with sixteen 366 nm, 8 W fluorescent lamps (e.g., Philips black light blue; emission spectrum, see the Supporting Information) as the irradiation source in dry, deaerated trifluorotoluene ( $c=2.5$  mM) as the solvent. [b] Yield of isolated product. [c] The enantiomeric excess was determined by chiral HPLC. [d] The irradiation time was 15 min.

#### Factors governing the stereoselectivity in the [2+2] photocycloaddition reaction:

A major outcome of the photophysical studies is the fact that they substantiate the previous assumption of a high cyclization rate  $k_{\text{cycl}}$  (i.e., a short triplet lifetime) favoring high enantioselectivity. Substrates **4**, **6**, and **7** show triplet state lifetimes in the order of 1 ns, whereas the triplet state lifetime of **2** is much higher. In the latter case the dissociation rate from catalyst (+)-**1** is apparently in the order of the cyclization rate ( $10^7$ – $10^8$  s<sup>-1</sup>) accounting for a large fraction of reactions to occur after dissociation from the catalyst. The enantioselectivity of the reaction **2** → **3** is consequently low (see above). As shown in Scheme 7, the cyclization step determines the absolute configuration of the product irrespective of its regioselectivity. An enantioface differentiation occurs in a 1,5,7-trimethyl-3-azabicyclo[3.3.1]nonan-2-one with benzoxazolyl substituents of any kind in position 7 because the substituent shields effectively one face of the quinolone double bond from an attack. The fidelity of this shielding is high even at ambient temperature as clearly seen by the enantioselectivities achieved with substrates **4** (88%  $ee$ ) and **7** (84%  $ee$ ) at ambient temperature. The slightly lower enantioselectivity in the reactions of 4-(hex-3-enyl)oxyquinolones (**6** → **14a**) (Table 2, entries 1 and 4) could be accounted for by their slightly lower cyclization rate. The decreased enantioselectivity observed for the crossed product **15** is likely due to the slower rate of six-membered ring formation.

The approach of a tethered olefin occurs in quinolones complexed to the enantiomer (–)-**1** of sensitizer (+)-**1** of course from the opposite face explaining the formation of *ent-17* and *ent-18* in significant enantiomeric excesses (Figure 7). To explain the lower enantioselectivity achieved



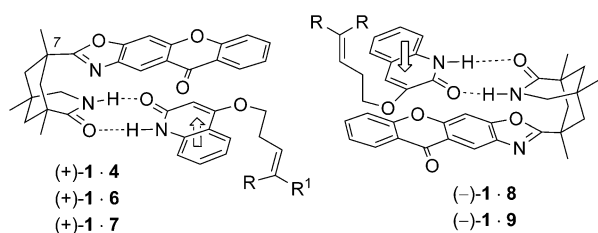


Figure 7. Preferred approach ( $\rightarrow$ ) of the tethered olefin in the complexes of (+)-**1** and (-)-**1** with the respective 4-alkenyloxyquinolones **4**, **6**, **7** (left) and 3-alkenyloxyquinolones **8**, **9** (right).

with substrates **8** and **9** (relative to substrates **4**, **6**, and **7**), the absorption properties of these compounds must be taken into account. Both quinolones **8** and **9** show a significantly stronger absorption at  $\lambda \approx 350$  nm in the UV/Vis spectrum, which allows for a relatively rapid background reaction under the irradiation conditions. When reactions were performed at room temperature in the absence of sensitizer (-)-**1** under conditions otherwise identical to the conditions of Table 3, yields of 21% (for *rac*-**17**) and 17% (for *rac*-**18**) were obtained after an irradiation time of ten minutes. In other words, the background reactions account for an *ee* loss of at least 20 percentage points.

From the lifetimes for the triplet intermediates T-DR (Scheme 7, Table 1) and the dissociation rate from templates (+)-**1** and (-)-**1** (see above) it is likely that a non-negligible fraction of these intermediates is still bound to the sensitizer before cyclobutane ring formation. This assumption is in agreement with the fact that the sensitizer influences the diastereo- and regioselectivity in the reaction of 4-(hex-3-enyl)oxyquinolones (**6**) (Scheme 4 vs. Table 2). Diastereoisomers (**14b**) and constitutional isomers (**15**), which lead to an increased steric repulsion with the xanthone moiety, are disfavored (Table 2).

## Conclusion

In this study a key principle for the design of chiral photocatalysts has been confirmed. The enantioselectivity determining step of the desired reaction must occur fast enough to compete with substrate dissociation from the photocatalyst. For the currently used xanthone **1**, this requirement asks for C–C bond-forming reactions on the ns timescale. As proven by transient absorption spectroscopy, the cyclization of substrates **4**, **6–9** does occur within this time window guaranteeing excellent selectivity for the formation of products **5**, **14**, and **16**. If the cyclization is slower, for example, for the formation of product **3** from **2** or of product **15** from **6**, the enantioselectivity decreases.

In addition, it became again evident in this study that the success of the enantioselective catalysis depends on an appropriate choice of excitation wavelength and on the absorption properties of the substrate and the respective substrate–photocatalyst complex. If excitation can occur in the absence of the photocatalyst, background reactions lead to a

deterioration of enantioselectivity, as observed for substrates **8** and **9**.

The transient absorption spectroscopy results not only corroborate this analysis but they also provide valuable data for further investigations. Although the enantioselective process within the substrate complexes depicted in Figure 7 appears understood, it is not yet clear how the energy transfer within this complex is accomplished on a molecular level. Operationally more difficult studies are required to investigate the substrate–photocatalyst complex by transient absorption spectroscopy. The data and spectra now obtained (Figures 4–6) present an excellent starting point for further work. Dexter energy transfer<sup>[30]</sup> is certainly conceivable and has been previously discussed<sup>[9,16]</sup> but requires to be proven in the context of further experiments. Work along these lines is ongoing in our laboratories.

## Experimental Section

**General:** All reactions sensitive to air or moisture, were carried out in flame-dried glassware under argon pressure using standard Schlenk techniques. Photochemical experiments were performed in flame-dried pyrex irradiation tubes (diameter: 1.0 cm, volume: 15 mL for low-temperature irradiation) under argon pressure. Irradiation experiments were performed in a Rayonet RPR-100 photochemical reactor (Southern New England Ultra Violet Company, Branford, CT, USA) equipped with fluorescence lamps (Philips black light blue 8 W,  $\lambda_{\max} = 366$  nm; Rayonet RPR-3000 Å,  $\lambda_{\max} = 300$  nm). For the photochemical reactions dry  $\alpha, \alpha, \alpha$ -trifluorotoluene was used and degassed by purging with argon in an ultrasonicating bath for 15 min. Flash chromatography was performed on silica gel 60 (Merck, 230–400 mesh) with the eluent mixtures given in the corresponding procedures. Thin layer chromatography (TLC) was performed on silica-coated glass plates (silica gel 60 F 254). Compounds were detected by UV ( $\lambda = 254$  nm, 366 nm) fluorescence. All solvents for chromatography were distilled prior to use. Preparative HPLC separations were performed on a Waters HPLC system (flow rate: 20 mL min<sup>-1</sup>; achiral stationary phase: XBridge C18 column, 5  $\mu$ m, 30  $\times$  150 mm; eluent: H<sub>2</sub>O/MeCN = 70:30, 1% trifluoroacetic acid) with a flame ionization detector. The temperature method is given for the corresponding compounds. Analytical HPLC was performed using a chiral stationary phase (Daicel ChiralCell, Chemical Industries, flow rate: 1.0 mL min<sup>-1</sup>, type and eluent are given for the corresponding compounds) and UV detection. IR: JASCO IR-4100. MS/HRMS: Thermo Scientific DFS HRMS. <sup>1</sup>H and <sup>13</sup>C NMR: Bruker AV-360 and AV-500 recorded at 300 K. Chemical shifts are reported relative to the solvent [CHCl<sub>3</sub>:  $\delta(^1\text{H}) = 7.26$  ppm,  $\delta(^{13}\text{C}) = 77.0$  ppm, [D<sub>2</sub>]DMSO:  $\delta(^1\text{H}) = 2.50$  ppm,  $\delta(^{13}\text{C}) = 39.5$  ppm] as reference. Apparent multiplets that occur as a result of accidental equality of coupling constants to those of magnetically non-equivalent protons are marked as virtual (virt.). The relative configuration of chiral products and the multiplicity of the <sup>13</sup>C NMR signals were determined by two-dimensional NMR spectra (COSY, NOESY, HSQC, HMBC). Specific rotations were determined by using a PerkinElmer 241 MC polarimeter (sodium vapor lamp). Melting points were measured on a Büchi 510 of the company Büchi and are not corrected.

**Transient absorption spectroscopy on multiple timescales:** The femtosecond broadband pump-probe setup has been described in detail elsewhere.<sup>[31]</sup> Briefly, a Ti/sapphire amplifier system (CPA 2001, Clark-MXR) with a repetition rate of 1 kHz was used to pump a noncollinear optical parametric amplifier (NOPA) which provides pulses with a center wavelength of 540–550 nm. After compression and frequency doubling in a BBO-crystal (100  $\mu$ m thickness) we achieved pump pulses with a center wavelength of 270–275 nm and sub-ps duration. The beam with a pulse energy of about 400 nJ was focused with a spot size of 100–150  $\mu$ m

(FWHM) into a 1 mm flow cell containing the sample solution with an optical density below 1 within the spectral probe range. A supercontinuum (290–750 nm) was generated and used as probe by focusing another part of the Ti/sapphire laser into a rotating CaF<sub>2</sub> (4 mm thickness) disk. The relative polarization of pump and probe pulses was set to the magic angle (54.7°) to avoid contributions from the rotational relaxation to the observed kinetics. A computer controlled delay line was used to set pump–probe delays up to 2 ns. After the interaction in the sample, the probe light was dispersed with a fused silica prism and detected with a 524 pixel CCD. The chirp of the white light was corrected for prior to data analysis. The resulting temporal resolution was better than 100 fs.

For transient absorption measurements on the ns timescale we used a pulsed ns laser system (NT242, Ekspla) with 1 kHz repetition rate and integrated OPO for spectral tunability, to pump the sample in a 1 mm flow cell (see above). The ns laser is externally triggered and is electronically synchronized with the Ti/sapphire amplifier system (see above), running at 1 kHz repetition rate as well. We still use the supercontinuum, generated by focusing the fs pulses into a CaF<sub>2</sub> disk for probing the sample. The pump–probe delay  $\Delta t$  is set by a computer controlled delay generator, which introduces a specified temporal delay  $\Delta t$  in the electronic trigger pulse from the master oscillator before the pulse triggers the release of the ns excitation pulse. This setup for transient absorption spectroscopy, combining two electronically connected laser sources, provides a temporal resolution better than 2.5 ns and allows recording transient absorption spectra up to temporal delays in the 100  $\mu$ s regime.

To obtain kinetics from the TA data we used a global data analysis that is based on a formalism developed by Fita et al.<sup>[32]</sup> and extracts decay associated difference spectra (DADS) from the transient data.<sup>[31]</sup> Before applying the global fit routine to our TA data, the wavelength scale was rescaled to a scale linear in  $\Delta E$  to avoid the enhancement of the weight of the long-wave components. The global fit analysis provides a global set of time constants  $\tau_i$  and the corresponding DADS  $A_i(\lambda)$ .

$$\Delta OD(\lambda, t) = \sum_i A_i(\lambda) \exp\left(-t/\tau_i\right) \quad (1)$$

Further data processing and the calculation of the species associated absorption spectra (SAS) were based on inserting the obtained DADS  $A_i(\lambda)$  into a sequential rate model.

**Actinometric measurements:** We used the previously mentioned ns laser system with integrated OPO, which provides a spatially, spectrally and energetically well-defined light beam, for photo-excitation of the sample solution in a transparent cuvette. A very similar approach, but using LEDs as light source for the determination of product quantum yields has been reported.<sup>[33]</sup> The irradiation was performed in a standard 10 mm cuvette containing about 3.8 mL sample solution, exhibiting an optical density of about 1.2 at the absorption maximum at 317 nm while stirring with a magnetic stirring bar. This ensures that more than 90% of the incident photons at  $\lambda = 317$  nm are absorbed. We measured  $P_{\text{trans}}$ , the light intensity transmitted by the sample solution, and  $P_{\text{ref}}$ , the light intensity transmitted by a reference solution comprising just solvent in a similar cuvette.

$$N_{\text{abs}} = \frac{(P_{\text{ref}} - P_{\text{trans}})\Delta t}{E_\gamma} \quad (2)$$

The decrease in absorption intensity of the starting material at 317 nm was used for the calculation of the amount of converted starting material within the irradiation time. In each case, we measured 3 data points for an over-all conversion of typically below 20% of the total amount of sample in the cuvette. The quantum yield then was the ratio of formed product molecules  $N_{\text{prod}}$  and absorbed photons  $N_{\text{abs}}$ .

**Representative procedure for the [2+2] photocycloaddition at short wavelength ( $\lambda \approx 300$  nm) leading to racemic products: 1,1-dimethyl-1,2,3,10b-tetrahydro-1H-furo[2',3':1,4]cyclobuta[1,2-c]quinolin-5(6H)-one (rac-18):** Compound **9** (61.0 mg, 0.25 mmol) was dissolved in  $\alpha, \alpha, \alpha$ -trifluorotoluene (100 mL,  $c = 2.5$  mmol L<sup>-1</sup>). The solution was irradiated at  $\lambda = 300$  nm (light source: RPR-3000 Å, emission spectrum, see the Supporting Information) at ambient temperature for 10 min. The solvent was

removed in vacuo and the resulting oil was purified by flash column chromatography (50 g silica, pentane/EtOAc=2:1). The racemic compound *rac*-**18** was obtained as a colorless solid (57.7 mg, 0.24 mmol, 95%).  $R_f = 0.62$  (EtOAc [UV]); m.p. = 158–160 °C; <sup>1</sup>H NMR (500 MHz, CDCl<sub>3</sub>, 303 K, TMS):  $\delta = 8.15$  (br s, 1H; NH), 7.15 (virt. td, <sup>3</sup> $J \approx 7.8$  Hz, <sup>4</sup> $J = 1.3$  Hz, 1H; H-8), 6.98 (virt. td, <sup>3</sup> $J \approx 7.6$  Hz, <sup>4</sup> $J = 1.1$  Hz, 1H; H-9), 6.90 (dd, <sup>3</sup> $J = 7.5$  Hz, <sup>4</sup> $J = 1.3$  Hz, 1H; H-10), 6.74 (dd, <sup>3</sup> $J = 7.9$  Hz, <sup>4</sup> $J = 1.1$  Hz, 1H; H-7), 4.45 (ddd, <sup>2</sup> $J = 9.0$  Hz, <sup>3</sup> $J = 7.7$  Hz, <sup>3</sup> $J = 3.1$  Hz, 1H; H-3 $\alpha$ ), 4.15 (virt. td, <sup>2</sup> $J \approx 3$  Hz, <sup>3</sup> $J = 6.5$  Hz, 1H; H-3 $\beta$ ), 3.29 (s, 1H; H-10b), 2.94 (virt. dt, <sup>3</sup> $J = 8.9$  Hz, <sup>3</sup> $J \approx 4$  Hz = 1.8 Hz, 1H; H-1a), 2.27–1.90 (m, 2H; H-2), 1.16 (s, 3H; CH<sub>3</sub>), 0.81 ppm (s, 3H; CH<sub>3</sub>); <sup>13</sup>C NMR (250 MHz, CDCl<sub>3</sub>, 303 K, TMS):  $\delta = 170.4$  (s, C-5), 136.5 (s, C-6a), 128.5 (d, C-10), 127.8 (d, C-8), 123.5 (d, C-9), 121.6 (s, C-10a), 115.8 (d, C-7), 78.3 (s, C-4), 71.0 (t, C-3), 56.6 (d, C-1a), 50.5 (d, C-10b), 34.9 (s, C-1), 27.8 (t, C-2), 26.4 (q, CH<sub>3</sub>), 24.8 ppm (q, CH<sub>3</sub>); IR (ATR):  $\tilde{\nu} = 2942, 2356, 1682, 1594, 1495, 1389, 1143, 1076, 1048, 973, 827$  cm<sup>-1</sup>; MS (EI, 70 eV):  $m/z$  (%) = 243 (1) [ $M^+$ ], 212 (1), 198 (2), 174 (3) [ $M^+ - C_5H_9$ ], 161 (100) [ $M^+ - C_6H_{10}$ ], 143 (5) [ $M^+ - C_6H_{12}O$ ], 133 (3) [ $M^+ - C_7H_{10}O$ ], 115 (5), 104 (3) [ $M^+ - C_8H_{11}O_2$ ], 89 (4) [ $C_7H_5^+$ ], 83 (7), 77 (3) [ $C_6H_5^+$ ], 67 (2), 55 (15); HRMS (EI):  $m/z$ : calcd for C<sub>15</sub>H<sub>17</sub>O<sub>2</sub>N: 243.1254; found: 243.1254.

**Representative procedure for the enantioselective [2+2] photocycloaddition under sensitized conditions at  $\lambda \approx 366$  nm (3a*S*,4a*S*,10b*S*)-4,4-dimethyl-2,3,4,4a-tetrahydro-furo-[2',3':2,3]-cyclobuta[1,2-c]-quinolin-5-(6H)-one (16):** Compound **7** (12.2 mg, 50.0  $\mu$ mol) and (+)-**1** (2.08 mg, 5.00  $\mu$ mol, 10 mol %) were dissolved in  $\alpha, \alpha, \alpha$ -trifluorotoluene (10 mL,  $c = 5$  mmol L<sup>-1</sup>), cooled to -25 °C and irradiated at  $\lambda = 366$  nm (light source: Philips black light blue; emission spectrum, see the Supporting Information) for 20 min. Silica (500 mg  $\rightarrow$  dry load) was added and the solvent was evaporated under reduced pressure. Following flash column chromatography (5 g silica, pentane/EtOAc=1:1), photoproduct **16** was obtained as a colorless solid (11.0 mg, 45.2  $\mu$ mol, 90%, 96% *ee*).  $R_f = 0.64$  (EtOAc [UV]); HPLC (chiral phase AD-H, *n*-hexane/*i*PrOH=90:10, 1 mL min<sup>-1</sup>,  $\lambda = 210$  and 254 nm):  $t_R = 12.6$  min [*ent*-**16**], 13.6 min [**16**]; m.p. = 122–126 °C;  $[\alpha]_D^{20} = +11.2$  ( $c = 0.9$ , MeOH) [96% *ee*]; <sup>1</sup>H NMR (500 MHz, CDCl<sub>3</sub>, 303 K, TMS):  $\delta = 8.35$  (brs, 1H; NH), 7.30 (d, <sup>3</sup> $J = 7.7$  Hz, 1H; H-10), 7.21 (virt. t, <sup>3</sup> $J \approx 7.7$  Hz, 1H; H-8), 7.05 (virt. t, <sup>3</sup> $J \approx 7.5$  Hz, 1H; H-9), 6.73 (d, <sup>3</sup> $J = 8.0$  Hz, 1H; H-7), 4.42–4.34 (m, 1H; H-2 $\alpha$ ), 4.09–3.99 (m, 1H; H-2 $\beta$ ), 3.02 (s, 1H; H-4a), 2.57 (d, <sup>3</sup> $J = 9.2$  Hz, 1H; H-3a), 2.10–2.04 (m, 2H; H-3), 1.21 (s, 3H; CH<sub>3</sub>), 1.12 ppm (s, 3H; CH<sub>3</sub>); <sup>13</sup>C NMR (126 MHz, CDCl<sub>3</sub>, 303 K, TMS):  $\delta = 168.5$  (s, C-5), 136.3 (s, C-6a), 129.5 (d, C-8), 127.7 (d, C-10), 124.2 (d, C-9), 124.0 (s, C-10a), 115.5 (d, C-7), 79.4 (s, C-10b), 68.9 (t, C-2), 58.1 (d, C-3a), 51.8 (d, C-4a), 34.8 (s, C-4), 27.8 (t, C-3), 26.1 (q, CH<sub>3</sub>), 24.8 ppm (q, CH<sub>3</sub>); IR (ATR):  $\tilde{\nu} = 2925$  (w, ArH), 2861 (w, C<sub>ar</sub>H), 1662 (s, C=O), 1594 (m, NH), 1381 (s), 1274 (s), 1139 (s), 1063 (s), 1039 cm<sup>-1</sup> (vs, C-O); MS (EI, 70 eV):  $m/z$  (%) = 243 (70) [ $M^+$ ], 161 (100) [ $M^+ - C_6H_{10}$ ], 82 (40), 67 (23), 55 (69), 44 (44); HRMS (EI):  $m/z$ : calcd for C<sub>15</sub>H<sub>17</sub>NO<sub>2</sub>: 243.1254; found: 243.1254.

**Single-crystal X-ray absolute structure determination of compound 21:** Formula: C<sub>13</sub>H<sub>12</sub>BrNO<sub>2</sub>;  $M_r = 294.14$ ; crystal color and shape: pale-yellow fragment, crystal dimensions = 0.15  $\times$  0.15  $\times$  0.20 mm; crystal system: triclinic; space group *P1* (no. 1);  $a = 6.4063(3)$ ,  $b = 9.8661(5)$ ,  $c = 10.3432(5)$  Å;  $\alpha = 114.362(2)$ ,  $\beta = 103.133(2)$ ,  $\gamma = 95.359(2)^\circ$ ,  $V = 566.91(5)$  Å<sup>3</sup>;  $Z = 2$ ;  $\mu(\text{MoK}\alpha) = 3.613$  mm<sup>-1</sup>;  $\rho_{\text{calcd}} = 1.723$  g cm<sup>-3</sup>;  $F_{000} = 296$ ;  $T = 123$  K;  $\theta$  range = 2.3–25.4°; data collected: 18004; independent data [ $I_o > 2\sigma(I_o)$ /all data/ $R_{\text{int}}$ ]: 3951/3951/0.048; data/restraints/parameters: 3951/0/307;  $R1$  [ $I_o > 2\sigma(I_o)$ /all data]: 0.0244/0.0247;  $wR2$  [ $I_o > 2\sigma(I_o)$ /all data]: 0.0658/0.0663; GOF = 1.098;  $\Delta\rho_{\text{max/min}} = 0.448/-0.329$  e Å<sup>-3</sup>. Flack parameter  $x = 0.045(7)$ . Hooft parameter  $y = 0.092(6)$ . For more details see the Supporting Information. CCDC-919729 (**21**) contains the supplementary crystallographic data for this paper. These data can be obtained free of charge from The Cambridge Crystallographic Data Centre via [www.ccdc.cam.ac.uk/data\\_request/cif](http://www.ccdc.cam.ac.uk/data_request/cif).

## Acknowledgements

This project was supported by the Deutsche Forschungsgemeinschaft (DFG) in the framework of the DFG Research Training Group "Chemical Photocatalysis" (GRK 1626). M.M.M. and M.W. acknowledge fellowship support by the GRK. R.A. is the recipient of an Alexander von Humboldt research fellowship. We thank Olaf Ackermann and Georg Rudolf (AK Sieber) for help with the HPLC analysis.

- [1] General reviews on [2+2] photocycloaddition reactions: a) J.P. Hehn, C. Müller, T. Bach in *Handbook of Synthetic Photochemistry* (Eds.: A. Albini, M. Fagnoni), Wiley-VCH, Weinheim, **2009**, pp. 171–215; b) S. A. Fleming in *Molecular and Supramolecular Photochemistry, Vol. 12* (Eds.: A. G. Griesbeck, J. Mattay), Marcel Dekker, New York, **2005**, pp. 141–160; c) P. Margaretha in *Molecular and Supramolecular Photochemistry, Vol. 12* (Eds.: A. G. Griesbeck, J. Mattay), Marcel Dekker, New York, **2005**, pp. 211–237; d) J. P. Pete in *CRC Handbook of Organic Photochemistry and Photobiology*, 2nd ed. (Eds.: W. Horspool, F. Lenci), CRC, Boca Raton, **2004**, pp. 71/1–71/14; e) T. Bach, *Synthesis* **1998**, 683–703; f) J.-P. Pete, *Adv. Photochem.* **1996**, *21*, 135–216; g) J. Mattay, R. Conrads, R. Hoffmann in *Methoden der Organischen Chemie (Houben-Weyl)*, Vol. E21c, 4th ed. (Eds.: G. Helmchen, R. W. Hoffmann, J. Mulzer, E. Schaumann), Thieme, Stuttgart **1995**, pp. 3085–3132; h) M. T. Crimmins, T. L. Reinhold, *Org. React.* **1993**, *44*, 297–588.
- [2] a) G. R. Evanega, D. L. Fabiny, *Tetrahedron Lett.* **1968**, *9*, 2241–2246; b) G. R. Evanega, D. L. Fabiny, *J. Org. Chem.* **1970**, *35*, 1757–1761; c) G. R. Evanega, D. L. Fabiny, *Tetrahedron Lett.* **1971**, *12*, 1749–1752.
- [3] a) E. C. Taylor, W. W. Paudler, *Tetrahedron Lett.* **1960**, *1*, 1–3; b) I. W. Elliott, *J. Org. Chem.* **1964**, *29*, 305–307; c) O. Buchardt, *Acta Chem. Scand.* **1964**, *18*, 1389–1396.
- [4] a) B. Loev, M. M. Goodman, K. M. Snader, *Tetrahedron Lett.* **1968**, *9*, 5401–5404; b) T. S. Cantrell, *J. Org. Chem.* **1974**, *39*, 3063–3070; c) R. G. Hunt, C. J. Potter, S. T. Reid, M. L. Roantree, *Tetrahedron Lett.* **1975**, *16*, 2327–2330; d) O. Buchardt, J. J. Christensen, N. Harrit, *Acta Chem. Scand. B* **1976**, *30*, 189–192; e) D. J. Haywood, S. T. Reid, *J. Chem. Soc. Perkin Trans. 1* **1977**, 2457–2458; f) C. Kaneko, T. Naito, M. Somei, *J. Chem. Soc. Chem. Commun.* **1979**, 804–805; g) C. Kaneko, T. Naito, *Chem. Pharm. Bull.* **1979**, *27*, 2254–2256; h) T. Naito, C. Kaneko, *Chem. Pharm. Bull.* **1980**, *28*, 3150–3152; i) C. Kaneko, T. Naito, N. Nakayama, *Chem. Pharm. Bull.* **1981**, *29*, 593–595; j) T. Chiba, M. Okada, T. Kato, *J. Heterocycl. Chem.* **1982**, *19*, 1521–1525; k) C. Kaneko, T. Naito, Y. Momose, H. Fujii, N. Nakayama, I. Koizumi, *Chem. Pharm. Bull.* **1982**, *30*, 519–525; l) T. Naito, Y. Momose, C. Kaneko, *Chem. Pharm. Bull.* **1982**, *30*, 1531–1534; m) C. Kaneko, T. Naito, Y. Momose, N. Shimomura, T. Ohashi, M. Somei, *Chem. Pharm. Bull.* **1983**, *31*, 2168–2171; n) C. Kaneko, N. Shimomura, Y. Momose, T. Naito, *Chem. Lett.* **1983**, 1239–1242; o) T. Naito, C. Kaneko, *Chem. Pharm. Bull.* **1983**, *31*, 366–369; p) T. Chiba, T. Kato, A. Yoshida, R. Moroi, N. Shimomura, Y. Momose, T. Naito, C. Kaneko, *Chem. Pharm. Bull.* **1984**, *32*, 4707–4720; q) S. Nonoyama, N. Yonezawa, K. Saigo, T. Hirano, M. Hasegawa, *Chem. Lett.* **1987**, 487–490; r) M. Sato, K. Kawakami, C. Kaneko, *Chem. Pharm. Bull.* **1987**, *35*, 1319–1321; s) C. Kaneko, T. Suzuki, M. Sato, T. Naito, *Chem. Pharm. Bull.* **1987**, *35*, 112–123; t) S. Nonoyama, N. Yonezawa, K. Saigo, M. Hasegawa, T. Hirano, *Bull. Chem. Soc. Jpn.* **1988**, *61*, 2387–2391; u) E. Sato, Y. Ikeda, Y. Kanaoka, *Liebigs Ann. Chem.* **1989**, 781–788; v) H. Suginome, K. Kobayashi, M. Itoh, S. Seko, A. Furusaki, *J. Org. Chem.* **1990**, *55*, 4933–4943; w) J. Kurita, T. Yamanaka, T. Tsuchiya, *Heterocycles* **1991**, *32*, 2089–2092; x) K. Kobayashi, M. Suzuki, H. Suginome, *J. Org. Chem.* **1992**, *57*, 599–606; y) M. Sakamoto, N. Sato, T. Mino, Y. Kasashima, T. Fujita, *Org. Biomol. Chem.* **2008**, *6*, 848–850; z) F. Yagishita, T. Mino, T. Fujita, M. Sakamoto, *Org. Lett.* **2012**, *14*, 2638–2641.
- [5] a) D. F. Cauble, V. Lynch, M. J. Krische, *J. Org. Chem.* **2003**, *68*, 15–21; b) S. Brandes, P. Selig, T. Bach, *Synlett* **2004**, 2588–2590; c) F. Yagishita, M. Sakamoto, T. Mino, T. Fujita, *Org. Lett.* **2011**, *13*, 6168–6171.
- [6] Review: J. C. Namyslo, D. E. Kaufmann, *Chem. Rev.* **2003**, *103*, 1485–1537.
- [7] a) T. Yamamuro, I. Tanaka, N. Hata, *Bull. Chem. Soc. Jpn.* **1971**, *44*, 667–671; b) T. Yamamuro, N. Hata, I. Tanaka, *Bull. Chem. Soc. Jpn.* **1973**, *46*, 29–34; c) F. D. Lewis, G. D. Reddy, J. E. Elbert, B. E. Tillberg, J. A. Meltzer, M. Kojima, *J. Org. Chem.* **1991**, *56*, 5311–5318.
- [8] H. Görner, T. Wolff, *Photochem. Photobiol.* **2008**, *84*, 1224–1230.
- [9] C. Müller, M. M. Maturi, A. Bauer, M. C. Cuquerella, M. A. Miranda, T. Bach, *J. Am. Chem. Soc.* **2011**, *133*, 16689–16697.
- [10] a) T. Bach, H. Bergmann, K. Harms, *Angew. Chem.* **2000**, *112*, 2391–2393; *Angew. Chem. Int. Ed.* **2000**, *39*, 2302–2304; b) T. Bach, H. Bergmann, *J. Am. Chem. Soc.* **2000**, *122*, 11525–11526; c) T. Bach, H. Bergmann, B. Grosch, K. Harms, *J. Am. Chem. Soc.* **2002**, *124*, 7982–7990; d) S. Breitenlechner, T. Bach, *Angew. Chem.* **2008**, *120*, 8075–8077; *Angew. Chem. Int. Ed.* **2008**, *47*, 7957–7959.
- [11] Reviews: a) J. Svoboda, B. König, *Chem. Rev.* **2006**, *106*, 5413–5430; b) D. M. Bassani in *Supramolecular Photochemistry* (Eds.: V. Ramamurthy, Y. Inoue), Wiley, Hoboken, **2011**, pp. 53–86.
- [12] T. Bach, H. Bergmann, B. Grosch, K. Harms, E. Herdtweck, *Synthesis* **2001**, 1395–1405.
- [13] D. S. Kemp, K. S. Petrakis, *J. Org. Chem.* **1981**, *46*, 5140–5143.
- [14] a) P. Selig, T. Bach, *Angew. Chem.* **2008**, *120*, 5160–5162; *Angew. Chem. Int. Ed.* **2008**, *47*, 5082–5084; b) P. Selig, E. Herdtweck, T. Bach, *Chem. Eur. J.* **2009**, *15*, 3509–3525.
- [15] Reviews: a) C. Müller, T. Bach, *Aust. J. Chem.* **2008**, *61*, 557–564; b) C. Yang, Y. Inoue in *Supramolecular Photochemistry* (Eds.: V. Ramamurthy, Y. Inoue), Wiley, Hoboken, **2011**, pp. 115–153.
- [16] C. Müller, A. Bauer, T. Bach, *Angew. Chem.* **2009**, *121*, 6767–6769; *Angew. Chem. Int. Ed.* **2009**, *48*, 6640–6642.
- [17] E. Ochiai, *J. Org. Chem.* **1953**, *18*, 534–551.
- [18] a) O. Buchardt, *Acta Chem. Scand.* **1963**, *17*, 1461–1462; b) A. Albini, E. Fasani, L. M. Dacrema, *J. Chem. Soc. Perkin Trans. 1* **1980**, 2738–2742; c) A. Albini, M. Alpegiani, *Chem. Rev.* **1984**, *84*, 43–71.
- [19] A. Bakowski, M. Dressel, A. Bauer, T. Bach, *Org. Biomol. Chem.* **2011**, *9*, 3516–3529.
- [20] F. Marsais, A. Godard, G. Queguiner, *J. Heterocycl. Chem.* **1989**, *26*, 1589–1594.
- [21] T. Nishi, F. Tabusa, T. Tanaka, H. Ueda, T. Shimizu, T. Kanbe, Y. Kimura, K. Nakagawa, *Chem. Pharm. Bull.* **1983**, *31*, 852–860.
- [22] a) D. Becker, M. Nagler, S. Hirsh, J. Ramun, *J. Chem. Soc. Chem. Commun.* **1983**, 371–373; b) D. Becker, M. Nagler, Y. Sahali, N. Haddad, *J. Org. Chem.* **1991**, *56*, 4537–4543; c) D. Becker, N. Klímovich, *Tetrahedron Lett.* **1994**, *35*, 261–264.
- [23] Review on the mechanism of the [2+2] photocycloaddition, see: D. I. Schuster, G. Lem, N. A. Kaprinidis, *Chem. Rev.* **1993**, *93*, 3–22.
- [24] C. Franco, J. Olmsted III, *Talanta* **1990**, *37*, 905–909.
- [25] Based on previous work (e.g., A. A. Abdel-Shafi, F. Wilkinson, *J. Phys. Chem. A* **2000**, *104*, 5747–5757), a bimolecular rate constant for triplet state quenching by oxygen can be estimated as  $k_q \approx 3 \times 10^9 \text{ M}^{-1} \text{ s}^{-1}$ . The minimum lifetime of a triplet species in air-equilibrated acetonitrile is consequently  $\tau_{\text{min}} \geq 1/[k_q \times 2.4 \text{ mM}] \approx 1.3 \times 10^{-7} \text{ s}$ . Oxygen quenching should not significantly influence the lifetime of a species with an intrinsically shorter lifetime than  $\tau_{\text{min}}$ . Indeed, as seen from Table 1, all intermediates relevant for the [2+2] photocycloaddition processes show lifetimes below 30 ns ( $3 \times 10^{-8} \text{ s}$ ).
- [26] S. J. Strickler, R. A. Berg, *J. Chem. Phys.* **1962**, *37*, 814–822.
- [27] For recent theoretical studies on intramolecular and intermolecular [2+2] photocycloaddition reactions, see: a) S. A. Bradley, B. J. Bresnan, S. M. Draper, N. W. A. Geraghty, M. Jeffares, T. McCabe, T. B. H. McMurry, J. E. O'Brien, *Org. Biomol. Chem.* **2011**, *9*, 2959–2968; b) J. R. Cucarull-González, J. Hernando, R. Alibés, M. Figueredo, J. Font, L. Rodríguez-Santiago, M. Sodupe, *J. Org. Chem.* **2010**, *75*, 4392–4401; c) K. Somekawa, Y. Oda, T. Shimo, *Bull. Chem. Soc. Jpn.* **2009**, *82*, 1447–1469; d) P. Jaque, A. Toro-Labbé, P. Geerlings, F. De Proft, *J. Phys. Chem. A* **2009**, *113*, 332–344.

- [28] a) G. Jones II, B. R. Ramachandran, *J. Photochem.* **1976**, *5*, 341–344; b) R. Gleiter, E. Fischer, *Chem. Ber.* **1992**, *125*, 1899–1911; c) D. Becker, Y. Cohen-Arazi, *J. Am. Chem. Soc.* **1996**, *118*, 8278–8284.
- [29] a) R. D. Small, J. C. Scaiano, *J. Phys. Chem.* **1977**, *81*, 2126–2131; b) J. C. Scaiano, *Tetrahedron* **1982**, *38*, 819–824; c) D. Becker, N. Haddad, Y. Sahali, *Tetrahedron Lett.* **1989**, *30*, 2661–2664; d) A. Rudolph, A. C. Weedon, *Can. J. Chem.* **1990**, *68*, 1590–1597; e) N. A. Kaprinidis, G. Lem, S. H. Courtney, D. I. Schuster, *J. Am. Chem. Soc.* **1993**, *115*, 3324–3325; f) D. Andrew, D. J. Hastings, A. C. Weedon, *J. Am. Chem. Soc.* **1994**, *116*, 10870–10882; g) J. F. D. Kelly, J. M. Kelly, T. B. H. McMurry, *J. Chem. Soc. Perkin Trans. 2* **1999**, 1933–1941; h) A. D. Cohen, B. M. Showalter, D. A. Brady, C. A. Kenesky, J. P. Toscano, *Phys. Chem. Chem. Phys.* **2003**, *5*, 1059–1063; i) X. Cai, P. Cygon, B. Goldfuss, A. G. Griesbeck, H. Heckroth, M. Fujitsuka, T. Majima, *Chem. Eur. J.* **2006**, *12*, 4662–4667.
- [30] D. L. Dexter, *J. Chem. Phys.* **1953**, *21*, 836–850.
- [31] U. Megerle, I. Pugliesi, C. Schriever, C. F. Sailer, E. Riedle, *Appl. Phys. B* **2009**, *96*, 215–231.
- [32] P. Fita, E. Luzina, T. Dziembowska, C. Radzewicz, A. A. Grabowska, *J. Chem. Phys.* **2006**, *125*, 184508.
- [33] U. Megerle, R. Lechner, B. König, E. Riedle, *Photochem. Photobiol. Sci.* **2010**, *9*, 1400–1406.

Received: February 27, 2013  
Published online: April 10, 2013

## **Appendix A7**

### **Electronic transient spectroscopy from the deep UV to the NIR: unambiguous disentanglement of complex processes**

*Eberhard Riedle, Maximilian Bradler, Matthias Wenninger,  
Christian F. Sailer, Igor Pugliesi*

Faraday Discussions 2013, 163, 139-158

Reproduced by permission of the Royal Society of Chemistry



## Electronic transient spectroscopy from the deep UV to the NIR: unambiguous disentanglement of complex processes

Eberhard Riedle, Maximilian Bradler, Matthias Wenninger, Christian F. Sailer and Igor Pugliesi

Received 5th February 2013, Accepted 11th February 2013

DOI: 10.1039/c3fd00010a

Complex multi stage relaxation and reaction pathways after the optical excitation of molecules makes the disentanglement of the underlying mechanisms challenging. We present four examples that a new transient spectrometer with excitation fully tunable from the deep UV to the IR and 225 to 1700 nm probing allows for an analysis with greatly reduced ambiguity. The temporal resolution of about 50 fs allows us to resolve all relevant processes. For each example there is a new twist in the sequence of relaxation steps that had previously been overlooked. In malachite green it appears that the importance of the phenyl twisting has been overemphasized and rather a charge transfer state should be considered. In TINUVIN P the predicted twisting as the driving motion for the ultrafast IC is confirmed and leads to a resolution of the earlier puzzle that the sub 5 ps regime shows kinetics deviating from a pure cooling process despite the sub ps proton transfer cycle. For the bond cleavage of Ph<sub>2</sub>CH Cl and Ph<sub>2</sub>CH Br the degree of electron transfer within the radical pair can now be determined quantitatively and leads to a profound understanding of the long term cation yield. For the first time coherent wavepacket motion in the photoproducts is reported. Last but not least the measurement of the GSB recovery in the deep UV allows for the surprising result, that even after S<sub>2</sub> excitation of cyclopentenones the triplet states are reached with near unity probability within a few picoseconds.

### 1 Introduction

Optical spectroscopy in a wide range of varieties is a prime source of microscopic information on molecular systems and processes. Simple continuous wave ultraviolet-visible (UV/vis) absorption allows the identification of the energies of excited electronic states and infrared (IR) measurements render typical vibrational modes that are used to identify the associated motives in the molecule. The

---

*Lehrstuhl für BioMolekulare Optik, Ludwig Maximilians Universität München, Oettingenstr. 67, 80538 München, Germany. E mail: Riedle@physik.uni-muenchen.de; Fax: (+49)089 2180 9202; Tel: (+49)089 2180 9210*

two regimes are complementary in many ways and the skilful choice or combination is often needed.

Modern time resolved versions of UV/vis and IR spectroscopy permit the observation of the temporal evolution of the system with well below 100 fs precision. Particularly in the UV/vis practically all relevant processes can now be resolved. The interpretation of the raw measurements does, however, require the identification of unambiguous signatures of the reaction intermediates and the eventual products. This is by far not trivial, as only the spectrum of the reactants is typically well known and possibly that of the product, if it can be isolated in sufficient quantity and purity. Any short lived intermediates can only be characterized by the transient measurement itself and so there is often a “chicken and egg” dilemma that a model of the reaction is needed to assign the observed spectral signatures and these would be of great help to develop the model.

As the structural motives that determine the vibrational frequencies are quite localized, *e.g.*, N-H or C-C stretches or specific bending motions in the fingerprint region, at least first guesses for the assignment are readily made. However, this also means that only moderate changes result in many regions of the IR spectrum due to the chemical transformation. Identifying the significant ones and isolating them from solvent signals can then become quite challenging. The electronic bands do change quite largely on the contrary, both in position and in strength. The problem there is the large homogenous and inhomogeneous width of each electronic transition. Sometimes even the decision of what is a separate electronic band or just a vibronic structure can become difficult.

Many of the seminal experiments in femtochemistry were done with fixed frequency pulses<sup>1</sup> and this - in retrospect - required a fair amount of chemical intuition for the analysis. Broadband transient measurements have, however, been developed continuously and the change from liquid based continuum generation to crystal based continua has allowed an ever widening application. Due to the intrinsically broad spectrum of a femtosecond IR pulse - relative to the typical  $15\text{ cm}^{-1}$  width of vibrational transitions - somewhat of an overview was originally easier to gain in this spectral range.<sup>2</sup> The coverage of a wide spectral range requires tuning the probe pulse repeatedly and performing the time scan at each setting. This is where UV/vis transient spectroscopy has an intrinsic advantage, as extremely broad continua are now available<sup>3,4</sup> and can be combined with detectors of a thousand or more pixels.

In this contribution we want to demonstrate the potential of a cutting edge broadband UV/vis/NIR transient spectrometer that will be briefly described in Sec. 2. We then present and discuss measurements on four sample systems ranging from ultrafast nonradiative decay, excited state proton transfer, and bond cleavage to ultrafast intersystem crossing. For all systems we find surprising new details that had been overlooked by the earlier investigations with limited spectral coverage. We thus can demonstrate that transient electronic spectroscopy is now becoming extremely powerful and the redundancy of information obtained in the measurements gives an unambiguous and clear picture of the complex dynamics. Combined with high level computations the energy flow in molecules after absorption of a photon and leading eventually to photochemistry can be traced most reliably.



## 2 Ultra-broadband transient spectroscopy with 50 fs resolution

The transient spectrometer used for our measurements relies on a fully tunable pump source and a broadband continuum for wavelength selective probing. The general setup has been described in detail<sup>4</sup> and is based on a kHz Ti:sapphire amplifier (CPA2001; Clark-MXR, Inc.). The pump pulses are derived from a blue pumped noncollinear optical parametric amplifier (NOPA) frequency doubled in a BBO crystal with typically 100  $\mu\text{m}$  thickness. The visible NOPA pulses are over-compressed in a fused silica prism compressor to precompensate for all dispersing elements after the doubling stage. With various mixing strategies and a possible intermediate continuum stage the range from 189 nm to 5  $\mu\text{m}$  can be covered without any gaps.<sup>5,6</sup> The pump pulse lengths can be adjusted to 30 fs or below from the deep UV to 1200 nm and are only slightly longer at longer wavelengths.

In the original setup we used a 775 nm pumped single filament supercontinuum that spans from 290 to 720 nm as the probe. Such a wide continuum is generated in a selected 5 mm  $\text{CaF}_2$  plate that is translated in a circular fashion to avoid optically induced damage. The plate is carefully oriented to avoid depolarization of the continuum.<sup>7,8</sup> The broadband probe light is dispersed in a fused silica prism and detected with a multichannel detector. The continuum chirp is corrected in the data postprocessing. The pump-probe delay up to 2 ns is adjusted with the help of a computer controlled delay line accurate to better than 10 fs. The overall temporal resolution is as good as 50 fs, mainly limited by residual group velocity mismatch between pump and probe in the 120  $\mu\text{m}$  solution sample. Transient spectrometers with parameters similar or close to ours are in use in a number of laboratories around the world.<sup>9–12</sup>

To access an even wider probe spectral range we alternatively pump the  $\text{CaF}_2$  based continuum generation by the frequency doubled or tripled Ti:sapphire

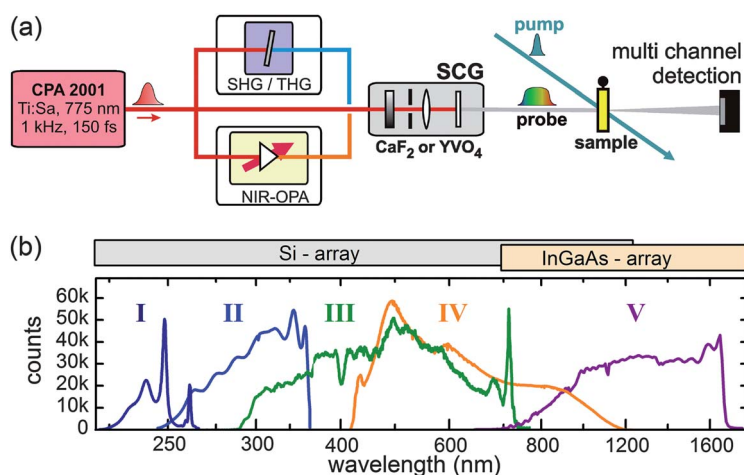


**Fig. 1** (a) Scheme of the supercontinuum generation with various harmonics of the Ti:sapphire amplifier or the output of a NIR OPA. (b) Spectra of the continua as seen on the spectroscopic multi channel detector.

output (see Fig. 1(a)). We find that significantly less pump energy is needed at these shorter wavelengths (387 and 258 nm) and therefore no damage is found even in prolonged operation. The resulting spectra are shown in Fig. 1(b). They span from close to the pump wavelengths down to 245 and 225 nm. The long wavelength cut-off is given by the dielectric filter used to suppress the high spectral power near the pump wavelength. Optimized filters with a smooth roll off could add some more spectral range in this vicinity to the probe pulse.

To access the near infrared (NIR) probe range we use a single-stage collinear optical parametric amplifier (OPA) to generate a red shifted continuum.<sup>3</sup> With the OPA signal at 1200 nm and the CaF<sub>2</sub> plate the useful continuum spans from 420 to 1100 nm. In this range the silicon based CCD or diode array can still be used. For the 750 to 1700 nm range we use the idler at 2100 nm to generate the continuum in a 4 mm YVO<sub>4</sub> crystal. As detector an InGaAs based 256 pixel detector (Series 2000CV2 camera with uncooled Hamamatsu G9203-256D detector; Entwicklungsbüro Stresing) was used.

All continua are single filament and can therefore be well collimated and focused into the sample cell. Their spectra are summarized in Fig. 1(b). They overlap sufficiently and in total span from 225 nm to 1.7  $\mu\text{m}$ . Typically two or three of the ranges are needed to cover the region of interest for a particular molecule. They are measured sequentially and then stitched together in the postprocessing to render the comprehensive manifold of transient spectra for all desired delay times.

### 3 Selection of sample molecules and processes

The development of the transient spectrometer described above has been motivated by our various investigations of ultrafast molecular and chemical dynamics. These range from photophysical process, *via* excited state electron and proton transfer to complex chemical reaction sequences. For this discussion we have chosen four examples that serve to demonstrate the newly available capabilities from the application point of view.

The first decision that has to be made in an ultrafast molecular experiment is the choice of the pump wavelength,  $\lambda_{\text{pump}}$ . As we have ultrashort pulses at all possibly needed wavelengths to our disposal, we choose  $\lambda_{\text{pump}}$  purely according to the energy level structure of the molecule. We strongly believe that this enhances the value of the results as we do not have to worry about some initial electronic relaxation that is inevitably connected to some vibrational excitation. As shortly discussed above, such a choice of pump wavelength is always possible with the existing nonlinear pulse generation schemes.

The choice of  $\lambda_{\text{pump}}$  can be made quite readily by inspecting the linear absorption spectrum of the sample. The spectra of the four substances are shown in Fig. 2. For 2,3,4,5-tetramethyl-2-cyclopentenone (TMCP) in cyclohexane there is an extremely weak  $S_1 \leftarrow S_0$  transition around 320 nm and a quite strong  $S_2 \leftarrow S_0$  transition below 250 nm. We excite TMCP at 228 nm to specifically investigate the relaxation from the  $S_2$  state. Diphenylmethylbromide (Ph<sub>2</sub>CH-Br) can be excited through the weak benzoic absorption at 270 nm. In 2-(2'-hydroxy-5'-methylphenyl)-benzotriazole (commercial name TINUVIN-P) ultrafast excited state intramolecular proton transfer (ESIPT) can be triggered by  $\pi-\pi^*$  absorption at 350 nm. The cationic dye malachite green (4-[(4-dimethylaminophenyl)phenyl-methyl]-

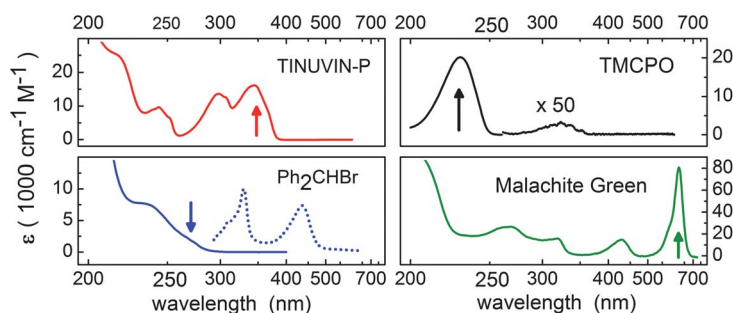


**Fig. 2** Absorption spectra of the molecules studied in this work. TMCPO: 2,3,4,5 tetramethyl 2 cyclopentenone. In the panel for  $\text{Ph}_2\text{CHBr}$  also the spectra of the benzhydryl radical and cation are shown (dotted line). The arrows indicate the pump wavelength.

*N,N*-dimethylaniline; MG) is known to laser spectroscopists as it made the first real femtosecond laser system, the colliding pulse mode locked laser (CPM) possible due to its saturability at the 620 nm emission wavelength of Rhodamine 6G. In the present report we reinvestigate the ultrafast dynamics after 620 nm excitation.

#### 4 Putting the analysis of the ultrafast dynamics in malachite green on a sound basis

Malachite green (MG, see Fig. 3(a)) is a cationic triarylmethane dye that absorbs strongly in the visible region. Since this absorption overlaps perfectly with the output of the CPM laser - it is actually used as a saturable absorber in this device - it was one of the first molecules investigated for its ultrafast dynamics. The early studies concentrated on the ground state bleach (GSB) recovery. Rather complex kinetics with a main time constant of 2.1 ps in methanol and a strong solvent dependence were found.<sup>13,14</sup> The solvent dependence is attributed to the viscosity of the solvent and it is postulated that an intermediate state  $S_x$  is reached after

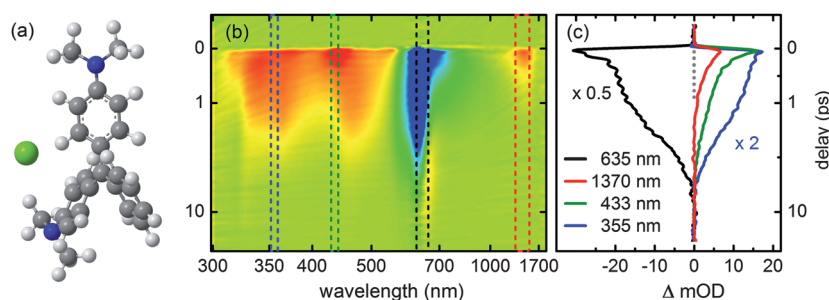


**Fig. 3** Transient spectroscopy of malachite green dissolved in ethanol. (a) Structure of the dye. (b) Manifold of transient spectra. Red colours indicate an increase in absorption, blue colours a decrease. The wavelength scale is roughly reciprocal to pronounce different energetic parts equally. The time scale is linear in the range of  $-1$  to  $+1$  ps and logarithmic beyond. (c) Selected kinetic traces at the maximum of the NIR absorption of the LE state (1420 nm), the broad excited state absorption in the UV (355 nm) and the GSB (620 nm).

excitation through torsion of the phenyl rings.<sup>14–19</sup> After relaxation from the  $S_x$  state to the ground state the geometrical relaxation and cooling of the hot  $S_0$  is thought to complete the cycle.

We investigated the dynamics of MG in ethanol after 620 nm pumping and utilizing the probe ranges III and V to cover the range from 300 to 1700 nm. The resulting manifold of the transient spectra is shown in Fig. 3(b). A pump–probe cross correlation of 35 fs in the NIR and slightly longer in the UV is reached and matches the resolution of previous one-<sup>14,20</sup> or two-colour pump–probe<sup>15</sup> and fluorescence up-conversion<sup>18</sup> measurements.

The strongest feature in the transient spectrum is the region of negative optical density around 635 nm (blue colours; Fig. 3(b)), where GSB and stimulated emission (SE) overlap. This is also the spectral region where most of the investigations were performed. In addition, the whole range from 300 nm to the GSB region and the NIR displays strong excited state absorption (ESA). A preliminary global fit analysis shows a 100 fs component with an increase of signal in the SE region and a decrease in the GSB region. This can be interpreted as the inertial motion of the optically prepared wavepacket away from the Franck–Condon point towards the equilibrium geometry of the excited electronic state  $S_1$  that leads to a time dependent red shift of the SE. Such an extremely fast dynamics was already reported previously.<sup>14,20</sup>

A second decay component of about 440 fs has major peaks in the decay associated spectrum (DADS) at 433 nm (with 33 nm width) and at 1400 nm (430 nm width). These peaks can be readily assigned to the ESA following  $S_1$  excitation and leading to the  $S_2$  and  $S_4$  excited electronic states. In the absorption spectrum, transitions to these two states are found at the matching positions of 428 and 255 nm (compared in Table 1). A third spectral feature with a positive amplitude in the DADS is found to be nearly coinciding with the  $S_1 \leftarrow S_0$  absorption band, but is significantly different in shape. If this feature was due to a change in the GSB, it would indicate an increase in GSB with time. There is no argument known to us that would predict such a change in the hundreds of fs range. Therefore we have to assign this feature to the  $S_3 \leftarrow S_1$  transient absorption (ESA). Finally a decrease in SE with a 440 fs time constant is found that reaches from 635 nm to 1100 nm. This matches the spontaneous emission spectrum within the limitation that certainly the stimulated emission in the sub-ps range does not originate from a thermalized  $S_1$  vibronic distribution. In summary, this means that the strong transient signal around the usual 620 nm pump

**Table 1** Absorption energies for the  $S_n \leftarrow S_0$  and  $S_n \leftarrow S_1$  transitions obtained from the cw spectrum of MG together with the  $S_n \leftarrow S_1$  transitions energies (widths in brackets) extracted from the transient absorption (TA) of MG. The time constants are obtained from single wavelength fits. “d” signals where the time constant cannot be determined due to spectral overlap, “a” signals no amplitude for the associated time constant

	$\lambda$ (nm) $S_n \leftarrow S_0$	$\lambda$ (nm) $S_n \leftarrow S_1$	$\lambda$ (nm) TA exp	$\tau_1$ (ps)	$\tau_2$ (ps)	$\tau_3$ (ps)
$S_1$	622			0.10	0.44	2.2
$S_2$	428	1372	1400 (430)	a	0.44	a
$S_3$	315	638	~635	d	d	d
$S_4$	255	432	433 (33)	a	0.33	1.7
ESA			355	a	a	2.0

wavelength of most investigations is the sum of GSB, SE and ESA. It follows that the undiscussed averaging over the spectral width of the pump/probe pulse will not lead to any unambiguous interpretation of the dynamics of MG.

To display the transient absorption at selected times more clearly, we extracted the spectrum of absorption change (black lines in Fig. 4) from the complete manifold shown in Fig. 3(b). We then added a constant fraction of the ground state absorption spectrum (grey line in all panels of Fig. 4) to obtain the momentary spectrum (blue lines) of the sub-ensemble of molecules that was initially excited. The rapid decay of the 1400 and 433 nm peaks is clearly seen, as are the changes in the 635 nm region. At 1 ps, there is a broad absorption beyond the ground state absorption remaining that decays with about 2 ps. At 2 ps the 622 and 428 nm bands are the only remaining signals. The 622 nm  $S_1 \leftarrow S_0$  absorption band has, however, not yet fully recovered. It is interesting to notice that the shape of the 622 nm band does not significantly change during the relaxation processes. This is surprising in view of the generally accepted interpretation that large amplitude torsional motions of the phenyl rings dominate the dynamics. We cannot rationalize how such motions do not lead to changes in the 622 nm band of more than the 3% upper limit we can deduce as maximum spectral change compared to the full GSB signal.

Kinetic traces at selected wavelengths are shown in Fig. 3(c). The fitted exponential decay constants are shown in Table 1. At 1400 nm we explicitly probe the  $S_1$  population through the  $S_2 \leftarrow S_1$  ESA. We find a relaxation time of 440 fs in good agreement with fluorescence measurements.<sup>21</sup> It should be noted that the largely increased probe range of our experiment allows for this unambiguous determination of the  $S_1$  lifetime by transient spectroscopy alone. At 433 nm there is an overlap between the specific  $S_4 \leftarrow S_1$  ESA and the very broad ESA that lasts into the ps range. The decay curve can be fitted with a first 330 fs exponential contribution that again signals the  $S_1$  decay and a further 1.7 ps components. At 355 nm there is no ground state absorption and we do not have to expect any GSB. At this wavelength we can therefore exclusively probe the intermediate state  $S_x$  that the  $S_1$  state relaxes to with the 440 fs time constant. The 2.0 ps decay is within experimental accuracy identical to the 1.7 ps component already found at 432 nm.

For the GSB recovery we need a 100 fs, a 440 fs and a 2.2 ps time constant. The first two most likely just result from the overlapping SE and ESA components. The

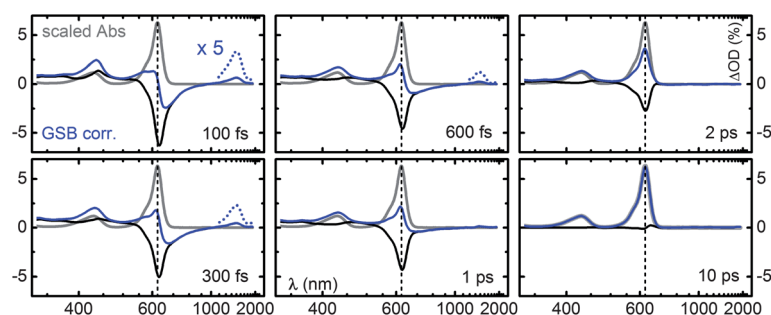


**Fig. 4** Selected transient spectra at the indicated pump-probe delays (black lines). For visualization of the underlying changes in malachite green dissolved in ethanol, an equal amount of absorption spectrum is added to each transient spectrum (blue lines). In this way the recovery to the absorption spectrum (grey line) of the sub-ensemble excited by the pump pulse can be recognized.

slightly longer 2.2 ps recovery time of the GSB as compared to the  $S_x$  decay is quite reasonable in view of cooling processes. Temporal signal oscillations of about  $226\text{ cm}^{-1}$  that can be attributed to a symmetric carbon–phenyl stretch vibration<sup>14,22,23</sup> are only found in the region from 605 to 635 nm. This must mean that a ground state wavepacket prepared by resonant stimulated Raman scattering is observed.

The extremely wide probe range of our measurements and the detailed analysis leads to the following conclusions. After  $S_1$  excitation MG relaxes to a state  $S_x$  that neither fluoresces below 900 nm nor carries any oscillator strength to the known higher electronic states. Instead a nearly 2 eV broad ESA band decaying with a time constant very close to the GSB recovery is found. This all points to a charge transfer (CT) character of the  $S_x$  state. Indeed, recent high level calculations predict such a character already for the  $S_1$  state<sup>24</sup> and for the related molecule crystal violet a relaxation mechanism involving charge redistribution has been proposed.<sup>25,26</sup> We suggest that the initially excited (local excited) state has an electronic character more similar to the ground state. This property would explain the very strong  $S_1 \leftarrow S_0$  absorption. The often discussed torsion of the phenyl rings starts after the initial 100 fs geometric relaxation and leads to a simultaneous change in the electronic character towards a CT state on the half-ps time scale. Charge recombination then takes about 2 ps to repopulate the  $S_0$  state with little optical signature from the “reverse” torsion of the phenyl rings.

From an extensive search of the literature it does not become clear, why repeatedly claims were made that the polarity of the solvent does not influence the dynamics of MG. It was always the viscosity that has been considered. If one, however, considers a series of alcohols with increasing size, not only the viscosity increases but also the polarity decreases. Future work should investigate this point by the reanalysis of existing data and solvent dependent transient spectroscopy. The solvation times of alcohols that are much longer than the ps times in the decay of excited MG are no intrinsic hindrance, as already a partial solvation can lead to efficient CT.<sup>27</sup> Given the capabilities demonstrated in this section, a final decision on the MG relaxation mechanisms should readily be possible.

## 5 An overlooked twisting isomerization in the proton transfer cycle of TINUVIN-P

TINUVIN-P is one of the best studied ESIPT systems.<sup>28–31</sup> After a 60–80 fs proton transfer the keto-type molecule relaxes to the electronic ground state with a 120–150 fs time constant. In the excited keto state a pronounced wavepacket motion is observed.<sup>31</sup> As the internal conversion (IC) was assumed to happen in the closed keto form originating from the optically excited enol form, the subsequent 600 fs decay found at probe wavelengths in the visible region was assigned to the proton back-transfer.<sup>29,30</sup> In the enol form a  $180^\circ$  twist around the central bond between the phenyl and the benzotriazole ring regenerates an identical conformation and a possible “isomerization” cannot be detected spectroscopically. In the keto-type form the same twist transfers TINUVIN-P from the closed form with the intramolecular hydrogen bond to the open form.<sup>32</sup>

The ultrafast proton transfer cycle leaves the TINUVIN-P in a highly vibrationally excited state. This is seen as a positive transient absorption below the  $S_1 \leftarrow S_0$  absorption edge at 367 nm and a decrease in absorption at shorter

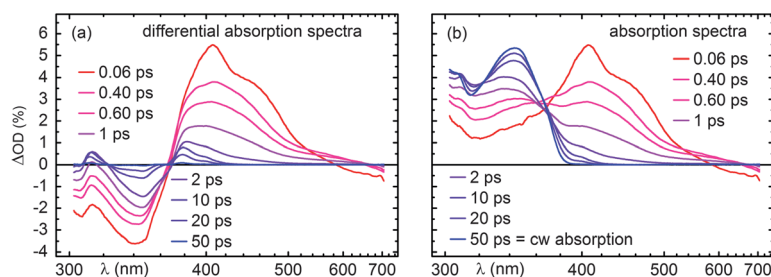


**Fig. 5** (a) Transient absorption changes at selected delay times for TINUVIN P in cyclohexane excited at 355 nm. (b) Absorption spectrum of the sub ensemble excited by the pump pulse.

wavelengths.<sup>33,34</sup> For times from 5 ps onward the relaxation of this transmission change can be well modelled with a cooling process. However, it was already realized in the earlier investigations that the cooling picture was not sufficient to explain the spectral evolution in the first few picoseconds.

With our broadband spectrometer we investigated the dynamics of TINUVIN-P in cyclohexane. The differential absorption spectra shown in Fig. 5(a) display a rich variety of kinetics in the first 50 ps. To allow for an easier discussion of the underlying dynamics, we added a suitable fixed fraction of the ground state spectrum to all traces. The resulting time dependent absorption spectrum of the sub-ensemble excited by the pump pulse (see Fig. 5(b)) is used to discuss the observations.

At 60 fs after the excitation depletion of the ground state absorption is clearly seen below 367 nm. In the blue spectral region a strong transient absorption is found that initially displays some vibronic structure. This initial absorption must be due to ESA from the enol- or keto excited state. The absorption extends into the UV and overlaps with the ground state absorption. A weaker structure between 500 and 600 nm that develops with some delay is assigned to the closed keto ground state in accordance with ref. 30. Beyond 600 nm stimulated emission is found. The SE decays very rapidly and therefore can be assigned to the excited keto-type state.

Kinetic traces at selected wavelengths are shown in Fig. 6. For clarity the traces are shown on an expanded scale in part (a,c) and over the full relevant range of 30 ps in part (b,d). At 684 nm we find a delay/increase of the SE with about 80 fs and a decay with 154 fs. Within the experimental precision this ESIPT and IC behaviour matches the previous reports.<sup>29,30</sup> At 551 nm we find a 144 fs increase of the signal and a 588 fs decay. Therefore we can confirm that in the 500 to 600 nm region the suggested proton back-transfer is observed and takes 600 fs.

At exactly the vibrationless 0–0 transition of the optically pumped  $S_1 \leftarrow S_0$  band (367 nm) we find an isosbestic point in the sub-ensemble spectra (Fig. 5(b)) at times beyond some ps. This is in close agreement with the earlier reports<sup>33,34</sup> and we can safely assign the decrease of absorption around 400 nm and the increase in the range around 350 nm to vibrational cooling. The spectral evolution of a cooling process does not render simple exponential decays with a wavelength independent decay time. Still, the value of 13 ps found at 344 nm near the band maximum gives a characteristic time constant of the cooling process. A very detailed resonance Raman study finds mode specific behaviour with time constants in the same range.<sup>35,36</sup> The traces at 362 and 375 nm, energetically



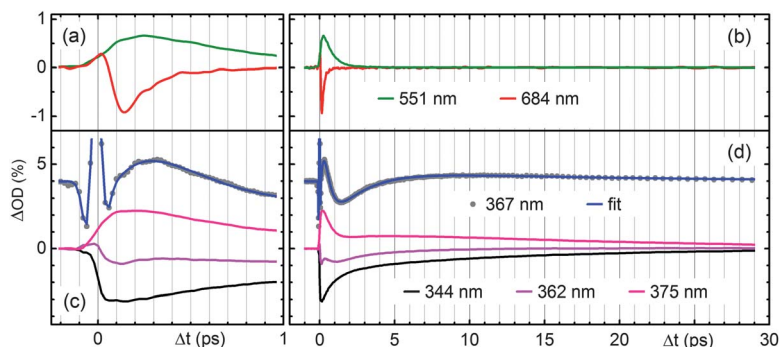


**Fig. 6** Selected kinetic traces at the spectral positions, where the various conformers and relaxation processes of TINUVIN P can be best differentiated. (a) and (c) show the traces within the first picosecond, while (b) and (d) show the range up to 30 ps. For clarity the coherent artefact due to the solvent cyclohexane has been subtracted from the traces except at 367 nm. The trace for 367 nm is multiplied by a factor of 4 and shifted upward.

slightly above and below the 0–0 transition consequently display quite complicated kinetics as many opposing effects contribute to the optical signal.

At exactly 367 nm the cooling does not influence the optical signal and the kinetics at this wavelength can therefore report the pure population evolution of the enol electronic ground state. We still have to assume that none of the other states involved in the full ES IPT and relaxation cycle contributes to the signal. Since the ES IPT itself proceeds in below 100 fs, the IC in 150 fs and the back-transfer from the closed keto-type form in 600 fs, this is a fairly safe assumption after about 1 ps. Inspection of the 367 nm trace (Fig. 6(c,d); grey filled circles for the experimental values and blue line for a multi-exponential fit) shows indeed an 80 fs decrease, a 150 fs increase and a 410 fs decrease. The vibrational cooling is seen as a very weak 15 ps decrease of the signal back to zero. Clearly there is another 2.2 ps contribution that was not seen in earlier work. In a global fit this time constant can be found as a prominent decay within most of the GSB range and the range around 450 nm. However, single wavelength fits show a systematic variation of the time constant due to the cooling and the overlap with the ESA.

To assign this 2.2 ps relaxation constant we return to the red region of the spectrum. The width of the spontaneous emission spectrum of the closed keto-type form of TINUVIN-P is known<sup>31</sup> and it is also established that the ground state closed keto-type form shows a mirror image to the fluorescence spectrum with a 0–0 transition at 625 nm.<sup>30</sup> Assuming a similar width and strength for emission and the absorption bands, only the region down to about 500 nm in the transient absorption spectrum can be assigned to the closed keto-type form. What is left to explain is the strong absorption in the range 380 to 500 nm and the 2.2 ps time constant.

It has been calculated, that the IC of the excited closed keto-type form proceeds *via* a conical intersection that involves a twisting around the central bond and a pyramidization.<sup>32</sup> A similar prediction backed up by experimental evidence was also made for the related 2-(2'-hydroxyphenyl)benzothiazole (HBT).<sup>37</sup> As a result of the twisting motion necessary for the extremely fast IC, parts of the molecules do not relax to the closed keto-type form but to the open keto-type form. This is



directly corroborated by transient IR spectroscopy<sup>38</sup> and in line with early indications.<sup>29,39</sup> In view of all the evidence we assign the 2.2 ps time constant in TINUVIN-P to the back-isomerization of the open to the closed keto-type form that is then followed by an even faster back-transfer of the proton to lead to vibrationally excited enol molecules. These are subsequently cooled by the solvent in 10 to 20 ps. The majority of the strong transient absorption in the blue is consequently assigned to the open form.

These additional species populated with the 150 fs IC can readily explain the difficulties discussed previously to model the cooling kinetics at times before 5 ps.<sup>34</sup> It is not yet clear what this means for the interpretation of the resonance Raman studies.<sup>35,36</sup> In summary, the relaxation cycle in UV-excited TINUVIN-P, that takes as little as some ten picoseconds for completion, involves forward ESIPT ( $\tau = 80$  fs), a branching in the IC to the closed and open keto-type form ( $\tau = 150$  fs), a back-twisting ( $\tau = 2.2$  ps), back-proton transfer ( $\tau = 600$  fs) and finally cooling ( $\tau = 15$  ps). One might ask oneself whether such a complex sequence is a rare exception or a more general occurrence. The ring opening of 1,3-cyclohexadiene comes to mind with the subsequent multi-step relaxation to the lowest energy tZt-conformer. In this system also highly complicated kinetics were reported.<sup>40</sup>

## 6 The generation and interconversion of benzhydryl radicals and cations by photolysis of diphenylmethylbromide

After UV excitation diarylmethylhalides undergo homolysis to the pair of a benzhydryl radical and halogen radical or heterolysis to the benzhydryl cation and the halogen anion. The overwhelming majority of investigations on this process and the subsequent interconversion between radical and ion pairs were performed without transient spectroscopy which renders spectra of the reactive intermediates, but rather by *a priori* chosen pump and probe pulse wavelengths. In addition, very intricate analysis with multiple exponential rates and a highly complex interpretation was deduced from these fixed colour recordings.<sup>41</sup> Last but not least, only ps resolution was employed, even though it had been shown that the initial processes proceed on the sub-ps time scale.<sup>42</sup>

We utilized 30 fs pulses at the first maximum of the absorption spectrum (270 nm; see Fig. 1) to excite either diphenylmethylchloride ( $\text{Ph}_2\text{CH}-\text{Cl}$ ) or diphenylmethylbromide ( $\text{Ph}_2\text{CH}-\text{Br}$ ). As the strong absorption features of the photolytic products  $\text{Ph}_2\text{CH}^+$  and  $\text{Ph}_2\text{CH}^\bullet$  are well separated from the absorption of the precursors, we can use the range III of our continuum generation for a full process analysis. The spectrum of  $\text{Ph}_2\text{CH}^\bullet$  at 330 nm and the one of  $\text{Ph}_2\text{CH}^+$  at 430 nm are shown as dotted lines in Fig. 1.

The manifold of transient spectra for  $\text{Ph}_2\text{CH}-\text{Br}$  in acetonitrile at various pump probe delays is shown in Fig. 7(a). It can be readily seen that the radical signal appears very early after the optical excitation and decreases in the ps range. The cation signal increases more slowly and then also decreases later. The kinetic traces shown in Fig. 7(b) give a more detailed view. They show the integrated signal over the full bands. The optical signal can be considered to be proportional to the species population within good approximation. The step in the rise of  $\text{Ph}_2\text{CH}^\bullet$  (blue line) at about 50% amplitude happens at 100 fs. In agreement with

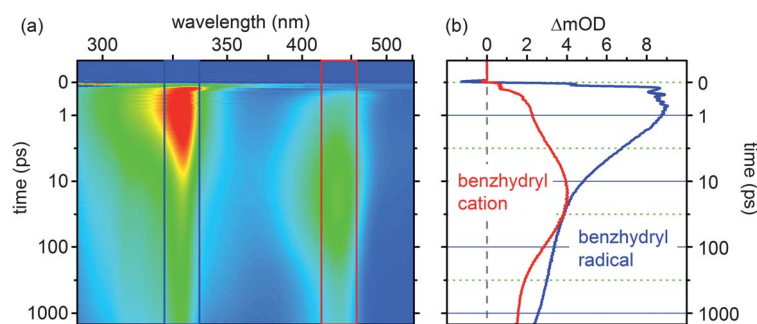


**Fig. 7** (a) Transient spectra after 270 nm excitation of diphenylmethylbromide in acetonitrile. Red colour indicates a large transient absorption, green an intermediate one and blue colours little. (b) Signal for the resulting benzhydryl radical (blue line) and benzhydryl cation (red line) integrated over the respective band.

the observation for  $\text{Ph}_2\text{CH-Cl}$ , where we observe such a step at 80 fs,<sup>43</sup> we assign this to the delayed generation of the radical. The excited state wavepacket propagates from the Franck–Condon region to a first conical intersection that leads part of the wavepacket to the radical product. The remainder of the wavepacket stays on the excited potential hypersurface and reaches a second conical intersection leading to the cation product. This takes a total time of 125 fs in  $\text{Ph}_2\text{CH-Cl}$  and 200 fs in  $\text{Ph}_2\text{CH-Br}$  (see step in the red line). This means that the cation does not appear until this later time. No more radical and cation population is generated at later times. The slight increase in the optical signals is rather due to an increase in transition strength due to solvation and planarization of the products.<sup>44</sup>

A close inspection of the product signal curves and the full set of transient spectra show significant modulations up to about 2 ps. The frequency is about  $300\text{ cm}^{-1}$  for the radical and  $350\text{ cm}^{-1}$  for the cation. To analyze these modulations, we compare the signal at the blue side of the radical absorption to that at the red side (see Fig. 8(a)). Clearly a  $\pi$  phase shift is seen that proves that the modulation is due to a vibronic wavepacket. In addition, we determined the position of the maximum of the radical and cation absorption for each delay.<sup>45,46</sup> The resulting temporal dependence of the peak position shows the already mentioned ps relaxation due to solvation and planarization and also the oscillations. This confirms the interpretation as a vibronic wavepacket. An analysis of the normal modes of the radical and cation suggests that these wavepackets correspond to a symmetric stretch motion of the phenyl rings relative to the central carbon. This is very similar to the situation in MG (see above). However, in the photolysis of  $\text{Ph}_2\text{CH-Br}$  the wavepacket motion is in the photochemical products. The bond cleavage proceeds so fast that an impulsive excitation of the vibrational motion occurs. The stabilization of the radical and the cation leads to an increased electron density in the vicinity of the central carbon. Such an increase in electron density leads in turn to an impulsive shortening of the bonds and the suggested vibrational motion.

In the time up to about 10 ps the radical population decreases while the population of the cation increases. This is due to electron transfer between closely spaced benzhydryl and bromine radicals leading to the ion pair. We find that a

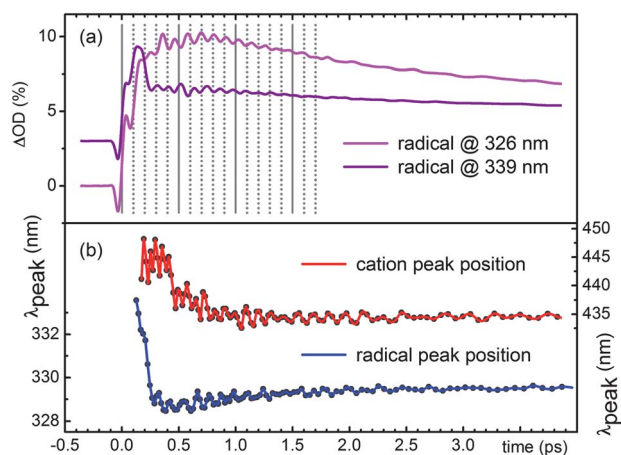


**Fig. 8** (a) Transient absorption changes after 270 nm excitation of Ph<sub>2</sub>CH Br on the low wavelength (326 nm) and high wavelength (339 nm) edge of the radical product band. (b) Temporal dependence of the peak position of the benzhydryl radical (blue curve) and cation (red curve) band.

stretched exponential describes this process best, just as in our recent analysis of Ph<sub>2</sub>CH–Cl.<sup>46</sup> The only difference is that for the chloride system an 11 ps time constant was found for this process compared to the shorter time constant of 2.1 ps in the bromide system. The decay of the radical population and the increase of the cation population with the identical temporal behaviour is direct proof of the interconversion by electron transfer. This finding is in contrast to the conclusions drawn from ps experiments on Ph<sub>2</sub>CH–Br.<sup>47,48</sup> Clearly the very fast termination of the electron transfer in the bromide system did not allow the correct interpretation in the earlier experiments with 20 ps resolution. The electron transfer is stopped by the depletion of closely spaced radical pairs.<sup>46</sup>

After the end of the electron transfer the remaining radical pairs separate by diffusion to give a stable population of free radicals. The ion pairs stick together for a longer time due to the Coulomb attraction. Therefore they can effectively undergo recombination and the reduced population of free ions eventually evolves (94 ps time for Ph<sub>2</sub>CH–Br and 138 ps for Ph<sub>2</sub>CH–Cl).

The complete set of transient data cannot be modelled anymore with the usual kinetic scheme of well defined species like contact pairs, solvent separated pairs and free species. Instead we developed a combined model of Marcus-type electron transfer and Smoluchowski-diffusion.<sup>46</sup> We have to assume an initial radical and cation pair distance distribution that extends far beyond the contact distance considered explicitly in earlier work.<sup>41,42,47,48</sup> The various processes are treated as distance dependent. The time dependent populations can then be deduced by integration over the full radial distribution for each delay time. The time dependent rates result from the convolution of the distributions with the distance dependent rates.<sup>46</sup>

The observation of the full range of optical signals connected with the photolysis of diarylmethylhalides with 50 fs temporal resolution renders many hitherto covered details on the dynamics. Hypotheses that have been carried on for decades can now finally be scrutinized. The investigation of complex and multistep chemical process is now possible in a most direct fashion. Together

with high level theoretical considerations the influence of conical intersections<sup>49</sup> and the microscopic arrangement can be investigated quantitatively. Since the breadth of optical signals renders a high degree of redundancy and cross checks, the ambiguity of many theories will be put to a serious test.

## 7 Direct determination of the triplet yield after $S_2$ excitation

One of the little mentioned understandings in ultrafast molecular dynamics seems to be that the rates connecting the originally excited state to the series of product states or chemical species are evaluated, presented and discussed, while the efficiencies and possible branching ratios are much less often put into the focus of the investigation. This stems from the fact that the yields of transient species are much less direct to determine compared to final product yields. For a hypothetical photochemical process leading from a precursor A to a stable product B the yield can readily be determined, as well established chemical means can be used to determine the product quantum yield. With modern illumination sources like high power LEDs this is extremely simple.<sup>50</sup> As a by-product one finds out which fraction returns to the reactant and effectively just undergoes a photophysical nonradiative relaxation.

For transient species or states the situation is much more difficult. Even if a time resolved measurement is available and able to uniquely identify the transient species - as exemplified in the sections above - one can still not rely on the Beer-Lambert law as the molar absorption coefficient  $\epsilon$  of the species is generally not known. So only the product of  $\epsilon$  and concentration can be determined. For the benzhydrylbromide photolysis discussed in Sec. 6 one can chemically stabilize the cation and actually measure the value of  $\epsilon$ . If in addition the fluence of the pump pulses at the sample position and all other relevant geometric parameters are determined, quantitative transient spectroscopy results that actually determines the time dependent yield of all species absolutely.<sup>46</sup>

More frequently other methods have been employed to determine the yield of intermediate species, particularly triplet states. Triplets are of special interest to chemistry as they are long-lived compared to singlet states and therefore can allow for diffusion controlled photo-initiated bimolecular processes like the ones found in photocatalysis<sup>51</sup> and photo-initiated organic synthesis. One method uses triplet-triplet energy transfer to a system with a known triplet absorption coefficient and the measurement of the resulting quencher triplet by spectral photometry can be used. However this procedure requires very careful calibration and a certain degree of assumptions. The oxygen production by triplet-sensitized photooxidation of 1,3-diphenylisobenzofuran is an example of actually producing a physically measurable specific product that should be proportional in amount to the amount of triplet molecules produced over a selected period.<sup>52</sup> Another spectroscopic method that requires many assumptions and checks is the measurements of the ESR spectrum that specifically can report the triplet concentration.<sup>53</sup> To decouple the triplet yield and the triplet absorption cross section, Van Stryland and coworkers have introduced a very elaborate double-pump method that relies on the partial saturation of transitions. This approach still has limitations given mainly by the molecular energy level structure.<sup>54</sup> The most direct method is the determination of the ground state bleach recovery. This

method relies on the ability to separate the time scales of the decay of the initially excited singlet and the resulting triplet in the GSB signal. This has been demonstrated by various single colour probe transient absorption measurements in the visible region.<sup>55–57</sup>

A more general application of the GSB recovery has so far been hampered by two issues. First, many systems of interest have their first strong absorption far in the UV. Second, a measurement at just one GSB wavelength still leaves the uncertainty that a superimposed ESA falsifies the interpretation. Both issues can now be solved with our extended probing range reaching as low as 225 nm. This is certainly sufficient to reach the strong absorption bands of almost any substance of chemical interest. By recording a full transient spectrum, the shape of the known ground state absorption spectrum can be used to unambiguously disentangle GSB and ESA or product contributions.

For an experimental demonstration we chose 2,3,4,5-tetramethyl-2-cyclopentenone (TMCPPO) in cyclohexane. As seen from the absorption spectrum displayed in Fig. 2, there is a very weak  $S_1 \leftarrow S_0$  absorption around 320 nm and a strong  $S_2 \leftarrow S_0$  absorption centred at 229 nm. The assignment of the spectrum and the qualitative picture of the dynamics are made in analogy to the closely related acrolein.<sup>58</sup> We pump the  $S_2$  state with 228 nm pulses of sub-60 fs duration. The transient spectra are measured with the three continuum ranges I–III (Fig. 1(b)). They display very broad structures (see Fig. 9(a)) and it becomes clear that such a wide probe range is needed for a clear interpretation. The spectrum at 0.15 ps pump–probe delay is dominated by the  $S_2$  state through its ESA and possibly direct stimulated emission. The TMCPPO relaxes to the  $S_1$  state with a time constant of 0.25 ps, a quite reasonable time for an IC mediated by a conical intersection. Subsequently the molecule relaxes to the triplet manifold within 4 ps. This is quite fast and the underlying mechanisms are presently under study (compare the scheme in Fig. 9(b)).

To determine the  $S_1$  and triplet yield, we evaluate kinetic traces at probe wavelengths that allow for a straightforward interpretation. A full analysis shows that a kinetic scheme purely based on population transfer cannot describe the observed dynamics. A more complex model incorporating solvation and vibrational relaxation has to be considered. At 400 nm we can see predominantly the  $S_2$

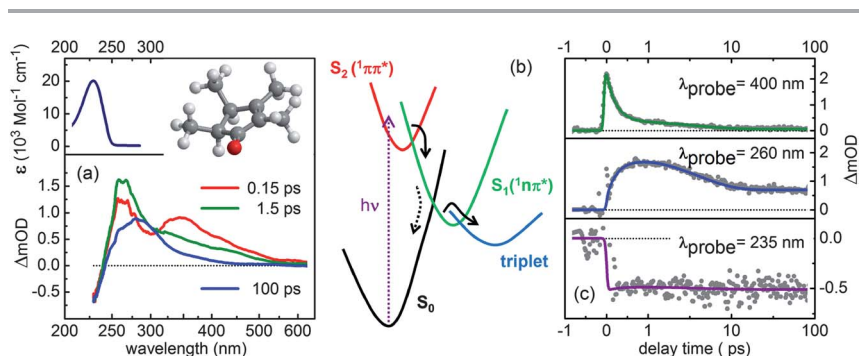


**Fig. 9** (a) Selected transient spectra after 227 nm excitation of TMCPPO in cyclohexane. The spectra were recorded in three parts and stitched afterwards. (b) Reaction scheme after  $S_2$  excitation. (c) Selected kinetic traces monitoring mainly the  $S_2$  population (400 nm), the  $S_1$  population (260 nm) and the GSB (235 nm).

state relaxation with a 0.25 ps exponential decay. At 260 nm the signal reports the  $S_1$  build-up and decay with 0.25 and 4 ps. Finally, at 235 nm the lack of any GSB recovery can be directly seen. Within the present experimental uncertainty given by signal fluctuations and the coherent contributions from the solvent and cell windows, we see no recovery of the GSB. This means that the whole  $S_2$  population initially generated by optical excitation transfers to the triplet. We can compare this to the previously reported triplet yield of the parent molecule cyclopentenone of also near unity.<sup>59</sup> While an ultrafast intersystem crossing (ISC) proceeding with such a high yield is not unreasonable when the vibrationless  $S_1$  state is excited, the finding of a unity yield after  $S_2$  excitation is surprising. The vibrational excess energy released in the  $S_2 \rightarrow S_1$  relaxation would easily suffice for IC to the electronic ground state as reported for acrolein.<sup>58</sup> High level quantum chemical calculations do indeed show a low lying conical intersection between the  $S_1$  and the  $S_0$  state. The fact that this process is highly inefficient while the ISC is highly efficient indicates that kinetic factors determine the dynamics and the branching ratio. That the triplet is accessed with near unity yield can be deduced from the transient spectra without any necessary assumptions as the GSB acts as an easily interpretable internal standard. The measurement is also corroborated by further recordings of TMCPO and 3-methyl-2-cyclopentenone in acetonitrile that also show near unity triplet quantum yield after  $S_2$  excitation.

## 8 Summary and conclusions

The four molecules investigated in this work all display complex multi-stage relaxation after optical excitation. This has in the past lead to investigations with partially contradicting interpretations and conclusions. The extremely broadband probe investigations now possible with about 50 fs temporal resolution render a detailed picture that allows an interpretation with unprecedented unambiguity. For each example a new twist in the story of the relaxation results that had been overlooked. In malachite green it appears that the importance of the phenyl twisting has been overemphasized and rather a charge transfer state should be considered. In TINUVIN-P the predicted twisting as the driving motion for the ultrafast IC is confirmed and leads to a resolution of the earlier puzzle that the sub-5 ps regime shows kinetics deviating from a pure cooling process. For the bond cleavage of  $\text{Ph}_2\text{CH-Cl}$  and  $\text{Ph}_2\text{CH-Br}$  the degree of electron transfer within the radical pair can now be determined quantitatively. The earlier single-wavelengths measurements with ps resolution lead to strongly contradicting conclusions. For the first time coherent wavepacket motion in the photoproducts is reported. Last but not least the measurement of the GSB recovery in the deep UV allows for the surprising result, that even after  $S_2$  excitation of cyclopentenones the triplet states are reached with near unity probability within a few picoseconds.

All these investigations were purely based on UV/vis/NIR transient spectroscopy. As similar problems have been tackled in the past with transient IR spectroscopy, we would like to ask ourselves how the two methods with state-of-the-art setups<sup>4,10 12,60 62</sup> compare. For the comparison a figure of merit is helpful. A sensible figure of merit seems to be the ratio of the broadest spectral probe range available to the smallest width found in the spectrum. In the IR vibrational transitions in solution are about  $15 \text{ cm}^{-1}$  wide and the whole spectrum covers about  $3000 \text{ cm}^{-1}$ . This gives a factor of 200. The spectral width in the electronic

spectrum is at least as wide as the homogeneous broadening determined by the pure electronic dephasing on the time scale of tens of fs. This converts to a linewidth of  $200\text{ cm}^{-1}$ . Our experimental setup can cover close to  $40\,000\text{ cm}^{-1}$  probe range and again a factor of 200 results. This means that transient electronic spectroscopy has finally caught up with transient IR spectroscopy with respect to detection width.

In both kinds of spectroscopies one has to identify the relevant spectral regions where the intermediates can be most unambiguously identified and tracked. The continua used in our setup (compare Fig. 1(b)) cover huge ranges and together with the highly resolving UV/vis/NIR detector arrays a first overview can be gained from a single time scan measurement requiring one or two hours. The temporal resolution is typically 50 to 100 fs, somewhat superior to the IR. Most importantly we find that the extension to the NIR allows for a qualitative new feature. We can always probe to the red of the GSB and SE region where only ESA or product bands can be located. Identifying the “last transition” in the NIR then allows to obtain the kinetics of the single species. This is nicely seen in the MG transient peak at 1400 nm assigned to the  $S_2 \leftarrow S_1$  transition. Once the kinetics of this species are deduced from the measurement, the full associated spectral components can be extracted and used to decompose the set of transient spectra. In a second step the next to last transition is tackled and so on leading to a complete picture of photoinduced dynamics, however complex it might be.

The quantitative determination of transition strengths is readily possible by comparison with the intrinsic standard of the GSB of known strength. This is then often helpful to determine the electronic character of the intermediate species by comparison to quantum chemical calculations. What our setup also provides is sufficient spectral reproducibility and resolution to allow the observation of shifts as small as 0.1 nm or  $10\text{ cm}^{-1}$ . These can be identified with solvation, ion or radical pairing,<sup>46</sup> and cooling. The temporal evolution of the shifts gives extra information on the dynamics.

It is also interesting to compare the ultra-broadband TA spectroscopy with fs-fluorescence spectroscopy (fs-FS) as it can be measured with up-conversion<sup>63,64</sup> or Kerr gating.<sup>65</sup> The reason that much effort is put into developing techniques of fs-FS is that the fluorescence is a very clean signature of the electronically excited molecule. There is no superposition in the signal by ESA or GSB as typically seen in TA spectroscopy with a limited detection range. As demonstrated in the examples of this work, ultra-broadband TA spectroscopy can fulfil the same condition by choosing the right spectral range, typically to the red of the GSB and stimulated emission. The well separated ESA transitions seen in this low energy part of the spectrum are also clean reporters of excited state dynamics. The great advantage is that the transient ESA signal can be measured with sub-50 fs temporal resolution, only reached by extremely well optimized fs-FS experiments.<sup>64</sup> Contrary to fs-FS, where an improvement in temporal resolution leads to a largely decreased signal strength and long averaging times, the TA spectroscopy can be performed quite quickly. We therefore expect that particularly transient NIR detection will be able to rival fs-Fs without the need for a dedicated setup.

Last but not least we want to address the detection and identification of vibronic coherences. In many one-colour pump-probe measurements much debate is needed to find out whether the observed modulations in the TA signal are due to vibrational wavepackets in the electronic ground state or to vibronic



wavepackets in an excited state. The first are a nice confirmation of our understanding of ultrafast experiments and the underlying molecular level structure, but they do not reveal much information beyond that already known from Raman spectroscopy and resonance Raman spectroscopy. Only the latter render real new information on the structure of the excited molecule and the course of reactions. We were able to report earlier that in ESIPT those modes contribute to the wavepacket signature that are intimately connected with the proton transfer by shortening of the donor–acceptor distance.<sup>66</sup> Now we even find that in the bond cleavage discussed in Sec. 6 the photoproducts display long lasting vibrational coherences. This can only be understood if the whole cleavage process proceeds coherently. It gives great hope that coherent control, *e.g.*, by double pulses or shaped pulses, can be used to control the branching ratio between homolysis and heterolysis and the yield of individual products. Also incoherent control by time delayed pulses of largely differing wavelengths might be feasible as the electron transfer, the recombination and the diffusional separation are understood in detail.

The newly available experimental capabilities should be able to revitalize the use of electronic spectroscopy for the elucidation and quantitative analysis of complex molecular and chemical processes. Unlike the typical use of UV/vis spectroscopy for stable species or just processes in the ms range, our strategy comes with 50 fs temporal resolution. As a consequence, even the shortest lived intermediates can be looked for. Unlike the earlier fs experiments the ultra-broadband detection allows the full range of spectroscopic knowledge to be utilized. We therefore think that the best is still to come for electronic spectroscopy and we look forward to a bright, visible future.

## Acknowledgements

We thank P. Lang and Oliver Schalk for experimental help, and R. de Vivie-Riedle, S. Thallmair and T. Tahara for stimulating discussions. Financial support of this work by the Deutsche Forschungsgemeinschaft through the SFB 749, the GRK 1626, and the excellence cluster ‘Munich Center for Advanced Photonics’ (MAP) is gratefully acknowledged.

## References

- 1 A. H. Zewail, *Angew. Chem., Int. Ed.*, 2000, **39**, 2586.
- 2 P. Hamm, S. Wiemann, M. Zurek and W. Zinth, *Opt. Lett.*, 1994, **19**, 1642.
- 3 M. Bradler, P. Baum and E. Riedle, *Appl. Phys. B: Lasers Opt.*, 2009, **97**, 561.
- 4 U. Megerle, I. Pugliesi, C. Schrieber, C. F. Sailer and E. Riedle, *Appl. Phys. B: Lasers Opt.*, 2009, **96**, 215.
- 5 M. Bradler, C. Homann and E. Riedle, *Opt. Lett.*, 2011, **36**, 4212.
- 6 C. Homann, P. Lang and E. Riedle, *J. Opt. Soc. Am. B*, 2012, **29**, 2765.
- 7 P. J. M. Johnson, V. I. Prokhorenko and R. J. D. Miller, *Opt. Express*, 2009, **17**, 21488.
- 8 I. Buchvarov, A. Trifonov and T. Fiebig, *Opt. Lett.*, 2007, **32**, 1539.
- 9 R. Huber, T. Köhler, M. O. Lenz, E. Bamberg, R. Kalmbach, M. Engelhard and J. Wachtveitl, *Biochemistry*, 2005, **44**, 1800.
- 10 A. N. Tarnovsky, W. Gawelda, M. Johnson, C. Bressler and M. Chergui, *J. Phys. Chem. B*, 2006, **110**, 26497.
- 11 T. A. Zeidan, Q. Wang, T. Fiebig and F. D. Lewis, *J. Am. Chem. Soc.*, 2007, **129**, 9848.
- 12 A. L. Dobryakov, S. A. Kovalenko, A. Weigel, J. L. Pérez Lustres, J. Lange, A. Müller and N. P. Ernstring, *Rev. Sci. Instrum.*, 2010, **81**, 113106.
- 13 E. P. Ippen, C. V. Shank and A. Bergman, *Chem. Phys. Lett.*, 1976, **38**, 611.
- 14 Y. Nagasawa, Y. Ando and T. Okada, *Chem. Phys. Lett.*, 1999, **312**, 161.



- 15 Y. Nagasawa, Y. Ando, D. Kataoka, H. Matsuda, H. Miyasaka and T. Okada, *J. Phys. Chem. A*, 2002, **106**, 2024.
- 16 D. Ben Amotz and C. B. Harris, *J. Chem. Phys.*, 1987, **86**, 4856.
- 17 M. D. Hirsch and H. Mahr, *Chem. Phys. Lett.*, 1979, **60**, 299.
- 18 A. Mokhtari, L. Fini and J. Chesnoy, *J. Chem. Phys.*, 1987, **87**, 3429; A. Mokhtari, A. Chebira and J. Chesnoy, *J. Opt. Soc. Am. B*, 1990, **8**, 1551.
- 19 F. Pellegrino, A. Dagen and R. R. Alfano, *Chem. Phys.*, 1982, **67**, 1982.
- 20 P. Sen, S. Yamaguchi and T. Tahara, *Faraday Discuss.*, 2010, **145**, 411.
- 21 N. H. Gottfried, B. Roither and P. O. J. Scherer, *Opt. Commun.*, 1997, **143**, 261.
- 22 M. J. Rosker, F. W. Wise and C. L. Tang, *Phys. Rev. Lett.*, 1986, **57**, 321.
- 23 K. A. Nelson and L. R. Williams, *Phys. Rev. Lett.*, 1987, **58**, 745.
- 24 A. Nakayama and T. Taketsugu, *J. Phys. Chem. A*, 2011, **115**, 8808.
- 25 M. M. Martin, E. Breheret, F. Nesa and Y. H. Meyer, *Chem. Phys.*, 1989, **130**, 279.
- 26 Z. R. Grabowski, K. Rotkiewicz and W. Rettig, *Chem. Rev.*, 2003, **103**, 3899.
- 27 U. Schmidhammer, U. Megerle, S. Lochbrunner, E. Riedle and J. Karpiuk, *J. Phys. Chem. A*, 2008, **112**, 8487.
- 28 S. R. Flom and P. F. Barbara, *Chem. Phys. Lett.*, 1983, **94**, 488.
- 29 M. Wiechmann, H. Port, W. Frey, F. Lärmer and T. Elsaesser, *J. Phys. Chem.*, 1991, **95**, 1918.
- 30 C. Chudoba, S. Lutgen, T. Jentzsch, E. Riedle, M. Woerner and T. Elsaesser, *Chem. Phys. Lett.*, 1995, **240**, 35.
- 31 C. Chudoba, E. Riedle, M. Pfeiffer and T. Elsaesser, *Chem. Phys. Lett.*, 1996, **263**, 622.
- 32 A. L. Sobolewski, W. Domcke and C. Hättig, *J. Phys. Chem. A*, 2006, **110**, 6301.
- 33 W. Frey and T. Elsaesser, *Chem. Phys. Lett.*, 1992, **189**, 565.
- 34 K. Lenz, M. Pfeiffer, A. Lau and T. Elsaesser, *Chem. Phys. Lett.*, 1994, **229**, 340.
- 35 V. Kozich and W. Werncke, *J. Mol. Struct.*, 2005, **735**, 145.
- 36 V. Kozich, J. Dreyer and W. Werncke, *Chem. Phys. Lett.*, 2004, **399**, 484.
- 37 M. Barbatti, A. J. A. Aquino, H. Lischka, C. Schrieber, S. Lochbrunner and E. Riedle, *Phys. Chem. Chem. Phys.*, 2009, **11**, 664.
- 38 O. F. Mohammed, S. Lubner, V. S. Batista and E. T. J. Nibbering, *J. Phys. Chem. A*, 2011, **115**, 7550.
- 39 P. F. Barbara, L. E. Brus and P. M. Rentzepis, *J. Am. Chem. Soc.*, 1980, **102**, 5631.
- 40 S. Lochbrunner, W. Fuss, W. E. Schmid and K. L. Kompa, *J. Phys. Chem. A*, 1998, **102**, 9334.
- 41 K. S. Peters, *Chem. Rev.*, 2007, **107**, 859.
- 42 M. Lipson, A. A. Deniz and K. S. Peters, *Chem. Phys. Lett.*, 1998, **288**, 781.
- 43 C. F. Sailer, N. Krebs, B. P. Fingerhut, R. de Vivie Riedle, E. Riedle, *Phys. Rev. Lett.*, submitted for publication.
- 44 B. P. Fingerhut, C. F. Sailer, J. Ammer, E. Riedle and R. de Vivie Riedle, *J. Phys. Chem. A*, 2012, **116**, 11064.
- 45 C. F. Sailer, R. B. Singh, J. Ammer, E. Riedle and I. Pugliesi, *Chem. Phys. Lett.*, 2011, **512**, 60.
- 46 C. F. Sailer, B. P. Fingerhut, S. Thallmair, C. Nolte, J. Ammer, H. Mayr, I. Pugliesi, R. de Vivie Riedle and E. Riedle, *ChemPhysChem*, 2013 (in print).
- 47 J. Dreyer and K. S. Peters, *J. Phys. Chem.*, 1996, **100**, 15156.
- 48 J. Dreyer, M. Lipson and K. S. Peters, *J. Phys. Chem.*, 1996, **100**, 15162.
- 49 B. P. Fingerhut, D. Geppert and R. de Vivie Riedle, *Chem. Phys.*, 2008, **343**, 329.
- 50 U. Megerle, R. Lechner, B. König and E. Riedle, *Photochem. Photobiol. Sci.*, 2010, **9**, 1400.
- 51 M. Wenninger and E. Riedle, in *Chemical Photocatalysis*, ed. B. König, DeGruyter, Berlin, 2013.
- 52 M. R. Detty and P. B. Merkel, *J. Am. Chem. Soc.*, 1990, **112**, 3845.
- 53 M. Guéron, J. Eisinger and R. G. Shulman, *Mol. Phys.*, 2006, **14**, 116.
- 54 D. Peceli, S. Webster, D. A. Fishman, C. M. Cirloganu, H. Hu, O. V. Przhonska, V. V. Kurdyukov, Y. L. Slominsky, A. I. Tolmachev, A. D. Kachkovski, R. R. Dasari, S. Barlow, S. R. Marder, D. J. Hagan and E. W. Van Stryland, *J. Phys. Chem. A*, 2012, **116**, 4833.
- 55 H. E. Lessing, A. von Jena and M. Reichert, *Chem. Phys. Lett.*, 1976, **42**, 218.
- 56 S. M. King, C. Rothe, D. Dai and A. P. Monkman, *J. Chem. Phys.*, 2006, **124**, 234903.
- 57 B. Lament, J. Karpiuk and J. Waluk, *Photochem. Photobiol. Sci.*, 2003, **2**, 267.
- 58 A. M. D. Lee, J. D. Coe, S. Ullrich, M. L. Ho, S. J. Lee, B. M. Cheng, M. Z. Zgierski, I. C. Chen, T. J. Martinez and A. Stolow, *J. Phys. Chem. A*, 2007, **111**, 11948.
- 59 R. Bonneau, *J. Am. Chem. Soc.*, 1980, **102**, 3816.
- 60 E. T. J. Nibbering and T. Elsaesser, *Chem. Rev.*, 2004, **104**, 1887.
- 61 E. T. J. Nibbering, H. Fidler and E. Pines, *Annu. Rev. Phys. Chem.*, 2005, **56**, 337.

Faraday Discussions

- 62 M. L. Groot, L. J. G. W. van Wilderen and M. Di Donato, *Photochem. Photobiol. Sci.*, 2007, **6**, 501.
- 63 X. X. Zhang, C. Würth, L. Zhao, U. Resch Genger, N. P. Ernsting and M. Sajadi, *Rev. Sci. Instrum.*, 2011, **82**, 063108.
- 64 C. H. Kim and T. Joo, *Opt. Express*, 2008, **16**, 20742.
- 65 B. Schmidt, S. Laimgruber, W. Zinth and P. Gilch, *Appl. Phys. B: Lasers Opt.*, 2003, **76**, 809.
- 66 S. Lochbrunner, A. J. Wurzer and E. Riedle, *J. Phys. Chem. A*, 2003, **107**, 10580.